Realization and Spectroscopy of the Quantum Spin Hall Insulator Bismuthene on Silicon Carbide

Dissertation zur Erlangung des
naturwissenschaftlichen Doktorgrades der
Julius-Maximilians-Universität Würzburg

vorgelegt von

Felix Reis

aus Aschaffenburg

Würzburg, 2021

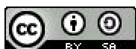

This document is licensed under the Creative Commons Attribution-ShareAlike 4.0 International License (CC BY-SA 4.0):
http://creativecommons.org/licenses/by-sa/4.0 This CC license does not apply to third party material (attributed to another source) in this publication.

Eingereicht am 18.03.2021

bei der Fakultät für Physik und Astronomie

1. Gutachter: Prof. Dr. Jörg Schäfer

2. Gutachter: Prof. Dr. Matthias Bode

3. Gutachter:

der Dissertation

Vorsitzender: Prof. Dr. Jens Pflaum

1. Prüfer: Prof. Dr. Jörg Schäfer

2. Prüfer: Prof. Dr. Matthias Bode

3. Prüfer: Prof. Dr. Ronny Thomale

im Promotionskolloquium

Tag des Promotionskolloquiums: 11.02.2022

Doktorurkunde ausgehändigt:

Abstract

Topological matter is one of the most vibrant research fields of contemporary solid state physics since the theoretical prediction of the quantum spin Hall effect in graphene in 2005. Quantum spin Hall insulators possess a vanishing bulk conductivity but symmetry-protected, helical edge states that give rise to dissipationless charge transport. The experimental verification of this exotic state of matter in 2007 lead to a boost of research activity in this field, inspired by possible ground-breaking future applications. However, the use of the quantum spin Hall materials available to date is limited to cryogenic temperatures owing to their comparably small bulk band gaps.

In this thesis, we follow a novel approach to realize a quantum spin Hall material with a large energy gap and epitaxially grow bismuthene, i.e., Bi atoms adopting a honeycomb lattice, in a $(\sqrt{3} \times \sqrt{3})$ reconstruction on the semiconductor SiC(0001). In this way, we profit both from the honeycomb symmetry as well as the large spin-orbit coupling of Bi, which, in combination, give rise to a topologically non-trivial band gap on the order of one electronvolt. An in-depth theoretical analysis demonstrates that the covalent bond between the Si and Bi atoms is not only stabilizing the Bi film but is pivotal to attain the quantum spin Hall phase.

The preparation of high-quality, unreconstructed SiC(0001) substrates sets the basis for the formation of bismuthene and requires an extensive procedure in ultra-pure dry H_2 gas. Scanning tunneling microscopy measurements unveil the (1×1) surface periodicity and smooth terrace planes, which are suitable for the growth of single Bi layers by means of molecular beam epitaxy. The chemical configuration of the resulting Bi film and its oxidation upon exposure to ambient atmosphere are inspected with X-ray photoelectron spectroscopy.

Angle-resolved photoelectron spectroscopy reveals the excellent agreement of probed and calculated band structure. In particular, it evidences a characteristic Rashba-splitting of the valence bands at the K point. Scanning tunneling spectroscopy probes signatures of this splitting, as well, and allows to determine the full band gap with a magnitude of $E_{\text{gap}} \approx 0.8\,\text{eV}$. Constant-current images and local-density-of-state maps confirm the presence of a planar honeycomb lattice, which forms several domains due to different, yet equivalent, nucleation sites of the $(\sqrt{3} \times \sqrt{3})$-Bi reconstruction.

Differential conductivity measurements demonstrate that bismuthene edge states evolve at atomic steps of the SiC substrate. The probed, metallic local density of states is in agreement with the density of states expected from the edge state's energy dispersion found in density functional theory calculations – besides a pronounced dip at the Fermi level. By means of temperature- and energy-dependent tunneling spectroscopy it is shown that the spectral properties of this suppressed density of states are successfully captured in the framework of the Tomonaga-Luttinger liquid theory and most likely originate from enhanced electronic correlations in the edge channel.

Zusammenfassung

Topologische Materie ist seit der Vorhersage des Quanten-Spin-Hall-Effekts in Graphen im Jahr 2005 eines der spannendsten Forschungsgebiete der gegenwärtigen Festkörperphysik. Quanten-Spin-Hall-Isolatoren besitzen zwar eine verschwindende Volumen-Leitfähigkeit, aber symmetriegeschützte, helikale Randzustände, welche verlustfreien Ladungstransport erlauben. Der 2007 erfolgte experimentelle Nachweis dieses außergewöhnlichen Materiezustands führte, inspiriert von möglicherweise bahnbrechenden zukünftigen Anwendungen, zu einem sprunghaften Anstieg der Forschungsaktivitäten auf diesem Gebiet. Jedoch ist der Nutzen der derzeit verfügbaren Quanten-Spin-Hall-Materialien aufgrund ihrer vergleichsweise kleinen Volumen-Bandlücken auf kryogene Temperaturen beschränkt.

In dieser Arbeit verfolgen wir einen neuen Weg, ein Quanten-Spin-Hall-Material mit einer großen Energielücke zu realisieren und wachsen Bismuten, ein Honigwabengitter aus Bi-Atomen, epitaktisch in einer $(\sqrt{3} \times \sqrt{3})$-Rekonstruktion auf den Halbleiter SiC(0001). Dadurch nutzen wir sowohl die Honigwaben-Symmetrie, als auch die große Spin-Bahn-Wechselwirkung von Bi aus, welche in Kombination zu einer topologisch nicht-trivialen Bandlücke in der Größenordnung eines Elektronenvolts führen. Eine eingehende theoretische Analyse zeigt, dass die kovalente Bindung zwischen den Si- und Bi-Atomen nicht nur den Bi-Film stabilisiert, sondern entscheidend zur Ausprägung der Quanten-Spin-Hall-Phase beiträgt.

Die Präparation unrekonstruierter SiC(0001)-Substrate hoher Güte ist der Grundstein für das Bismutenwachstum und erfordert die Anwendung einer aufwändigen Prozedur in hochreinem, trockenem H_2-Gas. Messungen mit Rastertunnelmikroskopie enthüllen die (1×1)-Periodizität der Oberfläche und glatte Terrassenebenen, welche für das Aufwachsen einzelner Bi-Lagen mittels eines dedizierten Molekularstrahlepitaxieprozesses geeignet sind. Die chemische Konfiguration der Filme und ihre Oxidation nach Kontakt mit Umgebungsluft wird mit Röntgenphotoelektronenspektroskopie untersucht.

Winkelaufgelöste Photoelektronenspektroskopie legt die exzellente Übereinstimmung zwischen gemessener und berechneter Bandstruktur offen. Insbesondere zeigt sie die charakteristische Rashba-Spinaufspaltung der Valenzbänder am K-Punkt. Messungen mit Rastertunnelspektroskopie beinhalten ebenso Hinweise dieser Aufspaltung, und ermöglichen die Bestimmung der vollständigen Größe der Bandlücke von $E_{\mathrm{gap}} \approx 0.8\,\mathrm{eV}$. Konstantstrom-Aufnahmen und Karten der lokalen Zustandsdichte bestätigen die Ausbildung eines planaren Honigwabengitters, welches aufgrund unterschiedlicher, jedoch äquivalenter Nukleationszentren der $(\sqrt{3} \times \sqrt{3})$-Bi-Rekonstruktion in mehreren Domänen auftritt.

Messungen der differenziellen Leitfähigkeit offenbaren, dass sich Bismuten-Randzustände an atomaren Stufen des SiC-Substrats ausbilden. Die gemessene, lokale Zustandsdichte und die gemäß der Energiedispersion des Randzustands in Dichtefunktionaltheorierechnungen erwartete Zustandsdichte stimmen – abgesehen von einem starken Abfall am Fermi-Niveau – überein. Mit temperatur- und energieabhängiger Tunnelspektroskopie wird gezeigt, dass die spektralen Eigenschaften dieser unterdrückten Leitfähigkeit erfolgreich im Rahmen der Tomonaga-Luttinger-Flüssigkeitstheorie beschrieben und wahrscheinlich durch verstärkte elektronische Korrelationen im Randkanal ausgelöst werden.

Contents

1 Motivation **1**

2 Methods for Surface Preparation & Analysis **5**

2.1 Dry Hydrogen Annealing . . . 5
2.2 Molecular Beam Epitaxy . . . 8
2.3 Scanning Tunneling Microscopy & Spectroscopy . . . 9
2.3.1 Scanning Tunneling Microscopy . . . 10
2.3.1.1 Working Principle . . . 10
2.3.1.2 Theoretical Description of the Tunneling Process . . . 12
2.3.2 Scanning Tunneling Spectroscopy . . . 14
2.3.2.1 Lock-In Amplifier Technique . . . 15
2.3.2.2 Measurement Modes . . . 16
2.4 Spatially-Averaging Techniques . . . 17
2.4.1 Low-Energy Electron Diffraction . . . 17
2.4.2 Photoelectron Spectroscopy . . . 18
2.4.2.1 Working Principle . . . 19
2.4.2.2 Angle-Resolved Photoelectron Spectroscopy . . . 21
2.4.2.3 X-Ray Photoelectron Spectroscopy . . . 23
2.5 Density Functional Theory . . . 24

3 Theoretical Concepts for 2D Topological Insulators **27**

3.1 Topological Insulators . . . 27
3.1.1 Topological Band Theory . . . 28
3.1.2 Chern Insulators . . . 29
3.1.3 Quantum Spin Hall Insulators . . . 32
3.1.4 Realizations of Quantum Spin Hall Insulators . . . 35
3.2 Interacting Electrons in 1D: Tomonaga-Luttinger Liquid Theory . . . 38

4 Theory of Group V-Monolayer-Substrate 2D Topological Insulators **43**

4.1 Bi(111) Crystal and Electronic Structure . . . 43
4.2 Freestanding Bi(111) Bilayer and Monolayer . . . 45
4.3 Planar Bismuthene on a SiC Substrate . . . 47
4.4 Spin-Orbit Coupling in Bismuthene on SiC . . . 51
4.5 Low-Energy Effective Modeling . . . 55
4.6 Nanoribbon Calculations: Edge States in Bismuthene on SiC . . . 58

5 Preparation of High-Quality SiC Substrates for Monolayer Epitaxy **61**

5.1 Structural and Electronic Properties of 4H-SiC . . . 61

5.2 Planar SiC(0001) Samples Prepared in Static Hydrogen Atmosphere 67
5.2.1 Influence of the Annealing Temperature 67
5.2.2 Influence of the H_2 Gas Purity 68
5.2.3 Layer-By-Layer Etching and Sublattice Orientation of 4H-SiC 70
5.3 Planar SiC(0001) Samples Prepared in Flowing Hydrogen Atmosphere . . . 72
5.3.1 Variation of the Gas Flow and Annealing Temperature 72
5.3.2 Detailed Investigation of the SiC(0001) Surface: Step Morphology, Atomic Resolution and Spectroscopy 75
5.4 SiC(0001) Samples Used for Bismuthene Growth 80

6 Epitaxial Growth and Structure of Bismuthene on SiC 83
6.1 Growth Process Guiding 83
6.1.1 Evaporation Procedure 83
6.1.2 LEED Characterization and Cycling of Bismuthene Growth 85
6.2 Film Growth Process 88
6.3 Domain Size and Coverage 92
6.4 Film Composition and Stability 94
6.4.1 XPS of Bismuthene on SiC 94
6.4.2 Stability of Bismuthene Films 98

7 2D Bulk Properties of Bismuthene on SiC 101
7.1 Morphological Overview 101
7.2 Ideal Honeycomb Lattice 103
7.2.1 Structural Properties 103
7.2.2 Electronic Properties 107
7.3 Surface Defects 111
7.3.1 Domain Boundaries 111
7.3.2 Point Defects 116
7.3.3 Antidots and Disordered Areas 119
7.4 Band Structure of Bismuthene 121
7.4.1 Low-Energy Band Structure 121
7.4.2 Valence Band Maximum at K 123
7.4.3 Detailed Comparison of ARPES and DFT Band Dispersion 126

8 1D Edge States of Bismuthene: Topological Protection vs. Correlations 131
8.1 Edge States Inspected with STM, STS and ARPES 131
8.1.1 Edge States at Extended Defective Areas of the Film 131
8.1.2 Armchair Edge States at SiC Substrate Steps 135
8.1.3 Search for the Edge States in ARPES 143
8.2 Helical Tomonaga-Luttinger Liquid in the Armchair Edge States 146
8.2.1 Characterization of the Zero-Bias Spectra 146
8.2.2 Temperature-Dependent Measurements 150
8.2.3 Discussion of Alternative Zero-Bias Anomaly Mechanisms 154

9 Conclusion 159

Appendix A Experimental Setups and Preparation Procedures **164**
A.1 Ex-situ SiC Preparation 164
A.2 Dry Hydrogen Annealing Setups and Process Guiding 165
A.3 STM Setup 168
A.4 ARPES and XPS Setup 169
A.5 Vacuum Suitcase 169

Appendix B Additional Information on 4H-SiC Substrates **170**
B.1 SiC Preparation and H Annealing Parameters in Literature 170
B.2 Polymorphism of SiC 170

Appendix C Additional Information on H Annealing of SiC Samples **172**
C.1 Miscut-SiC(0001) Substrates 172
C.2 Tested H Annealing Parameters in Flowing Gas Atmosphere 176
C.3 Etch Pits on Samples Prepared in 2 slm H_2 and 4 slm He Gas Flow 176
C.4 Surface Adsorbates and (Sub-)Surface Defects 177

Appendix D Additional Information on the Epitaxial Growth and Structure of Bismuthene on SiC **180**
D.1 Bismuthene Coverage and Domain Size on Different Samples 180
D.2 Details on XPS of Bismuthene 181
D.2.1 Fit Parameters at Varying Measurement Angle 181
D.2.2 Peak Ratios of Bi and Si at Different Sample Positions 183
D.2.3 Fit Parameters Before and After Air Exposure 184
D.3 Growth and STM on Miscut-SiC Substrates 185

Appendix E Additional Information on 2D Bulk Bismuthene **187**
E.1 STM and STS at High and Low Bias Voltage 187
E.2 LDOS Maps of the Bulk Lattice in STS and DFT 187
E.3 STS Band Gap Fits and Variation of the Stabilization Parameters 190
E.4 Ionization Discs around Disordered Areas 192
E.5 Energy Offset of Bands in ARPES ($h\nu = 47\,\mathrm{eV}$) and DFT 194

Appendix F Additional Information on the Edge States of Bismuthene **195**
F.1 Additional CCI and LDOS Maps of an Armchair Edge 195
F.2 Python Procedure Used for Analysis of the ZBA 196
F.3 Parameters of the ZBA Grid Spectroscopy Measurements 200
F.4 Influence of the Power-Law Exponent and Broadening Effects 201
F.5 Dynamical Coulomb Blockade Theory 202

Bibliography **204**

List of Publications **227**

Danksagung **228**

List of Figures

1.1 Insulators with Different Topological Character. 2

2.1 Gas Phase Chemistry During H Annealing. 6
2.2 Properties of SiC Samples Before and After H annealing. 7
2.3 Surface Reaction Kinetics and Growth Modes in MBE. 9
2.4 Tunneling Process and Imaging at Constant Current. 11
2.5 Energy Level Diagram During Tunneling Process. 14
2.6 STS with Lock-in Amplifiers. 15
2.7 Inelastic Mean Free Path of Electrons in Solids. 17
2.8 LEED setup and Ewald's Construction. 19
2.9 (Angle-Resolved) Photoemission. 22

3.1 Trivial and Twisted Bloch Bundles. 29
3.2 Haldane Model. 31
3.3 Tight-Binding Band Structure for Graphene. 34
3.4 Quantum Spin Hall Effect in HgTe/CdTe Quantum Wells. 35
3.5 Quantum Spin Hall Effect in WTe_2. 36
3.6 Mono-Elemental 2D Materials. 37
3.7 Tunneling Process in 2D and 1D Systems. 38
3.8 Scattering Processes in Linear Approximation. 41

4.1 Lattice and Electronic Structure of Bi(111). 44
4.2 Theoretical and Experimental Fermi Surface and Band Dispersion of Bi(111). 44
4.3 Freestanding Buckled Bi Bilayer and Planar Bi Monolayer. 46
4.4 Total Energy of Buckled and Planar Bi Films and Lattice Structure on a SiC Substrate. 48
4.5 Band Structure and DOS for Bismuthene on a SiC with Different DFT Functionals and 2D Brillouin Zone. 50
4.6 Lattice and Band Structure for One- and Two-Sided Bismuthane. 52
4.7 Orbital Projection of the Low-Energy Bands for Bismuthene on SiC. 52
4.8 $\mathbb{Z}_2$ Invariant, SOC Processes and Band Gap Magnitude as Function of SOC in Bismuthene on SiC and Related Compounds. 54
4.9 Low-Energy Model for Bismuthene on SiC. 57
4.10 Armchair and Zigzag Edge States in Bismuthene on SiC. 59

5.1 Crystal Structure of 4H-SiC. 62
5.2 Edge Terminations of 4H-SiC. 63
5.3 Step Terminations and Surface Morphology. 64
5.4 Ab-initio Band Structure Calculations and ARPES of 4H-SiC(0001) With and Without Dangling Bonds. 65
5.5 Charge Carrier Density and Fermi Level Position as Function of the Impurity Concentration in 4H-SiC. 66

5.6 LEED and STM of SiC(0001) after Annealing at Different Temperatures in Static H_2 Atmosphere. . . . 67
5.7 Influence of H_2 Gas Purity on the Probed Surface Structure. . . . 69
5.8 Morphology of SiC(0001) Samples after Static H_2 Annealing. . . . 71
5.9 STM and LEED on SiC(0001) Samples Prepared with Various Annealing Parameters. . . . 73
5.10 Surface Morphology of SiC(0001) Samples Prepared with Flowing H_2 Gas. . 76
5.11 Close-Up STM Image of SiC(0001) Surfaces. . . . 77
5.12 STS on 4H-SiC(0001) in Vicinity of a Step Edge. . . . 79
5.13 Pyrometer-Controlled Temperature During H_2 Annealing of SiC Samples. . 81
5.14 Overview STM Images of SiC(0001) Samples Prepared with Flowing H_2 and He Gas. . . . 82

6.1 Temperature Curve During Bi Deposition. . . . 84
6.2 Flow Chart for Evaluation of Grown Bismuthene Samples by LEED. . . . 86
6.3 Bi-Induced vs. Si-Induced $(\sqrt{3} \times \sqrt{3})$ Reconstruction. . . . 87
6.4 Influence of the Substrate's Temperature Gradient on Bismuthene Growth. 88
6.5 Film Coverage after Different Bismuthene Growth Cycles. . . . 91
6.6 Different Bismuthene Samples with Varying Coverage and Domain Size. . . 92
6.7 XPS Overview and Angle-Dependent Measurements of Bismuthene on SiC. 95
6.8 Stability of Bismuthene in Air. . . . 99

7.1 Large-Scale STM Image of Bismuthene Samples. . . . 101
7.2 Surface Morphology at Large and Small Bias Voltages. . . . 102
7.3 CCI and LDOS Maps in Occupied and Unoccupied States of Bismuthene. . 104
7.4 Structure of Bismuthene on SiC(0001). . . . 105
7.5 Atomic Resolution STM of Two Terrace Planes with Inequivalent C Sublattice Orientation. . . . 107
7.6 STS on 2D Bulk Bismuthene. . . . 108
7.7 Rashba Splitting Measured by STS and Predicted by DFT. . . . 110
7.8 Lattice Model Visualizing the Appearance of Domain Boundaries. . . . 112
7.9 High-Resolution STM of a Domain Boundary. . . . 113
7.10 Domain Boundary Type Analysis and Different Scenarios. . . . 114
7.11 Grid Spectroscopy of a Domain Boundary. . . . 115
7.12 Point Defect CCIs and LDOS maps in Occupied and Unoccupied States. . . 117
7.13 Lattice Sites and Electronic Properties of Point Defects. . . . 118
7.14 CCI, $\mathrm{d}I/\mathrm{d}V$ and Point Spectroscopy on Antidots and Disordered Areas. . . 120
7.15 ARPES Band Structure of Bismuthene. . . . 121
7.16 Comparison of ARPES and DFT Band Structure for Monolayer and Bilayer Bismuthene. . . . 122
7.17 ARPES CECs at Two Neighboring K Points. . . . 124
7.18 Linewidth Around K at Room and Low Temperature. . . . 125
7.19 Overlay of ARPES and DFT Band Structure. . . . 127
7.20 Binding Energy of Bands at High Symmetry Points. . . . 129

8.1 STM Scans of an Edge in Zigzag Geometry. 132
8.2 STS Measurements a ZZ-Like Boundary between Bismuthene and a Disordered Area. 134
8.3 Ball-and-Stick Model and 3D CCI in Vicinity of an AC Edge. 136
8.4 STS Measurements at a Step Edge of Bismuthene on SiC. 137
8.5 Differential Conductivity as Function of the Distance from the Edge. 138
8.6 Edge State Differential Conductivity Measured at the Upper and Lower Edge of a Step. 139
8.7 Grid Spectroscopy LDOS Maps and DFT Edge Simulations. 140
8.8 CCI and LDOS Mapping in the Occupied and Unoccupied States as well as the Bulk Band Gap. 142
8.9 High-Resolution ARPES Bandmap of Bismuthene on a Stepped SiC Substrate. 145
8.10 High-Resolution STS Across a SiC Step Edge. 147
8.11 ZBA Measurements as Function of the Stabilization Current. 148
8.12 High-Resolution STS at a Kinky Step Edge Section. 149
8.13 Temperature-Dependent ZBA Measurements and Power Law Exponent Alpha. 151
8.14 Zero-Bias Conductance as Function of the Temperature. 152
8.15 Universal Scaling of the ZBA. 153
8.16 Comparison of STS Curves and Disorder-Induced ZBA Modeling. 155
8.17 Schematic Diagram of the DCB. 156
8.18 Scaling of the ZBA Induced by the DCB. 157

A.1 Omicron Direct Current Sample Holder. 165
A.2 Setup for H_2 Annealing in Static Gas Atmosphere. 166
A.3 Setup for H_2 Annealing in Ultra-Pure Flowing Gas Atmosphere. 168

B.1 Polymorphism of SiC. 171

C.1 LEED of SiC Substrates with 2° and 4° miscut along $\langle 1\bar{1}00 \rangle$. 172
C.2 Comparison of SiC with 2° Miscut and Planar SiC(0001) in LEED. 173
C.3 STM Overview Image and 2D FFT of SiC Samples with 2° and 4° Miscut. 175
C.4 Etch Pits Observed on a SiC(0001) Sample Prepared in Flowing H_2 Gas. . . 177
C.5 Adsorption and Binding Sites of Defects on the SiC Surface and Their Spectroscopic Properties. 179

D.1 Analysis of Bismuthene Coverage and Domain Size on Different Samples. . 180
D.2 Angle-Dependent XPS Measurements - Fitting Parameters. 181
D.3 Angle-dependent XPS Data on H-Passivated SiC. 182
D.4 Bi-to-Si Peak Intensity at Different Lateral Positions of the SiC Wafer. . . . 183
D.5 Position-Dependent XPS Peak Ratios. 184
D.6 Coverage of Bismuthene on Miscut-SiC Substrates after Various Growth Attempts. 185
D.7 SiC Substrates with 4° Miscut after Bi Deposition. 186

D.8 Large-Scale STM Overview of Bismuthene on 4° SiC. 186

E.1 Bismuthene CCI and LDOS map at High and Low Bias Voltage. 187
E.2 CCI and LDOS Maps Recorded at Varying Bias Voltage. 188
E.3 DFT Simulations of the Bismuthene Surface at Constant Height and on an Isocharge Surface. 189
E.4 Fit Parameters for Band Gap Measurements on 2D Bulk Bismuthene. . . . 190
E.5 STS on 2D Bulk Bismuthene with Varying Setpoints. 191
E.6 LDOS Maps of Ionization Rings Around Defects. 193
E.7 Ionizationdisc and Ionizationring. 193
E.8 Bandedge Energy Difference at High Symmetry Points at $h\nu = 47\,\mathrm{eV}$. . . . 194

F.1 All CCI and LDOS Scans Recorded at a Perfectly Ordered Armchair Edge. 195
F.2 Influence of Thermal and Instrumental Broadening on TLL Modeling and Zero-Bias Conductance. 201

List of Tables

5.1 Electronic and Thermal Properties of Selected Semiconductor-Materials. . . 61

6.1 Inelastic Mean Free Path and Escape Depth of Bi, Si and C Core Levels. . . 95
6.2 Electronegativity of Selected Elements. 97

7.1 Energy Offset of Bands at High Symmetry Points at $h\nu = 80\,\mathrm{eV}$. 130
7.2 Energy Offset of Low-Energy Bands at High Symmetry Points at $h\nu = 80\,\mathrm{eV}$. 130
7.3 Energy Offset of Bands at High Symmetry Points in DFT HSE Band Structure Calculations. 130

A.1 Technical Specifications of the Commercially-Bought 4H-SiC Wafers. 164

C.1 Overview of Tested H Annealing Parameters. 176

E.1 Energy Offset of Bands at High Symmetry Points at $h\nu = 47\,\mathrm{eV}$. 194
E.2 Energy Offset of Low-Energy Bands at High Symmetry Points at $h\nu = 47\,\mathrm{eV}$. 194

F.1 ZBA Grid Spectroscopy Parameters. 200

List of Abbreviations

1D One dimension / one-dimensional

2D Two dimensions / two-dimensional

2° Miscut-SiC 4H-SiC(0001) samples with 2° miscut towards $\langle 1\bar{1}00 \rangle$

3D Three dimensions / three-dimensional

4° Miscut-SiC 4H-SiC(0001) samples with 4° miscut towards $\langle 1\bar{1}00 \rangle$

AC Armchair

ARPES Angle-resolved photoelectron spectroscopy

BZ Brillouin zone

CB Conduction band

CBM Conduction band minimum

CCI Constant current image

CEC Constant energy contour

DB Dangling bond

DCB Dynamical Coulomb blockade

DFT Density-functional theory

DOS Density of states

EBZ Effective Brillouin zone

EDC Energy distribution curve

GGA Generalized gradient approximation

H annealing Annealing in ultra-pure H_2 gas at atmospheric pressure

HSE Heyd-Scuseria-Ernzerhof

LDA Local density approximation

LDOS Local density of states

LEED Low-energy electron diffraction

MBE Molecular beam epitaxy

MDC Momentum distribution curve

NN Nearest neighbor

NNN Next-nearest neighbor

PBE Perdew-Burke-Ernzerhof

PES Photoelectron spectroscopy

QHE Quantum Hall effect

QSHE Quantum spin Hall effect

QSHI Quantum spin Hall insulator

RT Room temperature ($T \approx 295\,\mathrm{K}$)

STM Scanning tunneling microscopy

STS Scanning tunneling spectroscopy

TB Tight-binding

TI Topological insulator

TIBB Tip-induced band bending

TLL Tomonaga-Luttinger liquid

TR Time-reversal

TRIM Time-reversal invariant momenta

UHV Ultra-high vacuum

VB Valence band

VBM Valence band maximum

XPS X-ray photoelectron spectroscopy

ZZ Zigzag

1 Motivation

A major research area in contemporary solid state physics is devoted to the fabrication, characterization and optimization of heterostructures. These synthetic material systems are created by interfacing compounds with different electronic and structural properties. Certain heterostructures comprising semiconductors constitute particularly impressive examples for the intriguing physical phenomena that may evolve by suitable material combinations: transistors enabled the production of handy computation machines and thereby paved the way for the digital revolution, with far-reaching consequences for the way we work and live.

By 2020, this digital transformation extends to the interconnection of (industrial) objects via the so-called ”internet of things“ [1], implying the need to continue the development of devices with higher computational capacity and energy efficiency [2]. This is not limited to the optimization and re-design of existing technologies but comprises the synthesis of novel artificial materials that entail exotic physical phenomena and promise applicability in logic circuitry [3]. In this context, the discovery of graphene in 2004 [4] has been of outstanding importance for two reasons.

Firstly, graphene constitutes the first ever realized purely two-dimensional (2D) material, a state of matter that for a long time was believed to be unstable: thermodynamic fluctuations had been considered so large that they would lift the binding forces in 2D layers. It is most peculiar that overcoming this dogma has been accomplished with means that can be found in every household, namely graphite and adhesive tape [4]. This unexpected finding and the extraordinary physical properties of graphene, in particular the linear energy dispersion relation of occupied and unoccupied states in combination with a vanishing energy gap, triggered a vast research interest and the desire to realize similar materials for electronic applications. Meanwhile, a plethora of related elemental 2D materials including silicene, germanene, stanene, borophene, and many others have been realized, however involving much more complicated procedures [5–7]. All of them promise future applications in the fields of electronics, optoelectronics and energy conversion owing to the extraordinary physical properties of 2D crystals [5, 8].

Secondly, the discovery of graphene and its subsequent theoretical description by C. Kane and E. J. Mele as quantum spin Hall or $\mathbb{Z}_2$ topological insulator (TI) [11, 12] spotlighted the classification of matter in terms of topological invariants which had been pioneered after the discovery of the quantum Hall effect (QHE). The QHE appears in a 2D electron gas that is placed in a magnetic field $\vec{B}$, and is associated with a non-zero conductivity despite the presence of a bulk electronic band gap due to c_1 chiral edge states, where c_1 is the Chern number or TKNN invariant (see Fig. 1.1**a**) [13, 14]. F. D. M. Haldane tied in on this classification and, in a gedankenexperiment, created the Chern insulator, i.e., an insulator that exhibits chiral edge states due to a peculiar magnetic flux pattern and

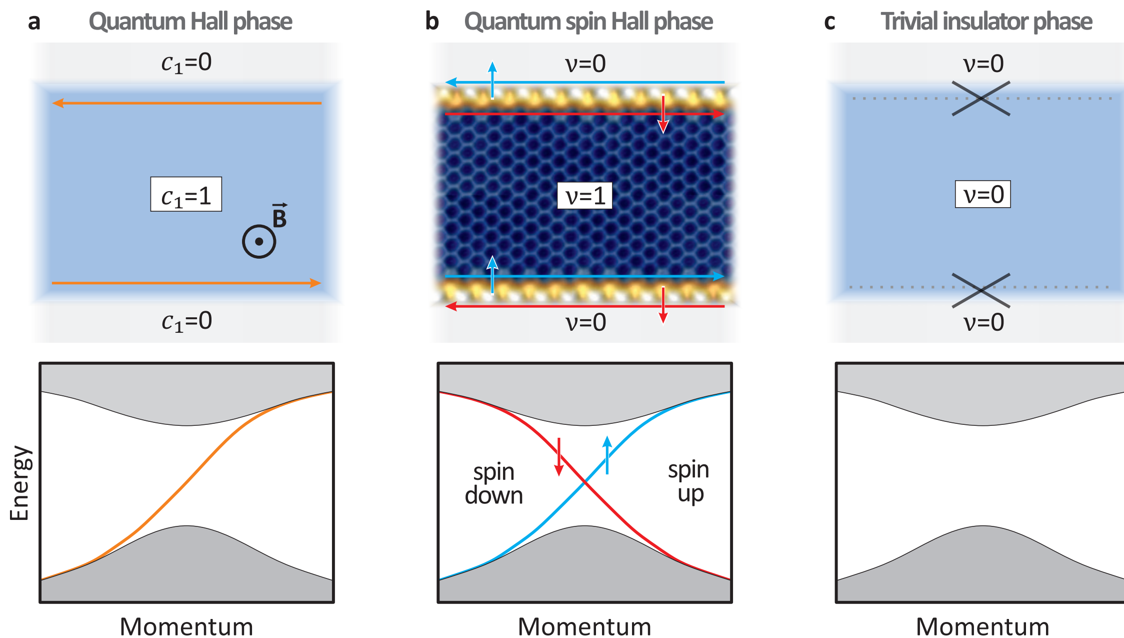

Figure 1.1 Comparison of phases with distinct topology. **a** The quantum Hall phase characterized by the Chern number $c_1 = 1$ evolves in a finite magnetic field $\vec{B}$ and is accompanied by chiral edge states at the boundary with a system with $c_1 = 0$. **b** Quantum spin Hall insulators with a topological invariant $\nu = 1$ exhibit helical edge states at the interface with an ordinary insulator ($\nu = 0$). **c** No helical edge states emerge between two insulators with $\nu = 0$. *Adapted from Ref. [9] under a Creative Commons 4.0 License (CC BY 4.0 [10]).*

sublattice potential in a honeycomb lattice [13, 14]. Eventually, Kane and Mele recognized that the requirements of this model are naturally realized in graphene in the presence of $U(1)_{\text{charge}}$ as well as time-reversal (TR) symmetry [14] and due to spin-orbit coupling (SOC), a relativistic effect that couples spin and orbital angular momentum of the electrons [11]. This leads to the quantum spin Hall effect (QSHE), compare to Fig. 1.1**b** [11]. Note that B. A. Bernevig and S.-C. Zhang likewise described the QSHE almost at the same time [15]. Shortly after, the quantized conductance resulting from the QSHE has been experimentally probed in the group of L. W. Molenkamp in HgTe/CdTe quantum wells following a proposal by B. A. Bernevig, T. L. Hughes and S.-C. Zhang, and the rise of topological materials began [16, 17].

What distinguishes $\mathbb{Z}_2$ TIs from conventional insulators? Again, a topological invariant ν is used to distinguish the two phases. TI systems with $\nu = 1$ exhibit an insulating bulk but gapless boundary states when having an interface with a material that belongs to a different, trivial topological class ($\nu = 0$) [14], see Fig. 1.1**b**. In contrast, no such edge state emerges when the topological invariant does not change at the interface (Fig. 1.1**c**). Remarkably, the electron's spin and momentum are locked in TI edge states, which are therefore helical. This property could eventually be utilized in revolutionary technological applications [11–13].

However, there is still a long route to go. Despite considerable efforts, a potential TI material promising real-world applications remains elusive for the following reasons. Firstly, insufficient bulk energy gaps render the spin-polarization of the helical edge electrons unusable due to the dominant contribution of trivial bulk electrons to the conductivity [18, 19]. Secondly, many candidate materials lack a substrate that does not alter the film properties

in a detrimental way [5, 19]. Thirdly, the preparation of certain monolayer crystals (such as WTe_2 [20]) in highest quality relies on exfoliation techniques, which is a non-scalable process [21].

Departing from the hitherto-established synthesis routes for QSHI systems, we try to resolve these issues via epitaxial growth of heterostructure consisting of a high-Z honeycomb layer on a suitable substrate. In particular, here, the substrate's impact on the structural and electronic properties is considered from the very beginning instead of focusing on the optimization of only the honeycomb layer.

Specifically, our system consists of bismuthene, i.e., a 2D Bi honeycomb lattice, and the wide-gap semiconductor silicon carbide (SiC). There are multiple benefits related to this system. On the one hand, bismuthene exploits both the honeycomb lattice symmetry and the large intrinsic SOC of Bi, which are prerequisites for obtaining a QSHI with an enhanced bulk band gap. On the other hand, the covalent bond between the Bi atoms and the SiC substrate does not only structurally stabilize the Bi film in a planar geometry but is decisive for the manifestation of a non-trivial TI phase. In this sense, the topologically non-trivial properties of the material system are emergent and result from the interplay of bismuthene and the SiC substrate, which constitutes a new paradigm to realize $\mathbb{Z}_2$ TI systems.

Scope of this thesis. This thesis aims at a complete description of the main characteristics of bismuthene on SiC, and covers the preparation as well as the analysis of the electronic and structural properties of both the SiC substrate and 2D Bi film.

Starting with Chapter 2, the methods used to fabricate and inspect the material system are described. Chapter 3 comprehensively introduces the theoretical framework and milestone experimental achievements of 2D TIs as well as the Tomonaga-Luttinger liquid (TLL) theory, which describes the characteristics of electrons in one dimension (1D). In Chapter 4, the topological properties of freestanding and substrate-supported Bi monolayers will be elaborated. Thereby, the relevance of the SiC substrate for the manifestation of a non-trivial topological phase will become clear. Chapter 5 deals with the properties and quality of the SiC surfaces prepared by a dedicated dry hydrogen annealing (H annealing) procedure. In Chapter 6, the Bi film growth and coverage as well as their chemical composition and inertness are evaluated. Chapter 7 provides a detailed discussion of the structural and electronic characteristics of 2D bulk bismuthene by means of scanning tunneling microscopy (STM and STS) and angle-resolved photoelectron spectroscopy (ARPES). The obtained results are compared to density-functional theory (DFT) calculations. In Chapter 8, the 1D edge states of bismuthene are scrutinized. The major part of this chapter is devoted to the edge states in armchair (AC) geometry ultimately focusing on their low-energy spectral properties, which are discussed in the context of the TLL theory.

2 Methods for Surface Preparation & Analysis

The fabrication and inspection of novel quantum materials requires the application of suitable experimental methods. This chapter summarizes the relevant physical processes and technical aspects required to understand the preparation and measurement methods as well as the calculations presented in Ch. 4–8.

This chapter starts with a description of the surface preparation procedures. In its first section, the preparation of unreconstructed, clean SiC substrate surfaces by annealing in an ultra-pure dry H_2 atmosphere, shortly named ”H annealing“ in the following, is introduced. The consecutive growth of Bi films on SiC is accomplished by molecular beam epitaxy (MBE), which is described in the following section.

The second part of this chapter is devoted to the methods used to analyze the structure as well as electronic and chemical configuration of bismuthene on SiC. All of them are based on purely quantum-mechanical processes and their significance is reflected in that the respective discoverers have been awarded with the Nobel Prize [22–26].

The experimental methods can be sorted into microscopic techniques, namely scanning tunneling microscopy (STM) and spectroscopy (STS), and spatially averaging techniques, which are low-energy electron diffraction (LEED) as well as photoelectron spectroscopy (PES) in angle-resolved mode (ARPES) and using X-rays (XPS).

The last section provides a short introduction to the basic principles of density-functional theory (DFT). The results obtained by DFT are crucially important for the identification of bismuthene on SiC as a topological insulator (TI) system and for understanding the observed physical phenomena.

2.1 Dry Hydrogen Annealing

The SiC substrates are prepared by an extensive combined ex-situ wet-chemical and in-situ dry-H_2 process. Before the H annealing is started, the commercial SiC wafer pieces undergo a pre-preparation phase consisting of degreasing and roughening in order to improve the electrical contact to the sample holder, which is discussed in App. A.1. The technical data of the wafers and the sample holder design are shown there, as well.

Necessity of dry H annealing. The growth of films with one monolayer thickness requires substrate surfaces with ultimate quality and as low as possible number of defects. Furthermore, Si dangling bonds (DBs), i.e., an unsatisfied valence with one missing electrons, present on a (1×1) surface, are employed to stabilize bismuthene in a flat geometry. This is in conflict with its tendency to form surface reconstructions that lower the surface free energy, just as observed on other semiconductor surfaces [27, 28]. The situation in SiC is further complicated by its outstanding chemical inertness and mechanical hardness [27, 29]. Conventional preparation procedures such as sputtering and annealing or wet-

chemical methods fail in case of SiC as they produce either Si-rich, C-rich, reconstructed or oxide-covered surfaces (see Refs. [29–35]). Only H annealing, also known as H etching, in H_2 gas at atmospheric pressure and temperatures higher than 1000°C has proven to provide the desired unreconstructed SiC surfaces [30, 31]. After the annealing process, the surface Si DB is passivated by H, which effects that the surface remains unreconstructed, atomically flat and remarkably stable against oxidation [31].

Etching process. In order to remove Si and C atoms from the surface, molecular H_2 must be dissociated into highly reactive atomic H. This process requires to overcome an activation energy as the standard enthalpy of H formation is positive ($\Delta_f H^0_{gas}(H) = +218.00\,kJ/mol$) [36]. In our case, this energy is provided by the hot substrate surface. The atomic H radicals preferably attach at sites with unsatisfied valence, such that crystal features with high number of DBs (e.g., substrate step edges or small SiC clusters on terraces) are etched faster, as visualized in Fig. 2.1. Eventually, the reaction products, namely silane (SiH_4) and methane (CH_4) molecules (see Fig. 2.1), are carried away by the gas flow. This leads to the generation of large and atomically smooth terraces, unless silane and methane dissociate in vicinity of the surface again. Silane is expected to be the more unstable molecule as its formation is energetically not favorable ($\Delta_f H^0_{gas}(SiH_4) = +34.31\,kJ/mol$), whereas the formation of methane is exothermic ($\Delta_f H^0_{gas}(CH_4) = -74.87\,kJ/mol$) [36, 37].

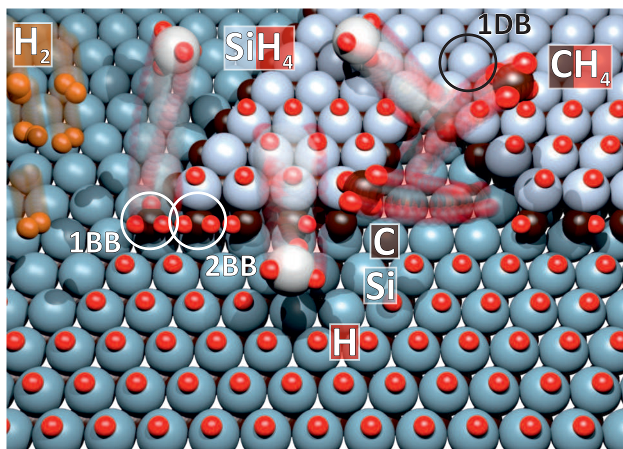

Figure 2.1 Visualization of the gas phase processes during H annealing. H radicals, which are created by dissociation of molecular H_2 at the hot sample surface, attach preferably at surface and step edge atoms due to their DBs (black circle). Eventually, when all backbonds (BBs, white circles) are lifted, silane (SiH_4) and methane (CH_4) molecules are formed. Remaining DBs on the Si surface or at step edges are H saturated, maintain a (1×1) reconstruction and are passivated against oxidation. *Adapted with permission from Ref. [37]. Copyright ©2016 American Chemical Society.*

H-passivated SiC surfaces. The influence of H annealing is summarized in Fig. 2.2. The as-received surfaces are full of irregular scratches with several nanometer depth and up to 200 nm width due to the mechanical polishing of the wafers, see Fig. 2.2**a**. Additionally, growth-related defects like pits and micropipes are observed. These defects are removed, and a regular stepped surface structure as shown in Fig. 2.2**b** is created by H annealing. The terraces are atomically smooth, several hundred nanometer wide and separated by mostly unit-cell high steps [38–42].

The long range order on the sample surface can be effectively inspected with LEED measurements, which are shown in Fig. 2.2**c** and **d** for a sample prepared with an HF dip and with subsequent H annealing, respectively. Both surfaces show a (1×1) LEED pattern, indicating a saturation of the DBs on both surfaces. However, the wet-chemically prepared samples exhibit an enhanced incoherent background compared to the H-annealed

surfaces and, more detrimental, studies carried out with LEED and XPS reveal a hydroxyl-terminated SiC surface (indicated by the Si^{+} peak in Fig. 2.2**e**) as well as additional contaminants like F [30, 31, 43].

Moreover, Fig. 2.2**e** demonstrates another remarkable feature of H-annealed SiC surfaces: the H saturation of DBs effectuates a passivation of the surface. XPS measurements carried out after exposure of a H-etched sample to ambient atmosphere for two days show that the Si2p core level peak remains completely unchanged. Although the presence of a certain amount of O is seen in survey scans (see, e.g., Ref. [31]), its O contamination is much smaller than, e.g., after a HF dip. Importantly, the monohydride electronically passivates the surface, as well, i.e., the surface Fermi level position corresponds to its bulk position and is not pinned to mid gap by impurity states [31, 44].

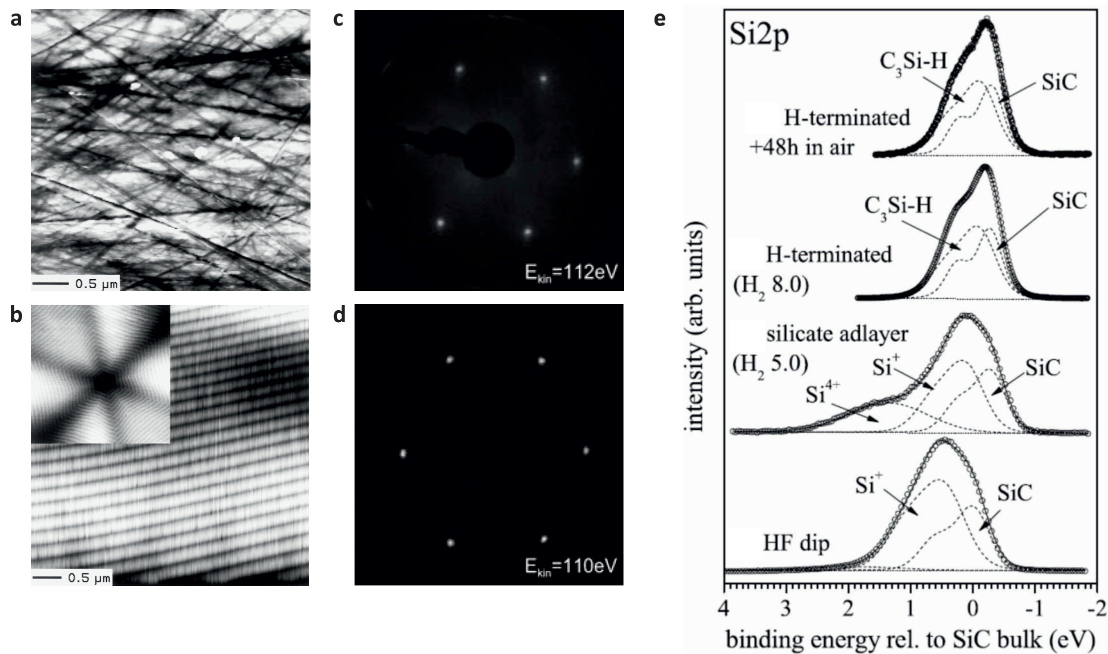

Figure 2.2 **a** and **b** Comparison of a 6H-SiC(0001) wafer surface as-received and after H annealing at 1600 °C. The atomic force microscopy images reveal that polishing scratches visible before H annealing (grayscale of the image is 7.5 nm) are effectively removed, resulting in a regular step pattern. The inset image ($20\,\mu m \times 20\,\mu m$) shows that steps evolve from a screw dislocation. **c** and **d** LEED images recorded after 6H-SiC(0001) surface preparation with an HF dip and by H annealing, respectively. Both surfaces exhibit a (1×1) structure but the spots on the H annealed surface are much sharper and the incoherent background is strongly reduced. **e** Surface-sensitive Si2p core level spectra recorded after preparation with various procedures. HF-dipped samples possess OH groups which cause a chemical shift (0.5 eV) of the Si peak position (Si^{+}) compared to SiC bulk spectra. H annealing with low-purity grade 5.0 gas causes the formation of a silicate adlayer with oxidation states Si^{+} and Si^{4+}, which are not observed when utilizing high-purity gas of grade 8.0. The absence of noticeable spectral changes after exposure to air for two days reflects that the SiC-H samples are passivated against oxidation. *Reprinted with permission from: Figs.* ***a/b*** *Ref. [41]. Copyright ©1998 TMS-The Minerals, Metals and Materials Society. Figs.* ***c/d*** *Ref. [31]. Copyright ©2004 IOP Publishing. Fig.* ***e*** *Ref. [45]. Copyright ©2006 Springer-Verlag.*

It is worth noting that it is indispensable to supply ultra-pure H_2 gas for the etching process [27, 31, 32, 41]. Using conventional H_2 gas with grade 5.0 or 6.0 results in the formation of a silicate adlayer reconstruction of the surface, see Fig. 2.2**e** [27, 46].

In our case, H annealing has been carried out using two different setups with a largely different process guiding, which are discussed in App. A.2. For an overview of the process

parameters reported in literature please consider App. B.1. The explored preparation parameters and the respective outcome of the annealing process as well as the physical properties of the prepared SiC surfaces are discussed in Ch. 5.

2.2 Molecular Beam Epitaxy

MBE is particularly well-suited to fabricate very thin films of high quality due to a rather low growth rate and its operation in ultra-high vacuum (UHV). It enables the epitaxial growth of a broad range of elements and/or molecules on proper substrates at low defect concentrations and with the possibility to abruptly vary the growth process, therewith permitting, e.g., to generate doping concentrations in semiconductors or layered heterostructures [47]. A comprehensive introduction to MBE is given in the book of M. Henini (Ref. [48]).

The basic methodology is very simple: a crucible is filled with a high-purity element or molecule, and is heated up, thereby generating a beam of atoms/molecules that is directed towards a crystalline surface [48], see Fig. 2.3**a** (I). The resulting flux depends on the crucible temperature and the material's vapor pressure. The interaction between the impinging species and substrate gives rise to chemisorption or physisorption. In the former case, a (strong) chemical bond between adsorbed element/molecule and substrate evolves, while in the latter case much weaker van der Waals forces act between the adatom and the substrate in the latter. Note that physisorption might be a preliminary stage of chemisorption [49].

Typical kinetic processes during MBE are sketched in Fig. 2.3**a**. The surface is kept at a suitable temperature T, providing enough thermal energy to allow the arriving atoms/molecules to migrate across the surface [Fig. 2.3**a** (II)] [48]. Some atoms will desorb without being attached, see Fig. 2.3**a** (III), whereas other traveling atoms minimize their energy by formation of bonds, e.g., via attaching to exposed step edges [Fig. 2.3**a**] (IV) and increasing grown terraces [Fig. 2.3**a** (V)]. Alternatively, the traveling atom sticks to clusters [Fig. 2.3**a** (VI)] [48, 50].

Based on the interaction strength and depending on the substrate lattice spacing as well as symmetry, the adsorbed species form crystalline layers. The resulting growth mode in heteroepitaxy crucially depends on the number of deposited layers and the lattice mismatch, which should be smaller than $\approx 10\%$ [48, 51]. Vanishing mismatch leads to a layer-by-layer Frank-van der Merwe (FM), see Fig. 2.3**b**, and small strain can be released via dislocations. In case of a larger lattice mismatch, a different growth mechanism occurs, namely the Stranski-Krastanov growth, which can be sorted into two different variants. In the first mode, the growth of a wetting layer and small, stable islands initiates simultaneously, whereas in the second mode, the formation of additional islands is suppressed until a complete wetting layer covers the surface (SK_1 and SK_2 in Fig. 2.3**b**, respectively). A wetting layer forms when the binding energy Φ_{AB} of adsorbed atom A and substrate B is larger than the binding energy between adsorbed atoms Φ_{AA} (wetting condition). Volmer-Weber-type (VW), where no wetting layer forms, is observed if the mismatch is too large or if $\Phi_{AA} > \Phi_{AB}$. Starting from a certain number of layers, the formation of large, ripening islands ($R_{1,2,3}$) is energetically favorable at any lattice mismatch [51]. In

the following experiments, the MBE parameters are adjusted such that a monolayer of Bi atoms remains on the SiC substrate and three-dimensional (3D) growth is absent.

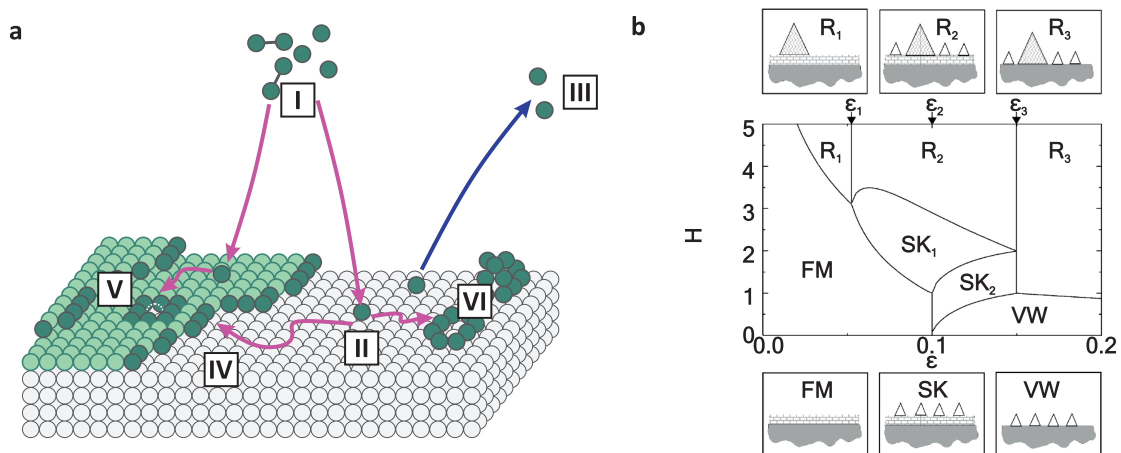

Figure 2.3 **a** Surface reaction kinetics during MBE. (I) Impinging molecular or atomic beam. (II) Migration of atoms upon arrival on the heated substrate. (III) Adsorbed atoms partially desorb from the surface. (IV) The diffusing atom attaches preferably to step edges or vacancies and (V) increases grown atomic layers. (VI) Alternatively, clustering of adsorbed atoms might occur. **b** Growth modes as function of lattice mismatch ϵ and number of grown layers H. Frank-van der Merwe growth (FM) occurs in layer-by-layer fashion (brick structure) on the substrate (gray underlay). In case of Volmer-Weber (VM) growth, the mismatch is too large and adsorbed atoms directly cluster in islands (structureless triangles). A wetting layer and small islands are observed in both Stranski-Krastanov (SK_1 and SK_2) modes. Eventually, at any lattice mismatch, ripening islands ($R_{1,2,3}$) evolve (triangles with wavy lines). *Fig. **b** Reprinted with permission from Ref. [51]. Copyright ©1997 American Physical Society.*

A typical MBE chamber is equipped with effusion cells, beam shutters, substrate heaters, in-situ characterization tools, mass spectrometers, beam flux monitors and cooled chambers walls to cause the condensation of unused beam fluxes [47, 48]. As in our special application MBE is not used to create layered heterostructures but only for the deposition of very thin layers, the latter three tools are not present. The bismuthene sample growth with MBE is described in Ch. 6.

2.3 Scanning Tunneling Microscopy & Spectroscopy

STM and STS offer the fascinating possibility to inspect conducting samples at the atomic scale and are among the most popular methods for surface analysis in the world. They are indispensable tools for the structural and electronic characterization of surfaces.

STM images display a convolution of structural and electronic properties of the surface, as will become apparent in the basic theoretical description of the method. Afterwards, we demonstrate that $\mathrm{d}I/\mathrm{d}V$ curves recorded with STS are representative of the sample's local density of states (LDOS) in first-order approximation. Naturally, the space for the description of STM/STS is limited in this thesis. For an in-depth discussion please consider the excellent books of R. Wiesendanger [52] and C. J. Chen [53].

2.3.1 Scanning Tunneling Microscopy

STM has been invented by G. Binnig and H. Rohrer in 1981. Originally interested in performing spectroscopy with a spatial resolution better than 100 Å they ended up with a novel type of microscope [22].

2.3.1.1 Working Principle

This section starts with the description of the working principle of STM, followed by a theoretical derivation of an expression for the tunneling current.

Tunneling effect. STM is based on quantum-mechanical tunneling between a tip and a sample, which are separated by a barrier of few angstrom in UHV. Its basic principle can be understood by considering a (1D) rectangular potential barrier of height Δ, see Fig. 2.4**a**. A particle with energy $E_0 < \Delta$ and mass m is described by the wave function Ψ and encounters the barrier at $z = 0$ from the left side. The solution of the stationary 1D Schrödinger equation [53]:

$$\left[-\frac{\hbar^2}{2m}\frac{d^2}{dz^2} + \Delta(z)\right]\Psi(z) = E\Psi(z) \tag{2.1}$$

reveals that the resulting wave function is exponentially damped, compare to Fig. 2.4**a**:

$$\Psi(z) = \Psi_0\, e^{-\kappa z} \quad \text{with} \quad \kappa = \frac{\sqrt{2m(\Delta - E_0)}}{\hbar}. \tag{2.2}$$

Here, Ψ_0 is the wave function at $z = 0$, see Fig. 2.4**a**, and κ is the decay constant. The probability density P of finding the particle within the barrier at position z is proportional to $|\Psi|^2$,

$$P \propto |\Psi_0|^2\, e^{-2\kappa z}. \tag{2.3}$$

Hence, the wave function penetrates into the barrier with finite probability. Of course the same considerations hold for a particle moving from right to left, as the depicted scenario is fully symmetric [53].

An STM setup with a metallic tip and sample separated by a vacuum barrier constitutes a similar scenario, see Fig. 2.4**b**. However, here, the application of a finite bias voltage lifts the symmetry of the system and a net transmission in one direction exists, which is detected as a tunneling current. This is the basic working principle of STM [53]. The transmission coefficient is highly sensitive on the barrier width d, i.e., the spacing between tip and sample. Typical values for the work function of tip and sample (≈ 4–5 eV) yield an amplitude decay of roughly a factor 10 per Å, which explains the extraordinary sensitivity and resolution of STM [22, 53, 54].

Data acquisition with STM. Fig. 2.4**b** visualizes the image acquisition in STM. The tunneling current depends exponentially on the tip-to-sample distance. Therefore, a metallic tip is approached towards the surface with a coarse piezo stack until a defined tunneling current I_T is detected at the applied tunneling bias V_T. Obviously, this requires

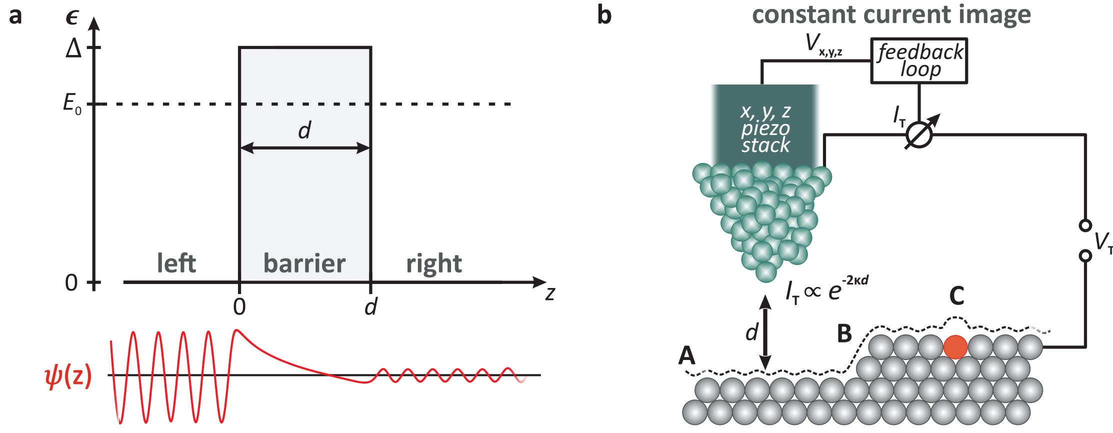

Figure 2.4 Working principle of STM. **a** Tunneling of a particle with energy E_0 through a rectangular potential barrier with height $\Delta > E_0$. The wave function Ψ (red curve, bottom) is exponentially damped but exhibits a finite amplitude within/after transmission through the barrier. **b** STM in CCI mode. A tip in tunneling contact is scanned across the surface while a feedback loop varies the elongation of the tip piezo such that the tunneling current I_T is kept constant. Note that the coarse piezo stack, which is used for the macroscopic approach of the tip, is not illustrated. I_T depends on the applied bias voltage, the tunneling matrix element, and exponentially on the distance to the surface, which enables a sub-ångström resolution and the examination of, e.g, the atomic corrugation (**A**), terrace steps (**B**), or impurities (**C**).

a conducting tip and sample. Note that the tunneling voltage V_T is applied to the tip, whereas the sample is grounded in our setup. Tunneling tips are usually made of W and electro-chemically etched. Further treatment occurs in UHV with electron bombardement, allowing to remove the insulating WO layer present on the tip after its preparation [55].
Conventionally, measurements are conducted in constant current imaging (CCI) mode, see Fig. 2.4**b**. Here, a feedback loop ensures that the tunneling current I_T is kept constant while the tip is scanned across the surface, which is achieved by elongation/retraction of the tip piezo. In this way, the tip probes a surface of constant LDOS if the tip's DOS and the tunneling matrix element do not change. The measurement electronics record the voltage $V_{x,y,z} \propto x,\, y,\, z$ applied to the piezos, which allows to visualize a surface contour with constant, integrated LDOS in the range from the Fermi level to eV_T [52].
The enormous advantage of CCI is that tip crashing is actively suppressed. Fig. 2.4 shows different situations that might be encountered by the tip. A sufficiently sharp tip might image the atomic corrugation of the surface (**A** in Fig. 2.4**b**). At terrace steps (**B** in Fig. 2.4**b**), the tip will be retracted/elongated in order to keep I_T constant. The presence of an impurity with a different electronic structure, even though it might be embedded in a "plane“ terrace, may cause a change of the tunneling probability and lead to the retraction (or elongation) of the tip, as well (**C** in Fig. 2.4**b**).
Alternatively, it is possible to image the sample surface in constant height mode. Here, as the name suggests, the feedback loop is deactivated and the variation of I_T is measured as the tip is scanned at constant height across the surface. Obviously, this mode bears an increased risk for crashes, such that all STM/STS measurements shown in Chs. 5–8 have been recorded exclusively with CCI.
Note that the tip's resolving power arises from a specific atom arrangement/configuration at its apex, and can be optimized only by non-controllable procedures, which are: (i) the

intentional intrusion of the tip into a (noble metal) crystal by few nanometers, such that it might pick up some of the crystal atoms; (ii) the application of voltage pulses up to 10 V between tip and sample, which cause a strip-off of the topmost atoms due to the strong electric field gradient at the apex [56]. This seemingly simple, yet violent methods have been established already by Binnig and Rohrer in their first experiments and are still used today [22, 53]. They are functional as the tunneling current is dominated by the contribution of the atom closest to the surface, meaning that a "minitip" attached to an arbitrarily shaped tip apex as sketched in Fig. 2.4**b** might be sufficient to provide atomic resolution [53].

We continue by a more formal theoretical description of the tunneling process in the next section.

2.3.1.2 Theoretical Description of the Tunneling Process

In the 1960s, metal-insulator-metal tunneling has attracted considerable research interest, in particular as a consequence of the rise of superconductivity [57]. In this context, J. Bardeen developed the idea to decouple the metal-insulator-metal system into two subsystems, which facilitates the calculation of the tunnel current and thereby enables a better interpretation of the observed phenomena. J. Tersoff and D. R. Hamann employed this approach and developed the first quantitative theory for STM [53, 57, 58].

In first order perturbation theory, the tunneling current I_T in their model reads [58]:

$$I_\mathrm{T} = \frac{2\pi e}{\hbar} \sum_{\mu,\nu} f(E_\mu)\left[1 - f(E_\nu + eV_\mathrm{T})\right] |M_{\mu\nu}|^2 \, \delta(E_\mu - E_\nu) \, , \tag{2.4}$$

where $f(E)$ is the Fermi function, V_T is the applied bias voltage, $M_{\mu\nu}$ is the tunneling matrix element, and E_μ/E_ν is the energy of the state ψ_μ/ψ_ν of probe and sample in the absence of tunneling, respectively.

Eq. 2.4 is simplified with rough physical approximations for a better understanding. In the limit of low T and small $V_\mathrm{T} \approx 10\,\mathrm{meV}$, Eq. 2.4 reduces to [58]:

$$I_\mathrm{T} = \frac{2\pi e^2}{\hbar} V_\mathrm{T} \sum_{\mu,\nu} |M_{\mu\nu}|^2 \, \delta(E_\nu - E_\mathrm{F})\delta(E_\mu - E_\mathrm{F}) \, . \tag{2.5}$$

If, in a gedankenexperiment, the tip wave functions are infinitely localized, Eq. 2.5 becomes [58]:

$$I_\mathrm{T} \propto \sum_{\nu} |\psi_\nu(\vec{r_0})|^2 \, \delta(E_\nu - E_\mathrm{F}) \, , \tag{2.6}$$

which signifies that the tunneling current is a function of the sample LDOS at the Fermi level, $|\psi_\nu|^2$, with $\vec{r_0}$ being the center of the (spherical) tip apex.

When attempting a more general treatment of Eq. 2.4, one faces the problem to evaluate the matrix element $M_{\mu\nu}$, which [58]:

$$M_{\mu\nu} = -\frac{\hbar^2}{2m} \int (\psi_\mu^* \nabla \psi_\nu - \psi_\nu \nabla \psi_\mu^*) \cdot \mathrm{d}\vec{\mathrm{S}}. \tag{2.7}$$

Here, $\int \mathrm{d}\vec{S}$ is an integral over a surface within the barrier separating the two sides represented by the wave functions ψ_μ and ψ_ν.
J. Tersoff and D. R. Hamann used an s-orbital tip wave function as a first approximation to calculate the matrix element and I_T, and obtained [52, 58]:

$$I_\mathrm{T} \propto \rho_\mathrm{T}(E_\mathrm{F})\, e^{2R\kappa}\, V_\mathrm{T} \sum_\nu |\psi_\nu(\vec{r_0})|^2\, \delta(E_\nu - E_\mathrm{F}), \tag{2.8}$$

where $\rho_\mathrm{T}(E_\mathrm{F})$ is the tip LDOS at E_F, R is the radius of the tip apex, and κ the decay constant, which is expressed by [59]:

$$\kappa = \frac{\sqrt{2m}}{\hbar}\sqrt{(\Phi_\mathrm{T} + \Phi_\mathrm{S})/2}, \tag{2.9}$$

with the electron mass m and the work functions Φ_T and Φ_S of tip and sample, respectively (see Fig. 2.5**a**). Note that the sum in Eq. 2.8 represents the LDOS of the sample, compare to Eq. 2.6. Furthermore, ψ_ν is exponentially damped, i.e., $|\psi_\nu(\vec{r_0})|^2 \propto e^{-2\kappa(R+d)}$, with d being the tip-sample separation.
C. J. Chen ameliorated this model by considering that real tip materials like W and PtIr are d-band metals. In W, which has been used as tip material throughout all experiments in this thesis, the vast majority of the density of states (DOS) at the Fermi level consists of d states. In particular, the highly localized W d_{z^2} orbitals enable the observed sub-ångström resolution in STM, which cannot be explained models assuming s states [60].

Finite-bias STM. The above considerations are constricted to very small applied bias voltages. As the substrate SiC and bismuthene (with exception of edge states) are semiconductors, most of the measurements are carried out using a sizable bias voltages up to several volt[1], where the above-derived equations are not applicable. The problem is resolved by employing a simpler theory, specifically the Wentzel-Kramers-Brillouin (WKB) theory for planar tunneling, where the probed current is expressed by [52, 59]:

$$I_\mathrm{T} = \int_0^{eV_\mathrm{T}} \rho_\mathrm{S}(r,\, E)\, \rho_\mathrm{T}(r,\, \mp E \pm eV_\mathrm{T})\, T(E,\, eV_\mathrm{T},\, r)\mathrm{d}E\ , \tag{2.10}$$

where $\rho_\mathrm{S}(r,\, E)$ and $\rho_\mathrm{T}(r,\, E)$ are the DOS of sample and tip, respectively, at location r and energy E with respect to their Fermi level. The polarity of the bias applied to the tip determines whether the current stems from electrons tunneling from the tip's occupied to the sample's unoccupied states ($V_\mathrm{T} > 0$), or from the occupied sample to unoccupied tip states ($V_\mathrm{T} < 0$), as illustrated in Fig. 2.5. The transmission probability T is [52, 59]:

$$T(E,\, eV_\mathrm{T}) = \exp\left[-\frac{2d\sqrt{2m}}{\hbar}\sqrt{\frac{\Phi_\mathrm{S}+\Phi_\mathrm{T}}{2} + \frac{eV_\mathrm{T}}{2} - E}\right]. \tag{2.11}$$

Here, the decay constant κ from Eq. 2.9 is modified and depends on the energy of the electron E as well as the bias voltage applied to the tip V_T. The latter governs the effective potential barrier that has to be overcome by the tunneling particles. Accordingly, states in the range of Fermi level to eV_T do not contribute equally to the probed current. If

[1]Note that V_T is generally smaller than the work functions of tip and sample.

$V_T < 0$, T is largest for the electrons from states at the Fermi level ($E = 0$), see Fig. 2.5**b**. In contrast, if $V_T > 0$, the current is dominated by electrons stemming from states with energy $E = eV_T$.

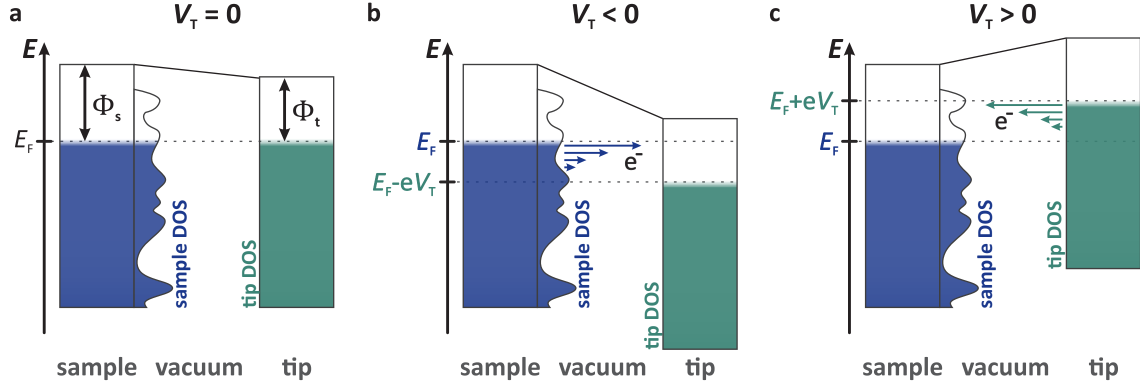

Figure 2.5 Bias dependence of the tunneling current. The tip LDOS is approximated to be constant. **a** In equilibrium tunnel contact, i.e., without applied bias voltage, the Fermi level of tip and sample are aligned. **b** If the applied bias voltage is negative ($V_T < 0$), tunneling occurs from occupied sample to unoccupied tip states. Note that the contribution from electrons at the Fermi level is largest (denoted by the arrow length). **c** At positive bias voltage ($V_T > 0$), the unoccupied sample states with electrons originating from occupied tip states are probed. The largest contribution is given by electrons with $E = eV_T$.

2.3.2 Scanning Tunneling Spectroscopy

The prospect of performing high-resolution spectroscopy was the initial goal of Binnig and Rohrer. STS, a natural extension of STM, offers the possibility to record $I_T(V)$ curves and to get insights to the LDOS at atomic resolution. In the following, the first part outlines the most important formulas, while the second part deals with the different measurement modes of STS.

The differential conductivity $\mathrm{d}I_T/\mathrm{d}V$ is calculated using Eq. 2.10 and reads [59]:

$$\left.\frac{\mathrm{d}I_\mathrm{T}}{\mathrm{d}V}\right|_{V=V_\mathrm{T}} = \rho_\mathrm{S}(r,\, eV_\mathrm{T})\,\rho_\mathrm{T}(r,\, 0)\,T(E = eV_\mathrm{T},\, eV_\mathrm{T},\, r) + \\ + \int_0^{eV_\mathrm{T}} \rho_\mathrm{S}(r,\, E)\,\rho_\mathrm{T}(r,\, \pm eV_\mathrm{T} \mp E)\,\frac{\mathrm{d}T(E,\, eV_\mathrm{T},\, r)}{\mathrm{d}V}\mathrm{d}E. \tag{2.12}$$

The first term consists of the LDOS of the tip at E_F, the sample LDOS at $E = eV_T$ and the transmission coefficient T. The second term incorporates the variation of T, which increases monotonically with V, such that additional features visible in $\mathrm{d}I_T/\mathrm{d}V$ can be attributed to the sample's LDOS at $E = eV_T$, i.e., $\mathrm{d}I_T/\mathrm{d}V \propto \rho_S(eV_T)$.

Again, one has to keep in mind that the bias polarity is important for the interpretation of the recorded spectra. While the above-considerations are valid in case of $eV_T > 0$ as the majority of the tunneling electrons originate from states with $E = eV_T$, see Fig. 2.5**c**, they are not a good approximation if $eV_T < 0$, because only a weak contribution I_T comes from states with $E = eV_T$, whereas the main contribution is given by electrons from the tip's Fermi level, see Fig. 2.5**b**. Obviously, the tip LDOS is becoming more and more relevant with increasing V_T [59].

2.3.2.1 Lock-In Amplifier Technique

Lock-in technique is used to improve the signal-to-noise ratio of spectroscopic data, especially of $\mathrm{d}I_\mathrm{T}/\mathrm{d}V$ measurements, which are highly susceptible to tiniest changes in the tip-sample distance. It is based on a lock-in amplifier, which adds a small sinusoidal modulation voltage V_mod with frequency ω_0 to the bias voltage V_T, resulting in a total voltage that is $V(t) = V_\mathrm{T} + V_\mathrm{mod}\sin(\omega_0 t)$. Consequently, the detected current is also modulated, see Fig. 2.6, and in a first order Taylor expansion expressed by [61]:

$$I_\mathrm{T}\Big(V(t)\Big) = I_\mathrm{T}\Big(V_\mathrm{T} + V_\mathrm{mod}\sin(\omega_0 t)\Big) \approx I_\mathrm{T}(V_\mathrm{T}) + \frac{\mathrm{d}I_\mathrm{T}}{\mathrm{d}V}\, eV_\mathrm{mod}\,\sin(\omega_0 t). \tag{2.13}$$

Hence, the amplitude of the resulting modulation current is proportional to $\mathrm{d}I_\mathrm{T}/\mathrm{d}V$, and, therefore, to the sample LDOS. However, it is rather small and must be separated from noise contributions.

This task is accomplished by the lock-in amplifier. The measured signal is convoluted with a reference signal that exhibits the very same frequency ω_0. An output is generated only when the frequency of reference and measured signal are identical, such that noise signals with arbitrary frequencies $\omega \neq \omega_0$ are removed. Additionally, uncorrelated contributions to the tunneling current are attenuated by a low-pass filter. A detailed discussion of the modulation technique for application in STS is found in Ref. [61]. Obviously, V_mod causes an

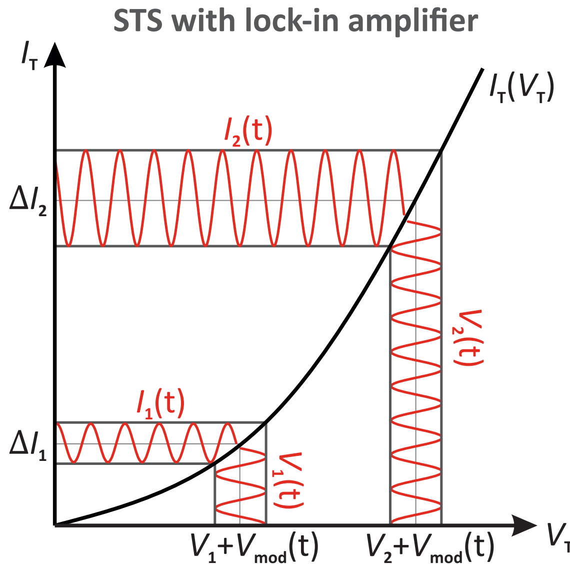

Figure 2.6 Illustration of the working principle of STS using a lock-in amplifier. During acquisition of an $I_\mathrm{T}(V)$ curve, a small sinusoidal voltage V_mod is added to the tunneling voltage V_T, which causes a modulation of the tunneling current I_T. Apparently, the amplitude of the resulting modulation current ΔI depends on the slope of $I_\mathrm{T}(V)$, compare ΔI_1 and ΔI_2, which is a function of the sample's LDOS in first order approximation. The probed signal is filtered to remove noise contributions and to obtain higher-quality signals.

averaging of the signal in a certain energy interval, with the upside of providing smoother signals. The downside is that the resulting energy resolution is finite and subtle details in the LDOS structure might be averaged out. Thus, depending on the inspected physical phenomenon, a careful adaption of the modulation amplitude is pivotal [61].

Additional broadening is caused by the finite probing temperature. Starting from Eq. 2.5, the influence of the temperature in the formulas describing I_T and $dI_\mathrm{T}/\mathrm{d}V$ is neglected. The overall signal is consequently a convolution of the sample LDOS ρ_S, the instrumental

broadening F_{instr}, temperature broadening F_{T} and the measured signal:

$$\mathrm{d}I_{\mathrm{T}}/\mathrm{d}V(eV_{\mathrm{T}}) \propto \Big(F_{\mathrm{T}} * F_{\mathrm{instr}}(V_{\mathrm{mod}}) * \rho_{\mathrm{S}}(eV_{\mathrm{T}})\Big). \tag{2.14}$$

Generally, the impact of these signal broadening effects is not relevant for the interpretation of STS measurements in this thesis with exception of the data discussed in Sec. 8.2.2. There, taking F_{instr} and F_{T} into account is of uttermost importance for a correct data evaluation and described there in more detail.

2.3.2.2 Measurement Modes

Complementary STS measurement modes are available and allow to probe different aspects of the sample LDOS. We employ three modes in this thesis, namely point spectroscopy and grid spectroscopy measurements as well as LDOS mapping, which will be shortly described in the following.

Point & grid spectroscopy measurements. Point spectroscopy curves allow the inspection of the sample LDOS at a specific point of the surface with high energy resolution. An $I_{\mathrm{T}}(V)$ (and optionally $\mathrm{d}I_{\mathrm{T}}/\mathrm{d}V$) curve is recorded at fixed tip-sample distance d, i.e., the feedback loop is deactivated during the voltage ramp from V_{start} to V_{end}. Before the ramp is initiated, the tip is stabilized at a stabilization voltage V_{st} and current I_{st}. As d is fixed, changes of the LDOS can be attributed to the sample LDOS provided that the tip LDOS is smooth and flat, which has to be assured before every measurement by preparation on a suitable, well-known material such as a Ag(111) crystal. Point spectroscopy curves are particularly helpful to identify strongly localized spectral features such as edge states in QSHIs.
Grid spectroscopy maps consist of a finite raster of single point spectroscopy curves recorded on the sample surface. They are very powerful tools as they contain the complete spectral information between V_{start} and V_{end} in a certain spatial margin. Unfortunately, the acquisition of a full $I_{\mathrm{T}}(V)$ curve at each point is vastly time consuming, and grid spectroscopy measurements with a duration up to the cryostat holding time ($\approx 50\,\mathrm{h}$) can be easily constructed. Consequently, the spatial extension x, y and resolution Δx, Δy as well as the energy resolution ΔE are limited, and the resulting setup constitutes a compromise. Nevertheless, grid maps are highly important tools for inspection of phenomena at small spatial extension, such as the influence of surface defects, or the edge state properties of bismuthene.

LDOS mapping. LDOS or $\mathrm{d}I/\mathrm{d}V$ maps are generated by detection of the $\mathrm{d}I_{\mathrm{T}}/\mathrm{d}V$ signal during the acquisition of a CCI. Again, a modulation voltage V_{mod} is added to the tunneling voltage V_{T}, such that the topographic image and the LDOS map at energy eV_{T} are collected in parallel. In order to avoid adjustment of the tip-sample distance as effect of the changes in $V_{\mathrm{T}}(t)$, the modulation frequency ω_0 must be higher than the feedback loop frequency of the STM.
In contrast to grid spectroscopy measurements, the great benefit from LDOS mapping is its potential to investigate the LDOS with high spatial resolution on extended areas. It can be used to inspect standing wave patterns arising from scattering of surface or edge

states around point defects and step edges, which are hardly recognizable in single point spectroscopy measurements. The scattering of the Shockley surface state on a Cu(111) crystal constitutes a very famous example of this application of LDOS mapping [62].
The high spatial resolution comes for the price of low spectral resolution, as only a single LDOS slice at eV_T is recorded. A more fundamental issue is the correct interpretation of the acquired data. The main problem is that the tip-sample distance z is continuously changing as result of the feedback loop at work. The topographic characteristics of the sample as well as the integrated LDOS from Fermi level to eV_T influence d. In turn, this affects the probed $\mathrm{d}I_\mathrm{T}/\mathrm{d}V$ signal, such that an unambiguous interpretation and assignment of features to electronic and structural sources is not trivial to impossible [59, 61].

2.4 Spatially-Averaging Techniques

Complementary to the microscopic scanning probe techniques discussed in the previous section, bismuthene on SiC has been investigated with a variety of spatially averaging methods, namely LEED, ARPES and XPS. These techniques employ electrons that are either diffracted at or emitted from the surface and contain information about the lattice symmetry and spacing as well as disorder, the band dispersion and chemical composition of the sample. Due to the short inelastic mean free path (IMFP) of electrons in solids in the probed energy range, see Fig. 2.7, all techniques are highly surface sensitive and ideal to inspect the properties of very thin films, such as bismuthene. In the following, a short survey of important formulas and information relevant for the interpretation of the experimental results is given.

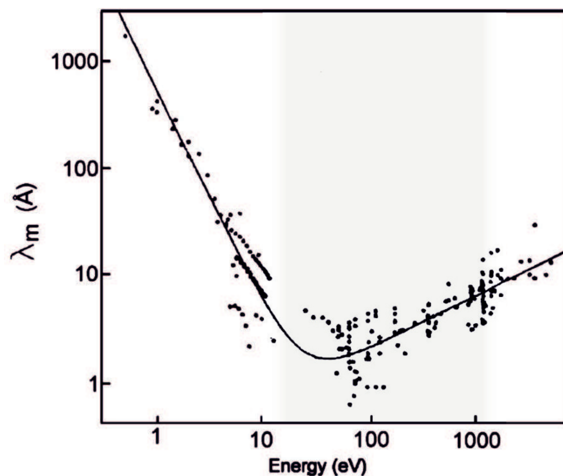

Figure 2.7 IMFP of electrons in various solids. The dots represent individual measured values and the solid line is a least squares fit. The gray shaded area indicates the energy range used in our experiments. Approximately, the IMFP is material-independent as the loss function is governed by the plasma frequency, while bonding properties are not important except for very low energies. The plasma frequency depends on the electron-electron distance that is roughly constant in all materials [63]. Thus, measurements in the depicted energy range are very surface sensitive with only few ångstrom probing depth. *Reprinted with permission from Ref. [64]. Copyright ©2003 Elsevier.*

2.4.1 Low-Energy Electron Diffraction

C. Davisson and L. H. Germer have discovered that electrons can be used as probes in diffraction experiments thanks to their wave-like behavior. LEED is typically conducted in the range of 30–200 eV, as the electrons' de Broglie wavelength $\lambda = \frac{h}{\sqrt{2mE_\mathrm{kin}}}$ (with the mass m and the kinetic energy E_kin of the electrons) is on the order of ångström and comparable

to the lattice spacing at these energies. The electrons are generated by an electron gun and accelerated by application of a defined potential towards the crystal. Electrons that are elastically scattered at the periodic sample surface give rise to interference phenomena, which are visualized on a fluorescent screen (see Fig. 2.8**a**) [65]. The collected information originates from the first one or two atomic layers (see Fig. 2.7). Hence, the corresponding reciprocal space consists of infinitely extended lattice rods instead of points in the direction normal to the surface, see Fig. 2.8**b** [65].

Geometric diffraction theory Constructive interference emerges when incoming and diffracted electron with wave vectors $\vec{k}_\mathrm{i}$ and $\vec{k}_\mathrm{o}$, respectively, fulfill the Laue condition, i.e., if their wave vector difference $\Delta\vec{k}$ corresponds to a reciprocal lattice vector $\vec{G}$ [65]:

$$\vec{k}_\mathrm{o} - \vec{k}_\mathrm{i} = \Delta\vec{k} = \vec{G}. \tag{2.15}$$

Note that $|\vec{k}_\mathrm{i}| = |\vec{k}_\mathrm{o}|$ due to the assumption of elastic scattering. Equivalently, the Laue condition is expressed by:

$$(\vec{k}_\mathrm{o} - \vec{k}_\mathrm{i}) \cdot \vec{R} = 2\pi n,\ n \in \mathbb{Z}, \tag{2.16}$$

where $\vec{R}$ is a lattice vector in real space.

Ewald's construction. The Laue condition can be visualized geometrically with help of the so-called Ewald construction, see Fig. 2.8**b**. The idealized flat and 2D surface with atom spacing $\vec{R}$ generates lattice rods in the reciprocal space. The center of the Ewald sphere is defined by the incident electron's wave vector $\vec{k}_\mathrm{i}$, which is aligned to a reciprocal lattice rod and determines the center of the reciprocal lattice (00). The radius of the sphere is fixed by the energy of the electron beam. Intersections of the sphere with the reciprocal lattice rods indicate constructive interference, which, in real space, become visible as diffraction spots on the fluorescent screen [65, 66].
With this theoretical considerations in mind and with geometric relations it is possible to assign the observed patterns on the fluorescent screen to the symmetry and spacing of the probed lattice. In our case, LEED patterns are used for a fast sample inspection after H annealing and Bi deposition (Chs. 5 and 6), in particular to check whether the desired surface reconstruction is present. More elaborate theories, namely the kinematic and dynamical theory, are required for evaluating the influence of more subtle details like point defects or faceting that lead to spot broadening and spot splitting, respectively [66, 67]. However, their analysis necessitates more sophisticated instrumentation such as spot profile analyzing LEED or $I(V)$-LEED, which is not used in the experiments presented in this thesis. A detailed discussion of LEED theory is found in Refs. [65] and [67].

2.4.2 Photoelectron Spectroscopy

The theory of PES is deeply linked to the quantum-mechanic interpretation of light and matter. Just as LEED employs the wave-like character of electrons, classically considered as particles, satisfactory understanding of PES is only possible when taking the particle-like character of light into consideration. It is based on the photoelectric effect, which has

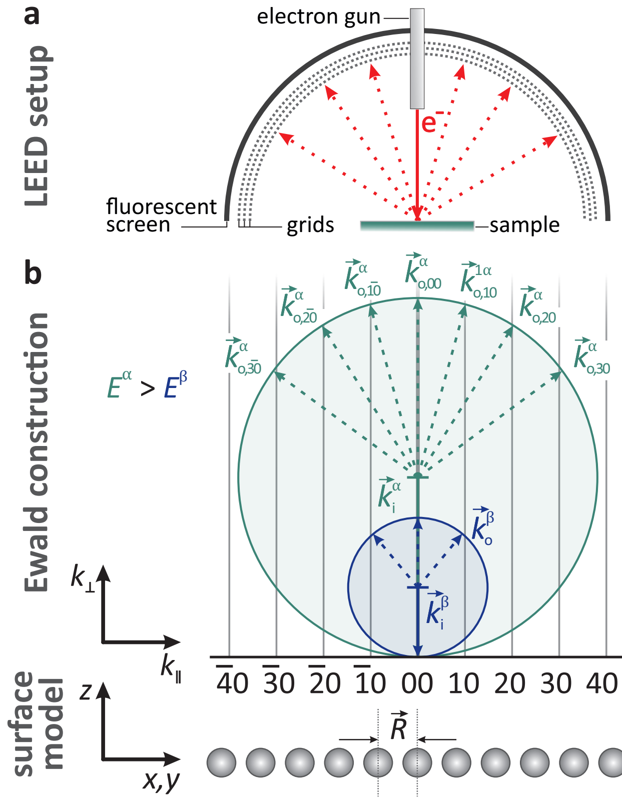

Figure 2.8 **a** Setup of a conventional LEED. An electron gun accelerates the electrons that approach the periodic crystal surface at normal incidence. The diffracted electrons are visualized on a half-spherical fluorescent screen, where the interference of incoming and diffracted electrons generates bright diffraction spots. A series of grids at proper potential assures that only elastically scattered electrons are imaged. **b** Ewald's construction in LEED. The high surface sensitivity of LEED implies that only the interference of electrons of the first or second atomic layer is represented on the screen and the reciprocal lattice converges to lattice rods instead of points. The Laue condition is fulfilled when the sphere, which is defined by the wave vector of the incident electrons $\vec{k}_\mathrm{i}$ and its absolute value $|\vec{k}|$ that is proportional to the beam energy E, intersects a reciprocal lattice rod.

been discovered by H. Hertz in 1887 [68] and theoretically interpreted by A. Einstein in 1905 [24].

With the development of proper methods and instrumentation advanced by K. Siegbahn in the 1950s [25], it became possible to use the photoelectric effect to probe the material stoichiometry and the chemical environment of the atoms with XPS, which today is among the most common methods in materials science. Based on this, more elaborate techniques have been developed in the later years, including ARPES, which provides insights into the material's electronic band dispersion.

Note that the discussion presented in this section is constricted to non-interacting electron systems, as correlation effects do not play a leading role in bismuthene on SiC apart from the edge states, which (unfortunately) are not detected in our PES experiments.

2.4.2.1 Working Principle

The theoretical description is initiated with the energy conservation law [69]:

$$E_\mathrm{kin} = h\nu - \Phi_\mathrm{W} - |E_\mathrm{bin}|. \tag{2.17}$$

An electron with binding energy E_bin is excited by a photon with frequency $h\nu$, and exhibits the kinetic energy E_kin after it has surmounted the material specific work function $\Phi_\mathrm{W} = E_\mathrm{vac} - E_\mathrm{F}$, i.e., the difference of vacuum (E_vac) and Fermi (E_F) energy, which is typically $4 - 5\,\mathrm{eV}$ in metals, see Fig. 2.9**a** [69]. Accordingly, it is evident that PES probes only occupied states of the sample. Note that Eq. 2.17 is true only under the assumption of an independent particle picture for the escaping electron, i.e., it does not account for correlations and is based on the sudden approximation. Specifically, this means

that interactions of the photoelectron and the $N-1$ particle system left behind after the excitation are neglected, and the electron is assumed to be instantaneously removed [70].

The measured core levels lineshapes $I(E_{\text{kin}})$ are usually described by a Voigt lineprofile. Broadening effects entering to the signal shape are, among others, the finite lifetime of the core hole (Lorentzian contribution) and instrumental broadening (Gaussian contribution). Similarly, the valence band (VB) spectra are affected by broadening effects and additionally through the DOS cutoff at E_{F} by the temperature-dependent Fermi distribution, as illustrated in Fig. 2.9**a**.

Three-step model. Often, the entire photoemission process is decomposed into three steps to facilitate its description [69]:

I Optical excitation of an initial to a final Bloch eigenstate by the photon.

II Propagation of the electron to the surface.

III Escape from the solid by transmission through the surface potential barrier.

Step (I) incorporates the information on the initial state of the electron and is detailed below. Step (II) depends on the effective mean-free path and is proportional to the probability that the electron reaches the surface without being affected by scattering processes leading to a loss of energy and wave vector information. Inelastic scattering processes produce a continuous background to the measured signal. Lastly, the transmission probability in step (III) depends on the kinetic energy of the electron E_{kin} and the material's work function Φ_{W} [69].

Strictly speaking, the phenomenological three-step model is not representative of the physical reality. Instead, a one-step model, in which the entire many-body system is treated within a single process and a Green's function is used to describe the single-particle removal function, has to be evaluated at the price of a far more complicated conceptual framework. Luckily, in many cases sufficient understanding is gained via the three-step model in combination with the sudden approximation [69, 70].

Fermi's golden rule. Mathematically, a formal description of the photoemission process is conventionally started with Fermi's golden rule, which describes the probability of an optical excitation between the N particle ground state Ψ_i^N and final states Ψ_f^N [69, 71]:

$$w_{fi} \propto |\langle \Psi_f^N | \vec{A} \cdot \vec{p} | \Psi_i^N \rangle|^2 \, \delta(E_f^N - E_i^N - h\nu). \tag{2.18}$$

The second term accounts for energy conservation between the final state with energy $E_f^N = E_f^{N-1} + E_{\text{kin}} + \Phi_{\text{W}}$ and initial state $E_i^N = E_i^{N-1} - E_{\text{bin}}^{\vec{k}}$ after excitation of a photoelectron by light of frequency ν. The photoelectron with energy E_{kin} exhibits a binding energy $E_{\text{bin}}^{\vec{k}}$ and wave vector $\vec{k}$ before the excitation. The first term in Eq. 2.18 depends on the interaction Hamiltonian $\vec{A} \cdot \vec{p}$, with the electromagnetic vector potential $\vec{A}$ and the electronic momentum operator $\vec{p}$. The term $\vec{A} \cdot \vec{p}$ evolves from the Hamiltonian H_{int}, which is obtained by replacing $\vec{p} \rightarrow (\vec{p} - e\vec{A})$ in the Schrödinger equation. The resulting quadratic term $\propto |\vec{A}|^2$ is often neglected assuming weak radiation fields, and $\nabla \cdot \vec{A} = 0$ with a possible exception at the surface. Under these assumptions, $\vec{p}$ can be transformed into a dipole operator [72].

The final state $\Psi_f^N = \mathcal{A}\Phi_f^{\vec{k}}\Psi_f^{N-1}$ is written as the product of the photoelectron wave function $\Phi_f^{\vec{k}}$ with wave vector $\vec{k}$ and the $(N-1)$ particle finale state wave function left behind after an electron is removed from the system (Ψ_f^{N-1}), and an operator $\mathcal{A}$ that accounts for the Pauli principle by assuring that the N-particle wavefunction is antisymmetric. The total transition probability is obtained by summation over all excited states (indexed by m) with wave functions Ψ_m^{N-1} and eigenenergies E_m^{N-1}. In the same way, the initial state $\Psi_i^N = \mathcal{A}\Phi_i^{\vec{k}}\Psi_i^{N-1}$ is expressed and $\Psi_i^{N-1} = c_{\vec{k}}\Psi_i^N$ is obtained by use of the annihilation operator of an electron with momentum $\vec{k}$ [69].

We use these expressions to evaluate the matrix element in Fermi's golden rule of Eq. 2.18 [69, 71]:

$$\langle \Psi_f^N | \vec{A} \cdot \vec{p} | \Psi_i^N \rangle = \underbrace{\langle \Phi_f^{\vec{k}} | \vec{A} \cdot \vec{p} | \Phi_i^{\vec{k}} \rangle}_{\text{dipole matrix el.} M_{fi}^{\vec{k}}} \times \underbrace{\langle \Psi_m^{N-1} | \Psi_i^{N-1} \rangle}_{(N-1)\text{-part. overlap int.}} . \tag{2.19}$$

It depends on the energy and polarization of the incident photon and the electron momentum [69]. The summation over all possible final states Ψ_m^{N-1} yields the PES signal $I(\vec{k}, E_{\text{kin}})$:

$$I(\vec{k}, E_{\text{kin}}) = \sum_{f,i} w_{fi} = \sum_{f,i} |M_{fi}^{\vec{k}}|^2 \sum_m |c_{mi}|^2 \delta(E_{\text{kin}} + E_m^{N-1} - E_i^N + \Phi_{\text{W}} - h\nu), \tag{2.20}$$

where $|c_{mi}|^2 = |\langle \Psi_m^{N-1} | \Psi_i^{N-1} \rangle|^2$ is the probability that the $(N-1)$-system ends up in the excited state m after excitation of an electron from state i. This probability strongly depends on the system that is investigated. If excited and initial $(N-1)$ particle state coincide, i.e., $\Psi_{m_0}^{N-1} = \Psi_i^{N-1}$ for a specific m_0 and all other $c_{mi} = 0$, the system is non-interacting and the probed intensity corresponds to a delta peak (if additionally the matrix element is non-zero, of course). In case of strongly interacting systems, many different c_{mi} are non-zero and the obtained spectral intensity is more complex. A theoretical description of the photoemission process for these systems is done in the framework of time-ordered one-electron Green's function formalism [69].

2.4.2.2 Angle-Resolved Photoelectron Spectroscopy

In ARPES, the photoelectron's momentum is resolved in addition to its kinetic energy, such that it is possible to image the dispersion relation $E(\vec{k})$ of the probed material. It can be deduced by geometric relations from the alignment positions of the sample, specifically from the emission angles φ (depending on the azimuthal rotation) and θ (depending on the polar and tilt angle), see Fig. 2.9**b**, as derived in the following.

As depicted in Fig. 2.9**c**, the electron momentum can be decomposed in a parallel and perpendicular component in reference to the sample surface. The respective components $K_\parallel$ and $K_\perp$ in vacuum are calculated via:

$$\hbar K_\parallel = \sqrt{2mE_{\text{kin}}} \sin(\theta), \tag{2.21}$$

$$\hbar K_\perp = \sqrt{2mE_{\text{kin}}} \cos(\theta), \tag{2.22}$$

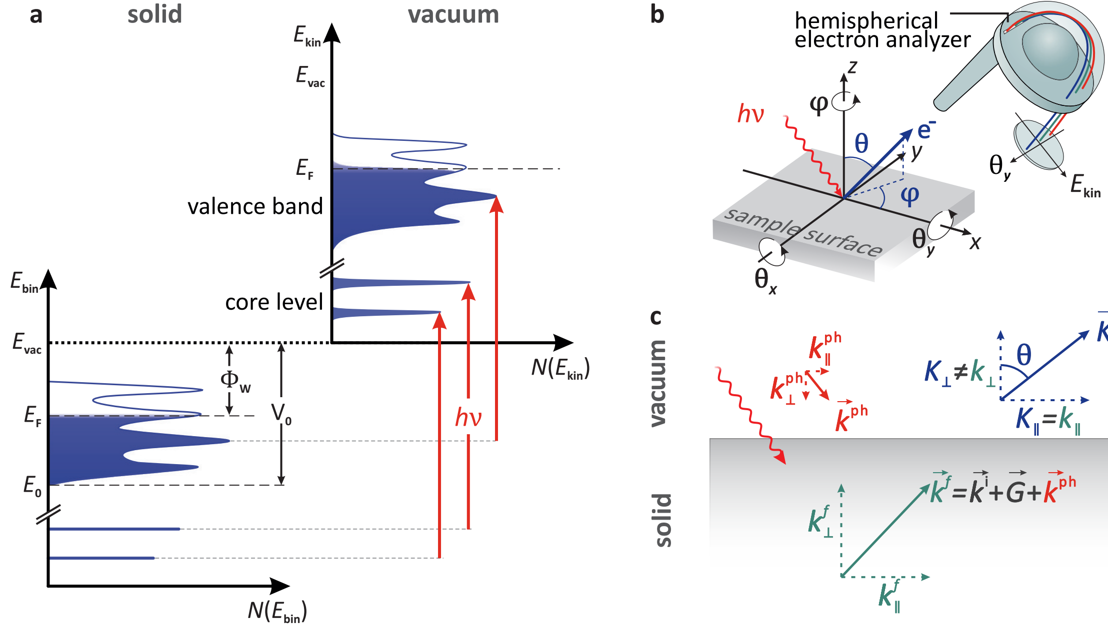

Figure 2.9 **a** Energetics in PES. Photons with energy $h\nu$ penetrate into the crystal and excite an electron in a core level or VB Bloch state. The energy and (in ARPES) the momentum distribution of the electrons is measured. Note that the detected DOS is broadened. **b** Geometry of an ARPES measurement. The escaping electrons are detected by a hemispherical electron analyzer and characterized in terms of E_{kin}, φ and θ, which allows to trace the material's band dispersion. **c** Kinematics of the photoemission process. The wave vectors of photon $\vec{k}^{\mathrm{ph}}$, initial state $\vec{k}^{\mathrm{i}}$, and final state within the crystal $\vec{k}^{\mathrm{f}}$ fulfill momentum conservation. $\vec{G}$ is a reciprocal lattice vector. When the electron escapes into vacuum, it exhibits a wave vector $\vec{K}$, with retained parallel but non-conserved perpendicular momentum due to the potential step at the surface. *Adapted with permission from Ref. [70]. Copyright ©2019 Springer Nature.*

where m is the electron mass. In the crystal, the photoelectron exhibits a wave vector $\vec{k}$ after excitation of an initial state $\vec{k}^{\mathrm{i}}$ by a photon $\vec{k}^{\mathrm{ph}}$. Note that the photon momentum in the ultraviolet energy regime ($h\nu < 100\,\mathrm{eV}$) corresponds to few percent of the extension of the Brillouin zone (BZ) radius only and is therefore negligible. For example, the distance of Γ and K point of bismuthene is $\approx 0.8\,\text{Å}^{-1}$, while the photon momentum at the He Iα line with $h\nu = 21.22\,\mathrm{eV}$ is only $\approx 0.008\,\text{Å}^{-1}$ [69].

The backtracing of the parallel component of the initial Bloch wave function $k^{\mathrm{i}}_{\parallel}$ is easier accomplished as it is conserved at the transition from solid to vacuum ($k^{\mathrm{f}}_{\parallel} = K_{\parallel}$) due to the translational symmetry in the xy plane of the surface, see Fig. 2.9**c**. Its calculation is straightforward:

$$k^{\mathrm{i}}_{\parallel} = K_{\parallel} - G_{\parallel}(-k^{\mathrm{ph}}_{\parallel}) = \frac{1}{\hbar}\sqrt{2mE_{\mathrm{kin}}}\,\sin(\theta) - G_{\parallel}\,(-k^{\mathrm{ph}}_{\parallel}). \tag{2.23}$$

Here, $G_{\parallel}$ represents an additional possible (parallel) momentum transfer by a reciprocal space vector, i.e., direct transitions and transitions involving momenta connected by $\vec{G}$ are both feasible scenarios.

The deduction of the perpendicular component requires more attention as it is not conserved at the interface of crystal and vacuum due to diffraction at the surface potential step [72]. To do so, different, rather complex approaches for experimental determination of the band dispersion are available [69]. Alternatively, $k_{\perp}$ is evaluated by adopting a

nearly-free electron model for description of the final states, i.e., $E_\mathrm{f}(\vec{k}) = \frac{\hbar^2|k^\mathrm{f}|^2}{2m} - |E_0|$, where $|k^\mathrm{f}|^2 = (k^\mathrm{f}_\parallel)^2 + (k^\mathrm{f}_\perp)^2$ and E_0 is the bottom of the VB, see Fig. 2.9**a** [69]. Then, one obtains:

$$k^\mathrm{i}_\perp = \frac{1}{\hbar}\sqrt{2m(E_\mathrm{kin}\cos^2(\theta) + V_0)} - G_\perp\,(+k^\mathrm{ph}_\perp), \tag{2.24}$$

where $V_0 = |E_0| + \Phi_\mathrm{W}$ is the so-called inner potential, which can be inferred from the periodicity of $K_\perp$ probed by tuning the photon energy in synchrotron experiments, or by optimizing the agreement with a DFT-computed band structure, see Sec. 2.5 [69, 70, 73]. 2D materials like bismuthene constitute a particularly easy case for determination of $k_\perp$, as in these systems, a dispersion along $k_\perp$ is absent by definition [69]. The ARPES measurements of bismuthene on SiC are shown in Ch. 7.

2.4.2.3 X-Ray Photoelectron Spectroscopy

The probed PES intensity may also be used to gain knowledge about the sample stoichiometry, which is particularly useful when, e.g., inspecting samples grown by a newly developed growth process or checking for the presence of oxidation states, as we have done for bismuthene. Such analysis is based on the core level intensity I_0, which is measured after illumination with X-ray light.

Background correction. The measured intensity $I_0(E_\mathrm{kin})$ has to be corrected for the inelastic background, i.e., signal produced by secondary electrons due to inelastic scattering processes when the electron is on its way to the surface [step (II) of the three-step model]. Frequently, this is done by a Shirley background correction, which is an iterative solution assuming that the background signal I_BG at E_kin is proportional to the number of electrons at higher kinetic energy $E'_\mathrm{kin} > E_\mathrm{kin}$. The intrinsic sample spectrum is approximated by the corrected intensity $I_c(E_\mathrm{kin})$ [71, 73]:

$$I^n_c(E_\mathrm{kin}) = I_0(E_\mathrm{kin}) - I_\mathrm{BG}(E_1)\left(\frac{\int_{E_\mathrm{kin}}^{E'_\mathrm{kin}} I^{n-1}_c(\epsilon)d\epsilon}{\int_{E_1}^{E'_\mathrm{kin}} I^{n-1}_c(\epsilon)d\epsilon}\right). \tag{2.25}$$

Here, n is the number of iterations (usually 5 are sufficient to obtain convergence), and $I_\mathrm{BG}(E_1)$ is the limit of the background correction at lower kinetic energy.

Parameters influencing I_c. The stoichiometry of the sample can be extracted with the obtained corrected intensity I_c up to a certain precision, depending on the accuracy with which certain experimental parameters are known. Obviously, the measured signal is proportional to the concentration N_α of species α in the sample. Additionally, it is affected by the photoionization cross section σ_α and other, technical parameters such as the photon flux J, the analyzer transmission T, and the detection efficiency D, such that overall the intensity is expressed with [71]:

$$I_c \propto N_\alpha \cdot \sigma_\alpha \cdot J \cdot T \cdot D. \tag{2.26}$$

Not all of these parameters are easily obtained and the photoionization cross section values are known only to a limited precision. Thus, the stoichiometry might be derived by

comparison to the probed signal of well-known reference samples, or is set in relation to other samples grown with different parameters but using identical measurement settings.

Varying emission angle. Depth profiling of samples is particularly interesting in case of thin film heterostructures and feasible by variation of the emission angle:

$$I(z) = I_0 \exp\left(-\frac{z}{\lambda_{\text{eff}}}\right) = I_0 \exp\left(-\frac{z}{\lambda \cos(\theta)}\right), \tag{2.27}$$

where I_0 is the number of excited electrons, z is the distance of the excited atom from the surface, and λ and λ_{eff} are the (effective) IMFP that is energy-dependent. Thus, electrons localized in varying depth z of the crystal are probed. Eq. 2.27 assumes that the trajectory of the photoelectron is a straight line of length $\frac{z}{\cos(\theta)}$. The overall signal is damped exponentially due to the inelastic scattering processes [73, 74]. Hence, the higher the emission angle, the more surface sensitive is the measurement, which is exploited in Ch. 6.

2.5 Density Functional Theory

DFT today is among the most popular electronic structure calculation methods [75, 76]. Its success is founded on the comparably low computational effort (for most of its implementations) and its high flexibility, allowing to simulate crystals and even heterostructures, in conjecture with fairly accurate results when used for systems where correlations are not dominant [75]. Hence, it enables and facilitates the quest of novel materials such as bismuthene on SiC. Indeed, it has been the starting point of this thesis because it allowed its identification as a quantum spin Hall insulator (QSHI) system, as will be outlined in Ch. 4.

Basic ideas of Hohenberg, Kohn and Sham. The year 1964 is seen as the birth year of DFT. P. Hohenberg and W. Kohn stated that the ground state wave function ψ_0 can be calculated when knowing the ground state density ρ_0 [77]. In turn, this implies that all observables of the N electron system are precisely determined and can be derived from ρ_0, as well [75, 76]. Moreover, the ground state energy E_0 associated with ρ_0 is lower than for any other $\rho \neq \rho_0$. This is used in a variational principle to minimize $E(\rho)$. The system energy $E(\rho)$ is described by density functionals, which can be split into a term that represents the interaction with an external potential v_{ext}, and other terms that do not involve the external potential, $F(\rho) = T(\rho) + V_{\text{ee}}(\rho)$ with the total kinetic energy $T(\rho)$ and Coulomb interaction $V_{\text{ee}}(\rho)$ [75].

W. Kohn and L. J. Sham provided concrete implementations of these functionals using reasonable approximations [78]. The kinetic energy $T(\rho)$ and the Coulomb interaction $V_{\text{ee}}(\rho)$ are replaced by the classical kinetic energy of non-interacting particles $T_0(\rho)$ and the Coulomb self energy $J(\rho)$, respectively [75]:

$$T(\rho) \rightarrow T_0(\rho) = -\frac{1}{2}\sum_i 2\int \psi_i^* \nabla^2 \psi_i, \tag{2.28}$$

$$V_{\text{ee}}(\rho) \rightarrow J(\rho) = \frac{1}{2}\int\int \frac{\rho_1 \rho_2}{r_{12}} dr_1 dr_2, \tag{2.29}$$

where the total density $\rho = 2\sum_i |\psi_i|^2$ is obtained as a Slater determinant of orthonormal states ψ_i and r_{12} is the distance of densities ρ_1 and ρ_2 at r_1 and r_2, respectively.
The error of these approximations is put into the exchange-correlation functional E_{XC}, which contains both kinetic and potential energies. Accordingly, the total Kohn-Sham energy functional reads [75]:

$$E(\rho) = T_0(\rho) + \int v_{\mathrm{ext}}\rho + J(\rho) + E_{\mathrm{XC}}(\rho) \ . \tag{2.30}$$

Finally, the Kohn-Sham equation is obtained by minimization of Eq. 2.30:

$$-\frac{1}{2}\nabla^2\psi_i \ + \ v_{\mathrm{KS}}\psi_i = \varepsilon_i\psi_i \ , \text{ where } \ v_{\mathrm{KS}} = v_{\mathrm{ext}} + v_{\mathrm{el}} + \frac{\delta E_{\mathrm{XC}}}{\delta\rho}. \tag{2.31}$$

Here, v_{KS} is the effective Kohn-Sham potential, v_{ext} is the potential energy of the crystal and v_{el} contains the Hartree-type Coulomb interaction between the charges [79]. The only term that is left over is the small but non-negligible exchange-correlation potential v_{xc} given by the functional derivative $\frac{\delta E_{\mathrm{XC}}}{\delta\rho}$ [75].
The intriguing and seemingly inconsistent finding is that Eqs. 2.29–2.31 describe the physical properties of an interacting many-body electronic system although the underlying theory is expressed with effectively independent particles. However, the quality of the description relies on the existence of a sufficiently precise and detailed solution for v_{xc}, which is the crux of DFT.

Approximations for the exchange-correlation functional. The first approximation for v_{xc} is given in the original Kohn-Sham paper, namely the local density approximation (LDA) [78]. It assumes that $E_{\mathrm{XC}}^{\mathrm{LDA}} = \int e_{\mathrm{XC}}^{\mathrm{HEG}}(\rho)$ only depends on the density at each specific position and is the same as in an homogeneous electron gas $e_{\mathrm{XC}}^{\mathrm{HEG}}(\rho)$. LDA is still used today, especially in systems where $\rho(r)$ varies slowly, but tends to overrate the strength of every bond by approximately 1 eV as result of the overestimation of correlation and underestimation of exchange energy [75, 76, 80].
Significantly better results are achieved with generalized gradient approximations (GGAs). They extend LDA by incorporating the gradient of the density in the functional approximation, such that the exchange-correlation energy reads $E_{\mathrm{XC}}^{\mathrm{GGA}} = \int e_{\mathrm{XC}}^{\mathrm{GGA}}(\rho, \nabla\rho)$. Among the manifold of published GGA implementations, differing in the choice of $e_{\mathrm{XC}}^{\mathrm{GGA}}(\rho, \nabla\rho)$, the parametrization of Perdew, Burke and Ernzerhof (PBE) [81] constitutes a very popular version and is used for most calculations of bismuthene on SiC shown in Chs. 4, 7 and 8. GGA approximations ameliorate the overbinding of the LDA functionals but still possess a tendency to exaggerate the localization of the so-called exchange-correlation hole, i.e., the reduced probability of finding another electron at r' if one is found at r, and therefore lead to overbinding [75].
Hybrid functionals, where v_{xc} is computed only partially by DFT (e.g., with GGA PBE) and combined with a certain amount ($\approx$ 20%) of the non-local, exact Hartree-Fock exchange, tremendously improve the error of calculated characteristics [75]. We used the hybrid functional in the implementation Heyd, Scuseria and Ernzerhof (HSE) [82] to attain more accurate values for band splittings and the band gap magnitude, which are used to compare to experimentally observed values in STS and ARPES (see Chs. 4, 7 and 8).

3 Theoretical Concepts for 2D Topological Insulators

Two-dimensional topological insulators (2D TIs), synonymously called quantum spin Hall insulators (QSHI) [13, 83, 84], host spin-polarized, metallic edge states that are strictly tied to the system's boundary. Intriguingly, these helical topological edge states are insensitive to single-particle backscattering as result of the interplay of strong spin-orbit coupling (SOC) and time-reversal (TR) as well as $U(1)_{charge}$ symmetry [13, 14].
However, the theoretical treatment in terms of a single particle picture proves to be insufficient in certain cases. In the limit of confinement to one dimension (1D), the description of excitations by individual quasi-particles in the framework of Fermi liquid theory, which is successfully applied to many two-dimensional and three-dimensional (2D and 3D, respectively) systems, fails. Instead, the impact of electronic correlations is enhanced and such (nearly) 1D systems are characterized by collective excitations of spin and charge, which is mathematically captured by the Tomonaga-Luttinger liquid (TLL) theory. Depending on the correlation strength, this might provoke a failure of the protection from backscattering due to two-particle processes.
As bismuthene on SiC belongs to the class of 2D TIs, the following chapter aims to provide a brief summary of important theoretical concepts. This comprises a general introduction to the theoretical description of TI materials as well as a summary of milestone experimental findings. Furthermore, a comprehensive introduction to the TLL theory, which is relevant for the data analysis in Ch. 8, is given. Note that the specific theory for bismuthene on SiC is discussed in much more detail in Ch. 4.

3.1 Topological Insulators

Topology, originally denoting a branch in mathematics, entered solid state physics with the Su-Schrieffer-Hegel model developed to describe polyacetylene in 1979 [85]. It became known to a broader public upon the discovery of the quantum Hall effect (QHE) by K. von Klitzing in 1980 [86] and the subsequent theoretical analysis by D. Thouless et al. [14, 87], who identified that the quantization of the Hall conductance and the appearance of chiral edge states in the QHE reflects the presence of topological order [13, 14, 88].
This section aims to provide an introduction to TI theory. In its first part (Sec. 3.1.1), we outline the difference between trivial and non-trivial insulators. In the second and third part, we explicitly inspect Chern insulators (Sec. 3.1.2) and QSHIs (Sec. 3.1.3). A summary of key properties of experimentally realized QSHI materials and the attempts to synthesize high-Z honeycomb systems is given in Sec. 3.1.4.
There exists a number of excellent reviews and books covering a broad range of aspects associated with topological matter, see, e.g., Refs. [13, 14, 83, 84, 89–94].

3.1.1 Topological Band Theory

Generally, insulators can be defined as materials with an energy gap between the filled and empty states, such that no current evolves when a finite potential gradient is present in the material. This definition comprises semiconductors and insulators, but also materials that exhibit the QHE, where equally-spaced Landau levels, which emerge in a 2D electron gas by a perpendicular magnetic field, are separated by an energy gap of $\hbar\omega_c$ (with the cyclotron frequency ω_c). Despite the band gap between the filled and empty levels, a finite, quantized Hall conductivity $\sigma = Ne^2/h$ directly proportional to the number of occupied Landau levels N is probed in a transverse electric field [13, 14].

The Bloch band theory, which exploits the crystal's translation symmetry, fails to explain this unconventional behavior of the QHE. Accordingly, a new classification scheme by topological invariants has been developed, which distinguishes between insulators in topologically trivial and non-trivial phases [13, 14]. Even though TIs are known for the intriguing states appearing at the system boundary, it is enough to inspect the properties of the bulk valence band (VB) Bloch wave functions to determine the topological character of a material [88, 89].

VB topology in crystals. A band structure evolves by mapping of the crystal momentum $\vec{k}$ to energy eigenvalues $E_\alpha(\vec{k})$, $\alpha = 1,...,2n$ in the Hilbert space with $2n$ electronic degrees of freedom via the Bloch Hamiltonian $H(\vec{k})$[2] [13, 88]. The corresponding eigenstates are the Bloch states $u(\vec{k})$. The wavevector $\vec{k}$ is defined in the periodic Brillouin zone (BZ), i.e., $\vec{k} + \vec{G} = \vec{k}$, where G is a reciprocal lattice vector [13]. A band is defined by the evolution of $E_\alpha(\vec{k})$ in the Brillouin torus with dimension $\mathbb{T}^d$, where d is the dimension of the crystal [88].

The ground state corresponds to the ensemble of filled eigenstates/VBs. Its wavevectors $u(\vec{k})$ are defined – up to a phase Φ – via the Schrödinger equation $H(\vec{k})u(\vec{k}) = E(\vec{k})u(\vec{k})$, i.e., they are invariant under the transformation $u(\vec{k}) \to e^{i\Phi(\vec{k})}u(\vec{k})$ [95]. One may think that the choice of the phase Φ is arbitrary and might be fixed by a proper gauge when varying k in the Brillouin torus, but this is not always the case. In certain cases, the wavevector path has to be separated into multiple segments, each with a specific phase [89]. In this (topologically non-trivial) case, the VB bundle exhibits a twisted topology [88].

To illustrate the notion of trivial and twisted VB bundles we use a Möbius strip. We decompose the circle $\mathbb{S}^1$, which is parametrized by the angle θ, into two semicircles $U_N = (0 - \epsilon, \pi + \epsilon)$ and $U_S = (-\pi - \epsilon, 0 + \epsilon)$, see Fig. 3.1**a**. The full circle is reconstructed by connecting U_N and U_S at the two transition regions $V_E = (-\epsilon, \epsilon)$ and $V_W = (\pi - \epsilon, \pi + \epsilon)$ (Fig. 3.1**a**), with two possible combinations of the transition function t_{NS} [88]:

$$t_{NS}(\theta \in V_E) : t \mapsto t \text{ and } t_{NS}(\theta \in V_W) : t \mapsto t, \tag{3.1}$$

or

$$t_{NS}(\theta \in V_E) : t \mapsto t \text{ and } t_{NS}(\theta \in V_W) : t \mapsto -t. \tag{3.2}$$

[2]Note that the Hamiltonian describes single-particle properties and interaction effects are neglected.

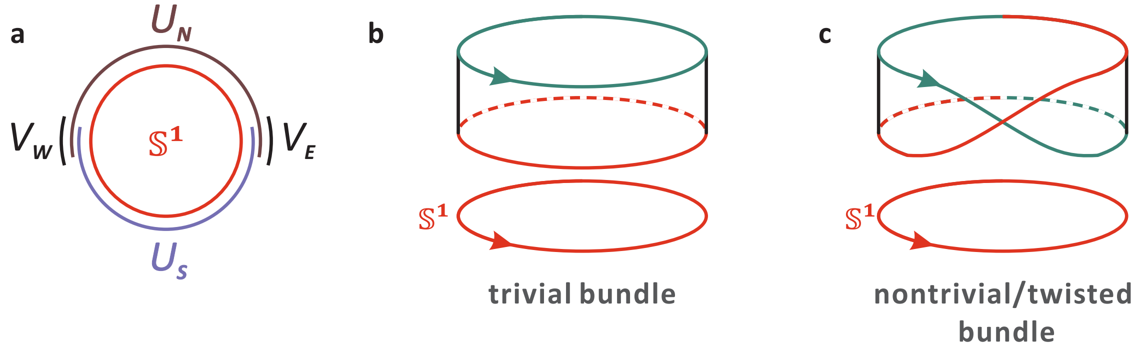

Figure 3.1 Möbius strip as an example for a twisted Bloch bundle. **a** The full circle $\mathbb{S}^1$ is generated by connection of the semicircles U_N and U_S at V_W and V_E, which can result in a **b** trivial or **c** twisted bundle. *Reproduced from Ref. [88].* *Copyright ©2013 Elsevier Masson SAS. All rights reserved.*

While the first case describes a cylinder and represents trivial vector bundle (Fig. 3.1**b**), the latter combination of transition functions corresponds to a twisted bundle (Fig. 3.1**c**) [88]. In contrast to the cylinder, the notion of "inner" and "outer" surface loses its meaning in case of a Möbius strip. Keeping this picture in mind, we continue the discussion by the description of two specific 2D insulators with non-trivial topology, namely the Chern insulator and $\mathbb{Z}_2$ insulator, which are characterized by the c_1 and ν topological invariant, respectively.

3.1.2 Chern Insulators

Any insulator minimally consists of an occupied and an unoccupied band, and can be described with a generic Hamiltonian of the form: [88, 89]

$$H(k) = h_0(k)\mathbb{1} + \vec{h}(k) \cdot \vec{\sigma}, \tag{3.3}$$

where $\mathbb{1}$ is the identity matrix and $\vec{\sigma}$ are the Pauli matrices. Solving the Schrödinger equation generates two eigenstates $u_\pm(k)$ and -energies $\epsilon_\pm(k) = h_0(k) \pm h(k)$ with $h(k) = \left\|\vec{h}(k)\right\|$. Note that h_0 is discarded in the following as it has no impact on the topological properties of the eigenstates [89].

We employ a transformation to spherical coordinates and parametrize $\vec{h}(k)$ with the polar angle $\theta \in [0, \pi)$ and azimuthal angle $\varphi \in [0, 2\pi)$: [88–90]

$$\vec{h} = h \begin{pmatrix} \sin\theta\cos\varphi \\ \sin\theta\sin\varphi \\ \cos\theta \end{pmatrix}, \tag{3.4}$$

and inspect the filled eigenstate $u_-(\vec{h})$. It reads:

$$u_-(\vec{h}) = \begin{pmatrix} -\sin\frac{\theta}{2} \\ \mathrm{e}^{i\varphi}\cos\frac{\theta}{2} \end{pmatrix} . \tag{3.5}$$

However, $u_-(\vec{h})$ is not well-defined in the limit $\theta \to 0$, because there, the x and y component become equally zero and φ cannot be defined, such that the phase $\mathrm{e}^{i\varphi}$ exhibits a

discontinuity [89]. An attempt to use a different gauge by multiplication of $u_-(\vec{h})$ with $e^{-i\varphi}$ will result in the same problem at $\theta \to \pi$ [88, 90].

Therefore, the only solution is to define u_- separately on the upper and lower hemisphere U_N and U_S, respectively:

$$u_-^S(\vec{h}) = \begin{pmatrix} -\sin\frac{\theta}{2} \\ \mathrm{e}^{i\varphi}\cos\frac{\theta}{2} \end{pmatrix} \text{ and } u_-^N(\vec{h}) = \begin{pmatrix} -\mathrm{e}^{i\varphi}\sin\frac{\theta}{2} \\ \cos\frac{\theta}{2} \end{pmatrix}. \tag{3.6}$$

The transition between U_N and U_S occurs on a circle $\mathcal{C} = U_N \cap U_S$ and is associated with a phase change $t_{NS} = \mathrm{e}^{i\varphi}$. The necessity for more than a single gauge, or differently speaking, the obstruction to smoothly transform the transition function to identity is the consequence of the non-trivial topology of the sphere [88].

Chern number. A direct evaluation of the topological properties can be accomplished by calculation of the Berry phase or Chern number c_1 with the so-called Berry connection $A = \frac{1}{i}\langle u_-(k)|\nabla_k|u_-(k)\rangle$ and the Berry curvature, which is $F(k) = \nabla_k \times A(k)$ [88, 89, 96]. The Chern number or Berry phase represents the phase acquired under an adiabatic cycle [95] and is obtained by integration of the Berry curvature over the Brillouin torus:

$$c_1 = \frac{1}{2\pi}\int_{\mathrm{BZ}} F \tag{3.7}$$

Eq. 3.7 is representative of the Berry flux in the BZ, which is a topological invariant that does not change unless the band gap is closed [13].

In case of the two band insulator model in Eq. 3.3, the evaluation of the Chern number reveals the field of a monopole, i.e., the singularity at $\theta = 0$ or $\theta = \pi$ (depending on the gauge), which gives rise to a non-trivial topology of the sphere [89, 90]. If no singularity is present, the filled eigenvector and the Berry connection are well-defined on the entire torus and the Chern number is zero, signaling a trivial topology [89]. In the following, the Haldane model as an explicit formulation of a two band insulator model is discussed. It is based on a graphene lattice, see Fig. 3.2**a**, with simultaneously broken inversion and TR symmetry. The former is lifted by inequivalent on-site energies of the triangular sublattices A and B, while the latter is suspended by introduction of a local magnetic flux designed such that it vanishes across the entire unit cell (see Fig. 3.2**b**) [88].

Haldane model. The nearest neighbor (NN) vectors a_i connecting both sublattices, and the next-nearest neighbor (NNN) vectors b_i between sites of the same sublattice, see Fig. 3.2, are: [88]

$$a_1 = \begin{pmatrix} \sqrt{3}/2 \\ 1/2 \end{pmatrix}, a_2 = \begin{pmatrix} -\sqrt{3}/2 \\ 1/2 \end{pmatrix}, a_3 = \begin{pmatrix} 0 \\ -1 \end{pmatrix} = -(a_1 + a_2), \tag{3.8}$$

$$b_1 = \begin{pmatrix} -\sqrt{3}/2 \\ 3/2 \end{pmatrix}, b_2 = \begin{pmatrix} -\sqrt{3}/2 \\ -3/2 \end{pmatrix}, b_3 = \begin{pmatrix} \sqrt{3} \\ 0 \end{pmatrix}. \tag{3.9}$$

In reciprocal space, the base vectors b_1^* and b_2^* corresponding to b_1 and b_2 are [88]:

$$b_1^* = 2\pi \begin{pmatrix} -1/\sqrt{3} \\ 1/3 \end{pmatrix}, \; b_2^* = 2\pi \begin{pmatrix} -1/\sqrt{3} \\ -1/3 \end{pmatrix}. \tag{3.10}$$

$\mathrm{K} = \frac{1}{2}(b_1^* + b_2^*)$ and $\mathrm{K}' = -\mathrm{K}$ are the Dirac points of the graphene lattice [88]. The Haldane Hamiltonian is defined as: [88]

$$H = t \sum_{\langle i,j \rangle} |i\rangle \langle j| + t_2 \sum_{\langle\langle i,j \rangle\rangle} |i\rangle \langle j| + M\Big[\sum_{i \in A} |i\rangle \langle i| - \sum_{j \in B} |j\rangle \langle j|\Big], \tag{3.11}$$

where $|i\rangle$ denotes a state at lattice site i, and $\langle i,j \rangle$ and $\langle\langle i,j \rangle\rangle$ correspond to NN and NNN sites connected with hopping amplitudes t and t_2, respectively. The last term generates an opposite on-site energy M at the sublattices A and B. TR symmetry is broken by local magnetic fluxes (see Fig. 3.2**c**), which are designed in such way that the Aharonov-Bohm phase Φ acquired by NN hoppings is zero, whereas it is non-zero and opposite for A/B sites in case of NNN (intra-sublattice) hopping, resulting in the following substitution: [88]

$$t \to t \text{ and } t_2 \to t_2 \mathrm{e}^{i\phi}. \tag{3.12}$$

The phase Φ acquired by a non-vanishing flux during the hopping process t_2 is used as a parameter to evaluate the phase diagram of the Haldane model as function of the ratio of M and ϕ, see Fig. 3.2**d**. It comprises four different sectors with distinct Chern numbers c_1, which is 0 for $|M|/t_2 > 3\sqrt{2}\sin\phi$ and ± 1 for $|M|/t_2 < 3\sqrt{2}\sin\phi$ [88]. The system is in an insulating state with a gap magnitude of $h_z(\mathrm{K}) = M - 3\sqrt{3}t_2\sin\phi = m$ and $h_z(\mathrm{K}') = M + 3\sqrt{3}t_2\sin\phi = m'$ unless at $|M| = 3\sqrt{2}t_2\sin\phi$, where the gap is closed, which signals a phase transition accompanied by the appearance of Dirac states at the Dirac points K and/or K′[3] [88].

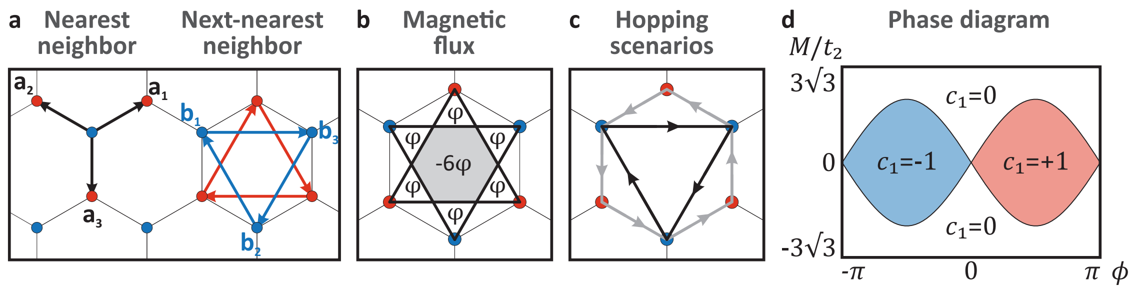

Figure 3.2 Haldane model for a honeycomb lattice with inequivalent sublattices A and B. **a** Lattice vectors in the Haldane model. NN lattice vectors a_i connecting the inequivalent sublattice atoms A and B (black arrows), and the NNN vectors b_i between equivalent species A and B (red/blue vectors). **b** Exemplary choice of the magnetic flux in the Haldane cell with $\Phi = \varphi/2$. **c** Hopping between NNN (triangular hopping path, black arrows) results in a non-zero flux, while NN hopping is associated with a vanishing flux (gray arrows). **d** Phase diagram of the Haldane model as function of M/t_2 and Φ. *Figs.* ***b*** *and* ***c*** *reproduced from Ref. [88].* *Copyright ©2013 Elsevier Masson SAS. All rights reserved.*

[3] Note that for graphene $[(M,\phi) = (0,0)]$ this phase transition occurs simultaneously at both Dirac points [88].

Edge states. Now we have a closer look on the Dirac states associated with this phase transition. Exemplary, we consider the interface of a non-trivial and trivial Haldane insulator with $c_1 = 1$ for $y < 0$ and $c_1 = 0$ for $y > 0$, respectively. Accordingly, one mass, say m at K, has to flip sign [$m(y < 0) < 0$ and $m(y > 0) > 0$ with $m(y = 0) = 0$] while the other mass $m' > 0$ at K′ remains unchanged [88]. The energy dispersion relation around K/K′ is linearized [88]:

$$H(q) = \hbar v_{\mathrm{F}} q \cdot \sigma_{2\mathrm{d}} + m\sigma_z, \tag{3.13}$$

where $q = (q_x, q_y)$ is a small wavevector around K/K′, $\sigma_{2\mathrm{D}} = (\sigma_x, \sigma_y)$, $m = h_z(\mathrm{K})$ and, for simplicity, $\hbar v_{\mathrm{F}} = 1$. As m is position-dependent, the Hamiltonian is expressed in space representation [88]:

$$H = -i\nabla \cdot \sigma_{2\mathrm{D}} + m(y)\sigma_z = \begin{pmatrix} m(y) & -i\partial_x - \partial_y \\ -i\partial_x + \partial_y & -m(y) \end{pmatrix}, \tag{3.14}$$

which, using the unitary matrix, is rotated to read as a Schrödinger equation [88]:

$$\begin{pmatrix} -i\partial_x & \partial_y + m(y) \\ -\partial_y + m(y) & i\partial_x \end{pmatrix} \begin{pmatrix} \alpha \\ \beta \end{pmatrix} = E \begin{pmatrix} \alpha \\ 0\beta \end{pmatrix}. \tag{3.15}$$

Eq. 3.15 is solved by $\Psi_{q_x}(x, y) \propto \mathrm{e}^{iq_x x} \exp\left[-\int_0^y m(y')\mathrm{d}y'\right] \begin{pmatrix} \alpha \\ \beta \end{pmatrix}$ with an eigenenergy $E(q_x) = E_{\mathrm{F}} + \hbar v_{\mathrm{F}} q_x$. This corresponds to a single chiral edge state crossing E_{F} at $q_x = 0$ with a positive group velocity v_{F}. If the interface with $c_1 = -1$ for $y < 0$ and $c_1 = 0$ for $y > 0$ is considered, a chiral left moving edge state evolves [88].

3.1.3 Quantum Spin Hall Insulators

Based on the Haldane model, C. Kane and E. Mele in 2005 described a model with spin-1/2 electrons and SOC [11, 12] that can give rise to the quantum spin Hall effect (QSHE). QSHI systems are characterized by a $\mathbb{Z}_2$ invariant in analogy to the previously discussed Chern number c_1, which is used to express the number of Landau levels in the QHE. However and in stark contrast to Chern insulators, quantum spin Hall systems comprise TR invariance [95].

Naturally, the TR operator Θ plays a crucial role. It relates the states at k and $-k$. Bloch Hamiltonians fulfilling TR invariance transform like [13, 88, 95]:

$$H(-k) = \Theta H(k)\Theta^{-1}. \tag{3.16}$$

As Θ is anti-involutive for spin $\frac{1}{2}$ particles, i.e., $\Theta^2 = -1$, TR symmetry implies the existence of two-fold degenerate eigenstates of the Hamiltonian, the so-called Kramers pairs. At certain high symmetry points of the Brillouin torus, namely the TR invariant momenta (TRIM) denoted Λ, k and $-k$ coincide under the TR operation as they are connected by reciprocal lattice vector G [13, 88].

Kane-Mele model and QSHE in graphene. Due to the spin degree of freedom, a minimal model for QSHIs consists of four bands, which are represented in a 4×4 Hermitian matrix. Hence, the basis of the vector space consists of 16 components, which are (may be) the unity matrix $\mathbb{1}$, five Dirac matrices Γ_i, $1 \leq i \leq 5$ and ten commutators $\Gamma_{ij} = \frac{1}{2i}[\Gamma_i, \Gamma_j]$ [12]. Accordingly, the (diagonal) Bloch Hamiltonian may be expressed by [12]:

$$H(k) = d_0(k)\mathbb{1} + \sum_{i=1}^{5} d_i(k)\Gamma_i + \sum_{i<j=1}^{5} d_{ij}(k)\Gamma_{ij}, \tag{3.17}$$

with the coefficients $d_i(k)$ and $d_{ij}(k)$ being symmetric and antisymmetric under $k \to -k$, respectively, such that $H(k)$ is TR invariant [12]. The Γ matrices are generated by tensor products of the spin-degree of freedom and a second degree of freedom. In the Bernevig-Hughes-Zhang model used for the prediction of the QSHE in HgTe/CdTe quantum wells, this additional degree is the orbital character associated with the lattice site [88]. However, in our study, the case of the Kane-Mele model for graphene is more relevant, where the additional degree of freedom is provided by the two sublattices A and B of the honeycomb lattice with the basis [88]:

$$(A,\, B) \otimes (\uparrow,\, \downarrow) = (A\uparrow,\, A\downarrow,\, B\uparrow,\, B\downarrow). \tag{3.18}$$

The representation of the Γ matrices is [88]:

$$\Gamma_1 = \sigma_x \otimes \mathbb{1}\ ,\ \Gamma_2 = \sigma_z \otimes \mathbb{1}\ ,\ \Gamma_3 = \sigma_y \otimes s_x\ ,\ \Gamma_4 = \sigma_y \otimes s_y\ ,\ \Gamma_5 = \sigma_y \otimes s_y\ , \tag{3.19}$$

with the Pauli matrices σ_i and s_i, which expand sublattice and spin operators, respectively. One possibility to calculate the $\mathbb{Z}_2$ invariant ν is based again on the obstruction to define a smooth gauge for the Bloch wave functions[4]. As a result of the constraints due to TR symmetry and in contrast to Chern insulators, the gauges at k and $-k$ are not independent. Consequently, the Berry curvature F and connection A around the effective Brillouin zone (EBZ), i.e., half instead of the full BZ of the VB bundle, is calculated [88, 89]:

$$\nu = \frac{1}{2\pi}\left[\oint_{\partial \mathrm{EBZ}} A - \int_{\mathrm{EBZ}} F\right] \pmod 2. \tag{3.20}$$

The resulting $\mathbb{Z}_2$ invariant ν is either 1, which constitutes an obstruction to define a continuous basis for the EBZ and signals a non-trivial topology, or 0 for a vanishing obstruction and in case of a trivial topology [88, 89].

Intrinsic vs. Rashba spin-orbit coupling. Solving Eq. 3.17 generates four bands of which two are occupied. It depends on the coefficients, specifically on the strength of SOC λ_{SO} and Rashba coupling λ_{R}, whether the system is a trivial insulator with $\mathbb{Z}_2 = 0$ or a QSHI/ $\mathbb{Z}_2$ TI ($\mathbb{Z}_2 = 1$).
To discuss the interplay of λ_{SO} and λ_{R}, we write down the explicit tight binding (TB) form of the Kane-Mele Hamiltonian [11, 12]:

[4]Refs. [88] and [89] review and compare different methods.

$$H = t \sum_{\langle i,j\rangle\alpha} c^\dagger_{i\alpha} c_{j\alpha} + i\lambda_{\mathrm{SO}} t \sum_{\langle\langle i,j\rangle\rangle\alpha\beta} \nu_{ij} c^\dagger_{i\alpha} s^z_{\alpha\beta} c_{j\beta} + \\ + i\lambda_{\mathrm{R}} \sum_{\langle i,j\rangle\alpha\beta} c^\dagger_{i\alpha} (\vec{s}_{\alpha\beta} \times \vec{d}_{ij})_z c_{j\beta} + \lambda_\nu \sum_{i\alpha} \xi_i c^\dagger_{i\alpha} c_{i\alpha}. \quad (3.21)$$

Here, the first term is the NN hopping term with hopping amplitude t. The second term arises from SOC and represents spin-dependent NNN hopping with $\nu_{ij} = \pm 1$, which depends on the orientation of the NN bonds $\vec{d}_1$ and $\vec{d}_2$ as well as on the electron spin that is represented by the Pauli matrix s^z. The third term with the vector d_{ij} between sites i and j is a NN Rashba-type SOC that stems from, e.g., the interaction with a substrate and, in contrast to all other terms, violates s^z conservation. Lastly, the fourth term accommodates a staggered sublattice potential with $\xi_i = \pm 1$, which might account for inequivalent atoms of the two sublattices (as, e.g, present in hBN) [11, 14].

The topological properties arising from the Hamiltonian in Eq. 3.21 are now discussed based on the ratio of λ_{SO}, λ_{R} and λ_ν. For $\lambda_{\mathrm{R}} = 0$, the system exhibits an energy gap with magnitude $|6\sqrt{3}\lambda_{\mathrm{SO}} - 2\lambda_\nu|$. If however $\lambda_{\mathrm{SO}} > \lambda_\nu$, the SOC is dominant and the system is a QSHI. This remains true even in the presence of the s_z violating Rashba term as long as $\lambda_{\mathrm{R}} < 2\sqrt{3}\lambda_{\mathrm{SO}}$. Similarly, the presence of a staggered potential leads to a decoupling of the two sublattices in a strong limit ($\lambda_\nu > \lambda_{\mathrm{SO}}$), leading to a trivial insulator phase. In contrast, gaps generated by the SOC term exhibit opposite signs at K and K$'$. Topologically distinct phases cannot be adiabatically transformed into each other without closing the gap, i.e., without a topological phase transition [11, 12].

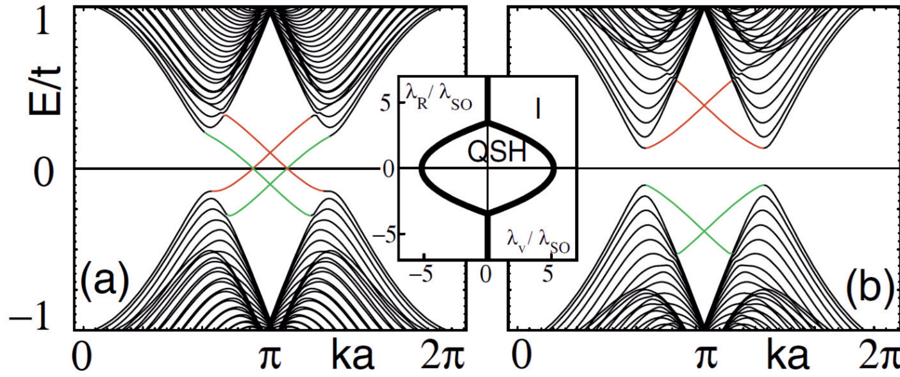

Figure 3.3 Band structure of a graphene zigzag (ZZ) nanoribbon. **a** Non-trivial and **b** trivial phase with $\lambda_\nu = 0.1t$ and $\lambda_\nu = 0.4t$, respectively. In both calculations, $\lambda_{\mathrm{SO}} = 0.06t$ and $\lambda_{\mathrm{R}} = 0.05t$. Edge states cross at π and are localized in the bulk gap in case of the non-trivial case. Colors depict the edge states localized at the two sides of the ribbon. The inset shows a phase diagram for $0 < \lambda_{\mathrm{SO}} \ll t$ as function of λ_ν and λ_{R}. *Reprinted with permission from Ref. [12]. Copyright ©2005 American Physical Society.*

Implications of a non-trivial $\mathbb{Z}_2$ phase. Now that the $\mathbb{Z}_2$ topological invariant is introduced we discuss the physical consequences associated with it. The trivial insulating phase exhibits edge states that do not traverse from valence to conduction band (CB), see Fig. 3.3**b**, such that they can be removed by a smooth deformation of the Hamiltonian without closing the band gap. These states are sensitive to backscattering. In contrast, in the QSHI phase, the system has a single pair of helical states bridging the band gap

at each edge (Fig. 3.3**a**). The helicity implies that any (single-particle) backscattering term containing a matrix element of type $\langle L, \downarrow| |R, \uparrow\rangle = 0$ will interfere destructively [14]. This property eventually causes the hallmark experimental signature of a QSHI, namely a quantized two-terminal conductance of $G_{\text{QSHE}} = \frac{2e^2}{h}$ associated with the single pair of spin-polarized edge states. As the edge states counter-propagate, there is a zero charge but non-zero spin current [13].
Moreover, the Kramers degeneracy of the edge states at the Dirac point is protected by TR symmetry, i.e., the Dirac point can be shifted in energy by smooth deformations of the Hamiltonian, but no band gap can evolve as long as only weak interactions, which do not violate TR symmetry, are present [83].
Notably, the protection from backscattering is constricted to single-particle processes and is persistent only as long as enhanced correlation effects are absent. Two-particle correlated backscattering might become relevant in case of sufficiently strong electronic interactions [97], as discussed in Sec. 3.2.

3.1.4 Realizations of Quantum Spin Hall Insulators

Despite huge efforts, the quantized conductance associated with the QSHE has been detected only in three systems up to now.

$\mathbb{Z}_2$ TI in quantum well structures. The first-ever fabricated QSHI, namely HgTe/CdTe quantum wells, see Fig. 3.4, has been grown in the group of L. Molenkamp after a prediction by B. A. Bernevig, T. L. Hughes and S.-C. Zhang [16]. The topological non-trivial

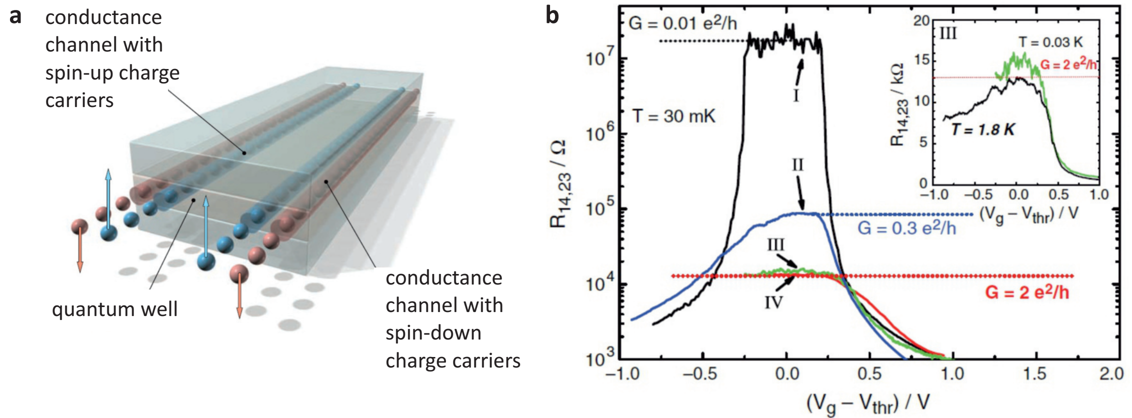

Figure 3.4 Edge channels in HgTe/CdTe quantum well structures. **a** Illustration of the helical quantum spin Hall edge channels residing at the boundary of the film. **b** Four terminal resistance for (I) normal ($d_{\text{HgTe}} = 5.5\,\text{nm}$) and (II, III, IV) inverted band ordering ($d_{\text{HgTe}} = 7.3\,\text{nm}$) as function of the gate voltage V_g at zero magnetic field and $T = 30\,\text{mK}$. The inset shows device III probed at $T = 30\,\text{mK}$ and $T = 1.8\,\text{K}$ with a linear scaling of the resistance. The corresponding Hall bar size (i.e., the distance of the contacts) is $(L \times W) = (20.0 \times 13.3)\,\mu\text{m}^2$ (I, II), $(1.0 \times 1.0)\,\mu\text{m}^2$ (III) and $(1.0 \times 0.5)\,\mu\text{m}^2$ (IV). Samples III and IV show a quantized conductance of $\frac{2e^2}{h}$. $R_{14,23}$ in sample II exhibits a too large resistance resulting from inelastic backscattering as the device dimensions exceed the inelastic mean free path. *Reprinted with permission from Ref. [17]. Copyright ©2007 American Association for the Advancement of Science.*

behavior emerges due to a band inversion in HgTe at a critical thickness $d_c > 6.3$nm [17, 98]. With a refined preparation procedure, the QSHE is observable up to $T = 15$K [99],

and by strain-engineering it is possible to increase the temperature-dependent energy gap significantly (up to $E_{\text{gap}} = 55\text{meV}$) [100]. Still, such low temperatures require to operate the device in LHe to avoid bulk excitations across the gap. Furthermore, charge puddles, i.e., local charge reservoirs, are a severe problem in HgTe, as they can cause a loss of the spin polarization [101, 102].

In a similar compound, namely InAs/GaSb quantum wells, strong indications of a helical edge state transport up to a temperature of $\approx 30\,\text{K}$ have been detected in the labs of G. Sullivan and R.-R. Du [103, 104], even though the band gap of the material is even smaller ($E_{\text{gap}} = 4\,\text{meV}$ [105]). The possibility of strong correlations in the edge states of InAs/GaSb has been investigated, as well [106].

WTe_2 as TI. Eventually, in 2018, the group of P. Jarillo-Herrero made a major step forward and measured the QSHE in monolayer flakes of $1T'$-WTe_2 encapsulated in hBN, see Fig. 3.5**a**. Again, the non-trivial band topology emerges due to band inversion with an inverted gap of $\approx 100\,\text{meV}$ magnitude. The quantized conductance is observed up to a temperature of almost $100\,\text{K}$ (Fig. 3.5**b**), rendering it accessible to measurement setups cooled with LN_2 [20]. However, the device design using flakes of hBN seems to set an intrinsic device size limit and seemingly does not allow for an automatized production process, such that the practical use of QSHIs based on WTe_2 is inherently limited.

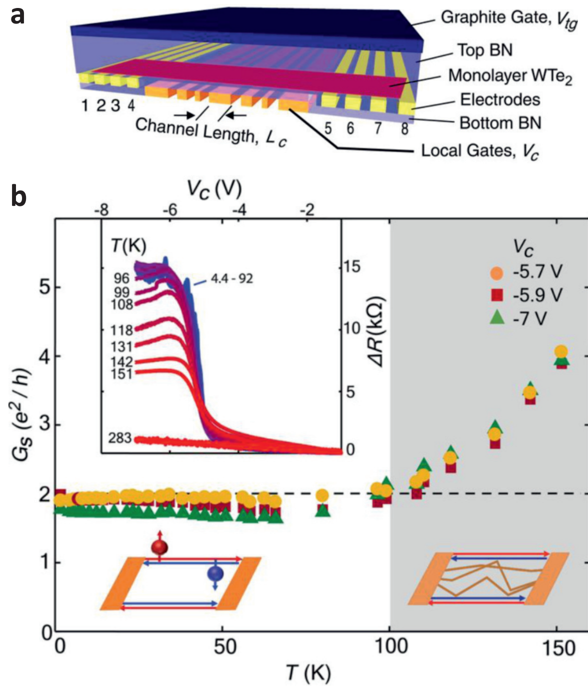

Figure 3.5 QSHE in WTe_2. **a** Device layout. The edge channel with length L_C is locally gated into the topological edge transport regime by tuning of V_C, while the rest of the material is pushed into a highly doped regime to ensure good contact with the electrodes by the top gate voltage V_{tg}. **b** The temperature dependence of the edge state conductance at different values of the gates voltage for a channel with 100 nm length reveals a quantized conductance of $\frac{2e^2}{h}$ up to $\approx 100\,\text{K}$. At higher T, bulk contributions lead to an increased conductance, as depicted in the sketch at the bottom of the diagram. The inset shows the drop of the offset resistance $\Delta R = R(V_C) - R(V_C = -1\text{V})$ plateau, i.e., the resistance change between undoped and doped regime, which is observed with increasing T due to bulk transport channels. *Reprinted with permission from Ref. [20]. Copyright ©2018 American Association for the Advancement of Science.*

Graphene and 2D Xenes. In honeycomb lattice materials it has not been possible to probe the QSHE until today for multiple reasons.

Unfortunately, the band gap of **graphene** is too small ($\approx 1\,\mu\text{eV}$) to be experimentally accessible [107, 108] because the intrinsically small SOC of the C atoms enters only as a second order term in the Kane-Mele Hamiltonian and is therefore minute.

Naturally, many groups attempted to exploit the honeycomb lattice geometry in materials "*beyond graphene*", i.e., honeycomb layers made of heavier elements, which should give

rise to substantially larger band gaps as result of an increased SOC strength. By 2020, many of these ”2D Xenes“[5] have been realized experimentally, see Fig. 3.6.
It should be noted that the synthesized 2D Xenes are not restricted to lattice formed by group IV and V elements, which are named in the following, but also include group III and VI elements or binary compounds [7]. For details beyond the scope of this short summary please consider reviews on this topic, see Refs. [5–7, 19, 109, 110].
Initially, the research community focused on group IVA elements because of their close relation to graphene. The investigated materials cover **silicene** ($E_{\mathrm{gap}} = 1.55\,\mathrm{meV}$ [111]), **germanene** ($E_{\mathrm{gap}} = 23.9\,\mathrm{meV}$ [111]), and **stanene** ($E_{\mathrm{gap}} \approx 100\,\mathrm{meV}$ [112]). Note that all of those materials, unlike graphene, cannot be exfoliated and exhibit buckling if they are not stabilized by a substrate [19].
However, the synthesized group IVA materials involve two major drawbacks. One major problem is that the topological properties are analyzed mostly for freestanding layers without accounting for interactions with the respective substrate, even though substrates may drastically affect the electronic properties, e.g., by imprinting strain on the honeycomb lattice [19]. A second problem is that many studies involve metallic substrates [19], which limits the use of spin-polarized edge states even if the honeycomb film remains in a topologically non-trivial regime. Exemplary, stanene is chosen to describe common difficulties. It has been synthesized on metallic substrates like Sb(111) [113], Ag(111) [114], and Bi_2Te_3 [115], where strain destroys the TI phase. Moreover, the fabrication on PbTe(111) [116] also did not result in a TI system as the p_z orbitals, which are highly important for the electronic properties of stanene, become passivated during growth. Lastly, flat stanene has been synthesized on Cu(111) [117]. Here, stanene exhibits a finite band gap and edge states in ribbon calculations. However, these features are far away from the Fermi level and coexisting with bulk bands [6, 117].
More recently, also graphene analogues in group VA of the periodic table moved into focus, specifically **phosphorene**, **arsenene**, **antimonene** and **bismuthene** [5, 6, 18, 109]. The latter two attracted the largest interest due to their enhanced SOC.

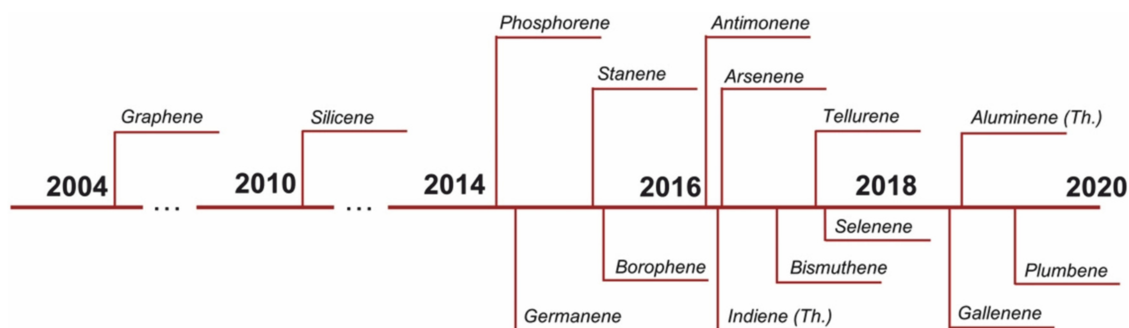

Figure 3.6 Timeline of predicted (denoted by *Th.*) and experimentally realized 2D materials. *Reprinted with permission from Ref. [5]. Copyright ©2019 John Wiley and Sons.*

The realizations of antimonene bear similar problems as the group IV-Xenes. It has been grown on Ag(111) in flat geometry [118] (metallic substrate), on Ge(111) [119] (metallic

[5]It should be noted that in literature, the use of the terms ”Xenes“ and ”graphene analogues“ is not limited to materials with a honeycomb lattice but also encloses 2D materials with different lattice symmetries.

Sb) and on $PdTe_2$ [120] (trivial insulator regime according to [121]).
"Bismuthene" and its topological edge states have been investigated in an STM study already in 2014 [122]. More precisely, the authors inspected a Bi(111) crystal, which consists of stacked, buckled Bi bilayers in ⟨111⟩ direction (see Sec. 4.1). However, Bi(111) exhibits also trivial, Rashba-split surface states, which hampers an unambiguous identification of non-trivial edge states and prohibits their use in transport devices. Fortunately, the edge states of bismuthene on SiC are localized in the band gap of the entire system, as will be detailed in Ch. 4.

3.2 Interacting Electrons in 1D: Tomonaga-Luttinger Liquid Theory

The precise description of interacting particles in solid state physics is an illimitable complex problem. Usually, however, experiments probe quantities on energy scales small compared to E_{F}, which enables a description in the framework of the Fermi liquid theory introduced by Landau in 1956 [123]. It founds on the notion of quasi-particles evolving out of a non-interacting Fermi gas by adiabatically switching on interactions. Surprisingly, these quasi-particles behave independently even in the presence of strong interactions but exhibit renormalized kinematic parameters, a finite lifetime and can be part of collective modes [123, 124].
The situation is fundamentally different in 1D electron systems, where the Fermi liquid model is generally not applicable as result of the collective character of any excitation, see Fig. 3.7. Adding a particle to a 1D system, e.g., by a tunneling tip, requires a collective propagation of all particles present along the 1D chain. This property is captured by the TLL theory. Its basic concepts are derived here, following the procedure and formulae outlined by S. Eggert in Ref. [125].

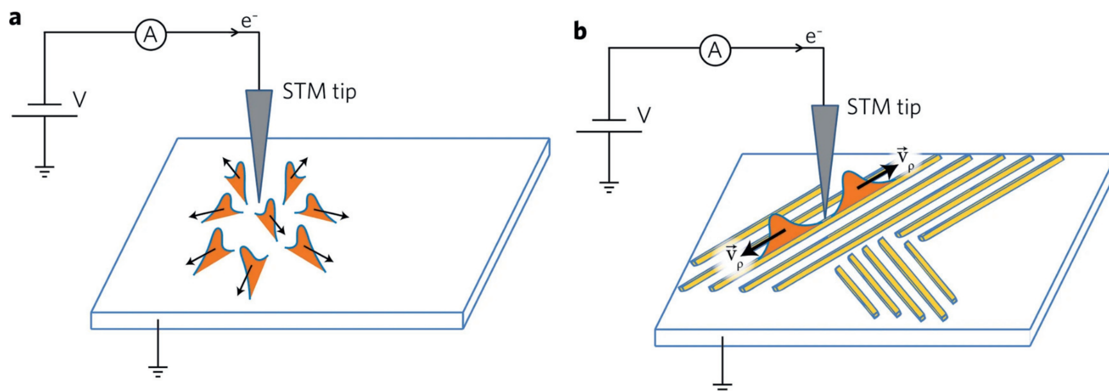

Figure 3.7 Tunneling process in **a** 2D and **b** 1D electron systems. **a** In general, the Fermi liquid description is valid in metals in 2D (and 3D). Independent quasi-particles propagate in all directions to minimize the interaction with other electrons. **b** This model fails in 1D systems, as here, any disturbance, e.g., by tunneling electrons, will cause a collective response of all particles along the chain. This requires a minimal excitation energy and leads to a suppression of the DOS at the Fermi level. *Reprinted with permission from Ref. [124]. Copyright ©2011 Nature Publishing Group.*

Bosonization. An excitation minimally comprises two particles, a particle and a hole, such that a theoretical description in terms of bosonic quasi-particles instead of fermions is expedient [123]. Any Hamiltonian can be expressed in second quantization with creation $c^\dagger_{k,\sigma}$ and annihilation $c_{k,\sigma}$ operators, where $\sigma = \uparrow / \downarrow$ denotes the spin of a state with wavevector k [125]:

$$H = \sum_{k,\sigma} \epsilon_k \, c^\dagger_{k,\sigma} \, c_{k,\sigma}. \tag{3.22}$$

For the treatment of interactions it will be useful to define a cutoff energy range around the Fermi level, among which a linear dispersion relation is approximated. In general, this might seem like a drastic simplification but the 1D bismuthene edge state scrutinized in Sec. 8.2 exhibits a fairly linear energy dispersion according to density functional theory (DFT), see Fig. 4.10. The cutoff energy is determined by a range Λ around the Fermi points $\pm k_\mathrm{F}$, and the Hamiltonian of left- and right-moving fermion with $-k_\mathrm{F}$ and $+k_\mathrm{F}$ is given by [125]:

$$H \approx \sum_{k=k_\mathrm{F}-\Lambda}^{k_\mathrm{F}+\Lambda} \epsilon_k \, c^\dagger_{k,\sigma} \, c_{k,\sigma} + \sum_{k=-k_\mathrm{F}-\Lambda}^{-k_\mathrm{F}+\Lambda} \epsilon_k \, c^\dagger_{k,\sigma} \, c_{k,\sigma}. \tag{3.23}$$

A Taylor expansion of the Hamiltonian yields the energy dispersion [125]:

$$\epsilon_k \approx \epsilon_{(-)k_\mathrm{F}} + (k \underset{(+)}{-} k_\mathrm{F}) \frac{\partial \epsilon_k}{\partial k}\bigg|_{k=(-)k_\mathrm{F}} + \mathcal{O}\big[(k \underset{(-)}{+} k_\mathrm{F})^2\big] \text{ for (left) right movers.} \tag{3.24}$$

Note that $\frac{\partial \epsilon_k}{\partial k}\Big|_{k=k_\mathrm{F}} = -\frac{\partial \epsilon_k}{\partial k}\Big|_{k=-k_\mathrm{F}} = v_\mathrm{F}$ defines the Fermi velocity. Furthermore, with $|k| < \Lambda$, it is convenient to introduce fermion operators $c^L_k = c_{-k_\mathrm{F}+k}/c^R_k = c_{k_\mathrm{F}+k}$ for left/right movers around the Fermi points $\pm k_\mathrm{F}$, which are used for definition of an effective Hamiltonian [125]:

$$H \approx \sum_{k=-\Lambda}^{\Lambda} v_\mathrm{F} \, k \, (c^{R\dagger}_k c^R_k - c^{L\dagger}_k c^L_k). \tag{3.25}$$

It is advantageous to express the particles with boson instead of fermion operators. A detailed derivation of the bosonic creation and annihilation operators, $b^{L/R\dagger}_k$ and $b^{L/R}_k$, respectively, and Eq. 3.28 is found in Ref. [125]. Boson and fermion operators are connected via [125]:

$$-i\sqrt{\frac{kN}{2\pi}} b^{R\dagger}_k = \rho^R_k = \sum_{k'} c^{R\dagger}_{k'+k} c^R_{k'} \text{ for } k > 0 \tag{3.26}$$

$$i\sqrt{\frac{kN}{2\pi}} b^{L\dagger}_k = \rho^L_{-k} = \sum_{k'} c^{L\dagger}_{k'-k} c^L_{k'} \text{ for } k > 0 \tag{3.27}$$

The operators shift all wave-vectors k' of right and left moving fermions by k. Using these operators, the Hamiltonian in Eq. 3.25 reads [125]:

$$H = \underbrace{\frac{\pi v_{\rm F}}{N}(n_R^2 + n_L^2)}_{\text{zero modes}} + \underbrace{v_{\rm F}\sum_{k>0} k\,(b_k^{R\dagger} b_k^R + b_k^{L\dagger} b_k^L)}_{\text{oscillator modes}}\,. \tag{3.28}$$

The zero modes determine the energy required to add a particle to the left-/right-moving branch and are expressed with the counting operators $n_{L/R}$, i.e., the total number of left/right movers with respect to the ground state. The oscillator modes shift a boson by the amount k. Note that $k = \dfrac{2\pi n}{N}$ denotes the level spacing of N particles.

Lastly, for discussion of electron-electron interactions, the definition of boson field operators, generated by a Fourier transform of the boson operators and describing the particle density at x, is beneficial [125]:

$$\Phi_R(x) = \Phi_0^{(L)R} + \sqrt{\pi}\frac{x}{l}n_{(L)R} + \sum_{x=1}^{\infty}\frac{1}{\sqrt{4\pi n}}\Big[e^{(\pm)iqx}b_n^{(L)R} + e^{(\mp)iqx}b_n^{(L\dagger)R\dagger}\Big], \tag{3.29}$$

where $\Phi_0^{L/R}$ are the canonical conjugate of the number operators $n_{L/R}$ and $q = \dfrac{2\pi n}{l}$. The boson field operators enable a compact expression of the Hamiltonian [125]:

$$H = a v_{\rm F}\int_0^l dx\,[(\partial_x\Phi_R)^2 + (\partial_x\Phi_L)^2], \tag{3.30}$$

with l being the length of the 1D chain. With these boson operators it is possible to solve the problem of interactions in 1D analytically.

Interactions in the spinless Luttinger liquid. The properties of 1D electrons at presence of electron-electron interactions are now inspected by introduction of the following generic density-density Hamiltonian [125]:

$$H_{\rm int} = \frac{1}{N}\sum_{k,k',\Delta k} c_k^\dagger c_{k-\Delta k}\,U(\Delta k)\,c_{k'}^\dagger c_{k'+\Delta k}, \tag{3.31}$$

where U is the interaction potential of states with wavevector difference $\Delta k = k - k'$. There are four different scattering scenarios, see Fig. 3.8, which are analyzed in the following. In general, the conclusions drawn in the following are limited to the range Λ or to states with approximately linear band dispersion as in our specific case.

Backward scattering. The scattering of left into right movers and vice versa is called backward scattering and associated with a large momentum transfer $\pm 2k_{\rm F}$, see Fig. 3.8**c**. The total momentum transfer is now expressed with a new parametrization $\Delta k = \pm(2k_{\rm F} + \delta k)$ with vanishing δk ($\delta k \to 0$) [125]:

$$H_{\rm backward} = \frac{1}{N}\sum_{k,k',\Delta k} g_1\,(\rho^R_{\Delta k}\rho^L_{-\Delta k} + \rho^L_{\Delta k}\rho^R_{-\Delta k})\,, \tag{3.32}$$

with the backward scattering amplitude $g_1 = U(2k_{\rm F} + \Delta k + k - k')$ that is assumed to be constant in the cutoff range Λ.

Forward scattering. In contrast to backward scattering, the momentum transfer is small for forward scattering ($\Delta k < \Lambda$). In particular, particles remain on the same branch before and after scattering. The interaction between particles on different branches is given by $g_2 = U(\Delta k)$ and within the same branch $g_4 = U(\Delta k)$, compare to Figs. 3.8**b** and **d**, respectively. The Hamiltonian H_{forward} reads [125]:

$$H_{\text{forward}} = \frac{1}{N} \sum_{\Delta k=-\infty}^{\infty} [g_2(\rho^R_{-\Delta k}\rho^L_{\Delta k} + \rho^L_{-\Delta k}\rho^R_{\Delta k}) + g_4(\rho^R_{-\Delta k}\rho^R_{\Delta k} + \rho^L_{-\Delta k}\rho^L_{\Delta k})] \quad (3.33)$$

$$= \frac{a}{\pi} \int_0^l dx\, [2g_2(\partial_x \Phi_R \partial_x \Phi_L)] + g_4[(\partial_x \Phi_R)^2 + (\partial_x \Phi_L)^2]. \quad (3.34)$$

In the last step, it is assumed that the scattering amplitude is momentum-independent due to a short-range potential. Obviously, in case of spinless particles, g_2 and g_1 cannot be distinguished, such that the backward scattering g_1 can be captured by proper refinement of the scattering amplitude g_2' [125, 126]. Furthermore, the structure of g_4 is contained already in the non-interacting case in form of the oscillator modes, see Eq. 3.28, and can be incorporated by a redefinition of the Fermi velocity $v_{\text{F}} \to v_{\text{F}}'$.

Eqs. 3.32 and 3.34 demonstrate the advantage of bosonization: they contain combinations of only two (bosonic) instead of four (fermionic) operators, which permits a substantially easier solution of the Hamiltonians [125].

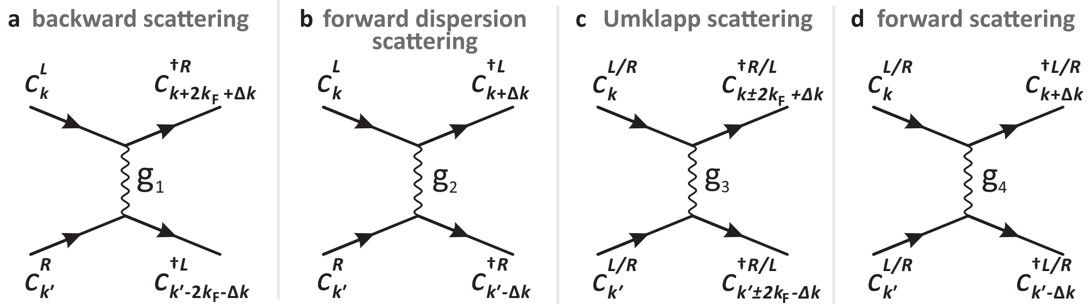

Figure 3.8 Scattering processes of electrons in a 1D system. **a** Backward scattering exchanges particles of left and right moving branch. **b** Forward dispersion scattering describes interaction between particles of left and right moving branch, as well, however the particles reside on their branch after the scattering event. Note that g_1 and g_2 are indistinguishable for spinless particles. **c** Umklapp scattering translates two particles from left to right branch or vice versa and is only relevant for half-filled bands. **d** Forward scattering of two particles on the same branch.

Umklapp scattering. The last scattering process, depicted in Fig. 3.8**c**, is the Umklapp scattering, where two left movers change into right movers and vice versa. The scattering wave vector is $\Delta k = \pm(4k_{\text{F}} + \delta k)$ and only relevant in systems with half band filling, which is why Umklapp scattering is usually neglected [123]. In our case, scanning tunneling spectroscopy (STS) and angle-resolved photoelectron spectroscopy (ARPES) data clearly demonstrate the absence of half-filling. Therefore, this process is not discussed here any further.

Bogoliubov transformation. The Hamiltonians of Eqs. 3.32 and 3.34 are re-formulated using counting operators, i.e., the Bogoliubov transformation, which reduces the problem

effectively to non-interacting particles. The Hamiltonian is then [125]:

$$H = a{v'}_{\mathrm{F}} \int_0^l dx\,\left((\partial_x \Phi_R)^2 + (\partial_x \Phi_L)^2 + \frac{2g_2'}{v_{\mathrm{F}}\pi} \partial_x \Phi_R \partial_x \Phi_L\right) \tag{3.35}$$

$$= a{v'}_{\mathrm{F}} \int_0^l dx\,\left((\partial_x \tilde{\Phi}_R)^2 + (\partial_x \tilde{\Phi}_L)^2\right), \tag{3.36}$$

and contains the backscattering process g_1 as well as the interaction g_4, which is incorporated by the renormalized velocity ${v'}_{\mathrm{F}} = v_{\mathrm{F}} + \frac{g_4}{\pi}$. In the last step, rescaled left and right mover fields are used [125],

$$\tilde{\Phi}_R - \tilde{\Phi}_L = \sqrt{K}(\Phi_L - \Phi_R) \text{ and } \tilde{\Phi}_R + \tilde{\Phi}_L = \frac{1}{\sqrt{K}}(\Phi_L + \Phi_R). \tag{3.37}$$

This finally introduces the Luttinger parameter $K = \sqrt{\frac{1 - g_2/(v_{\mathrm{F}}\pi)}{1 + g_2/(v_{\mathrm{F}}\pi)}}$ into the equations, which comprises the effect of all interactions [125].

Helical TLL. In contrast to conventional spinful TLLs, where the inclusion of the spin provides an additional degree of freedom to each particle, helical TLLs exhibit no further degrees of freedom because of the spin-momentum locking of helical particles. To account for the physical changes associated with consideration of the spin in helical TLLs, the interaction Hamiltonian (Eq. 3.31) is adapted to account for the spin degree of freedom:

$$H_{\text{int}} \rightarrow H'_{\text{int}} = \frac{1}{N} \sum_{k,k',\Delta k,\sigma,\sigma'} c^{\dagger}_{k,\sigma} c_{k-\Delta k,\sigma}\, U(\Delta k, \sigma, \sigma')\, c^{\dagger}_{k',\sigma'} c_{k'+\Delta k,\sigma'}. \tag{3.38}$$

The different scattering processes g_i, $i \in \{1, 2, 4\}$ have to be inspected separately for interacting particles with parallel spin orientation, i.e., $g_{i,\parallel}$, and with opposite spin, i.e., $g_{i,\perp}$. Note that Umklapp scattering g_3 is neglected, again.
The spin-momentum locking of the particles causes the absence of specific scattering processes, namely $g_{1,\perp/\parallel}$, $g_{2,\parallel}$ and $g_{4,\perp}$ [127, 128]. Firstly, backscattering is prohibited as it requires spin conservation while exchanging the chiral branch [127]. Secondly, forward dispersion scattering of particles with same spin orientation, $g_{2,\parallel}$, is incompatible with the helicity of the branches. Lastly, scattering on the same branch with orthogonal spins, i.e., $g_{4,\perp}$, is prohibited as well, as particles on the same branch must possess the same spin orientation [128].
Ultimately, the interactions $g_{2,\perp}$ and $g_{4,\parallel}$ are left over and the Luttinger parameter K changes to [128]:

$$K \rightarrow K^{\text{HLL}} = \sqrt{\frac{1 + g_{4,\parallel}/(v_{\mathrm{F}}\pi) - g_{2,\perp}/(v_{\mathrm{F}}\pi)}{1 + g_{4,\parallel}/(v_{\mathrm{F}}\pi) + g_{2,\perp}/(v_{\mathrm{F}}\pi)}}. \tag{3.39}$$

The implications in case of $K < 1$, i.e., repulsive interactions, are different for helical and conventional TLL. Whereas transport in ordinary TLLs is blocked by disorder or a Kondo impurity at $T = 0$ if $K < 1$, helical TLLs are more stable and circumvent single magnetic impurities as long as $K > 0.25$ [129]. A summary of the impact of further scattering scenarios on helical TLLs with varying interaction strength is provided in Ref. [129].

4 Theory of Group V-Monolayer-Substrate 2D Topological Insulators

Bismuthene on SiC represents the first realization of a new family of large gap two-dimensional topological insulators (2D TIs), which consists of a high-Z honeycomb monolayer film and a suitable substrate. In principal, the physics governing the topological transition and band gap opening is induced by the honeycomb geometry, and is not fundamentally different from graphene, the prototypical 2D system and honeycomb TI (see Sec. 3.1.3). However, bismuthene on SiC gains its intriguing properties by the beneficial influence of the substrate, which stabilizes the honeycomb layer in a planar configuration and drastically alters the electronic properties of the film. As will be explained following the description of Gang Li [18], a covalent bond between the substrate and the monolayer affects a so-called "orbital filtering", which drives the flat bismuthene lattice into a topologically non-trivial phase and allows to exploit the spin-orbit coupling (SOC) of the Bi atoms in first order [18, 130–133].This functionalization of the monolayer by the substrate constitutes a new route to tailor large-gap quantum spin Hall effect (QSHE) systems. The discussion will be limited to bismuthene on a SiC substrate. However, the description for other Gr. V elements such as As and Sb is very similar and can be found in Ref. [18].
The presence of Bi in many topological materials (pure Bi, binary/ternary compounds) results from the large SOC of the Bi valence electrons, which is a key ingredient for the occurrence of a non-trivial band topology [92, 134]. Hence, this chapter starts by a description of the properties of Bi(111) crystals. Thereafter, the properties of freestanding, single Bi layers with flat and buckled lattices are inspected, and lastly, a in-depth theoretical analysis of bismuthene on a SiC substrate is provided.

4.1 Bi(111) Crystal and Electronic Structure

Bulk Bi crystallizes in a rhombohedral structure with space group $R\bar{3}m$ [135, 136]. In its natural form, i.e., with isotope mass number $A_{\mathrm{Bi}} = 209$, it is typically considered the heaviest stable atom, although it is indeed weakly radioactive with a (very long) half-life of $(1.9 \pm 0.2) \times 10^{19}$yr [137]. Each Bi atom has the electron configuration $6s^2p^3$ and forms covalent bonds to three nearest neighbors (NNs) to attain a noble gas configuration in the outermost shell [138]. The lattice constants of the hexagonal system are $a = 4.538$ Å and $c = 11.823$Å at room temperature [139]. In $\langle 111 \rangle$-direction it forms stacks of buckled bilayers with ABCABC stacking sequence [140], see Fig. 4.1**a**, and strong intra- and weak interbilayer bonding. This is reflected in a larger bilayer distance ($d_2 = 2.347$Å) than buckling height ($d_1 = 1.594$Å) [135, 141], see Fig. 4.1**a** (side view). IV-Low-energy electron

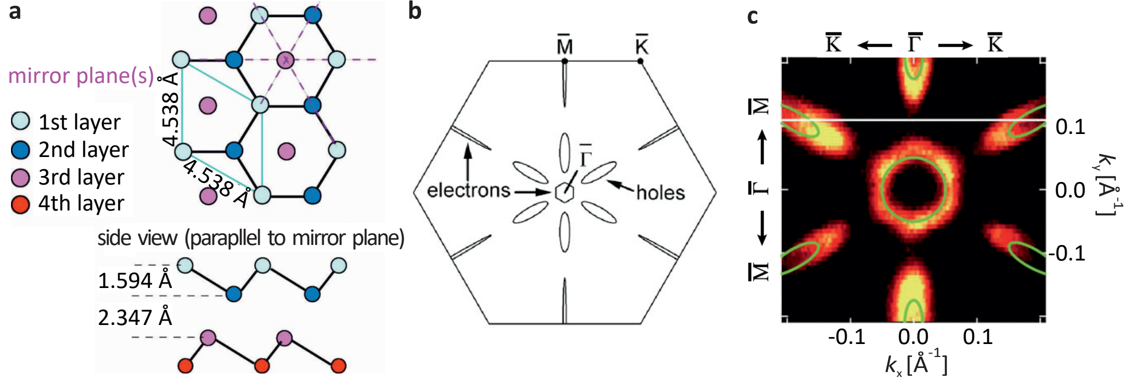

Figure 4.1 **a** Structure of truncated bulk Bi(111). Each Bi atom has covalent bonds with its three NNs (top view), forming bilayers consisting of two triangular sublattices. This produces a honeycomb-like structure [141]. The shorter intrabilayer distance and longer interbilayer distance can be seen in the side view. **b** Calculated surface BZ and **c** ARPES Fermi surface of Bi(111) at $h\nu = 21.22\,\text{eV}$. Both consist of hexagonal inner electron pocket and hole lobes in $\bar{\Gamma}\bar{\text{M}}$ direction. Green curves in panel **c** are fits to the measured band structure. *Reprinted with permission from Ref. [139] (Fig.* ***a****), Ref. [136] (Fig.* ***b****), and Ref. [142] (Fig.* ***c****). Copyright ©2005, 2003, and 2018, respectively, American Physical Society.*

diffraction (LEED) experiments confirmed that cleaved Bi crystals are terminated with intact bilayers and covalent bonds [139].

Bi(111) exhibits surface states which give rise to an enhanced conductivity but has a very low bulk conductivity ($3 \times 10^{17}\,\text{cm}^{-3}$) due to its semimetal character [135, 143]. In order to understand the mechanisms that lead to the increased surface conductivity, the calculated surface Brillouin zone (BZ) of Bi(111) and the Fermi surface probed by angle-resolved photoelectron spectroscopy (ARPES) is shown in Fig. 4.1**b**,**c**. The bands at the Fermi level, which comprise a hexagonal inner ring close to $\bar{\Gamma}$ and lobes in $\bar{\Gamma}\bar{\text{M}}$ direction, are reproduced in the band structure calculations only upon inclusion of SOC. SOC leads to a large Rashba-type spin splitting of the surface state band (black curve labeled S) in Fig. 4.2**a**. In direction $\bar{\Gamma}\bar{\text{M}}$, two bands, one with steep band dispersion (red curve labeled

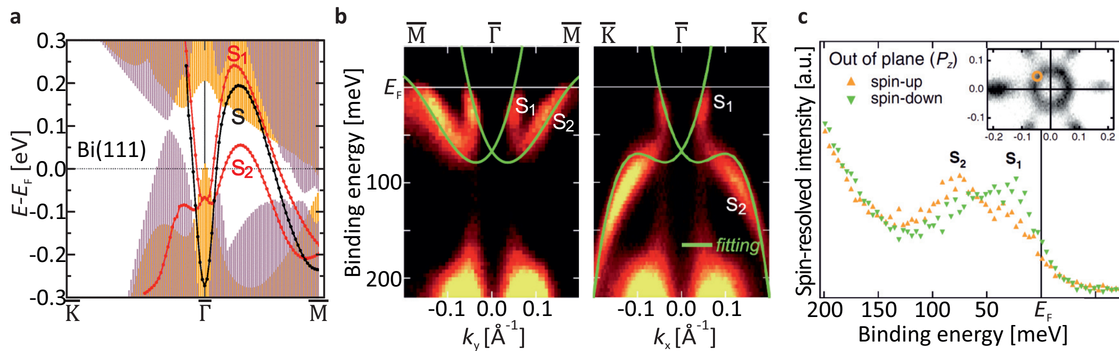

Figure 4.2 **a** Electronic structure and projected bulk band structure of Bi(111) with and without SOC. The surface states are calculated with (red) and without (black) SOC. The projected bulk bands with (yellow) and without (violet) SOC and their superposition (brown) is shown in the shaded areas. The strong impact of SOC is obvious. **b** Band dispersion of the surface state spin-split bands in $\bar{\Gamma}\bar{\text{M}}$ and $\bar{\Gamma}\bar{\text{K}}$ direction measured with ARPES at $h\nu = 21.22\,\text{eV}$. Green curves are fits to the band structure. The calculated band structure reproduces the Rashba splitting and the band dispersions very well. **c** Measurement of the out-of-plane spin polarization at the position indicated by the yellow circle in the inset. The two spin-split band S_1 and S_2 have opposite spin polarization. *Reprinted with permission from Ref. [134] (Fig.* ***a****) and Ref. [142] (Fig.* ***b****,* ***c****). Copyright ©2004 and 2018, respectively, American Physical Society.*

S_1) and a second band with lower band dispersion (red curve labeled S_2) intersect the Fermi level. Both bands are located in the projected bulk energy gap and degenerate only at the high symmetry points $\bar{\Gamma}$ and $\bar{\text{M}}$ [134–136]. Experimentally, the existence of these two surface bands is confirmed and the computed dispersions are well-reproduced, see Fig. 4.1**c** and 4.2**b**. Spin-resolved measurements (Fig. 4.2**c**) show that the two surface states S_1 and S_2 have opposite out-of-plane spin polarization while an in-plane spin polarization is not present, which is attributed to the C_{3v} crystal symmetry [142].
Already here the major influence of SOC on the electronic properties of Bi becomes apparent. We decompose the Bi(111) crystal into its individual layers and continue by examination of isolated Bi bilayers.

4.2 Freestanding Bi(111) Bilayer and Monolayer

Before inspecting bismuthene on a substrate, it is instructive to analyze the physical properties of freestanding Bi honeycomb layers in buckled and planar configuration. The physics governing both systems and their band structures are, despite their similar lattice structure, fairly different, especially in the context of topology [18].
For clarity it should be stated that the terms "bilayer" and "monolayer" are not sharply distinguished and both found in literature for a freestanding, buckled Bi(111) layer in honeycomb geometry. While the term "bilayer" is accentuating that there are two trigonal sublattices separated in z direction (compare to Fig. 4.1**a**), the term "monolayer" is emphasizing that the two sublattices are strongly bonded in a honeycomb ring and cannot be dissected from each other. In this thesis, I will name the *buckled* truncated bulk Bi(111) planes "(buckled) Bi bilayer" and a hypothetical *planar* configuration "(planar) Bi monolayer".

Freestanding, buckled Bi bilayer. The topological character of an isolated, freestanding buckled bilayer of Bi was claimed in one of the earliest papers about quantum spin Hall insulators (QSHIs) in 2006 by S. Murakami [141]. The author chose Bi as it combines many features that generally favor the existence of a 2D TI phase: (i) the honeycomb lattice that promotes a nontrivial $\mathbb{Z}_2$ invariant (in contrast to, e.g., square lattices) [11, 12]; (ii) the large spin splitting observed in the Bi surface states; (iii) the large diamagnetic susceptibility.
When reducing the number of stacked bilayers and approaching the 2D limit, Bi evolves from a semimetal to a semiconductor due to a shift of the electron pocket to higher energies, which is caused by quantum confinement [144], and has an energy gap throughout the BZ below or at a critical thickness of three bilayers [138, 140]. The theoretical analysis of the buckled Bi bilayers reveals an odd $\mathbb{Z}_2$ invariant [141, 145]. Consequently, ribbon calculations demonstrate the presence of a pair of spin-polarized edge states connecting the valence band (VB) to the conduction band (CB) [18, 140, 141]. Both p_x/p_y-derived σ orbitals and p_z-derived π orbitals are present and stabilize the isolated buckled Bi bilayer according to density-functional theory (DFT) [18, 146].
The emergence of one-dimensional (1D) edge states in buckled Bi bilayers is the consequence of a SOC-driven inversion of the VB and CB parities [18, 147]. Note that already

without SOC a buckled Bi bilayer has a direct band gap at Γ that is retained after SOC is considered in the calculations, see Fig. 4.3**a** [18, 147]. However, the orbital character of the bands is modified by SOC. This effect is most pronounced at Γ, where the main orbital contribution in presence of SOC originates from s orbitals in the VB and p orbitals in the CB, which is opposite without SOC, compare Fig. 4.3**b**,**c**. The same inversion takes place for the p_x/p_y and p_z orbitals [146]. Moreover, SOC causes touching bands to split in energy, and the band positions and dispersions are renormalized.

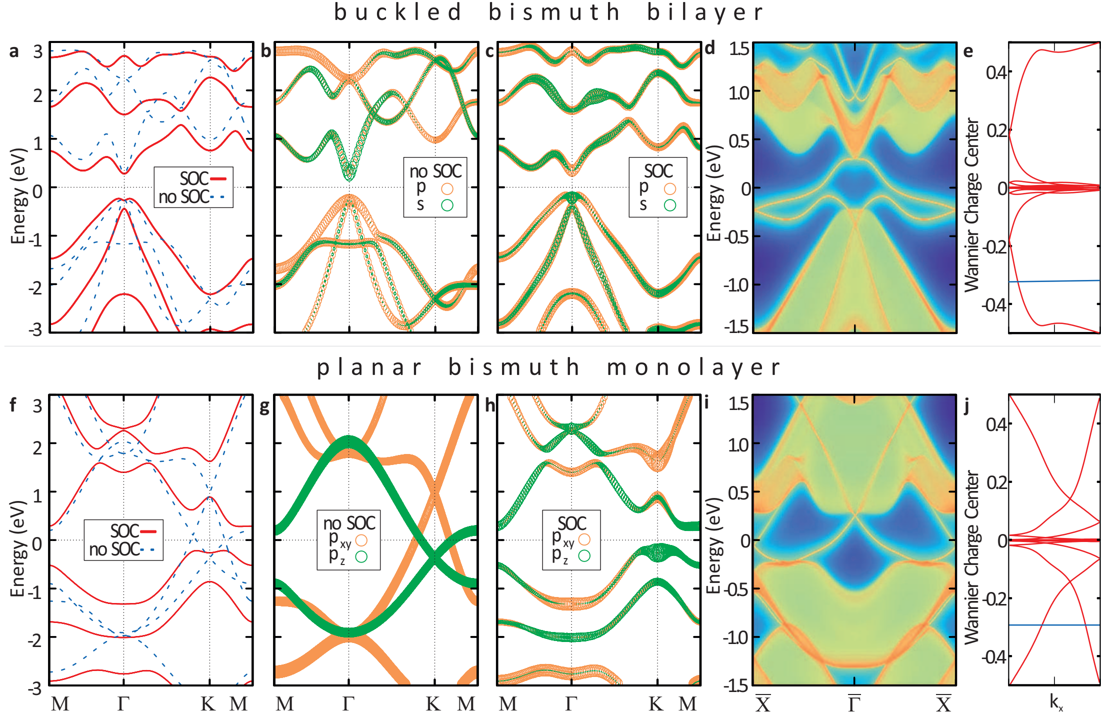

Figure 4.3 **a** Band structure, orbital character **b** without and **c** with SOC, **d** ZZ nanoribbon and **e** Wannier charge center calculation for a freestanding buckled Bi bilayer. **f-j** Same quantities as before but for a planar Bi monolayer. The two configurations exhibit a completely different band structure and orbital composition around E_{F}. **a** The energy gap of buckled bilayer Bi is found at Γ and present already without the inclusion of SOC. **b**, **c** Yet, the orbital character at Γ is changing and an inverted band structure is generated with presence of SOC. **g** In case of a freestanding, planar Bi monolayer no band gap but two bands with linear dispersion originating from p_z and p_x/p_y orbitals are observed at the Fermi level without SOC. **h** Accounting for SOC opens a band gap at K. **d**, **i** Edge states are generated in a ZZ nanoribbon calculation for both configurations. However, their topological character is different: a Wilson loop analysis shows **e** an odd number of crossings of a (blue) reference line with the Wannier charge centers (red line) in case of a buckled bilayer, but **j** an even number for the planar Bi monolayer. *Adapted from Ref. [18].*

Freestanding, planar Bi monolayer. Fig. 4.3**f-i** show the band structure and orbital decomposition of a freestanding, planar Bi monolayer. A comparison to the buckled Bi bilayer immediately reveals fundamental differences. Firstly, the system does not possess an energy gap in absence of SOC in the DFT calculations. Instead, two Dirac-like, crossing bands are present at the K point (blue dashed lines in Fig. 4.3**f**), which remind of the band structure of graphene [148]. The orbital projection reveals that the lower and upper crossing of bands arises from p_z and p_x/p_y orbitals, respectively (see Fig. 4.3**g**). Inclusion of SOC causes strong modifications of the band structure. Most importantly, it introduces a band gap around the Fermi level and mixes p_x/p_y and p_z orbitals, see Fig. 4.3**h**. A

camelback-like band dispersion in the VB and CB is replacing the Dirac-like bands at K (red line in Fig. 4.3**f**). An indirect band gap is defined by the VB maximum (VBM) and CB minimum (CBM) at K and M, respectively. Inversion symmetry is preserved both for the buckled bilayer and the planar monolayer, such that all bands are Kramers degenerate at every k point [18].

Edge states for freestanding, single Bi layers. Both the buckled and planar configuration host zigzag (ZZ) edge states, see Fig.4.3**d** and **i**, respectively. The buckled Bi bilayer is in a QSHI phase with $\mathbb{Z}_2 = 1$, as mentioned above, which is confirmed by an odd number of crossings of the Wannier charge center at a reference line [149, 150] (see Fig. 4.3**e**). In contrast, the planar Bi monolayer is in a trivial phase ($\mathbb{Z}_2 = 0$) with an even number of crossings (Fig. 4.3**j**) [18]. A comparative analysis in Ref. [132] analyzes the valence electron orbitals of the bands around E_F and provides a handwaving explanation for the different topology of buckled and planar Bi layers. While the existence of either p_z or p_x/p_y orbitals in a honeycomb lattice gives rise to a non-trivial topology with $\mathbb{Z}_2 = 1$, which can be described in the two-band Kane-Mele [11] and a four-band model [130], respectively, the combination of both models causes a trivial phase as an even number ($\mathbb{Z}_2 = 0$) results from the summation of two odd numbers [132].
Zhou et al. (Ref. [132]) offer two possible solutions to attain a topologically non-trivial phase: (i) use buckled Bi bilayers, or (ii) remove either p_x/p_y or the p_z orbitals from the low energy band structure. This so-called "orbital filtering" may be accomplished by a covalent bond between the Bi p_z and another half-filled orbital (which could be a H atom in the easiest case). This mechanism plays a pivotal role for bismuthene on a SiC substrate [18], and is therefore discussed in detail in the following.

4.3 Planar Bismuthene on a SiC Substrate

After the discovery of graphene, the modification of the low-energy electronic orbitals was first discussed in the context of ultracold atom optical honeycomb lattices in 2007 [151, 152], but only in 2014 in the context of QSHIs [130]. Since then, orbital selection or filtering mechanisms are proposed as promising way to tune the electronic properties and to enhance the size of the topological gap in numerous theoretical papers about group IV and V honeycomb lattices. The review articles in Refs. [19, 110, 153] discuss different methods of functionalization. This key word mostly denotes chemical adsorption of atoms and molecules on thin films [112, 154–158], though a less concise view includes external electric fields [130] and strain [138, 159], as well. Most of the studies have been carried out for freestanding layers that are functionalized with halogen atoms or hydrogen. In contrast, the idea to use a substrate to achieve the desired orbital situation was sparsely investigated, even though a substrate combines all the above-mentioned effects: it might form bonds with the film orbitals, implies the presence of an electric field gradient and imposes a lattice strain. Only recently some predictive studies involving a substrate in the calculations have been published [18, 131–133, 146, 160].
A suitable substrate for a QSHI material should fulfill at least two key properties: (i) its lattice constant and symmetry must match to the 2D adlayer, (ii) it should possess an

energy gap, i.e., it should be a semiconductor or insulator, such that charge transport occurs via the QSHI's helical edge states only.

To indentify candidate substrates for bismuthene, its lowest energy lattice constant is computed with DFT as a first step. Fig. 4.4**a** shows the total energy of a planar Bi monolayer (red triangles) and of a freestanding buckled Bi bilayer (black dots) with the corresponding buckling distance (blue squares) as function of the lattice constant. The strain (top horizontal axis) is calculated in reference to the lattice constant of a three-dimensional (3D) bulk Bi crystal. It can be seen that the buckled bilayer has the lowest total energy up to a lattice constant of ≈ 5 Å. This changes at the energy minimum of the planar film at $a_{\text{Bi-PL}} = 5.27$ Å, where the formation of a planar honeycomb film becomes energetically more favorable. At very large lattice constants ($a \gtrapprox 5.5$ Å) the buckling collapses and only the planar lattice configuration exists.

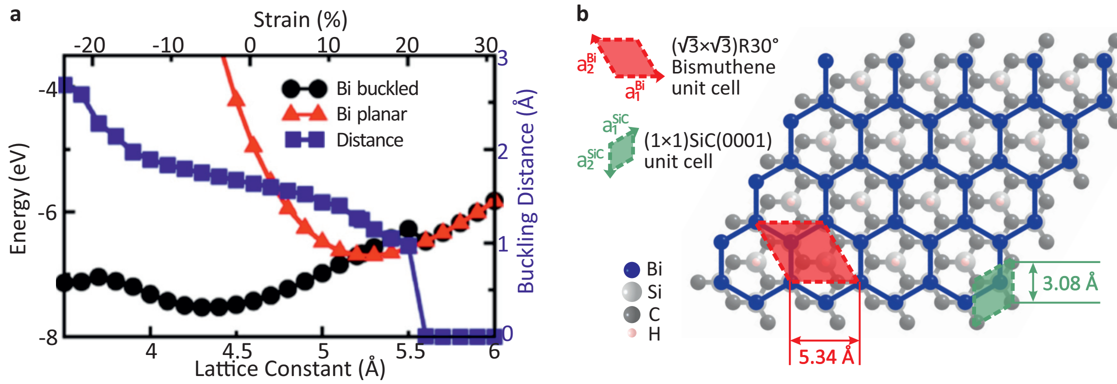

Figure 4.4 **a** Calculated total energy for a freestanding Bi film in buckled (black circles) and planar (red triangles) configuration. The buckling distance of the film is shown by blue squares. The total energy of the buckled and planar film exhibit a local minimum at $a_{\text{buckled}} = 4.33$ Å and $a_{\text{planar}} = 5.27$ Å, respectively [131]. A planar configuration is energetically favorable for large lattice constants ($a > 5.2$ Å). The strain is given in reference to the 3D bulk Bi crystal lattice constant. **b** A $(\sqrt{3} \times \sqrt{3})$-reconstruction on a 4H-SiC substrate has a lattice constant of $a_{\text{rt3-SiC}} = 5.34$ Å and is close to the minimum of the planar configuration. For clarity only the first SiC layer is shown in the top view. The side view shows that the Bi layer is positioned 2.75 Å above the SiC substrate and forms bonds with the Si dangling bond (DB). The unit cells and vectors are shown in red and green for bismuthene and SiC, respectively. *Fig.* ***a*** *adapted from Ref. [121] under a Creative Commons 3.0 License (CC BY 3.0 [161]). Fig.* ***b*** *from Ref. [162]. Reprinted with permission from AAAS.*

An initial study for Bi bilayers as well as Bi monolayers on various semiconducting or insulating substrates has been carried out by Huang et al. Ref. [160]. It claimed that hBN is suitable to stabilize a topological bilayer phase due to its weak interaction with the Bi film. Further proposals to realize bismuthene were provided by Zhou et al. [132, 133]. They use a Si(111) substrate patterned with H or halogen atoms, which prevent a substrate reconstruction, and place Bi atoms in a $(\sqrt{3} \times \sqrt{3})$ geometry on it. Before the Bi atoms may adsorb, the H or halogen atoms must be selectively removed, which, according to the authors, could be accomplished with a scanning-tunneling microscopy (STM) tip. It is obvious that this method does not allow to grow films larger than few nanometers. Leaving the experimental impracticality of these proposals aside, these papers provide an important step towards a realization of planar bismuthene, as the orbital filtering mechanism via a substrate is discussed for the first time. Finally, in 2015, SiC was identified as a suitable substrate to stabilize a QSHI phase of bismuthene [131].

Lattice structure. The geometric structure of a Bi monolayer on a SiC(0001) substrate is shown in Fig. 4.4**b**. The Bi atoms adopt a $(\sqrt{3} \times \sqrt{3}R30°)$ reconstruction with a lattice constant of $\sqrt{3}a_{\mathrm{SiC}} = a_{\mathrm{Bi.ene}} = 5.34\,\text{Å}$ on the substrate ($a_{\mathrm{SiC}} = 3.08\,\text{Å}$ [163, 164]), which is close to the calculated minimum total energy of the planar Bi monolayer. In particular, the planar configuration is energetically favorable at this atom spacing. The stabilization by the substrate ensures that the planar configuration is maintained, even though the buckled bilayer has overall a lower total energy.

The bismuthene unit cell and primitive vectors (red rhombus and arrows in Fig. 4.4**b**) are rotated by 30° with respect to the (1×1)-SiC unit cell and primitive vectors (green rhombus and arrows in Fig. 4.4**b**). The honeycomb lattice is composed of two triangular Bi sublattices offset by $\vec{a}_{\mathrm{i}}^{\mathrm{SiC}}, i = 1, 2$. The substrate is Si terminated and each Si atom has a half-filled orbital or DB that is created by the truncation of the surface. The adsorbed film has minimal energy when the Bi atoms are placed on the $T1$ site, i.e., directly on top of the Si atom [160]. This scenario favors the formation of a covalent bond between Bi and the surface Si atoms, such that the Si DB is passivated. The calculated Bi-Si distance after full relaxation is $2.75\,\text{Å}$ [162].

As evident in Fig. 4.4**b**, only two out of three Si DBs are saturated by Bi atoms while the remaining DB is passivated with H in the calculations [131, 160, 162]. The purpose of this technical trick is to avoid that the half-filled Si orbitals generate an artificial metallic band at the Fermi level. Photoemission measurements demonstrate that, in reality, the DBs on the SiC surface occupy a flat band at $\approx 1.8\,\mathrm{eV}$ binding energy, which is likely the result of a Mott-Hubbard metal-to-insulator transition [27, 165]. DFT, however, cannot account for any correlation effects and would predict metallic states. Note that the incomplete coverage supports the growth of three different, inequivalent bismuthene domains, which is discussed in Secs. 6.2 and 6.3, and investigated in detail in Sec. 7.3.1.

BZ and band structure. Based on this lattice model, the band structure of bismuthene on SiC has been computed by Gang Li and is shown in Fig. 4.5**a** along a path between the high symmetry points M-Γ-K-M (indicated by the turquoise line in Fig. 4.5**f**), first without accounting for SOC effects. Fig. 4.5**f** shows the hexagonal (1×1) surface BZ of SiC (white hexagon) and the $(\sqrt{3} \times \sqrt{3})R30°$ BZ of the Bi monolayer (blue hexagon), in which the high symmetry points of the hexagonal lattice Γ, M and K/K′ are marked with blue letters.

It was obtained by first-principle DFT [162] using a slab as shown in Fig. 4.4**b** consisting of bismuthene on top of two SiC bilayers. All remaining SiC DBs are passivated with H and at least 20Å of vacuum after the slab are included. The DFT calculation has been carried out in the framework of the Vienna Ab-Initio Simulation Package [166] using the projector augmented-wave method [167] and the generalized gradient approximation (GGA) functional in the parameterization of Perdew, Burke and Ernzerhof (PBE) [81], compare to Sec. 2.5. The bismuthene in-plane lattice constant has been fixed at $5.34\,\text{Å}$ in the calculations, while all other positions have been fully relaxed until the residual forces were smaller than $10^{-3}\,\mathrm{eV/Å}$.

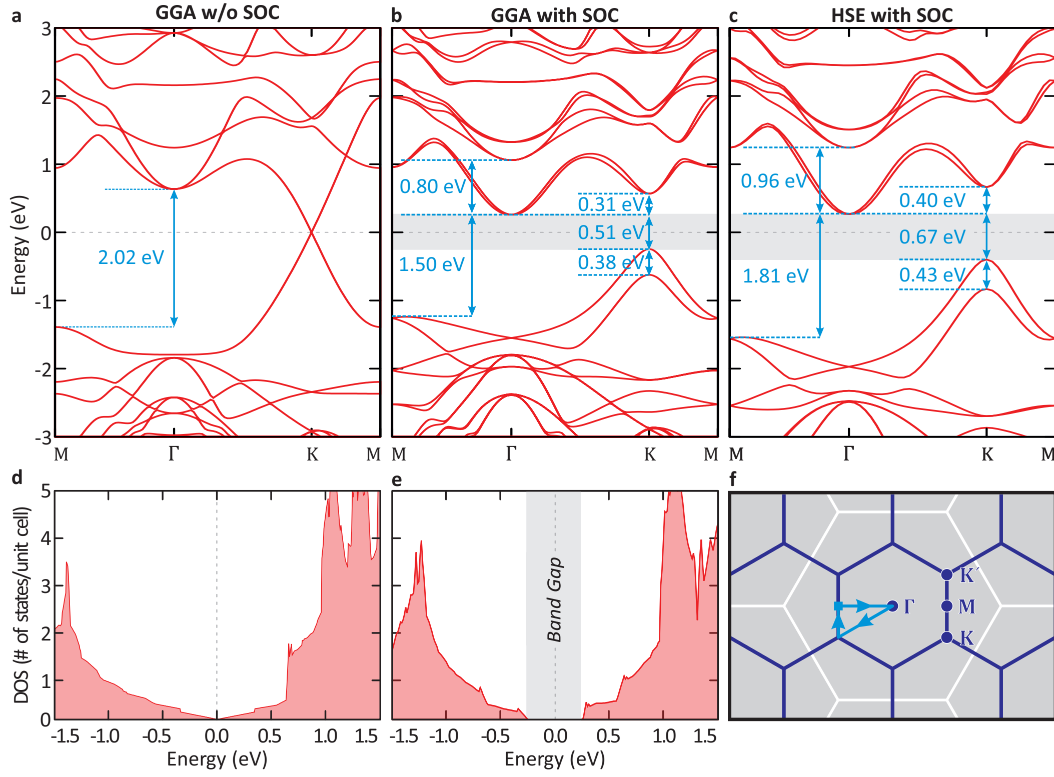

Figure 4.5 **a-c** DFT-computed band structure of bismuthene on SiC with different exchange functionals. **a**, **b** Band structure and **d**, **e** corresponding DOS obtained by use of the GGA exchange functional without and with SOC, respectively. Without SOC, a linear, Dirac-particle-like band dispersion at K is visible, which vanishes upon inclusion of SOC. An indirect band gap emerges and several formerly degenerate bands are split in energy, most clearly seen at the VBM at K. **c** Band structure calculated with the HSE hybrid exchange functional. Characteristic band apparent already in **b** are maintained but the band dispersion and binding energies are rescaled. **f** BZ of the $(\sqrt{3} \times \sqrt{3})$-reconstructed bismuthene layer (blue hexagon) with high symmetry points and (1×1) surface BZ of SiC (white hexagon). The turquoise arrows indicate the pathway shown in **a-c**. All calculations performed by Gang Li [168]. *Fig.* ***a-c*** *from Ref. [162]. Reprinted with permission from AAAS. Fig.* ***d, e*** *by courtesy of Gang Li [168].*

Band structure without SOC. All low-energy bands can be attributed to the Bi layer [131]. The parabola-shaped bands at ≈ -2 eV energy and Γ as well as the bands around M and at ≈ 1 eV are SiC-derived [169]. At the Fermi level, Dirac-like bands cross at the K point. Such a band dispersion is a fingerprint of a flat honeycomb structure and generated by the lattice symmetry (see also Sec. 4.5).

Band structure with SOC. The inclusion of SOC leads to strong modifications of the band dispersions, see Fig. 4.5**b**. Most importantly, the crossing states with linear energy dispersion vanish and give rise to a large (direct) band gap of ≈ 0.82 eV at K. The fundamental energy gap (visualized by the gray area in Fig. 4.5b) is indirect due to the CBM at Γ and slightly smaller ($\Delta_{\text{gap}}^{\text{GGA}} \approx 0.51$ eV). Secondly, band degeneracies are lifted, most prominently in the VBM at the K point, where the VB splitting amounts to $\Delta_{\text{R}}^{\text{GGA}} = 0.38$ eV (indicated by the turquoise dashed lines in Fig. 4.5**b**. Another large splitting (0.80 eV) is found in the unoccupied states at the CBM around Γ.

It is well-known that pure DFT underestimates band gap magnitudes [170, 171]. Hence, Gang Li additionally performed calculations using the Heyd-Scuseria-Ernzerhof (HSE) hybrid functional that uses a screened Coulumb potential to include the long-range part

of the Hartree-Fock exchange correlation [82], thereby enabling a better comparison to experimentally detected band gap and band splitting magnitudes. The HSE band structure is shown in Fig. 4.5**c**. Its characteristic features are identical to the GGA band structure calculation in Fig. 4.5**b**. However, the inclusion of the Hartree-Fock exchange affects a renormalization of all band positions. The magnitude of the rescaled energy gap is $\Delta_{\text{gap}}^{\text{HSE}} = 0.67\,\text{eV}$, and the VB splitting is enlarged to $\Delta_{\text{R}}^{\text{HSE}} = 0.43\,\text{eV}$.

DOS. The corresponding density of states (DOS) without and with SOC is displayed in Fig. 4.5**d** and **e**, respectively. Without SOC, a linearly increasing DOS is observed in both directions around the Fermi level. When accounting for SOC, a sharp increase of the DOS is reflecting the vanishing band dispersion around the VBM at low binding energies. In the same way, the minima at Γ and K in the CB give rise to two jumps of the DOS.

Comparison to freestanding, single Bi layers. A comparison of bismuthene on SiC substrate to freestanding, single Bi layers in Fig. 4.3 demonstrates that the monolayer/substrate systems behaves fairly different from unsupported layers and emphasizes the need to involve the substrate when aiming for a reliable description of the electronic properties of monolayers. While the CB dispersion of bismuthene on SiC reminds of the buckled Bi bilayer (see Fig. 4.3**a**), the VB dispersion of both structures is completely different and is rather similar to the planar Bi monolayer in Fig. 4.3**f**, although there, the VBM is not found directly at K but next to it.

4.4 Spin-Orbit Coupling in Bismuthene on SiC

The physical mechanisms generating the characteristic features of bismuthene on SiC can be well understood by comparison to complementary DFT studies. The two key properties of the band structure upon inclusion of SOC are: (i) a band gap at the K point with $\approx 1\,\text{eV}$ magnitude, and (ii) the of splitting of formerly degenerate bands. These properties can be reproduced by hydrogenation of a freestanding Bi honeycomb layer.

Rashba splitting. To understand the emergence on the band splittings we inspect the band structures calculated for two- and one-sided "bismuthane", see Fig. 4.6**a** and **b**, respectively. Importantly, the lattice constant for the hydrogenated Bi monolayers is identical to the lattice constant of bismuthene on SiC, i.e., $a = 5.34\,\text{Å}$ [131]. Therefore, differences/similarities can be ascribed to the presence and different H configurations. The band dispersions of the hydrogenated monolayers bear resemblance to bismuthene on SiC. The VB width in the BZ is small except for the pronounced maximum around K. Minima in the unoccupied states are at Γ and at slightly higher energy at K. A clear difference between the bismuthanes in Fig. 4.6 and bismuthene on SiC is evident regarding the parabola-shaped hole-like bands at Γ and at $\lessapprox -2\,\text{eV}$ energy in Fig. 4.5**b** and **c**, as they originate from SiC orbitals [131].

Differences between the two hydrogenated monolayers are found regarding their band degeneracy. While no band splitting is evident for the two-sided hydrogenated monolayer, bands with opposite spin character (red and green color in Fig. 4.6) possess different

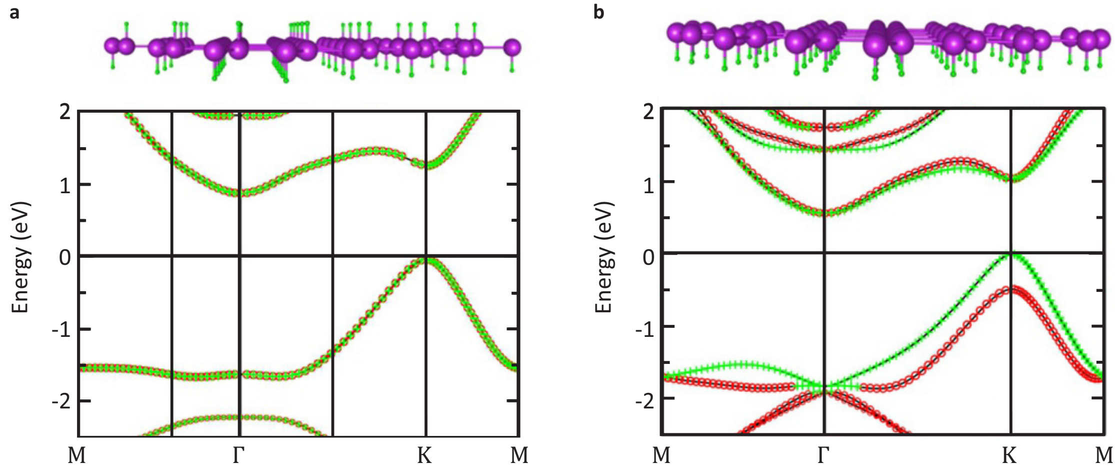

Figure 4.6 **a** Band structure for **a** two-sided and **b** one-sided bismuthane obtained by DFT calculations using the GGA exchange functional (including SOC). The in-plane lattice constant is fixed at 5.34 Å. The lattice geometry is shown in the top panels, and the spin character of the bands is encoded in red and green colors. **a** For two-sided bismuthane, H atoms are alternately placed on both sides of the Bi layer in contrast to one-sided bismuthane, where H atoms are on one side only. The band structure of both structures is very similar to bismuthene on SiC. However, split bands emerge only in one-sided bismuthane, suggesting that they originate from the broken inversion symmetry. *Adapted from Ref. [131] under a Creative Commons License (CC BY 3.0 [161]).*

energy expectation values for one-sided bismuthane. The magnitude of the band offsets are comparable to the magnitudes observed for bismuthene on SiC [131].

The only difference of two- and one-sided bismuthane is their different symmetry due to the ordering of the H atoms. Two-sided bismuthane conserves inversion symmetry, which is broken in one-sided bismuthane and bismuthene on SiC. This causes the appearance of the Rashba splitting [132]. The covalent bond between Bi and the substrate vitually acts like an extrinsic electric field on the bismuthene layer, making top and bottom face inequivalent [18, 107]. The overall reduced energy gap of one-sided (≈ 0.5 eV) with respect to two-sided (≈ 1 eV) bismuthane is a consequence of this Rashba splitting [11, 107, 131].

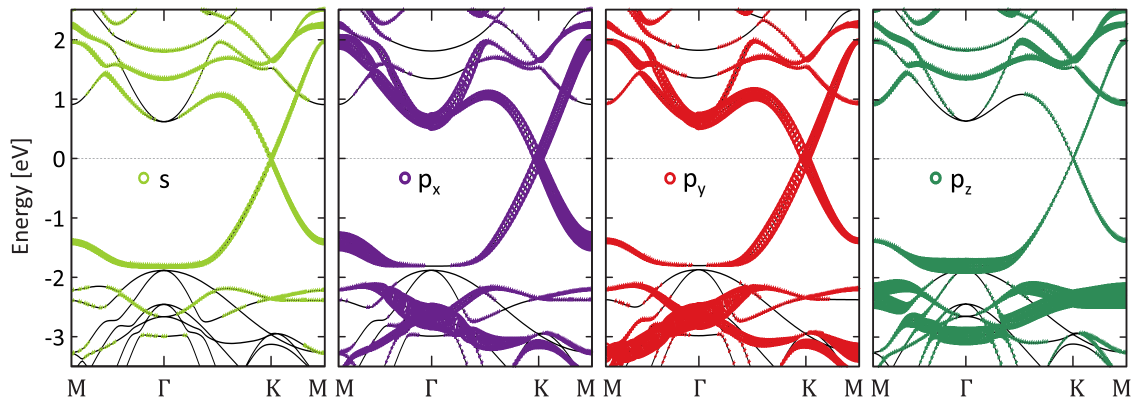

Figure 4.7 Projection of the orbital character of the low-energy electronic structure for bismuthene on SiC(0001). The size of the colored symbols corresponds to the relative weight of the respective orbital. Bands shown with black lines originate from the SiC substrate. The calculation is carried out without SOC. It demonstrates that σ-type bonds formed by hybridized s, p_x and p_y orbitals are dominant at K and close to E_F. The p_z orbital is pushed to higher binding energy due to the covalent bond with the Si substrate. Calculation by Gang Li [168]. *From Ref. [162]. Reprinted with permission from AAAS.*

Magnitude of the energy gap. Fig. 4.7 shows the decomposition of the low-energy bands of bismuthene on SiC into contributions from the Bi 6s and 6$p_{x,y,z}$ valence orbitals. The circle size corresponds to the relative weight of the orbital. Note that SOC is not included in these calculations, which results in a Dirac-like band dispersion at the Fermi level. The bands in vicinity of the K point are mainly derived from p_x and p_y orbitals with some minor contribution of the s orbital. They hybridize and form sp^2-type orbitals, leading to σ bonds in the plane of the bismuthene lattice [18, 146, 162]. In contrast, the p_z orbital and π bonds, which give rise to the bands at low energies in graphene, are not present at the Fermi level but shifted to significantly higher binding energy ($E - E_\mathrm{F} \approx -2\,\mathrm{eV}$). This is a result of the covalent bond to the substrate's Si DBs (or, likewise, to H in the case of bismuthanes), which pull the p_z orbitals to higher binding energy [18, 131, 132, 146, 162].
This constitutes the orbital filtering mechanism discussed in Sec. 4.2 and proposed by Zhou et al. ([132]), resulting in a four-band honeycomb lattice. To confirm its non-trivial topology, Gang Li checked that the Bloch wave functions cannot be smoothly defined along a closed path in half of the BZ, but must be described on separate sections, which are linked by the Berry connection, see Sec. 3.1. For a QSHI, the number of windings of the Berry connection along a non-contractable path is odd [172]. The numerical BZ is discretized into patches to extract the winding number [18, 162, 173], and the Berry connection is calculated around the boundary of each as shown in Fig. 4.8**a**. The analysis yields that $\mathbb{Z}_2 = 1$ for bismuthene on SiC, which confirms that the system is a QSHI [162].

SOC in graphene. In Fig. 4.5**c**, we have seen that the energy gap of bismuthene on SiC is tremendously enhanced in comparison to graphene (by a factor of 10^6 [174]), which can be understood by analysis of the SOC processes in both systems. At the K point, the bands of graphene and other flat honeycomb structures formed by group IV elements are composed of p_z orbitals. First-order, on-site SOC requires a spin-flip of electrons and therefore occurs only between different orbitals. Hence, it is absent for the p_z/π orbital of graphene. Moreover, the NN SOC of the π orbitals is not present due to a vertical reflection plane along the NN carbon atoms [174, 175]. Hence, SOC in graphene comes into play only as a second order process between next-nearest neighbors (NNNs) [11, 107], as illustrated in Fig. 4.8**b**. It is described by [175]:

$$|p^A_{z\uparrow}\rangle \overset{\xi_0/\sqrt{2}}{\rightarrow} |p^A_{+\downarrow}\rangle \overset{V}{\rightarrow} |s^B_{\downarrow}\rangle \overset{V}{\rightarrow} |p^A_{+\downarrow}\rangle \overset{\xi_0/\sqrt{2}}{\rightarrow} |p^A_{z\uparrow}\rangle\,, \tag{4.1}$$

$$|p^B_{z\downarrow}\rangle \overset{\xi_0/\sqrt{2}}{\rightarrow} |p^B_{-\uparrow}\rangle \overset{V}{\rightarrow} |s^A_{\uparrow}\rangle \overset{V}{\rightarrow} |p^B_{-\uparrow}\rangle \overset{\xi_0/\sqrt{2}}{\rightarrow} |p^B_{z\downarrow}\rangle\,, \tag{4.2}$$

where $|k^i_{\alpha\beta}\rangle$ denotes an electron in orbital $k_{(\alpha)}$ with spin $\beta = \uparrow / \downarrow$ and on sublattice $i = A/B$. Linear combinations of p_x and p_y orbitals form $|p_+\rangle = -\frac{1}{\sqrt{2}}(p_x + ip_y)$ and $|p_-\rangle = \frac{1}{\sqrt{2}}(p_x - ip_y)$. The SOC constant ξ_0 is the value obtained for coupling of the C 2p_x and 2p_z orbitals ($\xi_0 = 4\,\mathrm{meV}$) and V is the NN hopping amplitude [155, 175]. The entire SOC process can be deconvoluted into on-site SOC of the low-energy π and the high-energy σ orbitals, two consecutive hopping processes with strength V to a NNN, and another coupling of π and σ orbitals [175]. As SOC occurs twice, the process amplitude is scaled with ξ_0^2, resulting in an experimentally inaccessible band gap of $10^{-3}...10^{-2}$ meV [174, 175].

SOC in multiorbital honeycomb lattices. In a multiorbital low-energy Hilbert space, as present in bismuthene on SiC, different SOC processes are feasible. Here, the bands that form a Dirac cone at K without SOC are generated by the p_x and p_y orbitals. The availability of two orbitals per site enables on-site SOC, as sketched in Fig. 4.8**b**:

$$|p^A_{+\uparrow}\rangle \overset{\lambda_{\text{SO}}}{\to} |p^A_{+\uparrow}\rangle\,,\; |p^A_{+\downarrow}\rangle \overset{-\lambda_{\text{SO}}}{\to} |p^A_{+\downarrow}\rangle\,, \tag{4.3}$$

$$|p^B_{-\uparrow}\rangle \overset{-\lambda_{\text{SO}}}{\to} |p^B_{-\uparrow}\rangle\,,\; |p^B_{-\downarrow}\rangle \overset{\lambda_{\text{SO}}}{\to} |p^B_{-\downarrow}\rangle\,. \tag{4.4}$$

Here, λ_{SO} denotes the effective SOC strength. SOC takes place only once, making it a first-order process. Moreover, the coupling does not necessitate hopping to a NN or NNN, but occurs on-site. Lastly, the atomic SOC of Bi is 1.25 eV [176], resulting in an effective on-site SOC λ_{SO} on the order of ≈ 1 eV for the functionalized Bi monolayers [18, 155].

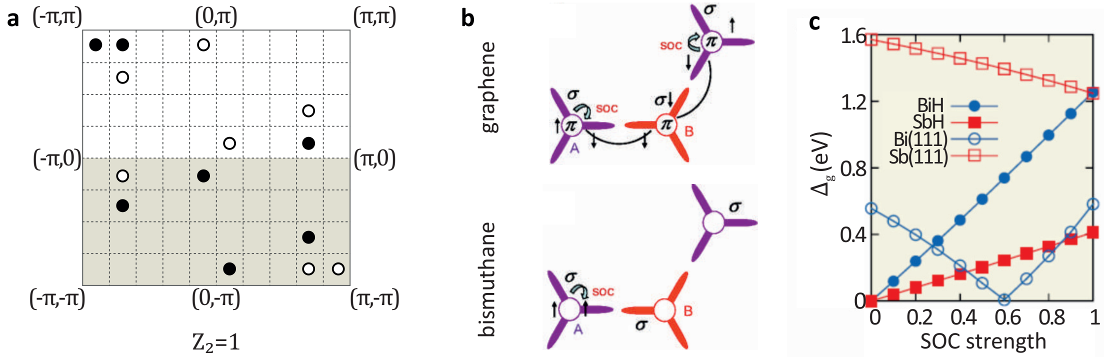

Figure 4.8 **a** $\mathbb{Z}_2$ invariant for bismuthene on SiC. The BZ is discretized in small plaquettes, around which the Berry connection is calculated (an empty field, empty circle and filled circle correspond to the value 0, +1 and -1, respectively). The sum over all plaquettes in half of the BZ (gray or white area) yields $\mathbb{Z}_2 = 1$, i.e., bismuthene on SiC is a QSHI [162]. **b** SOC processes in graphene and bismuthane. While SOC couples only NNN via a 2$^{\text{nd}}$ order process in graphene, the presence of p_x and p_y orbitals at low-energy bands in bismuthane allows for on-site, first-order SOC. **c** Band gap magnitude as function of SOC strength at Γ for buckled Bi/Sb bilayers [Bi(111)/Sb(111)] and at K for planar, hydrogenated Bi/Sb monolayers (BiH/SbH). While buckled Sb(111) is not a 2D TI as its SOC is too weak, buckled Bi(111) is in a QSHI phase driven by band inversion, which can be deduced from a closed gap at a certain SOC strength. In contrast, BiH and SbH are both Kane-Mele-type QSHIs, which results in a linear dependence of the energy gap magnitude and the SOC strength [146]. *Fig.* ***a*** *from Ref. [162]. Reprinted with permission from AAAS. Fig.* ***b*** *reprinted with permission from Ref. [155]. Copyright ©2014 American Physical Society. Fig.* ***c*** *reprinted from Ref. [146] under a Creative Commons 4.0 License (CC BY-NC-ND 4.0 [177]).*

Mechanisms for a non-trivial topology: band inversion vs. honeycomb lattice. It is important to distinguish the two mechanisms leading to non-trivial phases in a buckled Bi bilayer and in (orbital-filtered) planar bismuthene. While the topological phase of the first is caused by a band inversion, the latter is established by the honeycomb lattice geometry in combination with a SOC-induced band gap. In general, SOC does not directly determine the band gap magnitude in inversion-type 2D TIs, even though it is the driving force for the band inversion, which explains why it is found predominantly in materials containing (heavy) elements with large SOC like Cd, Te, Hg, or Bi. Still, the energy gap magnitude can be limited to small values due to hybridization effects, which can be tracked theoretically by variation of the SOC strength as shown in Fig. 4.8**c**. With increasing SOC strength, the energy gap shrinks until it closes and re-opens again with a non-trivial band

order. For Bi(111) bilayers, a band gap is found already without SOC, yet based on a trivial band order. This changes upon inclusion of SOC, see Fig. 4.3 and Ref. [146]. In contrast, SOC *does* scale the band gap in flat honeycomb lattices. Honeycomb systems possess a Dirac-like cone at the K point as a result of the lattice symmetry. SOC creates and scales the gap at K, which is reflected in the linear dependence of band gap magnitude and SOC strength in Fig. 4.8c. If, in addition, the low-energy bands arise from a multiorbital p_x/p_y structure and are formed by an element with large SOC (as Bi), the on-site SOC leads to huge energy gaps [18, 130, 132, 146, 155].

4.5 Low-Energy Effective Modeling

It is instructive to analyze a low-energy effective model that captures the SOC-induced mechanisms of bismuthene on SiC in quantitative formulae. If not stated otherwise, the following expressions are reproduced and summarize the procedures presented in Refs. [18, 162].

Dirac Hamiltonian without SOC. The description is started by a minimal four-band model using p_x and p_y orbitals, as those are predominantly found around the Fermi level, see Fig. 4.7. The eight basis wave functions of the four band model are:

$$|p^A_{x\uparrow}\rangle\,,\ |p^A_{y\uparrow}\rangle\,,\ |p^B_{x\uparrow}\rangle\,,\ |p^B_{y\uparrow}\rangle\,,\ |p^A_{x\downarrow}\rangle\,,\ |p^A_{y\downarrow}\rangle\,,\ |p^B_{x\downarrow}\rangle\,,\ |p^B_{y\downarrow}\rangle\,. \tag{4.5}$$

A/B indexes the sublattice site and $\uparrow$ / $\downarrow$ the spin. The Hamiltonians of the two spin orientations are identical and contain the following entries:

$$H^{\sigma\sigma}_{\uparrow\uparrow} = H^{\sigma\sigma}_{\downarrow\downarrow} = \begin{pmatrix} h^{AA}_{xx} & 0 & h^{AB}_{xx} & h^{AB}_{xy} \\ 0 & h^{AA}_{yy} & h^{AB}_{yx} & h^{AB}_{yy} \\ \dagger & \dagger & h^{BB}_{xx} & 0 \\ \dagger & \dagger & 0 & h^{BB}_{yy} \end{pmatrix}\,, \tag{4.6}$$

where

$$h^{AA}_{xx} = h^{BB}_{xx} = V^0_{pp\sigma}\,, \tag{4.7a}$$
$$h^{AA}_{yy} = h^{BB}_{yy} = V^0_{pp\pi}\,, \tag{4.7b}$$
$$h^{AB}_{xx} = V^1_{pp\pi} + \frac{1}{2}(3V^1_{pp\sigma} + V^1_{pp\pi})e^{i\frac{\sqrt{3}}{2}k_y}\cos\frac{k_x}{2}\,, \tag{4.7c}$$
$$h^{AB}_{xy} = h^{AB}_{yx} = i\frac{\sqrt{3}}{2}(V^1_{pp\sigma} - V^1_{pp\pi})e^{i\frac{\sqrt{3}}{2}k_y}\sin\frac{k_x}{2}\,, \tag{4.7d}$$
$$h^{AB}_{yy} = V^1_{pp\sigma} + \frac{1}{2}(V^1_{pp\sigma} + 3V^1_{pp\pi})e^{i\frac{\sqrt{3}}{2}k_y}\cos\frac{k_x}{2}\,. \tag{4.7e}$$

with the associated eigenvalues around K:

$$E_{1/2} = \frac{1}{4}\left[2(V^0_{pp\sigma}+V^0_{pp\pi})+3(V^1_{pp\pi}-V^1_{pp\sigma})\pm\sqrt{4(V^0_{pp\sigma}-V^0_{pp\pi})^2+9(V^1_{pp\pi}-V^1_{pp\sigma})^2}\right], \tag{4.8a}$$
$$E_{3/4} = \frac{1}{4}\left[2(V^0_{pp\sigma}+V^0_{pp\pi})-3(V^1_{pp\pi}-V^1_{pp\sigma})\pm\sqrt{4(V^0_{pp\sigma}-V^0_{pp\pi})^2+9(V^1_{pp\pi}-V^1_{pp\sigma})^2}\right]. \tag{4.8b}$$

$V^0_{pp\sigma}$, $V^0_{pp\pi}$, $V^1_{pp\sigma}$, $V^1_{pp\pi}$ are obtained by calculating the Slater-Koster integrals for p_x and p_y orbitals in a honeycomb lattice [178]. The Hamiltonian gives rise to two flat bands and two Dirac bands with linear energy dispersion, which cross at the K and E_F, and form the Dirac point, see Fig. 4.9**a** [133, 152]. The degeneracy at the Dirac point requires that the on-site matrix elements, i.e., $V^0_{pp\sigma}$ and $V^0_{pp\pi}$, are zero, leading to a reduced Hamiltonian:

$$H_{0,\uparrow\uparrow} = H_{0,\downarrow\downarrow} = \begin{pmatrix} 0 & 0 & h^{AB}_{xx} & h^{AB}_{xy} \\ 0 & 0 & h^{AB}_{yx} & h^{AB}_{yy} \\ \dagger & \dagger & 0 & 0 \\ \dagger & \dagger & 0 & 0 \end{pmatrix} , \tag{4.9}$$

with corresponding eigenenergies $E = 0, 0, \pm\frac{3}{2}(V^1_{pp\pi} - V^1_{pp\sigma})$ at K.

On-site SOC. A full mathematical description requires an expanded basis comprising the s and p_z orbital, resulting in a 16×16 Hamiltonian [18]. The intrinsic SOC couples spin and angular momentum due to the magnetic field induced by the electron motion in the charge field of the atoms. The coupling of p orbitals is calculated with the following integrals:

$$\langle p_y|\vec{L}\cdot\vec{S}|p_x\rangle = +i\sigma_z, \quad \langle p_x|\vec{L}\cdot\vec{S}|p_y\rangle = -i\sigma_z \ , \tag{4.10a}$$

$$\langle p_z|\vec{L}\cdot\vec{S}|p_x\rangle = -i\sigma_y, \quad \langle p_x|\vec{L}\cdot\vec{S}|p_z\rangle = +i\sigma_y \ , \tag{4.10b}$$

$$\langle p_z|\vec{L}\cdot\vec{S}|p_y\rangle = +i\sigma_x, \quad \langle p_y|\vec{L}\cdot\vec{S}|p_z\rangle = -i\sigma_x \ . \tag{4.10c}$$

Obviously, there exists an on-site coupling between p_x and p_y (σ band) orbitals by the $L_z\sigma_z$-term. The Hamiltonians for the on-site SOC of σ bonds read:

$$H^{\sigma\sigma}_{\mathrm{so}\uparrow\uparrow} = \lambda_{\mathrm{so}} \begin{pmatrix} 0 & -i & 0 & 0 \\ i & 0 & 0 & 0 \\ 0 & 0 & 0 & -i \\ 0 & 0 & i & 0 \end{pmatrix} \text{ and } H^{\sigma\sigma}_{\mathrm{so}\downarrow\downarrow} = \lambda_{\mathrm{so}} \begin{pmatrix} 0 & i & 0 & 0 \\ -i & 0 & 0 & 0 \\ 0 & 0 & 0 & i \\ 0 & 0 & -i & 0 \end{pmatrix} . \tag{4.11}$$

The are combined with the Hamiltonians $H_{0,\uparrow\uparrow}/H_{0,\downarrow\downarrow}$ in Eq. 4.9:

$$H^{\sigma\sigma}_{\uparrow\uparrow} = H^{\sigma\sigma}_{0,\uparrow\uparrow} + H^{\sigma\sigma}_{\mathrm{so}\uparrow\uparrow} = \begin{pmatrix} 0 & -i\lambda_{\mathrm{so}} & h^{AB}_{xx} & h^{AB}_{xy} \\ i\lambda_{\mathrm{so}} & 0 & h^{AB}_{yx} & h^{AB}_{yy} \\ \dagger & \dagger & 0 & -i\lambda_{\mathrm{so}} \\ \dagger & \dagger & i\lambda_{\mathrm{so}} & 0 \end{pmatrix} \text{ and} \tag{4.12a}$$

$$H^{\sigma\sigma}_{\downarrow\downarrow} = H^{\sigma\sigma}_{0,\downarrow\downarrow} + H^{\sigma\sigma}_{\mathrm{so}\downarrow\downarrow} = \begin{pmatrix} 0 & i\lambda_{\mathrm{so}} & h^{AB}_{xx} & h^{AB}_{xy} \\ -i\lambda_{\mathrm{so}} & 0 & h^{AB}_{yx} & h^{AB}_{yy} \\ \dagger & \dagger & 0 & i\lambda_{\mathrm{so}} \\ \dagger & \dagger & -i\lambda_{\mathrm{so}} & 0 \end{pmatrix} . \tag{4.12b}$$

The band structure for $H^{\sigma\sigma}$,

$$H^{\sigma\sigma} = \begin{pmatrix} H^{\sigma\sigma}_{\uparrow\uparrow} & 0 \\ 0 & H^{\sigma\sigma}_{\downarrow\downarrow} \end{pmatrix} , \tag{4.13}$$

is shown in Fig. 4.9**b**. It demonstrates that the $L_z\sigma_z$-term generates the large band gap of bismuthene on SiC.

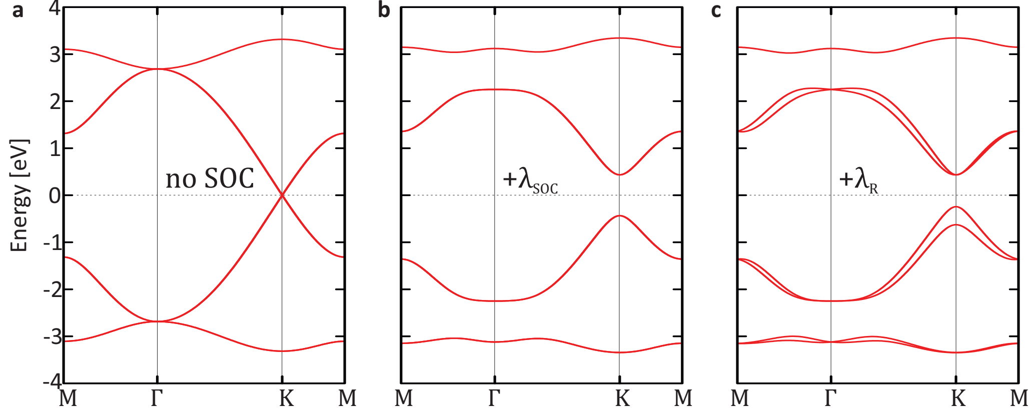

Figure 4.9 **a** Calculated band dispersion without SOC. A pair of Dirac states with steep dispersion crossing at K and two flat bands are observed. All bands are two-fold spin degenerate. **b** On-site SOC of p_x and p_y orbitals opens a huge band gap at K. **c** An E-field gradient, mimicking the effect of the covalent bond to the substrate, leads to a large Rashba-type spin splitting of the VBs and is a hallmark of bismuthene on SiC. Modeling and calculation done by Gang Li [168]. *From Ref. [162]. Reprinted with permission from AAAS.*

Rashba SOC. To complete the low-energy effective model and reproduce all key properties of the band structure it is necessary to consider the hybridization of σ and π bands. This is done with second-order perturbation theory of the π bands, which is motivated by the presence of mainly p_x and p_y orbitals around the Fermi level (see Fig. 4.7), and the desire to keep the model as simple as possible [18]. The full derivation of all matrix terms and approximations is found in Appendix D of Ref. [18]. In short, the $L_x\sigma_x + L_y\sigma_y$ term couples p_x/p_y with p_z orbitals, which exhibit a higher binding energy. Furthermore, to account for the substrate-induced potential gradient between top and bottom side of bismuthene, an effective electric field $\vec{E}$ is introduced in the equations. These effects generate a Rashba-like SOC in the σ bands, thereby lifting the spin-degeneracy, and are captured in the following Hamiltonian:

$$H^{\sigma\sigma}_{\uparrow\downarrow} = (H^{\sigma\sigma}_{\downarrow\uparrow})^\dagger = \lambda_R \begin{pmatrix} 0 & 0 & a & b \\ 0 & 0 & b & c \\ d & e & 0 & 0 \\ e & f & 0 & 0 \end{pmatrix} \text{, where} \tag{4.14}$$

$$a = -2\sqrt{3}i \exp(ik_y\sqrt{3}/2) \sin(k_x/2) \tag{4.15a}$$
$$b = [1 - \exp(ik_y\sqrt{3}/2)[\cos(k_x/2) + \sqrt{3}\sin(k_x/2)]] \tag{4.15b}$$
$$c = -2i[1 - \exp(ik_y\sqrt{3}/2)\cos(k_x/2)] \tag{4.15c}$$
$$d = -2\sqrt{3}i \exp(-ik_y\sqrt{3}/2) \sin(k_x/2) \tag{4.15d}$$
$$e = -[1 - \exp(-ik_y\sqrt{3}/2)[\cos(k_x/2) - \sqrt{3}\sin(k_x/2)]] \tag{4.15e}$$
$$f = 2i[1 - \exp(-ik_y\sqrt{3}/2)\cos(k_x/2)]\ . \tag{4.15f}$$

Low-energy effective Hamiltonian. The complete model Hamiltonian reproducing the essential characteristics of the low-energy bands of bismuthene on SiC is obtained by combination of Eqs. 4.13 and 4.14, and reads:

$$H^{\sigma\sigma}_{eff} = \begin{pmatrix} H^{\sigma\sigma}_{\uparrow\uparrow} & H^{\sigma\sigma}_{\uparrow\downarrow} \\ H^{\sigma\sigma}_{\downarrow\uparrow} & H^{\sigma\sigma}_{\downarrow\downarrow} \end{pmatrix}. \tag{4.16}$$

The resulting band structure is shown in Fig. 4.9**c**. This effective Hamiltonian contains four parameters, which are obtained by the fitting energy eigenvalues at the K point to the DFT band structure shown in Fig. 4.5**b**. The parameter values are $V^1_{pp\sigma} = 2.0\,\text{eV}$, $V^1_{pp\pi} = -0.21\,\text{eV}$, $\lambda_{so} = 0.435\,\text{eV}$ and $\lambda_R = 0.032\,\text{eV}$.

4.6 Nanoribbon Calculations: Edge States in Bismuthene on SiC

So far, the properties concern the 2D bulk electronic structure of bismuthene on SiC. An aspect that was not discussed until now are the 1D topological edge states, which are the hallmark feature of QSHIs and appear at the interface of a non-trivial and a trivial insulator. These topological states (i) connect VB and CB, bridging the bulk energy gap, and (ii) exhibit spin-momentum locking. The edge state energy dispersion and other key properties such as their charge distribution and spatial confinement to the edge can be studied with ribbon slabs, which can be based on a tight-binding (TB) model or computed with first-principle DFT.

TB ribbon model. Computations based on TB models bear the advantage that very large ribbons can be generated, such that hybridization effects between edge states across the film can be excluded. A ribbon is constructed by use of periodic boundary conditions to either the x or y axis of the unit cell, while the boundary along the other direction is kept open. A rectangular unit cell containing four Bi atoms, indicated by the red-shaded rectangular area between Fig. 4.10**a** and **c**, is used, which allows to switch between armchair (AC) and ZZ edge geometry by swapping the axes with periodic and open boundary conditions.

The parameters of the TB Hamiltonian are obtained from the ab-initio bulk DFT band structure calculation by projection on maximally localized Wannier functions (MLWF) [179, 180]. The MLWF span the same Hilbert space as the Bloch orbitals, however, they are located in real space. Both orbitals are linked by a Fourier transformation [180]. Only the three Bi 6p orbitals giving rise to the bands around E_F are considered in the calculations shown in Fig. 4.10, such that the dimension of the Hamiltonian including SOC is 24. The ribbon is built by repetition of 200 layers in AC/ZZ direction, which is enough to avoid a hybridization of the 1D edge states residing at both sides of the ribbon [162].

Both the AC and ZZ TB ribbon calculation of bismuthene on SiC reveal the existence of edge states that connect the VB and CB, see Figs. 4.10**a** and **c**. This is a strong indicator for the topological origin of the states. Importantly, additional edge states intraconnecting either the VB or CB, or residing entirely in the bulk gap are not observed. The red and blue curve show edge states localized at the two ribbon boundaries. The bulk bands

are visualized with the green shaded area. The band dispersion of the AC edge state is remarkably linear over a large range (> 1)eV. The Dirac point, formed by the crossing bands, is located slightly above the VBM. The ZZ edge ribbon exhibits a less simple band dispersion close to the bulk band edges, especially when emerging from the VB, where a pronounced local minimum between $\bar{\Gamma}$ and $\bar{X}$ is visible. Consequently, the Dirac point is located at lower energy than the VBM.

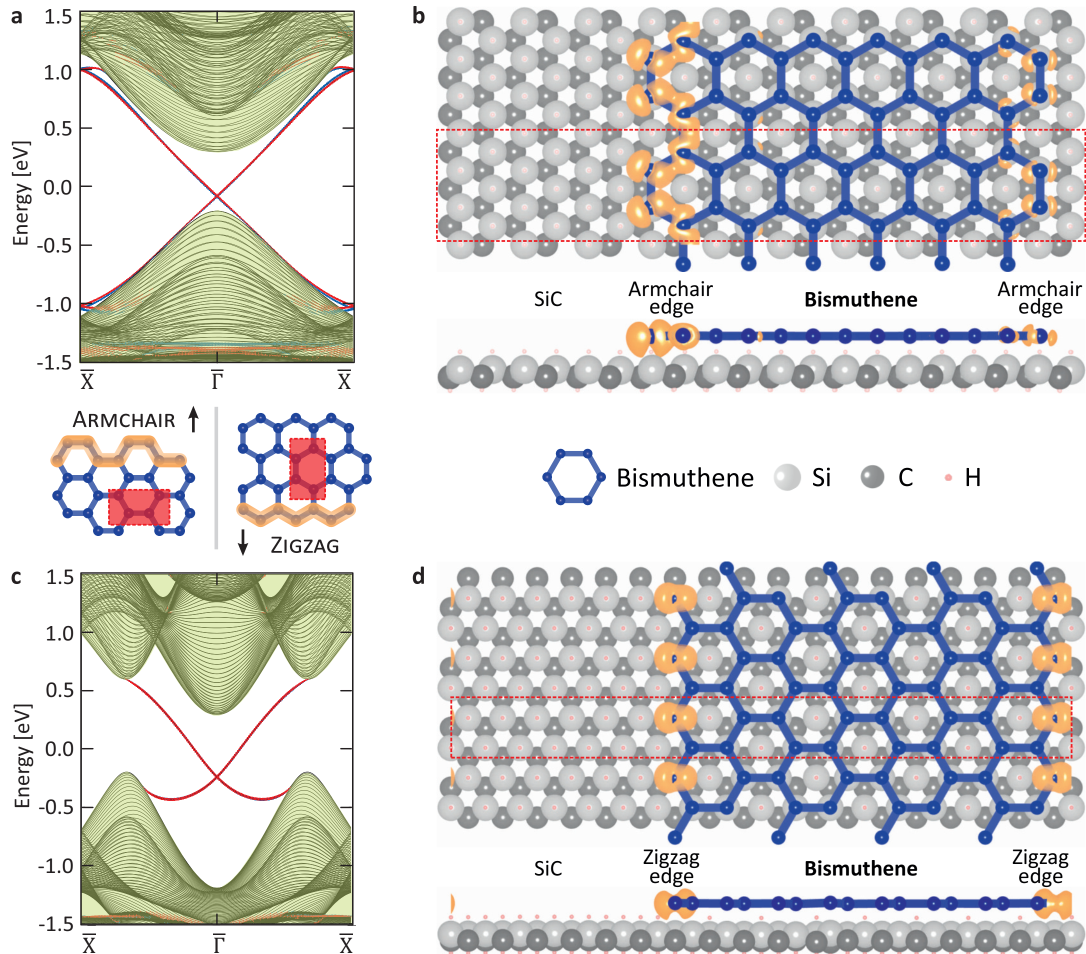

Figure 4.10 **a** AC and **c** ZZ TB ribbon band structure. AC and ZZ edge terminations and the respective TB unit cell (red rectangle) are sketched between the band structure plots. **a** The computed band structure of the AC edge shows a pair of spin-polarized states between the high-symmetry points $\bar{X} - \bar{\Gamma} - \bar{X}$ at either side of the bismuthene film with open boundary condition (red and blue curve), connecting VB and CB with an almost linear energy dispersion. The green shaded area shows bulk-derived states. **c** Similar observations hold for the band structure in ZZ edge geometry, however, there the energy dispersion is not linear close to the VBM and CBM, and the Dirac point is located below the VBM. Ab-initio DFT ribbon slabs in **b** AC and **d** ZZ geometry in topview (upper panel) and side view (lower panel). The corresponding unit cells are shown by the rectangular red dashed lines. The edge states' charge density is shown by orange clouds. Both AC and ZZ edge states are strongly confined to the Bi film boundary and rapidly decay in direction of the bulk lattice. The side view reveals that the edge states are derived from bismuthene without a significant contribution of the SiC substrate. All calculations are done by Gang Li [168]. *From Ref. [162]. Reprinted with permission from AAAS.*

First-principle DFT ribbon calculation. A complementary approach to model edge states is an ab-initio DFT ribbon slab computation of a crystal with an edge. This allows to investigate whether DBs created by truncation of the monolayer are rearranging due

to the potential gradient at the edge, which is excluded by the methodology of the TB Hamiltonian founding on the bulk band structure. Therefore, ab-initio calculations are indispensable to elucidate edge effects correctly [162, 180]. However, these ribbons involve large unit cells with a sizable number of atoms N, resulting in very costly calculations as the number of computation processes is $\propto N^3$ [180, 181]. Hence, the size of unit cell is limited and just large enough to avoid a hybridization of edge states across the film.
The ribbon unit cells used to compute AC and ZZ edge states are shown by the dashed red rectangles in Fig. 4.10**b** and **d**, respectively. In AC geometry, the ribbon slab consists of a Bi film with six unit cell width ($a^{\mathrm{Bi}}_{\mathrm{ACrib}} = 32.44\,\text{Å}$), which is placed on a SiC substrate with $a^{\mathrm{SiC}}_{\mathrm{ACrib}} = 53.5\,\text{Å}$ width. In the ZZ ribbon slab, the width of the Bi film and SiC substrate are $a^{\mathrm{Bi}}_{\mathrm{ZZrib}} = 33.98\,\text{Å}$ and $a^{\mathrm{SiC}}_{\mathrm{ZZrib}} = 56\,\text{Å}$, respectively. The obtained band dispersions are in accord with the TB-based ribbon calculations [162]. The substrate is significantly larger than the bismuthene layer width to ensure that left/right edge states are decoupled. Moreover, this gives insight to effects arising from the interaction of edge and substrate, relevant for the realistic scenario of incomplete growth of bismuthene on SiC. Note that the model comprises only a single SiC bilayer underneath the bismuthene film to keep the computation effort manageable.
Another useful feature of DFT calculations is the possibility to visualize states in real space. The iso-charge surface of the edge states, depicted by orange clouds in Fig. 4.10**b** and **d**, shows the charge distribution present in the energy gap, which exhibit a periodicity of 5.34 Å (ZZ ribbon) and 9.27 Å (AC ribbon). These additional states emerge at the last bismuthene row and are strongly confined to the edge. Their intensity drops to zero within 1–2 bismuthene unit cells. The side view images unveil that the charge clouds predominantly originate from Bi atoms, with negligible contribution by the SiC substrate. Left and right side AC edge of the bismuthene layer are inequivalent due to their symmetry with respect to the underlying C sublattice of the SiC bilayer, leading to an unequal edge potential. This leads to charge clouds with unequal intensity. This is in contrast to the edge in ZZ orientation, where the symmetry of left and right side in reference to the C atoms is identical [168].

5 Preparation of High-Quality SiC Substrates for Monolayer Epitaxy

The epitaxial growth of a monolayer system like bismuthene is based on the availability of a high-quality substrate. Therefore, considerable effort during the time of this thesis has been devoted to the preparation of 4H-SiC substrates with large, atomically flat terraces and a low defect density on by a suitable high-temperature H annealing process.
This chapter starts with a summary of the structural and electronic properties of 4H-SiC. Then, the quality of SiC surfaces obtained with different annealing setups and parameters is evaluated on the basis of low-energy electron diffraction (LEED), scanning tunneling microscopy and spectroscopy (STM and STS) measurements on the atomic scale.

5.1 Structural and Electronic Properties of 4H-SiC

SiC possesses a superior thermal conductivity, higher breakdown voltage and a wider band gap in comparison to Si, which is the most relevant semiconducting material in industry. Due to significant improvements of the crystalline quality achieved in the recent years, it gradually gains importance for application in high temperature and high power devices [182–184]. For the research community, SiC became highly relevant as it allows controlled and in-situ synthesis of graphene [185, 186]. An overview of the physical key parameters of SiC, its "parental" elements Si and C (in diamond modification), and other important semiconductor materials is shown in Tab. 5.1.

Crystal structure of 4H-SiC(0001). Both Si and C are group IV elements and possess a tetragonal coordination with four covalent bonds to neighboring C and Si atoms in SiC, see Fig. 5.1. Thus, both species are sp^3 hybridized and achieve a filled valence orbital [184, 188]. With this basic unit, a plethora of different SiC polytypes can be generated by variation of the stacking sequence along the [111] (cubic) or [0001] (hexagonal) direction and the orientation of adjacent bilayers (wurzite or zinc blende crystal structure) [184]. A more detailed description concerning the SiC polytypes is found in App. B.2. In case of

Properties	Ge	Si	GaAs	4H-SiC	C
Band gap (eV)	0.7	1.1	1.4	3.2	5.5
Breakdown Field (mV/cm)	0.1	0.3	0.4	3.0	20
Electron Mobility (cm^2/Vs)	3900	1450	8500	900	4500
Hole Mobility (cm^2/Vs)	1900	480	400	120	3800
Thermal Conductivity (W/cmK)	0.58	1.50	0.55	3.7	24
Maximum Electric Field (V/cm)	2.5×10^5	3×10^5	3.5×10^5	2.8×10^5	1×10^7

Table 5.1 Electronic and thermal properties of selected semiconductor materials. *Reprinted with permission from Ref. [187]. Copyright ©2014 Springer International Publishing Switzerland.*

4H-SiC, four SiC bilayers with stacking order *ABCBAB*... are piled up in [0001] direction (see also Fig. B.1). *A*, *B* and *C* denote the three different sites present in a hexagonal lattice that give rise to a close-packed structure.

The 4H-SiC periodicity along [0001] is $c = 10.08$ Å, i.e., four times the bilayer distance of 2.52 Å[6], see Fig. 5.1**a** [163, 164, 189]. The top-view of the (Si-terminated) 4H-SiC(0001) surface depicted in Fig. 5.1**b** shows the in-plane lattice constant $a^{\mathrm{SiC}} = 3.08$ Å [163, 164, 189], and reveals the overall trigonal structure of the SiC honeycomb bilayers as consequence of the buckling between Si and C atoms. This lattice may in principle give rise to two different edge terminations, namely a zigzag (ZZ) edge perpendicular to $[1\bar{1}00]$, and an armchair (AC) edge perpendicular to $[11\bar{2}0]$. The latter is also called open edge [190]. However, these edges in AC orientation are energetically unfavorable anyway and replaced by triangular, ZZ-terminated peninsulas during growth and etching [190], see Fig. 5.2 [190–194]. Consequently, a miscut along $\langle 1\bar{1}00 \rangle$ generates edges with higher degree of ordering than in $\langle 11\bar{2}0 \rangle$ direction [192, 194].

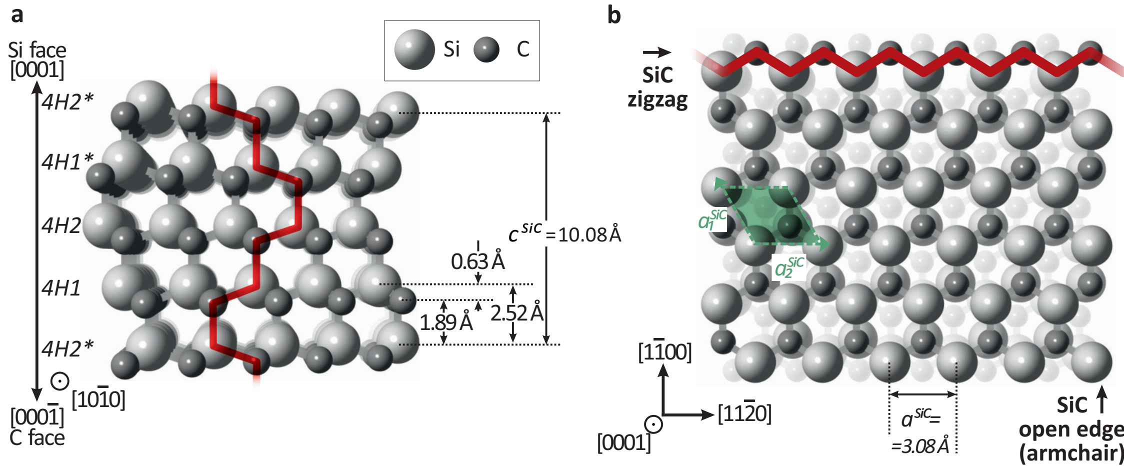

Figure 5.1 **a** Side view of the 4H-SiC crystal structure. Si and C atoms are shown in light and dark gray, respectively. 4H-SiC consists of stacked bilayers in [0001] direction. The red line highlights the stacking sequence. The in-plane lattice constant is $a^{\mathrm{SiC}} = 3.08$ Å, and the periodicity along [0001] is $c^{\mathrm{SiC}} = 10.08$ Å [163, 164, 189]. **b** Top view on 4H-SiC(0001). The SiC bilayers form buckled honeycombs, such that in principle two edge terminations are possible: ZZ (marked with the red line) and AC edges. The latter edge termination is not observed in experiments. The unit vectors and cell are shown by green arrows and the green rhombus, respectively.

Inspection of the lattice structure seen from $[11\bar{2}0]$ direction (Fig. 5.1**a**) highlights the stacking sequence, which is indicated by the red line [184, 195]. The bond orientation of neighboring bilayer pairs is always alternating between wurtzite and zincblende symmetry in 4H-SiC(0001). Consequently, the step height between adjacent terrace planes determines whether the C atom sublattice orientation is equal (for steps corresponding to an even number of bilayers, i.e., 2H, 4H,..) or rotated by 60° (for an odd number of bilayers), which will influence the resulting LEED pattern: in case only one C sublattice orientation is found at the surface, a trigonal LEED pattern is observed [42], while the presence

[6] In reality, the individual bilayer distances exhibit minute deviations from this idealized constant bilayer spacing, which, however, are not relevant for our purposes [164].

of both sublattice orientations on the surface planes causes a sixfold-symmetric LEED pattern [196].

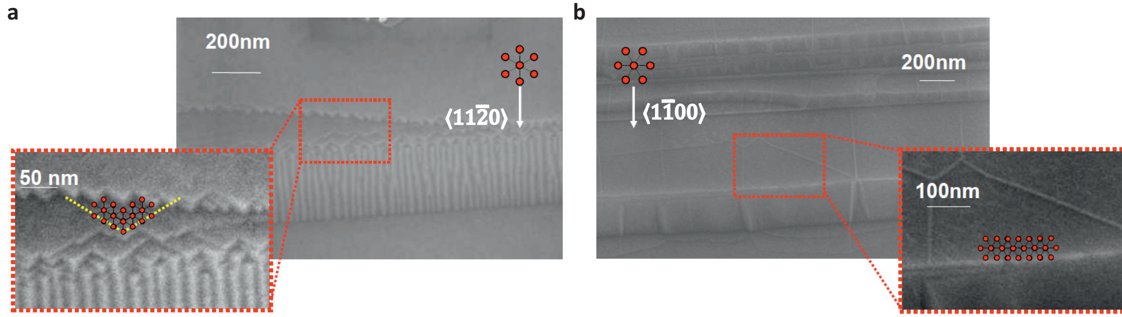

Figure 5.2 Scanning electron microscopy images of 4H-SiC(0001) samples prepared with miscut in **a** $\langle 11\bar{2}0\rangle$ and **b** $\langle 1\bar{1}00\rangle$ direction. While the latter leads to the formation of smooth step edges in ZZ direction, straight edges perpendicular to $\langle 11\bar{2}0\rangle$ are not seen but replaced by meandering segments of ZZ-terminated edges. *Republished with permission of Trans Tech Publications, Ltd., from Ref. [192]; permission conveyed through Copyright Clearance Center, Inc.*

Step Bunching Another characteristic of SiC surfaces is the (micro) step or, more precisely, bilayer bunching[7] observed on the Si-terminated surfaces of the 4H and 6H polytype. Bilayer bunching occurs due to different surface energies and surface diffusion velocities of the $H1/H1^*$ and $H2/H2^*$ (and, for 6H, additionally the $H3/H3^*$) layers, see Fig. 5.1**a**, which causes an imbalanced growth rate. The energy ΔU_{grow} for adding a new layer σ_{new} on a surface layer σ_{surf} is given by [197]:

$$\Delta U = E_0 - J^* \sigma_{\text{new}} \sigma_{\text{surf}} \tag{5.1}$$

where J^* represents the interaction strength with the neighboring bilayers. Correspondingly, ΔU_{grow} is: [198]

$$4H1 \text{ terrace: } \Delta U_{\text{grow}}^{4H1} = E_0 + 2.34\,\text{meV} = -\Delta U_{\text{etch}}^{4H2} \tag{5.2}$$

$$4H2 \text{ terrace: } \Delta U_{\text{grow}}^{4H2} = E_0 - 6.56\,\text{meV} = -\Delta U_{\text{etch}}^{4H1} \tag{5.3}$$

This energetic imbalance favors the formation of steps with half unit cell height. The evolution into full unit cell steps is related to the number of dangling bonds (DBs) created by the step termination, which is not equivalent for bilayer pairs: layers $H1/H2(/H3)$ have two DBs whereas the layers $H1^*/H2^*(/H3^*)$ have only one in $\langle 1\bar{1}00\rangle$ direction [197, 199, 200].
Similar considerations can be carried out for the etching process [190, 198]. The removal of $H1^{(*)}$ layers requires more energy than of $H2^{(*)}$ layers, and eventually causes the bilayers to merge into pairs, as indicated by the arrows with different lengths in Fig. 5.3 [190, 197, 198]. The higher stability of $H1^{(*)}$ layers and the varying number of DBs is reflected in the presence of half (2H) or full (4H) unit cell regular, straight steps perpendicular to the

[7] Note that *step bunching* is used in literature to describe two different processes: (i) the merging of two or more SiC bilayers up to one or few c^{SiC} unit cells, and (ii) the formation of large steps with a height of $\gg 10\,$nm. In order to avoid a misinterpretation the term *bilayer bunching* is used here for case (i) and *step bunching* for case (ii).

$\langle 1\bar{1}00\rangle$ direction for on-axis SiC(0001) [39, 201, 202].

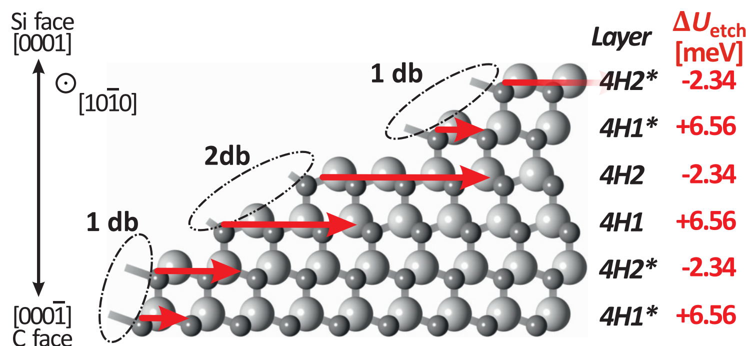

Figure 5.3 Sketch visualizing the bilayer etching in 4H-SiC during H annealing. $H2/H2^*$ layers possess a higher surface energy and are faster etched compared to $H1/H1^*$ layers, resulting in half unit cell (2H) steps. Bunching to full (4H) steps occurs due to the inequivalent number of DBs of the C edge atoms: $H1^*/H2^*$ layers have one, and $H1/H2$ layers have two DBs. The resulting etching velocity is visualized by the red arrows (not true to scale). *Adapted from Ref. [199] under a Creative Commons 4.0 License (CC BY 4.0 [10]).*

For substrates with a high miscut angle the presence of single unit cell steps is not favorable anymore. Instead, bunching into larger macro steps or so-called nanofacets is observed [194, 200, 202]. The higher the miscut, the higher is the number of bunched bilayers and eventually steps [202]. This trend is more pronounced on the Si- than C-face due to the different surface energies of both terminations [39, 203, 204].
Yet, it must be stated that the outcome of the etching process strongly depends on the precise choice of the H annealing parameters like the temperature [40, 202], the H_2 flow [205], the presence of additional gaseous etchants [40, 193] and the Si to C ratio in the gas phase [39]. Furthermore, the resulting surface morphology after the annealing depends on the sample itself. It is influenced by, e.g., the miscut angle [201], whether it is terminated by a Si or a C layer [190, 194], and by its doping level [206].

Band structure of 4H-SiC(0001). In order to be available to disentagle bismuthene- and SiC-derived states in ARPES, Gang Li performed a six layer slab DFT calculation of the 4H-SiC band structure. The calculations are based on the Heyd-Scuseria-Ernzerhof (HSE) exchange-correlation functional [207] and the projector-augmented wave method [208] implemented in the Vienna ab-initio simulation package [166].
The characteristics of the DB state resulting from the truncation of the crystal periodicity at the surface is inspected with special attention as it has a pivotal role for the formation of planar bismuthene on SiC. A calculation with unsaturated Si-DBs is shown in Fig. 5.4**a**. Not surprisingly, this leads to a metallic state with small band width ($\approx 0.57\,\text{eV}$) at the Fermi level as consequence of the partially filled Si sp^3 orbital. Such a finding must be interpreted critically because density-functional theory (DFT) calculations do not account for electronic correlations. Focusing on these states, Emtsev et al. [165] irradiated H-passivated 6H-SiC(0001) samples with high-intensity synchrotron light, which breaks the Si-H bond but allows to preserve the (1×1) reconstruction. Their angle-resolved photoelectron spectroscopy (ARPES) study reveals the presence of an additional state,

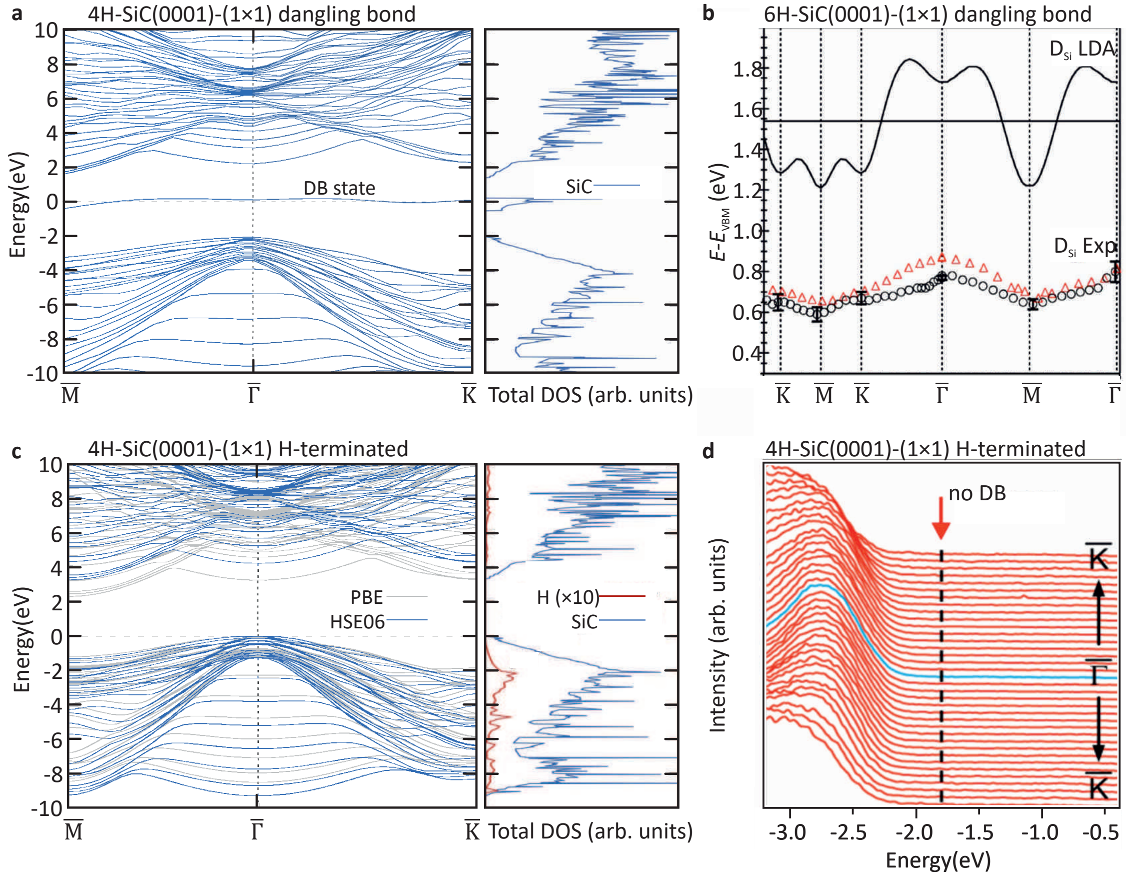

Figure 5.4 **a** Electronic band structure and corresponding total DOS of a six-layer slab 4H-SiC(0001) sample computed by DFT with the HSE exchange functional. Correlation effects are not taken into account. The Si DBs are not passivated, resulting in a half-filled flat band at the Fermi level. **b** DFT calculations for the closely-related 6H-SiC(0001) crystal with unpassivated Si DBs exhibit a band with similar dispersion (D_{Si} LDA). ARPES measurements after H desorption demonstrate the existence of a flat band at ≈ 1 eV binding energy, which leaves the system gapped. Circles and triangles correspond to measurements at $h\nu = 65$ eV and 110 eV. **c** DFT HSE band structure calculation like in **a** but with H-passivated DBs. The band at the Fermi level is removed and the system has a gap of ≈ 3.29 eV (blue lines). Gray lines represent calculations using the generalized gradient approximation (GGA) in the implementation of Perdew, Burke and Ernzerhof (PBE) [81]. The total DOS panel reveals that H-induced and SiC-derived states are coexisting and hybridizing. **d** Laboratory ARPES measurements ($h\nu = 21.22$ eV) of H-passivated 4H-SiC(0001) show no indications of a DB state. *Figs.* ***a***, ***c*** *Calculated and provided by courtesy of Gang Li [168]. Fig.* ***b*** *reprinted with permission from Ref. [165]. Copyright ©2006 American Physical Society. Fig.* ***d*** *adapted with permission from Ref. [37]. Copyright ©2016 American Chemical Society.*

which has a very small bandwidth (≈ 0.2 eV), but is shifted to a higher binding energy, see Fig. 5.4**b**. The authors conclude that the observed DB state is subject to electronic correlations and represents a fully occupied lower Hubbard band.

In a second calculation, the Si DBs are passivated by H atoms. As expected, the DB state visible in Fig. 5.4**a** vanishes in the computed band structure, see Fig. 5.4**c**. According to the calculations with the HSE exchange functional (blue lines), the system is a wide-gap semiconductor with a band gap of ≈ 3.29 eV [81], which matches very well to the experimental value of 3.27 eV [45]. ARPES measurements on H-passivated 4H-SiC(0001) with a laboratory He α light source (Fig. 5.4**d**), which leaves the Si-H bond unaffected, confirm the absence of a DB state. The inspection of the total density of states (DOS) (Fig. 5.4**c**) unveils that the VB maximum (VBM) and CB minimum (CBM) are composed

by SiC bands (blue lines), while bands with H character are at higher binding energies (red line in the total DOS plot).

Importantly, no SiC- or H-derived states are located directly at the Fermi level, neither for H-terminated nor for DB SiC surfaces, which is a prerequisite for the unimpeded inspection of Bi-induced states close to the Fermi level after the bismuthene growth.

Intrinsic and extrinsic charge carriers. The intrinsic charge carrier density of 4H-SiC is very low [$n_\mathrm{i} = 5 \times 10^{-9}\,\mathrm{cm}^{-3}$ at room temperature (RT)] as a result of its wide band gap [209]. Fig. 5.5**a** shows an Arrhenius plot comparing the intrinsic densities of 4H-SiC and Si. Such few charge carriers prohibit STM and ARPES measurements at low and even at RT. Therefore, doped SiC substrates are required for our purposes. Throughout all measurements in this thesis, n-type SiC substrates are used, where N is used as dopant and substitutes C atoms. The position of the Fermi level is pinned in vicinity of the VB/CB edge by the extrinsic carriers, almost independent of the doping level at $T < 300\,\mathrm{K}$ because of the very low density of intrinsic charge carriers [209], see Fig. 5.5**b**.

The ionization energy depends on the lattice site and ranges from $E_\mathrm{ion}^\mathrm{h} = 61\,\mathrm{meV}$ and

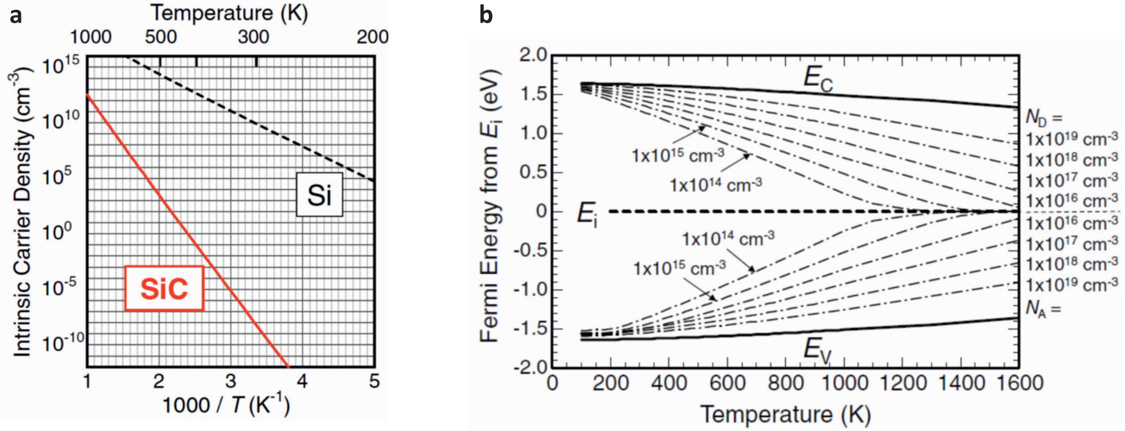

Figure 5.5 **a** Arrhenius plot comparing the intrinsic charge carrier density of 4H-SiC and Si. At 300 K, the intrinsic charge carrier density of SiC is 18 orders of magnitude lower than in Si as result of its much larger band gap. **b** Temperature-dependent Fermi level position for various doping concentrations in 4H-SiC. $E_\mathrm{i} = 0$ denotes the midgap position of the Fermi level. The Fermi energy is pinned close to the doping level energy due to the low intrinsic carrier density at $T < 300\,\mathrm{K}$. *Figs.* ***a*** *and* ***b*** *reprinted with permission from Ref. [209]. Copyright ©2015 The Japan Society of Applied Physics.*

$E_\mathrm{ion}^\mathrm{k} = 126\,\mathrm{meV}$ for hexagonal (h) and cubic (k) site (see Sec. B.2 for further information), such that at RT 80% to 100% are ionized, depending on the doping level [209, 210] . At a very high impurity concentration ($\geq 10^{19}\,\mathrm{cm}^{-3}$), the band gap size decreases and an impurity band is generated. The solubility limit of N atoms is $2 \times 10^{20}\,\mathrm{cm}^{-3}$ [209].

The commercial availability of those highly-doped 4H-SiC samples permits the detailed investigation of H-annealed SiC substrates with STM, STS and LEED, which is presented in the following sections of this chapter.

5.2 Planar SiC(0001) Samples Prepared in Static Hydrogen Atmosphere

Initially, a very simple setup was used to prepare H-terminated SiC samples, see Sec. A.2. Although the surface quality obtained with this instrumentation cannot compete with the quality obtained by a more sophisticated setup for annealing in flowing gas atmosphere (Sec. A.2), the small number of process parameters has proven to be instructional to understand the influence of two essential parameters, namely the annealing temperature and the H_2 gas purity. While the latter is hardly investigated in the majority of articles, the former is studied extensively using a large range of annealing temperatures from 800 °C to 1600 °C. The influence of both parameters is discussed in the first two subsections. Furthermore, an inspection of the 4H-SiC stacking sequence in as-prepared samples is feasible in consequence of a layer-by-layer removal (Sec. 5.2.3) [37].

5.2.1 Influence of the Annealing Temperature

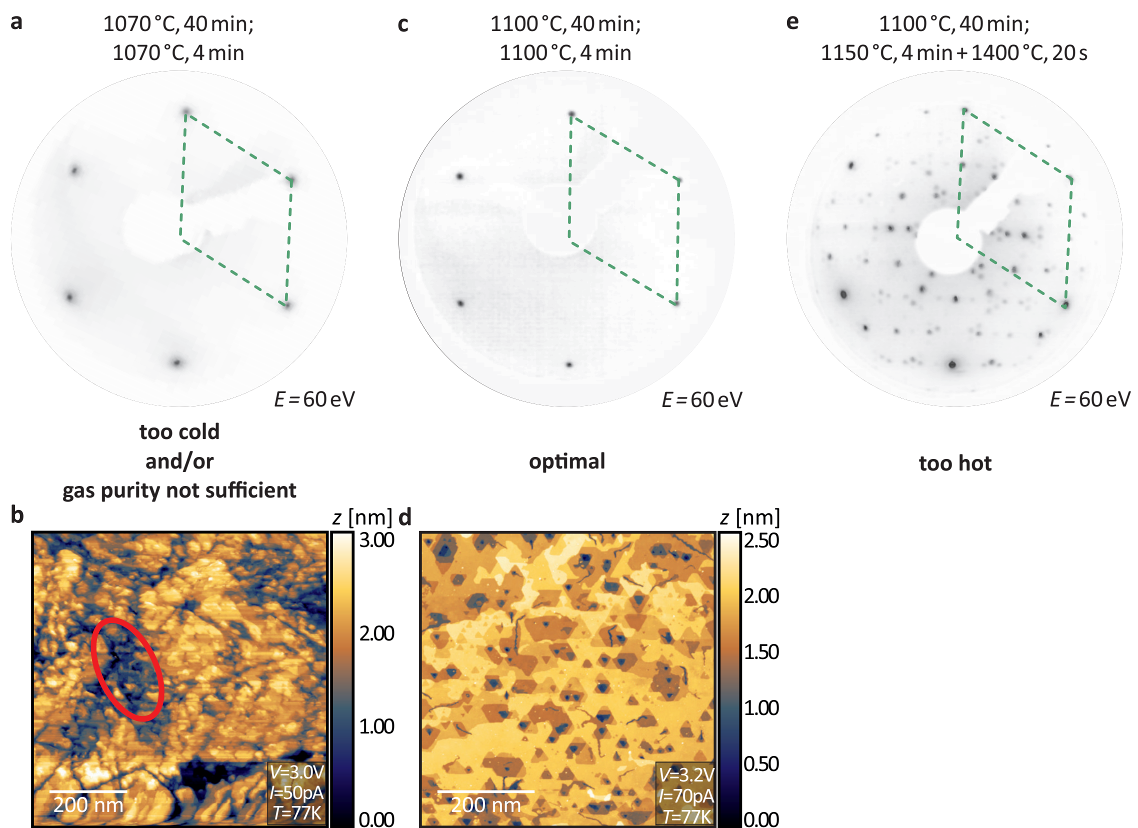

Figure 5.6 LEED and STM images of SiC(0001) substrates after two annealing steps in static H_2 at different temperatures. **a** A (1 × 1) LEED pattern with blunt diffraction spots is observed. The green dashed line depicts the (1 × 1) unit cell. **b** The corresponding STM image shows a very rough, ragged surface. Polishing scratches are clearly visible, and defined terrace planes are absent except for a small area marked by the red ellipsoid. **c** Sample annealed with a two-step H annealing process at slightly higher temperature. The LEED spots are considerably sharper and no background is seen. **d** The STM overview scan reveals the presence of flat terraces on the surface. Triangular cavities are reflecting the lattice symmetry. **e** LEED image of a SiC(0001) sample flashed at 1400 °C in the second step. The high temperature causes a Si depletion and the formation of a C-rich reconstruction on the surface. For this sample, no STM image has been recorded.

A direct adoption of the annealing temperatures reported in literature to our setup is difficult. Firstly, the sample in our case is heated by direct current (DC) through the sample, and secondly, its temperature is tracked with a pyrometer, which is in contrast to the heating methods and temperature readings implemented by most other research groups. Details on annealing parameters reported in literature are discussed in App. B.1.
Hence, temperatures at the lower limit of the reported range have been used in the initial experiments. Fig. 5.6**a** shows a LEED image of a SiC sample prepared at $T = 1070\,°\mathrm{C}$ in a two-step process as described in Sec. A.2. The LEED image shows a (1×1) reconstruction with six-fold symmetry, but the diffraction spots are faint and rather diffuse. A corresponding STM image (Fig. 5.6**b**) reveals that the majority of the surface is ragged and no signatures of ordered crystal planes, like flat terrace planes and ordered step edges are found, which explains the apparent noisy background due to incoherent elastic scattering of electrons in LEED [211]. A reduced corrugation is present only in a tiny area (marked by the red ellipsoid in Fig. 5.6**b**). Deep scratches with $> 100\,\mathrm{nm}$ length run through the surface and most probably are remainders of the wafer polishing process (compare to Fig. 2.2 and Ref.[212]), which indicates that the H annealing process did not remove enough material from the surface.
A LEED image of a second SiC sample prepared similarly but with slightly elevated temperature ($T = 1100\,°\mathrm{C}$) is shown in Fig. 5.6**c**. It exhibits much sharper diffraction spots than the first sample (Fig. 5.6**a**), indicative of a higher crystalline quality at the surface. The incoherent background is strongly reduced, as well. This is in line with the STM scan shown in Fig. 5.6**d**, which displays flat and uniform terrace planes separated by straight step edges along distinct directions. The peculiar trigonal symmetry of the step edge orientations is discussed later.
A further increase of the annealing temperature ($T^{\mathrm{ann},1}_{\mathrm{stat}} = 1100\,°\mathrm{C}$, $T^{\mathrm{ann},2}_{\mathrm{stat}} = 1150\,°\mathrm{C}$ and a short flash to $T^{\mathrm{ann},3}_{\mathrm{stat}} = 1400\,°\mathrm{C}$ for $t^{\mathrm{ann},3}_{\mathrm{stat}} = 20\,\mathrm{s}$) leads to a $(2\sqrt{13} \times 2\sqrt{13})$ surface reconstruction giving rise to the LEED pattern shown in Fig. 5.6**e**, which is not reported in literature so far. Obviously, the elevated temperature of $1440\,°\mathrm{C}$ causes a Si depletion of the surface because of the higher vapor pressure of Si compared to C[8]. This substrate does not provide the DBs necessary for the growth of bismuthene. Hence, an investigation with STM is omitted.

5.2.2 Influence of the H_2 Gas Purity

The H_2 gas purity is a second parameter that has been explored during the preparation of the first samples. In order that the H annealing process works, the supplied H_2 gas must be entirely dry with a purity degree of 8.0 or higher, otherwise, residual oxygen leads to the formation of a silicate adlayer [45]. In our case, the purification of the as-purchased H_2 5.0 gas in the first, simple annealing setup has been accomplished by gas filter cartridges with limited capacity (see Fig. A.2). Conventionally, large Pd diffusion cells are used for that task (e.g., in Refs. [32, 45]).
At a certain point, such a filter cartridge is used up and H_2 gas is contaminated with

[8] Several groups report the formation of a C-rich $(6\sqrt{3} \times 6\sqrt{3})$ instead of a $(2\sqrt{13} \times 2\sqrt{13})$ reconstruction upon Si depletion [212, 213]. Among other reasons, the observation of a different reconstruction in our case might be related to a different gas atmosphere (Si-rich, C-rich, etc.) in our setup, see also Sec. B.1.

O_2 and H_2O residuals. LEED and STM images of a SiC(0001) sample prepared with contaminated gas are shown in Fig. 5.7**a**, **e**, **i**. The very high background signal from incoherently diffracted electrons in LEED is immediately visible. The diffraction spots are intense but broad and with large halos. STM measurements (Fig. 5.7**e**) display step edges with similar triangular symmetry as in Fig. 5.6**d**, indicative of a functioning annealing process. The terraces themselves, however, are fully covered by irregular-formed clusters and no periodic atom arrangement is seen on the atomic scale (see Fig. 5.7**i**).

To put the filter into operation again it can be baked in high vacuum at $T > 100\,°C$ and simultaneously evacuated to remove H_2O molecules. The removal of O atoms requires the use of forming gas.

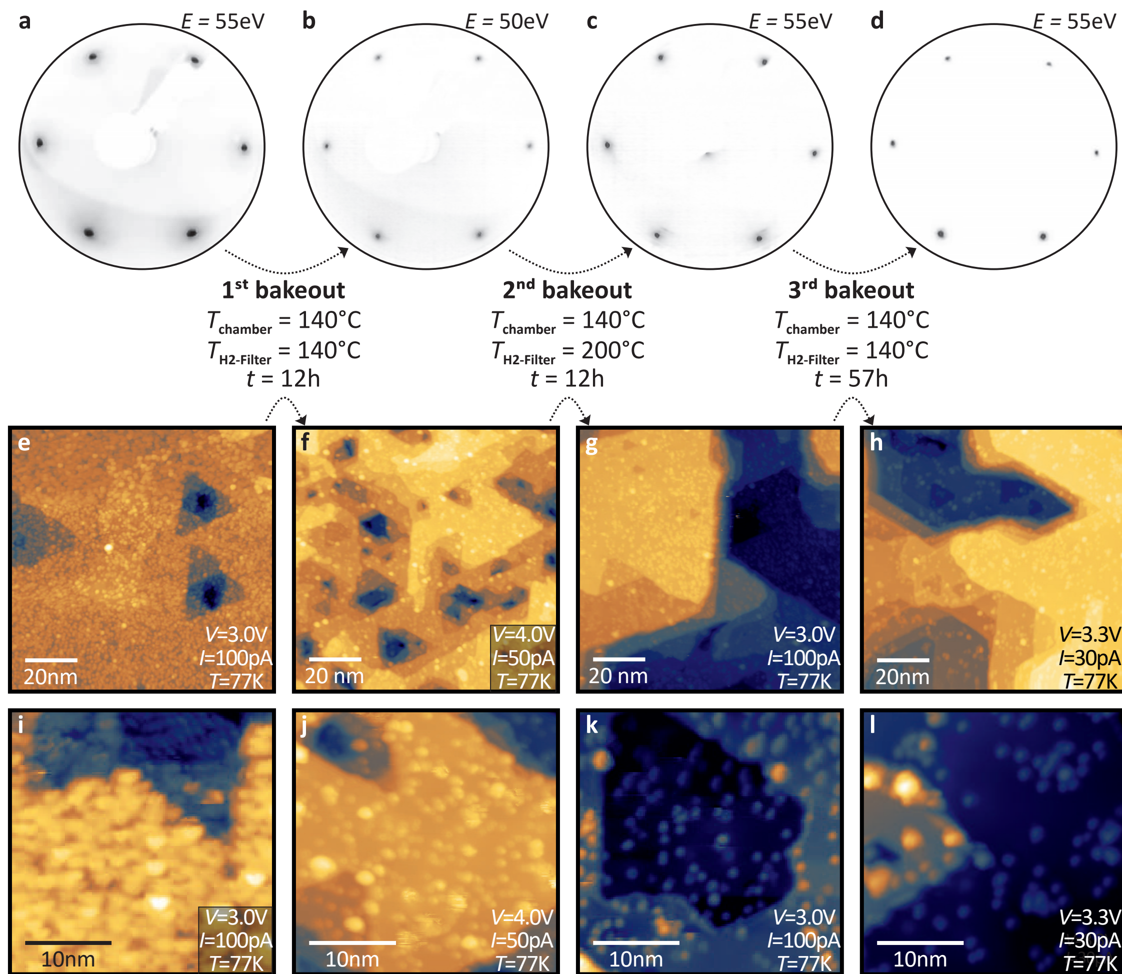

Figure 5.7 **a**–**d** LEED images and **e**–**h** STM measurements of SiC(0001) samples after high-temperature H annealing demonstrating the pivotal influence of the H_2 gas purity. Initially, the use-up of the filter capacity lead to O_2 and H_2O contamination during the annealing process. The LEED image (**a**) shows a (1×1) reconstruction but large spot halos and a high diffuse background. **e**, **i** The STM images show that the terrace planes are entirely covered with small, irregular clusters. **b** A bakeout of the filter cartridge at $T = 140\,°C$ causes an improvement of the LEED pattern. **f**, **j** The number of cluster visible in the STM images is strongly reduced and (small) defect free areas are visible. This trend is continued with two further bakeout processes (**c**, **g**, **k** and **d**, **h**, **l**). Finally, intense, sharp diffraction spots are seen in LEED, and atomically smooth areas on the scale of 5 nm × 5 nm are observed in the STM measurements .

The impact of this simple procedure is seen in Fig. 5.7**b**, **f**, **j**. The diffraction spots in LEED (Fig. 5.7**b**) become significantly sharper and the background is strongly reduced. The corresponding STM images demonstrate that atomically flat areas are present in between clusters (Fig. 5.7**f** and **j**). Additional bakeout cycles shown in Fig. 5.7**c**, **g**, **k** and in Fig. 5.7**d**, **h**, **l** point in the same direction and confirm the trend of improved surface quality in LEED and STM. Finally, the LEED image is free of noticeable background noise and exhibits sharp diffraction spots. The STM scan shows defect-free areas with 5nm$\times$5nm size, which is the optimum that can be produced with the simple SiC preparation setup. The the same time, a high density of big clusters is still present on the SiC(0001) surface in Fig. 5.7**l**. Furthermore, the surface is interspersed with many terrace steps.
Ultimately, these deficiencies lead to the assembly of a more elaborate setup for SiC preparation in flowing gas atmosphere. Before the therein prepared samples are investigated in Sec. 5.3, we make of use the manifold of visible terrace planes on the surface of samples treated in static H atmosphere to examine the SiC bilayer symmetry and stacking order of 4H-SiC.

5.2.3 Layer-By-Layer Etching and Sublattice Orientation of 4H-SiC

Fig. 5.8**a** displays an overview STM image on a SiC(0001) sample annealed in static H_2 atmosphere. Several terrace planes with varying height are visible and separated from adjacent planes by straight step edges along mostly three directions, resulting in depressions with triangular appearance pointing either "upwards" or "downwards".
Another remarkable feature is the occurrence of worm-like defects that cut deep trenches in the surface and stop at adatom defects (marked by green ellipsoids in Fig. 5.8**b**). The irregular shape of the edges and the expand of the defects indicates a faster etch rate than at regular steps. The observation that all the trenches end at defect clusters might indicate that these clusters act as catalyst in H_2 dissociation, but this is highly speculative.

Step height. We continue by inspection of the vertical displacement of different terrace planes. For this purpose, a line profile extracted in Fig. 5.8**b** (red line) is displayed in Fig. 5.8**c**. It demonstrates that the minimal separation of adjacent terrace planes corresponds to a single SiC bilayer (or 1H) step. Note that deviations from the theoretical value of $\frac{1}{4}c^{\mathrm{SiC}} = 2.52\,\text{Å}$ are the result of fluctuations of the probed apparent height on the heavily-doped 4H-SiC(0001) samples, as discussed in Refs. [214, 215]. Interestingly, the observation of single bilayer steps seems to be unreported in literature. Instead, majorly steps with half and full c^{SiC} height are reported [190, 197, 200]. The different finding in our experiments is likely related to a supposedly rather low temperature and etching rate during H_2 annealing, such that the variation of the thermodynamic stability of inequivalent bilayers is less relevant than in other studies.
Occasionally, also in our samples two 1H steps bunch to a 2H step. This happens when the lower-lying step edge exhibits a higher surface energy, which results in a faster etching rate of the lower terrace as discussed in the context of Fig. 5.3 [190, 197, 198, 200]. Further inspection discloses that the three predominant, i.e., more stable orientations switch by 60° for every other step, i.e., after a 2H-SiC(0001) sequence (see Fig. 5.8**a**, **b**). Reconsidering

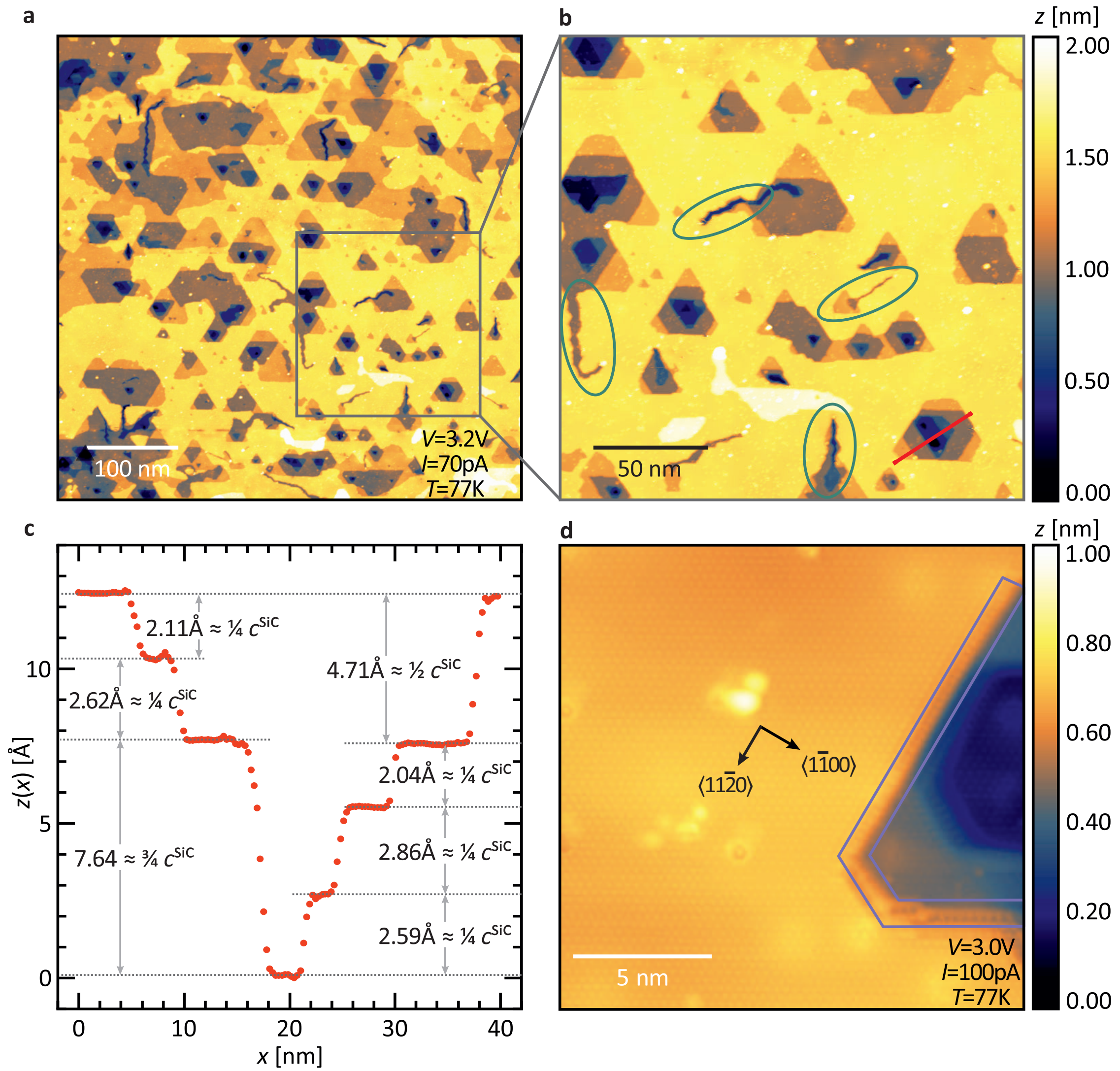

Figure 5.8 STM measurements on a SiC(0001) sample after a two-step annealing process in static H_2 gas atmosphere ($T_{\mathrm{ann},1/2} = 1100\,°\mathrm{C}$, $t_1 = 40\,\mathrm{min}$, $t_2 = 4\,\mathrm{min}$, $p = 950\,\mathrm{mbar}$). **a** A 500 nm STM scan shows that the terrace planes are eroded with deep cavities. The distinct triangular symmetry of step edges is conspicuous. The orientation along which straight edges are predominantly observed rotates after every other terrace step by 60 °. **b** The cavity walls are incised occasionally by irregular, worm-like defects (marked by green ellipsoids). **c** The line profile shows that 1H-SiC, i.e., ≈ 2.52 Å high steps are predominantly found on as-etched substrates. **d** A small scale STM image unveils that the (1×1) periodicity of the lattice is maintained at the step edge.

the lattice structure of 4H-SiC, we find that the bond orientation of SiC bilayer pairs switches between wurtzite and zincblende crystal symmetry (see Sec. B.2 and Fig. 5.3) after a 2H sequence, which implies that the number of DBs at the edges changes from one to two and vice versa. In literature, step edges with one and two DBs are called S_N and S_D steps, respectively [190, 216]. It is intuitively clear that S_N edge atoms are more stable than S_D atoms, as the latter are easier detached during the H annealing. Consequently, S_N edges are slower etched and predominantly observed. The 4H-SiC stacking sequence implicates that the orientation of S_N edges rotates by 60° after two bilayers.

Step periodicity and orientation. The high-resolution STM image shown in Fig. 5.8**d** focuses on the edge structure marked by the violet lines. At the edge, the (1×1) lattice

periodicity is preserved and an edge reconstruction is absent[9]. Furthermore, the edges in Fig. 5.8**d** (and also in Fig. 5.8**a**) clearly evolve in ZZ orientation along the $[11\bar{2}0]$ direction, while AC edges are not seen because their formation is energetically unfavorable (compare also to the discussion of Figs. 5.1 and 5.2). The observation of ZZ-terminated SiC step edges implies that the bismuthene edges at SiC steps follow an AC geometry due to the 30° rotation of the Bi $(\sqrt{3} \times \sqrt{3})$ superstructure, which is an important finding for the major part of the measurements analyzed in Ch. 8.

In conclusion, the H_2 annealing process in static gas atmosphere enables the preparation of unreconstructed 4H-SiC(0001) surfaces with atomically smooth terrace planes. Yet, unfortunately, a significant number of cluster-like defects is found on the surface of these SiC substrates, probably as a result of insufficient gas purity. A seemingly more fundamental problem is that the surfaces exhibit a high density of pits with several nanometer depth. Obviously, this is suboptimal for the growth of high-quality thin films. Therefore, the initial, simple SiC preparation setup was replaced with a more elaborate system. The SiC surfaces prepared in this new setup posses tremendously ameliorated characteristics, as will be described in the following.

5.3 Planar SiC(0001) Samples Prepared in Flowing Hydrogen Atmosphere

The newly designed SiC preparation setup, which is described in Sec. A.2, comprises mass flow controllers that enable the definition of newly a precisely controlled flow of gas, thereby providing an additional process parameter. Accordingly, this section starts with an exploration of samples treated with varying gas flows and gas mixtures in ultra-clean H_2 and He gas with a purity degree of 8.0 or better. Then, a prototypical SiC(0001) sample prepared with a dedicated standard annealing process is investigated in detail with LEED, STM and STS. Note that the discussion in this section is constricted to planar 4H-SiC(0001) substrates. Additionally, SiC samples with 2° and 4° miscut in $\langle 1\bar{1}00 \rangle$ direction, shortly named 2° and 4° Miscut-SiC, respectively, have been prepared and are analyzed in Sec. C.1.

5.3.1 Variation of the Gas Flow and Annealing Temperature

While in many publications, the gas flow rates are not stated explicitly [38, 42, 200, 217], it ranges from values as low as 0.5 lpm [205] and even 0.0 lpm, i.e., static annealing [31], to large throughput values of 10–20 lpm [32, 41, 194] if it is specified. Most studies, however, use a moderate flow rate of 1–6 slm [31, 40, 193, 205, 218–220]. The large spread of values and the fact that none of the above-listed publications shows STM images of SiC surfaces at the atomic scale motivated an annealing parameter series. For practical purposes, flow rates at the lower limit of the reported values have been chosen. Fig. 5.9 provides an exemplary overview of samples prepared with differing parameters using LEED and STM. All samples have been subject to the same ex-situ treatment, such that differences can be

[9]Note that a small double tip, clearly visible at the surface defects, creates the impression of a doubled edge in the lower segment parallel to the scale bar.

attributed to the variation of the annealing parameters. For a full overview of all tested annealing parameters (T_{ann}, H_2/He flow) we refer to Tab. C.1.

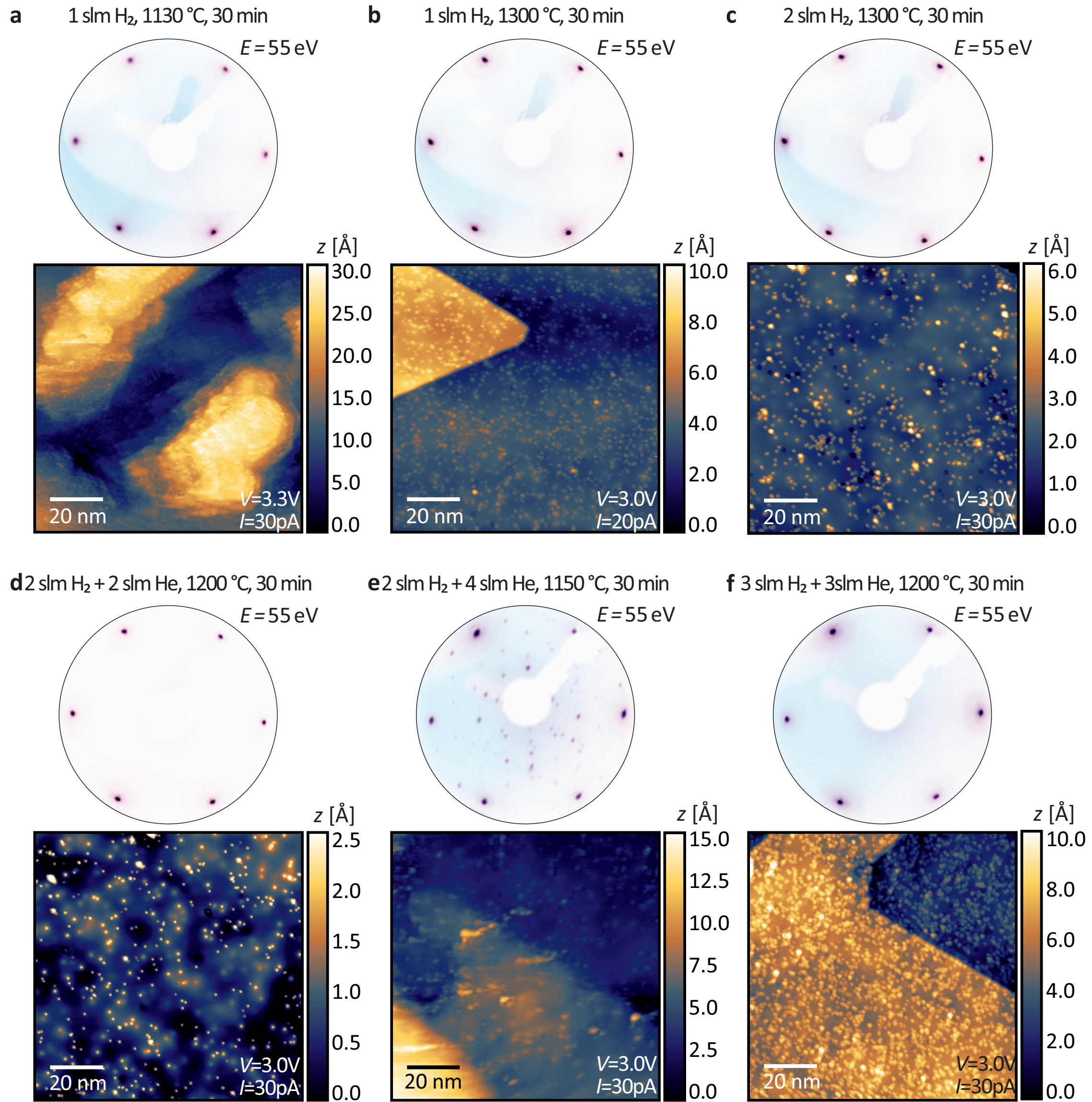

Figure 5.9 LEED and STM images of samples prepared with varying gas flow rates and temperatures. The annealing time is kept constant at $t = 30$ min. **a** A sample prepared with 1 slm H_2 gas flow and $T_{ann} = 1130$ °C exhibits only faint (1×1) spots in LEED. STM unveils a very rough surface, signaling insufficient material removal. **b** The treatment of the very same sample with the same gas flow as in **a** but at $T_{ann} = 1300$ °C results in sharper diffraction spots. The corresponding STM image reveals flat terrace planes. **c** A doubled H_2 gas flow does not cause significant improvements in comparison to **b**. **d** to **f** SiC(0001) samples annealed with admixture of He gas. **d** A sample annealed with 2 slm H_2 and 2 slm He exhibits by far the best surface. The LEED spots are very sharp and no background is noticeable. The surface defect density found in STM images is significantly lower than for the samples prepared with other annealing parameters. **e** A ratio of $H_2/\text{He} < 1$ leads to a large unit cell reconstruction despite a low annealing temperature. **f** A further increase of H_2 and He gas flow to 3 slm does not improve the result but leads to an enhanced defect density, which causes the pronounced halo around the spots in LEED.

Annealing in pure H_2. As a starting point, a SiC sample prepared with a flow of 1 slm H_2 is inspected. The temperature is set to $T_{ann} = 1130$ °C in analogy to the samples prepared in static gas atmosphere. Fig. 5.9**a** shows the corresponding LEED and STM

image. A (1×1) LEED pattern with large, diffuse diffraction spots surrounded by visible halos is observed. As expected, STM reveals a ragged, completely irregular surface. The overall etching rate seems too low to produce high-quality surfaces, and must be increased by a higher annealing temperature [217].

The very same sample is re-etched at $T_{\text{ann}} = 1300\,°\text{C}$, see Fig. 5.9**b**. Now, the LEED spots exhibit a pronounced maximum and the background noise is slightly reduced. The STM topography map shows a entirely different, but significantly improved surface morphology. Two flat terrace planes with an extent of $\approx 100\,\text{nm}$ are seen and separated by straight, regular step edges. This sample already demonstrates a major advantage of the preparation in flowing gas atmosphere: the prepared SiC(0001) surfaces are not interspersed with deep cavities as the samples annealed in static H_2 atmosphere described in Sec. 5.2, but exhibit smooth terrace planes. The most important goal is now to extensively reduce the high density of small defects visible on the SiC surface.

The necessity of higher temperatures compared to static annealing is attributed to the cooling by the gas flow. In the static annealing setup, the entire gas atmosphere was slowly heating up to such an extent that the outer chamber walls had temperatures higher than 50 °C at the end of an annealing process. The resulting elevated average kinetic energy of the molecules, especially in vicinity of the hot substrate, increases the probability of H_2 molecule dissociation and etching. In the flowing gas SiC preparation setup, the gas atmosphere is continuously exchanged and its temperature remains rather constant except in direct vicinity of the heated SiC wafer. Therefore, a higher energy transfer at the sample surface is required to overcome the H_2 dissociation energy and obtain reactive H radicals. A sample annealed with a doubled flow (2 slm H_2) but constant temperature ($T_{\text{ann}} = 1300\,°\text{C}$) is examined. Note that here a fresh SiC sample was mounted, such that the resulting sample surface does not benefit from a pre-treatment. The LEED pattern in Fig. 5.9**c** is very similar to 5.9**b**. The number of (cluster) surface defects, which most probably stem majorly from redeposited silane and methane molecules as outlined in Sec. 2.1, is probably slightly reduced but still rather high.

Admixture of He. The finding that increased gas flow rates might reduce the number of defects lead to the admixture of He gas during annealing. The idea is that the constant stream of gas causes the reaction products, i.e., silane and methane, to move away before a redeposition on the surface is possible. The secondary gas should (i) be inert, such that it does not influence the H_2 dissociation rate and formation of SiH_4 and CH_4; (ii) have an atomic mass comparable to H_2, such that both gas molecules cover similar volumes and possess similar kinematic properties; (iii) must be supplied in a sufficient purity to avoid detrimental gas contamination. He of purity degree 8.0 fulfills all these requirements.

A typical sample prepared by 2 slm H_2 and He gas flow is shown in Fig. 5.9**d**[10]. The LEED pattern of the sample shown in Fig. 5.9**d** is distinctly higher in quality than of the previous samples. The diffraction spots exhibit a very sharp maximum, whereas a spot halo or noticeable background noise are absent. The corresponding STM measurement discloses a considerably better surface, with comparably large areas up to $10\,\text{nm} \times 10\,\text{nm}$

[10] Note that the temperature has been lowered to $T_{\text{ann}} = 1200\,°\text{C}$ as a sample surface prepared at $T_{\text{ann}} = 1300\,°\text{C}$ reconstructs, which is attributed to a higher Si depletion than etching rate.

being defect-free. The absence of large clusters allows the perception of apparent height fluctuations, which do not seem to be caused by adsorbates but by sub-surface defects (e.g., vacancies or N doping impurities), like in other semiconductors [214, 215].
Samples processed with further increased gas flow rates are shown in 5.9**e** and **f**. Both substrates are prepared with the same overall gas flow of 6 slm, but with different H_2:He ratios [1:2 (**e**) and 1:1 (**f**)]. A ratio $H_2/He < 1$ (2 slm H_2 and 4 slm He) causes a failure of the annealing process. Clearly, diffraction spots additional to the (1×1) spots are visible but cannot be ascribed to a certain reconstruction because of poor diffraction pattern quality. In STM, the sample is hardly measurable, as the tip highly instable atop of the fuzzy area with higher charge density. Seemingly, the low H_2 partial pressure leads to a Si depletion of the surface already at $T_{ann} = 1150\,°C$[11]. The second sample (5.9**f**) treated with a flow ratio $H_2/He = 1$ and $T_{ann} = 1200\,°C$ shows a (1×1) LEED pattern but a very high cluster density in STM. Hence, a beneficial influence of the further increased gas flow rate cannot be confirmed.

5.3.2 Detailed Investigation of the SiC(0001) Surface: Step Morphology, Atomic Resolution and Spectroscopy

After exploration of the annealing parameters we set the surface characteristics of samples prepared in flowing gas into focus. We begin by inspection of surface morphology, i.e., the extent of the terrace planes as well as the orientation and height of terrace steps. The discussion is based on measurements conducted on the sample shown in Fig. 5.9**b**, however, all samples prepared with functional annealing parameters (Fig. 5.9**b**, **c**, **e** and **f**) exhibit comparable surface morphologies.

Step orientation. Accordingly, Fig. 5.10 shows CCIs recorded on a SiC(0001) substrate annealed with 1 slm H_2 flow and at $T_{ann} = 1300\,°C$. The 500 nm overview scan (Fig. 5.10**a**) reveals the presence large terraces with an extent of several 100 nm, comparable to values reported in literature for etching in flowing H_2. Importantly, deep etching pits are absent [41]. Yet, samples prepared in static and flowing gas atmosphere share the property that step edges connecting adjacent terraces are oriented predominantly along three directions. These directions rotate after a sequence of two SiC bilayers (i.e., after 2H steps). This is highlighted in the zoom-in image shown in Fig. 5.10**b**. For each terrace pair, extended straight edge segments are connected by a 120° angle, which are perpendicular to the white arrows in Fig. 5.10**b**. Step edges evolving in a direction reached by a 60° rotation in relation to these steps (i.e., perpendicular to the dashed white arrows Fig. 5.10**b**) are crystallographically equivalent but rarely seen, not really straight and with indents. The situation is reversed at the step edges formed with the lower or upper adjacent terraces. This alternating behavior is visualized by focusing on a certain step edge orientation roughly perpendicular to the red line profile in Fig. 5.10**a**, where green and purple rectangles indicate smooth and rough step edges, respectively.

[11] Close to the clamps of the DC sample plate, where the temperature is roughly 50°C lower than in the center, indeed a (1×1) reconstruction is found. Interestingly, the sample surface is very similar to the surface seen in Fig. 5.8 and shows pronounced triangular etch pits, see App. C.4

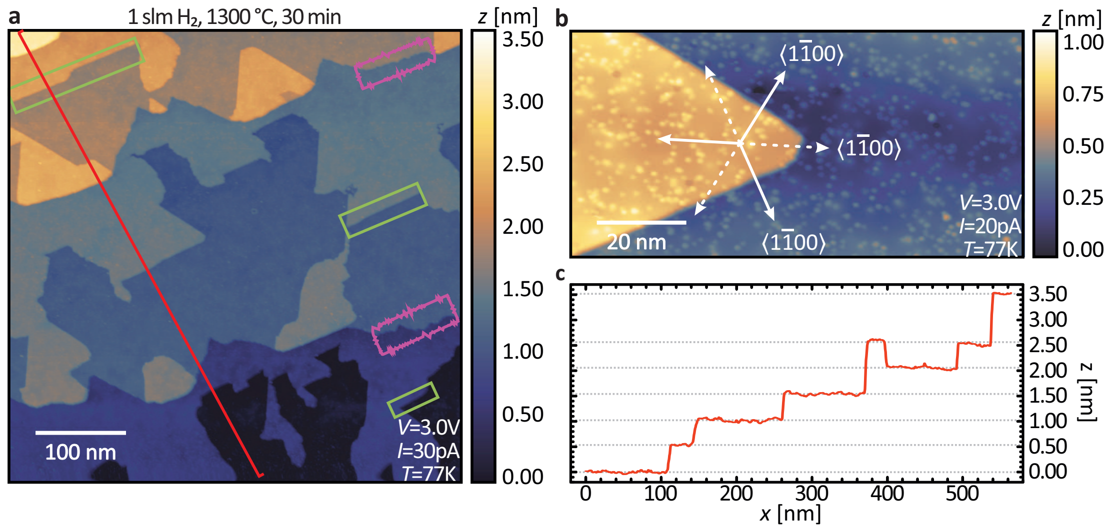

Figure 5.10 **a** Large scale STM scan of SiC(0001) samples prepared in ultra-pure H_2 gas flow. Terrace planes with several 100 nm extent are typical for 4H-SiC(0001) samples prepared in flowing gas atmosphere. Wide-stretched straight step segments are preferentially observed along three distinct directions that are rotated by 60° after each terrace step. The green (smooth edge) and purple (disordered edge) rectangles visualize that smooth, straight edges along this specific direction evolve at every other terrace step. **b** Zoom-in STM image. Straight step edges (solid white arrows) enclose a 120° angle while edges along the crystallographically equivalent orientation, which are rotated by 60° (dashed white arrow), are rarely seen for these two terrace planes. **c** The line profile reveals that 2H-SiC, i.e., $1/2c^{\text{4H-SiC}}$ step are predominantly found on the surface.

Step height. The stacking sequence of 4H-SiC has a major impact on the edge formation. Hence, the step height is determined with the red line profile shown in Fig. 5.10**c**. Clearly, $5\,\text{Å} \approx \frac{1}{2}c^{\text{4H-SiC}}$ steps are predominantly seen, and full 4H-SiC steps ($\approx 10\,\text{Å}$) appear only occasionally, while single bilayer steps are completely absent. The predominance of 2H steps can be explained by considering that the bilayers within the 4H-SiC stacking sequence possess inequivalent surface energies, i.e., $4H2/4H2^*$ layers are less stable and faster etched than $4H1/4H1^*$, see Fig. 5.3 [190, 197, 200]. Nevertheless, the finding of two bilayer steps on the surface deviates from many experimental reports (Refs. [194, 197, 200] with exception of Ref. [191] and a Monte Carlo study [190]). Although most articles report the initial bilayer bunching to half $c^{\text{4H/6H-SiC}}$ steps, a further bunching to full $c^{\text{4H/6H-SiC}}$ steps is frequently observed and attributed to the inequivalent number of DBs for the adjacent half $c^{\text{4H/6H-SiC}}$ steps.

There are two reasons that might explain these differences. Firstly, a major part of the above-cited studies investigates SiC substrates with miscuts $> 1°$ in $\langle 1\bar{1}00\rangle$ and $\langle 11\bar{2}0\rangle$ direction. For such substrates we find similar results as is discussed in Sec. C.1. Note that the predominance of 2H-SiC steps for on-axis SiC(0001) as well as the presence of full unit cell (4H) steps for samples with a miscut along $\langle 1\bar{1}00\rangle$ are claimed in a Monte-Carlo study [190]. Secondly, in those experiments, SiC is prepared at much higher temperatures (1600–1800 °C). Even though a direct comparison of the temperature readings might not be appropriate it is likely that the temperatures and therewith the etching rates are significantly enhanced. Considering the changes we found when moderately elevating temperature from the static (1H SiC steps) to dynamic annealing process (2H SiC steps), it does not seem unlikely that a further increase of T_{ann} might cause the differences between

out experiments and the cited articles.

The preferential formation of steps along three directions, which connect neighboring terrace planes, can be elucidated by consideration of the 4H-SiC(0001) crystal structure shown in Figs. 5.1 and 5.3. For each SiC bilayer and along a certain direction, there exists a ZZ termination with one DB (S_N edge), while the opposite edge has two DBs (S_D edge). During the etching process, S_D edges are gradually rearranged into the more stable S_N edges. Therefore, as indicated by solid and dashed white arrows in Fig. 5.10**b**, steps are preferably observed in the three equivalent S_N step orientations in Fig. 5.10**a**, while S_D edges are not seen. As discussed in Sec. 5.2.3, the orientation of the nearest neighbor (NN) bonds changes from wurtzite to zinc blende according to the stacking order of 4H-SiC for every other bilayer, see Figs. B.1 and 5.1. This causes a 60° rotation of the orientation of S_N steps and hence of the more stable edge orientations after a $2\text{H}/\frac{1}{2}c^{\text{4H-SiC}}$ sequence, as apparent in Fig. 5.10**a**.

Close-up STM measurement. In the following, we scrutinize the atomic arrangement of SiC(0001) surfaces. Fig. 5.11**a** shows a high-resolution STM scan. The red line profile (Fig. 5.11**b**) lies across the topmost atoms and shows a periodicity of 3.08 Å, i.e., the in-plane lattice constant of SiC [163, 164]. The green line profile in between the topmost

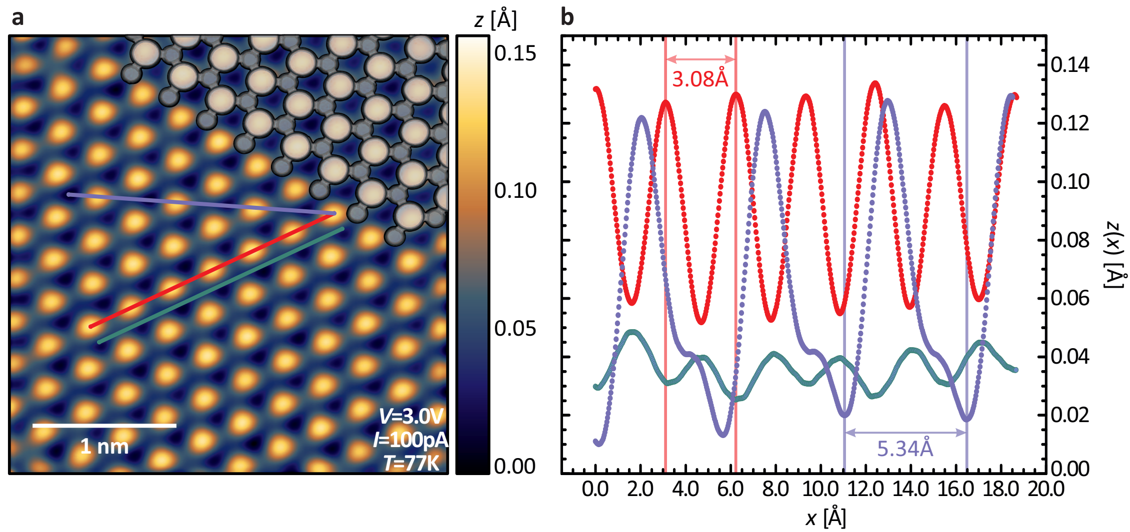

Figure 5.11 **a** Atomic resolution STM showing the well-ordered (1 × 1) SiC(0001) surface. The image is leveled with a polynomial background to improve the contrast of the sub-surface structure. Despite a low atomic corrugation, the bonds from the Si atoms to the C atoms are clearly observable. A ball-and-stick model of a SiC bilayer is overlaid to the measured image in the top right corner. Si and C atoms are represented by light and dark gray circles, respectively. **b** The red line profile is positioned above Si atoms and shows the expected periodicity of 3.08 Å. The parallel green line profile is located exactly in the middle between two rows of Si atoms. The violet line profile is oriented in the perpendicular crystallographic in-plane direction of the SiC lattice and shows both the position of the Si and C atoms.

atoms exhibits precisely the same periodicity, but with much smaller corrugation. By comparison with the structure model of the surface (Fig. 5.1) we conclude that peaks in both line profiles signal the positions of Si and C atoms.

A ball-and-stick model in the top right corner of Fig. 5.11**a** visualizes the lattice sites of both atom species. The Si atoms (light gray) and C atoms (dark gray) are connected by

three bonds. The missing fourth bond of the Si atoms is sticking out of the surface plane and passivated by H atoms during the H annealing process.
A third line profile in Fig. 5.11**b** (purple line) is rotated by 30° with respect to the other two. Here, three well-defined z levels are visible, which are attributed to Si (high peak), C (small peak) and the void site of the surface bilayer. The clearly detectable corrugation from the C sublattice leaves its fingerprints on the bismuthene lattice, as will be discussed in Sec. 7.2.1.

Spectroscopy on terrace plane and at step edge. The LDOS at the surface of the 4H-SiC(0001)-H samples may be probed with STS. Measurements are conducted on the bulk terrace and across a step edge to examine the presence of the expected wide band gap ($E_{\mathrm{gap}}^{\mathrm{4H\text{-}SiC}} = 3.27\,\mathrm{eV}$ [45]). Fig. 5.12**a** shows two terrace planes separated by a full 4H unit cell step ($\approx 10\,\mathrm{Å}$), visible in the line profile shown in Fig. 5.12**b**. The 4H stacking sequence implies that the C sublattice is oriented identically in relation to the Si lattice on both terrace planes, which can be deduced from magnified views of the line profiles (insets in Fig. 5.12**b**). Hence, C atoms form the last atom row of the topmost layer. Small bumps at the step wall (marked with gray dashed lines in Fig. 5.12**b**) might indicate the position of the four SiC bilayers (see again Fig. 5.1). Colored dots in the close-up STM scan in vicinity of the step edge (Fig. 5.11**c**) are related to the respective spectroscopy curves in Fig. 5.11**d** and **e**. The insets in Fig. 5.11**d** and **e** aim to allow a more precise evaluation of the band gap magnitude. However, the measurement precision is limited as it is not possible to stabilize the tip at energies lower than 2.5 eV impossible. All spectra exhibit very similar band onset energies, and no states are apparent in the band gap, neither on the terrace plane nor for the spectra recorded across the step edge. This will be important for the interpretation of the STS data at edges of bismuthene at SiC substrate steps.

Band gap magnitude. The heavy N doping of the used 4H-SiC(0001) substrates effectuates that the Fermi level is shifted from a midgap position towards to the CBM in all measurements. In our analysis, the band onset is defined by a linear extrapolation of the band edges in VB/CB towards the average value within the band gap. The best estimates are calculated as the mean of 18 individual measurements and the errors are obtained with the uncertainty of the linear fit. With this procedure, we determine the VB and CB onset to $(-2.83 \pm 0.21)\,\mathrm{eV}$ and $(1.51 \pm 0.093)\,\mathrm{eV}$, which results in an overall band gap of $E_{\mathrm{gap}}^{\mathrm{SiC,\,STS}} = (4.34 \pm 0.22)\,\mathrm{eV}$. This value is much larger than the literature value of $E_{\mathrm{gap}}^{\mathrm{SiC,\,lit}} = 3.27\,\mathrm{eV}$ [45], suggesting that the probed signal is strongly influenced by band bending effects. In literature, various sources of band bending are described, see, e.g., Ref. [221]. Among the possible reasons, surface band bending due to surface states can be excluded as the DB states are passivated by the H annealing process. In contrast, tip-induced band bending (TIBB), which is a common problem for band gap determination of semiconducting substrates with STS [222], is likely to contribute to the probed, too large band gap magnitude. TIBB occurs when a lack of free charge carriers results in an incomplete screening of the potential between tip and sample at the surface. Consequently, a finite electric field penetrates into the crystal, which acts as a dielectric and causes band bending [222]. Roughly speaking, the applied potential is partially compen-

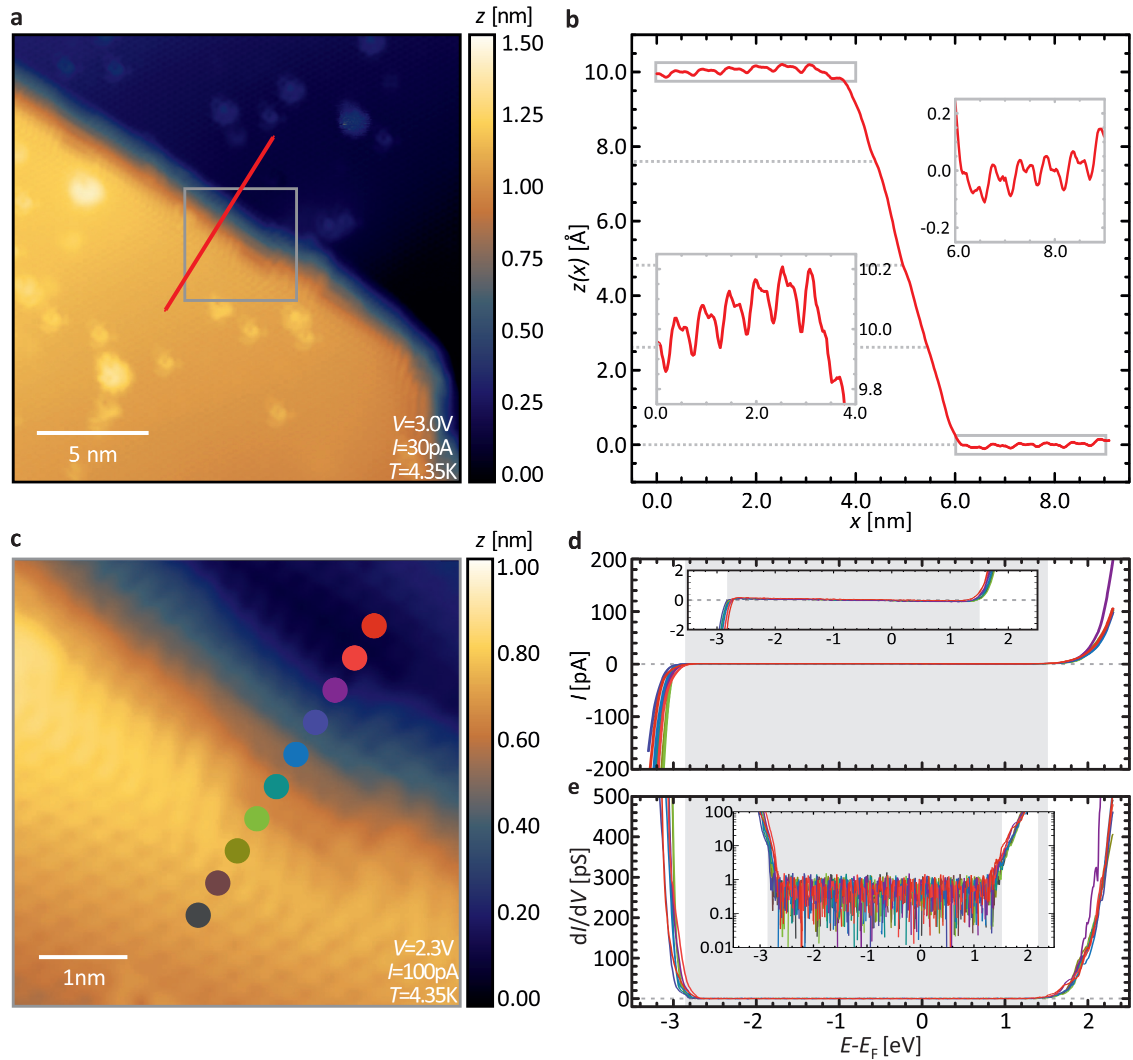

Figure 5.12 STS of H-annealed SiC(0001) on a plane terrace and across a 4H step. **a** Overview STM image showing two terrace planes. **b** The line profile along $\langle 1\bar{1}00 \rangle$ and marked in **a** reveals that both terraces are separated by a full 4H-SiC (c^{SiC}) step. The insets show magnified views of the z profile of upper and lower terrace. Si atoms (larger peaks) and C atoms (smaller peaks) are recognizable in the same ordering and indicate that the C sublattice orientation is equal on both terraces, as expected from a full step. **c** Close-up image marked with the light gray square in **a**. The colored circles indicate the measurement positions of the STS curves. **d** and **e** Corresponding $I(V)$ and $\mathrm{d}I/\mathrm{d}V(V)$ curves. The gray area behind the curves visualizes the band gap. No in-gap states are seen. $I_{\mathrm{st}} = 100\,\mathrm{pA}$, $V_{\mathrm{st}} = 2.3\,\mathrm{V}$, $T = 4.35\,\mathrm{K}$. Sample preparation according to Sec. 5.4.

sated by a polarization of the semiconducting material, such that the signal corresponding to an effectively reduced potential is probed. Consequently, both VB and CB onsets are observed at increased absolute energies.

The impact of TIBB depends on many experimental parameters such as the tip shape, the tunneling voltage, the material properties (intrinsic charge carrier concentration, dielectric function) as well as on the dopant type and concentration, and its quantitative evaluation is beyond the scope of this thesis. Nevertheless, we may draw some conclusions by comparison to related systems. P. Weidlich et al. (Ref. [214]) discuss the VB onset of p-doped GaAs with doping concentrations in a comparable range (10^{18}–$10^{19}\,\mathrm{cm}^{-3}$) as in our SiC samples. Even for high carrier concentrations of $p = 4 \times 10^{19}\,\mathrm{cm}^{-3}$, i.e., even for a rather complete screening, they calculate a VB shift of $\approx 0.5\,\mathrm{eV}$ and a small CB shift ($< 0.1\,\mathrm{eV}$) at $\|V\| =$

2 eV. An order of magnitude lower p-doping causes a band bending as large as 1.5 eV. This indicates that TIBB might easily explain the observed deviation from the literature value. Another interesting detail concerns the Fermi level position, which does not seem to be determined by the N impurity ionization level ($E_N^{ion} = E_{CB} - 61\,\text{meV}$) as one would expect in a SiC sample with an as high doping concentration, see Fig. 5.5**b**. Interestingly, Seyller et al. also stated difficulties in generating a flat band condition for n-doped 6H-SiC(0001) samples, even though this is no problem for p-type or in 6H-SiC(000$\bar{1}$) samples [31, 45]. Instead, they observe a band bending of 0.6 eV, which is attributed to a small number (0.2% of a monolayer) of DBs resulting from incomplete H passivation. In Sec. C.4, characteristic surface defects regularly found on SiC substrates are inspected with STM and STS measurements. We may not assign one of the probed defects to Si DBs with hich confidence. Yet, importantly, none of these defects introduces impurity states close to the Fermi level.

5.4 SiC(0001) Samples Used for Bismuthene Growth

Practical considerations with the main goal to keep the duration of the annealing as short as possible lead to a slight modification of the annealing process. It is derived from the 2 slm H_2/2 slm He annealing process, which generated the highest-quality SiC surfaces, and has become our standard recipe for preparation of 4H-SiC(0001) substrates.
Based on the experiences with different preparation parameters a significantly shorter two-step process has been implemented. The pyrometer-controlled sample temperature during the procedure is displayed in Fig. 5.13. It possess plateaus at two distinct annealing temperatures, $T_{ann1} = 1250\,°\text{C}$ ($T_{ann1} = 1230\,°\text{C}$) and $T_{ann2} = 1180\,°\text{C}$ ($T_{ann} = 1150\,°\text{C}$) for planar SiC(0001) [2° / 4° Miscut-SiC] samples[12]. The individual procedure steps are the following:

I A rapid sample heat up to T_{ann1}. Overshooting to temperatures higher than $\approx 1300\,°\text{C}$ must be avoided as this might cause the formation of a C-rich reconstruction.

II The first higher temperature T_{ann1} aims to remove deep polishing trenches and to reduce the surface roughness. Due to the high reaction rate at T_{ann1}, a duration of only 2 min proves to be sufficient. If a sample is reused, this step is omitted and the annealing process starts with step IV.

III The temperature is rapidly lowered to T_{ann2}.

IV Annealing at T_{ann2} focuses on increasing the size of defect-free areas by a lowered etching rate, therewith reducing the number of newly generated and probably redeposited SiH_x and CH_x molecules.

V The slow reduction of the temperature is used to affect an incremental decay of the H_2 dissociation and etching rate, again with the goal to gradually reduce the density of etching products[13].

VI At a reasonably low temperature, the cool down rate is increased.

[12]Miscut samples require lower preparation temperatures as they tend to reconstruct more easily. This is probably caused by their lower surface stability, resulting from the higher density of step edge atoms with less backbonds to the bulk crystal.

[13]A new process guiding, focusing on an even longer duration of this step, indicates that the formation of

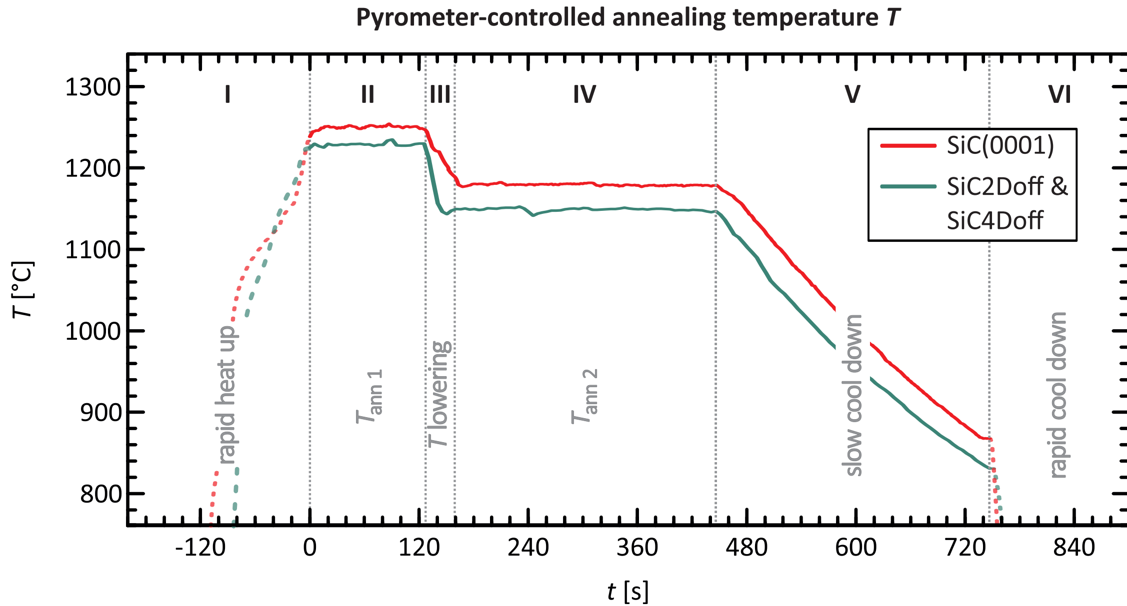

Figure 5.13 Pyrometer-controlled SiC substrate temperature recorded during the standard H annealing process. The sample heating starts as soon as the chamber is filled with a pressure of $p = 950\,\mathrm{mbar}$ of H_2/He gas. The entire process time is about 12 min.

This modified annealing process has a duration of only ≈ 12 min, approximately one third of the processes used before. Despite that, it produces SiC samples of highest quality, see Fig. 5.14. The surface morphology apparent in the STM scan in Fig. 5.14**a**, with terrace planes of several 100 nm width and straight step edge segments, is typical for as-prepared samples. The perception of the LDOS variation at large scales on the surface is clearly visible due to the low z corrugation. Fig. 5.14**b** shows a smaller CCI with three terrace planes. The line profile shown in Fig. 5.14**c** reveals that the terraces are still separated by 2H-SiC steps.

The step edges of the upper terrace constitute perfect examples of the preferential orientation of the step walls along the three distinct directions that possess only one DB, the S_N steps (indicated by the full lines of the white hexagon in Fig. 5.14**b**). Similarly, the lower-lying terrace step exhibits two DBs (S_D step) in this direction according to the 4H stacking sequence (dotted lines of the white hexagon in Fig. 5.14**b**), and visualizes the meandering step edges resulting from the faster etching. The defect density in Fig. 5.9**d** is kept fairly low.

Accordingly, the 4H-SiC(0001) samples prepared with the modified annealing process shown in Fig. 5.13 provide a suitable substrate to stabilize bismuthene. The epitaxial growth process will be detailed in the following chapter.

straight step edges without indentations profit from a controlled, slow cool down [223].

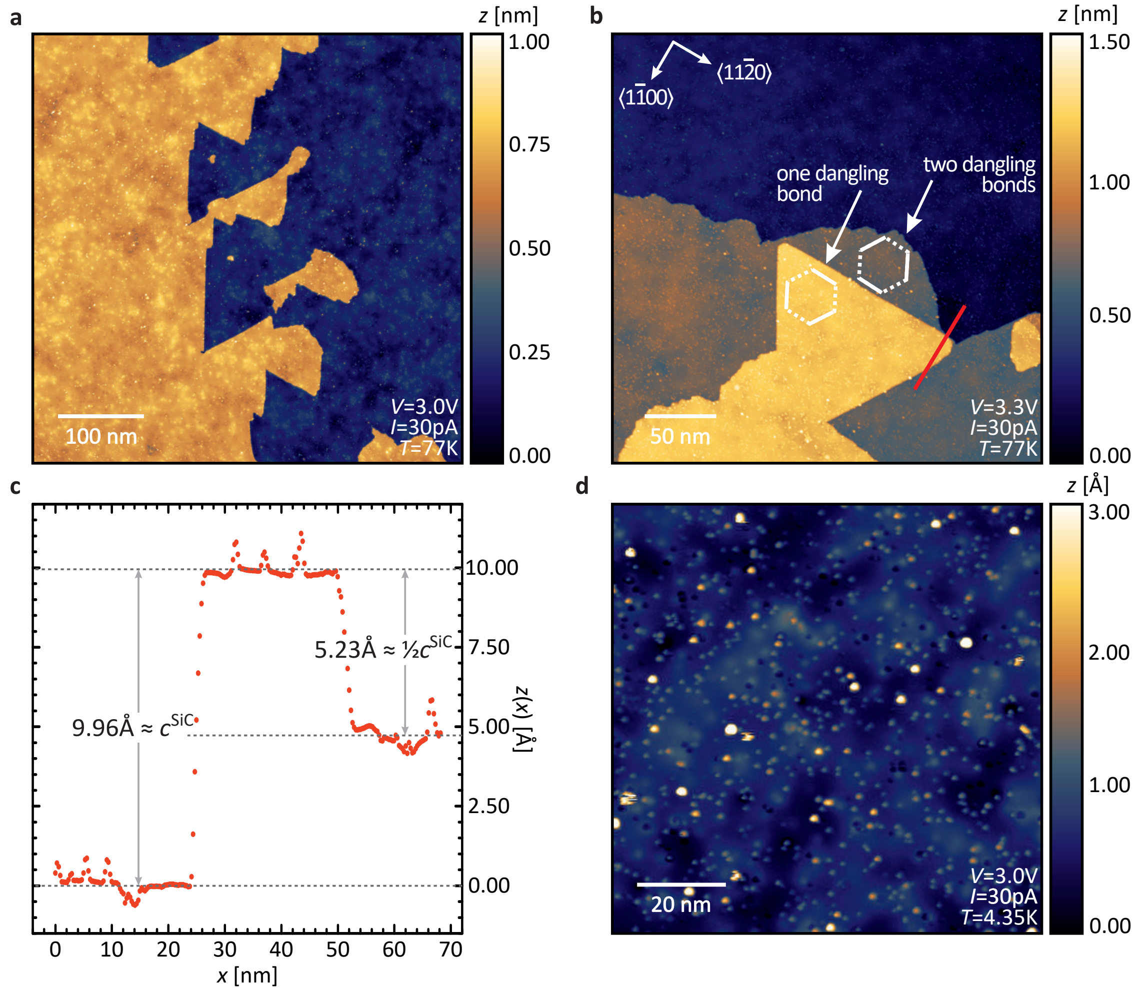

Figure 5.14 STM images of samples prepared with the modified H_2 and He gas annealing process at two temperatures in Fig. 5.13. **a** The overview scan demonstrates the presence of very large terrace planes with several 100 nm width. **b** The upper terrace has perfect straight step edges along three directions. The white hexagon denotes edges with presumably one (full line) and two (dotted line) DBs. The profile marked by the red line is shown in **c**. It shows that half ($\frac{1}{2}c^{\mathrm{SiC}}$) and occasionally full unit cell steps (c^{SiC}), but not single bilayer steps ($\frac{1}{4}c^{\mathrm{SiC}}$) evolve during the H annealing. **d** The smaller STM image enables the perception of LDOS fluctuations caused by crystal imperfections. The point defect density is fairly low.

6 Epitaxial Growth and Structure of Bismuthene on SiC

The formation of Bi honeycombs on SiC is accomplished with a dedicated molecular beam epitaxy (MBE) process requiring dynamic and precise control of the substrate temperature. In principal, the two key growth process steps are (i) the H desorption from and (ii) the Bi accumulation on the SiC surface.

A cautious process guiding is necessary because the H atoms are released at a temperature that provides (almost) enough energy for the formation of a Si-rich surface reconstruction, which would render the substrate useless for bismuthene growth. Hence, often several growth attempts are required to achieve satisfying results, as will be discussed in the first section of this chapter. Moreover, we use scanning tunneling microscopy (STM) and low-energy electron diffraction (LEED) to inspect the surface reconstructions, the growth mode and the morphological characteristics of different bismuthene samples with varying quality. Lastly, based on X-ray photoelectron spectroscopy (XPS) measurements, the chemical properties and the stability of grown films is discussed.

6.1 Growth Process Guiding

Bismuthene attains its peculiar electronic properties only if a covalent bond between Bi atoms and the SiC substrate develops. Obviously, this implicates that the H atoms passivating the Si dangling bonds (DBs) on the surface after annealing in dry H_2 (H annealing) must be released. The H desorption can be accomplished either by thermal energy or by light with proper intensity and energy. Although the latter option seems attractive, it is not feasible unless working with a synchrotron beam[14]. Therefore, thermal desorption by direct current (DC) heating of the substrate is the method of choice.

6.1.1 Evaporation Procedure

During the growth procedure, the temperature is monitored and controlled with a pyrometer. The corresponding temperature curve is shown Fig. 6.1. As for the gas phase process in Fig. 5.13, the purpose of the individual steps is shortly outlined in the following:

I The SiC sample is pre-heated to initiate the growth by a well-defined temperature, independent of the substrate's resistance and earlier preparation steps (e.g. STM measurements at low temoerature, transfer, degas, etc.).

II Rapid increase to $T_{\text{deso}} \approx 600\,°\text{C}$. During this ramp, the effusion cell shutter is opened at $T = 500\,°\text{C}$ (marked by the black dot in Fig. 6.1).

[14]Desorption of H with lab-based He light and other high-energy and -intensity light sources have been attempted and are discussed in Ref. [224]. Unfortunately, these methods are not successful for practical application during bismuthene growth.

III H desorption from the surface. This is the most critical step and discussed in detail below.

IV Rapid reduction from desorption (T_{deso}) to accumulation (T_{accu}) temperature. The latter is comparable or slightly lower than the temperature of the Bi cell T_{Bi}.

V The sample temperature is kept constant to achieve long-range ordering of the impinging Bi atoms. The duration of this step varies, depending on T_{Bi}.

VI Ultimately, the temperature is lowered rapidly to avoid a re-evaporation of bound Bi atoms from the SiC surface, which occurs within few seconds at $T > 430\,°\text{C}$. The shutter closure is delayed by 3 s. An earlier shutter closure results in a Bi-deficient surface, whereas a later closure provokes the presence of Bi multilayers. At zero heating current, the sample temperature slowly cools down until it is in thermal equilibrium with its surroundings.

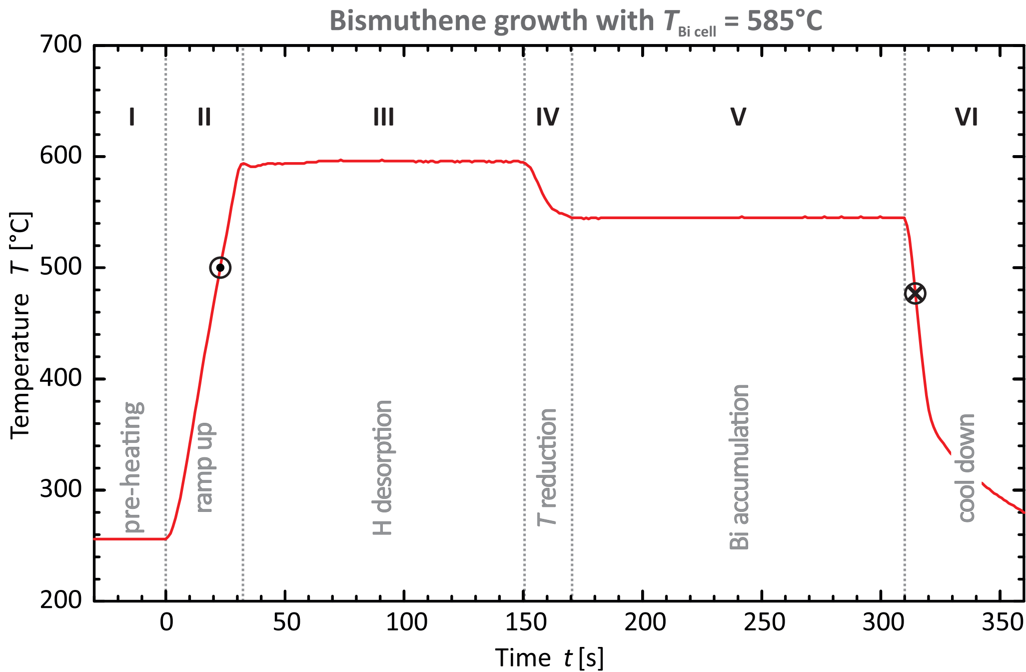

Figure 6.1 Pyrometer-controlled substrate temperature during the evaporation of Bi on SiC(0001) substrates. The circle and cross denote the temperature at which the Bi effusion cell shutter is opened and closed, respectively.

It must be clearly stated that the understanding of the mechanisms during the growth is rather rudimentary as a dedicated growth chamber was lacking while most of the experiments presented in this thesis have been conducted. In particular, the chamber layout prevented the monitoring of the substrate temperature in its evaporation position, which hampered systematic film growth studies. Only recently this became possible in a newly built chamber. Nevertheless, based on the experience gathered with about 50 grown samples, steps that are decisive for the obtained film quality can be named.

H desorption. As mentioned in the introductory words of this chapter thermal H desorption bears the danger of obtaining a Si-rich surface reconstruction. Seyller et al. reported that H desorption is accompanied by simultaneous formation of a $(\sqrt{3}\times\sqrt{3})$-Si reconstruction and occurs around 700 °C [31]. Although recent results suggest that this is not the

case[15], both processes occur at almost the same temperature, which makes the desorption (step III) highly critical. A $(\sqrt{3} \times \sqrt{3})$Si-reconstructed SiC substrate must be annealed in H_2 atmosphere again, as it prohibits makes the formation of a covalent bond between Bi and Si unfeasible. The high risk of obtaining a Si-rich surface reconstruction is tackled by lowering the desorption temperature: initially, we used $T_{deso} \approx 650$–$670\,°C$ for 10–20 s and later lowered it to $T_{deso} \approx 600\,°C$, which is kept longer time to compensate the reduced probability of H release. Attempting to lower T_{deso} even further seems absolutely reasonable.

Shutter opening and closure. The shutter is opened already at 500 °C. In this way, Bi atoms are continuously impinging on the surface during the desorption period. It is not clear whether this Bi "counter pressure" helps to avoid the formation of a Si-rich phase – this must be clarified by further studies. However, the delayed shutter closure at the end of the growth process, which is targeted to compensate the time until the temperature is below 400 °C and bismuthene remains stable on the sample, is necessary to obtain a decent sample coverage.

T_{Bi} and T_{accu}. The accumulation temperature T_{accu} and Bi effusion cell temperature T_{Bi} are closely linked. In contrast to T_{Bi}, the precision of our sample temperature measurement is not clear since the emissivity of polished SiC samples is unknown but would be required for a reliable pyrometric temperature measurement. The successful growth of bismuthene might indicate that the pyrometer reading is reasonably close to the real sample temperature. At the typically used effusion cell temperature ($T_{Bi} = 585\,°C$), the vapor pressure of Bi is very high ($p_{Bi} = 1 \times 10^{-3}$ mbar). Again, a lowering of T_{Bi} and T_{accu} seems plausible with the goal to generate fewer lattice nucleation sites, as this might lead to larger domains. This issue will be discussed in more detail in Secs. 6.2, 6.3 and 7.3.1.

Despite the fact that key process steps require further exploration to gain a decent understanding of the relevant mechanisms, meanwhile a high success rate trending to 90% has been achieved, even though often more than one growth attempt is necessary. Whether or not bismuthene has formed on SiC is decided with inspection by LEED, which provides a fast and robust tool to judge the film quality and coverage. Hence, the next subsection describes the criteria that have to be fulfilled to indicate a successful bismuthene formation.

6.1.2 LEED Characterization and Cycling of Bismuthene Growth

The outcome of a growth attempt is analyzed by LEED immediately after termination of the Bi deposition. The evaluation process is schematized in the flowchart diagram shown in Fig. 6.2.

The LEED examination starts with $E = 55$ eV beam energy. In case that an intense $(\sqrt{3} \times \sqrt{3})$ reconstruction is visible, the beam energy is lowered to 50 eV, as will be detailed later. If, instead, the $(\sqrt{3} \times \sqrt{3})$ spots have a low intensity or are very broad, the deposition is incomplete and not worth an examination in STM, such that the substrate temperature is elevated to $\leq 550\,°C$ with the intention to re-evaporate all Bi atoms from the surface.

[15] Recent investigations indicate that H atoms can be removed without obtaining a $(\sqrt{3} \times \sqrt{3})$-Si reconstruction [223]. Instead, the desired (1×1) reconstruction is maintained upon H desorption.

The left and right picture in the middle row of Fig. 6.2 exemplary display diffraction patterns with intense and weak $(\sqrt{3} \times \sqrt{3})$ spots, respectively. After the desorption, the sample's LEED pattern is re-inspected to confirm the presence of a (1×1) periodicity and exclude the possibility of a Si-induced $(\sqrt{3} \times \sqrt{3})$ reconstruction. If the latter is found, the sample must be H annealed again, as indicated in the lowest row of Fig. 6.2.

Bi- vs. Si-induced $(\sqrt{3} \times \sqrt{3})$ spots. Besides a Bi-induced also a Si-induced $(\sqrt{3} \times \sqrt{3})$ reconstruction might form during the evaporation procedure, and either fully cover the surface or coexist with the bismuthene patches. Therefore, the question arises whether one can distinguish the two reconstructions. Theoretically, within kinematic LEED theory, the observed LEED pattern and intensities depend on the structure factor F, which is

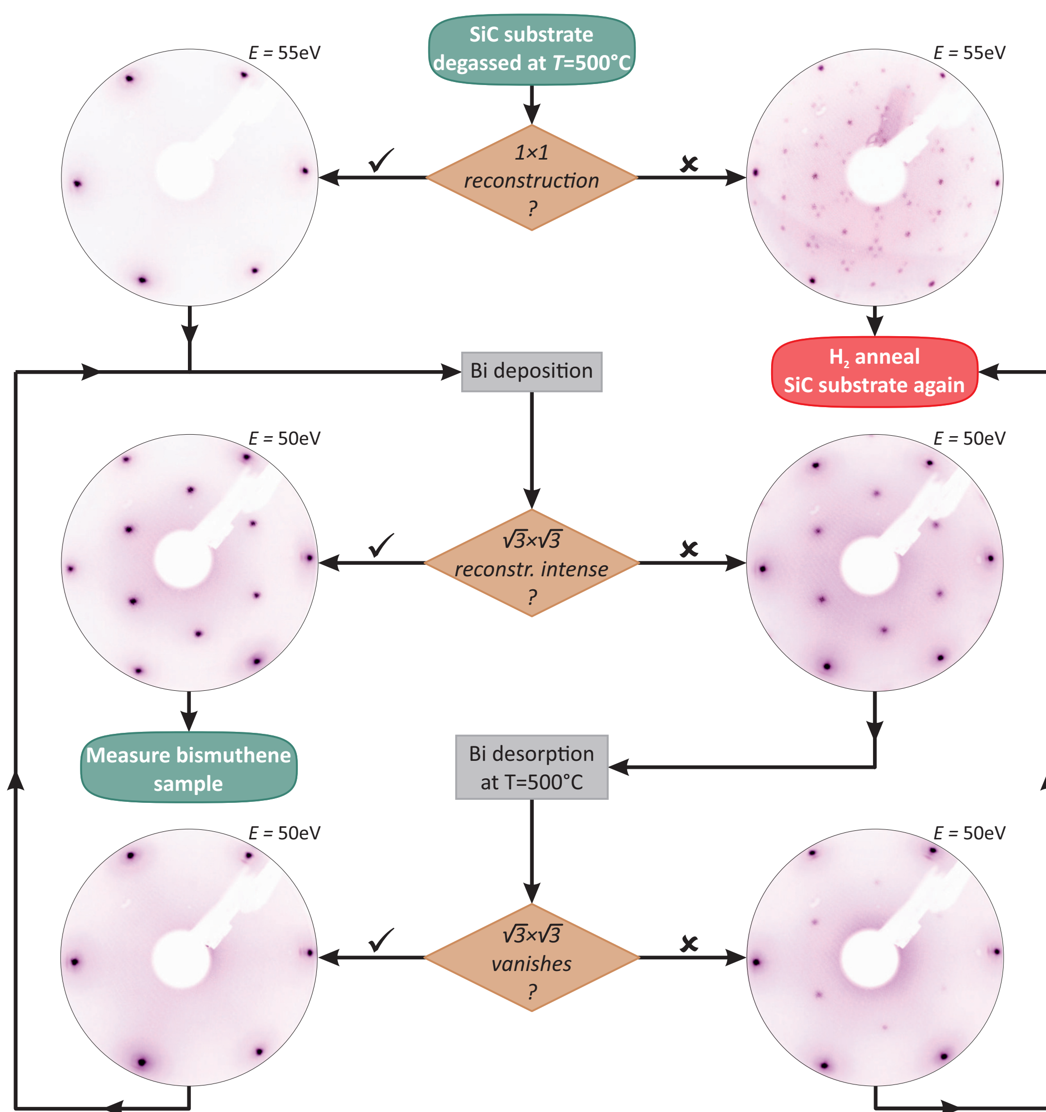

Figure 6.2 Flow chart visualizing the evaluation of the quality of bismuthene/SiC samples with LEED. Subsequent to each preparation step, i.e., after transfer from the H annealing setup to the growth chamber, the sample degas at $T = 500\,°\mathrm{C}$, the Bi deposition and, a possible Bi desorption, the surface periodicity is checked with LEED. As long as a (1×1) reconstruction is regained after Bi desorption the sample can be re-used for further growth attempts. More often than not several deposition cycles are required until a decent $(\sqrt{3} \times \sqrt{3})$ reconstruction is found. Alternatively, the cycle is terminated when spots additional to (1×1) appear on Bi-desorbed samples.

composed of the atomic structure factors and the position of the respective atoms within the unit cell [67]. Both parameters are different for Bi and Si superstructures, as the $(\sqrt{3} \times \sqrt{3})$-Si reconstruction forms a triangular lattice with only 1/3 monolayer coverage with respect to the topmost Si layer [225], whereas Bi atoms arrange in a 2/3 monolayer reconstruction, see Fig. 4.4. For a quantitative analysis, $I(V)$ LEED, which takes the underlying substrate into account, is necessary [67]. Fortunately, a differentiation of both phases with high certainty is possible even with conventional LEED by variation of the probing energy E.

Bi-induced and Si-induced $(\sqrt{3} \times \sqrt{3})$ reconstructions on SiC samples with 4° miscut in $\langle 1\bar{1}00 \rangle$ direction (4° Miscut-SiC) are shown in Fig. 6.3**a**–**c** and **d**–**f**, respectively. The LEED images are acquired at 50 eV and 55 eV. The averaged line profiles across (1×1) and $(\sqrt{3} \times \sqrt{3})$ spots are shown in Fig. 6.3**c** and **f** and normalized to the (1×1) peak intensity, which reveals differences between the Bi- and Si-rich surface. For a Bi reconstruction, the

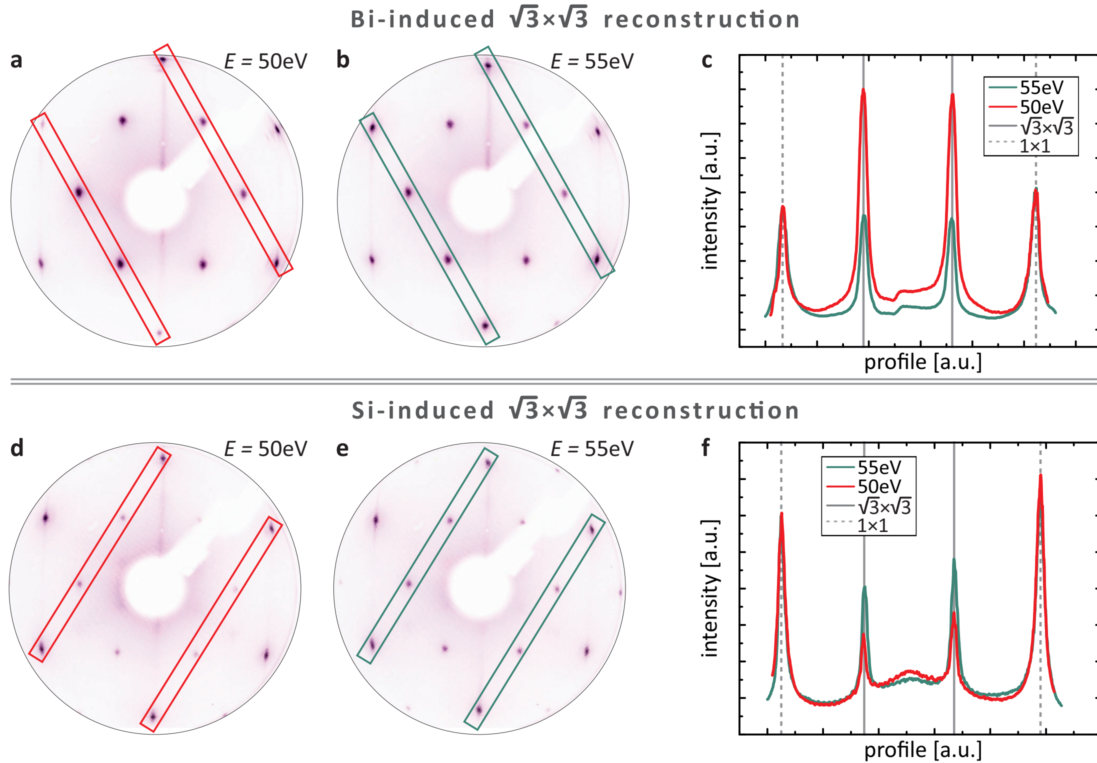

Figure 6.3 LEED images and corresponding line profiles for a **a-c** Bi-induced and **d-f** Si-induced $(\sqrt{3} \times \sqrt{3})$ reconstruction on a 4° Miscut-SiC substrate. The line profiles are averaged in the areas marked by the red and green rectangles. To account for a possible C sublattice-induced intensity variation of the (1×1) spots upon beam energy change (see Fig. C.2), the spot intensity corresponding to both bond configurations, i.e., $4H1/4H2$ and $4H1^*/4H2^*$ (see Fig. 5.1**a**), is included by averaging two areas. $(\sqrt{3} \times \sqrt{3})$ and (1×1) spots are marked by solid and dashed gray vertical lines in **c** and **f**, respectively. The intensities are normalized to the (1×1) spot intensity. While for a Bi-induced reconstruction the relative intensity of the $(\sqrt{3} \times \sqrt{3})$ spots is distinctly higher at 50 eV than at 55 eV, the opposite trend is observed on a Si-induced $(\sqrt{3} \times \sqrt{3})$ reconstruction, which allows to distinguish both phases.

ratio of $(\sqrt{3} \times \sqrt{3})$ to (1×1) spot intensities becomes lower when increasing the beam energy from 50 eV to 55 eV. In contrast, the opposite trend is seen for the Si-induced reconstruction, i.e., the $(\sqrt{3} \times \sqrt{3})$ spots gain intensity at the higher probing energy.

With this method one can decide quickly whether an inspection of the sample with STM is worth a try or not. Another indicator of heavily reconstructed SiC substrates is the appearance of a (3×3) diffraction pattern after the evaporation of Bi.

Influence of T-gradient on bismuthene formation. Every mounted SiC sample possesses a unique lateral temperature gradient as a consequence of the DC heating being sensitive to variations of the sample resistance (varying clamping pressure, contact area, etc.). Fig. 6.4 exemplary demonstrates that the success of the growth process is strongly influenced by this temperature variation. Although the gradient is generally in the range of only ≈ 5–20 °C, it is large enough to have a major impact on the growth success. Most probably, this results from the required high precision of the temperature regulation during the H desorption.

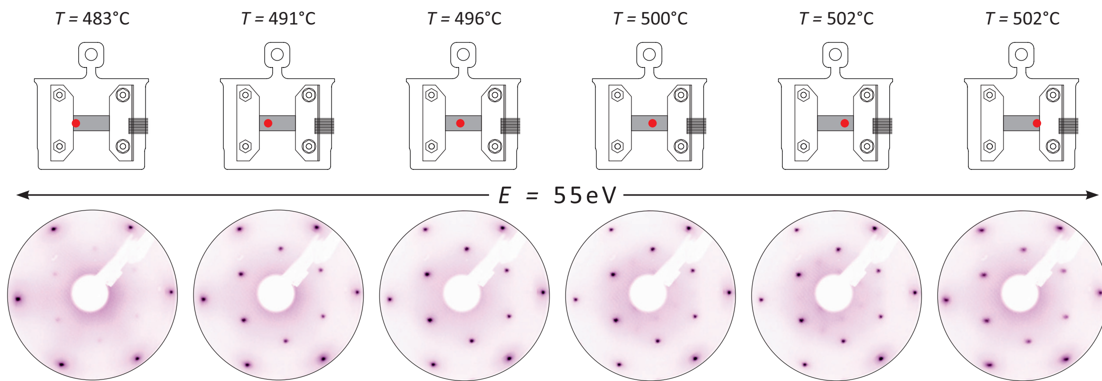

Figure 6.4 LEED pattern of a sample after Bi deposition at different lateral positions of the SiC wafer (indicated by red dots). In consequence of the DC heating, the SiC substrate exhibits a temperature gradient across the sample, which is usually less than 20 °C. Still, this variation can be detrimental for the success of the growth process. For the specific sample shown here, the desired temperature and an intense Bi-induced $(\sqrt{3} \times \sqrt{3})$ pattern are present only in the central area of the wafer, whereas the temperature is too high (right half of images) or too low (left two images) during H desorption in vicinity of the contact clamps.

If T_{deso} is too high, weak $(2\sqrt{3} \times 2\sqrt{3})$ Bragg peaks additional to (1×1) or $(\sqrt{3} \times \sqrt{3})$ appear in the image, as seen the right half of LEED images in Fig. 6.4. Bi desorption demonstrated that the SiC substrate is reconstructed at these positions. In contrast, if the temperature is too low (two left LEED images in Fig. 6.4) the Si–H bond is cracked only with small probability, such that major parts of the surface remain H-passivated, which leads to faint Bi-induced $(\sqrt{3} \times \sqrt{3})$ spots.
The required precision of the sample temperature regulation emphasizes that a redefinition of the growth process, involving an even lower H desorption temperature, could be advantageous to reduce the risk of a failure of the growth attempt.

6.2 Film Growth Process

The tentative course of action during growth frequently results in an incomplete H desorption and bismuthene surface coverage, such that several growth cycles are required until a decent film quality is attained. In this section, a side-by-side comparison of LEED and STM as well as scanning tunneling spectroscopy (STS) measurements after the initial and

two subsequent Bi growth cycles on the very same sample elucidates that the improvement of the LEED pattern is indeed linked to an increased bismuthene coverage of the sample. Moreover, measurements after different deposition steps demonstrate that the Bi film grows in domains.

Isolated Bi islands. Fig. 6.5**a** shows LEED images of a sample after the first Bi deposition and a subsequent post-anneal ($T = 400\,°\mathrm{C}$, $t = 10\,\mathrm{min}$)[16]. The ratio of the $(\sqrt{3} \times \sqrt{3})/(1 \times 1)$ spot intensities is higher at 50 eV than 55 eV beam energy, suggesting the presence of bismuthene islands. However, the Bi-induced $(\sqrt{3} \times \sqrt{3})$ pattern has a rather low intensity compared to very intense (1×1) spots, suggesting that major parts of the substrate are not covered with bismuthene.

Indeed, the corresponding STM constant current image (CCI) shown in Fig. 6.5**b** reveals that only a minor portion of the surface is covered by small islands. The different surface areas, i.e., the islands and the lower-lying terrace plane, possess a defined, constant height level. A large number of characteristic point defects seen in the lower plane, compare to Fig. C.5, indicates that this area represents the bare SiC substrate surface, which lead to the intense (1×1) LEED pattern. Accordingly, the islands seem to give rise to the $(\sqrt{3}\times\sqrt{3})$ spots. The small point-like clusters scattered across the substrate area might be leftover Bi atoms/clusters from the growth process. The local density of states (LDOS) map (see Sec. 2.3.2.2) in Fig. 6.5**c** shows a high $\mathrm{d}I/\mathrm{d}V$ signal at the positions of the clusters, while a constant signal is found both on the islands as well as on the SiC substrate. The corrugation observed in the line profile (Fig. 6.5**d**) is up to 4 Å. A direct comparison of the value measured in STM and predicted by DFT is not reasonable due to the LDOS contribution to the apparent height measured with STM. Moreover, the apparent height of the SiC substrate and probably also of the bismuthene film is not constant but exhibits long-range LDOS fluctuations (see, e.g., Fig. 5.14**a**). For a quantitative evaluation of the layer height above the substrate it is necessary to use atom-resolved q-plus atomic force microscopy (AFM). Still, the density-functional-theory-(DFT)-predicted height of bismuthene above the SiC substrate of 2.75 Å is reasonably close to our probed value (Fig. 4.4**b**).

Altogether, the coverage of the sample surface is insufficient. The observation of the bare substrate on large portions of the surface might indicate that the H desorption was not successful, rendering the formation of a covalent bond between Si and Bi atoms impossible. Hence, additional growth cycles are required.

Isolated Bi islands and disordered Bi. We skip the second/third attempt and present measurements conducted on the sample after the fourth growth cycle and a post anneal ($T = 405\,°\mathrm{C}$, $t = 10\,\mathrm{min}$) in Fig. 6.5**e**–**h**. The LEED pattern displayed in Fig. 6.5**e** is similar to Fig. 6.5**a**. Again, the $(\sqrt{3} \times \sqrt{3})$ diffraction spot intensity is higher at 50 eV than at 55 eV beam energy, thereby suggesting the presence of bismuthene domains. At the same, time both (1×1) as well as $(\sqrt{3} \times \sqrt{3})$ spots are faint and broad, and the background signal around the (0,0) spot is considerable.

[16] Note that a sample temperature up to $T \leq 400\,°\mathrm{C}$ leaves the surface unchanged. Higher temperatures affect the desorption of Bi from the surface. Heating up to $T = 400\,°\mathrm{C}$ is particularly useful after sample transfers with our ultra-high vacuum (UHV) suitcase or long-time storage in UHV, as weakly bound adsorbates may be removed.

The overview STM image (Fig. 6.5**f**) displays a surface that can be separated in two areas. A minor portion of the surface area is covered by isolated islands with a low-corrugation surface, similar to the islands found in Fig. 6.5**b**, while the majority of the surface is seemingly disordered, which makes an evaluation of the LDOS map (Fig. 6.5**g**) hardly feasible. A close inspection of the STM scan reveals one-dimensional (1D) trenches, which are running through the meandering islands (compare to the line profile in Fig. 6.5**h**). As we will see later in Secs. 7.1 and 7.3.1, these lines with distinguished apparent height mark domain boundaries (DBs) in the bismuthene film.

The observed surface morphology is distinctly different from the one shown in Fig. 6.5**b**. The size and corrugation of the bismuthene islands is comparable, but the area in between is rough and ragged instead of smooth and flat. The reduced corrugation range in the line profile (Fig. 6.5**h**) suggests that either disordered Bi, or Si DBs are present on top of the SiC surface. In any case, the coverage of the sample is still insufficient. Furthermore, the tip is not stable in the areas with disordered appearance unless using voltages suitable for tunneling on the bare substrate. This precludes the investigation of the lattice structure at low bias voltages in the range of $\pm 1\,\mathrm{eV}$.

Closed Bi film. After a further cycle of Bi growth a much improved bismuthene film coverage is found on the sample. As incomplete H desorption was assumed in the earlier attempts, the desorption temperature was increased by $5\,^{\circ}\mathrm{C}$. Additionally, the accumulation temperature was lowered by $\approx 20\,^{\circ}\mathrm{C}$ to attain a higher sticking probability. The LEED pattern (Fig. 6.5**i**) indicates the presence of bismuthene on the sample and shows reduced background as well as increased spot intensities compared to the previous cycles (Fig. 6.5**f**). The STM image in Fig. 6.5**j** demonstrates that an almost closed film, which is occasionally interspersed with disordered areas, has formed. These disordered areas are discussed in Sec. 7.3.3. Domain boundaries are now clearly visible as 1D features, even though they exhibit an inconstant z signal in CCI because of a different tunneling voltage than in Fig. 6.5**f**. The corresponding LDOS map (Fig. 6.5**k**) likewise displays the domain boundaries with absolute clarity. The line profile (Fig. 6.5**l**) demonstrates the low z corrugation of the islands except for regions covered by disordered areas and point defects, which are visible as depressions with reduced apparent height in the CCI (Fig. 6.5**j**) and will be discussed in Secs. 7.3.2 and 7.3.3.

Growth of bismuthene films. The measurements recorded on samples with incomplete coverage (Figs. 6.5**a**–**d** and **e**–**h**) nicely illustrate the growth process of bismuthene. Bi islands nucleate simultaneously at several sites on the crystal. It is not clear whether point defects or adsorbates serve as strong nucleation centers, or if this is a statistical process driven purely by the H desorption. Subsequently, those independent domains become larger and eventually merge if their honeycomb centers are separated by $n\vec{a}_1^{\mathrm{Bi}} + m\vec{a}_2^{\mathrm{Bi}}$ ($n, m \in \mathbb{Z}$) bismuthene lattice constants. Alternatively, they form domain (see Fig. 7.8). The structural and electronic properties of domain boundaries will be inspected in more detail in Sec. 7.3.1. In the following section, we quantitatively evaluate the domain size and surface coverage of exemplary bismuthene films.

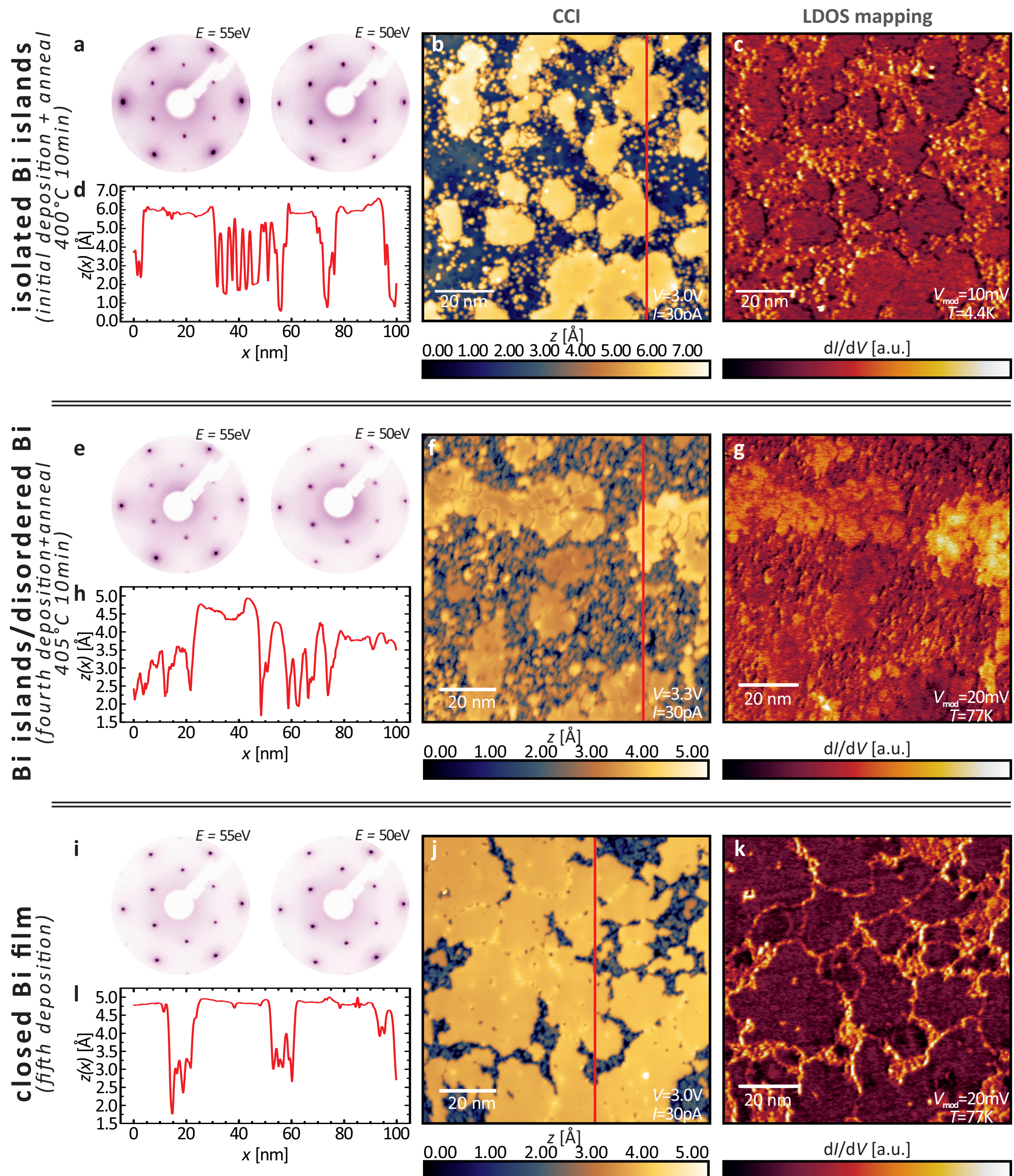

Figure 6.5 LEED, STM and LDOS measurements recorded on the very same sample after **a**–**d** the initial Bi deposition, **e**–**h** the fourth, and **i**–**l** the fifth growth cycle. **a**, **e**, **i** The LEED background signal and spot width are continuously reduced from **a** to **e** to **i**, resulting in the highest quality LEED pattern after the fifth Bi deposition. Throughout all attempts an increasing ratio of the $(\sqrt{3} \times \sqrt{3})/(1 \times 1)$ spot intensities is found when lowering the beam energy from 55 eV to 50 eV, which is indicative of bismuthene formation. STM images are used to understand the differences found in LEED. **b** After the first growth attempt, isolated islands and small clusters distributed on top of a smooth surface, i.e., the SiC substrate surface, are seen. **d** The islands are clearly identifiable in the LDOS map, as well. **f** After the fourth deposition, islands with smooth surfaces are interspersed by ragged, disordered segments instead of flat terraces. **g** The ragged surface causes by an inconstant LDOS signal. **j** After the last deposition step, smooth islands are dominantly observed on the sample. **k** Clear improvements are visible in the LDOS map, as well: the smooth $\mathrm{d}I/\mathrm{d}V$ signal generated by the islands is only occasionally intersected by higher charge density (domain boundaries and disordered areas). **d**, **h** and **l** The line profiles demonstrate that the corrugation is highest (up to 4 Å) for the sample with islands on a bare substrate (**a**–**d**), and clearly reduced ($\approx$ 2.5 Å) after several deposition cycles (**h** and **l**). All line profiles are oriented from bottom to top of the images.

6.3 Domain Size and Coverage

The coverage of SiC surfaces with bismuthene was already content of the section before. In this section, it is evaluated quantitatively to characterize several, exemplary samples, as it is one principal criterion to assess the quality of a grown film. Another aspect not referred to in Sec. 6.2 is the average domain size, which is crucial for conducting and interpreting future transport measurements. A edge states might emerge around each domain, in the best case, the average domain size is large enough that only one domain is contacted. In the worst scenario, a vast number of domains is contacted and all their edge states are contributing to the probed current, the such that the detection of a quantized conductance, even if present, is hardly possible. Note that a thorough description of domain boundaries and other surface defects is shifted to Sec. 7.3. Here, we aim to present quantitative numbers related to the growth process.

As explained in the discussion of Fig. 6.5 it is possible to distinguish the regular bismuthene lattice from the area covered by other structures in high bias survey LDOS maps. Therefore, large scale CCIs and LDOS maps of different samples are analyzed in terms of (i) coverage and (ii) domain size. As it will become apparent, both figures are varying significantly from sample to sample.

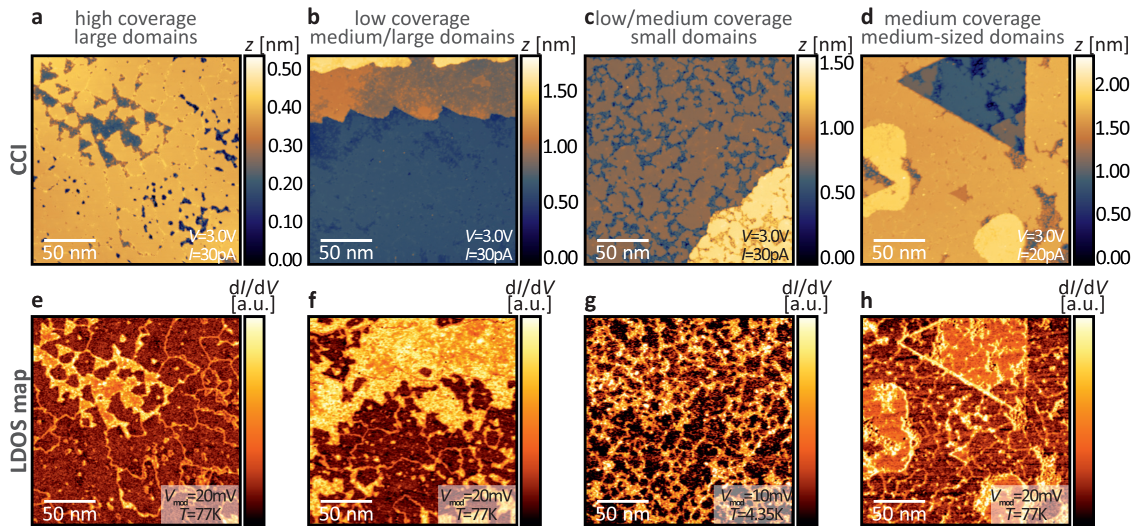

Figure 6.6 Comparative view of four different bismuthene samples with significant variations of coverage and domain size. **a**–**d** The upper row shows CCIs and is used to analyze the surface coverage with bismuthene. Only the area covered by plane domains is used, whereas disordered regions and the area covered by defects or domain boundaries are excluded. The bismuthene-covered surface area varies from ≈ 51% (**c**) to ≈ 76% (**a**). **e**–**h** LDOS maps are used to extract the domain size present on the surface of the specific sample, as domain boundaries are visible as lines with higher/lower charge density in dI/dV (depending on the bias voltage). Before the analysis mask is generated, all dI/dV images have been smoothed with a 2 pixel Gaussian function to improve the signal-to-noise ratio. The average maximum inscribed radius of a domain ranges from 3.6 nm for sample **c**/**g** to 7.4 nm for sample **a**/**e**. Further characteristic numbers can be found in App. D.1. As some domains are cut at the boundaries of the scan frame, the evaluated numbers represent the lower limit of the domain size.

Coverage. In Fig. 6.6, STM CCIs (**a**–**d**) and LDOS maps (**e**–**h**) of four different bismuthene samples are displayed. The coverage is analyzed by inspection of the CCIs and

defined as the area covered by bismuthene domains, excluding apparent point defects, disordered regions and domain boundaries. The mask shown in Fig. D.1 visualizes the evaluated areas.

The coverage of the four samples shown in Fig. 6.6**a**–**d** is 76.4%, 53.9%, 50.9% and 65.3%, respectively. In case of the sample with the highest coverage (Fig. 6.6**a**) only a small portion of the surface area is apparently disordered. This is in stark contrast to the sample in Fig. 6.6**b**, where major parts of the surface are rough, in particular on the mid-level terrace, which is even more obvious in the LDOS map (Fig. 6.6**f**). A comparison to the sample in Fig. 6.6**c**/**g**, which exhibits a similar coverage, is interesting: while the disordered areas shown in Fig. 6.6**b** are fairly large and connected, a manifold of small trenches intersecting the bismuthene domains reduce the covered surface in Fig. 6.6**c**. In the former case (Fig. 6.6**b**), the appearance of disordered areas is likely caused by a substrate reconstruction, as $(2\sqrt{3} \times 2\sqrt{3})$ spots are observed in addition to (1×1) and $(\sqrt{3} \times \sqrt{3})$ spots in LEED. In the latter case (Fig. 6.6**c**), it can be attributed either to an incomplete H desorption or unsatisfactory Bi accumulation on the surface, i.e., the Bi flux has been too low in relation to the sample temperature and the domains did not reach their ultimate extension. Lastly, the sample shown in Fig. 6.6**d** seemingly exhibits partially reconstructed regions, as well, but to a much smaller extent than the one shown in Fig. 6.6**b**.

Domain size. The LDOS maps shown in Fig. 6.6**e**–**h** reveal the presence of domain boundaries, which sometimes are hard to detect in CCI scans. It is immediately evident that the boundary of the domains encloses highly irregular-shaped areas, especially for domains with large average diameter. Therefore, the most relevant quantity is the inscribed disc radius. This quantity expresses the maximum distance of, e.g., contacts in a transport experiment that are safely within a single domain. In Figs. 6.6**a**–**d**/**e**–**h**, the average (maximum) value is 7.4 nm (29.7 nm), 5.2 nm (19.3 nm), 3.6 nm (12.7 nm) and 4.9 nm (22.2 nm), respectively. Interestingly, the sample with the best coverage also possesses the largest domains (Fig. 6.6**a**/**e**). However, the sample with the lowest coverage has domains of comparable size (Fig. 6.6**b**/**f**). The sample displayed in Fig. 6.6**c**/**g** has by far the smallest maximum domain size.

Still, it is clear that it is unlikely to contact only one or even a few domains in future transport experiments, such that the average domain size must be substantially increased. The formation of domains of bismuthene is an intrinsic problem that comes along with the reconstruction that is formed by Bi atoms on the SiC substrate. Two possible approaches to avoid or minimize the problem are available: either SiC must be replaced by a different substrate that fulfills all important criteria (semiconducting or insulating band structure, atomically smooth and clean surfaces, suitable lattice constant), which, unfortunately, is not available at the moment, or the average domain size must be enlarged by tuning of the growth parameters.

An obvious strategy is the reduction of Bi nucleation sites, such that impinging Bi atoms attach to existing instead of forming new domains, which probably has happened in Fig. 6.6**c**/**g**. This might be achieved by a reduction of the Bi flux that is, considering that only one monolayer is grown, very high ($p_{\mathrm{Bi}} = 1 \times 10^{-3}$ mbar), and/or an increase of the accumulation temperature (T_{enrich}), such that the atoms remain highly mobile on the

surface. Clearly, this must be compensated by longer growth times. Moreover, it must be ascertained that the Si-H bonds are homogeneously released, which is a tricky problem. A simple prolongation of the desorption time t_{deso} or a higher desorption temperature T_{deso} bears the danger of generating a Si-reconstructed substrate surface (which might have happened in Fig. 6.6**b**/**f**).
Finding optimal growth parameters is time consuming and – in particular – requires precise control of all relevant parameters. In our case, this concerns the Bi flux as well as the temperature during Bi accumulation and shutter closure (growth phase V and VI in Fig. 6.1). While a reproducible Bi flux and shutter closure can be achieved by use of a state-of-the-art MBE machine, it is in principal not possible to obtain a precisely regulated and reproducible substrate temperature with DC heating[17]. Therefore, a growth process based on a different heating method as, e.g., radiation or laser heating, must be developed.

6.4 Film Composition and Stability

In this section, X-ray photoelectron spectroscopy (XPS) measurements on bismuthene films are analyzed. In the first part, as-grown bismuthene samples are investigated. In the second part, the stability of bismuthene films is explored by performing XPS after sample storage in a glovebox atmosphere and in ambient air. While the former leaves the sample unaffected, the latter procedure is harmful to bismuthene films.

6.4.1 XPS of Bismuthene on SiC

An XPS survey scan ranging from 0...1000 eV binding energy is shown in Fig. 6.7. The sample presented here has been grown in the LT-STM preparation chamber and transferred in-situ to the photoemission chamber (see App. A.5). This comprises two load lock transfers ($p_{\mathrm{LL}} \approx 1 \times 10^{-7}$ mbar) and a rest time of at least 2 h in the UHV suitcase. If bismuthene samples were highly susceptible to oxidation, one would expect to identify an O peak. However, no traces of O are seen in the survey scan of Fig. 6.7. Instead, the spectrum signals the presence of Si, C and Bi only.
The inset of Fig. 6.7 shows spectra recorded with higher energy resolution and varying emission angle. At finite emission angle θ (measured relative to the surface normal), the probed intensity $I(\theta)$ is described by Eq. 2.27 [73, 74]:

$$I(\theta) \propto \exp\left(-\frac{z}{\lambda_{\mathrm{eff}}}\right) = \exp\left(-\frac{z}{\lambda\cos(\theta)}\right), \tag{6.1}$$

where z is the shortest distance between emitting atom and the surface, and λ is the inelastic mean free path (IMFP). Thus, measurements at varying angle θ effectively reduce the escape depth $\lambda_{\mathrm{eff}} = \lambda\cos(\theta)$ of the photoelectrons, which can be utilized to vary the surface sensitivity of the collected XPS spectra. An estimation of the IMFP and escape depth of electrons from different core levels is helpful to interpret the recorded data. In first order approximation, the IMFP depends on the plasmon energy of the specific material

[17] For future transport experiments it is anyway necessary to replace the highly n-doped SiC with semi-insulating SiC wafers (or at least with semi-insulating layers on top of a doped SiC substrate).

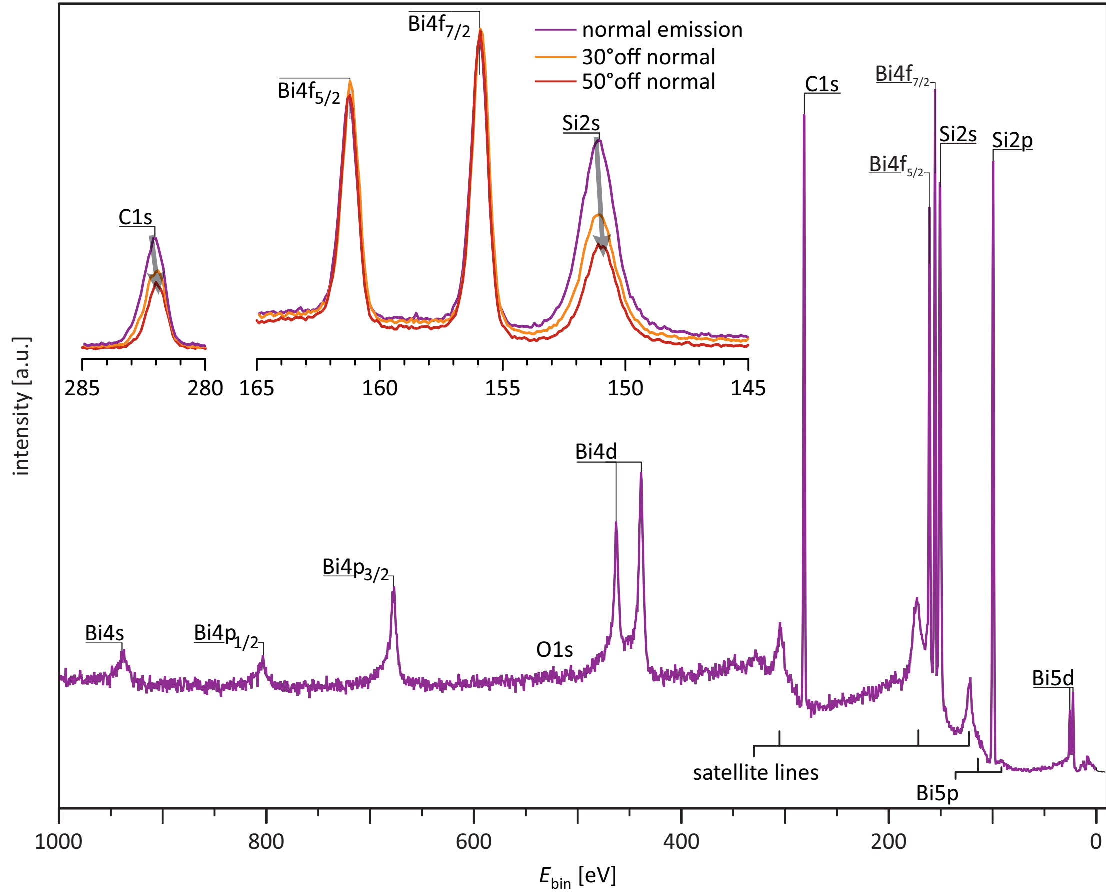

Figure 6.7 XPS of bismuthene on SiC. The Al K_α line is used as photon source. The sample is degassed at $T \approx 350\,°\text{C}$ for $t = 10\,\text{min}$ to remove weakly-bound adsorbates after the transfer. Importantly, no O peak is seen, even though the sample has been transferred between different UHV chambers. The peaks in the survey scan originate from Si, C and Bi orbitals, and the inset shows higher resolution and angle-dependent measurements of these peaks. The probed intensity of Si and C peaks is normalized to the Bi4f peak area, and the ratio of the Bi4f$_{7/2}$ to Bi4f$_{5/2}$ peaks is fixed to be 4 to 3 according to the multiplicity of the total angular momentum. Both Si/Bi and C spectra are background-corrected with a Shirley function. Measuring at finite angle instead of normal emission leads to a strong increase of the Bi/Si and Bi/C peak ratios. Gray arrows in the Si2s and C1s peaks are a guide to the eye and visualize the slightly reduced binding energies of the spectra with higher surface sensitivity. This behavior is absent for the Bi4f peaks.

and the kinetic energy of the photoelectrons. It is calculated with a modified Bethe formula [226] and listed in Tab. 6.1. Even though these numbers might constitute only a rough estimate it is clear that only few SiC bilayers (≈ 5...10) in addition to the topmost Bi layer provide contributions to the signal.

Core level	C1s	Si2s	Bi4f
λ [Å]	21.1	31.0	25.0
$\lambda_{\text{eff}}^{\text{NE}}$ [Å]	21.1	31.0	25.0
$\lambda_{\text{eff}}^{30°}$ [Å]	18.3	26.8	21.7
$\lambda_{\text{eff}}^{50°}$ [Å]	13.6	19.9	16.1

Table 6.1 IMFP λ and escape depth d_α as function of the emission angle α for important core levels of bismuthene on SiC upon excitation with an Al K_α X-ray light source. The values are calculated with a modified Bethe formula according to Ref. [226].

The Bi4f orbital. The Bi4f core level exhibits two spin-orbit split peaks, namely the $Bi4f_{7/2}$ and $Bi4f_{5/2}$ peak, which are separated by $\Delta E(\text{Bi4f}) = (5.31 \pm 0.01)\,\text{eV}$ in Fig. 6.7. Detailed information about the peak fitting is found in Fig. D.2. This compares well to the value reported in literature ($\Delta E_{\text{lit}}(\text{Bi4f}) = 5.30\,\text{eV}$) [227]. Moreover, the absolute binding energies of the Bi peaks is in agreement with values obtained by Dharmadikari et al. in a study of Bi thin films [227]. The two Bi4f peaks can be fitted reasonably good with a single Voigt profile within our experimental resolution. However, the fit curves do not reproduce a small shoulder at higher binding energies, which is present in throughout all measurements and in both Bi4f peaks. The reason for this remains unclear. Oxygen contamination of the surface would cause a BiO peak with a higher binding energy but with a much larger energy shift ($\Delta E_{\text{bin}}(\text{BiO-Bi}) \approx 2.5\,\text{eV}$ [227]) than observed in the spectra of Fig. 6.7.

The peak area ratio of $Bi4f_{7/2}$:$Bi4f_{5/2}$ core levels is fixed to 4:3 according to the multiplicity of the total angular momentum. However, this results in a small systematic underestimation of the $Bi4f_{5/2}$ core level peak height, while the fit curve maximum of the $Bi4f_{7/2}$ peak is slightly too high. A similar finding and possible explanation for these observations has been reported recently in BiPd films [228]. The authors ascribe the apparent deviations to modifications of the orbital angular momentum. In solids without inversion symmetry, a finite potential gradient will be present and leads to Dresselhaus and/or Rashba spin-orbit coupling, which causes an overall enlarged total angular momentum $J = L \pm S$, with L and S being the orbital and spin quantum numbers, respectively. Consequently, an increasing branching ratio $[2(L-S)+1] : [2(L+S)+1]$ is observed, especially for heavy elements [228]. Bismuthene on SiC as a monolayer-on-substrate system exhibits a strong electric field gradient perpendicular to the surface, see Sec. 4.4, such that the ingredients described in Ref. [228] are fulfilled. If the area ratio of $Bi4f_{5/2}$ and $Bi4f_{7/2}$ is not fixed during the fitting procedure, we extract $L_{\text{eff}}^{\text{Bi4f}} = 4.8$ for the Bi4f orbitals in normal emission, which agrees very well with the value obtained in Ref. [228] ($L_{\text{eff}}^{\text{Bi4f}}(\text{BiPd}) = 4.9$). We leave the peak area ratio of 4:3 fixed nonetheless, mainly because the authors of Ref. [228] state that the above-described interpretation is not well-established in literature. Moreover, other sources for the suboptimal peak fitting, e.g., a suboptimal background correction or an asymmetric peak shape, cannot be excluded. Lastly, the fitted spectra are not used to determine the absolute binding energies but are compared to the spectra probed at other emission angles.

Apparently, the Bi/Si and Bi/C peak area ratio is strongly increasing with higher emission angle. The peak intensity of the substrate core levels Si2s and C1s is reduced as result of the lower probing depth of photoelectrons under finite emission angle, rendering the signal of the spin-orbit split Bi4f levels more dominant in comparison to Si and C. This is in agreement with the structural model of bismuthene on SiC. Unfortunately, the absolute ratio of the Bi4f and Si2s peak areas, or maximum probed intensities of different samples is fluctuating substantially, even if the samples exhibit the band structure characteristic for bismuthene on SiC (compare, e.g., Fig. 6.7 to the spectrum probed after storage in a glovebox in Fig. 6.8). This is the result of the relatively large probed area in our setup. Moreover, the temperature gradient due to DC substrate heating during growth causes a considerable variation of the Bi/Si ratio even within a single sample, see Fig. D.4.

Element	H	C	O	Si	Bi
η	2.2	2.55	3.44	1.9	1.9

Table 6.2 Electronegativity η (on the Pauling scale) of elements present in pristine and air-exposed bismuthene on SiC samples. From Ref. [232].

Consequently, a quantitative evaluation of the Bi/Si ratio is not very meaningful and not discussed here any further, but is provided in Figs. D.2 and D.3.

Substrate core levels. The Si2s peak is fitted by a single Voigt profile. However, the fit curves shown in Fig. D.2 reveal that the peak intensity towards the side with higher binding energy is not reproduced well by the fit curves. Despite numerous attempts, no convergence was obtained when the fitting procedure is initiated with more than one Voigt peak, such that no clear indication of a Si state at higher binding energy, which would, e.g., be caused by the presence of oxygen [229], is given. A shoulder at lower binding energies due to the clustering of Si atoms during H etching [230] is not apparent, as well. The fit values of the angle-dependent measurements (see inset of Fig. D.2) show a small shift to lower binding energies at increasing emission angles ($\Delta E_{\text{bin}} \approx -0.1$eV). A possible interpretation of this behavior is based on the lower electronegativity of Bi compared to C, see Tab. 6.2. This indicates that, in comparison to bulk SiC, more charge is localized around the Si atoms of the topmost layer(s), leading to a more efficient screening of holes after the photoemission process [231]. If this was true, such a surface chemical shift to lower E_{bin} for higher emission angles should be present also for H-passivated SiC(0001), see Tab. 6.2, even though the shift is expected to be smaller. Measurements on a SiC-H sample demonstrate that this is indeed the case (Fig. D.3). A comparison of bismuthene on SiC to bare H annealed SiC demonstrates an enhanced binding energy of the Si2s core level in the latter type of samples. At normal emission, the peak center energy is $E_{\text{bin}}^{\text{SiC-H}}(\text{Si2s}) = (152.7228 \pm 0.0053)\,\text{eV}$ compared to $E_{\text{bin}}^{\text{Bi/SiC}}(\text{Si2s}) = (152.5301 \pm 0.0097)\,\text{eV}$, see Figs. D.2 and D.3. Note that all errors are generated by the fit procedure. The same shift is seen for C1s peak, as detailed below. An alternative explanation for the evident behavior might be surface band bending, which may evolve when two semiconductors are brought into contact [221]. Of course it is possible that both mechanisms contribute to the observed trend.

In contrast to the Si2s line, the C1s line is fitted considerably better by two Voigt profiles (see Figs. 6.7 and D.2). The total fit curve can be decomposed in a main (C1s) peak at lower and a smaller (C1s-H$_x$) peak at higher binding energy. Both peaks are separated by $\approx$ 0.55 eV. The area ratio of C1s:C1s-H$_x$ peaks increases for higher emission angle, i.e., the main peak weight at lower E_{bin} is becoming more dominant at the surface. The interpretation of this observation is difficult. The appearance of a C side peak separated from the main (bulk SiC) peak by 0.47±0.03 eV was reported in H-passivated 6H-SiC(0001) and 6H-SiC(000$\bar{1}$ samples by Seyller *et al.* (see, e.g., Ref. [31]). In photon energy-dependent measurements they find an increasing relative weight of the shoulder peak with decreasing probing depth, and attribute this to H-passivated C atoms at the terrace steps [in case of 6H-SiC(0001)] and/or the surface atoms [in case of SiC(000$\bar{1}$]. Step edge C atoms bound

to H (Si_3CH) appear to have a higher binding energy than bulk C atoms (Si_4C) due to the stronger electronegativity of H than Si, see Tab. 6.2. For our samples, this interpretation seems wrong: even when assuming that the sample is not fully covered with bismuthene and large parts are still H passivated after the Bi growth as for the samples analyzed in Sec. 6.2, the increasing ratio of C1s:C-H_x with higher emission angles is contradicting the expected trend, such that a satisfying explanation cannot be provided at this point. An alternative explanation of the shoulder by hydrocarbons on the surface (C_xH_y) may be excluded as such species should be observed at a larger chemical shift ($\approx 2\,\text{eV}$ [31]).
A different aspect, i.e., the slight reduction of the binding energy of both C peaks in measurements with higher surface sensitivity is in line with the observations made for the Si2s peak. Again, both interpretations, namely surface chemical shift due to the Bi adsorption or surface band bending, might lead to the probed trends.

6.4.2 Stability of Bismuthene Films

For future experiments that require lithographic processing it is crucial to gain knowledge about the stability of bismuthene films outside vacuum. This comprises two possible conditions, which pose different demands on the film's robustness: bismuthene samples transferred into (i) a glovebox with dry N_2 atmosphere, and (ii) ambient air. XPS is ideally suited to investigate changes of surface chemical properties of our samples after they have been moved outside ultra-high vacuum (UHV). In particular, possible oxidation states of the Bi atoms can be immediately identified.

XPS after glovebox handling. We start the investigation with a sample that remained in a glovebox for 5h, which would be enough to encapsulate the surface with a protective layer. The glovebox is equipped with a CF flange, such that samples can be loaded by attaching our UHV suitcase without transport through air. The glovebox is filled with N_2 gas of purity $\leq 99.9999\%$, which is further purified by internal filters, such that the final O_2 and H_2O partial pressures are $< 0.1\,\text{ppm}$. Prior to XPS measurements, weakly-bound hydrocarbons are desorbed with an anneal at $T = 400\,°\text{C}$. Fig. 6.8 shows an XPS survey scan as well as detailed views of the Bi4f, Si2s, C1s and O1s peaks[18]. A small but noticeable O1s contamination is seen after the sample was in the glovebox. On the other hand, no BiO-related peak can be detected. Spectra of the bulk crystal species Si and C possess the same characteristics as samples that remained in UHV. The Si2s line is fitted with a single Voigt profile and does not seem to be noticeably shifted to higher binding energy, like one expect upon the presence of O atoms on the surface [230]. The C1s line is composed of two lines and has the same peak energies as the sample kept in UHV (see Fig. D.5).

XPS after air exposure. The spectral characteristics drastically change after the sample has been transferred to ambient air for 5 min (Fig. 6.8). At first, no annealing step is executed. The most obvious change in the spectra is the appearance of peaks next to the

[18]Note that the Si/Bi peak area ratio observed here is largely different from the spectrum in Fig. 6.7 (compare to Figs. D.2 and D.5, as well). Nevertheless, both samples feature a bismuthene-induced band dispersion with similar quality as the aforementioned sample in angle-resolved photoelectron spectroscopy (ARPES)

$Bi4f_{7/2}$ and $Bi4f_{5/2}$. Quantitative analysis reveals a shift of $\Delta E_{\mathrm{bin}} = (2.53 \pm 0.01)$ eV with respect to the Bi4f peaks. The absolute binding energies correspond well to published values on BiO thin films and pure BiO powder [227]. The peak area ratio of BiO/Bi is ≈ 2.9, which means that the major part of Bi atoms is oxidized and bismuthene samples are not robust to contact with ambient air, presumably as a consequence of the large electron affinity of O_2 and/or H_2O. An inspection of the O1s peak shows that, compared to the

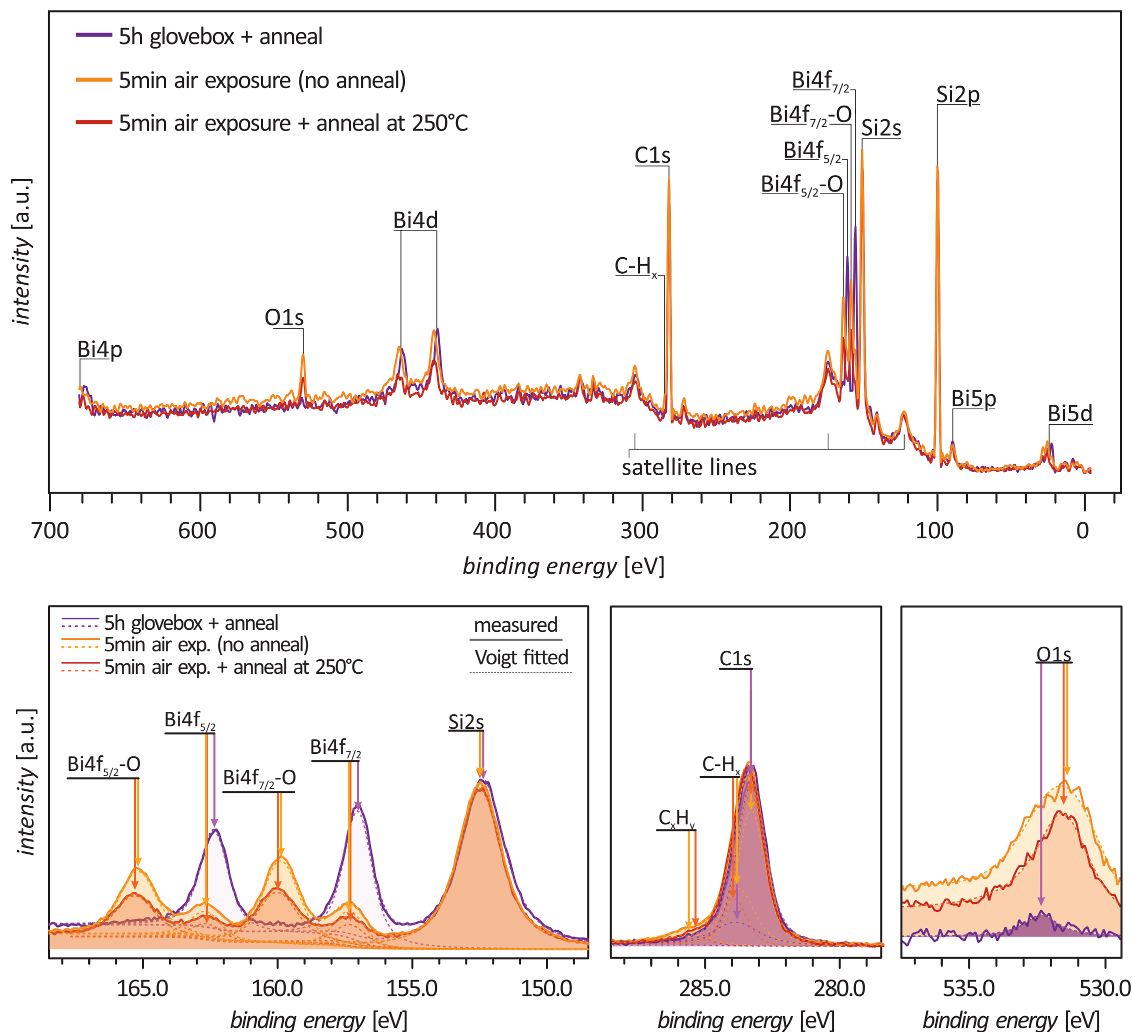

Figure 6.8 XPS spectra recorded with a Al K_α line. The spectra shown here are normalized to the Si2s peak area to allow a comparison of the Bi(O) peak area ratios. Calculated binding energy shifts and peak area ratios are shown in Fig. D.5. Purple line: Spectra recorded after the bismuthene sample was transferred back and forth between UHV and a glovebox filled with dry N_2 atmosphere (H_2O<0.1 ppm, O_2<0.1 ppm), and remained there for $t = 5$ h. Apart from a small O peak at $E_{\mathrm{bin}}(\mathrm{O}) \approx (532 \pm 1)$ eV no relevant modifications of the surface chemistry can be identified. In particular, neither a shift of the Bi4f peaks nor the appearance of a BiO peak is seen. Orange line: Spectra after the sample was exposed to ambient air for $t = 5$ min. A large BiO peak is observed both for the $Bi4f_{7/2}$ and $Bi4f_{5/2}$ core level states, indicating that bismuthene cannot resist O_2 and/or H_2O molecules. Red line: Annealing at moderate temperatures ($T = 250$ °C for $t = 10$ min) does not reduce the BiO peaks but seemingly causes a loss of Bi from the surface. Furthermore, the BiO:Bi peak area ratio becomes higher instead of lower after the thermal treatment.

spectra after the glovebox exposure, (i) the O peak area is substantially increasing, (ii) the peak binding energy is decreasing by roughly -0.9 eV, and (iii) the peak's full width at half maximum is strongly increasing, as well. The O spectra are fitted with a single

Voigt profile, but due to low count rates it cannot be excluded that it should be actually deconvoluted into two or more components. The shift to lower energy indicates that the O atoms present after the glovebox are (electronically) differently coordinated than the O atoms of the sample that remained in air. Based on the observation of BiO peaks one could argue that a reduced binding energy might be the consequence of the relatively low electronegativity of the Bi atoms.

Annealing after air exposure. An attempt to mildly anneal the oxidized sample surface at $T = 250\,°\mathrm{C}$ to remove oxygen contaminants is shown in Fig. 6.8. Unfortunately, the BiO to Bi peak ratio does not decrease but becomes even larger (BiO/Bi ≈ 3.16) after annealing. Furthermore, the overall Bi count rates are becoming lower, such that it seems as if Bi is desorbing from the surface. Annealing of other samples exposed to O or organic solvents containing O at higher temperature ($T = 400\,°\mathrm{C}$), i.e., the standard annealing temperature used to remove weakly bound adsorbates, which usually can be kept for hours, resulted in a complete loss of the Bi signal in XPS, in line with the measurement presented here. In contrast, the C1s hydrocarbon shoulder seems to be reduced, showing that the annealing process in principle works. Additionally, in both cases, a (1×1) reconstruction has been observed in LEED after the annealing step. Seemingly, the presence of O releases or at least substantially weakens the covalent bond formed by Bi and the Si atoms.
Altogether, bismuthene on SiC is a remarkably robust material, considering that one of its main ingredients is a monolayer of Bi atoms only. It keeps its initial chemical properties almost unaffected when being handled in a dry N_2 glovebox atmosphere for several hours. The long survival time in a standard glovebox atmosphere opens prospects to protect bismuthene layers by suitable capping layers. A lithography-free stamping technique with pre-integrated contacts in hBN layers, as proposed by Telford et al., might be a promising way to do so [233]. With this method, they successfully contact bilayer graphene and suppress degradation effects in air for several months.

7 2D Bulk Properties of Bismuthene on SiC

In this chapter the properties of the two-dimensional (2D) bulk bismuthene lattice are described in detail. Scanning tunneling microscopy (STM) and spectroscopy (STS) as imaging and spectroscopic techniques, respectively, are ideal to inspect the structural and electronic properties on the nanometer scale. The analysis comprises the characteristics of defect-free areas as well as distinct surface defects regularly observed on the film. Complementary to that, the band structure of bismuthene on SiC is probed by angle-resolved photoelectron spectroscopy (ARPES) and compared to density-functional theory (DFT) calculations.

7.1 Morphological Overview

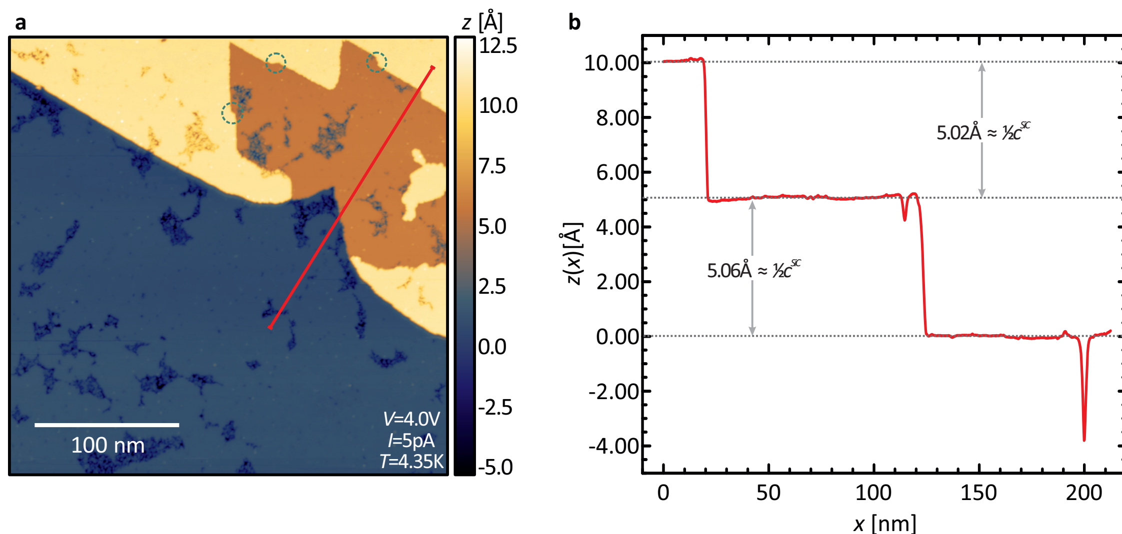

Figure 7.1 Overview STM image and corresponding line profile on bismuthene on SiC(0001). **a** The CCI displays smoothly covered surfaces, which are occasionally intersected by areas with random boundary and inconstant apparent height. The step edges are oriented predominantly along three directions that switch by 60° for adjacent terraces, as for bare SiC samples after H_2 annealing. **b** The line profile reveals that terraces are separated by ≈ 5 Å, corresponding to half a unit cell steps of 4H-SiC in ⟨0001⟩ direction.

We start with a short description of the sample morphology. Fig. 7.1**a** shows an overview STM constant-current image (CCI) of a bismuthene sample. To interpret the observations correctly it is important to check the step heights. The line profile shown in Fig. 7.1**b** reveals that adjacent terraces are separated by ≈ 5 Å. This corresponds to the typical step height observed on planar, H-annealed 4H-SiC samples, see Fig. 5.10, and suggests that – despite a very high Bi vapor pressure (see Sec. 6.1) – a Bi film with homogeneous thickness has grown. Large areas of the sample surface in Fig. 7.1 appear entirely smooth

and connected, which is nicely seen in the line profile. However, small areas with irregular boundary, showing a reduced apparent height and higher roughness, are present, as well.

Bias dependence. The overview image in Fig. 7.1 is recorded at high bias voltage, which means that the tunneling voltage is compatible with measurements on bare SiC samples. This allows to scan large surface areas, including areas not covered by bismuthene but by irregular structures or even bare SiC surfaces (as in Fig. 6.5), at a reduced risk that the tip changes or crashes. However, at such high bias, the atomic structure is generally hard to reveal as it enables the tunneling of electrons to all states disposable from E_F to the applied bias voltages. A substantially smaller tunneling voltage must be used to resolve the atomic structure of bismuthene. Fig. 7.2 shows two high quality CCI and local density of states (LDOS) maps, one recorded at high and the other at low V, to demonstrate how the surface appearance changes when switching from high to low bias[19] As shown in Sec. 6.3,

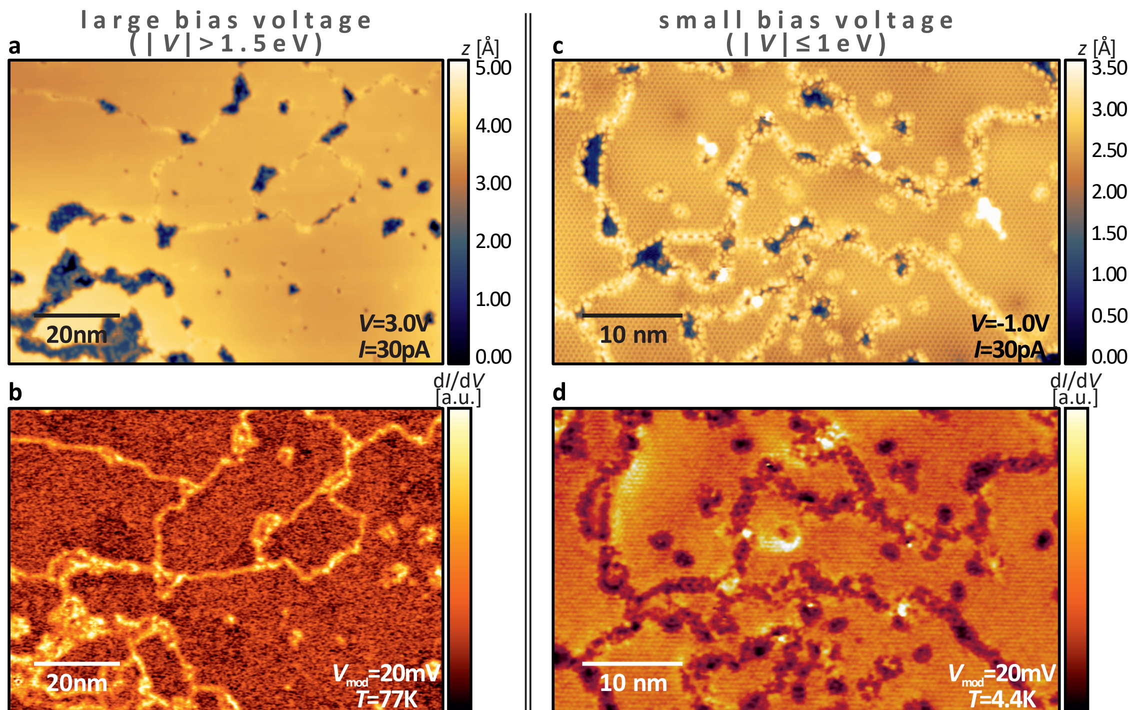

Figure 7.2 **a**, **c** STM and **b**, **d** LDOS map at **a**, **b** high and **c**, **d** low bias voltage showing how the appearance of characteristic features changes. Certain properties are visible even at high bias voltage, such as the domain size and bismuthene coverage. Others, like the atomic lattice structure, domain boundary structure and all defects become visible only at low tunneling voltage.

measurements at high bias voltage allow to evaluate the film coverage and domain size by the different z or LDOS signal of the regular bismuthene lattice and defective structures. The scan shown in Fig. 7.2**a** displays thin lines with inconstant, but rather enhanced apparent height compared to the smooth surrounding planes, which are caused by domain boundaries and much better seen in the LDOS map recorded simultaneously to the CCI and shown in Fig. 7.2**b**. Apart from these structures with one-dimensional (1D) character,

[19] Note that the displayed maps at high and low bias are not recorded on the same surface area. They have been chosen nevertheless as both constitute representative scans with particularly high quality. Measurements allowing a one-to-one comparison are shown in Fig. E.1.

point-like defects and large, disordered areas with inhomogeneous z and $\mathrm{d}I/\mathrm{d}V$ signal are evident both in the CCI and LDOS map.
A much more detailed picture in $z/\mathrm{d}I/\mathrm{d}V$ emerges at reduced bias voltage (Figs. 7.2**c** and **d**). Most importantly, the formerly smooth planes in the CCI (Fig. 7.2**c**) now exhibit a fine corrugation in a honeycomb arrangement, and a structure with the same periodicity is present in the LDOS map (Fig. 7.2**d**). Moreover, the different surface defects obviously have a fairly complicated fine structure. In the case of the domain boundaries, an intriguing pearl necklace-like structure appears in the CCI (Fig. 7.2**c**). The defective areas, which give rise to an inconstant z and $\mathrm{d}I/\mathrm{d}V$ signal, are surrounded by edges with enhanced apparent height. Small protrusions on plane terraces indicate point defects.
In the following sections the above-listed features are analyzed in detail. We begin with the properties of the ideal honeycomb lattice, and then describe the characteristics of the different surface defects, namely domain boundaries, disordered areas and point defects.

Bismuthene on miscut SiC substrates. The discussion of the 2D bulk bismuthene properties in the following is limited to samples grown on nominally planar 4H-SiC substrates. Bismuthene samples grown on SiC(0001) substrates with 2° and 4° miscut in $\langle 1\bar{1}00 \rangle$ direction possess the very same structural and electronic properties, as summarized in App. D.3. However, STM and STS measurements on their surface are much more demanding due to the high density of full unit cell steps with a height of $c^{\mathrm{SiC}} = 10.08\,\mathrm{Å}$ (see Sec. C.1). The high step density is intended to enhance the edge state signal in relation to the bulk intensity in ARPES measurements. In STM, however, it causes frequent tip instabilities, rendering the interpretation of the collected data overall more complicated.

7.2 Ideal Honeycomb Lattice

The description of the honeycomb lattice includes structural as well as electronic properties of the surface in the absence of defects. Depending on the specific sample such defect-free areas have a diameter of 5–20 nm.

7.2.1 Structural Properties

We begin the discussion of structural properties with Fig. 7.3. The honeycomb pattern suggested by the CCIs is immediately evident. However, STM is sensitive both to structural properties and the LDOS, causing the appearance in STM to be highly bias dependent. This is pointed out in the theoretical work by Miwa et al. [234] in the course of a persistent discussion provoked by the question whether a $(\sqrt{3} \times \sqrt{3})$ superstructure after Bi deposition on Si(111) originates from Bi atoms arranged in a trimer or honeycomb geometry (Refs. [234–237]).

Bias-dependent measurements. In order to exclude that the honeycomb structure is observed only at individual probing energies, Fig. 7.3 shows four CCIs (**a**– **d**) and LDOS maps (**e**–**h**) recorded at different bias voltages in the occupied as well as in the unoccupied states. Measurements at additional probing energies are found in Fig. E.2. The CCIs display a honeycomb pattern throughout the shown sequence (and also in all

measurements in Fig. E.2). The honeycomb structure becomes weaker and the corrugation eventually vanishes at $|V > 1.5\,\mathrm{eV}|$, such that an almost featureless surface similar to the measurement shown in Fig. 7.2**a** is pictured. Altogether, the observation of a honeycomb pattern both in occupied as well as unoccupied states is a strong indicator for the presence of a honeycomb lattice like assumed in the theory calculations in Ch. 4, and is incompatible with a Bi trimer structure [234].

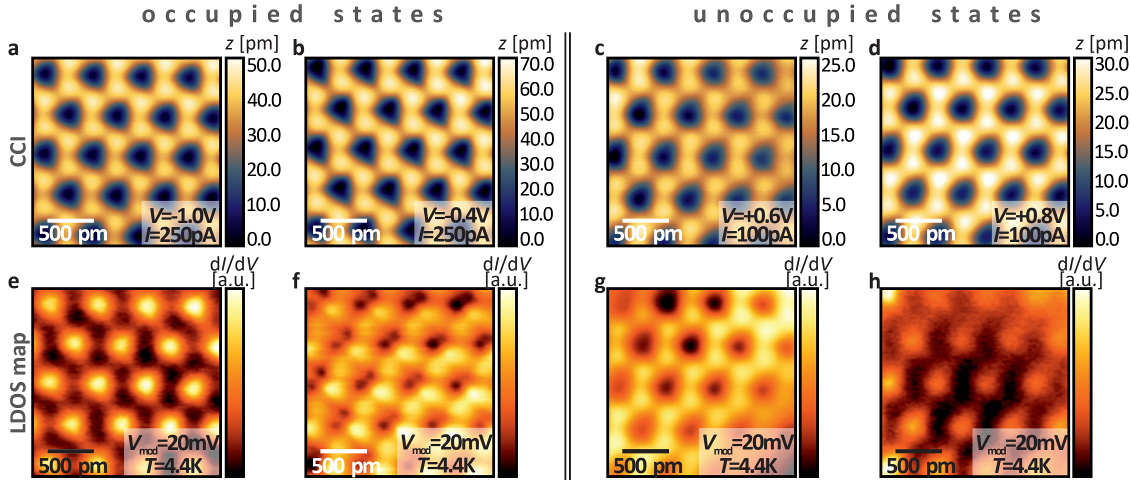

Figure 7.3 **a**–**d** CCI and **e**–**h** LDOS map of bismuthene on SiC(0001). **a**–**d** All CCI scans demonstrate that the Bi atoms adsorb in a honeycomb geometry. A small triangular distortion is seen in all measurements but more pronounced in the occupied states (**a**,**b**). In general, the corrugation is higher in the occupied states and the honeycomb pattern is more easily resolved. **e**–**h** The corresponding LDOS maps similarly exhibit a honeycomb pattern. Both in occupied and unoccupied states we find an inversion of the dI/dV signal strength at a certain absolute value of the applied bias voltage, such that a higher LDOS is observed at the lattice site of the SiC substrate that is not covered by a Bi atom.

The LDOS maps similarly display a honeycomb structure, but here, interesting bias-dependent changes are observable. Close to the Fermi level (the middle two columns in Fig. 7.3) the LDOS coincidences with the CCI, i.e., the measured dI/dV signal is high/low when the measured apparent height in the CCI is high/low. At larger absolute scanning voltages this trend is inverted and the honeycomb pattern in the LDOS maps is generated by areas with lower dI/dV signal, while a high LDOS is probed in the center of the CCI honeycombs (see Fig. E.2, as well).

DFT calculations representing STM measurements at constant height and constant isocharge surfaces performed by Gang Li similarly confirm the presence of a honeycomb pattern in the occupied and unoccupied states and are shown in Fig. E.3. However, no inversion of the contrast is observed in the simulation with increasing absolute voltage, neither in the constant height nor isocharge surface simulations. Even though a direct comparison is not appropriate as the simulated constant height STM images and isocharge maps are unfortunately neither to CCI nor to dI/dV(V_{const}) maps fully compatible (see App. E.2 for more details), we want to emphasize possible differences between both the real-world and theoretical structure, and what might give rise to these different results.

Obviously, the structure model used in the simulations might cause such differences. A reinspection of Fig. 4.4 recalls that in the calculation, the Si site of SiC, which is not covered

by a Bi atom, is passivated by a H atom to avoid the appearance of a metallic band in DFT as a result of the deficiencies of DFT (compare to the discussion in Sec. 4.3). However, there is no reason to assume that specific Si sites are H passivated in the real material, at least not immediately after Bi deposition. This is supported by the observation of domains centered around different Si sites on the surface (see Sec. 7.3.1). Yet, the dangling bond might become passivated as H is the main residual gas in ultra-high vacuum (UHV) [238, 239]. Thus, on the one hand, the observation of an elevated charge density in the center of the honeycomb of the LDOS maps in Fig. 7.3 could be an indicator that the dangling bond remains indeed unpaired. The fact that the contrast inversion in dI/dV occurs not around E_{F}, but at higher energy is compatible with the observation of strongly correlated bands on H-desorbed SiC surfaces [165]. On the other hand, it cannot be excluded that additional effects, such as different tunneling matrix elements close to the band edges of valence and conduction band (VB and CB, respectively), cause or contribute to the discrepancy between experiment and theory.

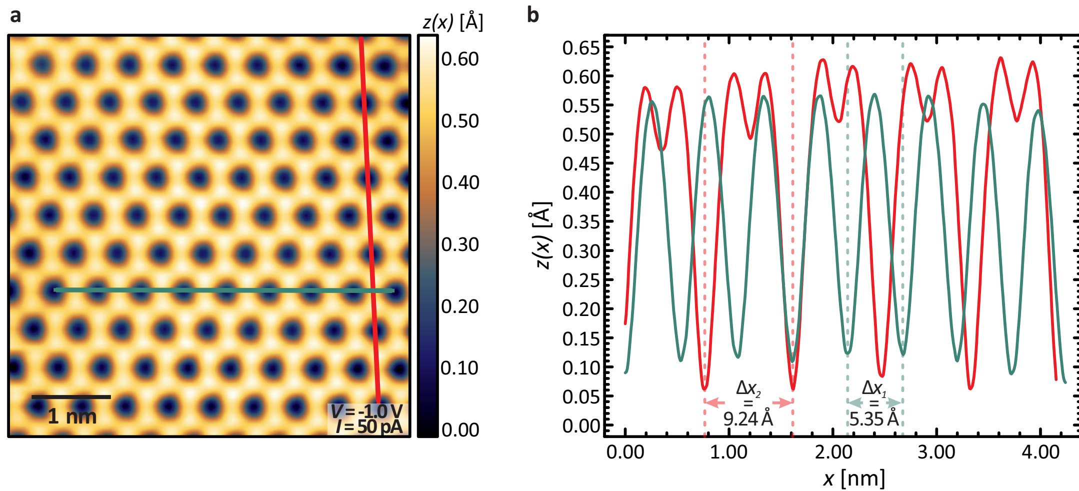

Figure 7.4 **a** Atomic resolution STM CCI showing a defect-free 5 nm × 5 nm bismuthene lattice. For optimized view of the honeycomb structure, long-range potential fluctuations are removed by leveling of the background with a polynomial plane of order 3. The Bi atoms arrange in a perfect honeycomb structure: The overall corrugation is < 1 Å, i.e., fairly low. **b** The line profile parallel to the ZZ (green) orientation features the bismuthene lattice constant of $a_{\mathrm{Bi.ene}} = 5.34$ Å $= \sqrt{3} \times a_{\mathrm{SiC}}$. The profile in AC direction (red) runs across both sublattices and the SiC lattice site, which is not covered by Bi. The corrugation of both Bi atoms is smaller than 0.04 Å, and no systematic height difference between both sublattice sites is apparent.

Lattice parameter. The lattice parameter of the Bi honeycombs is evaluated with help of the high resolution CCI presented in Fig. 7.4**a** and two line profiles. The green profile in Fig. 7.4 reveals the spacing of adjacent honeycombs, which is 5.34 Å and coincides with the bismuthene lattice constant $a_{\mathrm{Bi.ene}}$ calculated by DFT and shown in Fig. 4.4. This confirms that the $(\sqrt{3} \times \sqrt{3})$ superstructure observed in low-energy electron diffraction (LEED) signals the presence of bismuthene on the surface. The atomic corrugation is on the order 50 pm and hence rather low, which might be related to the question whether or not the lattice site in the center of the honeycombs is passivated with H atoms.

Another aspect predicted by the first-principles calculations is the absence of buckling caused by tensile strain on bismuthene, leading to a fully planar configuration of the two Bi sublattices (see Fig. 4.4**a**). Such a completely flat honeycomb lattice has been reported recently for the related, substrate-stabilized compounds stanene on Cu(111) [117] and antimonene on Ag(111) [118]. To confirm the planar lattice structure of the grown film, a linecut capturing both sublattices sites of bismuthene is shown in Fig. 7.4**b**. As presumed, no buckling in the honeycomb pattern is perceivable within the resolution of the tunneling microscope, which is in line with the calculations by Hsu et al. [131] and the calculations of Gang Li presented in Fig. 4.4. Note that the red line profile intersects the bismuthene film in armchair (AC) orientation and exhibits a periodicity of $9.24\,\text{Å} = 3 \times a_{\text{SiC}}$, which will be retrieved later in Ch. 8.

Triangular lattice symmetry. A subtle detail visible in the CCIs of Fig. 7.3**a**–**d** is a weak triangular symmetry imprinted on the "hexagonal" lattice. It appears in the DFT calculations shown in Fig. E.3, as well, and is best seen in the occupied states for the chosen simulation parameters. In case of the most comparable systems, i.e., flat stanene (Sn-induced (2×2) reconstruction on Cu(111) [117]), and flat antimonene (Sb-induced $(\sqrt{3} \times \sqrt{3})R30°$ reconstruction on Ag(111) [118]), a honeycomb lattice with perfect hexagonal symmetry is present. A comparison to the bismuthene lattice model shown in Fig. 4.4**b** suggests that this triangular pattern originates from the substrate C sublattice, which induces a threefold rotational symmetry to the total system. If this were true, one would expect a reversal of the triangular orientation after a half unit cell steps in $\langle 0001 \rangle$ direction ($\frac{1}{2}c_{\text{SiC}}$) according to the stacking order of 4H-SiC, see Fig. 5.1. For stanene/Cu(111) and antimonene/Ag(111), the different adsorption sites of Sn/Sb atoms and crystal symmetry of the substrates do not result in a threefold rotational symmetry [117, 118].

This assumption is confirmed by an atomic resolution image capturing two terraces separated by $\approx 5\,\text{Å} = \frac{1}{2}c_{\text{SiC}}$ in $\langle 0001 \rangle$ direction is displayed in Fig. 7.5. A zoom-in image on either terrace demonstrates that the above-described threefold symmetry is imprinted on the honeycombs both on upper and lower terrace. As expected, the orientation of the inner triangle is opposed, i.e., its orientation is rotated by 60° when changing between the two surface planes, which is indicated by the small red and green colored triangles in Fig. 7.5. The overlay of the SiC bilayer in the small-scale images in Fig. 7.5 is a guide to the eye and visualizes the position of the C sublattice atoms, which is deduced from the underlying lattice model of the DFT simulations shown in Fig. E.3. Physically, this finding indicates that the presence of the C atoms in the first SiC bilayer comes along with an increased charge density compared to the void sites in this layer, which pushes the LDOS of the bismuthene bonds further out to vacuum to minimize potential energy. This equally affects both sublattice atoms. Consequently, an impact on the electronic structure is not expected.

The STM measurements shown in the section demonstrate the formation of a honeycomb lattice induced by the Bi deposition. However, the question whether the Bi film is only one monolayer thick remains open, although the sensitivity to the C sublattice supports this assumption. In the following section, we analyze STS measurements, which allow to probe the energy-dependent LDOS, to confirm the presence of monolayer bismuthene.

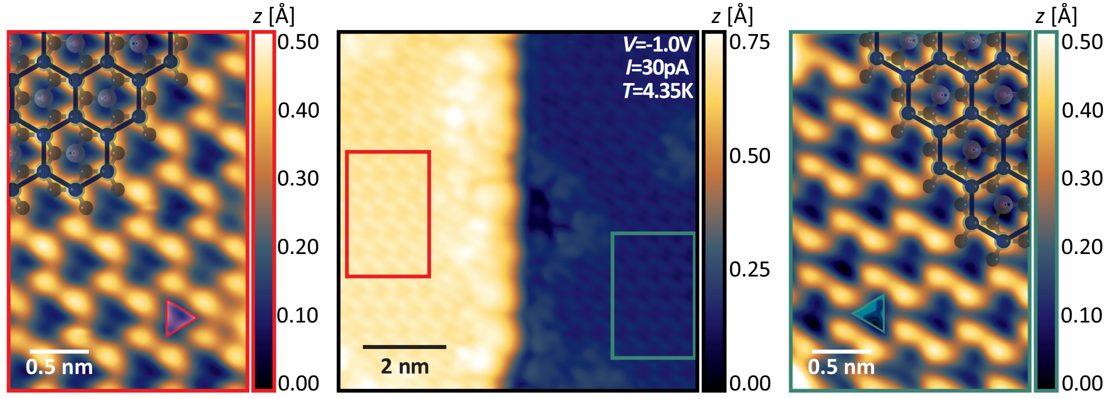

Figure 7.5 The atomic resolution STM image shown in the center captures two terrace planes separated by $\frac{1}{2}c_{\mathrm{SiC}} \approx 5\,\text{Å}$. The red and green rectangle in the main image mark the area shown in the zoom-in view at either side. A triangular distortion of the honeycombs is apparent on both terraces, but its orientation is rotated by 60° between both planes (pointing to the right (left) on the upper (lower) terrace, as indicated by the small red (green) colored triangle). This suggests that this observation is related to the C sublattice orientation. A ball-and-stick model of Bi on SiC (Bi atoms and bonds appear as dark blue dots and lines; Si, C, and H atoms are light gray, dark gray, and pink spheres) is overlaid in the top left and right corner to illustrate this finding.

7.2.2 Electronic Properties

A particularly meaningful property helping to distinguish between monolayer and multiple layer systems is the large band gap of 2D bulk bismuthene predicted by DFT (see Fig. 4.5). Bulk denotes all areas not close to a boundary of the film. As the overview STM measurements have shown, structural irregularities evolve around domain boundaries, defects, or atomic steps, see Fig. 7.2**c**. Hence, careful selection of the tip position is necessary during the data acquisition is pivotal.

Fig. 7.6**a** shows an STM image with very high resolution. Colored circles mark the different high symmetry points of the lattice: the two inequivalent Bi atoms on both sublattices (light and dark brown/blue), the Si site not covered by Bi (light and dark red), and the bonds between two Bi atoms (light and dark green). STS curves recorded at these positions are extracted from a grid spectroscopy measurement (see Sec. 2.3.2.2) with high resolution. The light and dark colors indicate whether the STS curve stems from the upper or lower domain in the CCI/LDOS map (Fig. 7.6**b**/**c**), which are separated by a domain boundary. The corresponding $\mathrm{d}I/\mathrm{d}V$ curves are displayed in Fig. 7.6**d-f**. The overview diagram (Fig. 7.6**d**) visualizes that a large band gap separates the VB and CB of bismuthene, which is persistent at low $\mathrm{d}I/\mathrm{d}V$ signal (see inset of Fig. 7.6**d**). The light and dark green curves represent spectra measured on the upper and lower domain, respectively. The small energy offset between both $\mathrm{d}I/\mathrm{d}V$ signals will be discussed later.

Band gap magnitude. The band gap magnitude is evaluated by use of the diagram with logarithmic scale (inset in Fig. 7.6**d**). The VB and CB edge are extrapolated to the average noise limit signal of the measurement, which gives rise to the finite conductance of 1 pS in the band gap (the fit curves are found in Fig. E.4). With this procedure, we determine a band gap magnitude of $E_{\mathrm{gap}}^{\mathrm{STS}} = (831 \pm 35)\,\mathrm{meV}$. The detected band gap magnitude varies only weakly upon variation of the STS stabilization parameters. Details

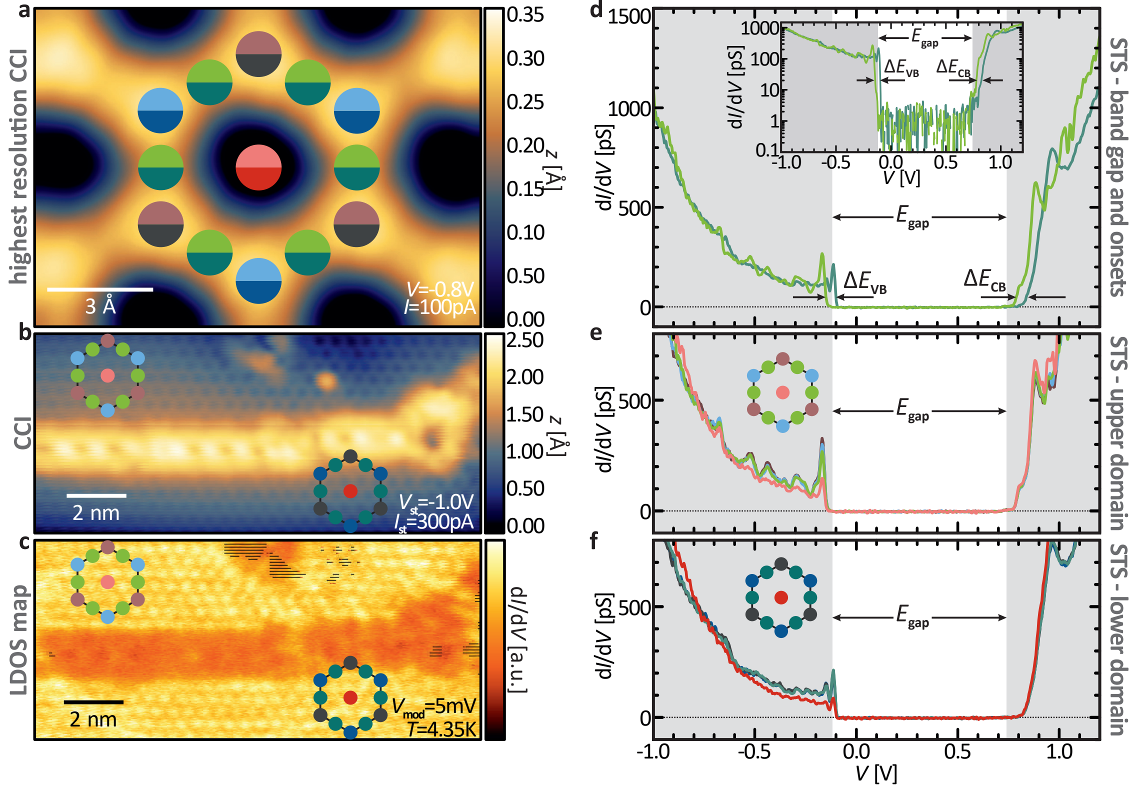

Figure 7.6 STS on bulk bismuthene samples. **a** Colored markers in the high resolution STM image indicate distinct high symmetry points of the honeycomb lattice. Lighter and darker colors correspond to spectra from the upper and lower domain visible in **b**/**c**, respectively. **b** CCI and **c** LDOS map recorded during acquisition of the grid spectroscopy measurement. The CCI reveals that the probed area is intersected by a domain boundary. **d** Single-point STS curves measured on top of the bond between Bi atoms on the upper (light green) and lower (dark green) domain. A large gap of $E_{\mathrm{gap}}^{\mathrm{STS}} = (831 \pm 35)\,\mathrm{meV}$ (fitting procedure see Fig. E.4) is evident on both domains and indicated in the panels **d**–**f** by the gray shaded areas. Moreover, the band edges of VB and CB are rigidly shifted. The inset shows a plot with logarithmic $\mathrm{d}I/\mathrm{d}V$ scale. **e** and **f** STS curves measured at different positions of the honeycomb lattice, compare to **a**, of upper and lower domain, respectively. The curves acquired atop the bond as well as atop the Bi atoms of both sublattices are practically identical, whereas on both domains, the $\mathrm{d}I/\mathrm{d}V$ signal probed in the center of the honeycomb (light/dark red) is slightly lower at the VB edge and higher at $V < -0.5\,\mathrm{V}$ in comparison to the other lattice positions. Grid parameters (see Sec. 2.3.2.2 for their definition): $V_{\mathrm{ini}} = -1.0\,\mathrm{V}$ to $V_{\mathrm{end}} = +1.2\,\mathrm{V}$, $V_{\mathrm{mod}} = 5\,\mathrm{mV}$, $V_{\mathrm{st}} = -1.0\,\mathrm{V}$, $I_{\mathrm{st}} = 300\,\mathrm{pA}$, $\Delta x = \Delta y = 0.25\,\mathrm{Å}$. All $\mathrm{d}I/\mathrm{d}V$ curves are averages of at least three spectra of equivalent lattice positions within the same but not from the other domain.

on this are found in App. E.3. This is a huge value and exceeds all experimental band gap magnitudes identified on (candidate) 2D topological insulator (TI) materials by far (see Ref. [240] for a recent review article). Moreover, the obtained value is substantially larger than the band gap predicted by DFT calculations shown in Fig. 4.5, which is $\Delta_{\mathrm{gap}}^{\mathrm{HSE}} = 0.67\,\mathrm{eV}$ (calculated with the Heyd-Scuseria-Ernzerhof (HSE) exchange correlation functional [207]). However, this is not surprising as DFT tends to underestimate the band gap magnitudes [170, 241]. Still, experimentally determined and calculated gap value are reasonably close. This provides strong evidence for the formation of monolayer bismuthene, especially as the band gap of bilayer bismuthene is only $\lesssim 100\,\mathrm{meV}$ according to DFT [162] (see also Fig. 7.16).

Variation of the band onsets. The light and dark green curve in Fig. 7.6**d** are recorded on the upper and lower domain, respectively, and evidently exhibit different band onset energies. In the VB and CB, the offset between lower and upper domain is calculated to $\Delta E_{\mathrm{VB}} = (40 \pm 11)$ meV and $\Delta E_{\mathrm{CB}} = (49 \pm 68)$ meV, respectively, indicating a rigid shift of the LDOS. The large error for the CB reflects the difficulty to define the slope around the CB minimum (CBM) correctly. This rigid shift of the band structure is regularly observed and not a property of this specific bismuthene sample. In general, the probed Fermi level position varies in a range of less than 150 meV, and importantly, the Fermi level always remains within the 2D band gap. The grid spectroscopy measurement shown in Fig. 7.6 demonstrates the presence of these fluctuations within a single measurement, such that the observed offset cannot be attributed to changes of the tip condition.

As both measurement areas are separated by few nanometers only an impact of macroscopic parameters such as the distance to the metal contact clamp to the sample holder can be ruled out. Two possible explanations might cause the observed fluctuations. Firstly, irregular surface defects might induce a surface band bending and lower/raise the Fermi level position. As will be discussed in Secs. 7.3.2 and 7.3.3, defects influence the electronic properties of bismuthene, some of them at comparably large distance. Secondly, as described in Sec. 5.3, fluctuations of the apparent height have been observed with STM on bare SiC samples. These are likely caused by intrinsic SiC defects and (extrinsic) N doping atoms, which give rise to variations of the LDOS and could induce local variations of the Fermi energy, which might be translated to bismuthene.

STS curves at different sites of the honeycomb lattice. At first glance, no apparent differences are visible in Fig. 7.6**e**/**f** upon comparison of spectra recorded at different high symmetry positions of the honeycomb lattice. A close inspection of the occupied states reveals that STS curves recorded in the honeycomb center (light/dark red colored spectra in Fig. 7.6) exhibit a marginally lower and a slightly enhanced differential conductivity at $-0.5\,\mathrm{V} < V < E_{\mathrm{F}}$ and $V < -0.5\,\mathrm{V}$, respectively, with respect to the other measurement points, which is in agreement with the observations made for the LDOS maps in Figs. 7.3 and E.2.

Fermi level position. An aspect not discussed so far is the position of the Fermi level, which is located much closer to the VB maximum (VBM) than CBM in all inspected bismuthene samples, although, as mentioned, its specific value is slightly varying between different and even within a single sample. In general, we estimate $(E_{\mathrm{CBM}} - E_{\mathrm{F}}) \approx 3 \times (E_{\mathrm{F}} - E_{\mathrm{VBM}})$. Here, E_{CBM} and E_{VBM} denote the energy of the CBM and VBM, respectively. The reason for this p-doping of the samples is not known. As also the averaged Fermi level position is changing from sample to sample, the observed behavior might arise due to the contact resistance between the SiC substrate and the sample holder. Apart from this technical aspect, possible reasons comprise Fermi level pinning by defects, and more generally, varying sample quality and cleanliness (defect density, average domain size, coverage, etc.). Unfortunately, these properties cannot be controlled with high accuracy in the present fabrication process, such that it is impossible to verify one or the other reason for the Fermi energy fluctuation.

Comparison of dI/dV and the density of states (DOS) in DFT. The dI/dV curve probed on bulk bismuthene is highly reproducible and represents approximately the sample's LDOS (see Sec. 2.3.2), which renders a comparison of the measured STS signal and the DFT-calculated DOS feasible. Fig. 7.7 displays the LDOS generated by both methods. Overall, the measured and computed (L)DOS possess large similarities, even though the precise band offsets and the band gap magnitude do not coincide as measured values are systematically larger than calculated ones. This is a general deficiency of DFT, which underestimates the band gaps and splittings in semiconductors [171, 241]. Note that the displayed DOS (Fig. 7.7**b**) is generated by use of the generalized gradient approximation (GGA) in in the parametrization of Perdew, Burke and Ernzerhof (PBE) [81], which is well-known to severely underestimate band gap magnitudes [242]. Calculations with the HSE hybrid functional [241] lead to significantly better results concerning these quantities [241, 242]. However, HSE calculations are computationally more demanding. In the case of bismuthene on SiC, this is a particularly relevant problem, as the inclusion of SiC substrate layers is pivotal for the electronic properties of bismuthene. Due to this, the band structure calculations based on this exchange functional, which are shown in Fig. 4.5, do not possess a sufficiently dense k mesh to generate a DOS plot with decent resolution.

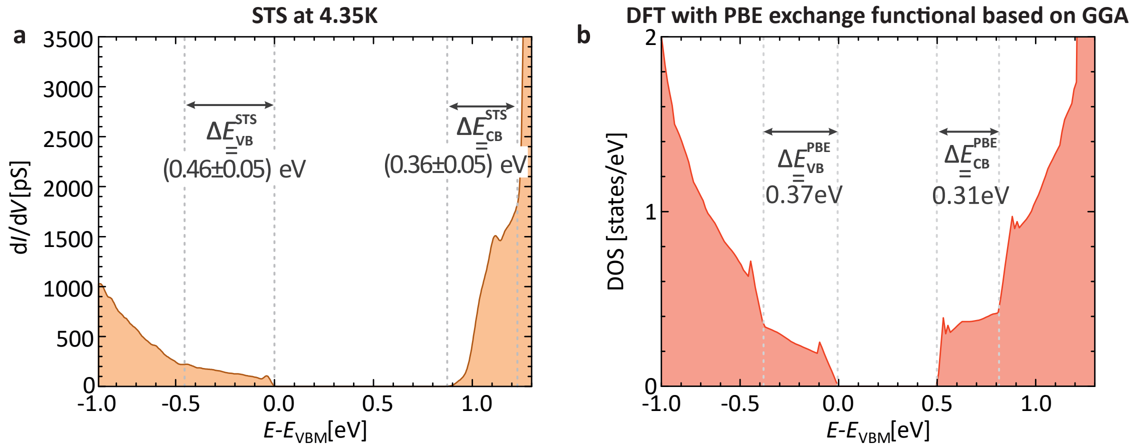

Figure 7.7 Comparison of **a** the experimental dI/dV signal (V_{mod} = 10 meV) and **b** the bismuthene bulk DOS calculated by DFT with PBE exchange functional. Note that the energy is shown in reference to the VBM because DFT fails to predict the precise Fermi level position in the bulk band gap. The estimated band offset errors account for the ambiguity to localize the change of slope in dI/dV. The PBE exchange functional is well-known to underestimate band-splittings and the band gap [171, 243]. Still, the experimental and theoretical value of $\Delta E_{\mathrm{VB/CB}}$ and E_{gap} are reasonably close. Furthermore, the similarity between the STS dI/dV signal and DFT DOS is clearly apparent. DFT calculation by Gang Li [162, 168].

Hence, instead of a one-to-one comparison, we extract the offsets between bands from the HSE band structure plot in Fig. 4.5**c** to compare to experimental values. They are $\Delta E_{\mathrm{VB}}^{\mathrm{HSE}} = 0.43\,\mathrm{eV}$, $\Delta E_{\mathrm{CB}}^{\mathrm{HSE}} = 0.40\,\mathrm{eV}$ and (as already mentioned) $E_{\mathrm{gap}}^{\mathrm{HSE}} = 0.67\,\mathrm{eV}$, and denote the offset of first and second VB, second and first CB, and the band gap. In STS experiments, a band onset becomes visible by a sudden increase of the differential conductivity at energies with a high DOS, i.e., at band minima/maxima, where the energy dispersion is small. Experimentally, the band offsets are determined by a fit of linear functions to lower/higher energies around the change of slope in the LDOS. They are

$\Delta E_{\mathrm{VB}}^{\mathrm{STS}} = (0.46 \pm 0.05)\,\mathrm{eV}$, $\Delta E_{\mathrm{CB}}^{\mathrm{STS}} = (0.36 \pm 0.05)\,\mathrm{eV}$, and $E_{\mathrm{gap}}^{\mathrm{STS}} = (0.83 \pm 0.04)\,\mathrm{eV}$, and compare very well to the computed values, apart from the already discussed mismatch of the band gap magnitude.

Apart from quantitative agreement, the resemblance of the experimental LDOS and the theoretical DOS is apparent. Yet, the experimentally derived conductivity of the occupied states is generally significantly lower than in the unoccupied states, while in the DFT PBE calculation, the difference of the DOS between valence and CB is much less pronounced. The reason for this discrepancy is the tunneling process. Note that the abrupt change of $\mathrm{d}I/\mathrm{d}V$ in the VB and CB indicates two different scenarios: in case of the occupied states, it signals the split VB that appears in DFT calculations upon inclusion of SOC at K, whereas in the CB, it indicates two local band minima at Γ and K (see to Fig. 4.5). The assumption that the $\mathrm{d}I/\mathrm{d}V$ signal represents the sample's LDOS is a rough simplification and is based on a constant tunneling matrix element. As the VBM and CBM are at K and Γ, respectively, this is not necessarily the case. In general, the wave function of states with $k_{||} \neq 0$ is damped more rapidly compared to states with $k_{||} = 0$, i.e., states at Γ, which results in a relatively lower current signal of the former [244].

While DFT predicts all key ingredients observed by STS on the defect-free bismuthene surface, i.e., the band gap magnitude as well as characteristic band splittings in the VB and CB, it naturally fails to calculate the extended surface defects that evolve on a real sample. The signatures of these characteristic defects are studied in the following.

7.3 Surface Defects

The surface of bismuthene on SiC exhibits a variety of surface defects, which can be sorted into three different categories. Firstly, 1D domain boundaries evolve as a consequence of bismuthene growing in a surface reconstruction on SiC. Secondly, as in any real-world crystal, bismuthene exhibits point defects. Thirdly, enlarged defective areas with irregular boundary, which enclose parts not covered by the honeycomb lattice, are present on the bismuthene surface. In this section, the properties of these defects are analyzed with STM and STS measurements.

7.3.1 Domain Boundaries

Bismuthene growths in a $(\sqrt{3} \times \sqrt{3}R30°)$ reconstruction on SiC, as evident in LEED (see Sec. 6.1.2) and by inspection of lattice constant in STM (see Sec. 7.2.1). STM images and STS measurements in combination with the theoretical modeling demonstrate that only two out of three Si sites become occupied by Bi atoms (Fig. 4.4). This causes a certain ambiguity, as the honeycomb lattice may nucleate around three different, but equivalent Si sites (A/B/C), as illustratey by the ball-and-stick model in Fig. 7.8, which gives rise to three domains that eventually cannot merge when the surface filling with bismuthene increases. The formation of peculiar interface structures between domains is frequently observed in materials that form a reconstruction on a substrate. In the context of topological materials, they emerge, e.g., in stanene on Cu(111) [117], where they evolve as result of a (2×2) reconstruction of Sn on Cu(111), and in $1T'$-$\mathrm{WSe_2}$ [245].

Edges that exhibit a periodic structure in AC orientation (parallel to $\langle 11\bar{2}0\rangle$) are observed only at the interface of domains with "disordered" areas (compare to Fig. 7.2**b**), but not between neighboring bismuthene domains.
In contrast, ordered domain boundaries are observed in zigzag (ZZ) direction parallel to $\langle 1\bar{1}00\rangle$ (see Fig. 7.2**b**). The analysis of the schematic model in Fig. 7.8 visualizes that in principle two types of domain boundaries, each with three orientations, could evolve. These two types are distinguished by the lateral distance of the (Bi-void) A/B/C sites, around which the domains are centered, which is expressed in units of the SiC lattice constant a_{SiC}. The gaps between domains separated by domain boundary type I and type II are $d_{\mathrm{I}} = (3n+1) \times a_{\mathrm{SiC}}$ and $d_{\mathrm{II}} = (3n+2) \times a_{\mathrm{SiC}}$, respectively ($n \in \mathbb{N}$ in both cases).

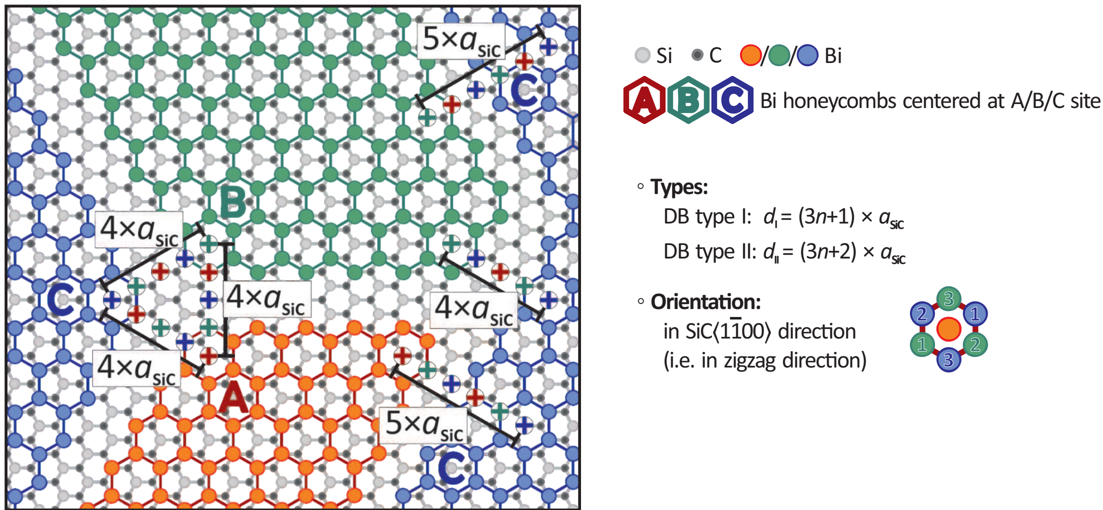

Figure 7.8 Schematic lattice model visualizing the appearance of domains on bismuthene on SiC. The bismuthene lattice can be centered around three different Si sites as only two out of three sites are covered by Bi atoms. Consequently, this gives rise to three domains that cannot merge. All ordered domain boundaries are oriented in ZZ direction in our measurements. Two boundary types with different domain spacing d_i, with i either I or II, can be generated theoretically although in reality, only type I exists.

Structural properties of domain boundaries. These theoretical considerations are now confronted with domain boundaries found in STM measurements. Fig. 7.9**a** displays a high resolution STM image of a domain boundary. A 1D structure with a pearl necklace-like pattern and $\approx 5\,$nm length, which is terminated by a kink (left side) and a change/absence of the characteristic domain boundary periodicity (right side), is observed. Its orientation along $\langle 1\bar{1}00\rangle$, i.e., a ZZ termination of honeycombs, can be immediately deduced from the scan.
Line profiles parallel to the domain boundary reveal a period doubling, most clearly seen in the central row (turquoise line in Fig. 7.9) but also in the two outer profiles on the domain boundary (light green and blue lines), whereas the usual bismuthene lattice constant is found nearby on the bulk lattice (orange profile in Fig. 7.9). At the chosen tunneling parameters, the detected apparent height increases by $\approx 1.5\,$Å with respect to the bismuthene lattice plane, see the red and purple profile in Fig. 7.9**b**. It will be shown later that this increased height is related to an enhanced LDOS in the band gap of bismuthene.

The calculated lateral distance between both domains reveals that the probed structure is a type I domain boundary ($d \approx 19 \times a_{\text{SiC}}$).

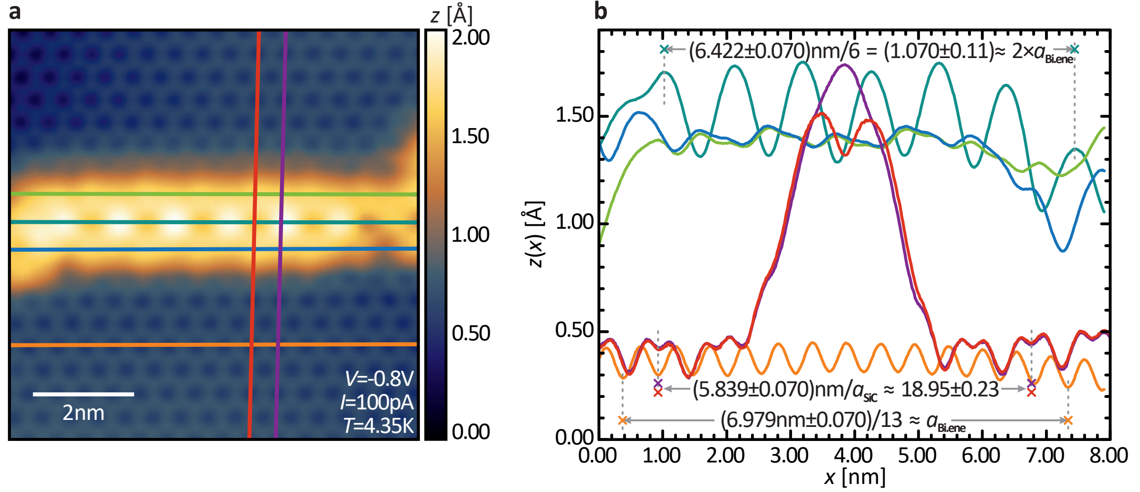

Figure 7.9 **a** High resolution STM image of an ordered domain boundary. A pearl necklace-like structure is observed. The orientation in ZZ direction $\langle 1\bar{1}00 \rangle$ is evident. **b** Line profiles corresponding to the colored lines in **a** are presented. Profiles run from left to right and top to bottom. All profiles parallel to the 1D structure reveal a period doubling with respect to the orange line on bulk bismuthene. The separation of both domains is determined with profiles perpendicular to the 1D boundary and allows a clear identification as type I domain boundary.

Indeed, only type I domain boundaries are experimentally observed. This empirical finding is visualized with an atomic resolution STM image comprising several domains in Fig. 7.10**a**. Line profiles across different domain boundaries are shown in Fig. 7.10**b**. The length of all profiles is equal, and they are positioned at equivalent positions along a domain boundary to highlight that the characteristic features of all profiles coalesce. In particular, the spacing of all analyzed domains is the same and identifies all domain boundaries to be of type I, while type II boundaries are absent. DFT modeling of the underlying structure could help to reveal why only type I boundaries seem to develop during growth.
The overview CCI in Fig. 7.10 demonstrates that the domain boundary length fluctuates between 1...10 nm, but domain boundaries with more than 10 nm length and perfect ordering have not been measured to date. Instead, domain boundaries are terminated frequently by kinks or incorporate a phase shifts, which interrupt the doubled periodicity. Both aspects are visualized in Fig. 7.10**c**. Occasionally, domain boundaries are found in special configurations, such as in Fig. 7.10**d**, where two boundaries form a sharp kink, or in Fig. 7.10**e**, where three domains merge at a single point.

Electronic properties of domain boundaries. The peculiar corrugation of domain boundaries motivates an inspection of their electronic signature. For this purpose, a representative domain boundary is shown in Fig. 7.11. The CCI in Fig. 7.11**a** serves to portray the surrounding area of the domain boundary. The domain boundary itself is defect-free and terminated by a kink (left side) and disorder (right side). Colored markers in the CCI in Fig. 7.11**b**, which has been recorded during a high-resolution grid spectroscopy, indicate the measurement positions of STS curves along the 1D structure shown in Fig. 7.11**c**.

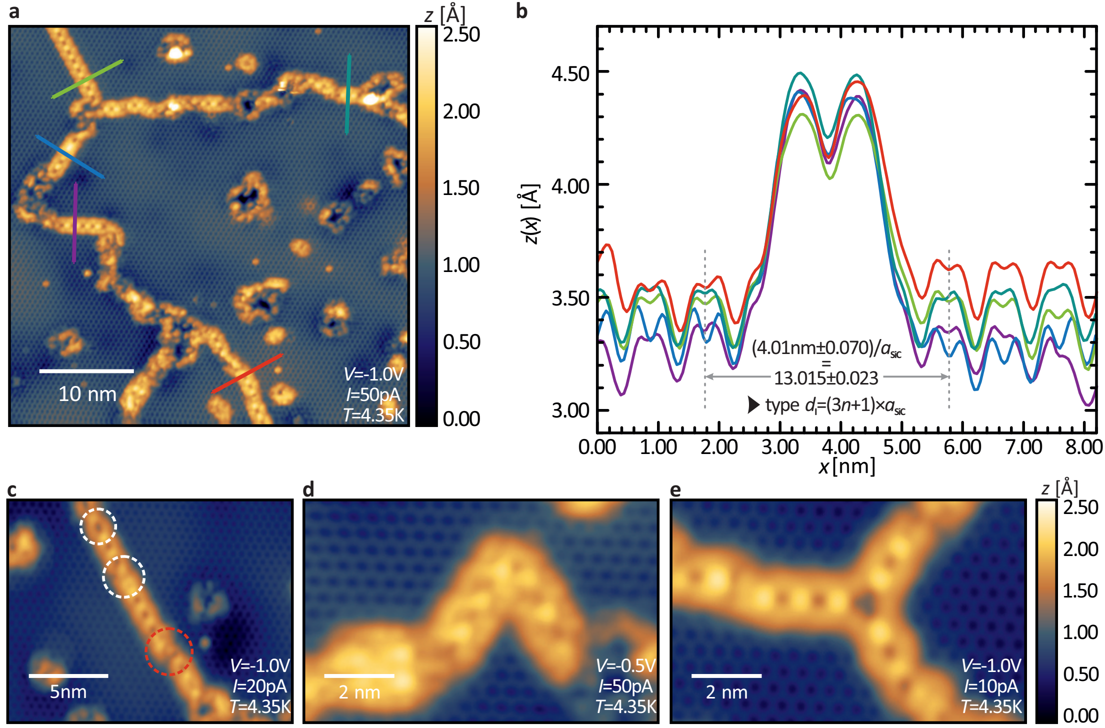

Figure 7.10 **a** Atomic resolution STM image mapping several domains. The formation of ordered boundaries along three directions is apparent. **b** The corresponding line profiles show that all inspected domain boundaries are of type I. The length of defect-free domain boundaries is varying significantly. **c**–**e** Different domain boundary scenarios. **c** Long domain boundary with several phase shifts (white dashed circles) terminated by a kink (red dashed circle). **d** Corner-shape of two domain boundaries. **e** Three different domain boundaries merging at one point.

The measured $\mathrm{d}I/\mathrm{d}V$ signal is fairly different in comparison to the bulk bismuthene spectra described in Sec. 7.2.2. It contains a manifold of peaks in the entire bulk band gap (and beyond) instead of a wide energy gap. The conductivity at zero bias seems suppressed, however, analysis of other domain boundaries demonstrates that this is not always the case. Spectra measured at different lateral positions along the domain boundary may give rise to peaks at equal energy but with varying $\mathrm{d}I/\mathrm{d}V$ signal. Reproducible peak energies are marked with black arrows in Fig. 7.11**c**, and the corresponding (grid) LDOS maps are shown in Fig. 7.11**d**.

At first we focus on energies corresponding to occupied bulk states, which are highlighted by the gray shaded areas in Fig. 7.11**c**. The LDOS maps on both domain reproduce the LDOS signal of bulk bismuthene (see Fig. 7.3), despite close proximity to the domain boundary ($< 1\,\mathrm{nm}$). Interestingly, atop the 1D structure seen in the topographic CCI, the LDOS signal is displaying reduced or enhanced $\mathrm{d}I/\mathrm{d}V$ signal and additional structure. The period doubling observed in the CCI images (see, e.g., Fig. 7.11**a**) is seen in the LDOS maps, as well, and serves as a marker to determine the domain boundary length. Importantly, no energy-dependent modulations are seen in the LDOS maps as long as those are recorded at energies well inside the VB/CB.

Different structures are evident when LDOS maps close to or within the 2D bulk bismuthene band gap are inspected. Remarkable LDOS modulations reminding of standing waves are apparent. The number of maxima/minima is linearly increasing with the probing

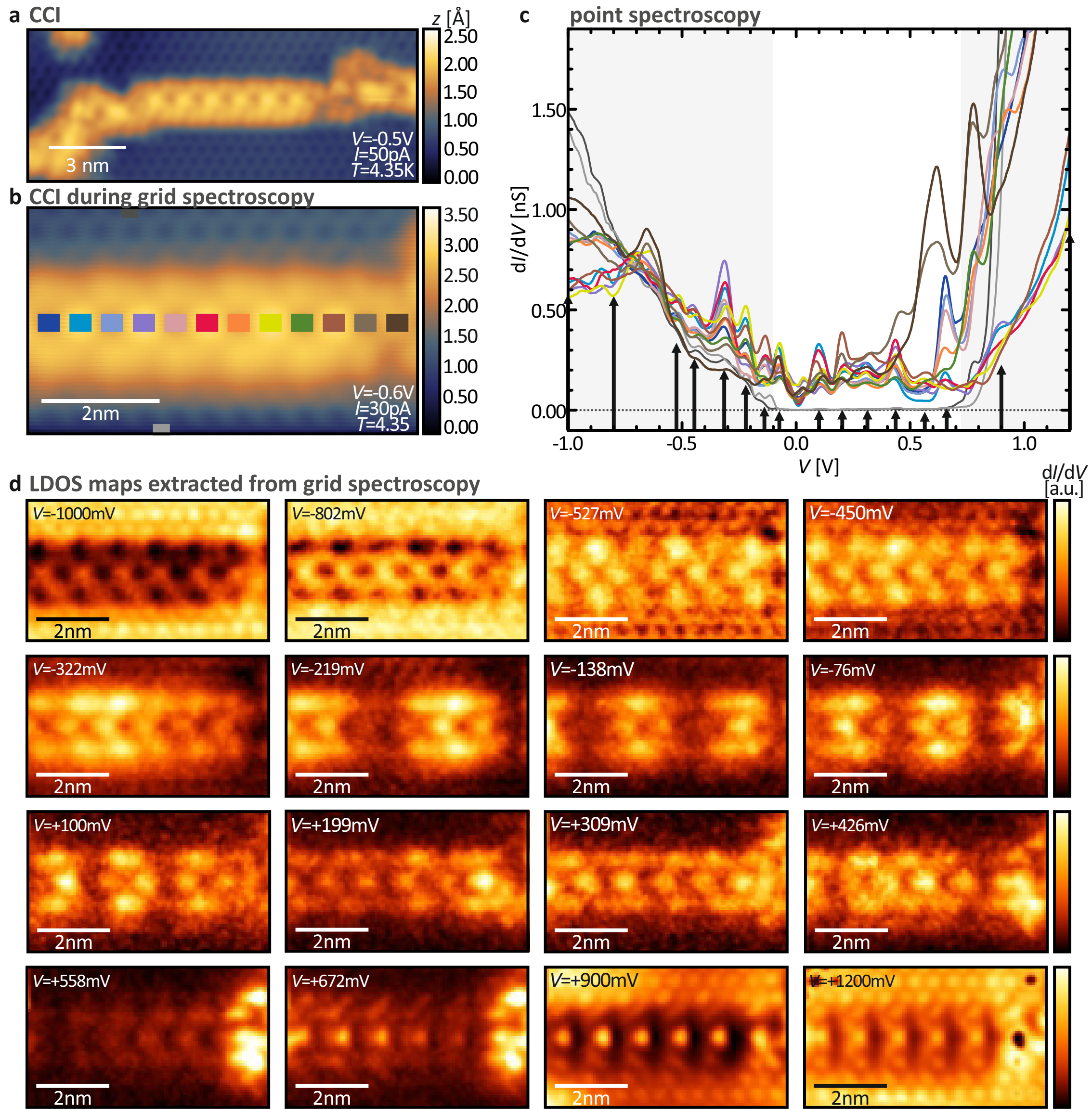

Figure 7.11 Grid spectroscopy of a domain boundary. **a** The overview CCI image shows the surroundings of the domain boundary. **b** CCI recorded during a high-resolution grid spectroscopy ($V_{\text{st}} = -1.0\,\text{V}$, $I_{\text{st}} = 500\,\text{pA}$, $V_{\text{mod}} = 5\,\text{mV}$, $\Delta x = \Delta y = 0.6\overline{6}\,\text{Å}$, $V_{\text{ini}} = -1.0\,\text{V}$, $V_{\text{end}} = +1.2\text{V}$, 601 points). Gray shaded areas denote bismuthene bulk state contributions to the signal, and colored squares indicate the measurement position of the extracted spectra shown in **c**. To improve statistics, 5×5 spectra are averaged with exception of bulk spectra (light/dark gray rectangle), where only 4 spectra are averaged to maintain enough distance to the domain boundary. **c** The $\mathrm{d}I/\mathrm{d}V$ spectra far away from the boundary (light/dark gray line) show the bismuthene bulk spectral properties described in Sec. 7.2.2. In contrast, spectra measured on top of the domain boundary possess a completely different $\mathrm{d}I/\mathrm{d}V$ signature with a manifold of peaks in the bulk gap. Black arrows mark reproducible maxima. **e** The grid LDOS maps (2 pixel Gaussian filtering) corresponding to the different maxima pointed out by arrows in **c** are displayed and reveal quasi-particle interference.

energy from one ($V = -322\,\text{mV}$) to three ($V = -138\,\text{mV}$ and/or $V = -75\,\text{mV}$). Starting from four maxima and more, an unambiguous identification is not possible anymore.

The interpretation of this quasi-particle interference is not at all trivial. Domain boundaries break the periodicity of the bismuthene lattice, and provide a ZZ edge, which is accompanied by an edge state connecting VB and CB in DFT (see Fig. 4.10), but only if the domain boundary constitutes a topologically trivial defect (see Sec. 3.1.2). In fact, in this case not only one but two edge states should emerge, with one being contributed by

each of the adjacent domains. Moreover, the spatial proximity of both edge states might cause tunneling between both sides and in the end even induce a gap to the system (see, e.g., Refs. [246] and [247]). A direct observation of such coupled interface states with an imaging techniques like STM/STS has been lacking and only recently achieved by the group of M. Crommie in $1T$'-WSe_2 [245, 248]. In Ref. [245], they analyze both trivial and non-trivial topological interface states.

Yet, in the case of domain boundaries in bismuthene it is not clear whether the observed behavior stems from coupled topological states. More precisely, it is not known whether an atomic rearrangement takes place when domain boundaries evolve during bismuthene growth. Hence, it is unclear whether the domain boundaries involve a lattice structure that gives rise to ZZ edge states, or whether a different atomic arrangement causes the appearance of trivial edge states. The differentiation of both scenarios (helical vs. trivial edge states at domain boundaries) is highly complex and interest of current research.

As strong LDOS contributions to the CCI signal are manifest, atom-resolved atomic force microscopy is the method of choice to unveil the atomic structure, which can be used in a second step to simulate the 1D defects by DFT. Yet, even without further theory backup we can state that domain boundaries do not show the smooth $\mathrm{d}I/\mathrm{d}V$ signal expected from modeling of an ideal ZZ edge (Fig. 4.10) but host in-gap states that might be detrimental to the helical transport. To circumvent these problems the average domain size has to be increased substantially, as discussed in Secs. 6.3 and 9.

7.3.2 Point Defects

Point defects emerge during crystal growth and result from, e.g., atom vacancies, stacking faults, or the incorporation of chemical impurities in the crystal lattice. In the following, the properties of few frequently observed, exemplary defects are described.

Fig. 7.12 shows a CCI (**a**,**c**) and LDOS map (**b**, **d**) recorded in occupied (**a**/**b**) and unoccupied states (**c**/**d**) of bismuthene. The probed surface area encloses four point defects with varying extent and shape. Measurements at a different bias voltage demonstrate the strong bias dependence of the defect shape and probed apparent height with respect to the surrounding honeycomb lattice.

A bismuthene lattice model is placed on top of the CCI scan in Fig. 7.13**a** to identify the defect site in relation to the underlying lattice. It reveals that all defects are centered around the central honeycomb site, i.e., the site not covered by Bi atoms with exception of the divacancy defect (defect no. 2 in Fig. 7.12), which evolves from two missing Bi atoms.

Spectroscopic properties of point defects. To examine the LDOS of the respective point defect, a high-resolution grid spectroscopy measurement is recorded. The CCI representing the probed surface area is shown in Fig. 7.13**b**. The diagram in Fig. 7.13**c** shows the conductivity averaged within the area of the colored squares in Fig. 7.13**b** on top of the defects.

An STS curve on the regular bismuthene lattice is extracted, as well, to confirm that the usual bulk spectrum is recovered at a certain distance from the point defects. Indeed, the purple curve in Fig. 7.13**c** reproduces the key characteristics that are evident in Fig. 7.6.

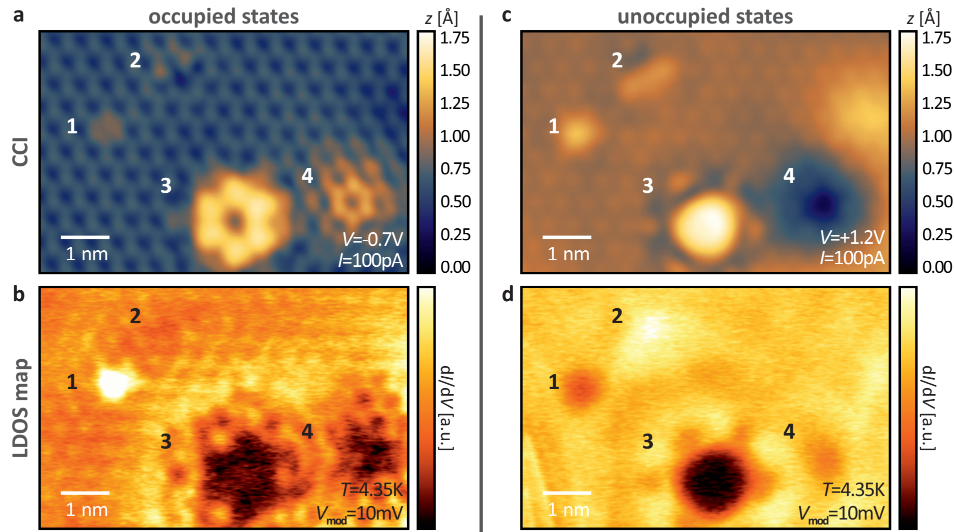

Figure 7.12 Scan area including four regularly found point defects on bismuthene. **a** and **c** CCI and **b** and **d** LDOS map in the occupied and unoccupied states, respectively. The defects' shape and probed apparent height with respect to surrounding regular bismuthene plane changes upon variation of the bias voltage. For an easier identification we name the defects (1) *enhanced honeycomb center*, (2) *Bi divacancy* $V_{2\mathrm{Bi}}$, (3) *flower* and (4) *isolated honeycomb* defect according to their shape.

Bi divacancy defect. The STS curve measured on top of the *Bi divacancy defect* (orange curve in Fig. 7.13**c**) is very similar to the bulk $\mathrm{d}I/\mathrm{d}V$ signal. The conductivity in the unoccupied states is lower and lacks the pronounced increase of the LDOS visible at $\approx +1.0\,\mathrm{eV}$ in the bulk spectrum (purple curve), but in particular, the commonly observed band gap is apparent. It is interesting to note that a single Bi vacancy has not been observed, whereas the divacancy defect is frequently found. This is in contrast to flat stanene on Cu(111), where mono- and divacancy defects are both found [117]. Furthermore, the nearest and next-nearest neighbor Bi atoms on one side parallel to the line connecting the two missing atoms always feature an increased apparent height in the occupied states, whereas the opposite trend is seen in the unoccupied states (compare to Fig. 7.12**a**/**c**). This broken symmetry is always observed, even though all Bi atoms next to the vacancies possess the same number of unbound orbitals. Supposedly, a small lattice relaxation lowers the strain that comes along with missing atoms. An increased apparent height is found likewise in case of the Sn-divacancy for stanene on Cu(111) [117], but on one side perpendicular instead of parallel to the line connecting the missing atoms. This difference could be related to a different symmetry with respect to the underlying substrate.

Isolated honeycomb defect. The $\mathrm{d}I/\mathrm{d}V$ curve recorded on top of the *isolated honeycomb defect* (red marker in Fig. 7.13**b**) also exhibits comparably small differences in reference to the bulk $\mathrm{d}I/\mathrm{d}V$ signal. The band gap magnitude is slightly lowered, and the LDOS in VB and CB band are enhanced and reduced, respectively, compared to a typical bulk spectrum. All surrounding Bi atoms are affected in the very same way and a sixfold symmetry is seen. A defect with very similar appearance is observed on graphene/hBN films by Wong et al. and appointed to intrinsic hBN substrate defects [249], such that point defects present on top of or within the SiC substrate might cause their occurrence.

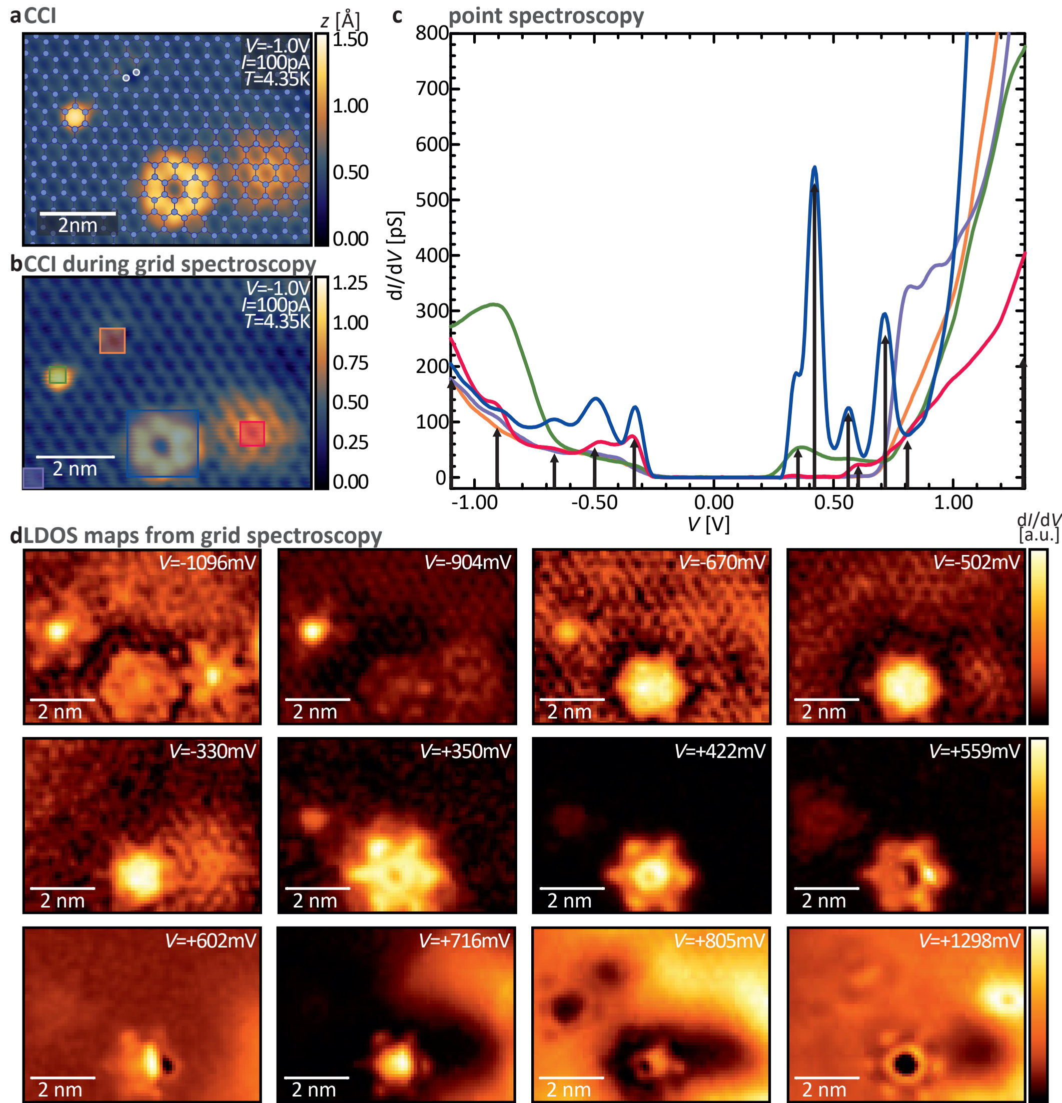

Figure 7.13 **a** CCI with overlaid bismuthene lattice model to identify the lattice site of all defects. **b** CCI measured during acquisition of a high resolution grid spectroscopy ($V_{\mathrm{st}} = -1.0\,\mathrm{V}$, $I_{\mathrm{st}} = 100\,\mathrm{pA}$, $V_{\mathrm{mod}} = 10\,\mathrm{mV}$, $\Delta x = \Delta y = 1\,\mathrm{Å}$, $V_{\mathrm{ini}} = -1.4\,\mathrm{V}$, $V_{\mathrm{end}} = +1.6\mathrm{V}$, 501 points). Colored squares indicate where spectroscopy curves have been extracted for the respective defect. **c** Averaged $\mathrm{d}I/\mathrm{d}V$ signal. The purple spectrum measured at distance from defects reproduces regular bulk bismuthene signal. In comparison, STS curves recorded on the flower and enhanced honeycomb center defect show strong deviations. **d** Grid LDOS maps displayed at distinct peak energies (marked by black arrows) in the STS curves in **c**. The LDOS maps are smoothed by a Gaussian filter (width 2 pixel).

Enhanced honeycomb center and flower defect. STS curves measured on top of the other two defects have a distinctly different characteristics. The spectrum recorded on the *enhanced honeycomb center* (green curve in Fig. 7.13**c**) exhibits a strongly reduced band gap magnitude ($\approx 0.5\,\mathrm{eV}$) and a peak around $E - E_{\mathrm{F}} \approx -0.9\,\mathrm{eV}$. Given that this defect is in the center of the honeycomb it might emerge due to the presence of either a DB (in case that the major part of Si DBs become passivated by H after growth) or of an additional (unknown) atom/molecule. In comparison to the *isolated honeycomb defect* it is interesting to note that a threefold symmetry is observed in some LDOS maps (best seen at $V = -904\,\mathrm{meV}$ and $V = +805\,\mathrm{meV}$). Such an effect might be related to the C sublattice of the SiC bilayer. Moreover, we find an ionization ring around the defect center

in the LDOS at higher binding energy (not shown), which is reported for similar systems due to charged point defects (bulk or surface dopants) [249–251].
The *flower defect* spectrum exhibits the most drastic deviations from the bulk spectrum. This comprises a significant reduction of the band gap magnitude as well as the presence of pronounced peaks.

LDOS maps of point defects. Although it is difficult to assign the physical reason giving rise to the formation of the respective defects it is important to check whether the point defects modify the LDOS signal only locally or have a long-range influence, especially as some lower the band gap magnitude. For this purpose, grid LDOS maps at certain peak energies (indicated by black arrows in Fig. 7.13**c**) are displayed in Fig. 7.13**d**. As expected from the point spectroscopy curves in Fig. 7.13**c**, it is the *flower defect* that has the largest impact range in the LDOS maps. With increasing bias voltage pulsating patterns with hexagonal symmetry appear. The signal emerges in the defect center and then spreads out across to the defect but remains localized within the boundary indicated by modified apparent height in the CCI image. Similarly, also the other defects do not cause modifications at large distance, at least not in the mapped energy range close to/within the bulk band gap. However, ionization rings evolve around the *enhanced honeycomb center defect* and around the *flower defect* at high binding energies ($E - E_\mathrm{F} < -1.2\,\mathrm{eV}$), implicating that a harmful influence in transport experiments cannot be excluded.

7.3.3 Antidots and Disordered Areas

Apart from reproducible crystal imperfections like point defects and 1D domain boundaries, bismuthene also hosts irregular, extended 2D defects on its surface. These defects enclose areas with varying size by meandering boundaries like shown in the STM image in Fig. 7.14**a**. On some samples, the surface area covered by disorder is even exceeding the area of the bismuthene lattice, compare to Figs. 6.6, 7.2 and 7.1. The defective areas are separated from the bismuthene plane by a boundary of increased apparent height. The smallest versions of these defective areas may be called "antidots“, while defective regions with larger extension are called "disordered areas“, as usually no periodic substructure is found in their inner area, neither in topographic scans (see magnified views on several defects in Fig. 7.14**b**–**d**) nor in the corresponding $\mathrm{d}I/\mathrm{d}V$ maps recorded during a grid spectroscopy of the defects (Fig. 7.14**e**–**g**). It is assumed that both antidots and disordered areas evolve due to suboptimal epitaxial growth, as their frequency of occurrence varies significantly between different samples. Bismuthene samples with a high percentage of such defects seem to be grown on partially reconstructed SiC substrates.
Although the boundaries follow arbitrary directions and terminations, in some cases segments with well-ordered AC and ZZ edges are seen (see area enclosed by the dotted white ellipsoid in Fig. 7.14**b**). As these edges constitute a termination of the regular bismuthene lattice, they might host an edge state, which motivates spectroscopic measurements.
Unfortunately, the point spectroscopy curves shown in Fig. 7.14**h**–**j** reveal that no reproducible but seemingly arbitrary $\mathrm{d}I/\mathrm{d}V$ curves are detected. Sharp peaks similar to what is observed for certain point defects in Sec. 7.3.2 seem to stem from defect ioniza-

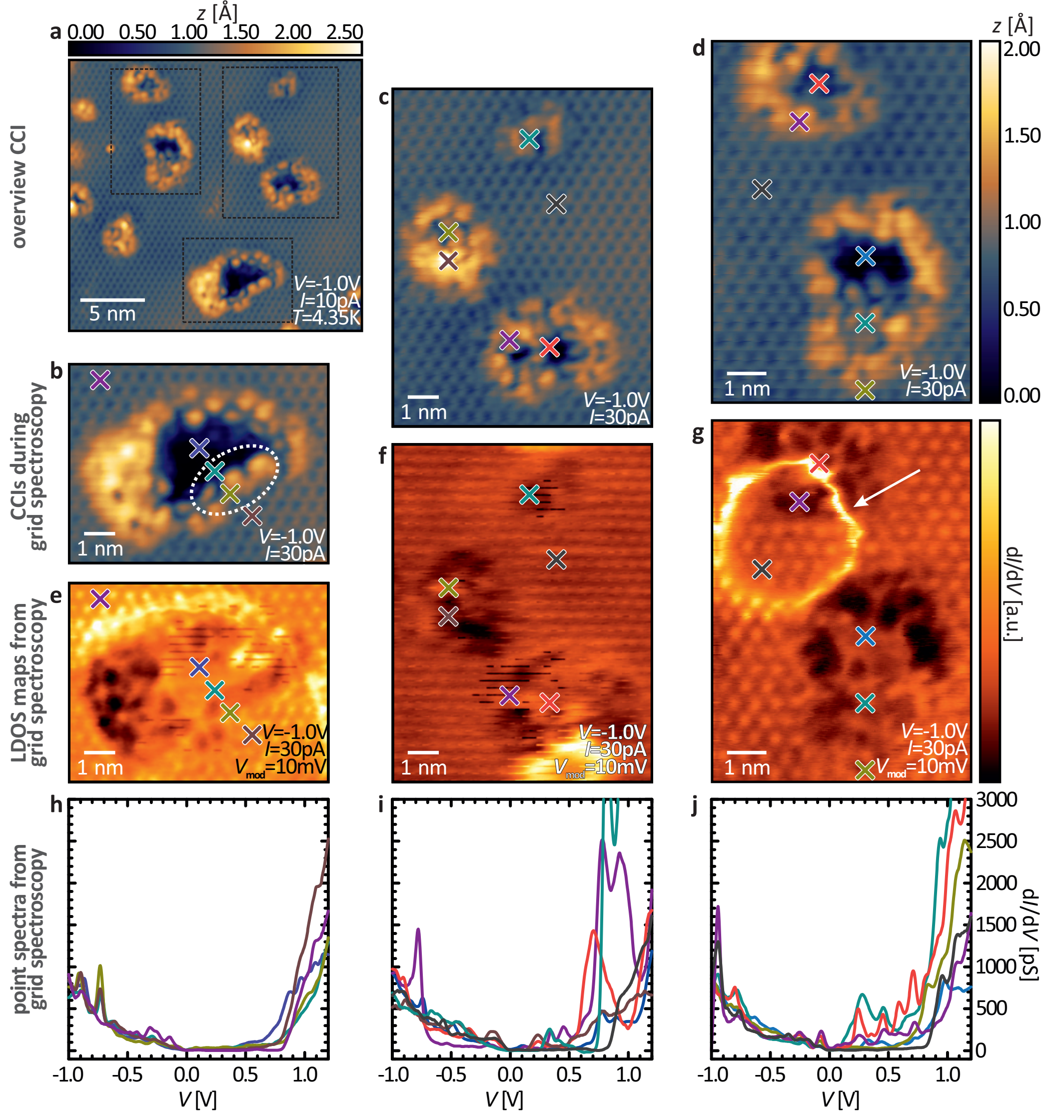

Figure 7.14 Investigation of antidots and disordered areas with STM and STS. **a** Overview CCI of a bismuthene surface possessing several of those surface imperfections of few nanometer diameter. The defect's boundary is meandering in arbitrary directions and displays partially ordered sections both in ZZ and AC orientation. **b–d** CCIs and **e–g** LDOS maps recorded during a series of grid spectroscopy measurements. Neither in the CCI nor LDOS scan a periodic structure is seen in the inner area of the defects. The white dashed ellipsoidal line in **b** marks an ordered AC edge segment, and the white arrow in the LDOS map in panel **g** highlights an ionization ring arising from a charged defect. Colored crosses mark positions of individual point spectroscopy curves displayed in **h–j**. The STS curves exhibit a manifold of position-dependent sharp peaks. No pattern is recognizable, suggesting that the peaks stem from statistically-arranged defect clusters. Scan parameters: $V_{\mathrm{st}} = V_{\mathrm{ini}} = -1.0\,\mathrm{eV}$, $V_{\mathrm{end}} = +1.2\,\mathrm{eV}$, $I_{\mathrm{st}} = 300\,\mathrm{pA}$, $V_{\mathrm{mod}} = 10\,\mathrm{meV}$, $\Delta x = 2.99...2.43\,\text{Å}$, $\Delta y = 2.37...2.44\,\text{Å}$, 601 points per spectrum.

tion levels [250]. This is supported by the observation of ionization rings in the LDOS map of Fig. 7.14**g** (see also App. E.4). Therefore, presentation of LDOS maps for antidots/disordered areas is omitted at this stage. Interestingly, a completely different $\mathrm{d}I/\mathrm{d}V$ signal evolves when the disordered area is not enclosed by a single domain but connects minimally two domains, as will be discussed in Sec. 8.1.1.

Evaluation of the surface defects. It has been shown that the point defects as well as the defective areas and domain boundaries introduce impurity levels in the band gap

of bismuthene, which could trap charge carriers or provide reservoirs of trivial electrons when quantum transport experiments will be eventually carried out. Thus, clearly, their appearance should be avoided as far as possible. Detailed growth studies are required to diminish their density, as, depending on the defect type, different aspects of the growth process have to be optimized. The reduction of the point defect density might be achieved by an as-clean-as-possible epitaxy under the best possible vacuum conditions and with Bi material of highest purity. The other two defects are intimately related to the peculiar epitaxy process described in Sec. 6.1. It is likely that the disordered areas emerge when either the H desorption fails or the substrate becomes too hot, such that a Si-rich $(\sqrt{3}\times\sqrt{3})$ reconstruction takes place. Accordingly, this critical step must be studied and regulated with high precision. The domain boundaries result from the ambiguity introduced by the different, but equivalent Si atoms, at which the $(\sqrt{3}\times\sqrt{3})$ Bi reconstruction might nucleate, such that it is not possible to avoid their appearance completely. Instead, one must aim to enlarge the average domain size. This might be accomplished by lowering the density of Bi nucleation sites by reduction of the Bi vapor pressure, while the thermal energy provided by the substrate is maintained or raised, such that atoms preferably attach to already grown domains to lower their free energy.

7.4 Band Structure of Bismuthene

Complementary to a microscopic method like STS, we use ARPES to explore the momentum-resolved energy dispersion of bismuthene, making a detailed comparison to the band structure computed by DFT feasible.

7.4.1 Low-Energy Band Structure

We start the ARPES analysis by inspection of the low-energy band structure, which is predicted to exhibit a characteristic Rashba-split VBM around the K point. Fig. 7.15**a** shows an ARPES band structure plot measured along a pathway connecting the high symmetry points of the hexagonal lattice in k space, i.e., Γ, M, and K.

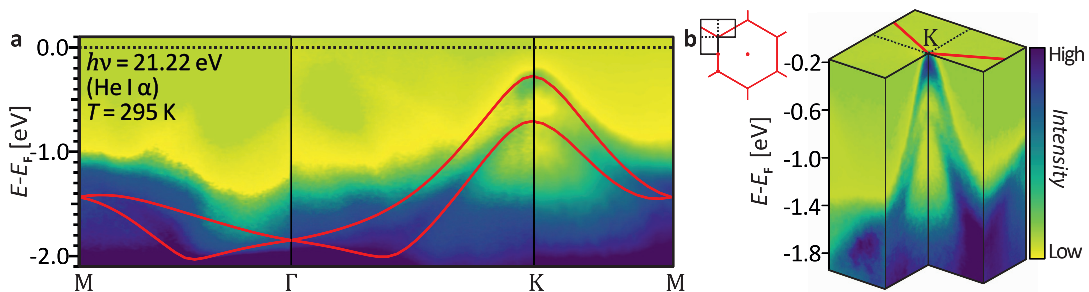

Figure 7.15 **a** ARPES of bismuthene on SiC measured in the homelab setup with an unmonochromatized He lamp (see Sec. A.4). The measured spectral function at low binding energies is governed by two bands around the K point. The band maximum is located clearly below the Fermi level, i.e., a band gap is present. The DFT band structure calculation shown by red curves is a guide to the eye and corresponds to the band structure in Fig. 4.5**c**. **b** A 3D cut around the K point visualizes that two cones with hole-like band dispersion are centered at the K point.

Indeed, in the range of $E - E_F > -1.0\,\mathrm{eV}$, two bands that feature a hole-like dispersion in K-Γ as well as in K-M direction are visible, in agreement with the DFT calculations shown in Fig. 4.5**c**. The binding energy offset of both bands ($\approx 0.5\,\mathrm{eV}$) is better seen in the three-dimensional (3D) cut shown in Fig. 7.15**b**. Importantly, the maximum of the upper band exhibits a clear offset from E_F, i.e., a band gap is present, although its full magnitude cannot be probed with ARPES.

Monolayer vs. bilayer bismuthene. STM and STS probe primarily the first layer of the system, hence, the growth of several bismuthene layers cannot be fully excluded, even though many indications for formation of monolayer bismuthene have been gathered so far. Therefore, we compare the ARPES-measured band structure to the DFT-computed band structure for mono- and bilayer bismuthene in Fig. 7.16.

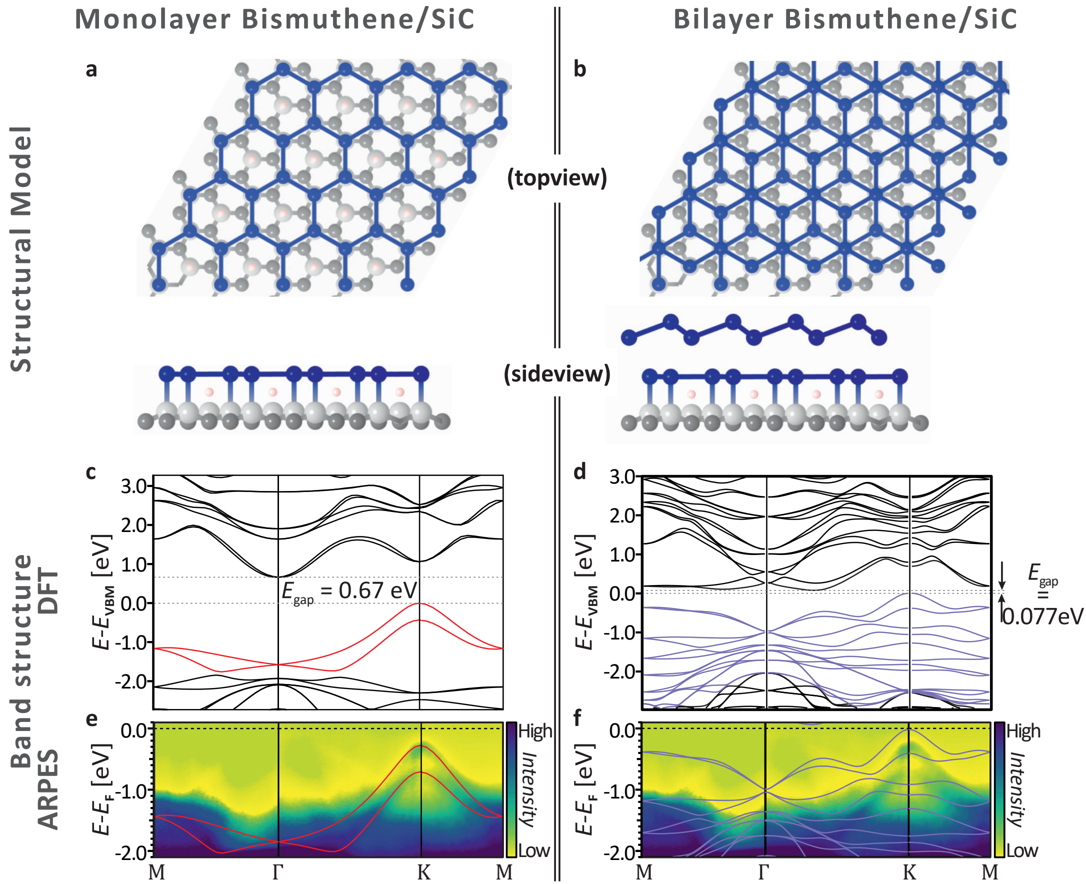

Figure 7.16 Structural model for **a** monolayer and **b** bilayer bismuthene on SiC. Left and right column compare the **c**/**d** DFT band structure, and the **e**/**f** ARPES band map with overlaid DFT band structure of both model structures. Red and violet colored curves in **c**/**e** and **d**/**f** highlight bands that are (at least partially) included within the energy range of the measured band structure. **e** The measured ARPES band structure (He I line, $h\nu = 21.22\,\mathrm{eV}$, $T = \mathrm{RT}$) fits very well to the DFT-predicted band dispersions. **f** Huge differences are found when comparing the experimental ARPES and the computed DFT band dispersion of bilayer bismuthene. The predicted band gap for bilayer bismuthene is only $E_{\mathrm{gap}}^{\mathrm{bilayer}} = 0.077\,\mathrm{eV}$ and smaller than the energy offset of the VBM and E_F in ARPES ($\approx 0.2\,\mathrm{eV}$). The DFT band structures are obtained by the HSE hybrid functional (monolayer bismuthene) and GGA functional (bilayer bismuthene). Band structure calculations were provided by Gang Li [168].

The structural model for monolayer bismuthene has been shown in Fig. 4.4 but is shown here again (Fig. 7.16**a**) to facilitate a side-by-side comparison to structure of bilayer bis-

muthene (Fig. 7.16**b**). In bilayer bismuthene, two Bi honeycomb lattices are stacked in a Bernal (AB) stacking sequence, which is commonly observed for bilayer graphene epitaxially grown on SiC [252, 253]. One of the two Bi atoms is positioned directly on top of a first layer Bi atom, while the other one occupies the SiC site at which no Bi atom adsorbs in the first layer. Furthermore, the second, buckled Bi layer is aligned by weaker van der Waals forces instead of covalent bonds.

The band structure computed by first-principles DFT is shown in Fig. 7.16**c** and **d** for both materials. The second layer with different lattice structure gives rise to additional bands present in bilayer bismuthene on SiC. In particular, near the Γ point, where no band is evident in the energy range of $E - E_{\mathrm{VBM}} = 0\,\mathrm{eV}$ to $E - E_{\mathrm{VBM}} = -1\,\mathrm{eV}$ for monolayer bismuthene, two bands are seen, and four instead of two bands are found around the K point. The VB is still formed by two hole-like bands at K, but their splitting is slightly larger and energy dispersion is strongly reduced. Most importantly, the band gap magnitude is lower by roughly one order of magnitude.

With these observations in mind, an overlay of calculated and experimental band structure is shown in Fig. 7.16**e** and **f** for mono- and bilayer bismuthene, respectively. Large differences are evident in case of bilayer bismuthene, with none of the above-described features being present. In particular, the experimentally-probed offset between VBM and Fermi level is approximately two times larger than the computed band gap magnitude for bilayer bismuthene. Moreover, the second band maximum of the two bands along the way from K to Γ and M is clearly not observed.

The next sections provide a more detailed inspection of band structure. A comparison of the probed spectral weight in ARPES and the binding energy of bands DFT is accomplished with synchrotron-light-based ARPES measurements. At first, however, the VBM at the K point is scrutinized.

7.4.2 Valence Band Maximum at K

The Rashba-split VB is characteristic for the Bi/SiC system as it is induced by the covalent bond between Bi and Si atoms. Constant energy contours (CECs), displaying the intensity distribution in the 2D k space at variable binding energy, are used to visualize the band dispersions. Fig. 7.17 shows CECs from E_{F} to $E - E_{\mathrm{F}} = -1.2\,\mathrm{eV}$ in steps of $0.1\,\mathrm{eV}$.

Probed high symmetry points. The captured k space area is sketched in the top left panel of the figure. It includes K, M and K′ as high symmetry points. Additionally, a graph with larger k space extension can be found in the bottom right panel of Fig. 7.17. Directly at the Fermi level two circular points with high intensity are found. Upon lowering of the probing energy, the band maxima evolve to a ring-like contour starting from $E - E_{\mathrm{F}} = -0.3\,\mathrm{eV}$. At $E - E_{\mathrm{F}} = -0.6\,\mathrm{eV}$ a second band maximum, i.e., the lower VB, becomes visible within the contour of the first VB, and at around $E - E_{\mathrm{F}} = -1.2\,\mathrm{eV}$, an increased intensity is emerging directly in the middle of the line connecting K and K′ line point, which is the M point.

Band dispersion. In the energy range of $E - E_{\mathrm{F}} = -0.3...-1.0\,\mathrm{eV}$ the contour of both VBs in CECs shown in Fig. 7.17 noticeably deviates from a ring-like shape and is

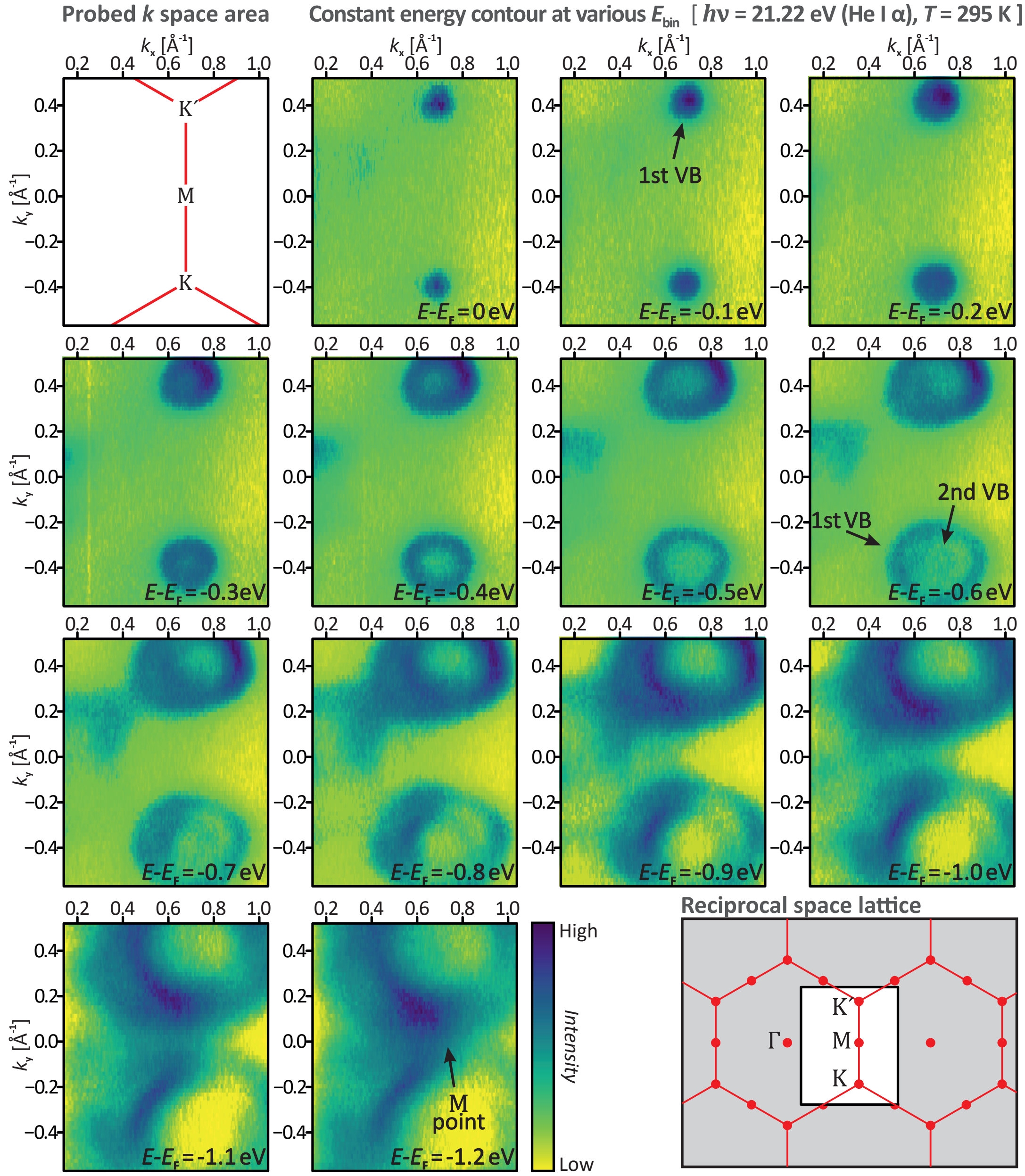

Figure 7.17 ARPES CECs including the neighboring K′/K points at varying binding energy. The probed k space area is shown in the sketch in the top-left corner. All CECs are averaged in a range of $dE = 25$ meV around the given energy. The data has been recorded with the homelab ARPES setup. Already at the Fermi level a weak, point-like signal originating from the VBM is seen at the K/K′ point, which gradually evolves to an oval contour with increasing radius at higher binding energies, until a second but weaker maximum is visible directly at K′/K and $E - E_F \approx -0.6$ eV. Finally, at around $E - E_F \approx -1.2$ eV, the M point emerges between K and K′.

rather oval. Very close to E_F, only a circle is seen, and in the lower limit of the displayed energy range ($E - E_F = -1.1 \ldots -1.2$ eV) the CEC eventually has a circular shape, again. A comparison of the CECs of both VBs reveals that the triangular symmetry of the band contour is more pronounced in case of the upper VB, best seen in the CEC at $E - E_F = -0.8$ eV. This reflects very well the slightly steeper band dispersion along K–M as compared to K–Γ direction that is evident in the band structure calculations shown in Fig. 4.5**c**/Fig. 7.16**c**. Likewise, the more uniform dispersion of the lower VB in K–Γ and K–M direction is reproduced by the DFT calculations.

It is worth noting that around K and K′ the identical band dispersion is observed. This could be expected, as neither in the theoretical modeling nor in STM any difference between the Bi atoms sitting on different sublattice sites is evident. The slightly lower signal strength of K with respect to K′ in this measurement is most likely caused by a frequently observed drop of the He light intensity over the duration of the measurement.

VB linewidth. The energy as well as momentum linewidth of the bismuthene bands at the K/K′ point seems relatively large. Among a manifold of sources causing linewidth broadening, thermal broadening is the easiest to check as it only requires a measurement of the band structure at low temperature. Therefore, two measurements of the very same sample at the K point are conducted and shown in Figs. 7.18**a** and **b**, with the sample being at room temperature (RT) and cooled down to $T = 10\,\mathrm{K}$, respectively.

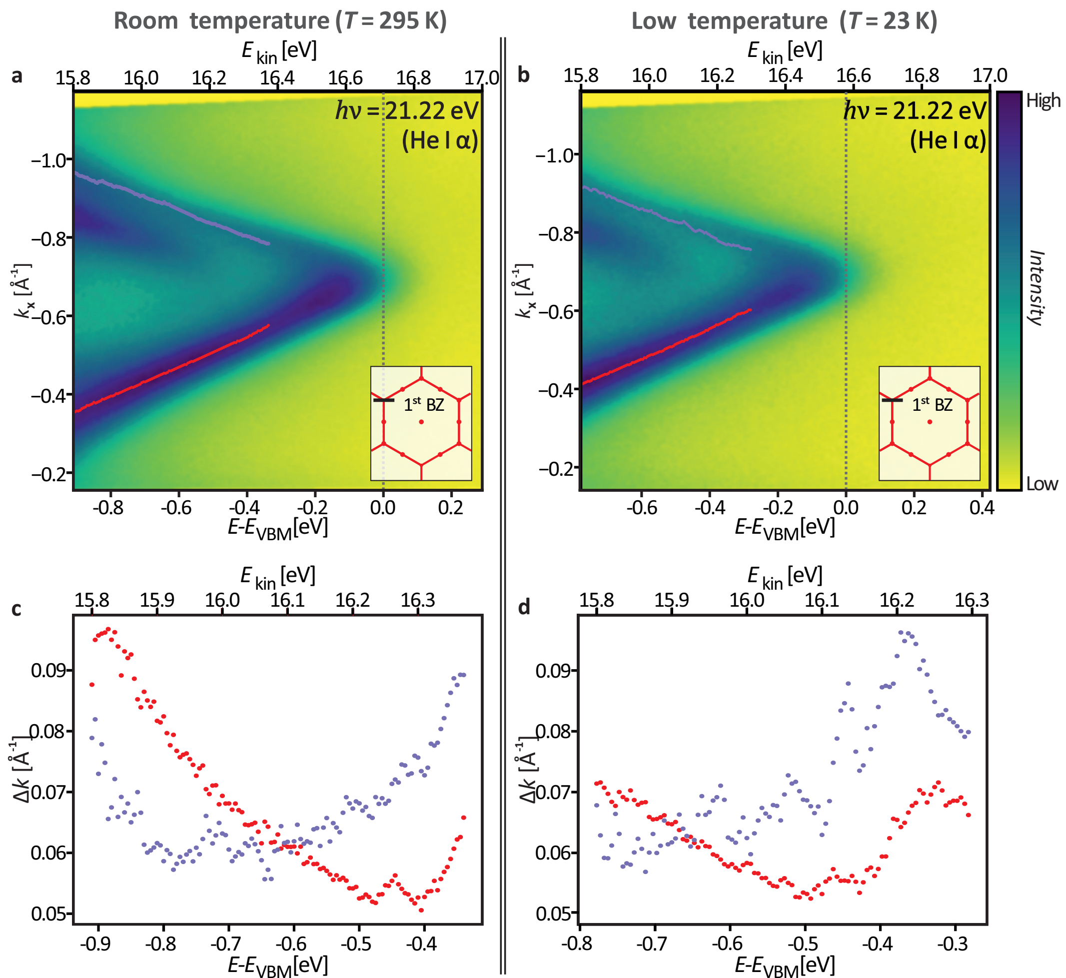

Figure 7.18 **a**, **b** Close-up bandmap around K and **c**, **d** linewidth at room (295 K) and low temperature (23 K), respectively. The bandmap's position in k space is sketched in the inset at the bottom right. A direct comparison of the bandmaps at RT (**a**) and low temperature (**b**) reveals that the entire band structure is shifted to higher binding energy at reduced temperature due to charging. Apart from that, both plots appear very similar. The red and violet profile indicate the energy at which the linewidth of the upper VB is fitted. Measurements at low temperature do not feature a reduced linewidth, suggesting that the thermal broadening is not the limiting parameter.

At first glance, both ARPES bandmaps seem to be fairly comparable. In both cases, the two Rashba-split VBs are clearly perceivable, although the mapped intensity of both bands

is different: while the lower half ($k_x > -0.65\text{Å}^{-1}$) of the first VB, which is located in the first Brillouin zone (BZ) (see sketch of measurement geometry in the inset of Figs. 7.18**a**, **b**), is more intense and the upper half ($k_x < -0.65\text{Å}^{-1}$) seems more faint, this trend is reversed for the 2nd VB at lower kinetic energy. This results from the peculiar measurement geometry. To reach the K point, the sample surface normal is rotated towards the He light source, resulting in an illumination that is not symmetric with respect to k_x (i.e., the direction M–Γ–M)[20].

The linewidth is determined by fitting Gaussian profiles to the extracted MDCs. As the sample is apparently charging at low temperature, an energy scale given in reference to the VBM ($E - E_{\text{VBM}}$) instead of the Fermi level is shown in addition to the kinetic energy (E_{kin}). The results of the MDC fitting procedure of the upper VB are shown in Fig. 7.18**c** and **d**. The fitted linewidths of both measurements are very similar. Close to the Fermi level, at $E - E_{\text{VBM}} = -0.3...-0.4\,\text{eV}$, the fitted width increases in both measurements and both branches, which is the result of the very broad maximum of the upper VB, whereas the minimal linewidth is found at $E - E_{\text{VBM}} = -0.5\,\text{eV}$.

Generally, the fitted Δk values at room and low temperature are almost identical, and are rather increasing in the latter case. Hence, thermal broadening does not have a significant contribution to the detected linewidth. Final state broadening in the photoemission process should be a negligible factor, as well, because of the (per definition) 2D electronic structure of bismuthene and the associated vanishing perpendicular electron momentum $k_\perp$ [69]. In contrast, the imaginary part of the self-energy including scattering rates, e.g., due to electron-plasmon, electron-electron, or electron-phonon coupling, might contribute to the observed broadening, even though the latter comprises a temperature-dependence and consequently is not the decisive factor [69, 254]. However, considering the surface structure and defects probed by STM in Secs. 6.3 and 7.3, respectively, it is probable that the small domain size as well as the amount of disorder, i.e., the surface's roughness, might be the main reason for the large linewidth of the broad bands [255–257]. Finally, the fluctuation of the chemical potential evidenced with STS, see Fig. 7.2.2, might contribute to the signal broadening in energy and therewith in k, as well.

7.4.3 Detailed Comparison of ARPES and DFT Band Dispersion

In contrast to our laboratory light sources, the highly-brilliant synchrotron light probes only a small sample spot, is monochromatized, polarized, and allows tuning of the photon energy. In order to compare the band dispersion in more detail, bandmaps recorded at two photon energies, namely $h\nu = 47\,\text{eV}$ and $h\nu = 80\,\text{eV}$, at which the bismuthene band structure is probed with particularly high count rates and richness of detail are shown in Fig. 7.19. The larger photon energies translate into larger k space sections that are mapped with a single frame by the spectrometer, see Fig. 7.19**a** and **c**.

The measured band structure data is displayed as a second derivative image (energy axis) to improve the visibility of the bands. All features are found in the original images, as well (compare to Fig. 7.20 and E.8). Like in Fig. 7.18, the energy scale is given in reference

[20] Accordingly, this effect is not seen in ARPES measurements probing a K point with symmetric illumination in reference to M–Γ–M, see Fig. 8.9.

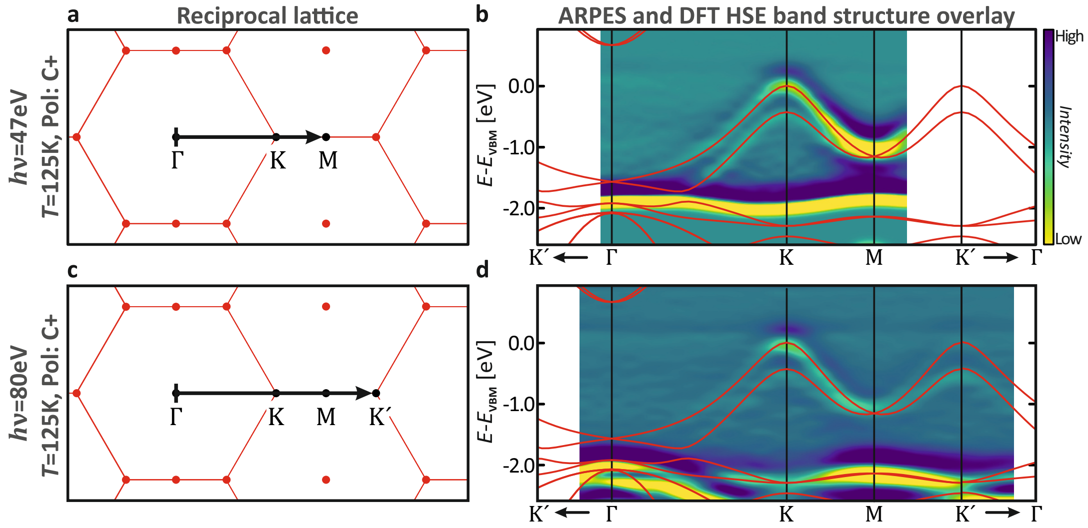

Figure 7.19 Direct comparison of DFT and 2nd derivative (along the energy axis) ARPES band structure maps. **a**/**c** Pathway in reciprocal space and **b**/**d** ARPES band structure map recorded with $h\nu = 47\,\text{eV}$ and $h\nu = 80\,\text{eV}$ overlaid with DFT HSE calculations (red curves), respectively. **b** The dynamic range of the bandmap is adapted to the Rashba-split VBs at K. The dispersion of the upper VB can be fully tracked along Γ-K-M while the lower VB is not visible close to Γ. The overlay of the computed band structure unveils the excellent agreement between experiment and theory. **d** At higher photon energy ($h\nu = 80\,\text{eV}$) the dynamic range of the image is optimized to bands at increased binding energy, which possess a much higher intensity than the bands near the Fermi level. The band dispersion at K-M-K′ coincides with the theoretical modeling. Close to Γ, bands with strong or pure SiC character are seen, some of which (partially) not evident in the measured data. Nevertheless, decent agreement is found here, as well. The experimental band structure is displayed as second derivative image and smoothed prior to and after derivation with a Gaussian function. Both ARPES bandmaps have been recorded at the high-resolution endstation of the SIS beamline at the Swiss Light Source with C+ light polarization and at $T = 125\,\text{K}$.

to the VBM, as the sample was charging due to the reduced measurement temperature ($T = 125\,\text{K}$). The dynamic range of the bandmap recorded at $h\nu = 47\,\text{eV}$ (Fig. 7.19**a**, **b**) is limited to highlight the two Rashba-split VBs along the entire pathway along Γ–K–M. Therefore, the false color map is featureless at $E - E_{\text{VBM}} < -2.0\,\text{eV}$. The overlay of measured and DFT-computed band dispersion shows a very high degree of congruence. This concerns the VB splitting and curvature at the K point, as well as their degeneracy at M and the different band velocity of upper and lower band in direction K–Γ.

At higher photon energy ($h\nu = 80\,\text{eV}$, Fig. 7.19**c** and **d**), the probed k space section extends to the next K′ point. Here, the dynamic range of the image is adopted to all bands in the entire energy range. The energy dispersion of the VB is still traceable from K to M, but becomes noticeably weaker from M–K′. Nevertheless, the very close agreement between the experimental data and the DFT band structure is evident.

Also the third and fourth band at higher binding energy (around $E - E_{\text{VBM}} \approx -2.00\,\text{eV}$), which have a weaker dispersion and cross the M point, are intense along K–M–K′ in the ARPES experiment, and exhibit the same dispersion in the calculation. A fifth band is seen in experiment and theory, as well, but very close to the limit of the measurement range, such that only a small part is captured.

In vicinity of the Γ point, a manifold of bands is observable. The third and fourth band exhibit high intensity in direct vicinity of Γ and vanish on the way from Γ to K. At

slightly increased binding energy, Si-derived bands with hole-like dispersion are found in the computed band structure, one with large and one with small effective mass [165]. The heavy hole band is clearly detectable in the 2nd derivative image. In case of the light-hole band, a definitive assignment is difficult but a weak feature with seemingly correct energy dispersion is seen at the very bottom of the displayed energy range.

Band energies at high symmetry points in experiment and theory. A quantitative evaluation of band energies is motivated by the very high degree of congruence between ARPES and DFT band structure obtained by a simple overlay. As the Fermi level position is not fixed in DFT calculations for systems with a fundamental band gap, it is not reasonable to compare absolute binding energy values. Instead, meaningful results are obtained by calculation of the binding energy offset of bands at high symmetry points. This is accomplished by use of line profiles in the rawdata and 2nd derivative ARPES bandmaps ($h\nu = 80\,\text{eV}$), both in the images with full and limited dynamic range shown in Fig. 7.20**a**, **b** and **e**, **f**, respectively. Note that the very same analysis is found in Fig. E.8 for the ARPES data detected at $h\nu = 47\,\text{eV}$. Fig. 7.20**a**/**b** displays an ARPES bandmap with a dynamic range that allows the evaluation all bands in the given energy range. The line profiles (Fig. 7.20**c** and **d**) reveal the presence of intensity maxima at certain energies. To obtain the respective energy of the band in reference to the VBM, these maxima are fit with Gaussian functions in the 2nd derive image line profile. The tabulated values shown in Tabs. 7.1 and 7.3 allow a comparison of the energy offsets obtained by ARPES and according to the DFT HSE band structure calculation, respectively. Note that Γ_1, which belongs to the bismuthene VBs, is not seen in the data due to the vanishing photoemission intensity of these bands in vicinity of Γ (see Fig. 7.19**e**/**f**), and is not found in Tab. 7.1.
For the energy offset of the Rashba-splitted first and second VB at K/K′ we find perfect agreement between ARPES and DFT. Moreover, the energy offset of the band crossing the K point at higher binding energy (K_4 in Tabs. 7.1 and 7.3) in relation K_1/K_2 is almost identical in experiment and theory. We extend the analysis and include bands at other high symmetry points. The theory-predicted offsets for $E(K_{1,2}) - E(M_1)$ and $E(K'_{1,2}) - E(M_1)$ are slightly too large ($\approx 0.2\,\text{eV}$), whereas the values coincide in case of the energy offset of the M point (M_1 and M_2, see Tabs. 7.2 and 7.3). At Γ, only $E(\Gamma_2) - E(\Gamma_3)$ can be evaluated, where the DFT-predicted value is slightly too small ($\approx 0.1\,\text{eV}$).
In general, the energy offset of the bands at M and Γ with respect to the VBM is predicted too large in DFT ($\approx 0.2\,\text{eV}$). This is not surprising, as a renormalization of the valence band width due to electron-electron or electron-phonon interactions, i.e., the real part of the self-energy, are reflected in the spectral function probed ARPES measurements but not in DFT (see, e.g., Refs. [69, 257]), which computes ground state properties.
Fig. 7.20**e**/**f** shows an ARPES bandmap focusing on the Rashba-split VBs, and in particular the 2nd derivative image allows a comparison of the band dispersion around K and K′, which should be identical according to the DFT calculations in Fig. 4.5. Again, we highlight the bands at low energy in a practical way by limiting the dynamic range of the ARPES bandmap to these bands of highest interest. The photoemission intensity is much higher in the first BZ (i.e., at K) than in the second BZ (i.e., at K′), see Fig. 7.20**e** and compare to the sketch of the displayed k space area in Fig. 7.19. Still, their identical band

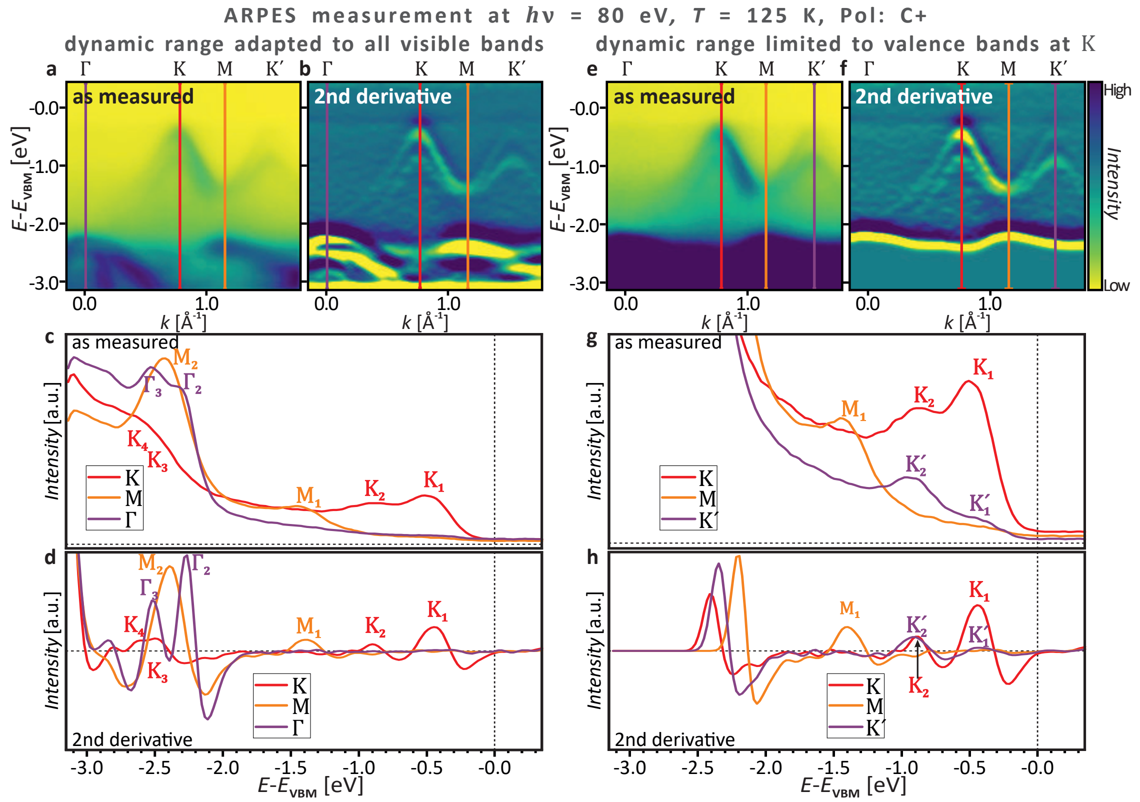

Figure 7.20 ARPES band structure EDCs are used to determine the binding energy offset of bands at high symmetry points of the BZ. The energies are given in relation to the VBM. **a** ARPES bandmap and **b** corresponding 2nd derivative image at $h\nu = 80\,\text{eV}$. **c** and **d** The line profiles at K, M and Γ extracted from the original and 2nd derivative image, respectively, exhibit a series of peaks (K_1–K_4, M_1–M_2, Γ_1–Γ_3). **e**–**h** Same quantities as **a**–**d** but limited dynamic range to focus on the Rashba-split VBs of bismuthene. Note that the displayed intensity range in the line profile in **g** is cropped to allow a better perception of the peaks at low energy. At K/K′, two maxima separated by $\approx 0.5\,\text{eV}$ are evident and originate from the VBs. The bandmaps have been measured at the high-resolution endstation of the SIS beamline (Swiss Light Source). All bandsmaps are smoothed with a Gaussian function, and the 2nd derivative images are additionally smoothed with a Gaussian function before and after twofold derivation along the energy axis.

dispersion around K and K′ is obvious, especially in Fig. 7.20**f**. The dispersion around the M point is now clearly visible and exhibits a local minimum between K and K′. The line profiles shown in Fig. 7.20**g** highlight the two distinct maxima at K and K′ corresponding to the first (K_1, K'_1) and second (K_2, K'_2) maximum of the Rashba-split valence bands. The calculated fitting values, obtained with higher accuracy in Fig. 7.20**h**, are shown in Tab. 7.2. As presumed, identical peak positions are obtained for K_1/K'_1 and K_2/K'_2.
Overall, the quantitative analysis of the energy offset between bands at high symmetry points unveils that the experimental system is described very well by the DFT hybrid-functional calculation shown in Fig. 4.5**c**. Minor discrepancies are observed for the M point in relation to other high symmetry points, which are probably related to the deficiencies of DFT in predicting accurate band positions [76, 80] and might arise from interactions of the photoelectron with its surroundings [257]. In contrast, excellent agreement is found for the VB splitting induced by the Rashba SOC. The presented ARPES experiments further substantiate that bismuthene has been epitaxially grown on SiC, and is correctly described by the theoretical model presented in Ch. 4.

	$\mathbf{K}_2$	$\mathbf{K}_3$	$\mathbf{K}_4$	$\mathbf{M}_1$	$\mathbf{M}_2$	$\mathbf{\Gamma}_2$	$\mathbf{\Gamma}_3$
$\mathbf{K}_1$	0.45±0.11	2.15±0.24	2.35±0.14	0.94±0.08	1.95±0.04	1.82±0.04	2.06±0.04
$\mathbf{K}_2$		1.70±0.26	1.90±0.17	0.49±0.13	1.50±0.11	1.37±0.11	1.61±0.11
$\mathbf{K}_3$			0.20±0.27	−1.21±0.25	−0.20±0.24	−0.33±0.24	−0.09±0.24
$\mathbf{K}_4$				−1.41±0.15	−0.40±0.13	−0.53±0.13	−0.29±0.13
$\mathbf{M}_1$					1.01±0.07	0.88±0.07	1.12±0.08
$\mathbf{M}_2$						−0.13±0.01	0.11±0.02
$\mathbf{\Gamma}_2$							0.24±0.02

Table 7.1 Energy offset $E(\mathrm{X}_i^{\mathrm{row}}) - E(\mathrm{X}_j^{\mathrm{col}})$ of bands at high symmetry points. The values are obtained by fitting maxima in the line profiles of the second derivative ARPES band map at $h\nu = 80\,\mathrm{eV}$ (Fig. 7.20**b**/**d**). All energies are given in electronvolt.

	$\mathbf{K}_2$	$\mathbf{M}_1$	$\mathbf{K}'_1$	$\mathbf{K}'_2$
$\mathbf{K}_1$	0.443±0.020	0.950±0.018	−0.030±0.091	0.468±0.026
$\mathbf{K}_2$		0.507±0.025	−0.472±0.093	0.025±0.031
$\mathbf{M}_1$			−0.979±0.092	−0.482±0.030
$\mathbf{K}'_1$				0.498±0.094

Table 7.2 Energy offset $E(\mathrm{X}_i^{\mathrm{row}}) - E(\mathrm{X}_j^{\mathrm{col}})$ of bands at high symmetry points. The values are obtained by fitting maxima in the line profiles of the second derivative ARPES band map with reduced dynamic range at $h\nu = 80\,\mathrm{eV}$ (Fig. 7.20**f**/**h**). All energies are given in electronvolt.

	$\mathbf{K}_2$	$\mathbf{K}_3$	$\mathbf{K}_4$	$\mathbf{M}_1$	$\mathbf{M}_2$	$\mathbf{\Gamma}_2$	$\mathbf{\Gamma}_3$
$\mathbf{K}_1$	0.430	2.295	2.469	1.159	2.144	1.925	2.075
$\mathbf{K}_2$		1.866	2.039	0.729	1.714	1.495	1.645
$\mathbf{K}_3$			0.174	-1.137	-0.152	-0.370	-0.221
$\mathbf{K}_4$				-1.130	-0.325	-0.544	-0.394
$\mathbf{M}_1$					0.985	0.766	0.881
$\mathbf{M}_2$						-0.361	-0.069
$\mathbf{\Gamma}_2$							0.150

Table 7.3 Energy offset $E(\mathrm{X}_i^{\mathrm{row}}) - E(\mathrm{X}_j^{\mathrm{col}})$ of bands at high symmetry points according to the DFT HSE band structure calculation (see Fig. 4.5**c**). All energies are given in electronvolt.

In this chapter, the discussion has been limited to properties of the sample excluding edges. Based on the evidence gathered for the formation of bismuthene on SiC, we continue by the analysis of edge states, which are predicted to reside at the boundaries of the bismuthene layer, see Sec. 4.6.

8 1D Edge States of Bismuthene: Topological Protection vs. Correlations

This last chapter deals with the properties of bismuthene edge states. In the first section (Sec. 8.1), different edge state scenarios apparent on the sample surface are discussed, namely edge states residing at the boundary of bismuthene and defective film segments (Sec. 8.1.1) and, more extensively, edge states at the boundary generated by atomic steps in the SiC substrate (Sec. 8.1.2). In Sec. 8.1.3, it is attempted to detect edge states with angle-resolved photoelectron spectroscopy (ARPES) measurements. Lastly, correlation effects in the AC edge states are scrutinized by elaborate and extensive scanning tunneling spectroscopy (STS) measurements in the second part of this chapter (Sec. 8.2).

8.1 Edge States Inspected with STM, STS and ARPES

Honeycomb lattices like bismuthene exhibit two elementary edge terminations, namely zigzag (ZZ) and armchair (AC) edges, which have been introduced in Sec. 4.6. Both can be easily distinguished due to their different lattice periodicity and symmetry[21].
Segments of ordered edges are occasionally found at the interface of bismuthene and large disordered areas where a regular bismuthene lattice did not grow. Furthermore, edges in AC orientation evolve at step edges of the SiC substrate. As will be described, these AC edge states provide an ideal platform to investigate edge state properties with scanning tunneling microscopy (STM) and STS measurements. Moreover, it is tried to map the k space dispersion of these states with ARPES, as their density is easily increased by bismuthene growth on miscut SiC substrates.

8.1.1 Edge States at Extended Defective Areas of the Film

We begin the analysis of edge states by revisiting the defective film regions described in Sec. 7.3.3. Defective means that those areas do not exhibit a regular bismuthene lattice, but lack a periodic structure and are seemingly disordered according to their appearance in STM. In contrast to the disordered areas in Sec. 7.3.3, these areas are larger and not enclosed by a single bismuthene domain, but connect at least two of them.
An exemplary constant-current image (CCI) and corresponding local density of states (LDOS) map shown in Fig. 8.1**a** and **b**, respectively, exhibits several defective areas with smaller and larger extension. In the CCI image (Fig. 8.1**a**) these areas are clearly identifiable as they are separated from the regular, flat bismuthene lattice by a boundary with increased apparent height. The areas themselves exhibit a lower z signal at the given measurement parameters.

[21] This different symmetry has important consequences for the behavior of the edge states in magnetic fields [258].

The LDOS map in Fig. 8.1**b** shows that the LDOS is not periodic as on a regular bismuthene lattice, but inconstant, like within domain boundaries and small antidots. No long range pattern is recognizable[22]. In the following, a specific boundary between bismuthene and a disordered area, marked by the gray square in Figs. 8.1**a**/**b**, is inspected.

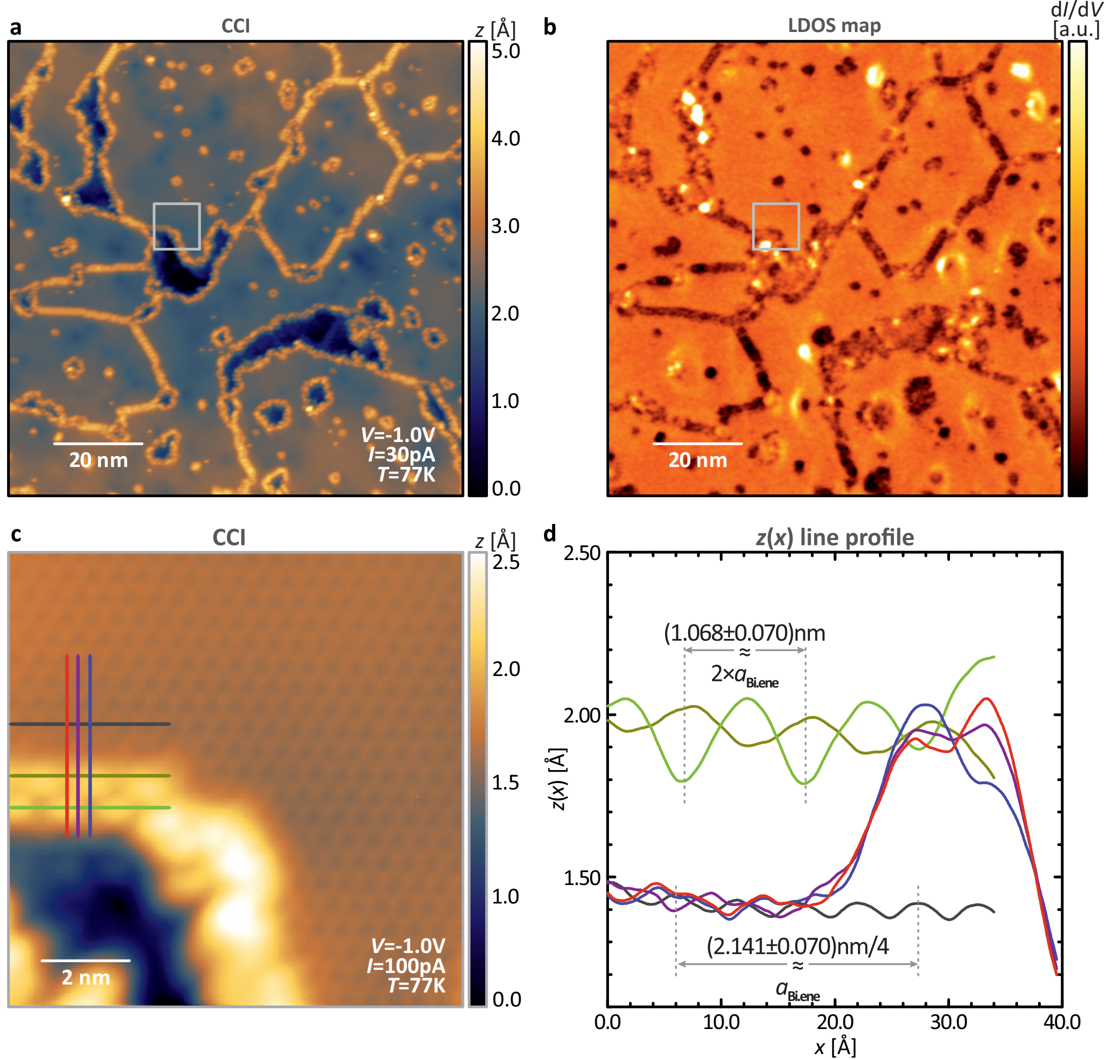

Figure 8.1 **a** STM CCI scan and corresponding **b** LDOS map of a bismuthene film. Apart from smaller, isolated disordered areas surrounded by a single domain also larger defective regions with boundaries to several domains are found. **c** The smaller STM scan (marked by the gray square in **a**/**b**) shows a regular bismuthene lattice and an area with lower z signal. At the interface of both structures, a tube with increased apparent height, which possesses partially ordered sections, is found. **d** The black line profile shows the corrugation of bismuthene with a periodicity of $a_{\mathrm{Bi.ene}} = 5.34\,\text{Å}$. The dark and light green profiles parallel to the black profile demonstrate a doubling of the lattice periodicity at the interface. Line profiles perpendicular to the boundary (red, purple, blue) show that the z signal sharply increases when the interface is approached. Moreover, they reveal that the area with increased apparent height has a width of several nanometers.

Structural properties. Fig. 8.1**c** shows the respective area with higher resolution. The perfectly smooth bismuthene structure (compare to the black line profile in Fig. 8.1**d**) and

[22]The biggest of those areas located in the lower-right quadrant of Fig. 8.1**a**/**b** seems to exhibit a short range periodic structure, which, however, cannot be assigned to a constant spacing by inspection of line profiles. The apparent periodicity and could arise from a weak double tip.

the defective film area are separated by a boundary with increased apparent height and few nanometer width, which evolves in ZZ geometry in this small scan frame[23].
The line profiles perpendicular to the edge (blue, purple and red profile in Fig. 8.1**c**/**d**) reveal a sharp increase of the measured apparent height (≈ 0.5 Å), which has a width of about 2 nm. Line profiles in parallel to the edge (light and dark green curves in Fig. 8.1**c**/**d**) demonstrate that large, circular clouds forming a ZZ pattern come along with a doubling of the lattice constant. Both the increased apparent height and the doubled periodicity might be caused by additional atoms, edge reconstructions, or edge states at the boundary as well as combinations of these effects. STM is not able to disentangle structural and electronic properties. However, with STS, it is possible to check whether additional states are localized at the edge.

Point spectroscopy towards the boundary. Therefore, a grid spectroscopy measurement probing the surface area around the interface has been acquired and is displayed in Fig. 8.2. The very same CCI of Fig. 8.1 is shown in Fig. 8.2**a** with colored markers that indicate the position of the corresponding $\mathrm{d}I/\mathrm{d}V$ curves in Fig. 8.2**b**. The black curve recorded at few nanometer distance from the interface structure shows a zero $\mathrm{d}I/\mathrm{d}V$ signal between the valence and conduction band (VB and CB, respectively), as on bulk bismuthene (see Sec. 7.2.2). The white area between the gray shaded areas in Fig. 8.2**b** indicates the band gap (≈ 800 meV). The situation changes as soon as the ZZ-like edge is approached. Step by step, the magnitude of the energy gap is reduced and eventually filled with a non-zero signal connecting the VB and CB. The signal is fairly smooth and, within the gap, rather constant. Thereby, it is fundamentally different to the peaky signal that has been described in case of the point defects and disordered areas in Secs. 7.3.2 and 7.3.3, respectively. Remarkably, the signal sharply increases when the ZZ-like edge is approached from the side of the bismuthene lattice but does not seem to drop as fast towards the other, disordered side. In comparison to typical bulk $\mathrm{d}I/\mathrm{d}V$ curves (black curve) we note a reduced conductivity in the valence band, and more distinctly, a peak that gradually evolves at $E \approx 0.6$ eV, which reminds of a van Hove singularity [259]. Additionally, a dip at zero bias is seen throughout all spectra with enhanced conductivity.
The average conductivity in the band gap is estimated by fitting a linear function in the energy range of $E = +0.1...+0.5$ eV to the measured $I(V)$ curves. The calculated $I(V)$ slope is roughly representative of the average conductivity in the band gap, as the fitted energy range excludes the influence of the zero-bias dip and the peak in the CB, but does not account for the finite curvature observed in some spectra.
The resulting average $\mathrm{d}I/\mathrm{d}V$ value is shown in Fig. 8.2**c** next to the z line profile. The red dot-line and black curve in Fig. 8.2**c** reveal that the increase of the $\mathrm{d}I/\mathrm{d}V$ and z signal go hand in hand on the side where the regular bismuthene lattice is found. Both quantities reach their maximum roughly at the position of the bright, circular feature in the CCI (marked by the gray shaded area in Fig. 8.2**c**). Towards the other side of the edge, the $\mathrm{d}I/\mathrm{d}V$ signal remains rather constant and is in any case not dropping

[23] Note that locally, also edges in AC geometry are found at the boundary of these defective areas but their discussion is omitted as the AC edges at SiC substrate steps (see Sec. 8.1.2) provide a better alternative.

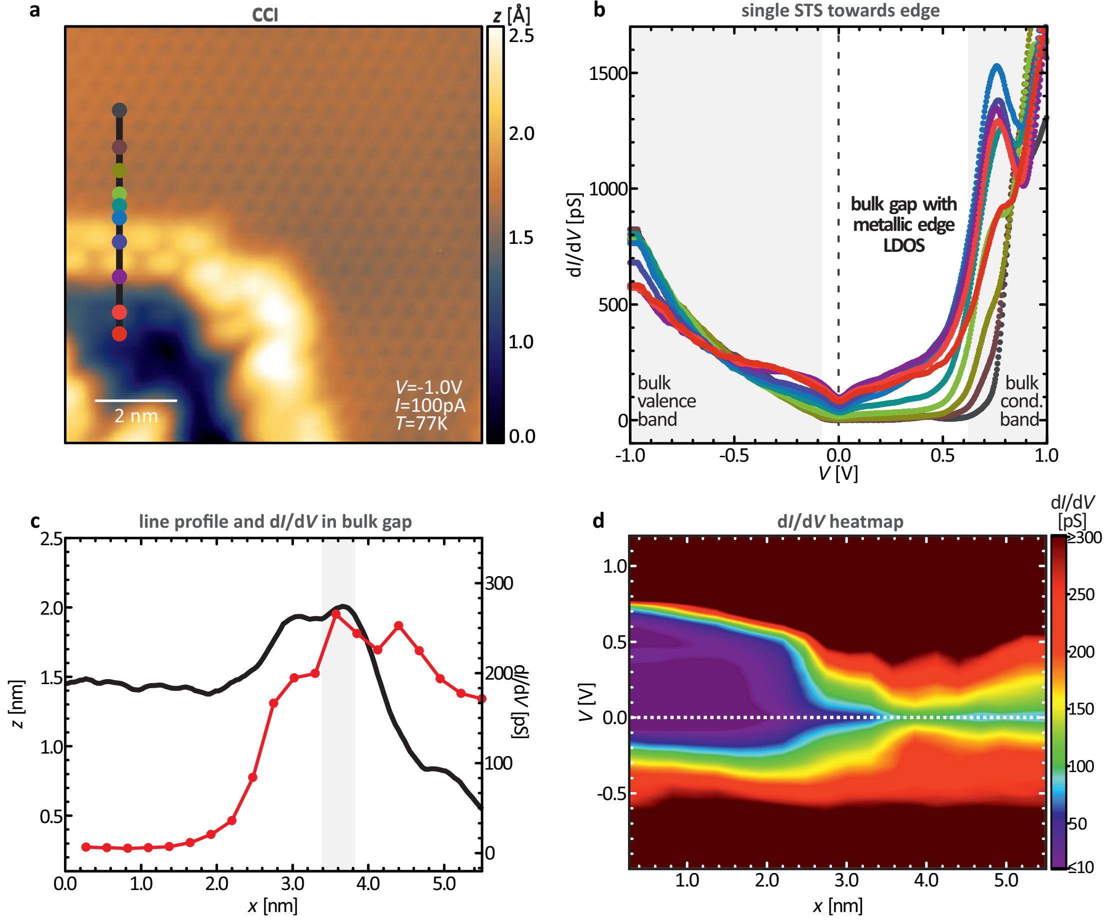

Figure 8.2 Electronic properties at a ZZ-like interface of bismuthene and a defective film segment. **a** Atomic resolution CCI with colored dots that mark the position of single STS curves extracted from a grid spectroscopy measurement. **b** Differential conductivity in vicinity of the boundary. Far away from the edge the bismuthene bulk band gap ($\approx 0.8\,\text{eV}$) is retrieved. When approaching the boundary by following the colored dots in **a**, the band gap magnitude shrinks and eventually, a non-zero conductance throughout the gap is observed. The measured $\mathrm{d}I/\mathrm{d}V$ signal reaches its maximum value at the ZZ clouds (gray dashed line in **c**) and does not drop as fast as expected towards the defective area. **c** Line profile (black line underneath the colored dots in **a**) and average $\mathrm{d}I/\mathrm{d}V$ signal in the bulk band gap (red dot-and-line curve) generated by a linear fit to the $I(V)$ curves in the range of $E = 0.1\text{–}0.5\,\text{eV}$. **d** The heatmap visualizes the presence of a gap on the side of bismuthene. However, it is not or much slower retrieved towards the defective area (same x axis as in **c**). Measurement parameters: $V_{\text{st}} = -1.0\,\text{V}$, $I_{\text{st}} = 300\,\text{pA}$, $V_{\text{mod}} = 10\,\text{mV}$, $\Delta x = \Delta y = 2.5\,\text{Å}$, $x_{\text{range}} = 8\,\text{nm}$, $y_{\text{range}} = 6\,\text{nm}$, $V_{\text{ini}} = -1.0\,\text{V}$, $V_{\text{end}} = 1.2\,\text{V}$, 601 points per curve.

as fast as expected regarding the probed z profile. The heatmap in Fig. 8.2**d** basically confirms this trend. Whereas it evidences the large bulk gap on the side of bismuthene, it shows a finite conductivity in the band gap if the spectra are recorded on the side of the defective/unstructured area.

The observation that the vastly different spectral signature of defective areas with larger and smaller extension, which described here and in Sec. 7.3.3, respectively, is puzzling. While the former exhibit a smooth $\mathrm{d}I/\mathrm{d}V$ signal in the band gap, the latter has been characterized by pronounced peaks. This difference might be related to, e.g., the covered surface area, which is significantly larger in case of the measurement shown in Fig. 8.2 than in Fig. 7.14, or to the number of adjacent, inequivalent domains (which is four and one in case of Figs. 8.2 and 7.14, respectively). Further studies with STS are required to

resolve and better understand the physical mechanisms that give rise to a metallic signal and peaks in those disordered regions of the lattice.

Comparison to the density-functional theory (DFT) modeling of a ZZ edge. The observation of a metallic LDOS at a ZZ termination of a bismuthene film is expected according to the nanoribbon calculations presented in Fig. 4.10**c**/**d**. The steep increase towards the apparent boundary with a fitted exponential growth constant of $\xi = (3.6 \pm 0.1)\,\text{Å}$, i.e., less than a bismuthene lattice constant, is the result of the large band gap of bismuthene and reflects a strong localization at the edge. The decay constant can be estimated by $\xi_{\text{theo}} = \hbar v_{\text{F}}/\Delta$ [260]. Here, $\hbar$ is the reduced Planck constant, $\Delta = 830\,\text{meV}$ the magnitude of the energy gap in our experiments, and $v_{\text{F}}^{\text{zz}} = 3.1 \times 10^5\,\text{m}\,\text{s}^{-1}$ denotes the Fermi velocity of ZZ edge states predicted by DFT [168]. Thereby, the decay constant is calculated to $\xi_{\text{theo}}^{\text{zz}} = 2.4\,\text{Å}$, which is reasonably close to the experimentally determined value.

The observed smooth LDOS signal is in accord with the edge state picture, as they connect the VB and CB with an almost constant band slope in the energy range of the band gap. According to the DFT model (see Fig. 4.10**c**), a strong deviation from a linear band slope is expected only when the edge states merge into and ultimately coexist with bulk states. The peak observed at $E \approx 0.6\,\text{eV}$ could be indicative of the CB minimum (CBM) at Γ in the one-dimensional (1D) ZZ projection of the bismuthene band structure (compare to Fig. 4.10**c**). In particular, it is expected that the peak associated with the CBM at Γ is more pronounced than its counterpart of the VB maximum (VBM) at K, as $k_{||} \neq 0$ reduces the tunneling matrix element [244].

Albeit those findings seem to match to the interpretation in terms of a 1D ZZ edge state, the spectra observed at the interface of bismuthene with a disordered region provoke questions. Firstly, the inspected edge section with an apparent ZZ structure is only a few nanometer long, while afterwards, the boundary follows a contour that mixes ZZ and AC segments. Hence, it is not clear why the LDOS should coincide with the DFT-computed DOS for a nanoribbon with ZZ boundary. In addition, the edge structure features a lattice constant doubling due to structural reconstructions or a rearrangement of the orbitals at the edge, which is not comprised in DFT, as well. Lastly, the finding that the metallic $\text{d}I/\text{d}V$ signal is hardly reduced when measuring on the disordered area raises doubts whether the observed metallicity might arise (at least partially) from the material in these regions.

Hence, studies that inspect and resolve the structure within the defective areas (e.g., with AFM at atomic resolution) are a first step towards the clarification whether the observed metallic LDOS is derived from topological edge states or from trivial states.

8.1.2 Armchair Edge States at SiC Substrate Steps

Bismuthene samples naturally host a second type of edge states that provide a more clear and reproducible experimental scenario than the edge states appearing randomly at the interface with extended defective surface areas. In particular, the appearance of these states does not rely on deficiencies in the film growth but is bound to surface steps in the SiC substrate, which terminate bismuthene films and thereby generate edges in AC

geometry. Hence, this type of edge state can be fabricated in a controlled way and high number by the use of suitable miscut SiC substrates (see Sec. C.1), which makes those edge states extraordinarily interesting. Fig. 8.3 illustrates this experimental scenario that will be extensively discussed in the leftover of this thesis.

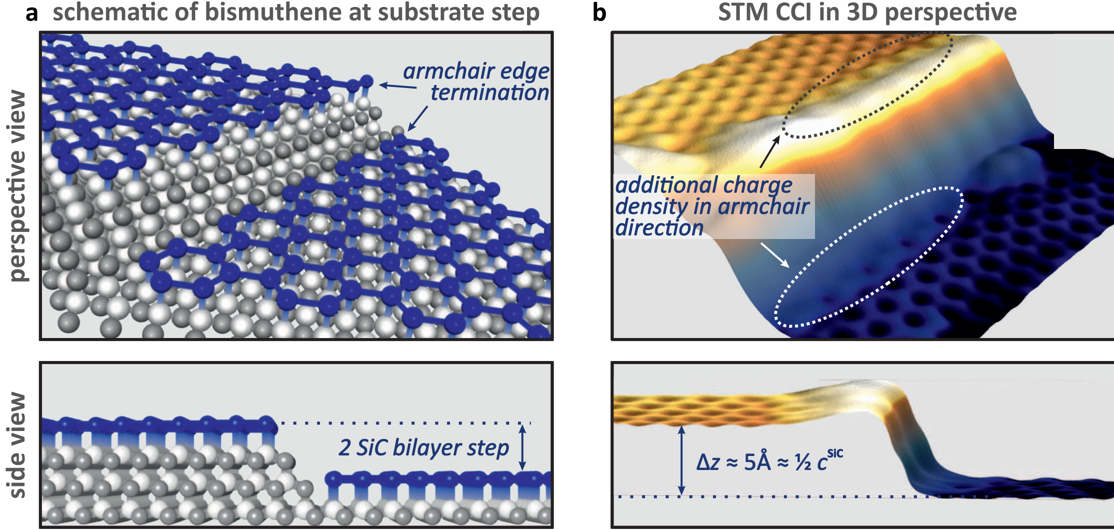

Figure 8.3 Bismuthene AC edges at a SiC substrate steps. **a** The ball-and-stick lattice model shows two bismuthene terraces and the underlying SiC substrate in perspective and side view. ZZ edges at steps of the SiC substrate lead to AC edges of the bismuthene film as a result of the $(\sqrt{3} \times \sqrt{3})R30°$ reconstruction. **b** 3D view of a CCI of two bismuthene terraces separated by $\Delta z \approx 5\,\text{Å} \approx \frac{1}{2}c^{\text{SiC}}$, i.e., half a lattice constant in $\langle 0001 \rangle$ direction. The regular bismuthene lattice is seen on the two terrace planes while directly at the edge, an increased apparent height, which partially follows an AC contour, is probed.

The left panel of Fig. 8.3 shows a ball-and-stick model of bismuthene at a SiC substrate step. Two bismuthene planes are located on the upper and lower terrace, and are separated by a step corresponding to two SiC bilayers (see side view of Fig. 8.3**a**), i.e., the type of step most frequently observed on SiC substrates (and bismuthene samples). The step gives rise to an edge in AC geometry. This is a consequence of the ZZ termination of SiC step edges, see Sec. 5.1, which transform into edges with AC symmetry due to the 30° rotation of the $(\sqrt{3} \times \sqrt{3})R30°$-Bi lattice with respect to the (1×1) SiC lattice.

A CCI in three-dimensional (3D) representation (Fig. 8.3**b**) displays the experimental realization of this setting in STM. The corrugation of the honeycomb lattice is clearly visible on both terrace planes, which are separated by $\Delta z \approx 5\,\text{Å} \approx 1/2 \cdot c^{\text{SiC}}$, as sketched in the side view of Fig. 8.3**b**. Intriguingly, directly at the upper and lower edge of the step, an additional, slightly elevated structure following an AC pattern is present, which is more easily seen at the upper terrace plane, where the Bi film faces vacuum.

Point spectroscopy towards a step edge. STS is used to inspect the electronic properties of the edge in detail. As Fig. 8.3**b**, Fig. 8.4**a** shows a CCI that captures two bismuthene planes, which are separated by an atomic step corresponding to two SiC bilayers. Again, an increased apparent height is localized at the film boundaries, which, however, seems disordered, especially at the upper edge.

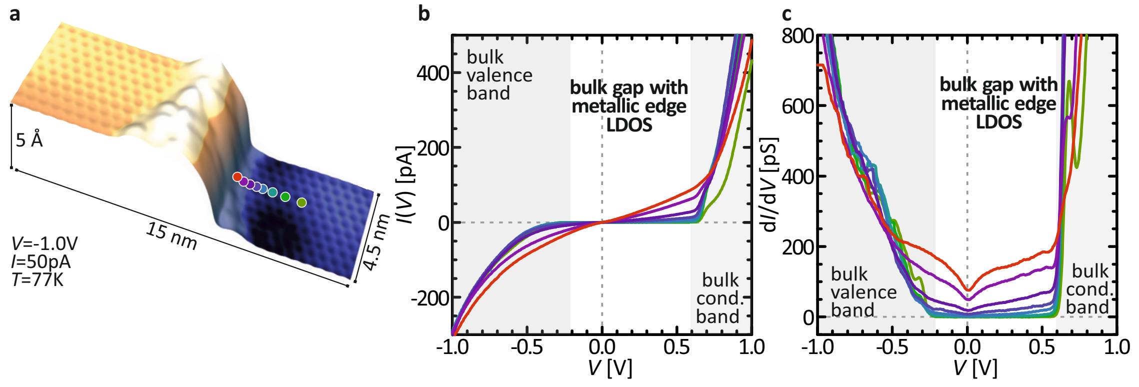

Figure 8.4 STS measurements in vicinity of a SiC step. **a** Visualization of the measurement geometry. Colored dots indicate where **b** $I(V)$ and **c** $\mathrm{d}I/\mathrm{d}V$ curves are acquired. **b** At few nanometer lateral distance from the edge a fully gapped band structure in the range of $E \approx -0.2\,\mathrm{eV}$ to $E = +0.6\,\mathrm{eV}$ is visible and marked by gray shaded areas. When the step edge is approached, a finite, non-zero and roughly constant slope of the $I(V)$ curve is detected. **c** Correspondingly, the $\mathrm{d}I/\mathrm{d}V$ signal is smooth and relatively constant apart from a pronounced dip at zero-bias, which will be discussed in Sec. 8.2. Tunneling parameters of the grid spectroscopy in **b**/**c**: $V_{\mathrm{st}} = -1.0\,\mathrm{V}$, $I_{\mathrm{st}} = 300\,\mathrm{pA}$, $V_{\mathrm{mod}} = 10\,\mathrm{mV}$, $\Delta x = 1.5\,\text{Å}$, $\Delta y = 1.3\,\text{Å}$, $x_{\mathrm{range}} = 11.9\,\mathrm{nm}$, $y_{\mathrm{range}} = 0.9\,\mathrm{nm}$, $V_{\mathrm{ini}} = -1.0\,\mathrm{V}$, $V_{\mathrm{end}} = 1.2\,\mathrm{V}$, 601 points per curve.

$I(V)$ and $\mathrm{d}I/\mathrm{d}V$ curves measured at the positions indicated by the colored dots in Fig. 8.4**a** are shown in Fig. 8.4**b** and **c**, respectively. The first measurement point (dark green dot/curve) is located at about five lattice constants distance from the step wall and the corresponding $\mathrm{d}I/\mathrm{d}V$ signal evidences the fully developed bismuthene band gap. This changes when the step edge is gradually approached. An almost constant slope in the $I(V)$ curves shown in Fig. 8.4**b** is evolving in the energy gap. Accordingly, the corresponding $\mathrm{d}I/\mathrm{d}V$ curves (Fig. 8.4**c**) feature a finite, metallic LDOS localized at the step edge, which is smoothly derived from the bulk states.

As the symmetry relations of bismuthene and the SiC lattice imply the predominance of AC edges at atomic steps, we may compare the detected $\mathrm{d}I/\mathrm{d}V$ signal to the AC nanoribbon calculations in Fig. 4.10**a**. Intriguingly, the measured signal compares very well to the DFT-computed AC edge dispersion. The quasi-linear energy dispersion within, but also beyond the bulk band gap in theory (Fig. 4.10**a**) should give rise to an almost constant LDOS signal. Moreover, it is expected that the edge state DOS adopts smoothly to the bulk DOS, as the calculated edge band structure does not feature minima or maxima in the probed energy range. Both these theory-derived signatures are evident in the probed $\mathrm{d}I/\mathrm{d}V$ signal.

In contrast, an obvious difference between experiment and theory is apparent around the Fermi level, where the differential conductivity is pronouncedly reduced in STS. This feature will be elaborated later in Sec. 8.2.

We estimate the $\mathrm{d}I/\mathrm{d}V$ signal in the band gap by fitting a linear function to the recorded $I(V)$ data. The calculated average $\mathrm{d}I/\mathrm{d}V$ signal, which is shown in Fig. 8.5**a**, reveals the steep increase of the conductivity on the upper and lower bismuthene lattice when the step edge is approached. Importantly, two well-distinguishable, sharp $\mathrm{d}I/\mathrm{d}V$ maxima, which are located at the edge of the upper and lower Bi film, are observable, whereas the average differential conductivity is clearly dropping in between, i.e., across the SiC step

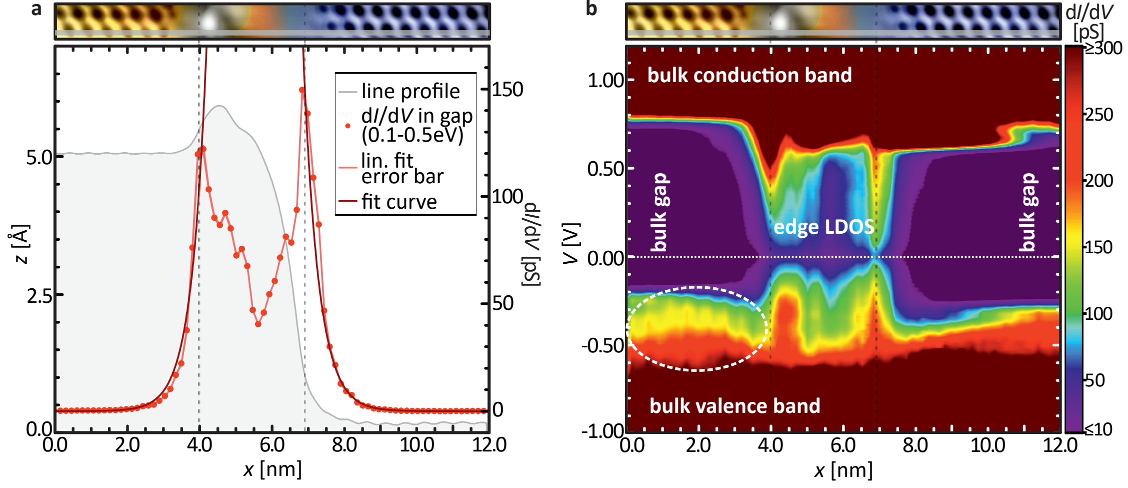

Figure 8.5 **a** Differential conductivity in the bulk band gap and **b** heatmap as function of the lateral position across the step. **a** The average $\mathrm{d}I/\mathrm{d}V$ signal in the band gap (red dot-line curve) is estimated with a linear function, which is fitted to the $I(V)$ curve in the energy range of $E = +0.1...+0.5\,\mathrm{eV}$. The gray line and shaded area show the CCI z signal along the corresponding line. At both sides of the step edge a sharp maximum differential conductivity (marked by the gray dashed lines) is calculated. The dark red lines show exponential fit curves. **b** The heatmap reveals that the edge state signal clearly drops in the area between both bismuthene terraces. The gray line in the CCI on top of both panels indicates the position at which the spectra and line profile have been measured. The measurement and tunneling parameters are the same as in Fig. 8.4.

edge atoms. The calculated points are fitted with an exponential function to estimate the decay length ξ, which yields $\xi_{\mathrm{up}} = 4.1 \pm 0.3\,\text{Å}$ and $\xi_{\mathrm{lo}} = 4.2 \pm 0.1\,\text{Å}$ for the upper and lower step edge, respectively. As discussed for the states residing at the boundary with defective film areas, the finding of such a fast decay towards the bulk is expected [260]. With the Fermi velocity apparent in DFT calculations of the AC edge ribbon ($v_{\mathrm{F}}^{\mathrm{ac}} = 4.9 \times 10^5\,\mathrm{m\,s^{-1}}$ [168]), and the measured band gap of $\Delta = 830\,\mathrm{meV}$ we estimate the decay constant to $\xi_{\mathrm{theo}}^{\mathrm{ac}} = 3.9\,\text{Å}$, which is very close to the value evidenced in STM/STS.

The heatmap shown in Fig. 8.5**b** visualizes that the non-zero edge state signal is laterally strongly confined and surrounded by a gapped LDOS on both bismuthene terraces and across the SiC step. The STS signals probed on the upper and lower plane exhibit minor differences but overall seem very similar. The modulations of the signal strength in the occupied states and on the upper terrace, which follow the periodicity of the bismuthene lattice and are marked by the white dashed ellipse in Fig. 8.5**b**, result from the varying intensity of the VB edge signal on bismuthene bonds and the site of SiC that is not covered by Bi, see Fig. 7.6**e**/**f**.

Furthermore, the heatmap directly visualizes that the VB and CB edges of upper and lower bismuthene plane are shifted by $\approx 100\,\mathrm{meV}$. Importantly, the Fermi level is offset from the VB edge by at least $150\,\mathrm{meV}$. At the same time, the rigid shift of the band edges indicates that the zero-bias dip is not inherent part of the band structure but pinned to the Fermi level.

This is further elucidated in a side-by-side comparison of single spectra measured on upper and lower bismuthene terrace. Fig. 8.6**a** and **b** display the $\mathrm{d}I/\mathrm{d}V$ signal with equidistant spacing from the respective edge as indicated by the colored dots in the CCI on top of

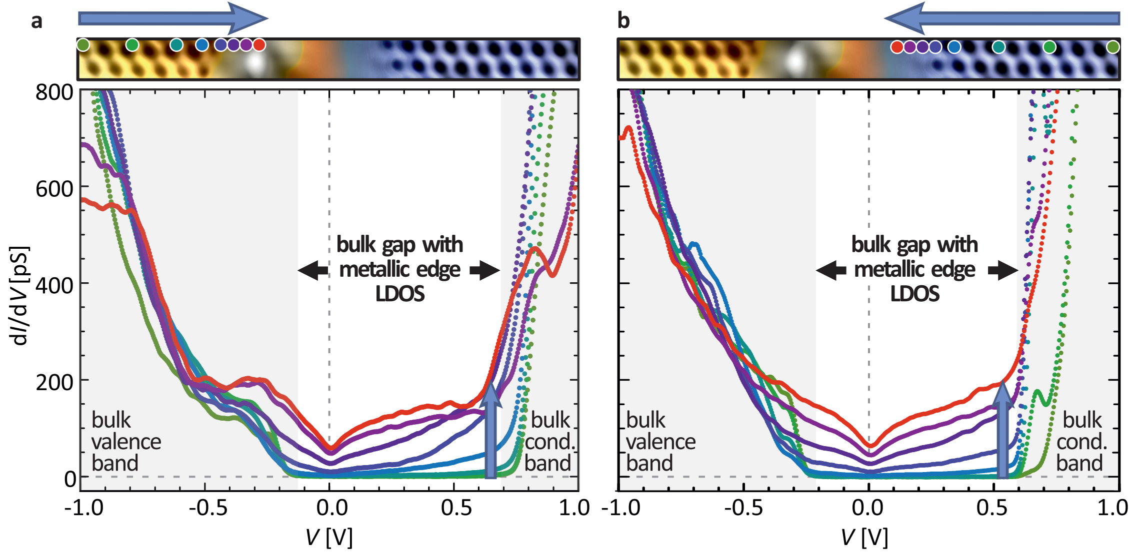

Figure 8.6 Single $\mathrm{d}I/\mathrm{d}V$ spectra as function of the distance from the step on the **a** upper and **b** lower bismuthene terrace. Colored dots in the CCI on top of the diagrams indicate the measurement positions. The spectra acquired at both film edges share many key properties. In particular, the entire band gap is filled with a smooth, non-zero differential conductivity signal and a dip is present in both measurements. Minor differences are found regarding their relative LDOS, especially close to the VBM and the Fermi level position. Measurement parameters as in Fig. 8.4.

both diagrams. The detected LDOS of upper and lower terrace shares many key features, in particular, the rather constant and smooth LDOS apart from the dip at zero bias. Yet, the $\mathrm{d}I/\mathrm{d}V$ curves on the upper plane directly at the edge (pink and purple curve in Fig. 8.6) differ from the signal on the lower terrace and from the spectra on the upper plane recorded at larger distance from the edge, as well (especially at $E - E_\mathrm{F} = \pm 1\,\mathrm{eV}$). The white structural disorder at the upper step edge might be the source of this behavior and causes an edge termination that mixes AC and ZZ sections. Note that the question whether the edge states persists against disorder is explicitly investigated in Fig. 8.8.

High-resolution grid spectroscopy. To scrutinize the edge state properties further, experimental LDOS maps are compared to DFT-computed edge state simulations. A very high resolution grid spectroscopy measurement has been recorded and is shown next to the AC edge modeling in Fig. 8.7 for this purpose. The dashed lines in Fig. 8.7**a**/**b** serve as a guide to the eye and are aligned to Bi atoms of the last and third to last row from the edge in the DFT simulations[24] (Fig. 8.7**c** and **d**). The theoretical simulations themselves in Fig. 8.7**c**/**d** are aligned with respect to the CCI (Fig. 8.7**a**) and LDOS maps (Fig. 8.7**b**). Fig. 8.7**a** shows the CCI acquired during the grid. It exhibits an AC edge located at the upper terrace of a SiC step edge and represents a reproducible experimental case. The honeycomb pattern of the bulk lattice merges into a periodic AC edge with increased apparent height and LDOS. The LDOS probed on bulk honeycombs is retrieved in the grid LDOS map with lowest energy ($E = -1.0\,\mathrm{eV}$), while the $\mathrm{d}I/\mathrm{d}V$ signal strength at the edge is very low.

[24]Note that the DFT constant height simulations do not account for tunneling effects like the finite tip resolution or varying tunneling matrix elements. Hence, a one-to-one comparison to experimental CCI/LDOS maps is not appropriate.

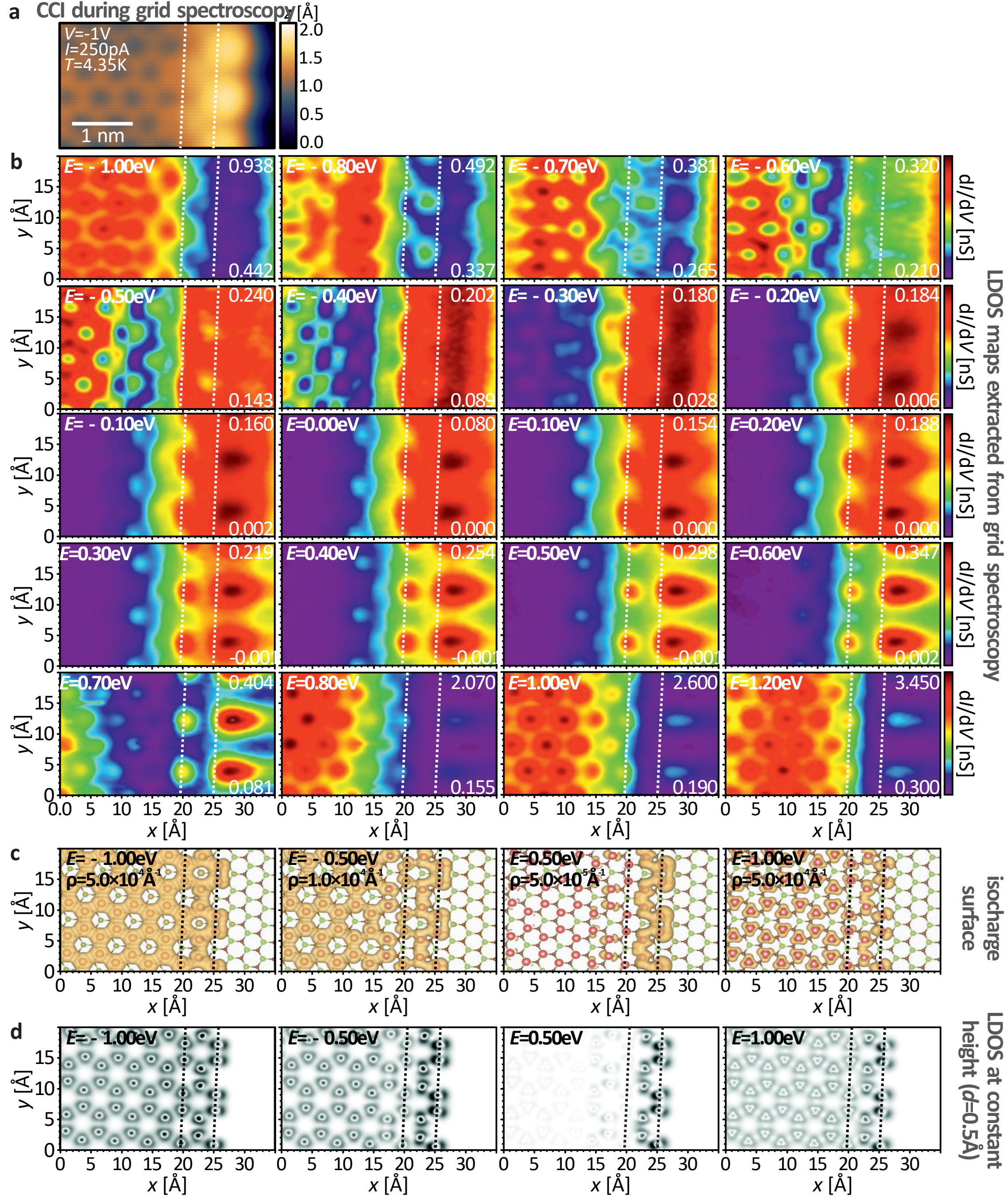

Figure 8.7 High-resolution grid spectroscopy of the AC edge state. **a** CCI recorded during the grid spectroscopy. Its quality is comparable to a normal CCI and indicates that piezo drift is absent. **b** Grid LDOS maps at varying energy. The white numbers to the right of each slice denote the lower and upper limit of the differential conductivity. Dashed lines and white AC pattern serve as guide to the eye to facilitate the comparison to **c**, **d**. Both the honeycomb pattern in the bulk as well as the AC pattern at the edge are perceivable. Within the bulk gap, a non-zero $\mathrm{d}I/\mathrm{d}V$ signal is found only at the edge. **c** Isocharge surface and **d** constant height STM simulation for an AC edge nanoribbon. The displayed cutout is adopted to the grid spectroscopy frame. At $E = +0.5\,\mathrm{eV}$ the bulk LDOS vanishes and a finite LDOS is apparent only at the edge. The dashed lines are positioned at the third to last and last row of Bi atoms. Tunneling parameters of the grid spectroscopy: $V_{\mathrm{st}} = -1.0\,\mathrm{V}$, $I_{\mathrm{st}} = 250\,\mathrm{pA}$, $V_{\mathrm{mod}} = 30\,\mathrm{mV}$, $\Delta x = \Delta y = 0.5\,\text{Å}$, $x_{\mathrm{range}} = 3.5\,\mathrm{nm}$, $y_{\mathrm{range}} = 2.0\,\mathrm{nm}$, $V_{\mathrm{ini}} = -1.0\,\mathrm{V}$, $V_{\mathrm{end}} = 1.2\,\mathrm{V}$, 601 points per curve. *Simulations in Fig.* **c**, **d** *calculated and provided by courtesy of Gang Li [168].*

This changes when the probing energy is increased. Step by step, more structure becomes visible in the surface area where the edge state is presumably located according to the CCI

(Fig. 8.7**a**) and DFT images (Fig. 8.7**c**/**d**). Gradually, AC patterns become more intense in the second to last and last row of Bi atoms ($E \geq -0.7\,\text{eV}$). Around $E = -0.5\,\text{eV}$, the edge and bulk dI/dV signals are equally strong. As soon as the probing energy enters the band gap, i.e., from $E = -0.2\,\text{eV}$, only the edge state signal is seen until the honeycomb lattice is recovered at slices corresponding to energies in the CB (i.e., at $E > +0.6\,\text{eV}$).

A discrepancy of theory and experiment seems present regarding the position of highest dI/dV signal in the gap along the AC contour. In contrast to the theoretical model (Figs. 8.7**c**/**d**), the maximum LDOS in the experiment (Fig. 8.7**b**) is probed precisely in between pairs of nearest neighbor (NN) Bi atoms at the edge, i.e., at the site of the underlying SiC surface that is not covered by a Bi atom. Several reasons could explain this finding. Of course it is possible that the alignment of experimental scans and DFT simulations is done falsely. This scenario cannot be fully excluded, however all other alignments generated larger inconsistencies between the probed LDOS maps and the DOS expected by DFT. Moreover, tunneling effects (variations of the matrix elements, finite resolution) are entirely disregarded in the simulations, which might result in deviating observations in STM/STS. Lastly, the observed LDOS might arise from the presence of additional states in real bismuthene samples, which are coexisting with the AC edge states and localized at the edge. As the periodicity of the AC edge is retained in all slices, it does not seem likely that an edge reconstruction takes place. However, it is possible that the Si dangling bond (DB), which is leftover after the Bi atoms cover two out of three Si sites, might give rise to an additional LDOS signal in the constant energy slices within the band gap.

Yet, it must be emphasized that the presented LDOS maps exhibit periodic structures that can be fully traced back to the AC edge geometry.

LDOS mapping. Topological states feature the extraordinary property of suppressed single-particle backscattering, which persists even in the presence of weak interactions and disorder [122, 261–263]. In a material with conventional metallic states, abrupt changes of the local potential due to defects in the lattice , like step edges or impurities, cause scattering of metallic states and may lead to quasi-particle interference, as has been demonstrated, e.g., on the surface of noble metal crystals [62]. In contrast, the absence of single-particle backscattering in topological materials has been claimed on two-dimensional (2D) as well as 3D TIs (see, e.g., Refs. [122, 261, 264]).

A special section of a step edge, see Fig. 8.8**a**, has been probed to investigate this key characteristic on bismuthene. It shows an extended, about 12 nm long and seemingly defect-free AC edge, which comprises two kinks. The edge state has been probed by CCI and LDOS maps at tunneling voltages corresponding to VB and CB states as well as to the bulk band gap. A selection of recorded topographic and LDOS maps is shown in Fig. 8.8**a** and **b**, respectively. The full set of measurements is present in Fig. F.1. The scan frame width is shrinked to a narrow range around the edge in the bulk gap to avoid tip crashes.

The AC edge pattern is manifest in all measurements in Fig. 8.8**a** and the periodicity of bismuthene is visible in the bulk lattice. The corrugation is strongly developed in the occupied states as well as bulk energy gap and is much lower in the unoccupied states, especially for the LDOS maps at large positive bias voltage. As in case of the grid LDOS maps in Fig. 8.7, the dI/dV signal (Fig. 8.8**b**) at the edge is low in comparison to the

strength arising from bulk states but gains relative weight as soon as the bulk band edges are approached. This affects the CCI scans, as well, as the AC contour spreads further out into the bulk lattice at energies close to the VB and CB edges.

Line profiles positioned on top of the edge charge density in the CCI and LDOS maps are plotted in Fig. 8.8**c** and **d**, respectively, to conduct a more detailed analysis. At first glance, peaks and valleys are piled up regularly at the very same locations of the AC edge. The periodicity of minima/maxima in Fig. 8.8**c** yields the AC edge periodicity of $a_{\mathrm{ac}} \approx 9$ Å. No additional periodic structure is present in the profiles, even though the amplitude of the LDOS in Fig. 8.8**d** is modulated at energies $E > 1.1$ eV. This, however, occurs at energies corresponding to bulk states, while no modifications are seen within the band gap.

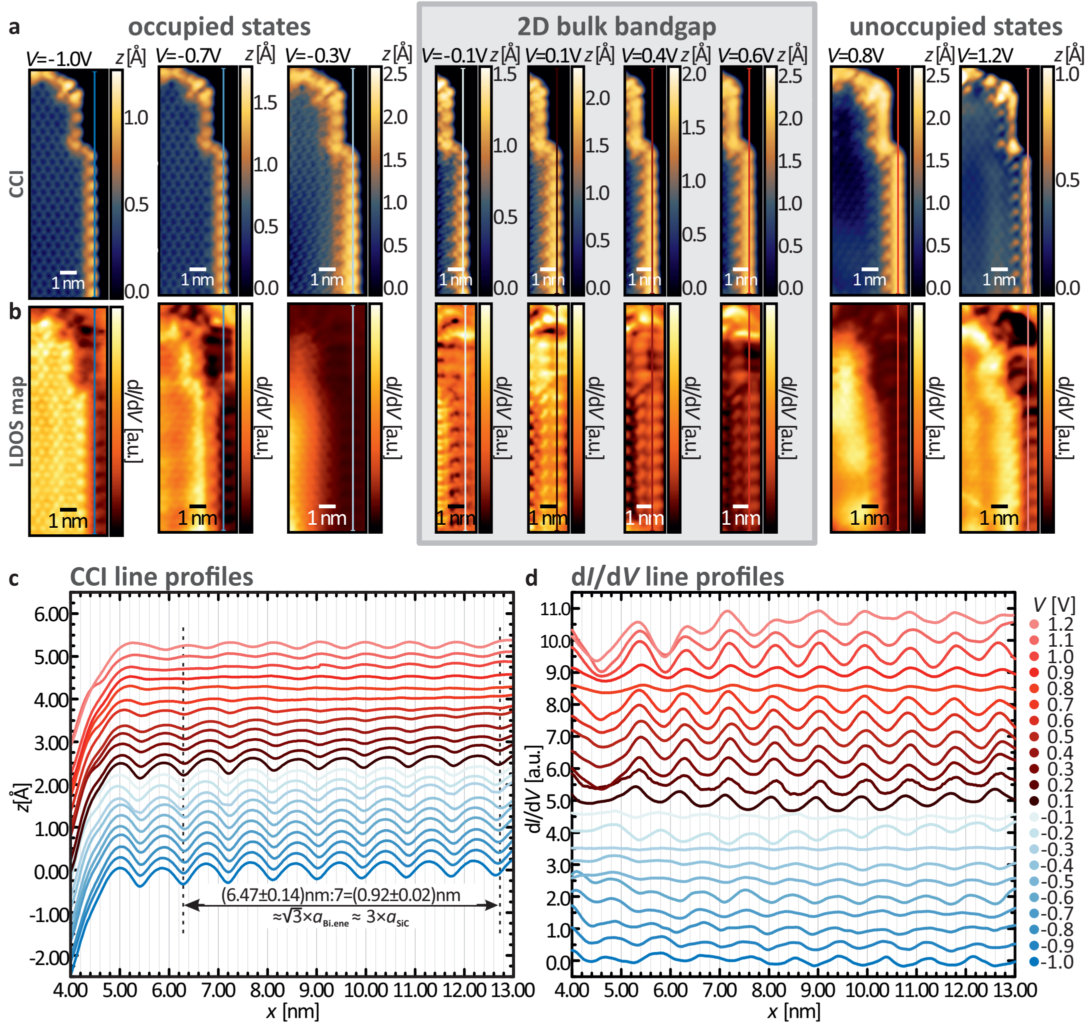

Figure 8.8 **a** CCI and **b** LDOS maps at an AC edge with perfect ordering (additional energies are shown in Fig. F.1). Despite the pronounced kinks, only the periodicity of an AC edge is seen throughout all measurements, whereas additional structures are absent. Note that the scan frame width is partially confined to a narrow channel around the edge to avoid tip crashing in the bulk band gap. **c** and **d** Line profiles generated at the edge in the CCI and LDOS maps, respectively (marked by colored lines). The curves are aligned with help of an additional line profile in the bulk lattice. Only the periodicity of an AC edge is present, both in the CCI and LDOS profiles. The line profiles are offset by 0.2 Å (CCI) and 0.5 (LDOS). All measurements recorded at $T = 4.35$ K and with $I = 100$ pA. $V_{\mathrm{mod}}(V = \pm 0.1\,\mathrm{V}) = 10$ mV, $V_{\mathrm{mod}}(V = \pm 0.2\,\mathrm{V}) = 20$ mV and $V_{\mathrm{mod}} = 30$ mV in all other scans. The scans have been background-corrected with a polynomial plane of order 3.

Absence of backscattering signatures. Neither around the kinks nor at other positions along the edge any sign of backscattering processes are evident, which further substantiates that the metallic states discussed in this section may be regarded as the realization of the topologically protected AC edge states predicted by DFT.

It is interesting to note distinct differences between the grid LDOS maps shown in Fig. 8.7 and the LDOS maps simultaneously recorded to the CCI maps at a kinky edge segment shown in Fig. 8.8. The wave lines in Fig. 8.8**d** are phase shifted by 180° as soon as the unoccupied bulk states are probed, whereas the switch occurs earlier (already approximately when the bulk gap is entered) in the grid measurement (Fig. 8.7). The alignment of the profiles in the different CCI/LDOS maps in Fig. 8.8 might be erroneous but has been carried out with high diligence using a second line profile in the bulk lattice as a reference, such that a possible misalignment may be excluded with high confidence. In contrast, as always, it cannot be excluded that the tip condition is different in the two measurements, which might lead to different tunneling matrix elements and cause the observed deviations. Yet, also the different measurement methodology of both experiments might give rise to the apparent differences. In a grid spectroscopy measurement, the entire LDOS is probed at fixed distance, which depends on the stabilization current/voltage ($V_{\mathrm{st}} = -1.0\,\mathrm{V}$, $I_{\mathrm{st}} = 250\,\mathrm{pA}$ in Fig. 8.7). Of course, this distance may vary as function of the lattice site and the allocated orbitals, but is thereafter kept constant. In contrast, in LDOS mapping, the situation is more complicated. The tip-to-sample distance is continuously adapted to maintain a constant current at the applied voltage, which changes in every scan and thereby the integrated LDOS in the range of E_{F} to eV_{T} available for tunneling electrons according to Eq. 2.10. Consequently, a complex interplay of parameters influences the probed $\mathrm{d}I/\mathrm{d}V$ signal strength in LDOS mapping, such that the grid measurement in Fig. 8.7 seems more reliable concerning the imaging of the LDOS intensities at the AC edge.

Yet, here we want to stress that the LDOS maps in Fig. 8.8 cover a large spatial range and are used to confirm the absence of modulations caused by single-particle backscattering processes, for which they are perfectly appropriate.

8.1.3 Search for the Edge States in ARPES

The discovery of metallic states bound to SiC step edges motivated the preparation of bismuthene on miscut SiC samples, which are presented in Sec. C.1. By epitaxial growth of bismuthene on these substrates we may (i) drastically enhance the edge state density on a sample and (ii) fix their orientation, which is defined via the miscut direction, rendering a controlled investigation with ARPES feasible. Hence, we attempted to visualize the 1D edge states of bismuthene with ARPES measurements on such bismuthene samples, a goal that has been prohibited by the structure of the QSHI materials (quantum wells, exfoliated flakes) realized to date.

Fig. 8.9 shows ARPES measurements conducted on a high-quality bismuthene sample grown on a substrate with 4° miscut in the $\langle 1\bar{1}00 \rangle$ direction (4°-Miscut SiC). The 1D Brillouin zone (BZ) in AC direction is sketched in Fig. 8.9**a**. As the crystal momentum perpendicular to the edge is lost in case of 1D states, the 1D BZ features only two high

symmetry points, i.e., $\bar{\Gamma}$ in the center and $\bar{X}$ at the boundary. Additionally, the relation between the 1D and 2D BZ of bismuthene is visualized in Fig. 8.9. The high-resolution ARPES bandmap in Fig. 8.9**b** shows a close-up scan of the Rashba-split VB[25] By comparison with the nanoribbon calculations in Fig. 4.10 it becomes clear that the edge states are derived from the VB. However, at first glance no bands with the linear energy dispersion of the edge state are visible.

One may doubt whether the edge state signal in comparison to the total signal is large enough to allow its perception. This can be roughly estimated by a back-of-the-envelope calculation. The STS measurements revealed that the states are constricted to a very narrow channel at the film edge and decay exponentially within ≈ 4 Å, i.e., within roughly one bismuthene unit cell. Moreover, edge states appear both at the upper and lower edge of a terrace step. STM measurements on bare 4°-Miscut SiC samples have demonstrated an average terrace width of about 15 nm, corresponding to about 30 bismuthene unit cells. Consequently, the edge state signal extends over 1/15 of the surface area. This indicates that it is much weaker than the bulk signal but may be identified with a detailed inspection. Accordingly, momentum distribution curves (MDCs) of the VBM are shown in Fig. 8.9**c**. Again, both upper and lower VB are seen. On top of the upper band maximum one might perceive a slow fade out of the intensity. Interestingly, the width of the signal becomes rather broader than narrower at lower binding energies, which seems compatible with the DFT calculations that locate the merging of the edge states in the Dirac point directly ahead of the band maximum at K. Starting from there, the branches reopen again due to their linear energy dispersion.

Nevertheless, an unambiguous recognition of an edge state is not possible. In particular, we may not trace a dispersion of bands with high confidence even though we devoted considerable experimental efforts to reach this goal.

Possible reasons that cause the absence of edge states in ARPES. Many reasons bedevil the observation of 1D edge states in ARPES. One source of smeared-out features, as seen between the VBM and the Fermi level, could be temperature broadening, as the measurement in Fig. 8.9**b/c** is conducted at room temperature. Yet, similar experiments carried out at low temperature basically produce the same result.

Another obvious issue on the probed bismuthene samples is disorder, which might give rise to a featureless DOS at the Fermi level. Some parts of the AC edges are perfectly ordered like the one presented in Fig. 8.8, but others, as shown in Fig. 8.4, exhibit disordered edge structures, which will cause a broadening of the detected signal. Structural disorder is also introduced by the step edges of miscut samples. Albeit they are highly oriented and predominantly straight, they possess frequent indents and a varying terrace width (compare to Fig. C.3 and Sec. D.3).

A further aspect, which complicates the observation of edge states, is the position of the Fermi level at low energy within the band gap. This problem is particularly severe in case of miscut samples, where the VBM and E_{F} are often offset by only 100 meV, which makes the

[25] Note that here, the K point can be probed by rotating the sample around an axis that does not change the symmetry of the sample normal with respect to M–Γ–M, resulting in a symmetric illumination and equally intense VB branches in this direction.

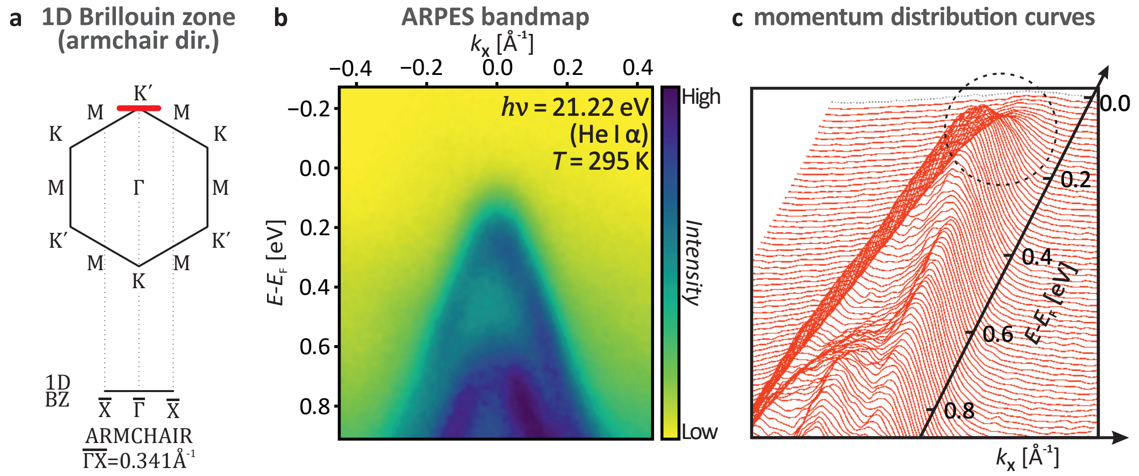

Figure 8.9 High-resolution ARPES bandmap at K on a bismuthene sample grown on a 4°-Miscut SiC substrate. **a** Sketch of the 1D BZ of bismuthene in AC direction and its relation to the 2D BZ. The red line indicates the probed k space area. **b** The ARPES image shows the Rashba splitting of the VB. Apart from the bulk bands, no additional states are visible. **c** The inspection with MDCs shows that weak spectral weight between the VBM and E_F (gray dotted line) is present. However, clear signatures of bands with linear dispersion are not observed.

perception of additional, weak dispersing bands much harder. It was attempted to increase the Fermi level position by surface doping with K atoms[26], which works but at the same time introduces a significant amount of disorder on the surface. Inverse photoemission seems not useful due to its comparably low energy resolution and count rates.

Similarly, the floating Fermi level energy found in STS (see Fig. 8.6) might cause a broadening of the VBM, hampering the identification of edge states even further.

Technically, the observation of edge states in our setup is complicated by the lack of a monochromatized He light source. The search for the edge states at momenta off the K point, where the band structure does not possess bulk derived bands, has been attempted but failed due to replica of (SiC) bands at higher binding energy, which are caused by satellites of our He light source. Moreover, due to the fixed excitation energy, it cannot be excluded that final state effects lead to reduced edge state signals. Fortunately, these issues may be easily solved by experiments at a synchrotron.

The prospect of a first-ever observation of 1D edge states with an imaging technique is motivating further efforts despite all these problems, especially as bismuthene on SiC has several crucial advantages in comparison to other QSHI materials. Firstly, it is fabricated epitaxially, which allows a further increase of the edge state density by use of proper SiC substrates. Secondly, it is a surface system (in contrast to HgTe/CdTe quantum wells), which makes the use of low-energy photoemission with high momentum and energy resolution feasible, and renders the edge state observation with ARPES in principle possible.

Yet, in the following, we turn back to a microscopic sample inspection and scrutinize the strongly suppressed LDOS at the Fermi level with high-resolution STS measurements.

[26] Further information on K doping of bismuthene studied with ARPES and STM/STS are found in Refs. [265] and [266].

8.2 Helical Tomonaga-Luttinger Liquid in the Armchair Edge States

The bismuthene edge states described in Sec. 8.1.2 are laterally highly confined. Such spatial constriction to 1D inevitably raises the relevance of electronic correlations in any system with conducting electrons, regardless whether they are materials with trivial or non-trivial topology [267]. Even though elastic single-particle backscattering in topological insulators (TIs) is prohibited as long as time-reversal (TR) invariance is preserved [12, 13], backscattering might appear nonetheless via two-particle processes, i.e., correlations caused by the Coulomb interaction between electrons [14, 263, 268]. Correlation effects evolve predominantly at the Fermi level and can cause a suppression of the DOS, just as is apparent in the $\mathrm{d}I/\mathrm{d}V$ spectra of the edge state measurements in Fig. 8.4. Hence, it is a reasonable assumption that correlations might play an important role in bismuthene edge states.

Interacting 1D electron systems may be studied in the framework of the Tomonaga-Luttinger liquid (TLL) theory, which exhibits a suppression of the LDOS at the Fermi level at presence of repulsive interactions. However, also other mechanisms might give rise to a reduced signal around zero bias, in particular disorder resulting in a Coulomb gap and a dynamical Coulomb blockade (DCB), which is a result of charging effects in low-dimensional structures [269, 270]. Therefore, a thorough investigation to unveil the underlying physics of such an anomaly observed around zero-bias (ZBA) is imperative and presented in the following.

8.2.1 Characterization of the Zero-Bias Spectra

As a starting point, STS spectra towards and across a SiC step are revisited with special attention to the energy range of $\pm 100\,\mathrm{meV}$ around the Fermi level. This means that the $\mathrm{d}I/\mathrm{d}V$ signal close to E_F is measured with better statistics and higher resolution. For this purpose, the modulation voltage needs to be reduced to $V_\mathrm{mod} = 1\,\mathrm{meV}$ to avoid that subtle details are averaged out [61, 244].

Fig. 8.10 shows STS spectra recorded across a step with $\frac{1}{2}c^\mathrm{SiC}$ height. The two measurements are identical except for their stabilization parameters. The left column (Fig. 8.10**a**–**c**) displays spectra recorded with a tip stabilization at voltage V_st, which is well inside the bulk states. The corresponding grid measurement is used to assure that the ZBA feature is bound to the step edge. Indeed, by following the colored dots in Fig. 8.10**b** and inspecting the respective spectra in Fig. 8.10**a**, we find that the signal strength grows while it retains its shape, until a V-shaped ZBA is seen directly at the edge.

The heatmap in Fig. 8.10**c** visualizes that the ZBA is strongly confined to the step edge region and exhibits a very steep increase of the signal strength towards the edge. Moreover, the STS curves are particle-hole symmetric, compare also to the plots in Fig. 8.10**a**.

Spectra shown in the right column (Fig. 8.10**d**–**f**) are recorded with tip stabilization at $V_\mathrm{st} = V_\mathrm{ini} = -100\,\mathrm{mV}$, which provides an even better signal-to-noise ratio for the ZBA but bears the danger of an inconstant or failing tip stabilization if the measurement is recorded at too large distance from the edge, as the bulk VB has a vanishing DOS at E_F.

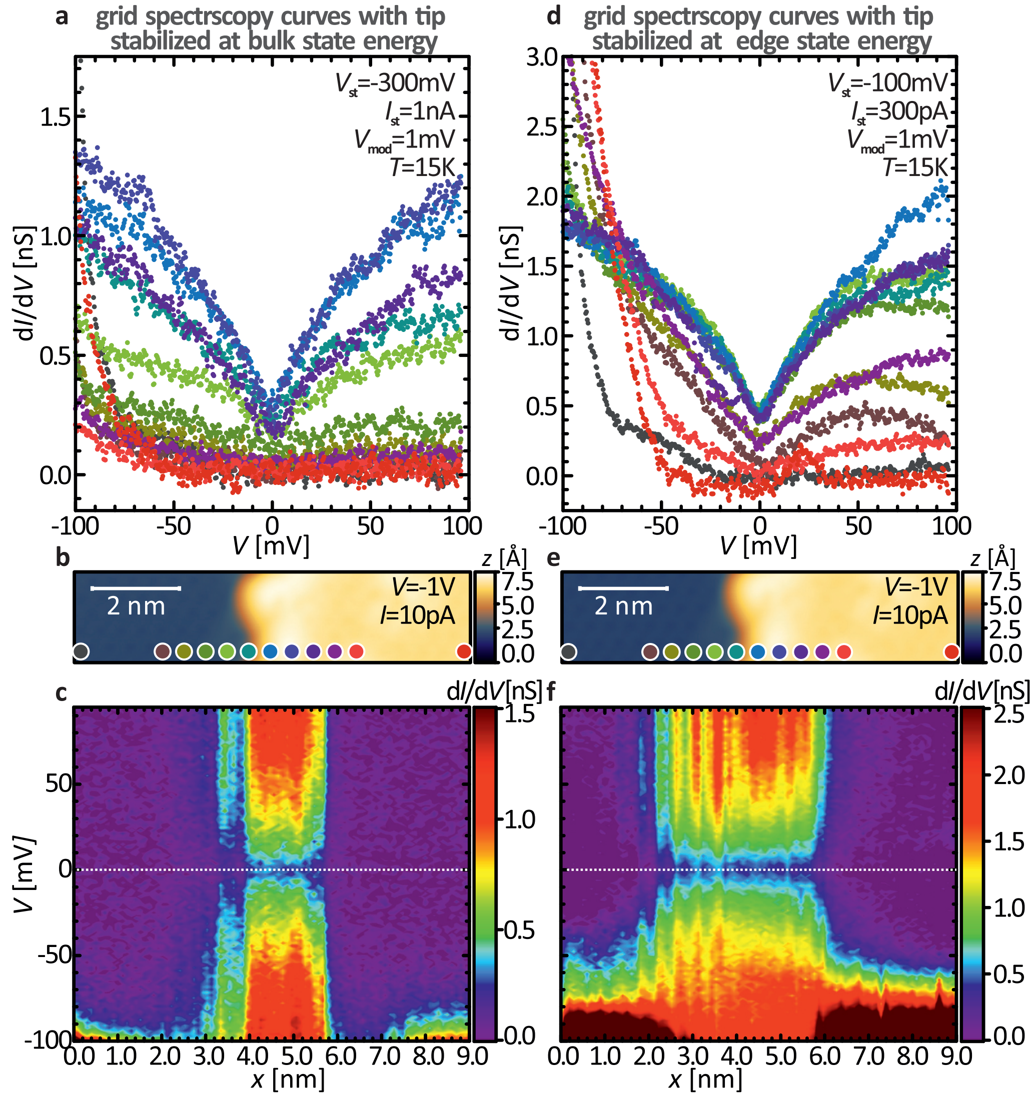

Figure 8.10 Grid spectroscopy measurements across a SiC step edge with focus on a small energy range around the Fermi level. **a** Single STS curves in the energy range of ±100 meV. The lateral position at which the spectra are recorded is indicated in the CCI shown in **b**. The tip stabilization before acquisition of the $I(V)$ curve is carried out at energies corresponding to bulk states ($V_{st} = -300$ meV, $I_{st} = 1$ nA) to see whether the zero-bias anomaly is constrained to the edge, which is the case. **c** The heatmap demonstrates that the zero-bias dip is seen only in a range of $\approx \pm 1.5$ nm around the step. **d**–**f** The same measurements as in **a**–**c** but with $V_{st} = -100$ meV and $I_{st} = 300$ pA to improve the signal-to-noise ratio. **f** The better statistics highlight the bulk lattice periodicity in the heatmap. Further measurement parameters (both grid measurements): $V_{mod} = 1$ mV, $\Delta x = 1.0$ Å, $\Delta y = 2.0$ nm, $x_{range} = 9.0$ nm, $y_{range} = 2.0$ nm, $V_{ini} = -0.1$ V, $V_{end} = 0.1$ V, 501 points per curve.

The dI/dV curves in Fig. 8.10**d** demonstrate the improved signal quality, as the ZBA spectra exhibit a significantly reduced scattering of measurement points in comparison to the spectra in Fig. 8.10**a**. At the same time, the spectra recorded at a certain lateral distance from the edge on the bulk lattice are influenced by the overwhelming LDOS of the bulk VB for the chosen stabilization parameters, resulting in a highly asymmetric shape (olive, dark green, and purple spectrum in Fig. 8.10**d**/**e**) or are enhancend to a degree that the zero conductance line vanishes (black, brown, and light red spectrum in Fig. 8.10**d**/**e**). The rippling pattern apparent in the heatmap (Fig. 8.10**d**) is caused by the varying LDOS at different lattice sites, compare to the discussion of Fig. 8.5**b**, and

is pronounced due to the stabilization very close to the VB edge for the measurement in Fig. 8.10**d**–**f**. Besides this, the heatmap reveals that the spectra at the edge, i.e., in the region from $x \approx 3.0 ... 6.0\,\text{nm}$, are particle-hole symmetric to a reasonable extent. As seen, both options, i.e., measurements with tip stabilization in the bulk VB or directly at $V_{\text{st}} = V_{\text{ini}} = -100\,\text{mV}$, basically lead to the same results. Hence, depending on the alignment of the bulk states with respect to the Fermi level, they are both used in the following measurements in this section.

ZBA as function of the stabilization current. In the STS curves of Fig. 8.10, we compensated the lower differential conductivity in the range $-100\,\text{meV} < E - E_{\text{F}} < +100\,\text{meV}$ for the measurement with $V_{\text{st}} = -300\,\text{mV}$ by adjustment of the stabilization current. However, it is important to check whether the detected signal is sensitive to the current setpoint, as too high values might induce a band bending due to a too large electric field between tip and sample [222, 251].
Fig. 8.11 displays a series of zero-bias spectra recorded with varying stabilization current ranging from $I_{\text{st}} = 10\,\text{pA}$ to $I_{\text{st}} = 1\,\text{nA}$, i.e., a variation of two orders of magnitude. The $z(t)$ signal during the incremental rise of I_{st} is depicted in Fig. 8.11**a** and reveals that the increase of the current affects a change of the tip position z by roughly $2\,\text{Å}$. Note that $z(I = 10\,\text{pA}) = 0\,\text{Å}$ is taken as reference and negative values indicate that the tip is approached to the sample surface.

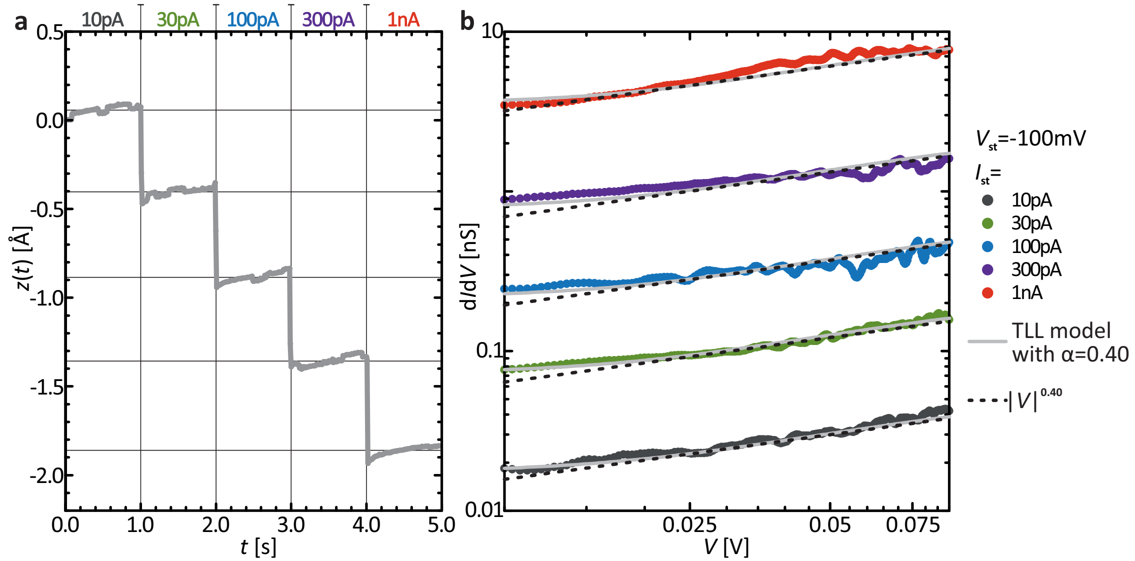

Figure 8.11 Zero-bias STS curves as function of the stabilization current. **a** The $z(t)$ signal visualizes the exponential dependence of the tunneling current on the spacing between tip and sample. **b** STS curves at zero bias. A logarithmic scale is used to show all measurements in a single viewgraph. Even though the $\mathrm{d}I/\mathrm{d}V$ signal varies by two orders of magnitude, the zero-bias signal is mostly unchanged. Black dashed and gray solid curves depict a power law with $|V|^{0.40}$ and a TLL model (Eq. 8.3) with $\alpha = 0.40$, respectively. Additional spectroscopy parameters: $V_{\text{mod}} = 1\,\text{mV}$, $V_{\text{ini}} = -0.1\,\text{V}$, $V_{\text{end}} = 0.1\,\text{V}$, 501 points per curve and $T = 4.35\,\text{K}$.

Despite this large variation of I_{st} the spectra do not show systematic changes and remain mostly uninfluenced in the double logarithmic plot in Fig. 8.11**b**. The almost linear slope upon logarithmic plotting suggests a power-law behavior of the LDOS at low bias. Therefore, the experimental $\mathrm{d}I/\mathrm{d}V$ curves are compared to a power-law function proportional

to $|V^{0.40}|$ (black dashed curves in Fig. 8.11**b**), which yields a decent agreement, however, systematic deviations are apparent very close to E_F, in particular in the spectra recorded with $I_\mathrm{st} = 30/100/300\,\mathrm{pA}$. A better description of the functional form of the data is obtained with an equation that expresses the DOS of a TLL (gray solid curves in Fig. 8.11**b**), which will be introduced in Sec. 8.2.2. Note that the specific value of $\alpha = 0.40$ will be motivated later in this section.

ZBA at a kinky edge segment. In a next step, we examine the ZBA at structural irregularities, which are expected to act as scattering potentials. Fig. 8.12**a** shows a CCI displaying a pronounced, almost 90° kink of the edge contour at the upper terrace, which is an ideal studying case for this purpose. A grid spectroscopy measurement (boundaries indicated by the gray rectangle in Fig. 8.12**a**) recorded at $T = 95\,\mathrm{K}$ is used to extract STS curves along a path along the step edge kink. The corresponding spectra are shown in Fig. 8.12**b**. Note that the spectra shown here are normalized according to the procedure shown in App. F.2 as they are used in fit routines later.
Intriguingly, the spectra seem to be entirely unaffected by the scattering potential provided by the step edge corner. All STS curves exhibit a particle-hole symmetric $\mathrm{d}I/\mathrm{d}V$ signal. The fact that the ZBA signal is robust despite the scattering potential of the kink is another indicator for the topological protection of the bismuthene edge states against single-particle backscattering.

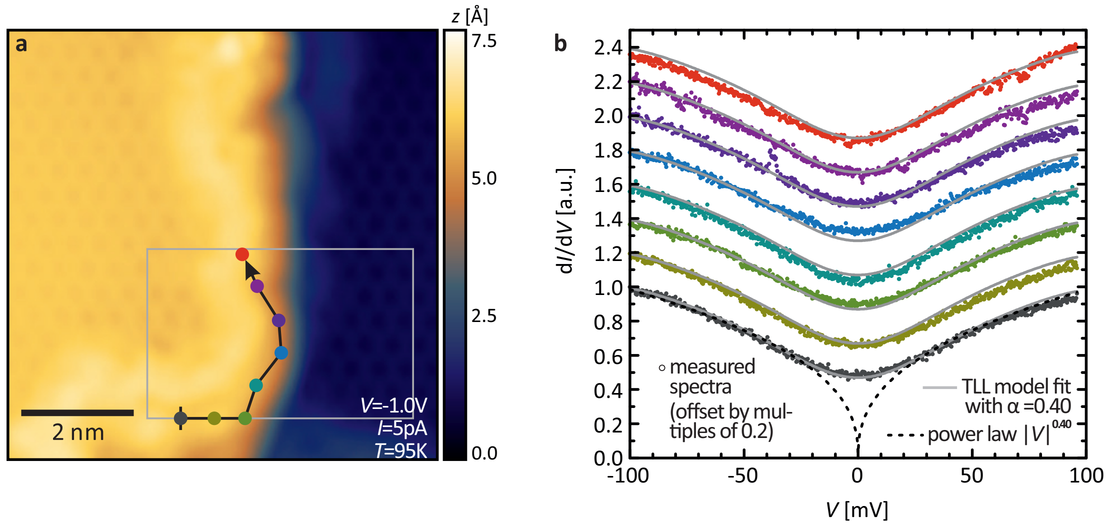

Figure 8.12 STS spectra recorded at a kinky section of a step edge. **a** The CCI shows two bismuthene terraces separated by an atomic step of the SiC substrate. The upper step edge shows a pronounced, almost 90° kink. **b** Single STS curves extracted from the grid spectroscopy measurement. The grid extension is indicated by the gray rectangle in **a**. The selected spectra are marked by colored dots and follow the contour of the step edge. The signal close to zero-bias remains unaffected despite the scattering potential that is most probably induced by the kink. Spectra are fitted with Eq. 8.3 and an exponent of $\alpha = 0.40$. Note that the presented measurement is conducted at $T = 95\,\mathrm{K}$, which causes a much smoother and less steep signal directly at $E = E_\mathrm{F}$. Tunneling parameters of the grid spectroscopy: $V_\mathrm{st} = -0.3\,\mathrm{V}$, $I_\mathrm{st} = 300\,\mathrm{pA}$, $V_\mathrm{mod} = 1\,\mathrm{mV}$, $\Delta x = 0.5\,\mathrm{Å}$, $\Delta y = 5.0\,\mathrm{Å}$, $x_\mathrm{range} = 4.7\,\mathrm{nm}$, $y_\mathrm{range} = 3.0\,\mathrm{nm}$, $V_\mathrm{ini} = -0.1\,\mathrm{V}$, $V_\mathrm{end} = 0.1\,\mathrm{V}$, 601 points per curve.

A power-law curve proportional to $|V^{0.40}|$ serves as a guide to the eye (black dashed curve in Fig. 8.12**b**). The linear axes scaling visualizes that a mere power law fails to describe

the spectral shape around the Fermi level, see black dashed line in Fig. 8.12**b**. Furthermore, it is obvious that the signal minimum is much more rounded in comparison to the spectra shown in Fig. 8.10. As the measurement parameters are the same as in Fig. 8.10**a**–**c**, it is reasonable to assume that the variation of the measurement temperature causes the change in the signal shape. Remarkably, the broadening of the zero-bias dip is reproduced by the functional form of the DOS according to TLL theory, which is shown by the gray solid curves in Fig. 8.12**b**.

8.2.2 Temperature-Dependent Measurements

The strong modification of the spectral shape when comparing the measurements at $T = 15\,\mathrm{K}$ and $T = 95\,\mathrm{K}$ motivates systematic temperature-dependent experiments. As stated in the opening remarks of this section, the strongly confined 1D states observed at SiC substrate steps on bismuthene films may serve as an ideal platform for enhanced electronic correlations, which, in case of a QSHI edge state, are described theoretically by the (helical) TLL model. Its DOS is expressed by [271]:

$$\rho_{\mathrm{TLL}}(eV, T) \propto T^{\alpha} \cosh\left(\frac{eV}{2k_{\mathrm{B}}T}\right) \left|\Gamma\left(\frac{1+\alpha}{2} + i\frac{eV}{2\pi k_{\mathrm{B}}T}\right)\right|^{2}. \tag{8.1}$$

Here, ρ_{TLL} is the DOS associated with a TLL, e the elementary charge, V is the tunneling voltage, T the temperature, k_{B} the Boltzmann constant, and $\Gamma(x)$ the Gamma function. Most importantly, α constitutes the power-law exponent that enters the formula in temperature and energy and is its only free parameter.
For comparison with experimental data it is mandatory to include thermal and instrumental broadening in the fit routine. Thermal broadening (F_{T}) is relevant as Eq. 8.1 is based on the assumption of leads, i.e. the sample and the tip in our case, at $T = 0\,\mathrm{K}$, which are at the finite measurement temperature in reality. To account for this thermal broadening the derivative of the Fermi distribution, [271]

$$F_{\mathrm{T}} = \mathrm{d}f/\mathrm{d}E = \left(\frac{1}{4k_{\mathrm{B}}T}\right) \mathrm{sech}^{2}\left(\frac{eV}{2k_{\mathrm{B}}T}\right), \tag{8.2}$$

is included in the fit formula. Instrumental broadening F_{instr} is governed by the modulation voltage, but also introduced via noise of the power supply and offset-voltage noise in the current-voltage-converter, which are hard to quantify but often give a major contribution to this type of broadening [61]. Instrumental broadening is estimated by a Gaussian curve with suitable width and convoluted with the other functions (compare to App. F.2). The resulting total model function is:

$$\mathrm{d}I/\mathrm{d}V(eV) \propto \left(F_{\mathrm{T}} * F_{\mathrm{instr}}(V_{\mathrm{mod}}) * \rho_{\mathrm{TLL}}(eV, T)\right). \tag{8.3}$$

The heavy impact of thermal and instrumental broadening on the modeling curve is demonstrated in Fig. F.2.

Data processing. Before the experimentally probed STS spectra may be fit with the above-described formula it is mandatory to normalize spectra obtained at different dis-

tances from the edge and from various experimental runs. The Python code and fit procedure are described in detail in App. F.2.

The most important step in data preparation is the normalization of the spectra. As the lock-in data exhibits a higher quality, it is scaled with an auxiliary function to mimic the physically meaningful, numerically derived $I(V)$ curves, and is then normalized. In this way, the full spectral information like the signal curvature (proportional to the TLL exponent α) and the zero bias conductance (which increases proportional to α, as well) is transported, while the optimal quality is maintained. Most importantly, the as-prepared normalized $\mathrm{d}I/\mathrm{d}V$ curves possess α as the only free fit parameter.

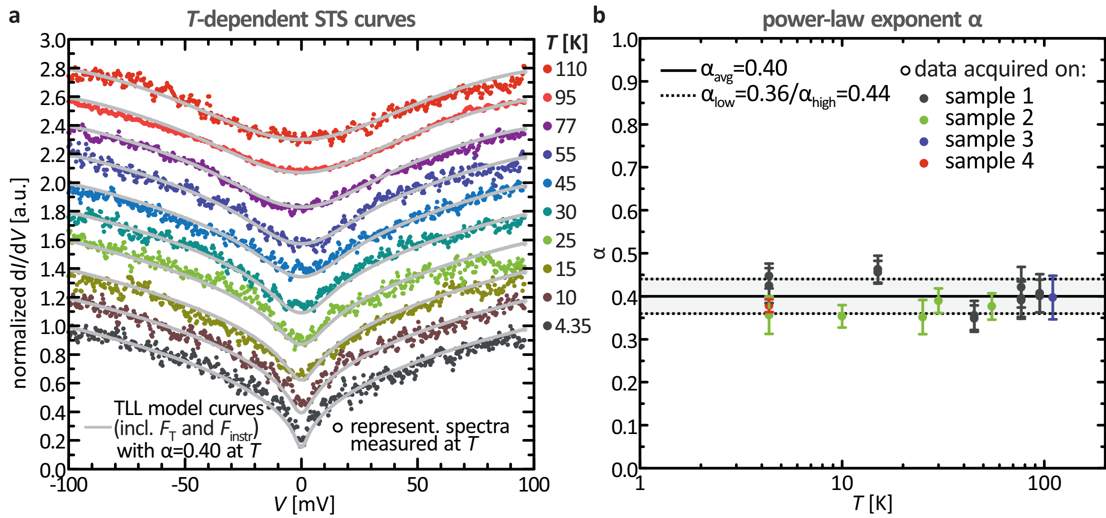

Figure 8.13 Temperature-dependent ZBA measurements. The temperature is varied between $T = 4.35\,\mathrm{K}$ and $T = 110\,\mathrm{K}$, i.e., covering almost two orders of magnitude. **a** Spectra recorded at different temperatures show that the zero-bias dip is most pronounced at the lowest accessible temperature and gradually becomes filled up when the temperature is increased. Note that the spectra are shifted by 0.2. The displayed points are generated by binning of three measurement points. Fits with TLL formula (Eq. 8.3) at the given temperature and with $\alpha = 0.40$ reproduce the detected spectra very well. **b** Power-law exponent α obtained at different temperatures, measurement runs and samples. The average value is $\alpha = 0.40 \pm 0.04$ and visualized by the gray shaded area. Details on the spectroscopy measurements in App. F.3.

Representative ZBA curves at varying probing temperature. Fig. 8.13**a** shows representative ZBA curves measured at variable temperature T ranging from 4.35 K up to 110 K. The tunneling spectra continuously evolve with the increasing temperature. More precisely, the LDOS signal around the Fermi level, which is a pronounced V-shaped depression at $T = 4.35\,\mathrm{K}$, becomes steadily smoother and the differential conductivity at zero bias increases. In contrast, the curvature of the signal at larger bias voltage, i.e., at $|eV - E_\mathrm{F}| > 50\,\mathrm{meV}$, remains rather unaffected upon variation of the temperature.

The measured STS curves are reproduced with accuracy by the TLL formula including thermal and instrumental broadening (Eq. 8.3). We inspect Eq. 8.1 to understand the spectral characteristics. Whereas the tunneling rate and hence the $\mathrm{d}I/\mathrm{d}V$ signal at $eV = 0\,\mathrm{eV}$ behaves like $\propto T^\alpha$ for $eV \ll k_\mathrm{B}T$ in Eq. 8.1, it is proportional to V^α at larger bias voltages (i.e., $eV \gg k_\mathrm{B}T$) [271, 272]. As mentioned, it is important to account for broadening due to finite temperature and instrumental resolution, see Fig. F.2.

The model curves are generated with a power-law exponent $\alpha = 0.40$. It is determined as average fit value obtained by analysis of 20 grid spectroscopy measurements and on four different samples (see Tab. F.1). Naturally, the individual values of α are varying but clearly follow a trend line around 0.40. The error ($\sigma_\alpha = 0.04$) corresponds to the standard deviation obtained when averaging the individual $\alpha(T)$ values shown in Fig. 8.13**b**.

Zero-bias conductance. We perform a complementary analysis by examination of the STS zero-bias conductance $\rho_0(T)$ measured at different temperatures, which is proportional to T^α according to the TLL theory [271, 272]. The representative STS spectra at varying T are shown again in Fig. 8.14**a**, but this time, the spectra are not offset to visualize that the differential conductivity at zero bias ρ_0 increases together with the temperature.

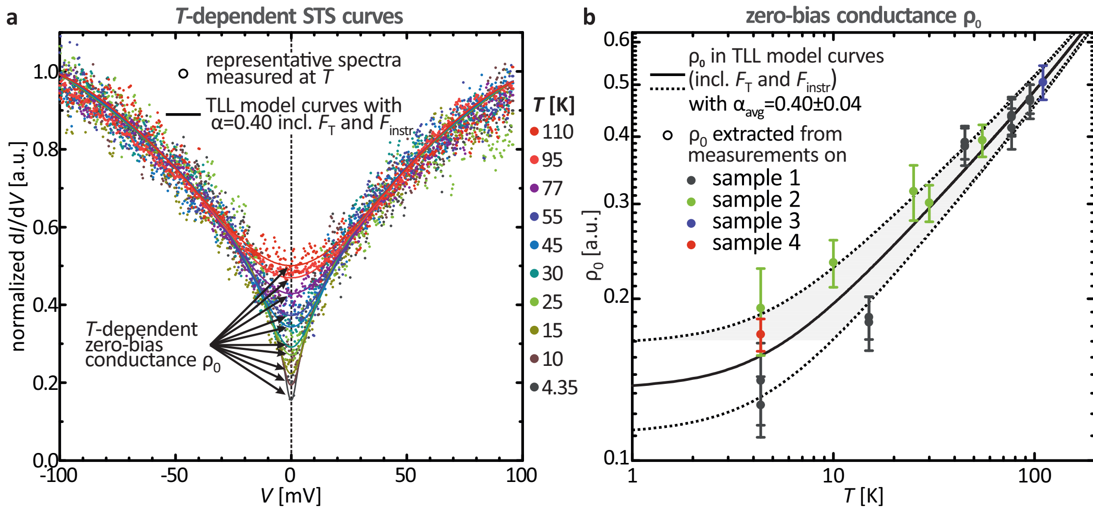

Figure 8.14 Temperature-dependent STS curves and corresponding TLL fits with $\alpha = 0.40$. Spectra are not filtered and not offset to visualize the increase of the zero-bias conductance ρ_0 with temperature T. **b** Double-logarithmic plot of ρ_0 as function of the temperature. The black line represents ρ_0 calculated with the TLL formula including temperature and modulation voltage broadening (Eq. 8.3), and with the exponent $\alpha = 0.40$. The dotted curves correspond to $\alpha = 0.36$ and $\alpha = 0.44$. The color of the dots indicates different samples. The determined zero-bias conductance is in agreement with a power-law exponent $\alpha = (0.40 \pm 0.04)$ for all measurements .

The colored model curves in Fig. 8.14**a** are a guide to the eye and computed with $\alpha = 0.40$. For analysis of $\rho_0(T)$, the STS spectra are fitted by the procedure described in App. F.2, leaving α a free parameter. Then, ρ_0 is extracted from the optimal model curve.

Fig. 8.14**b** shows the average values and error bars of $\rho_0(T)$. The logarithmic scaling affects that the zero-bias conductance ρ_0 at $T > 10\,\mathrm{K}$ exhibits a linear dependence on T in the diagram, as expected due to the power-law dependence T^α in Eq. 8.1. At very low T, i.e., for $T \leq 10\,\mathrm{K}$, $\rho_0(T)$ does not continue to decrease linearly, mainly as a result of instrumental broadening. This is apparent in the model curves with and without F_T and F_instr shown in Fig. F.2**b**.

The values obtained experimentally are captured by the margin of the averaged $\rho_0(T)$ curve, which confirms that the zero-bias conductance is well described by Eq. 8.3 and with a power-law exponent of $\alpha = 0.40 \pm 0.04$.

Universal scaling. Lastly, the power-law scaling in temperature and energy may be made evident in a single graph by a proper rescaling of the plot axes. This *universal scaling* is a hallmark of TLL systems and causes a collapse of all spectra onto a single curve. Consequently, the representative dI/dV curves (8.13**a**) are re-used and shown with rescaled axes in Fig. 8.15. Indeed, all STS spectra are superposed and within the margin of the (rescaled) model curve with $\alpha = 0.40 \pm 0.04$, which highlights the indications of a TLL formation in bismuthene AC edge states.

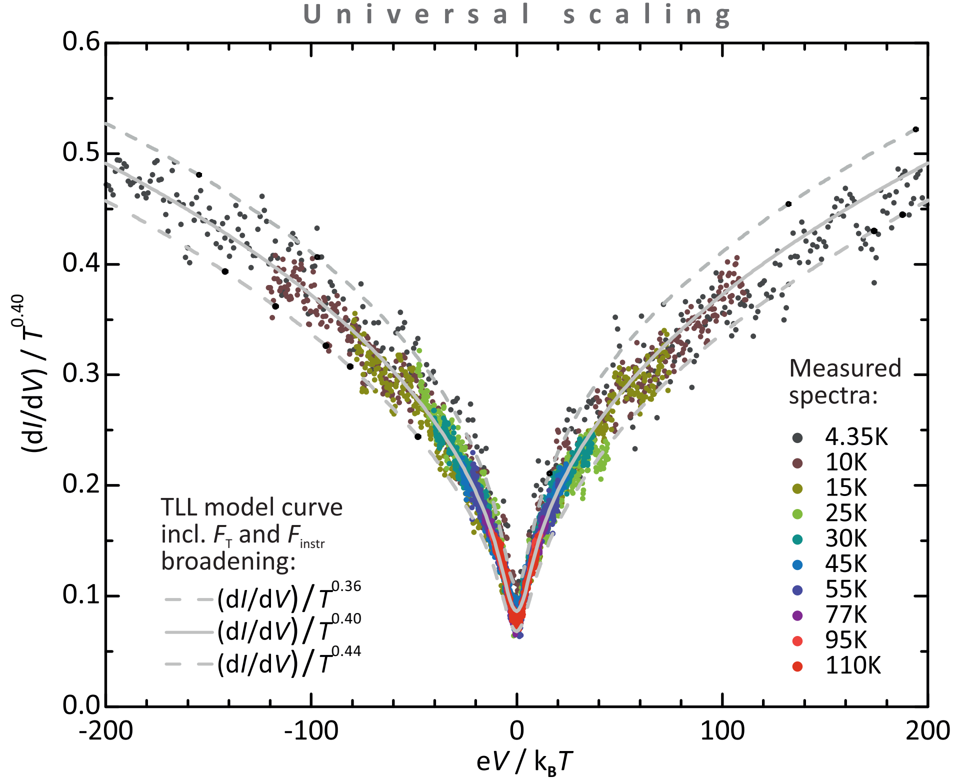

Figure 8.15 Universal scaling of the ZBA STS curves recorded at different probing temperature. All spectra collapse onto a single curve, which provides strong evidence for the formation of a TLL. The full and dashed gray lines correspond to the TLL model curve with $\alpha = 0.40$ and $\alpha = 0.36/0.44$. Again, temperature and modulation broadening is included during calculation of the TLL model. All spectra are within the margin provided by the error in α. Experimental curves are presented after binning with a window of three measurement points.

Luttinger parameter. Based on this finding we may calculate the Luttinger parameter K, which is a measure of the interaction strength within the edge channel and related to experimentally detectable quantities, namely the power-law exponent α, via [268]:

$$\alpha = \frac{1}{2}(K + K^{-1} - 2). \tag{8.4}$$

Note that Eq. 8.4 is based on the theory for a helical Luttinger liquid with counterpropagating, spin-polarized edge states, which has half the degrees of freedom compared to trivial TLL systems. The prefactor in a regular Luttinger liquid, in which the electron spin and momentum are independent, changes from $\frac{1}{2}$ to $\frac{1}{4}$ [268, 273]. Our assumption of a helical TLL is based on the experimental evidence that the realization and theoretical

description of bismuthene on SiC coincide and derived from the non-trivial $\mathbb{Z}_2$ invariant in DFT. Yet, no direct experimental evidence for the helicity of the TLL in AC edge states can be provided by STS. With these assumptions and with $\alpha = 0.40 \pm 0.04$ according to our experiments we calculate $K = 0.42 \pm 0.02$ in the AC edge states of bismuthene.

As stated above, K is a measure for the strength of electronic interactions. More precisely, $0 \leq K < 1$ indicates repulsive interactions while $K > 1$ is found in systems with attractive interactions. Obviously, $K = 1$ constitutes the non-interacting case [127]. The theoretical description of helical Luttinger liquids is limited to renormalization group methods. Microscopic models have not been found to date due to the complexity of the problem [129]. Within the methodology of the renormalization group analysis, repulsive interactions are further categorized into weak ($1/2 < K < 1$) and strong ($0 \leq K < 1/2$) repulsive interactions. In case of $0 \leq K < 3/8$, a gap is introduced in the DOS due to quenched disorder [129, 274]. Hence, bismuthene on SiC is positioned in the regime of strong interactions in this framework.

TLL in other 2D TI materials. Besides these theoretical exercises we may compare the obtained Luttinger parameter to values found in other 2D TI materials. Experimentally, K has been determined in InAs/GaSb quantum wells with transport experiments ($K_{\mathrm{exp}}^{\mathrm{InAs/GaSb}} = 0.21$) as well as theoretically estimated ($K_{\mathrm{th}}^{\mathrm{InAs/GaSb}} = 0.22$) in Ref. [106]. The authors state that the material is accordingly in the strong interaction regime, in which two-particle backscattering may occur at low energies. However, the theory used to calculate the experimental value of K founds on changes of the gate voltage with a degree of precision that is technically hard to achieve. Alternatively, the observed spectral signatures may be explained by the presence of Kondo impurities, which would result in $K_{\mathrm{th,\ alt.}}^{\mathrm{InAs/GaSb}} \approx 0.82$ (see Ref. [127] for details).

Furthermore, the Luttinger parameter in HgTe/CdTe quantum wells is estimated theoretically by Teo and Kane ($K_{\mathrm{th}}^{\mathrm{HgTe/CdTe}} \approx 0.8$) [274]. This indicates that the edge states in HgTe/CdTe are in the weak interaction regime.

Based on their approach it is also possible to provide a theoretical estimate of the Luttinger parameter in bismuthene on SiC [275]. The description is based on momentum-independent, long-range Coulomb interactions in the edge states, and employs knowledge about the dielectric constant of SiC, the Fermi velocity in DFT as well as the experimentally probed extension of the edge state. Therewith, the Luttinger parameter is calculated to $K_{\mathrm{th}}^{\mathrm{Bi/SiC}} = 0.5 \pm 0.1$, which agrees with the value determined experimentally. In the framework this description, the reduced Luttinger parameter K arises from the enhanced influence of the Coulomb interaction due to the strong edge state confinement in bismuthene on SiC in comparison to, e.g., HgTe/CdTe quantum wells: whereas the extension of the edge state in HgTe/CdTe is 30 nm [274], it is only < 1 nm in bismuthene, see Sec. 8.1.2.

8.2.3 Discussion of Alternative Zero-Bias Anomaly Mechanisms

The observation of universal scaling of the STS makes a strong case for the formation of a state that may be described by the TLL theory. Yet,the finding of a ZBA and even the coincidental agreement of power-law exponent for T and E (i.e., universal scaling) is

not exclusive to TLL systems but might evolve due to a different physical origin, as well. Hence, the remainder of this section is devoted to the discussion of alternative mechanisms that might explain our experimental findings. Given the energy scale at which the ZBA occurs, the symmetric shape around zero bias, and the physical system in which it appears, i.e., bismuthene on SiC as described in Chs. 7 and 8, the most relevant candidate theories are a disorder-induced Coulomb gap and the DCB. In contrast to the TLL theory, the ZBA-like behavior is not an intrinsic property of the edge states itself, but arises from the electric properties of the surrounding physical system.

Disorder-induced ZBA. In low-dimensional metals, a ZBA might appear due to the presence of weak disorder. Long-range Coulomb interactions in 1D systems cause an exponentially suppressed DOS at zero bias.

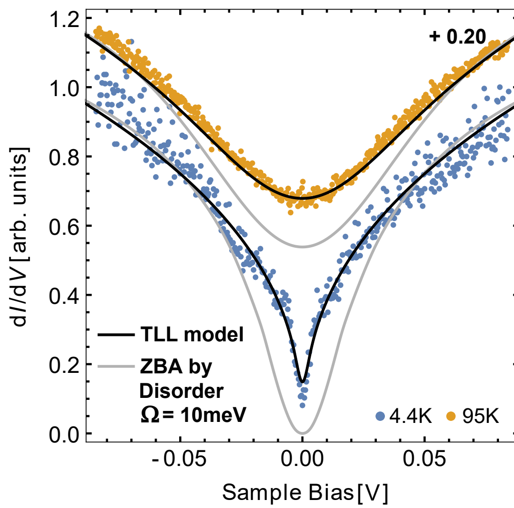

Figure 8.16 Comparison of measured STS curves at 4.35 K (blue dots) and 95 K (orange dots), and model curves computed for a TLL with $\alpha = 0.41$ (black lines) as well as for a disorder-induced ZBA (gray line). Clearly, the TLL model curve reproduces the power-law behavior present in the experimental spectra. In contrast, the curves generated by Eq. 8.6 show only poor agreement with the measured $\mathrm{d}I/\mathrm{d}V$ spectra. *Figure reprinted from Ref. [275].*

The DOS generated by such a metallic Coulomb gap at finite T is expressed by [269]:

$$\rho(V,T) \approx \rho_0 \coth\Big(\frac{eV}{2k_\mathrm{B}T}\Big)\, 2T \int_0^\infty dt\, \frac{\sin(eVt/k_\mathrm{B})\cos(\sqrt{2e\Omega t/k_\mathrm{B}})}{\sinh(\pi t T)} \times \tag{8.5}$$

$$\times \exp\Big[-\sqrt{\frac{\Omega}{\pi}} \int_0^\infty dV' \, \frac{1-\cos(V't)}{V'^{3/2}\tanh(eV'/2k_\mathrm{B}T)}\Big], \tag{8.6}$$

where $\Omega = f_0^2/(32\pi D_0)$ is used as fit parameter in Fig. 8.16 and depends on the strength of electron-electron interaction f_0 and the diffusion coefficient D_0, which is related to the elastic mean free path l via $D_0 = v_\mathrm{F} l$ (v_F is the Fermi velocity). Hence, D_0 reflects the amount of disorder in the system. Note that the authors of Ref. [269] state that their derivation is strictly valid only in 2D, where the derived functional form of the DOS in the presence of disorder resembles an Efros-Shklovskii Coulomb gap, but extended to describe 1D systems.

Nevertheless, Eq. 8.6, in which Ω is the only free fit parameter, is used to compare to our experimental data in Fig. 8.16. It is apparent that the fit curves reproduce the higher energy part of the measured spectra but completely fail to reproduce the spectral shape in direct proximity to E_F. This is a consequence of their different functional form. While our spectra exhibit a power-law dependence in T and V, Eq. 8.6 comprises an exponential

suppression of the DOS, and can therefore be ruled out with high confidence. In contrast, the TLL modeling curves shown for comparison reproduce the dI/dV signal very well.

DCB. A further mechanism that may give rise to a ZBA is the DCB, which appears when the charging energy of the surface upon current injection is too small to overcome the total capacitance of the system. A DCB is generally absent in perfect conductors[27] but a relevant effect in systems where a high-impedance contact is formed between the substrate, i.e., the drain and an intermediate, nanoscale object [277, 278].

Schematically, the DCB can be abstracted by a double junction as in Fig. 8.17 [270, 277]. The first junction, the so-called T junction, is formed by the (metallic) tip and an island on the surface, and characterized by the tunneling resistance R_T and the tunneling capacitance C_T. The latter is unknown but typically on the order of $C_\mathrm{T} \leq 1\,\mathrm{aF}$ [270, 277], while the former is determined by the tunneling parameters $R_\mathrm{T} = V/I_\mathrm{T}$. The second junction evolves between the island and the surrounding dissipative environment, i.e., the substrate. In this model, the differential conductivity can be calculated with [279]:

$$\frac{dI}{dV}(eV) = \frac{1}{R_\mathrm{T}}[1 + 2\int_0^\infty dt\, \frac{\pi k_\mathrm{B}^2 T^2}{\hbar^2}\,\mathrm{Im}[e^{J(t)}]\cos(\frac{eVt}{\hbar})\,\mathrm{csch}^2(\frac{\pi k_\mathrm{B} T t}{\hbar})\,t]. \tag{8.7}$$

Additional information of the DCB modeling is found in App. F.5.

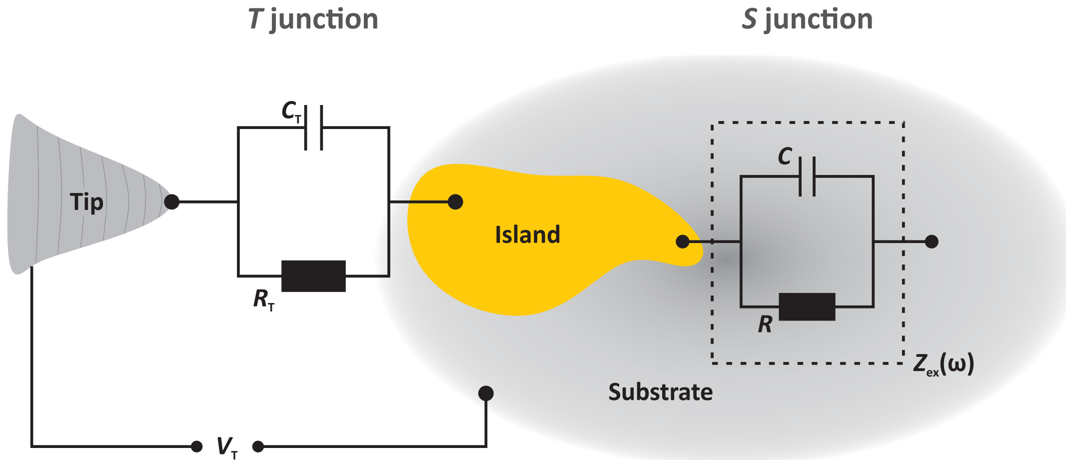

Figure 8.17 DCB model scheme. The tunneling process between the metallic tip and substrate is subdivided into two stages by introduction of an intermediate stage (yellow island). This setup is characterized by two RC junctions in a serial connection. A ZBA can be induced in STS measurements if the potential energy due to the applied bias voltage eV is smaller than the charging energy of the system, which depends on the total capacitance C_Σ of the of T and S junction. *Figure adapted from Ref. [275].*

With use of Eq. 8.7 a numerical simulation of DCB is feasible. The results are presented in Fig. 8.18 for different combinations of R and C_Σ. The differential conductivity is rescaled by $T^{2\alpha'} := T^{2R/R_\mathrm{K}}$, and the energy axis is rescaled with $k_\mathrm{B}T$ to see whether the modeled curves at varying T collapse on a single curve, as is observed for the STS curves in our

[27] Note that at very low temperatures ($T < 1\,\mathrm{K}$) a DCB might appear and limit the energy resolution even in a perfect conductor [276].

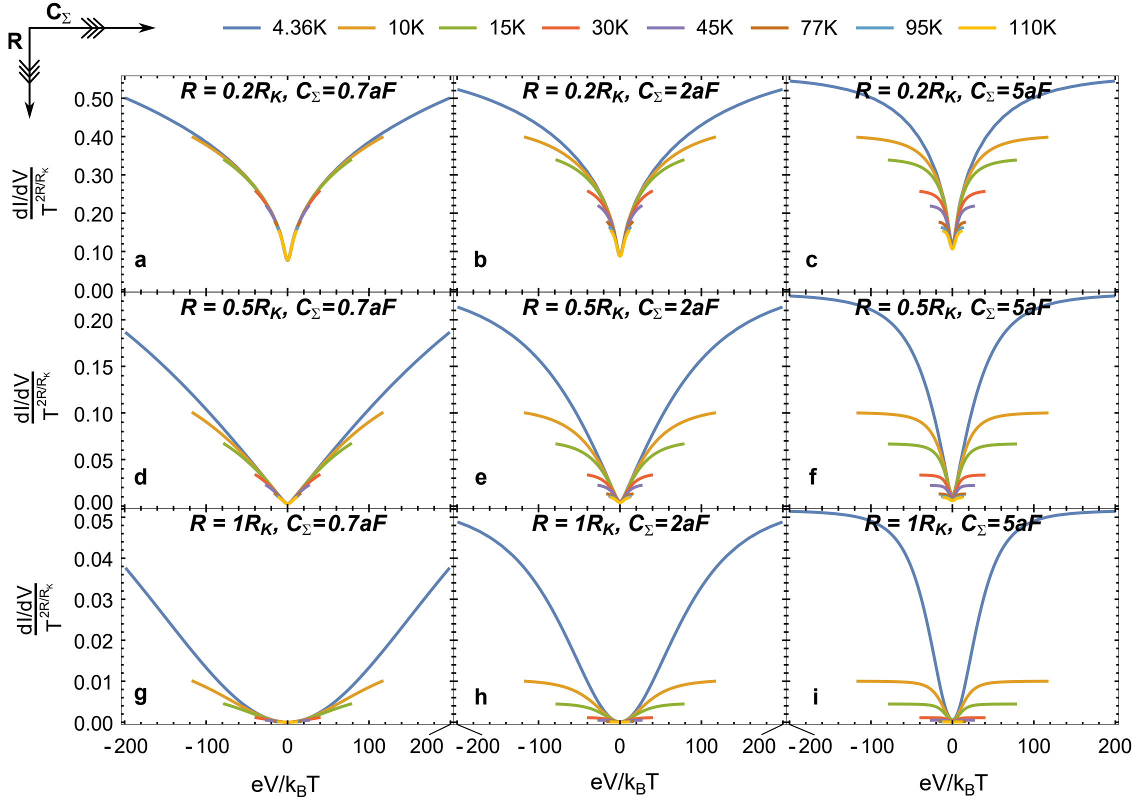

Figure 8.18 Scaling of the ZBA induced by the DCB as function of R and C_Σ. The energy and differential conductivity axis have been rescaled by $k_\mathrm{B}T$ and T^{2R/R_K}, respectively. Universal scaling in the energy range, in which the ZBA is found in STS experiments, is observed only for the specific combination of $R = 0.2R_\mathrm{K}$ and $C_\Sigma = 0.7\,\mathrm{aF}$, whereas the model curves are scaling differently in all other cases. *Figure reprinted from Ref. [275].*

experiments. Indeed, this superposition of the spectra is observed for a specific choice of the parameters.

The collapse of all spectra for $R = 0.2R_\mathrm{K}$ and $C_\Sigma = 0.7\,\mathrm{aF}$ can be understood by inspection of the formula in Eq. 8.7. theoretical description of the DCB. In the limit of low energy $eV \to 0$ and temperature $T \to 0$, Eq. 8.7 simplifies to [280]:

$$I(V) = \frac{\exp(-\alpha'\gamma)}{\Gamma(\alpha'+2)}\,\frac{V}{R_\mathrm{T}}\Big(\frac{e|V|}{\hbar(RC)^{-1}}\Big)^{\alpha'}, \tag{8.8}$$

with the Euler constant γ and $\alpha' = R/R_\mathrm{K}$. After derivation, we obtain:

$$\frac{dI}{dV}(eV) \propto |V|^{\alpha'}. \tag{8.9}$$

This constitutes a power-law dependence similar to the one in Eq. 8.1, which is a hint that the DCB formalism can be mapped onto a TLL formula and was explicitly demonstrated in Ref. [278]. This underlines that both effects have to be distinguished carefully against each other. In the following, we argue that it is not likely that the ZBA in bismuthene on SiC originates from a DCB.

The DCB is based on the presence of a capacitive island with poor electrical contact to the substrate, i.e., the S junction. The bismuthene edge channels on SiC could, in principal, constitute such a scenario. The characteristic parameters that enter the DCB

modeling are R and C. The larger R and the smaller C, the higher the impact of charging effects in the recorded STS spectra [277]. This means that the DCB is firmly linked to the extension of the edge segment. More specifically, $R = \gamma_\mathrm{R} A^{-1}$ and $C = \gamma_\mathrm{C} A$ (with the resistivity per inverse unit area γ_R, the capacitance per unit area γ_C and the area covered by the edge channel A). While γ_R and γ_C are unknown but are related to the material system and should be fixed, A depends on the width and length of the edge channels. As the latter varies and depends on the domain size, A constitutes a local property and changes in A are directly related to the detected $\mathrm{d}I/\mathrm{d}V$ signal. In particular, Fig. 8.18 demonstrates that the modeled, temperature-dependent $\mathrm{d}I/\mathrm{d}V$ signal is highly sensitive to R and C, and universal scaling is found only for a specific set of parameters in the range $-200 < eV/k_\mathrm{B}T < 200$.

In the presented experiments we measured the ZBA on four independent samples, see Figs. 8.13/8.14, and on various spots on each sample. As discussed in Sec. 6.3, the size of the bismuthene domains, and therefore of the edge channel length, varies significantly. Moreover, the tunneling parameters and thereby the tip-sample separation have been changed between different measurements (compare to Tab. F.1), as well, see Fig. 8.11. It seems likely that all these differences should become apparent in the probed spectra. Ming et al. have convincingly demonstrated how the enumerated parameters affect the detected $\mathrm{d}I/\mathrm{d}V$ signal [277].

Here, however, no systematic deviations are found in between different measurements despite this large variability, which makes the observation of universal scaling due to a DCB rather unlikely. Instead, given the strong 1D character of the AC edge states, it seems probable that the ZBA is observed due to intrinsic properties of the material system and indicates TLL-like physics in the bismuthene edge channels.

9 Conclusion

The scope of this thesis has been the realization of bismuthene on a 4H-SiC(0001) substrate and its characterization with imaging as well as spectroscopic techniques. The heterostructure constitutes one of the rare systems in the quantum spin Hall insulator (QSHI) material class where a monolayer and its substrate are treated as an entity from the beginning instead of focusing on the properties of the honeycomb film only. The formation of a large band gap in experiments emphasizes the need to involve the substrate when designing QSHI systems.

Summary. An in-depth theoretical description reveals the mechanisms that drive bismuthene on SiC into a topologically non-trivial phase. The covalent bonds between the Si and Bi atoms stabilize fully planar Bi honeycombs, which form a $(\sqrt{3} \times \sqrt{3})\mathrm{R}30°$-reconstruction with negligible lattice mismatch on SiC. Moreover, they remove the contributions of p_z orbitals to the bands at low energy. Still, hopping between p_x and p_y orbitals is feasible, which paves the way for the formation of a large, topologically non-trivial energy gap (theoretical estimate by DFT $E_{\mathrm{gap}}^{\mathrm{th}} \approx 700\,\mathrm{meV}$). The surface potential gradient due to the presence of the substrate leads to a characteristic Rashba-splitting ($\approx 430\,\mathrm{meV}$) of the valence bands at the K point. The computed edge band structure, based on nanoribbon calculations, confirms the existence of topological edge states both in armchair (AC) and zigzag (ZZ) orientation.

As the presence of Si dangling bonds (DBs) on the SiC surface is pivotal to obtain the non-trivial topological phase, the preparation of high-quality, unreconstructed 4H-SiC substrates in (0001) orientation as well as with 2° and 4° miscut towards $\langle 1\bar{1}00 \rangle$ with annealing in a H_2 atmosphere is the first step towards the realization of bismuthene. The impact of the hydrogen annealing parameters, specifically the annealing temperature, time, and gas flow rate is explored in an on purpose-built chamber. The results demonstrate that the use of H_2 gas with ultimate purity is absolutely imperative. In addition to annealing in pure H_2 atmosphere, an increased flow rate by admixture of He gas is beneficial to reduce the defect density found in scanning-tunneling microscopy (STM) measurements. The (1×1) periodicity observed in low-energy electron diffraction (LEED) and STM after the H annealing signals the H passivation of the Si DBs in the topmost substrate layer.

Detailed STM studies show smooth 4H-SiC(0001) surfaces with several hundred nanometer wide terraces and predominantly steps with half unit cell height in $\langle 0001 \rangle$ direction, which are terminated by edges in ZZ orientation. Moreover, they reveal long-range potential fluctuations caused by crystal defects, N doping impurities, and the presence of a manifold of surface defects. Scanning-tunneling spectroscopy (STS) measurements demonstrate the presence of a wide band gap, even though a discrepancy to reported literature values is found, most probably due to tip-induced band bending (TIBB).

The main task during the epitaxial growth of bismuthene on SiC is the removal of the H passivation, whereas the formation of a $(\sqrt{3} \times \sqrt{3})$-Si-reconstructed surface must be avoided. This is complicated by the fact that both processes occur at comparable activation energies. This is accomplished by a special evaporation procedure, which comprises a highly dynamic temperature regulation of the SiC substrate via direct current (DC) heating.

The obtained Bi monolayer films are characterized by LEED as well as STM. Their surface coverage and domain size fluctuates significantly due to the variable temperature caused by the DC heating. A Bi re-evaporation process on unreconstructed SiC samples is feasible and often leads to an improved bismuthene coverage of the surface (up to 80%). The small average domain size ($\approx$ 10 nm) resulting from the presence of different, but equivalent nucleation sites of the $(\sqrt{3} \times \sqrt{3})$R30°-Bi reconstruction constitutes a more severe problem that must be resolved for future quantum transport experiments.

X-ray photoelectron spectroscopy (XPS) is used to inspect the stability of the grown bismuthene films. In ultra-high vacuum (UHV), they maintain their chemical and physical properties up to several months. In contrast, exposure to ambient air leads to the irreversible oxidation of the Bi atoms. The finding that bismuthene maintains its initial electronic and chemical properties in a glovebox filled with dry N_2 gas (residual H_2O and O_2 smaller than 0.1ppm) for a comparably long time (i.e., several hours) is encouraging and might enable the film capping in a glovebox atmosphere.

The morphological inspection of grown Bi films with STM shows the presence of step heights corresponding to multiples of SiC bilayers without exception, indicating that the synthesized film has grown homogeneously. Overview scans reveal that the flat honeycomb lattice is accompanied by typical point, but also extended surface defects, i.e., one-dimensional (1D) domain boundaries and disordered areas with arbitrarily-oriented boundaries, in which no bismuthene lattice has grown.

At the interface of these disordered areas and bismuthene, the height, as measured by STM, appears to be increased. A closer inspection with STS demonstrates the presence of defect states in the bulk band gap, which are characterized by spikes in $\mathrm{d}I/\mathrm{d}V$ as long as the probed disordered area is enclosed by a single bismuthene domain. Surface point defects exhibit similar electronic properties.

The 1D domain boundaries evolve when bismuthene domains centered around different nucleation sites of the $(\sqrt{3} \times \sqrt{3})$R30°-reconstruction encounter each other, and constitute a reproducible, distinctive feature of bismuthene on SiC. The pearl-necklace structure apparent in STM gives rise to standing wave patterns in grid spectroscopy measurements. To date, it is not possible to resolve whether this quasi-particle interference is caused by interacting topological edge states or their trivial counterparts.

Within the resolution of the STM, the ideal, defect-free honeycomb lattice is entirely flat. The nominally sixfold symmetry of the honeycomb lattice is affected by the presence of the C sublattice in the topmost SiC bilayer, which causes the appearance of a weak triangular pattern. Local-density-of-states (LDOS) maps demonstrate that the honeycomb symmetry is persistent both in the occupied as well as unoccupied states. STS curves unveil a huge band gap of $E_{\mathrm{gap}}^{\mathrm{exp}} \approx 800\,\mathrm{meV}$, fairly comparable to the theoretically predicted value.

Angle-resolved photoelectron spectroscopy (ARPES) is used to explore the band struc-

ture of bismuthene on SiC. Excellent agreement of the density-functional-theory (DFT)-predicted and experimentally-probed band dispersion in k space is found. It is worth to note that the magnitude of the valence band's Rashba splitting at the K point determined by the complementary methods ARPES, STS and DFT coincides, which makes a strong case for the formation bismuthene on SiC as described in theory.

Edge states are a key attribute of QSHIs and inspected in detail with STM and STS. A clear-cut situation is encountered at atomic steps of the SiC substrate. The preference of the substrate to form ZZ edges at atomic steps translates into AC edges of bismuthene, which grows in a $(\sqrt{3} \times \sqrt{3})$R30° reconstruction. The additional charge density apparent at these boundaries exhibits the periodicity of an AC edge and is caused by a highly-localized edge LDOS signal (decay length $\xi = 4.3\,\text{Å}$), which is found at the edges of both the upper and lower bismuthene film. Importantly, the observed signal spans the entire two-dimensional (2D) bulk band gap and reveals a close-to-constant LDOS as expected from the band structure based on nanoribbon calculations, except for a pronounced dip at zero bias. The absence of modulations in the $\mathrm{d}I/\mathrm{d}V$ signal at a kinky section of the step supports the assumption that the observed LDOS arises from topological edge states.

Lastly, the suppressed LDOS at the Fermi level is scrutinized with high-resolution STS. Here, too, the V-shaped $\mathrm{d}I/\mathrm{d}V$ signal probed at the step edge remains unaffected by an almost 90° kink. Such a scenario would be expected to cause quasi-particle interference if it was encountered by trivial states not protected from single-particle backscattering.

The edge state's confinement to a narrow 1D channel with less than a nanometer width raises the relevance of possible electronic correlations. Therefore, temperature-dependent measurements covering more than two orders of magnitude are inspected. Excellent agreement of model curves and experimental LDOS as well as universal scaling in energy and temperature demonstrate that the edge states can be described in the framework of Tomonaga-Luttinger liquid (TLL) theory. The collected data originates from four different samples as well as different tips and sample spots. Therefore, it seems unlikely that the observed behavior is caused by a dynamical Coulomb blockade, which mimics the collapse of the rescaled spectra only for one specific set of parameters. Other reasons for the observed dip can be excluded with high confidence.

Based on the fitted model curves and the assumption that the LDOS stems from helical edge states, a power-law exponent $\alpha = 0.40 \pm 0.04$ is extracted and translates into an edge state interaction parameter $K^{\mathrm{exp}} = 0.42 \pm 0.02$. A theoretical estimate of the Luttinger parameter for edge states of bismuthene on SiC yields the same magnitude ($K^{\mathrm{th}} = 0.5 \pm 0.1$). This indicates that AC edge states are in the regime of strongly repulsive interactions, in which correlated two-particle scattering might be a relevant process at low energies.

Outlook. Ultimately, outstanding agreement between the experimental data and the theoretical modeling has been found for many structural and electronic characteristics of bismuthene on SiC. Yet, as a first step towards real-world applications, it is desirable to clarify whether its edge states indeed exhibit the quantized conductance of $2e^2/h$ associated with QSHIs. At present, this is hampered by the following reasons.

Substrate conductivity. An important step towards the realization of quantum transport devices involving bismuthene is the development of a growth process on a non-conducting

SiC surface. So far, all samples have been grown on highly N-doped SiC samples. For the determination of the transport characteristics, a pristine edge state conduction without the contribution of trivial bulk electrons must be achieved. This may be accomplished in two ways. The obvious solution, i.e., growth on insulating SiC substrates, requires the definition of an entirely new growth process that does not involve DC heating but employs a different technique (e.g., radiative laser heating). Ideally, this heating method would also give rise to a more homogeneous sample temperature and lead to more reproducible growth results. Alternatively, one could use insulating SiC layers grown on top of N-doped, conducting SiC samples. Naturally, this solution might provide a faster access to bismuthene devices, as one could rely on the established growth recipe. Moreover, the conducting SiC substrate layers could serve as the backgate in transport experiments, which is anyway required.
Domain size. Furthermore, the domain size has to be increased to a level where lithography becomes feasible by carrying out systematic growth studies. At present, the applicable growth parameters are limited by the temperature required for desorbing the H atoms passivating the Si DB. Frequently, it is high enough to cause a Si-rich $(\sqrt{3}\times\sqrt{3})$ reconstruction. If it was possible to obtain H-free SiC surfaces that remain unreconstructed, e.g., by prolonged heating at lower temperature, the Bi deposition rate could be lowered substantially, resulting in fewer nucleation centers. Again, a more reliable and homogeneous substrate temperature would be highly beneficial to carry out these systematic studies.
Topological character of the domain boundaries. Even if the domains are enlarged, it will be mandatory to resolve whether the states emerging at the domain boundaries within the bulk band gap constitute topologically trivial or non-trivial states. While the former might appear due to a structural relaxation of the lattice at the interface between two domains, the latter could appear as the domain boundary constitutes an edge of each bismuthene domain. At the moment, a reliable theoretical description of the domain boundaries is not feasible. Their atomic structure cannot be resolved with STM due to the intrinsic contribution of the LDOS and structure to the probed current. Hence, the suggestion to inspect the samples with atomic force microscopy, which may provide the same resolution as STM but resolves structural properties much better, is quite obvious.
Capping layer. Lastly, a suitable capping layer protecting bismuthene from degradation in ambient air must be found. A promising candidate material is hBN, which has been successfully used to cap graphene samples and transition metal dichalcogenides, and would allow to fall back to established techniques. Of course, a capping layer prohibits the inspection of samples with STM/STS and ARPES. Optical spectroscopy might be a suitable method to characterize the electronic properties of bismuthene samples after capping.

If these problems can be resolved, the surface system bismuthene on SiC offers fascinating opportunities, which arise from its production via epitaxial growth and comprise, e.g., the straightforward control of the armchair edge state density and direction by choice of SiC substrates with suitable miscut, or the possibility to manipulate its topological properties by overgrowth with superconducting or magnetic materials. However, the most distinctive feature, which distinguishes bismuthene on SiC from any other TI compound known to date, is certainly its large bulk band gap at the Fermi level, rendering it a candidate material to observe the QSHE at room temperature.

Appendices

A Experimental Setups and Preparation Procedures

A.1 Ex-situ SiC Preparation

Three types types of wafers were 4H-SiC wafers were used for the measurements conducted within this thesis. Their technical data is summarized in Tab. A.1.

Sample mounting. The SiC substrate strips are mounted on an Omicron direct current sample holder, see Fig. A.1, where the sample is hovering over the Mo plate and the clamps are electrically decoupled, such that a potential difference over the semiconductor sample can be applied. The current accompanying the voltage drop heats up the wafer piece. Advantages of this so-called direct current heating (DC heating) are its cleanliness, as in the first place only the substrate is heated, and its high dynamic range, as a reduction/increase of the applied current is directly reflected in a drop/raise of the temperature. The main disadvantage is that the temperature over the entire sample is not homogeneous, which is a problem for preparation recipes that require a very percise temperature regulation. In order to minimize the influence of the Schottky barrier between semiconductor surface and metal clamps, a thin, flexible piece of metal foil is wrapped around the stripe ends, compare to Fig. A.1. Rh has proven to deliver the best compromise of low resistance ($2.1\,\Omega$cm vs. $7-14\,\Omega$cm without foil) and stability against hydrogen embrittlement during annealing [281].
A further measure to improve the electrical contact with the DC plate metal clamps is the roughening of the wafer stripe edges with a diamond scratching pen, which is intended to crack the surface oxide layer and to enlarge the contact area between clamp and SiC surface (visible at the left, slightly opaque edge in Fig. A.1).

Wet-chemical treatment. After that, the SiC samples are rinsed with ultra-pure organic solvents, i.e., acetone, isopropanol and methanol, to remove grease and other organic remnants of the polishing procedure.
Additional wet-chemical treatment in Caro's acid and subsequent etchnig in buffered HF, as described in the majority of published papers (see also App. B.1), was used during

Short name	planar	2°off	4°off
Miscut in $\langle 1\bar{1}00\rangle$	($< 0.5°$ in all dir.)	2°	4°
Resistivity (Ωcm)	0.01–0.03	0.01–0.03	0.015–0.028
Roughness (nm)	< 0.2	–	<0.5
TTV/Bow/Warp (μm)	$\leq 25/\leq 25/\leq 25$	$\leq 15/\leq 15/\leq 15$	$\leq 15/\leq 25/\leq 25$
Micropipe Dens. (cm^{-2})	–	–	< 15
Thickness (μm)	330 ± 25	330 ± 25	350
Piece size (mm × mm)	2.5×12	2.5×12	2.5×10

Table A.1 Technical data of the different types of 4H-SiC wafers as specified by the manufacturer used for the experiments in this thesis. The Si-face is epi-ready, the C-face optically polished. All wafers are N doped.

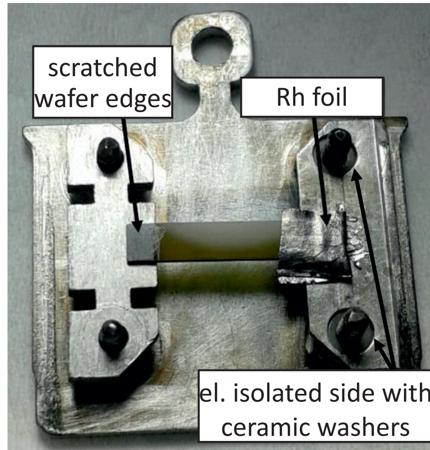

Figure A.1 Omicron direct current sample holder with a SiC sample, which is used for the preparation of bismuthene on SiC. The right side of the sample holder is electrically insulated from the rest of the setup and therewith enables to apply a voltage between both sides of the semiconductor strip. This enables to direct current heating of the substrate. The edges of the SiC wafer are roughened and wrapped in Rh foil to improve the electrical contact toe the sample holder.

the initial experiments but did not provide any advantage over samples prepared without them and has therefore been omitted.

At the end of the ex-situ preparation, the SiC substrate/sample holder is blow-dried with N_2 gas, such that particles from, e.g., the scratching procedure are removed, and thereafter, the sample is transferred into the H_2 annealing chamber.

A.2 Dry Hydrogen Annealing Setups and Process Guiding

The in-situ preparation starts with a thorough degas up to 1000°C. The pressure is kept lower than $p_{\text{degas}}^{\text{H2 cham.}} < 1 \times 10^{-7}$ mbar. The high temperature leads to a slight Si depletion, but removes weakly bound adsorbates and the oxide layer on the surface [30, 33]. After that the sample is cooled down by gradually reducing the current through the sample. The execution of this process step requires several hours and is the most time-consuming in-situ step in the entire bismuthene production.

The H_2 annealing step has been conducted in two different setups with a largely different process guiding, which are described separately in the following.

H Annealing in Static Gas Atmosphere

Setup for static H annealing. The original setup of for annealing in static H_2 atmosphere consists of a CF63 double cross, which is placed on top and can be separated via a gate valve from a Pfeiffer pump stand. The sample is introduced by the vacuum suitcase consisting of a transfer rod, a *CapaciTorr D100* NEG pump by SAES Getters, and its receptable is contacted with feedthroughs, such that the sample can be heated with direct current and monitored with pyrometric temperature control via the top viewport. The pressure is measured with a piezoresistive pressure gauge. Gas bottles of purity 5.0 are attached with simple aluminum pressure reducers, and the gas is additionally filtered to higher purity with a filter from SAES Getters. A fine dosage valve allows a precise control of the gas pressure. Note that this setup does not comprise a load lock chamber, such that it had to be baked prior to annealing of every sample.

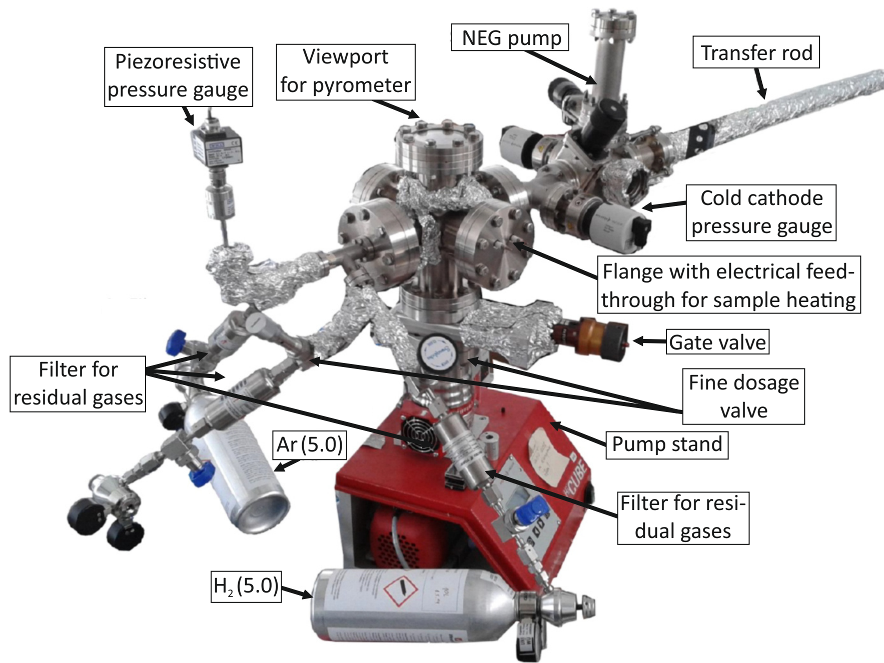

Figure A.2 Chamber for annealing in dry, static H_2 gas. Important components are labeled.

Process guiding in static gas atmosphere. The chamber is decoupled from the turbo pump by closing the gate valve. Subsequently, it is slowly filled with purified H_2 gas until the pressure reading shows $p_{H2} = 950\,\text{mbar}$. After that, the DC heating is restarted and the current-controlled power is raised until a temperature of $T_{\text{stat}}^{\text{ann},1} \approx 1050\text{–}1150\,°\text{C}$ is displayed on the pyrometer (emissivity $\eta = 85\%$ for all measurements). The required heating current largely depends on the specific sample, which is a consequence of varying contact area (Rh foil, scratching) and clamping pressure. Typically, 2–3 A and 15–25 V are required. During the annealing time ($t_{\text{stat}}^{\text{ann},1} \approx 20\text{–}40\,\text{min}$) these values have to be reduced continuously to account for the heating of the (static) H_2 gas atmosphere. Finally, the sample temperature is reduced by slowly reducing the current. In order to guarantee a save removal of the H_2 gas from the chamber it is waited until the hot gas atmosphere has cooled down. Then the turbo pump is restarted and the gate valve is opened.
When the base pressure is lower than $p < 5 \times 10^{-8}\,\text{mbar}$ the valve is closed and the procedure is repeated. Annealing time and temperature are lowered to $T_{\text{stat}}^{\text{ann},2} \approx 1000\text{–}1150\,°\text{C}$ and $t_{\text{stat}}^{\text{ann},2} \approx 2\text{–}4\,\text{min}$, respectively, while the other parameters remain unchanged.
The first step is intended to remove polishing damage from the surface. The purpose of the second step is to supply a cleaner gas atmosphere, as, in contrast to the reports in literature, no H_2 gas flow is used. This causes an increasing amount of Si- and C-based molecules (SiH_4 and CH_4 and fractions of it) in the chamber over time, such that the probability of their redeposition might increase.
Ultimately the sample is transferred in the UHV suitcase, which is attached to the STM chamber load lock for surface analysis.

H Annealing in Ultra-Pure Flowing Gas

Setup for flowing gas H_2 annealing. When designing the new SiC preparation setup special attention was given to the elimination of the deficiencies of the static annealing setup. In particular, this concerns the H_2 gas purity. To avoid residual contamination of the process gas only UHV compatible connections are used. Upon gas bottle exchange an Ar gas of purity 6.0 is used to purge the lines of H_2 and He. In this way, it is assured that large quantities of air are removed, especially O_2 and H_2O, and therewith extendes the lifetime of the gas purifying filters. Furthermore, the entire gas rack is drafted such that all tubes can be baked at $T = 120\,°C$ and evacuated by a turbo pump. To provide optimal gas cleanliness in the first, place only H_2 and He gas of purity 8.0 is used. In this way, an ultra-pure process gas is entering the annealing chamber. He gas is admixed to H_2 gas to increase the gas flow.

The vacuum chamber itself still consists of a 6-way CF63 cross. Sample receptacle and the pyrometer-controlled temperature measurement remain unchanged, as well. The chamber evacuation is done with a turbo pump and external rotary vane pump to achieve a pressure in the range of 2×10^{-10} mbar. Chamber and turbo pump can be separated with a gate valve.

An important change is the additional pumping port that leads to a pressure regulator, which keeps the chamber pressure constant while a continuous flow of gas is precisely controlled with the mass flow controllers. The pressure regulator is connected to a scroll pump, where the H_2/He gas mixture is strongly diluted with dry N_2 gas before it is pumped to outer air. In this way, the H_2 gas concentration becomes smaller than the (lower) explosive limit of 4% [282].

Another bottleneck of the old setup, which was the necessity to break the vacuum after every single sample, was circumvented by implementation of a load lock chamber. Three samples can be introduced, subsequently annealed and loaded to the vacuum suitcase, allowing for a significantly faster work flow than previously.

H_2 annealing in flowing gas atmosphere. The process control for the newly-designed H_2 annealing chamber starts similarly with decoupling the chamber from the turbo pump with a gate valve as soon as the base pressure after the intial degas is better than 1×10^{-9} mbar. Then, the scroll rough pump is started and the pressure regulator is set to $p_{\text{set}}^{\text{ann}} = 950\,\text{mbar}$. a specific gas flow rate of H_2 and most of the times He is defined and the chamber fills up until the pressure regulator starts to work to maintain the desired process pressure. The specific values of H_2 and He flow are discussed later in Sec. 5.3.

At this point, a continuous flow of H_2 and He and a steady pressure is present and the substrate DC heating is initiated. As the gas atmosphere is constantly flowing and does not heat up, a higher sample temperature and accordingly heating current is required to crack H_2 molecules on the semiconductor surface. Typically, values in the range of 2.5–3.2 A and 19–21 V are required to reach the annealing temperature $T_{\text{flow}}^{\text{ann,1}} = 1230\,°C$, which is kept for $t_{\text{flow}}^{\text{ann,1}} \approx 2\,\text{min}$. Then, the temperature is slightly lowered $T_{\text{flow}}^{\text{ann,1}} = 1150\,°C$ and kept there for $t_{\text{flow}}^{\text{ann,2}} \approx 5\,\text{min}$. Note that a full exchange of the gas atmosphere is not necessary anymore as it is constantly renewed. After that the sample current is ramped

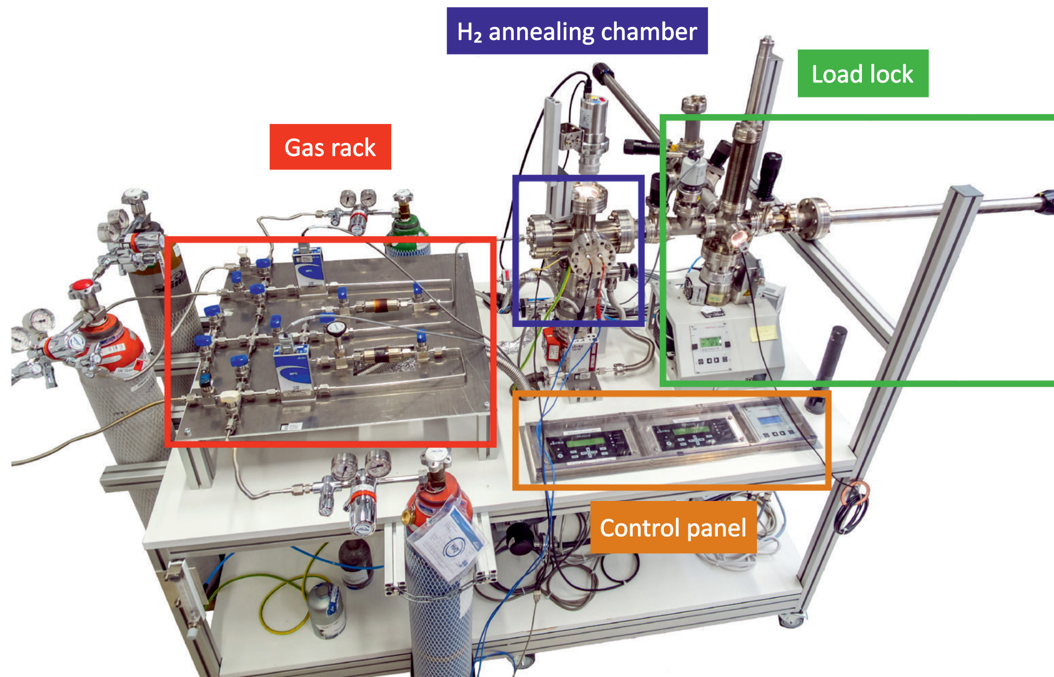

Figure A.3 Setup for H_2 annealing in ultra-pure flowing atmosphere.

to 0 A within $\approx$ 7 min. Finally, the chamber is evacuated and the sample is transferred in the UHV suitcase.

The first higher temperature step is implemented to attain a high as possible etching rate, leading to a smooth surface and large terraces. However, the high temperature bears the danger that the surface becomes C-rich under our annealing conditions. Therefore, the temperature is lowered in the second step to ensure a stoichiometric surface termination.

A.3 STM Setup

The STM is part of a UHV setup consisting of a preparation and analysis chamber. Both feature a base pressure of $p = 3 \times 10^{-11}$mbar.

The preparation chamber comprises a manipulator allowing for DC heating and indirect heating via a heating element below the sample receptacle. The manipulator exhibits a yxz translational and rotational degree of freedom around the manipulator axis. A low-temperature effusion cell from *Dr. Eberl MBE-Komponenten GmbH* is used for Bi deposition. An optical *SPECTALEED* instrument from *Scienta Omicron GmbH* (formerly known as Omicron NanoTechnology GmbH) is part of the chamber, as well.

The STM and STS measurements presented in this thesis have been performed in a commercial *LT STM* setup from *Scienta Omicron GmbH*. Its LHe cryostat exhibits a maximum hold time of $\approx$ 50h, and the lowest measurement temperature is $T = 4.35$ K. The probing temperature is measured at the sample stage, which is connected to the inner cryostat via three stainless steel cones (cooling and sample exchange position) or three springs (measurement position). The piezostack consists of a coarse xyz piezo and a tip piezo. The

sample stage is equipped with a Si diode heating element, allowing to raise the probing temperature up to $\approx 130\,\mathrm{K}$. A lock-in amplifier from *SRS* is connected to the system.

A.4 ARPES and XPS Setup

The ARPES and XPS setup are attached to a separate UHV chamber with a base pressure around 3×10^{-10}mbar. A *Phoibos 100* hemispherical electron analyzer from *SPECS Surface Nano Analysis GmbH* with 24meV energy resolution is the central part of the setup. A *UVS 300* He duoplamatron lamp from *SPECS Surface Nano Analysis GmbH* with $h\nu = 21.22$eV is used for UV PES experiments. A six-axis manipulator (*Carving* from *SPECS Surface Nano Analysis GmbH*) allows to probe the entire k space. The sample receptacle can be cooled with LHe flow cryostat. The XPS measurements are conducted with a Al K$\alpha_{1,2}$ line. Neither the He lamp nor the X-ray gun are monochromatized. Due to the poor thermal contact of the SiC substrates mounted on the DC sample holder (see Fig. A.1) and the cooled manipulator, the lowest measurement temperature for these samples has been checked with a Si diode attached to such a substrate and is $T = 23\,\mathrm{K}$.
Moreover, the sample periodicity after transfer from the growth chamber via the vacuum suitcase (see Sec. A.5) may be checked with an optical LEED by *SPECS Surface Nano Analysis GmbH*.

A.5 Vacuum Suitcase

Due to the high Bi vapor pressure during growth and the growth routine developed for bismuthene samples (see Sec. 6.1), Bi epitaxy is carried out in a dedicated growth chamber. To allow the sample inspection with low-temperature STM/STS and ARPES, the grown samples have to be transferred to different chambers, which is accomplished with two home-built vacuum suitcases. Both consist of a transfer rod, a sample garage that allows the transportation of up to eight samples, a cold cathode gauge by *Pfeiffer vacuum* and a non-evaporable getter pump *CapaciTorr* from *SAES Getters*. A gate valve from *VAT* separates the samples that are stored at $p_{\mathrm{suitcase}} < 1 \times 10^{-9}$ mbar from ambient atmosphere.

B Additional Information on 4H-SiC Substrates

B.1 SiC Preparation and H Annealing Parameters in Literature

Before heating the sample in H_2 gas atmosphere it is treated with standard wet-chemical treatment procedures in organic solvents or RCA cleaning procedure [283] in order to degrease the sample as supplied by the manufacturer. Many authors also include a step in acids and/or buffered HF solution to remove the surface oxide layer prior to introduction in the H etching chamber [31, 32, 40–42, 200–202, 284, 285].
The H annealing is commonly done in a quartz tube reactor, which in most cases was a hot or cold wall chemical vapour deposition chamber evacuated with a turbo molecular pump to a pressure of around 1×10^{-6} mbar or better. Sample heating is usually accomplished by a graphite susceptor heated with high-frequency inductive radiation or halogen lamps [31, 32, 40, 42, 200, 201, 284, 285]. Xie et al. coat the susceptor with BN to avoid contamination with residual SiC from previous preparations [40], while others aim to achieve a stoichiometric atmosphere by on-purpose coating with SiC (see, e.g., [32, 201]). Sample heating with a hot Ta strip was also reported [41].
The H_2 gas is filled into the chamber up to atmospheric pressure (e.g. [31, 40, 201]) or slightly below ([32, 201]), and a gas flow of $5 - 20$ lpm is applied [32, 285]. Then, the sample is heated for $10 - 80$ min up to temperatures ranging from 1000°C [31, 44, 285] to 1600°C [40, 41, 200]. This large variety in temperature results from different methodologies for temperature measurement (by a thermocouple or pyrometric; on a sample plate or graphite susceptor block; etc.), such that a direct transfer to our setup is not reasonable. It was also pointed out that additional, ad-mixed gases might increase (e.g., HCl [40]) or decrease (e.g., propane [286]) the etch rate and influence the surface morphology [287].

B.2 Polymorphism of SiC

Depending on the stacking order different lattice structures can be constructed with the basic unit of tetragonally-coordinated Si and C atoms, which leads to more than 200 SiC polytypes [184]. The most important polytypes are 4H-SiC, which is the polytype with lowest overall crystal energy [288] and is used as a substrate for bismuthene growth, and 6H-SiC (not described here), while 3C-SiC and 2H-SiC conspire the fundamental polytypes. Here, "C“ and "H“ is denoting their cubic and hexagonal crystal structure, respectively, while the number denotes the A, B and C bilayer plane periodicity in the $\langle 111 \rangle$ (cubic) or $\langle 0001 \rangle$ (hexagonal) stacking direction [184]. A, B, and C denote the lattice sites giving rise to a close packed structure in the hexagonal lattice (see Fig. B.1**a**). The difference between cubic and hexagonal stacking is illustrated in Fig. B.1**b**: for the cubic structure, nearest neighbor bonds of an adjacent Si/C pair are rotated by 60° in stacking direction (so-called *staggered* orientation [289]), giving rise to a zinc blende crystal structure, while for a hexagonal stacking the bonds are mirrored in a plane perpendicular to the SiC bilayer bond direction (wurtzite structure, *eclipse* orientation [289]. These

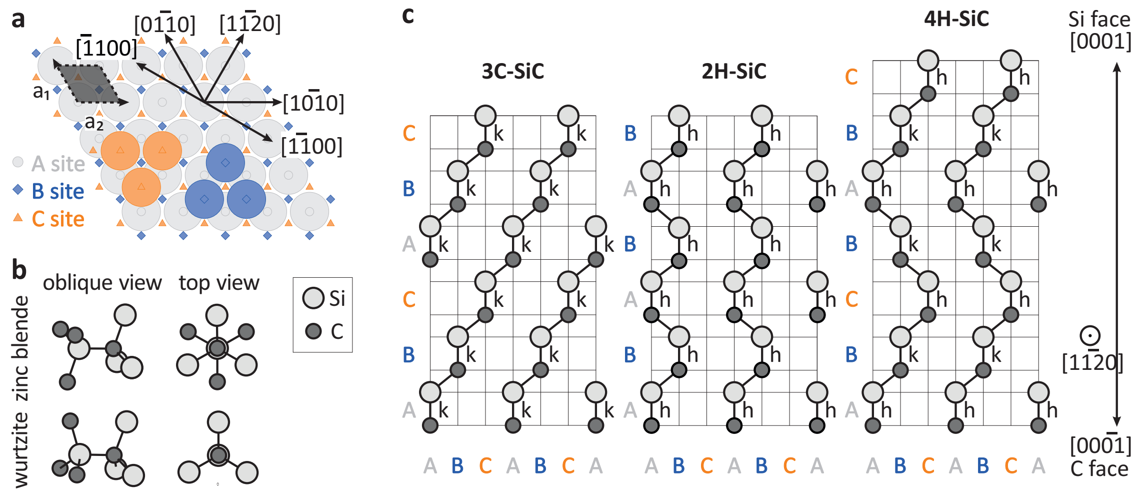

Figure B.1 **a** Three different sites A, B, C give rise to a close-packed structure. Certain high-symmetry directions are denoted with black arrows. **b** The nearest neighbor bonds of adjacent Si and C atoms along ⟨0001⟩ direction are either rotated by 60°, giving rise to a zinc blende crystal structure, or aligned, resulting in a wurtzite structure. **c** Stacking order of SiC bilayers in a plane along ⟨11$\bar{2}$0⟩ direction. The 3C-SiC and 2H-SiC structures are purely zinc blende and wurtzite, respectively, with all atoms sitting on k and h sites. Other polytypes, such as the 4H-SiC structure shown on the right, are mixtures of both fundamental polytypes. The 4H stacking sequence is $ABCBABCB...$. *Fig.* ***c*** *adapted with permission from Ref. [184]. Copyright ©2007 Springer Nature.*

two scenarios are energetically almost degenerate, which gives rise to the large number of different stacking sequences, i.e., polytypes [196], of which some are illustrated in Fig. B.1**c**. For 3C-SiC, the stacking order is $ABCABC...$, resulting in a pure zinc blende structure and an overall cubic lattice. The other extreme case is the 2H-SiC polytype, which crystallizes in a hexagonal pure wurtzite structure with order $ABAB...$. Consequently, each atom is sitting on cubic k or hexagonal h sites in the two cases. All other polytypes are composed by a mixture of h and k sites [184, 188, 195].

C Additional Information on H Annealing of SiC Samples

C.1 Miscut-SiC(0001) Substrates

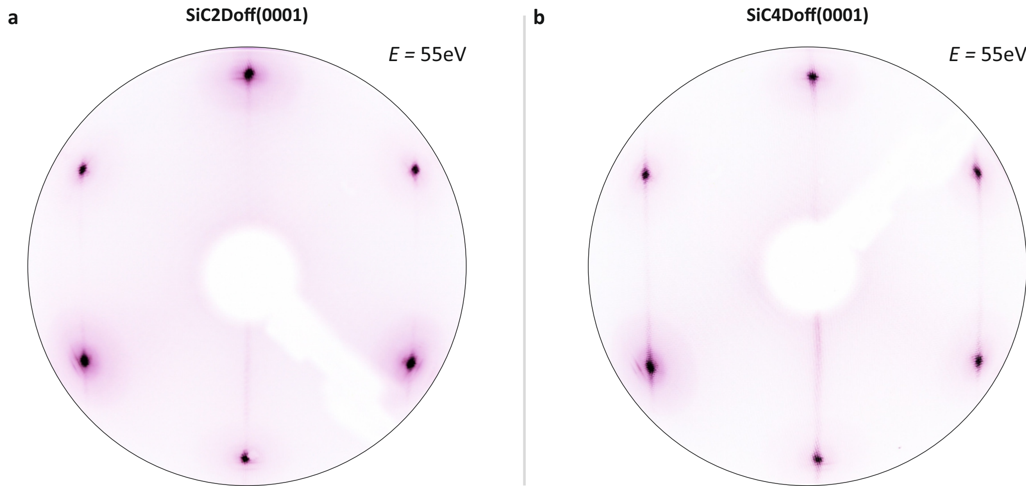

Figure C.1 LEED images recorded on **a** 2° Miscut-SiC and **b** 4° Miscut-SiC Substrates. Both images show intense (1×1) diffraction spots and a low background signal. A threefold-symmetric spot intensity is observed, in difference to nominally on-axis SiC samples. 1D stripes are seen due to the additional periodicity in the miscut direction. Note: the image recorded of the 2° Miscut-SiC sample is rotated by 90° clockwise with respect to the measurement geometry in order to align the crystallographic directions of both samples, which are different due to an inverted wafer cutting direction.

All samples displayed in the main text have been nominally on-axis 4H-SiC(0001) wafers with very large terrace planes, such that only a minor portion of the sample surface is covered by edge states of bismuthene at substrate step edges. With the intention to increase the edge state density on bismuthene, miscut SiC samples have been prepared, as well, namely 4H-SiC 2°off(0001) and 4°off(0001) towards $\langle 1\bar{1}00 \rangle$ direction (named shortly 2° Miscut-SiC and 4° Miscut-SiC, respectively).

Measurements and DFT calculations on the Si-terminated 6H-SiC(0001) surface propose a step bunching to single, full unit cell steps for vicinal angles in $\langle 1\bar{1}00 \rangle$ direction, independent of the precise value of miscut[28] [190, 194]. Only large miscut angles provoke the bunching of several unit cell steps. Therefore, the terrace width is calculated with $d(\alpha) = c^{\mathrm{SiC}} / \tan(\alpha)$, where $c^{\mathrm{SiC}} = 10.08\,\text{Å}$ is the full 4H lattice constant, and yields $d^{\mathrm{th}}(2°) = 28.9\,\mathrm{nm}$ and $d^{\mathrm{th}}(4°) = 14.4\,\mathrm{nm}$. These values are small compared to terrace planes with hundreds of nanometer extension found on planar 4H-SiC(0001) samples and suitable to drastically increase the edge state signal in relation to the bulk signal.

[28] Small miscut angles in $\langle 11\bar{2}0 \rangle$ direction lead to half unit cell high steps, as found on the nominally on-axis SiC(0001) substrates [190, 194].

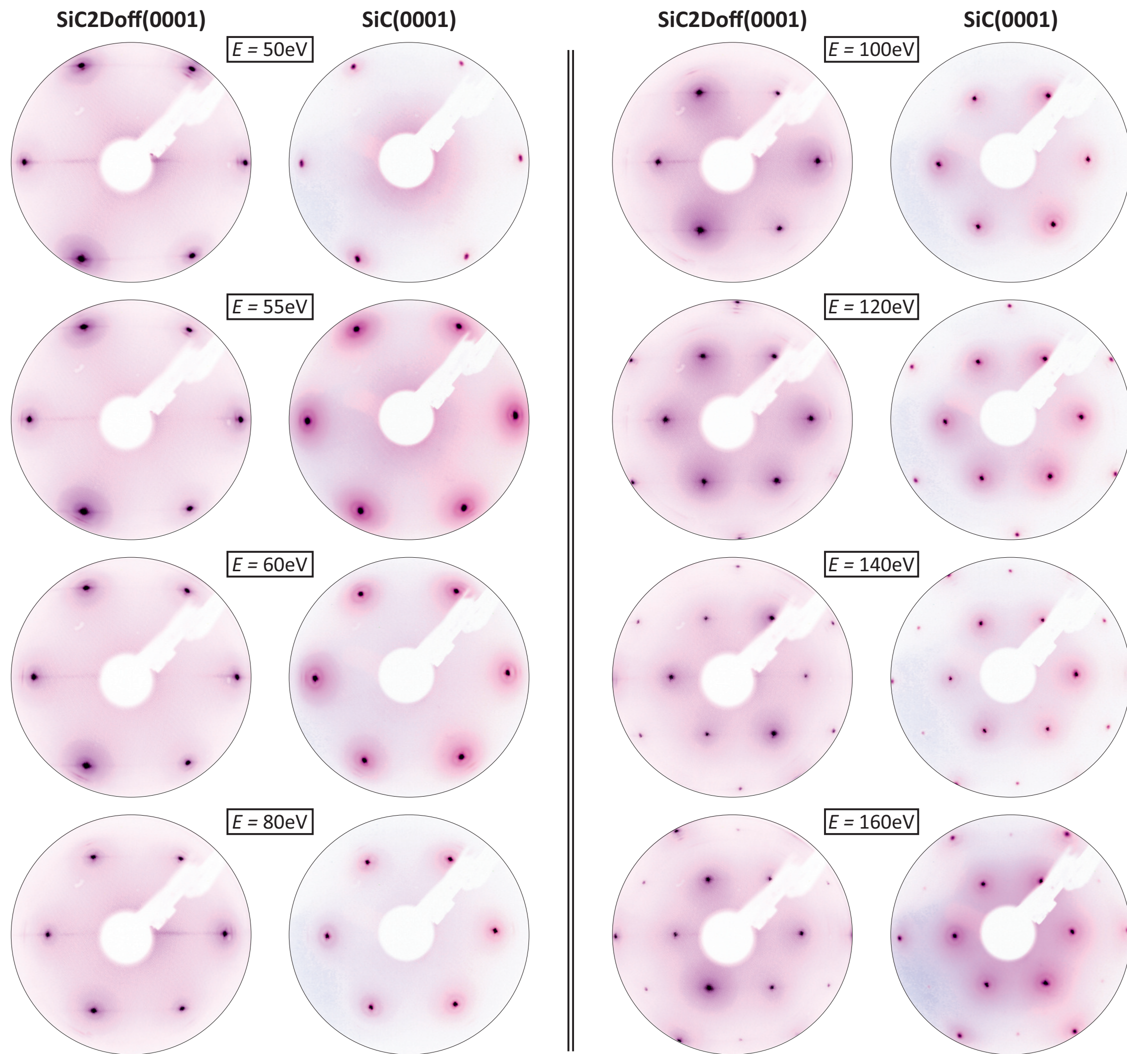

Figure C.2 Whereas a distinct triangular imbalance of the spot intensity is found at certain energies on the 2° Miscut-SiC samples, a sixfold symmetric diffraction pattern is observed for planar samples. The same observations are found on 4° Miscut-SiC samples.

LEED. Fig. C.1**a**, **b** show LEED images of 2° Miscut-SiC and 4° Miscut-SiC samples recorded after a two-step H_2 annealing process as described in Sec. 5.4. Both LEED images display a (1×1) reconstruction with negligible background intensity and sharp diffraction spots. A feature not observed for on-axis 4H-SiC samples is an imbalance of the diffraction spot intensity, which is in turn better seen on the 2° Miscut-SiC sample shown in Fig. C.1**a**. The effectively threefold-symmetric diffraction pattern might be the result of the preferential existence of one specific SiC bilayer domain at the surface, i.e 4H1/2 or 4H1*/2*, which differ by a 60° rotation of the Si–C bond directions (compare to Fig. 5.1). In other words, mostly full 4H-SiC unit cell steps should be present within the coherence length of the LEED spot. In contrast, an equal distribution of 4H1/2 and 4H1*/2* bilayers at the surface caused by dominantly half unit cell steps as found on planar SiC(0001) substrates evokes a hexagonal LEED pattern (see, e.g., Fig. 5.10) [196].

A sequence of LEED images acquired at different energies is shown in a comparative way for 2° miscut and planar samples in Fig. C.2 and confirms this finding. The crystallographic directions at which higher intensity spots are imaged are dependent on the probing energy.

A noticeable switch occurs, e.g., between 140 eV and 150 eV. Notably, this flip of high intensity directions occurs at the very same energies on 4° Miscut-SiC samples.
Another distinct property not observed in LEED images of planar samples is the existence of a faint, stripe-like intensity along one direction. The off-axis orientation of the sample normal introduces a superlattice periodicity that is equal to the step distance [290]. If the variation of this periodicity is small or even fixed, as for vicinal surfaces with high miscut, a spot splitting into subspots appears [290]. The spacing of these subspots is proportional to the inverse of the step distance $1/d\alpha$ and consequently very small in our case, as the terrace width (> 140 Å) is fairly large compared to the in-plane interatomic distances of SiC (≈ 3 Å). Furthermore, variations of the step distance that might be present in our etched samples will cause a blurring of the subspots. An inspection with high-resolution spot-profile analysis LEED (SPA-LEED) instead of conventional LEED is required to resolve these details, which is beyond the scope of this work[29].

STM. In order to inspect the surface structure, large scale STM images are conducted and shown in a side-by-side comparison for 2° Miscut-SiC and 4° Miscut-SiC in Fig. C.3**a** and **b**, respectively. The STM images reveal terrace planes strongly confined in $[1\bar{1}00]$ direction, while their extent in $[11\bar{2}0]$ direction is beyond the limits of the depicted scan frame. Well-known surface defects similar to the ones discussed in Fig. C.5 are visible due to a small z derivative signal added to the CCI scans. The step edges are mostly straight, although perfect ordering is absent, with frequent insections at the step edges. Occasionally, larger indentations of the step edge are seen (more pronounced for the 2° Miscut-SiC sample).
A 200 nm line profile displayed in Fig. C.3**c** and **d** discloses that the terrace width is varying significantly and a much higher step density is found on the 4° Miscut-SiC sample. Moreover, it demonstrates that the terrace planes are separated exclusively by full 4H-SiC steps ($\Delta z \approx 10$ Å) on both samples, which causes the threefold-symmetric LEED pattern shown in Figs. C.1 and C.2. The evidenced bilayer bunching to 4H-c^{SiC} steps is in line with DFT predictions for small miscut angles in $[1\bar{1}00]$ by Borovikov and Zangwill [190], and it is in contrast to the predominantly observed 2H-c^{SiC} steps apparent for on-axis substrates annealed in flowing gas atmosphere.
In order to get an unbiased estimate of the average terrace width, a 2D Fast Fourier transform (2D FFT) of the measured scan frames is shown in Fig. C.3**e** and **f**, even though much larger scan frames would be desirable for better statistics. As the atomic corrugation is not resolved by this scan frame, the only contributor to peaks observed in the FFT is the additional periodicity produced by the stepped surface. Indeed, a high intensity is found in the direction of the miscut, which resembles rather a row than isolated peaks due to the step width variation. Nevertheless, the line profiles shown in Fig. C.3**g** and **h** unveil peaks both for 2° Miscut-SiC and 4° Miscut-SiC samples. In case of the smaller miscut and for few samples analyzed, a main peak corresponding to an average terrace width of $d^{\mathrm{exp}}(2°) \approx (27 \pm 2)$ nm is extracted apart from smaller, less relevant peaks. This compares pretty well to the calculated theoretical width ($d^{\mathrm{th}}(2°) = 28.9$ nm). The 2D FFT pattern

[29] An analysis of 4° Miscut-SiC samples with SPA-LEED in terms of the average terrace width and variation dependent on the H_2 preparation parameters can be found by the interested reader in Ref. [291]

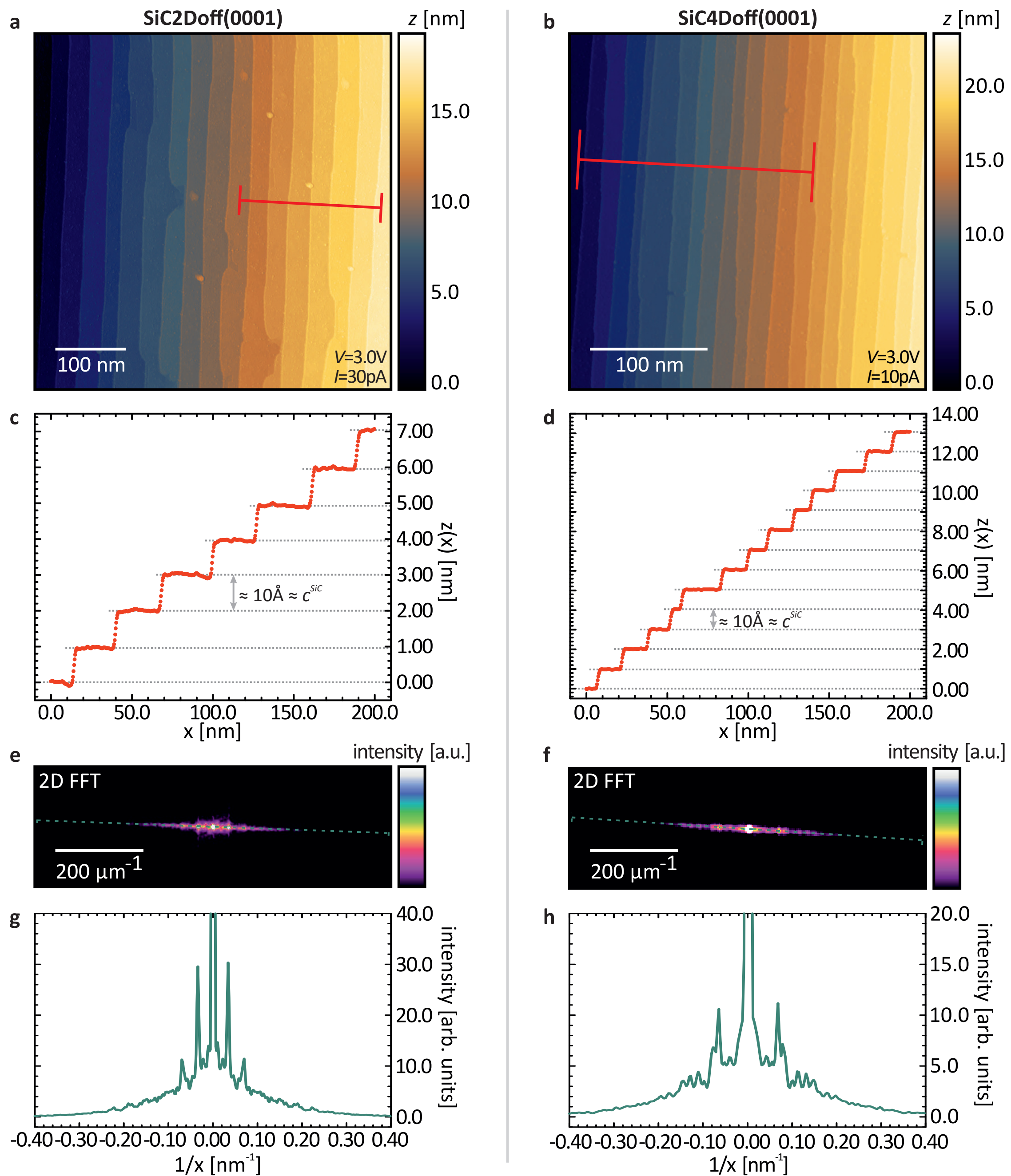

Figure C.3 Large scale STM image showing the morphology of **a** 2° and **b** 4° Miscut-SiC samples. Due to the high z range a small amount of the horizontal derivative is added to the CCI for improved perception of the structure while the original z scale bar is maintained. The data is leveled such that the normal of the planes is pointing out-of-plane. In reality it is inclined by 2° and 4°. Both images demonstrate the presence of parallel, mostly straight step edges after the etching. Only rarely, larger indentations are observed, more pronounced on the 2° Miscut-SiC sample. **c** and **d** Line profiles ($x = 200\,\text{nm}$) extracted and averaged in the area marked by the red bar in **a** and **b**. Notably, full 4H-SiC unit cell steps are found. The average terrace width of 4° Miscut-SiC is approximately half as large as on 2° Miscut-SiC. **e** and **f** 2D FFT and corresponding line profiles (**g** and **h**) of the STM images shown in **a** and **b**.

of several 4° Miscut-SiC samples shows a clear peak corresponding to $d^{\text{exp},1}(4°) \approx 15\,\text{nm}$, which matches very well to the theoretical value for 4° miscut ($d^{\text{th}}(4°) = 14.4\,\text{nm}$). Recent results indicate that the step width variation can be controlled to a certain extent by parameter tuning during H_2 annealing [223].

Conclusion. The 2° and 4° Miscut-SiC surfaces produced by H_2 annealing are of comparable quality as the planar samples. Notably and in contrast to on-axis substrates only 4H-SiC unit cell high terrace steps are found. This is of high importance for research on the influence of the spin-orbit interaction on the spin-split band structure or the Spin-Berry curvature, both deducible from circular dichroic spin-resolved ARPES [292].

C.2 Tested H Annealing Parameters in Flowing Gas Atmosphere

H_2 fl. [slm]	He fl. [slm]	p_{ann} [mbar]	$T_{ann1/2}$ [°C]	$t_{ann1/2}$ [min]	LEED	STM terrace	STM steps	STM #defects
1	-	950	1130/-	30/-	(1×1)	ragged	absent	-
1	-	950	1300/-	30/-	(1×1)	flat	defined	high
2	-	950	1300/-	30/-	(1×1)	flat	defined	moderate
3	-	950	1400/-	30/-	(reconstr.)	ragged	absent	-
2	2	950	1300/-	30/-	(reconstr.)	ragged	absent	-
2	2	950	1200–1230/-	30/-	(1×1)	flat	defined	low
2	2	950	1250/-	30/-	(reconstr.)	-	-	-
2	4	950	1150/-	30/-	(reconstr.)	-	-	-
3	3	950	1200/-	30/-	(1×1)	flat	defined	very high
2	2	950	1250/1180	2/10	(1×1)	flat	defined	low

Table C.1 Overview on all tested H annealing parameters in flowing gas atmosphere, the respective outcome examined with LEED, and, if applicable, STM. Steps are called "defined" in case they are sharp, straight and showed a preference for certain crystallographic directions.

C.3 Etch Pits on Samples Prepared in 2 slm H_2 and 4 slm He Gas Flow

The predominance of 2H steps for SiC samples prepared in flowing gas is in contrast to 1H steps mainly seen on samples prepared in static gas atmosphere. We attribute the bilayer bunching to the higher temperature of the process in flowing gas, causing much faster etching rates. This assumption is substantiated by findings on a sample prepared with 2 slm H_2/4 slm He gas flow, see Fig. C.4. The STM image recorded close to the clamping shields (Fig. C.4**b**), where the temperature is lower than in the central wafer area, resembles surfaces after static H_2 annealing, with triangular cavities and 1H steps despite a high gas flow.

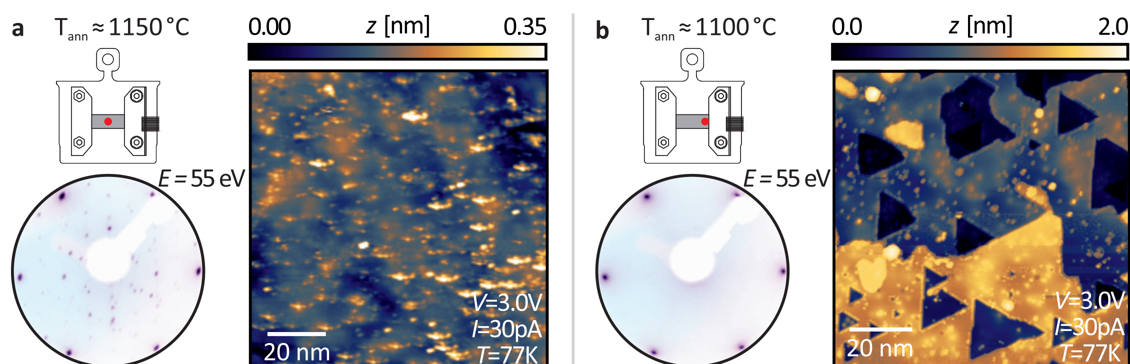

Figure C.4 LEED and STM measurements on a sample prepared with 2 slm H_2 and 4 slm He gas flow for 30 min. At the sides of the wafer stripe, the temperature is roughly 50 °C lower than in the center (where it is usually measured) due to the gradient induced by the DC heating. **a** The LEED pattern in the center reveals the formation of a reconstruction, leading to a high corrugation surface in STM. **b** Close to the clamping sheet, the temperature during H annealing is only ≈ 1000 °C, i.e., sufficiently low to avoid a reconstruction according to the (1 × 1) surface periodicity in LEED. STM measurements display plane terraces, which are eroded by triangular-shaped cavities and separated by single bilayer steps, as found on samples prepared in static H_2 atmosphere.

C.4 Surface Adsorbates and (Sub-)Surface Defects

In the following, characteristic surface imperfections present after the H annealing are discussed. Fig. C.5 shows a high quality 50 nm × 50 nm STM image. The obvious long-range fluctuations of the apparent height are caused by impurity inhomogeneities and found similarly in related doped semiconductors [214, 215]. A plethora of small, localized defects with a lateral extension of 5–10 Å is found, which are marked with colored frames in the central image and shown in the surrounding magnified scan frames (Fig. C.5**a**–**j**). A semi-transparent SiC ball-and-stick model is used to identify the defect site in relation to the topmost bilayer. Additionally, an $I(V)$ curve and the corresponding differential conductivity $\mathrm{d}I/\mathrm{d}V$ measured on top of the respective defect are shown in Fig. C.5**k** and **l**. The quality of the acquired data is rather poor due to the sharp raise of conductivity close to the VB and CB of SiC.

Impurities in SiC, which are visible in STM, stem either from native defects, i.e., vacancies and antisite defects in a bilayer at or close to the surface, or (fractions of) molecules that are redeposited during the H_2 gas etching process.

As the density of defects with rather high corrugation seems to rise with increasing etching rate, compare Fig. 5.9, one could assume that these are at least partly redeposited etching products, namely silane, methane and fractions thereof. The probed radius in the range of 5 Å is considerably larger than the length of Si–H ($d_{\text{Si-H}} = 1.48$ Å) and C–H ($d_{\text{C-H}} = 1.09$ Å) reported in literature [293], however, these seeming deviations must be handled with care as STM in CCI mode probes a surface of constant charge density. Moreover, the measured image constitutes a convolution of the surface and the tip geometry, which leads to an increase of the apparent object size. Considering both aspects, the defects apparent in Fig. C.5, especially **a**–**g**, could constitute redeposited molecules from the gas phase. The corresponding spectroscopic measurements on top of these defects (Fig. C.5**a**–**g**) do not exhibit remarkable characteristics and show an unaffected band gap magnitude.

In contrast, the differential conductivity probed on top of the defects shown in Fig. C.5**h**–

j is slightly different from the ordinary bulk SiC signal in Fig. 5.12. The small apparent height ($z < 1\,\text{Å}$) and large lateral spread compared to the defects shown in Fig. C.5**a**–**g** suggests that the defects are located (presumably) within deeper lying layers of the SiC crystal and constitute either intrinsic SiC defects or N impurities.

The most basic native defects are vacancies, antisites and interstitials [294, 295]. Their formation and ionization energies strongly depend on the growth conditions (C-rich, Si-rich, or stoichiometric), the doping type, the adsorption site (h- or k-site) and the charge state [295–297]. Not all of these parameters are known or can be precisely determined, which prohibits a detailed discussion. However, it is clear that both vacancy defects at Si (V_{Si}^{q}) and C (V_{C}^{q}) sites as well as the simplest antisite defects C_{Si} and Si_{C}, i.e., a C atom at a Si site and vice versa, are accompanied by structural relaxations, as the electronegativity and bond lengths of Si and C atoms differ ($\eta_{\text{C}} = 2.55\,\text{eV}$ and $\eta_{\text{Si}} = 1.90\,\text{eV}$ [298]). Moreover, many of the defects might exist in either charge neutral or (several) charged states [295]. Both aspects might lead to the apparent crystal distortion seen in Fig. C.5**h**–**j**.

Additionally, external defects due to the N impurities must be present in the n-doped 4H-SiC samples. The wafer resistivity is specified as 0.015–0.028 Ω cm, which corresponds to a dopant density in the range of $\approx 10^{18}$–$10^{19}\,\text{cm}^{-3}$. A comparison with the SiC crystal density shows that N atoms are substituting one out of roughly 10^4 to 10^5 atoms [299, 300]. Calculations indicate that N atoms replace C atoms (N_{C}) because of a much lower formation energy as on Si atom sites [209, 301, 302]. The electronegativity of N ($\eta_{\text{N}} = 3.04\,\text{eV}$) is higher than of C, but the difference is still smaller than between C and Si atoms [298]. Accordingly, the covalent radii of C ($r_{\text{cov}}^{\text{C}} = 0.77\,\text{Å}$) and N ($r_{\text{cov}}^{\text{N}} = 0.75\,\text{Å}$) are very similar, while Si favors bonds with larger extent ($r_{\text{cov}}^{\text{Si}} = 1.10\,\text{Å}$) [302]. From this viewpoint, structural deformations as for, e.g., native SiC antisite defects in any case must be significantly smaller than for those defects if present at all. However, also N doping atoms exist in a charge neutral state (and with an additional electron compared to the surrounding atoms) or are ionized, which causes a screening of the leftover positive ion by free charge carriers. The same mechanism causes very similar charge density fluctuations as observed in Fig. C.5 in Zn-doped GaAs samples [214].

Ultimately, the fluctuations of the apparent height seen in CCI scans of the SiC surface can be explained by the presence of native or extrinsic N defects. The spectroscopic measurements atop of all defects demonstrate that the bandgap remains mostly unaffected by the point defects. An in-depth analysis requires additional STM and STS measurements, but must include DFT-simulated STM images of different SiC native defects, N impurities and etching products or complementary measurements with atomic-resolution AFM as presented in Ref. [303] to disentangle structural and electronic properties.

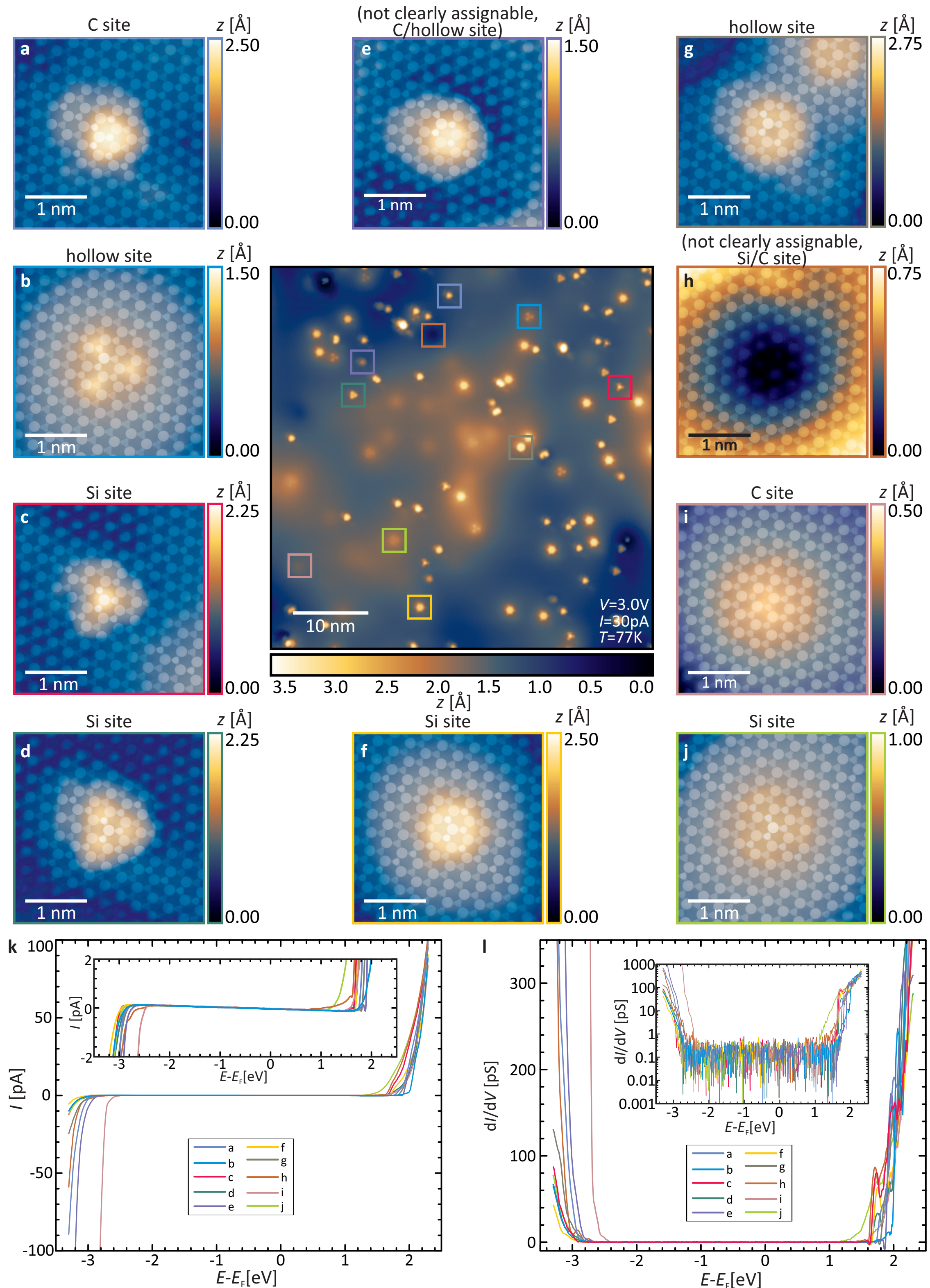

Figure C.5 **a–j** Overlay of the defects shown in Fig. C.5 and a SiC bilayer ball-and-stick model to investigate the adsorption or binding sites of the corresponding defect. **k** $I(V)$ curve and corresponding **l** differential conductivity $\mathrm{d}I(V)/\mathrm{d}V$ measured directly on top of each defect ($I_{\mathrm{st}} = 100\,\mathrm{pA}$, $V_{\mathrm{st}} = 2.3\,\mathrm{V}$). The SiC(0001) sample was prepared with in 2 slm H_2/2 slm He gas flow at 1200 °C for 30 min.

D Additional Information on the Epitaxial Growth and Structure of Bismuthene on SiC

D.1 Bismuthene Coverage and Domain Size on Different Samples

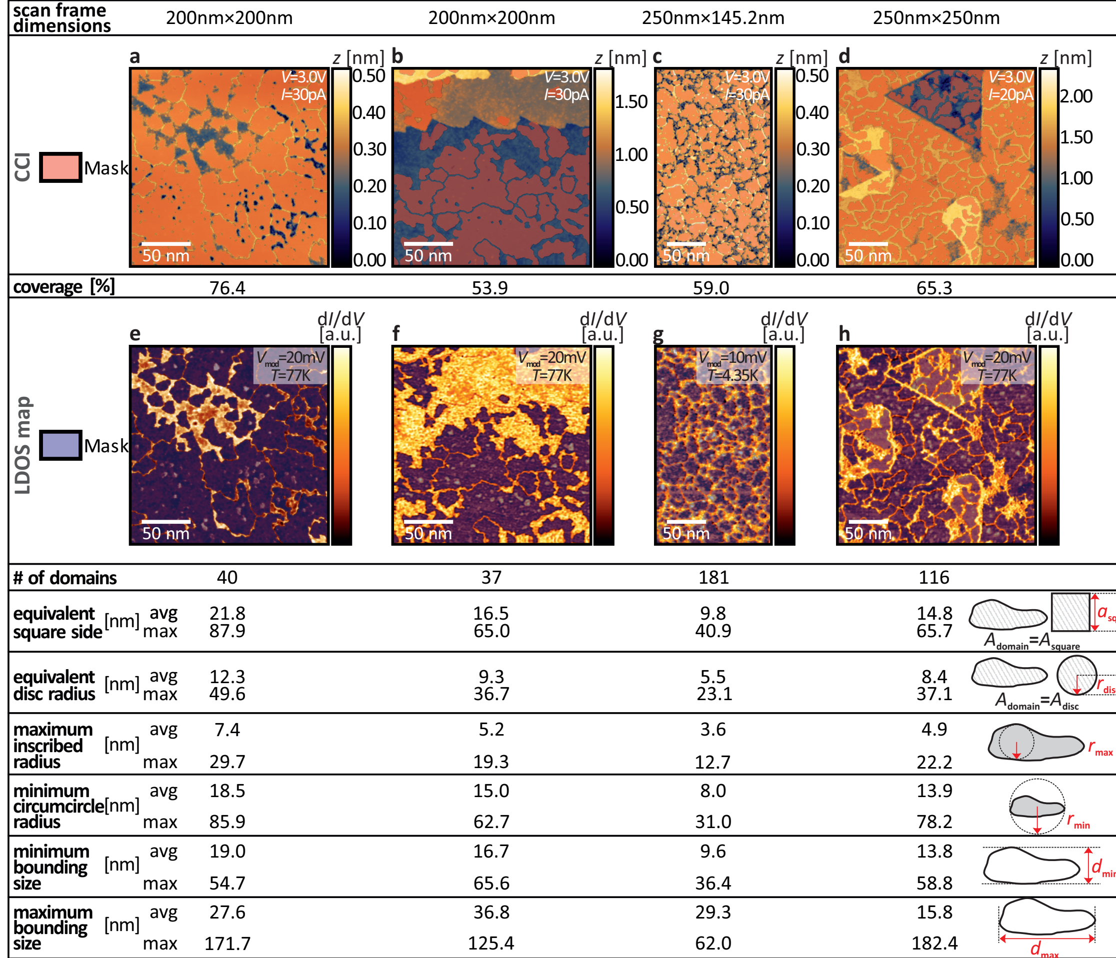

			a / e	b / f	c / g	d / h
scan frame dimensions			200nm×200nm	200nm×200nm	250nm×145.2nm	250nm×250nm
coverage [%]			76.4	53.9	59.0	65.3
# of domains			40	37	181	116
equivalent square side	[nm]	avg	21.8	16.5	9.8	14.8
		max	87.9	65.0	40.9	65.7
equivalent disc radius	[nm]	avg	12.3	9.3	5.5	8.4
		max	49.6	36.7	23.1	37.1
maximum inscribed radius	[nm]	avg	7.4	5.2	3.6	4.9
		max	29.7	19.3	12.7	22.2
minimum circumcircle radius	[nm]	avg	18.5	15.0	8.0	13.9
		max	85.9	62.7	31.0	78.2
minimum bounding size	[nm]	avg	19.0	16.7	9.6	13.8
		max	54.7	65.6	36.4	58.8
maximum bounding size	[nm]	avg	27.6	36.8	29.3	15.8
		max	171.7	125.4	62.0	182.4

Figure D.1 Analysis of four different samples in terms of bismuthene coverage and average/maximum domain size in CCIs (**a**–**d**) and LDOS maps (**e**–**h**), respectively. The meaning of the different domain size properties is depicted in the sketch at the right side of the table.

Masks in the CCI scans and LDOS maps in Fig. D.1 are generated by the threshold grain analysis implemented in the free and open-source software *Gwyddion* [304]. The provided masks have been manually corrected by comparison of both CCI and LDOS map to account for erroneously masked areas due to the inconstant and peaky signal in disordered areas, and for the hard-to-interpret signature of domain boundaries.

D.2 Details on XPS of Bismuthene

D.2.1 Fit Parameters at Varying Measurement Angle

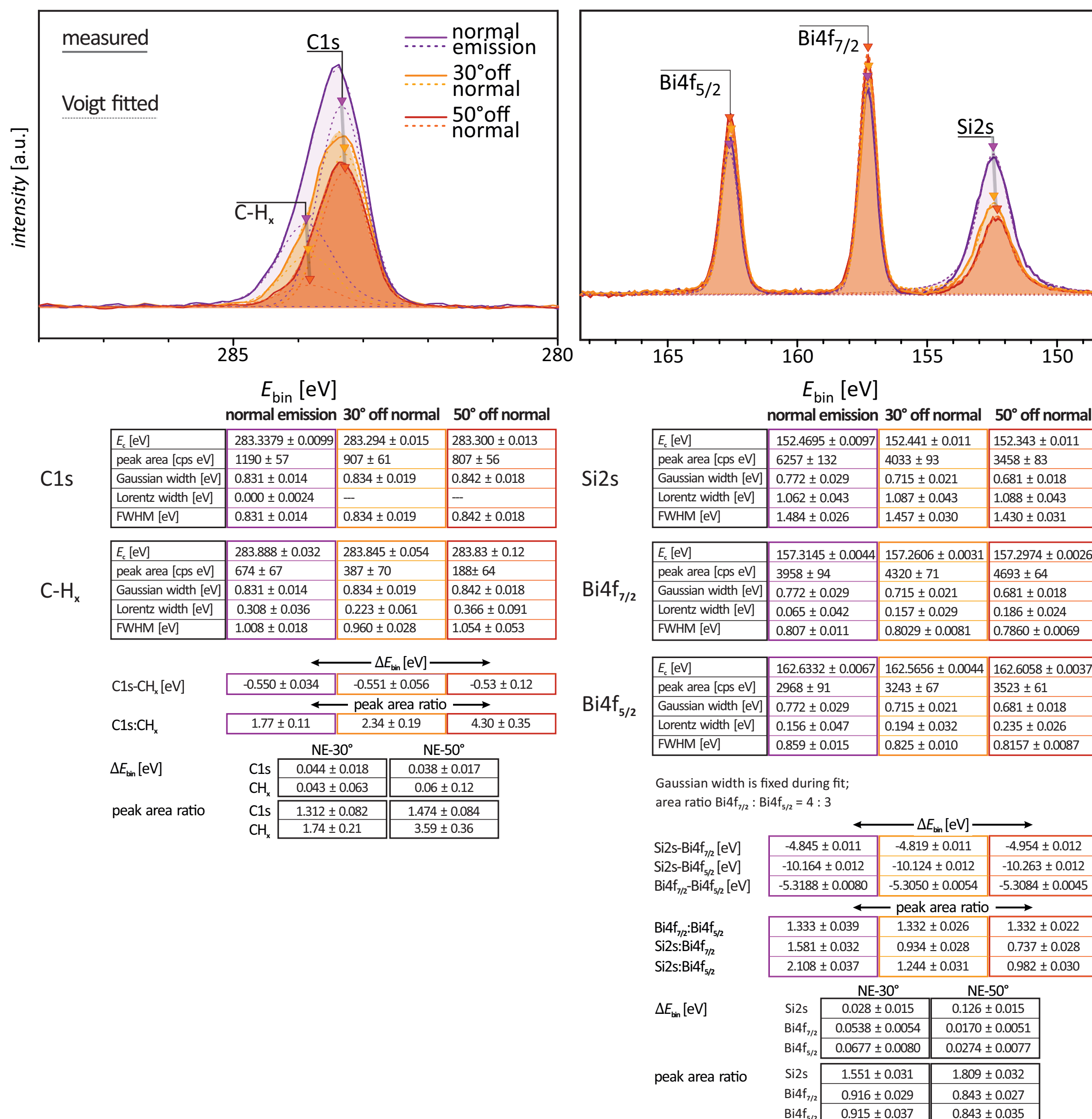

C1s

	normal emission	30° off normal	50° off normal
E_c [eV]	283.3379 ± 0.0099	283.294 ± 0.015	283.300 ± 0.013
peak area [cps eV]	1190 ± 57	907 ± 61	807 ± 56
Gaussian width [eV]	0.831 ± 0.014	0.834 ± 0.019	0.842 ± 0.018
Lorentz width [eV]	0.000 ± 0.0024	---	---
FWHM [eV]	0.831 ± 0.014	0.834 ± 0.019	0.842 ± 0.018

C-H$_x$

	normal emission	30° off normal	50° off normal
E_c [eV]	283.888 ± 0.032	283.845 ± 0.054	283.83 ± 0.12
peak area [cps eV]	674 ± 67	387 ± 70	188± 64
Gaussian width [eV]	0.831 ± 0.014	0.834 ± 0.019	0.842 ± 0.018
Lorentz width [eV]	0.308 ± 0.036	0.223 ± 0.061	0.366 ± 0.091
FWHM [eV]	1.008 ± 0.018	0.960 ± 0.028	1.054 ± 0.053

	normal emission	30° off normal	50° off normal
	← ΔE_{bin} [eV] →		
C1s-CH$_x$ [eV]	-0.550 ± 0.034	-0.551 ± 0.056	-0.53 ± 0.12
	← peak area ratio →		
C1s:CH$_x$	1.77 ± 0.11	2.34 ± 0.19	4.30 ± 0.35

		NE-30°	NE-50°
ΔE_{bin} [eV]	C1s	0.044 ± 0.018	0.038 ± 0.017
	CH$_x$	0.043 ± 0.063	0.06 ± 0.12
peak area ratio	C1s	1.312 ± 0.082	1.474 ± 0.084
	CH$_x$	1.74 ± 0.21	3.59 ± 0.36

Si2s

	normal emission	30° off normal	50° off normal
E_c [eV]	152.4695 ± 0.0097	152.441 ± 0.011	152.343 ± 0.011
peak area [cps eV]	6257 ± 132	4033 ± 93	3458 ± 83
Gaussian width [eV]	0.772 ± 0.029	0.715 ± 0.021	0.681 ± 0.018
Lorentz width [eV]	1.062 ± 0.043	1.087 ± 0.043	1.088 ± 0.043
FWHM [eV]	1.484 ± 0.026	1.457 ± 0.030	1.430 ± 0.031

Bi4f$_{7/2}$

	normal emission	30° off normal	50° off normal
E_c [eV]	157.3145 ± 0.0044	157.2606 ± 0.0031	157.2974 ± 0.0026
peak area [cps eV]	3958 ± 94	4320 ± 71	4693 ± 64
Gaussian width [eV]	0.772 ± 0.029	0.715 ± 0.021	0.681 ± 0.018
Lorentz width [eV]	0.065 ± 0.042	0.157 ± 0.029	0.186 ± 0.024
FWHM [eV]	0.807 ± 0.011	0.8029 ± 0.0081	0.7860 ± 0.0069

Bi4f$_{5/2}$

	normal emission	30° off normal	50° off normal
E_c [eV]	162.6332 ± 0.0067	162.5656 ± 0.0044	162.6058 ± 0.0037
peak area [cps eV]	2968 ± 91	3243 ± 67	3523 ± 61
Gaussian width [eV]	0.772 ± 0.029	0.715 ± 0.021	0.681 ± 0.018
Lorentz width [eV]	0.156 ± 0.047	0.194 ± 0.032	0.235 ± 0.026
FWHM [eV]	0.859 ± 0.015	0.825 ± 0.010	0.8157 ± 0.0087

Gaussian width is fixed during fit;
area ratio Bi4f$_{7/2}$: Bi4f$_{5/2}$ = 4 : 3

	normal emission	30° off normal	50° off normal
	← ΔE_{bin} [eV] →		
Si2s-Bi4f$_{7/2}$ [eV]	-4.845 ± 0.011	-4.819 ± 0.011	-4.954 ± 0.012
Si2s-Bi4f$_{5/2}$ [eV]	-10.164 ± 0.012	-10.124 ± 0.012	-10.263 ± 0.012
Bi4f$_{7/2}$-Bi4f$_{5/2}$ [eV]	-5.3188 ± 0.0080	-5.3050 ± 0.0054	-5.3084 ± 0.0045
	← peak area ratio →		
Bi4f$_{7/2}$:Bi4f$_{5/2}$	1.333 ± 0.039	1.332 ± 0.026	1.332 ± 0.022
Si2s:Bi4f$_{7/2}$	1.581 ± 0.032	0.934 ± 0.028	0.737 ± 0.028
Si2s:Bi4f$_{5/2}$	2.108 ± 0.037	1.244 ± 0.031	0.982 ± 0.030

		NE-30°	NE-50°
ΔE_{bin} [eV]	Si2s	0.028 ± 0.015	0.126 ± 0.015
	Bi4f$_{7/2}$	0.0538 ± 0.0054	0.0170 ± 0.0051
	Bi4f$_{5/2}$	0.0677 ± 0.0080	0.0274 ± 0.0077
peak area ratio	Si2s	1.551 ± 0.031	1.809 ± 0.032
	Bi4f$_{7/2}$	0.916 ± 0.029	0.843 ± 0.027
	Bi4f$_{5/2}$	0.915 ± 0.037	0.843 ± 0.035

Figure D.2 Fit parameters of angle-dependent XPS measurements of the C1s, Bi4f and Si2s lines of Bi/SiC(0001). Below the analysis of single peaks, binding energies offsets and peak area ratios are displayed. All spectra recorded after excitation with the Al K_α line. The spectra at different angles are probed with the same parameters and not normalized to display changes of the intensity. Clearly, the substrate peak C1s and Si2s count rates are strongly reduced at increasing emission angles. Moreover, both species show a small shift to lower binding energies in the more surface sensitive measurements. This can be attributed to a surface chemical shift or surface band bending.

Comparison of angle-dependent XPS on SiC(0001)-H and Bi/SiC(0001)

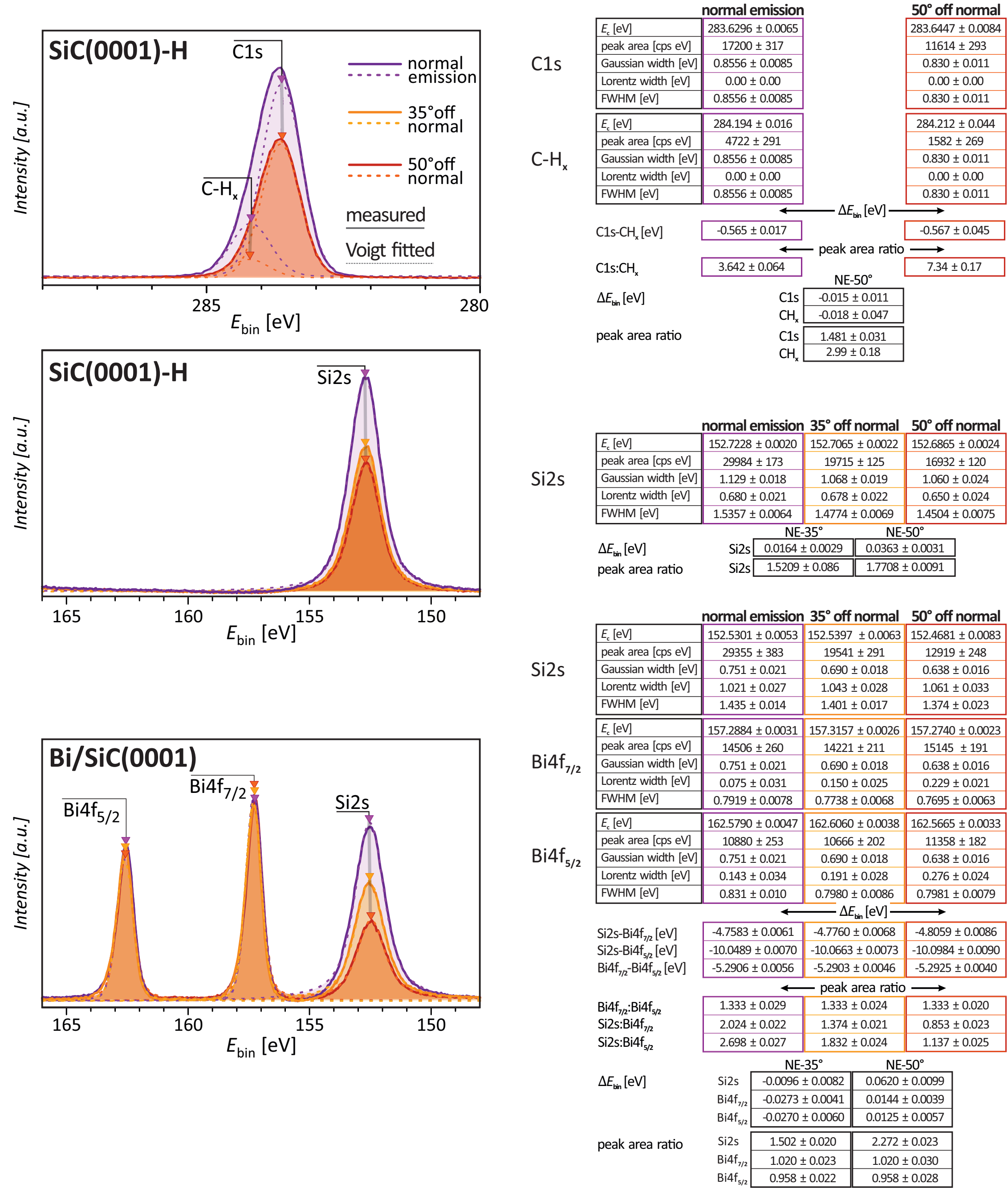

C1s / C-H$_x$ (SiC(0001)-H)

		normal emission	50° off normal
C1s	E_c [eV]	283.6296 ± 0.0065	283.6447 ± 0.0084
	peak area [cps eV]	17200 ± 317	11614 ± 293
	Gaussian width [eV]	0.8556 ± 0.0085	0.830 ± 0.011
	Lorentz width [eV]	0.00 ± 0.00	0.00 ± 0.00
	FWHM [eV]	0.8556 ± 0.0085	0.830 ± 0.011
C-H$_x$	E_c [eV]	284.194 ± 0.016	284.212 ± 0.044
	peak area [cps eV]	4722 ± 291	1582 ± 269
	Gaussian width [eV]	0.8556 ± 0.0085	0.830 ± 0.011
	Lorentz width [eV]	0.00 ± 0.00	0.00 ± 0.00
	FWHM [eV]	0.8556 ± 0.0085	0.830 ± 0.011
ΔE_{bin} [eV]	C1s-CH$_x$ [eV]	-0.565 ± 0.017	-0.567 ± 0.045
peak area ratio	C1s:CH$_x$	3.642 ± 0.064	7.34 ± 0.17

		NE-50°
ΔE_{bin} [eV]	C1s	-0.015 ± 0.011
	CH$_x$	-0.018 ± 0.047
peak area ratio	C1s	1.481 ± 0.031
	CH$_x$	2.99 ± 0.18

Si2s (SiC(0001)-H)

		normal emission	35° off normal	50° off normal
Si2s	E_c [eV]	152.7228 ± 0.0020	152.7065 ± 0.0022	152.6865 ± 0.0024
	peak area [cps eV]	29984 ± 173	19715 ± 125	16932 ± 120
	Gaussian width [eV]	1.129 ± 0.018	1.068 ± 0.019	1.060 ± 0.024
	Lorentz width [eV]	0.680 ± 0.021	0.678 ± 0.022	0.650 ± 0.024
	FWHM [eV]	1.5357 ± 0.0064	1.4774 ± 0.0069	1.4504 ± 0.0075

		NE-35°	NE-50°
ΔE_{bin} [eV]	Si2s	0.0164 ± 0.0029	0.0363 ± 0.0031
peak area ratio	Si2s	1.5209 ± 0.086	1.7708 ± 0.0091

Si2s / Bi4f$_{7/2}$ / Bi4f$_{5/2}$ (Bi/SiC(0001))

		normal emission	35° off normal	50° off normal
Si2s	E_c [eV]	152.5301 ± 0.0053	152.5397 ± 0.0063	152.4681 ± 0.0083
	peak area [cps eV]	29355 ± 383	19541 ± 291	12919 ± 248
	Gaussian width [eV]	0.751 ± 0.021	0.690 ± 0.018	0.638 ± 0.016
	Lorentz width [eV]	1.021 ± 0.027	1.043 ± 0.028	1.061 ± 0.033
	FWHM [eV]	1.435 ± 0.014	1.401 ± 0.017	1.374 ± 0.023
Bi4f$_{7/2}$	E_c [eV]	157.2884 ± 0.0031	157.3157 ± 0.0026	157.2740 ± 0.0023
	peak area [cps eV]	14506 ± 260	14221 ± 211	15145 ± 191
	Gaussian width [eV]	0.751 ± 0.021	0.690 ± 0.018	0.638 ± 0.016
	Lorentz width [eV]	0.075 ± 0.031	0.150 ± 0.025	0.229 ± 0.021
	FWHM [eV]	0.7919 ± 0.0078	0.7738 ± 0.0068	0.7695 ± 0.0063
Bi4f$_{5/2}$	E_c [eV]	162.5790 ± 0.0047	162.6060 ± 0.0038	162.5665 ± 0.0033
	peak area [cps eV]	10880 ± 253	10666 ± 202	11358 ± 182
	Gaussian width [eV]	0.751 ± 0.021	0.690 ± 0.018	0.638 ± 0.016
	Lorentz width [eV]	0.143 ± 0.034	0.191 ± 0.028	0.276 ± 0.024
	FWHM [eV]	0.831 ± 0.010	0.7980 ± 0.0086	0.7981 ± 0.0079
ΔE_{bin} [eV]	Si2s-Bi4f$_{7/2}$ [eV]	-4.7583 ± 0.0061	-4.7760 ± 0.0068	-4.8059 ± 0.0086
	Si2s-Bi4f$_{5/2}$ [eV]	-10.0489 ± 0.0070	-10.0663 ± 0.0073	-10.0984 ± 0.0090
	Bi4f$_{7/2}$-Bi4f$_{5/2}$ [eV]	-5.2906 ± 0.0056	-5.2903 ± 0.0046	-5.2925 ± 0.0040
peak area ratio	Bi4f$_{7/2}$:Bi4f$_{5/2}$	1.333 ± 0.029	1.333 ± 0.024	1.333 ± 0.020
	Si2s:Bi4f$_{7/2}$	2.024 ± 0.022	1.374 ± 0.021	0.853 ± 0.023
	Si2s:Bi4f$_{5/2}$	2.698 ± 0.027	1.832 ± 0.024	1.137 ± 0.025

		NE-35°	NE-50°
ΔE_{bin} [eV]	Si2s	-0.0096 ± 0.0082	0.0620 ± 0.0099
	Bi4f$_{7/2}$	-0.0273 ± 0.0041	0.0144 ± 0.0039
	Bi4f$_{5/2}$	-0.0270 ± 0.0060	0.0125 ± 0.0057
peak area ratio	Si2s	1.502 ± 0.020	2.272 ± 0.023
	Bi4f$_{7/2}$	1.020 ± 0.023	1.020 ± 0.030
	Bi4f$_{5/2}$	0.958 ± 0.022	0.958 ± 0.028

Figure D.3 Comparative angle-dependent XPS measurements on bare H-passivated SiC and bismuthene on SiC. All spectra are recorded with a Al K_α line. The C1s line measured on a SiC-H sample shows the key features that are observed in Fig. D.2, i.e., the peak consisting of two Voigt profiles, a slight reduction of the binding energy at increasing photoemission angle and an increase of the peak area ratio of main peak to side peak at lower and higher binding energy, respectively. With increasing emission angle, a decreasing binding energy of the Si2s peak both on the bare SiC-H and Bi/SiC sample is observed. The shift is larger for the Bi covered substrate.

D.2.2 Peak Ratios of Bi and Si at Different Sample Positions

One may think of using the Si2s/Bi4f peak area ratio as a tool to judge the bismuthene coverage and quality of the sample. As visualized by Fig. D.4 this is not possible, at least not with our XPS spectrometer. Mainly, this is because of the large probing spot of the XPS source on the order of ≈ 1 mm, which is averaging over many domains and sample spots with different substrate temperature causing a failure (too low/too high) during growth. XPS performed with highly focused synchtron radiation could be useful to evaluate the Si/Bi ratio of bismuthene with a higher degree of reliability. Conventional LEED possesses a beam diameter of ≈ 1 mm, as well, and similarly averages the diffraction patterns reliant on the coherence length of the electrons (≈ 100 Å) of many different sample spots. In contrast to XPS, LEED is performed quickly and is therefore used as a first analysis tool.

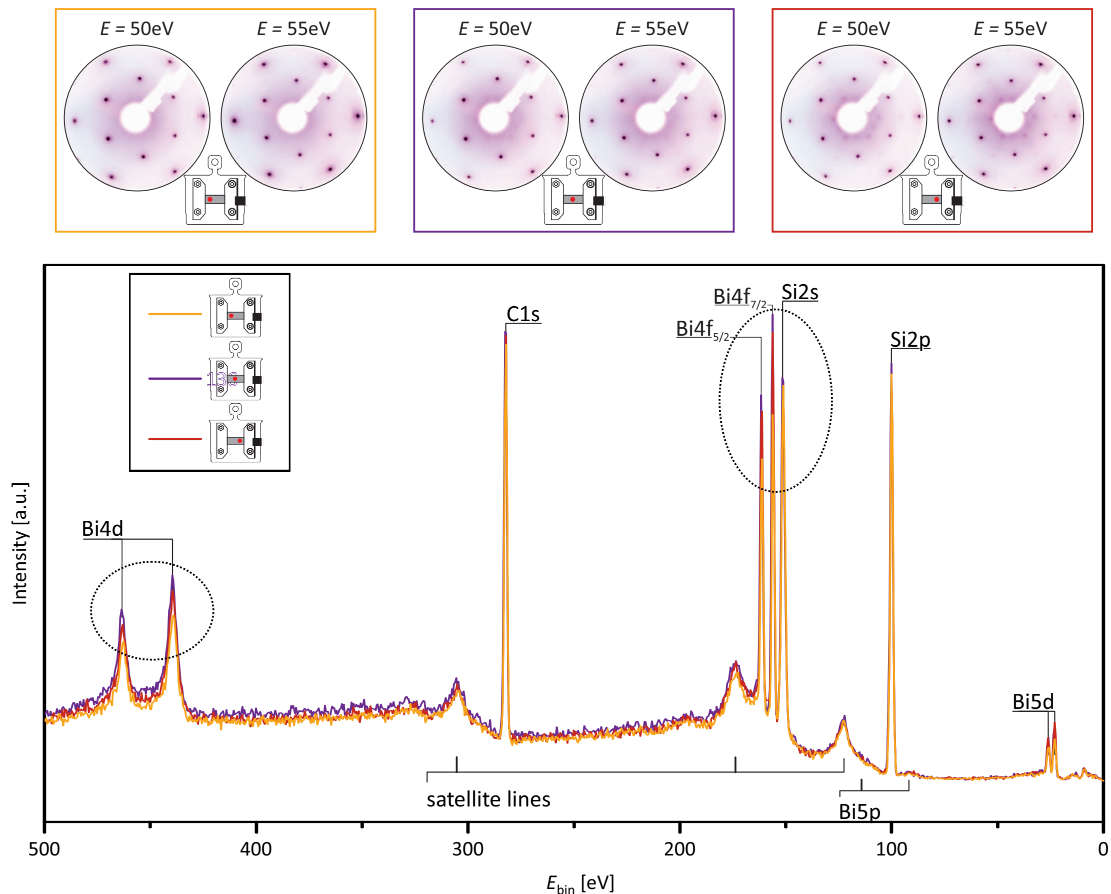

Figure D.4 LEED and XPS overview spectra recorded at different lateral positions of the SiC wafer. XPS measurements are conducted with the Al K_α line. Even though all measurements show the $(\sqrt{3} \times \sqrt{3})$ diffraction pattern characteristic for the formation of bismuthene at 50 eV and 55 eV beam energy, significant changes of the Si2S/Bi4f peak area ratio are seen (marked by dotted curves), especially when comparing the spectrum recorded at the left (orange curve) and the center (purple curve). The spectra at the right edge (red curves) and center (purple curve) of the sample seem to be very similar, but in LEED, noticeable (3×3) spots are seen in the LEED pattern of the right edge. Therefore, peak area ratios are not a suitable tool to judge whether (high quality) bismuthene has formed on the sample or not.

D.2.3 Fit Parameters Before and After Air Exposure

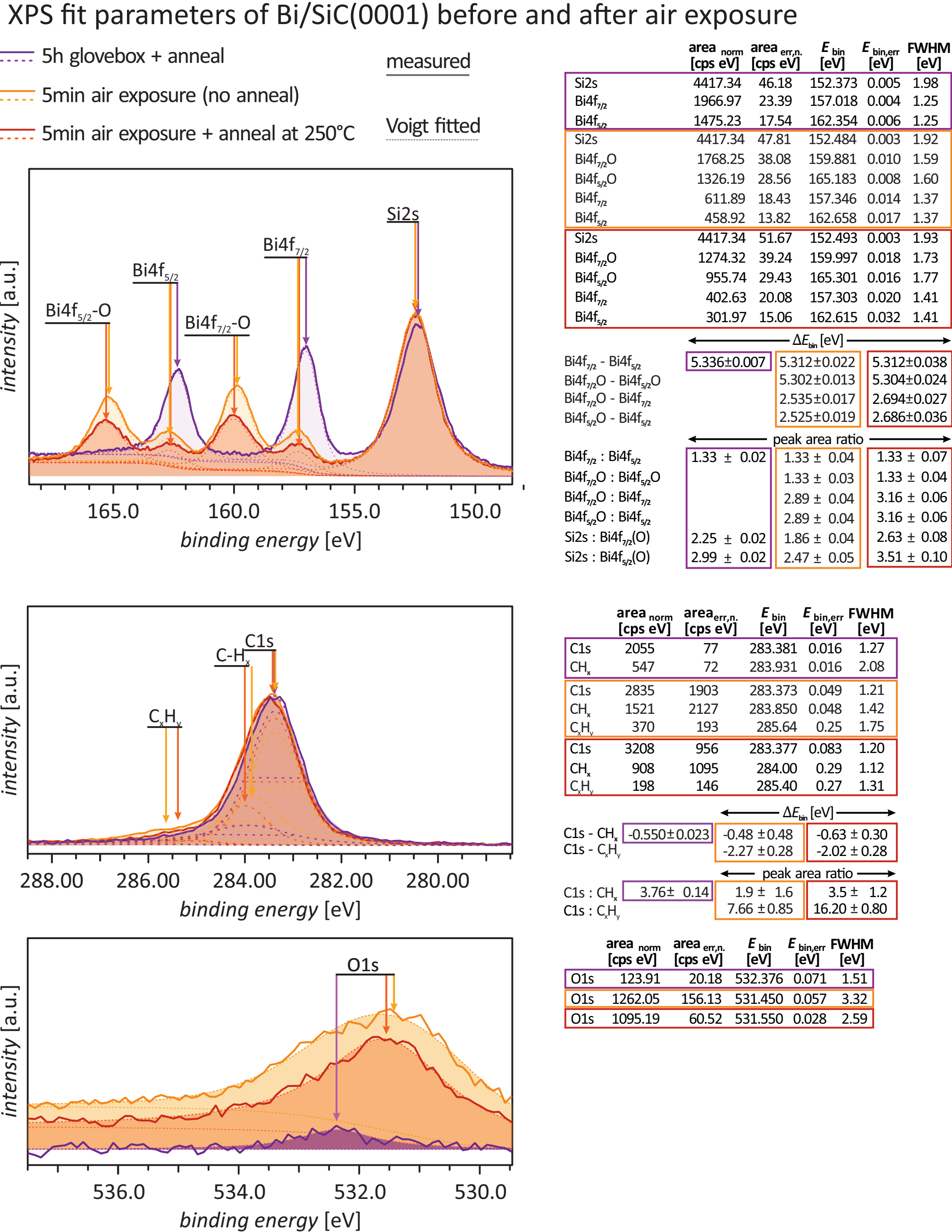

	area $_{norm}$ [cps eV]	area $_{err,n.}$ [cps eV]	E_{bin} [eV]	$E_{bin,err}$ [eV]	FWHM [eV]
Si2s	4417.34	46.18	152.373	0.005	1.98
Bi4f$_{7/2}$	1966.97	23.39	157.018	0.004	1.25
Bi4f$_{5/2}$	1475.23	17.54	162.354	0.006	1.25
Si2s	4417.34	47.81	152.484	0.003	1.92
Bi4f$_{7/2}$O	1768.25	38.08	159.881	0.010	1.59
Bi4f$_{5/2}$O	1326.19	28.56	165.183	0.008	1.60
Bi4f$_{7/2}$	611.89	18.43	157.346	0.014	1.37
Bi4f$_{5/2}$	458.92	13.82	162.658	0.017	1.37
Si2s	4417.34	51.67	152.493	0.003	1.93
Bi4f$_{7/2}$O	1274.32	39.24	159.997	0.018	1.73
Bi4f$_{5/2}$O	955.74	29.43	165.301	0.016	1.77
Bi4f$_{7/2}$	402.63	20.08	157.303	0.020	1.41
Bi4f$_{5/2}$	301.97	15.06	162.615	0.032	1.41

	ΔE_{bin} [eV]		
Bi4f$_{7/2}$ - Bi4f$_{5/2}$	5.336±0.007	5.312±0.022	5.312±0.038
Bi4f$_{7/2}$O - Bi4f$_{5/2}$O		5.302±0.013	5.304±0.024
Bi4f$_{7/2}$O - Bi4f$_{7/2}$		2.535±0.017	2.694±0.027
Bi4f$_{5/2}$O - Bi4f$_{5/2}$		2.525±0.019	2.686±0.036

	peak area ratio		
Bi4f$_{7/2}$: Bi4f$_{5/2}$	1.33 ± 0.02	1.33 ± 0.04	1.33 ± 0.07
Bi4f$_{7/2}$O : Bi4f$_{5/2}$O		1.33 ± 0.03	1.33 ± 0.04
Bi4f$_{7/2}$O : Bi4f$_{7/2}$		2.89 ± 0.04	3.16 ± 0.06
Bi4f$_{5/2}$O : Bi4f$_{5/2}$		2.89 ± 0.04	3.16 ± 0.06
Si2s : Bi4f$_{7/2}$(O)	2.25 ± 0.02	1.86 ± 0.04	2.63 ± 0.08
Si2s : Bi4f$_{5/2}$(O)	2.99 ± 0.02	2.47 ± 0.05	3.51 ± 0.10

	area $_{norm}$ [cps eV]	area $_{err,n.}$ [cps eV]	E_{bin} [eV]	$E_{bin,err}$ [eV]	FWHM [eV]
C1s	2055	77	283.381	0.016	1.27
CH$_x$	547	72	283.931	0.016	2.08
C1s	2835	1903	283.373	0.049	1.21
CH$_x$	1521	2127	283.850	0.048	1.42
C$_x$H$_y$	370	193	285.64	0.25	1.75
C1s	3208	956	283.377	0.083	1.20
CH$_x$	908	1095	284.00	0.29	1.12
C$_x$H$_y$	198	146	285.40	0.27	1.31

	ΔE_{bin} [eV]		
C1s - CH$_x$	-0.550±0.023	-0.48 ±0.48	-0.63 ± 0.30
C1s - C$_x$H$_y$		-2.27 ±0.28	-2.02 ± 0.28

	peak area ratio		
C1s : CH$_x$	3.76± 0.14	1.9 ± 1.6	3.5 ± 1.2
C1s : C$_x$H$_y$		7.66 ±0.85	16.20 ± 0.80

	area $_{norm}$ [cps eV]	area $_{err,n.}$ [cps eV]	E_{bin} [eV]	$E_{bin,err}$ [eV]	FWHM [eV]
O1s	123.91	20.18	532.376	0.071	1.51
O1s	1262.05	156.13	531.450	0.057	3.32
O1s	1095.19	60.52	531.550	0.028	2.59

Figure D.5 XPS fit parameters of spectra measured after a bismuthene sample has been exposed to (i) a dry N_2 glovebox atmosphere for 5 h (purple curve), (ii) 5 min ambient air (orange curve), (iii) 5 min ambient air and a subsequent mild annealing at 250 °C (red curve). All spectra are recorded with the Al K_α line and normalized to equal Si2s peak areas. (i) The bismuthene film remains almost unaffected by the glovebox atmosphere (H_2O, O_2<0.1 ppm). Only a small O peak ($E_{\text{bin}} \approx 532$ eV) is found. Importantly, no BiO-related peaks are present, in contrast to the measurement conducted after the sample was transferred to air for 5 min. (ii) Here, intense BiO peaks appear, at ≈ +2.5 eV higher binding energy than the two spin-orbit split Bi4f peaks, compatible to measurements on Bi(O) thin films in literature [227]. (iii) The total Bi peak area is reduced after the thermal treatment, even though as-grown samples do not show Bi loss when heated to $t = 400$ °C for hours, indicating that the oxidation is irreversible.

D.3 Growth and STM on Miscut-SiC Substrates

Bismuthene grows on miscut SiC substrates and the observed lattice structure and morphology of the surface is identical to what is described for planar samples in Ch. 7. Samples on substrates with two miscut angles have been grown, and selected images recorded on the corresponding samples are displayed in the following.

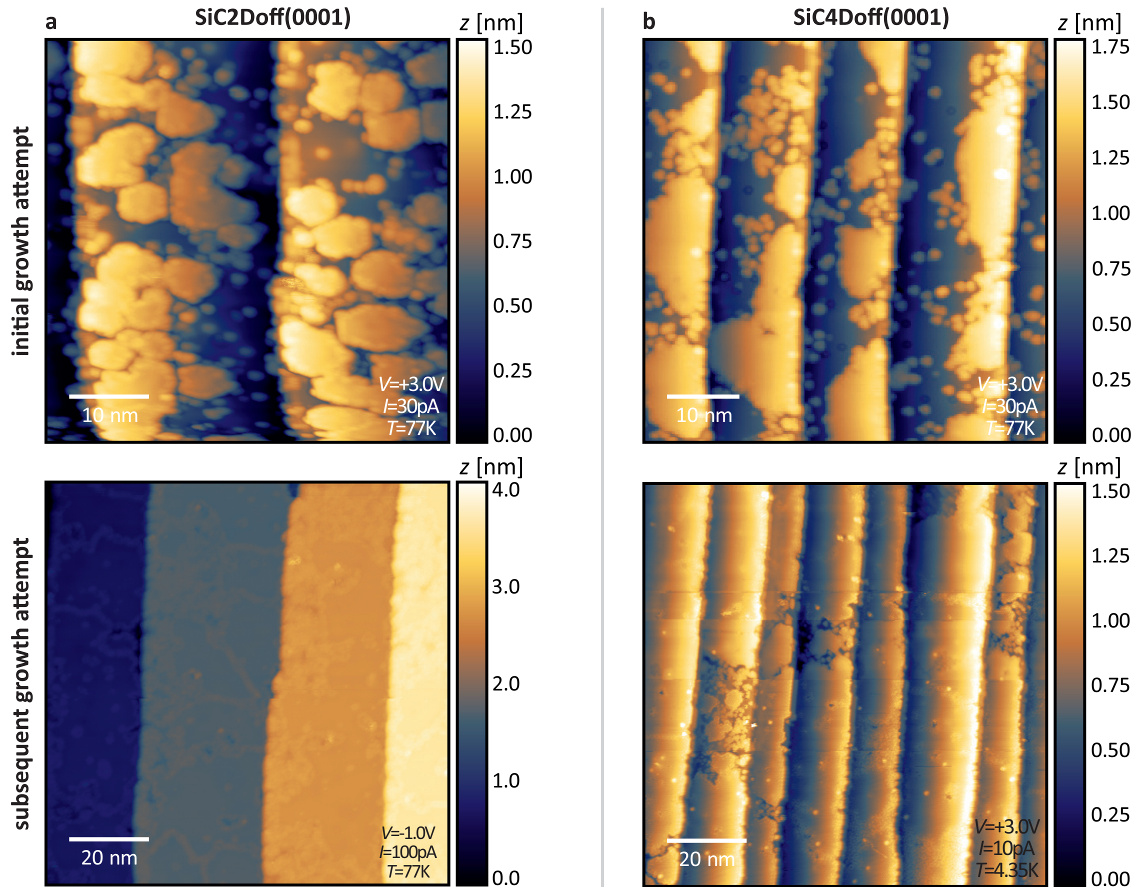

Figure D.6 STM overview images of **a** bismuthene grown on 2° Miscut-SiC and **b** 4° Miscut-SiC substrates. The upper and lower row depict the surface after the initial and a subsequent growth cycle, respectively (compare to Fig. 6.2). The results are in line with the osbervations for planar samples, compare to Fig. 6.5. Often, the substrate is covered only by isolated bismuthene islands and areas with blank SiC substrate are seen after the first growth attempt. The surface filling with bismuthene increases after a second growth cycle. Interestingly, the coverage close to a step edge seems higher on the upper than on the lower edge of a terrace, which might indicate a higher probability to bind impinging Bi atoms there.

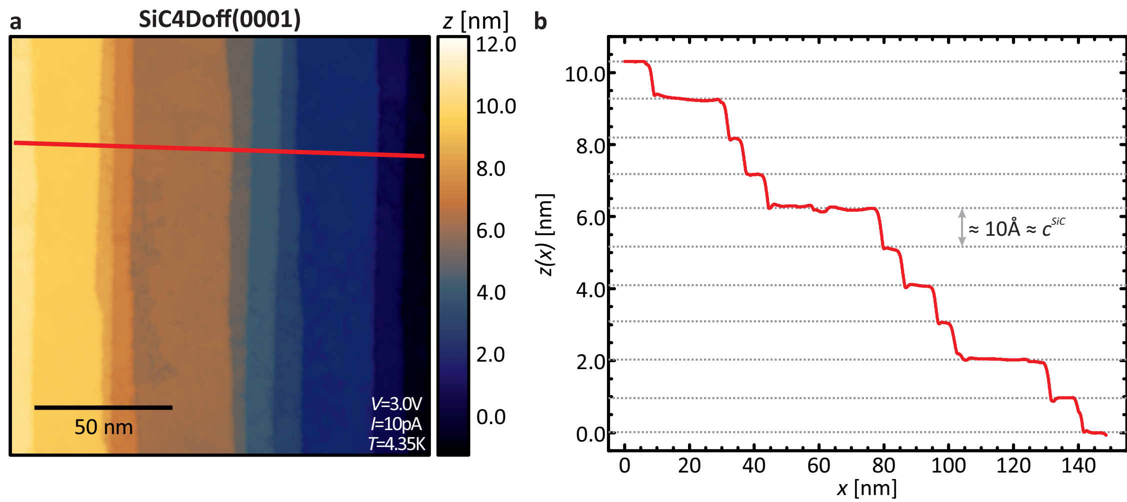

Figure D.7 **a** Overview STM image after Bi deposition on a SiC4Doff substrate. As on bare miscut substrates, straight steps spread from the bottom to the top of the image. The surface of the terraces is mostly smooth but exhibits disordered areas, best seen in the central, wide brown-colored terrace at $z \approx 6\,\text{nm}$. **b** A line profile is used to check the height of the atomic steps. Clearly, all terrace planes are separated by full 4H SiC ($c^{\text{SiC}} = 1.008\,\text{nm}$) unit cell steps.

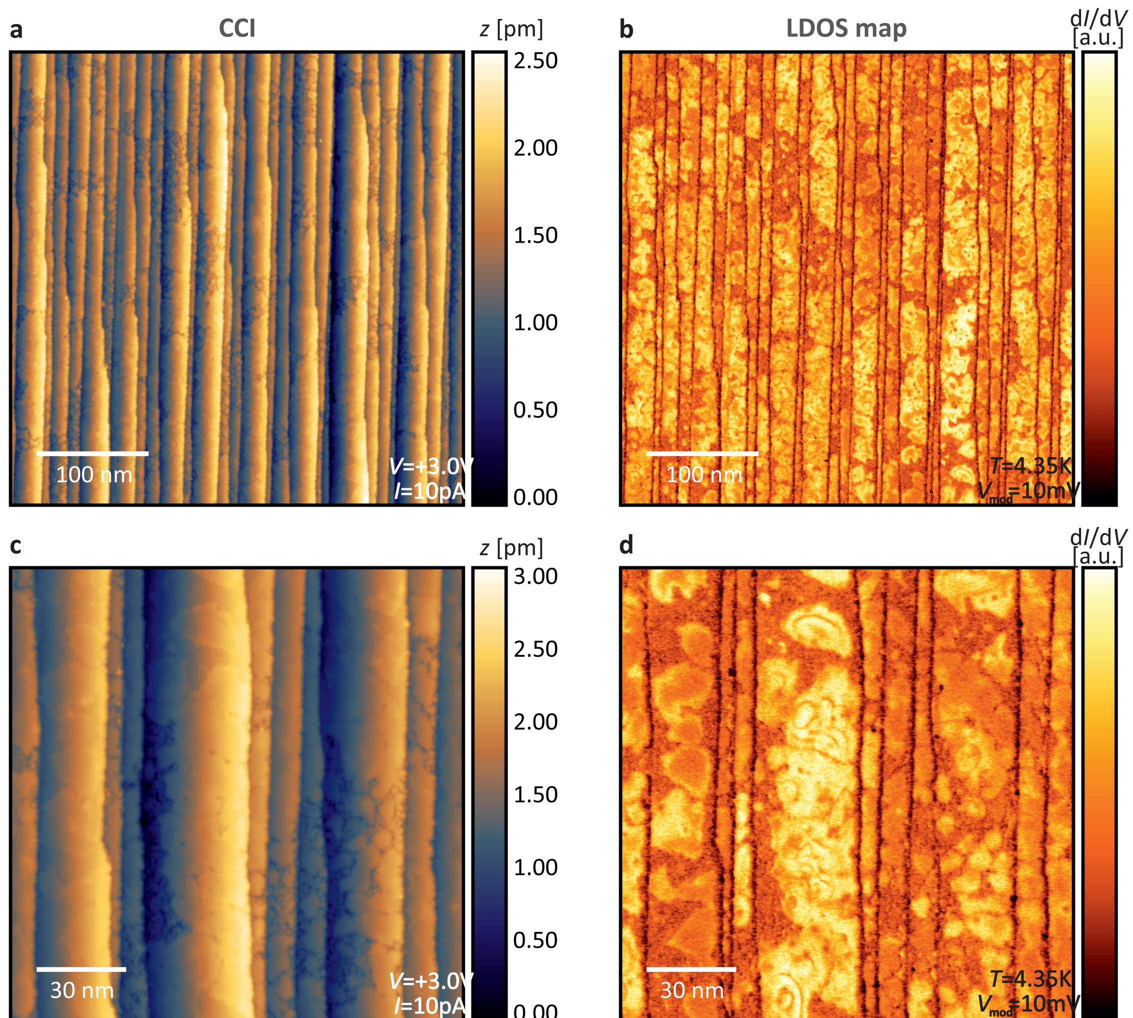

Figure D.8 Large scale STM overview image of bismuthene grown on a SiC4Doff(0001) substrate. **a**, **c** and **b**, **d** show CCIs and LDOS maps, respectively. As on planar SiC substrates, the CCI and LDOS maps allow to judge coverage and domain size.

E Additional Information on 2D Bulk Bismuthene

E.1 STM and STS at High and Low Bias Voltage

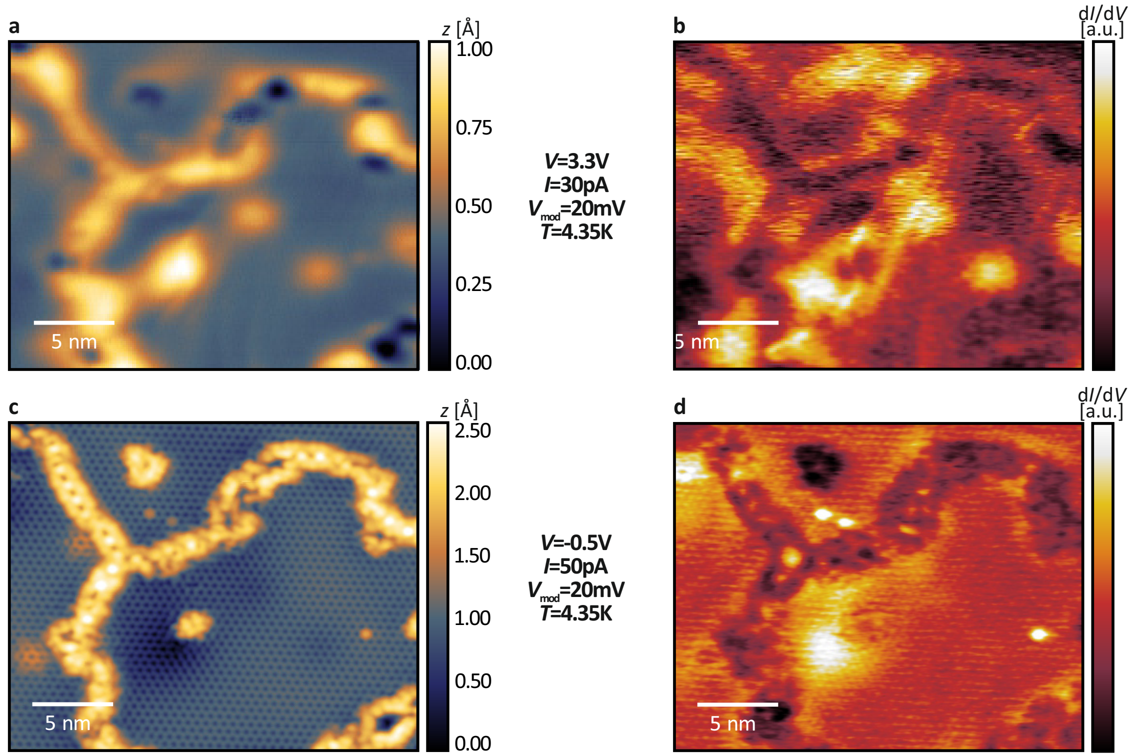

Figure E.1 **a**, **c** CCI and **b**, **d** LDOS map recorded on the very same sample area at **a**, **b** high and **c**, **d** low bias voltage. It reveals that key features like domain boundaries and some defects are seen in CCI and LDOS map even at high tunnel voltage as result of their distinct electronic properties. The honeycomb lattice structure and the substructure of the domain boundaries are resolved only in low bias voltage measurements.

The CCI and LDOS images displayed in Fig. E.1 show the very same sample region probed at high and low tunneling bias, enabling a one-to-one comparison of the evolution of characteristic surface structures when when switching from high to low bias.

E.2 LDOS Maps of the Bulk Lattice in STS and DFT

All CCIs and LDOS maps shown in Fig. E.2 indicate the presence of a honeycomb lattice. The threefold symmetry is induced by the C sublattice of the SiC substrate and apparent in the DFT simulations at constant height and isocharge, as well, see Fig. E.3.
A detailed comparison between experiment and theory, e.g., in terms of bias-dependent LDOS maps and simulations is omitted, as none of the two simulation methods is directly comparable to STM/STS experiments. In principle, simulations at constant height, see Fig. E.3**a**, could be mimicked experimentally by constant height imaging of the sample surface. However, this bears an increased risk of tip crashes and has therefore not beeen

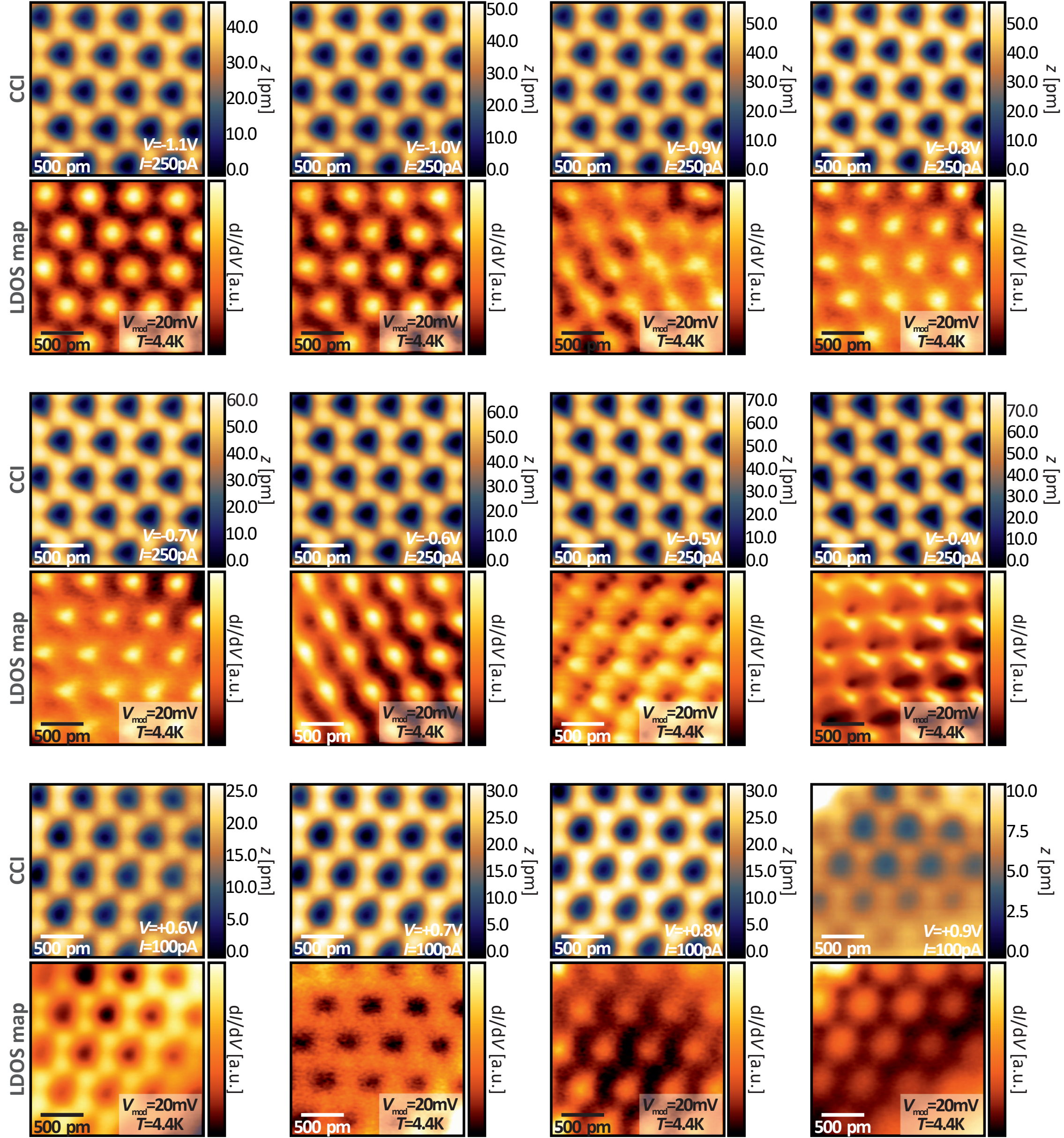

Figure E.2 CCI and LDOS maps recorded at a large number of different bias voltages. A honeycomb lattice/pattern is perceivable throughout all scans. The triangular symmetry induced by the substrate is best seen in the scans of occupied states and close to the Fermi level.

carried out. Furthermore, the simulated images do not account for variations of the tunneling matrix element or the finite tip resolution relevant to STM/STS data. In case of simulated isocharge surfaces (Fig. E.3**b**), a comparison is not sensible, as well, as it is not clear how an isocharge value is translated into experimental parameters. Lastly, the simulated probing energies are hardly comparable to the experimental tunnel voltages because of the deficiencies of the GGA functional, on which the simulations are based, in determining precise band positions [243].

Nevertheless, all DFT simulations demonstrate the presence of a honeycomb pattern at all energies, in agreement with the recorded CCI and LDOS maps.

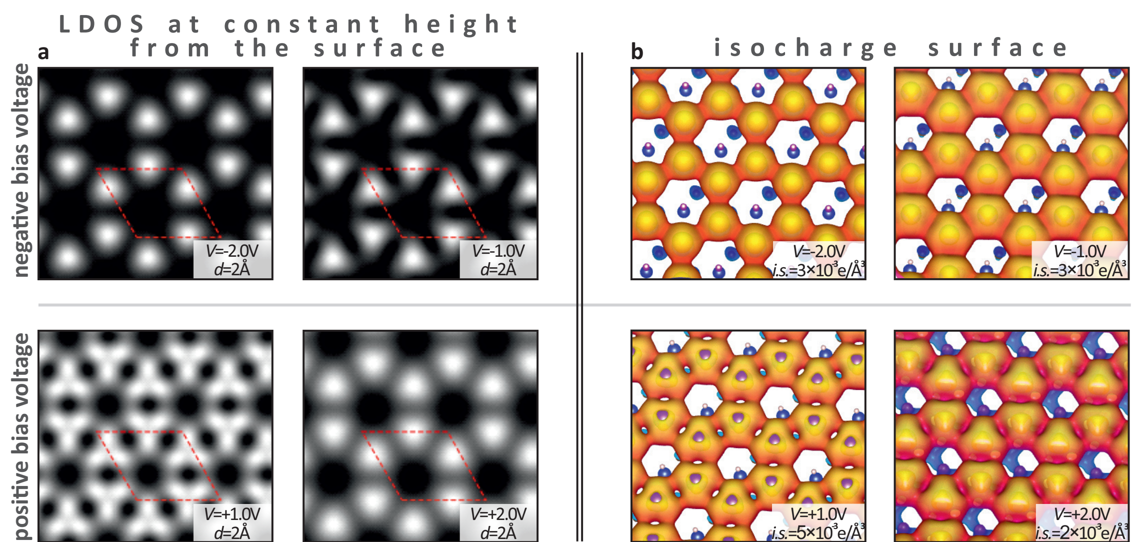

Figure E.3 DFT simulations based on the lattice structure shown in Fig. 4.4. **a** Simulated LDOS at constant height from the surface. **b** An isocharge surface at certain bias voltages, which are measured in relation to the VBM. All simulations display a honeycomb geometry, as observed in the experiment. Interestingly, the triangular symmetry of the honeycombs that is induced by the C sublattice is captured in the simulations, as well, and best seen in the simulation at constant height at $V = -1.0\,\text{eV}$. *Simulations calculated and provided by courtesy of Gang Li [168].*

E.3 STS Band Gap Fits and Variation of the Stabilization Parameters

Fig. E.4 illustrates the procedure used for determination of the band gap magnitude on bismuthene.

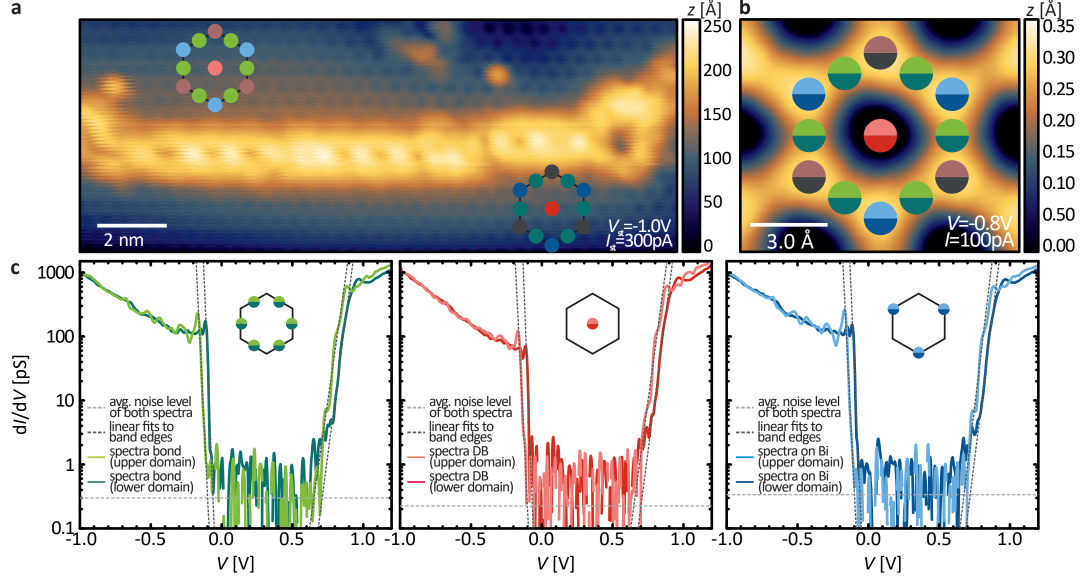

Note: Spectra on Bi atoms are displayed only for one sublattice as they are equivalent.

d

	Bonds		Dangling Bond (DB)		Bi atoms	
	upper domain	lower domain	upper domain	lower domain	upper domain	lower domain
VBM [meV]	-116.4±5.5	-75.7±9.9	-121±25	-82±31	-116.2±7.6	-75.4±11
CBM [meV]	705±62	759±35	702±110	751±39	720±150	765±34
E_{gap} [meV]	822±62	835±36	823±110	832±50	836±150	840±36
	VB	CB	VB	CB	VB	CB
Δ*E* [meV]	41±11	54±71	39±40	48±116	41±13	45±154

Figure E.4 Procedure for determination of the band gap magnitude in STS measurements. **a** Overview CCI visualizing that spectra of two domains are shown. **b** Atomic resolution CCI with markers that indicate positions at which the spectra shown in **c** are recorded. **c** The band edges in the STS spectra are used to calculate the band gap magnitude. Fits with a linear function are extrapolated to the average zero line within the band gap. A small, rigid offset of the LDOS is seen between the lower and upper domain consistently at all measurement positions. **d** Tabulated energies of the VB maximum and CB minimum as well as the corresponding energy gap. The energy difference of VB and CB onset observed between lower and upper domain is shown in the lowest row. Grid spectroscopy parameters: $V_{\mathrm{st}} = -1.0\,\mathrm{V}$, $I_{\mathrm{st}} = 300\,\mathrm{pA}$, $V_{\mathrm{start}} = -1.0\,\mathrm{V}$, $V_{\mathrm{end}} = +1.2\,\mathrm{V}$, $V_{\mathrm{mod}} = 5\,\mathrm{mV}$, $\Delta x = \Delta y = 0.25\,\mathrm{Å}$, $x_{\mathrm{range}} = 17\,\mathrm{nm}$, $y_{\mathrm{range}} = 6.5\,\mathrm{nm}$, $T = 4.35\,\mathrm{K}$, 601 points per spectrum.

Variation of the STS stabilization parameters. All spectra up to know are measured with identical stabilization parameters. Fig. E.5 shows $\mathrm{d}I/\mathrm{d}V$ curves acquired with largely varying values of V_{st} and I_{st}. Importantly, even the spectrum with the smallest tip-to-sample distance, i.e., $V_{\mathrm{st}} = -0.5\,\mathrm{eV}$ and $I_{\mathrm{st}} = 0.3\,\mathrm{nA}$ (blue curve in Fig. E.5), exhibits a band gap of $(801 \pm 58)\,\mathrm{meV}$. The analysis of the measurements with larger tip-sample distance yields slightly larger band gap magnitudes. The biggest band gap is extracted

from the measurement with $V_{\mathrm{st}} = -1.5\,\mathrm{V}$ and $I_{\mathrm{st}} = 1.5\,\mathrm{nA}$ and is $(861 \pm 114)\,\mathrm{meV}$ (green curve in Fig. E.5). Fig. E.5 suggests that shifts of the VB maximum rather than of the CB minimum cause the slight variations of the band gap magnitude, and the fit values confirm this observation, which might be caused by tip-induced band bending [214].

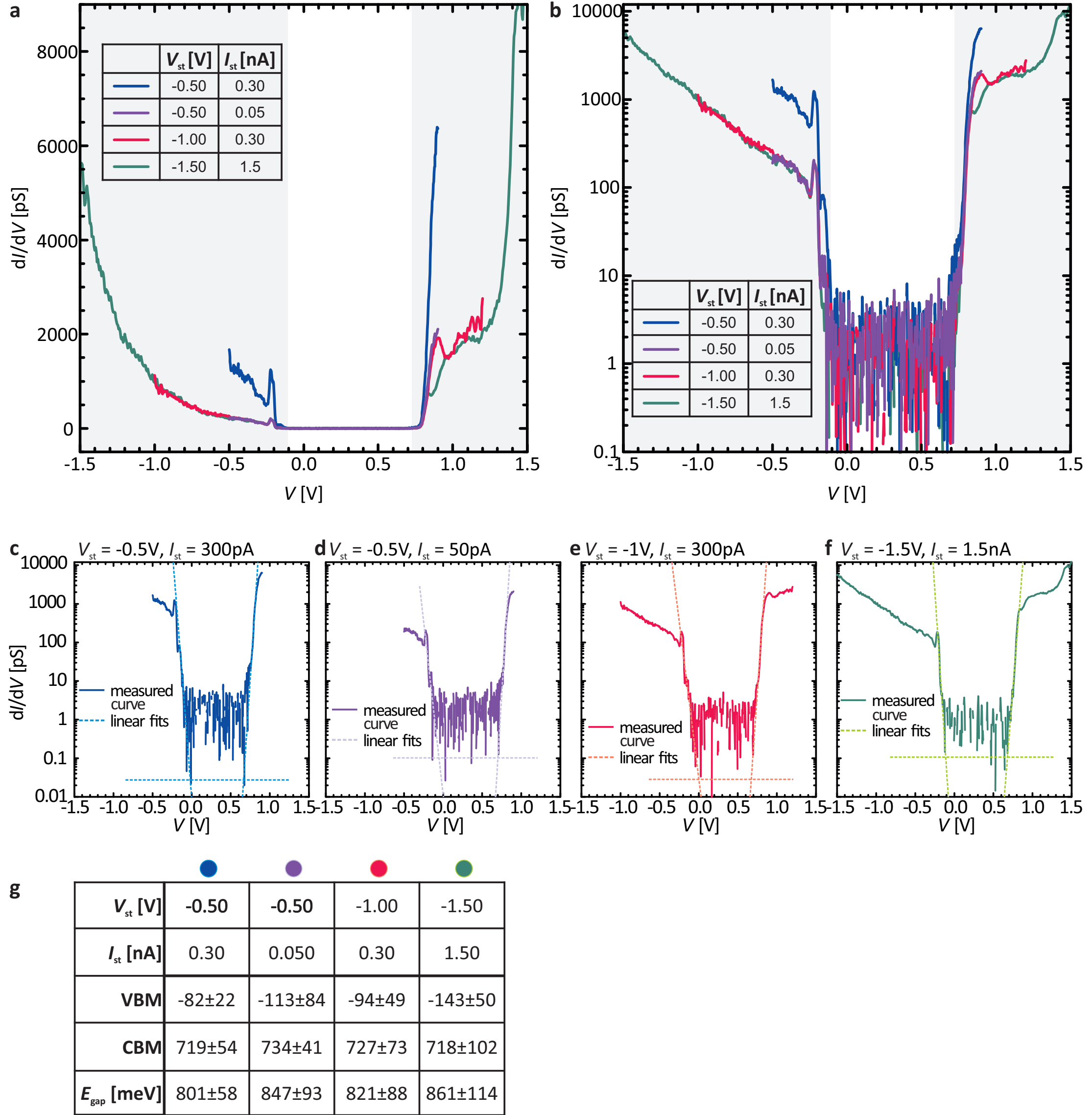

V_{st} [V]	-0.50	-0.50	-1.00	-1.50
I_{st} [nA]	0.30	0.050	0.30	1.50
VBM	-82±22	-113±84	-94±49	-143±50
CBM	719±54	734±41	727±73	718±102
E_{gap} [meV]	801±58	847±93	821±88	861±114

Figure E.5 Point spectroscopy measurements recorded with varying tip stabilization parameters with **a** linear and **b** logarithmic axis scaling. Gray shaded areas denote the presence of bulk states. Stabilization parameters are shown in the diagrams. In all measurements, the following parameters are fixed: $V_{\mathrm{mod}} = 10\,\mathrm{mV}$, $T = 4.35\,\mathrm{K}$, and 601 points per spectrum. **c–f** Fit curves used to determine the band gap magnitude for the different setpoints. Lighter colored dashed lines are linear fits to band edges and the average zero line, while darker colors show the measured spectra. Note that the zero current line seems to be misaligned, but negative $\mathrm{d}I/\mathrm{d}V$ values, which emerge during the numerical derivation of the $I(V)$ curves, are obviously not plotted with logarithmic scaling. **g** The analysis of the band edge energies reveals that the VB edge exhibits a small systematic shift, whereas the CB edge energy seems fixed. This could be related to tip-induced band bending. For all spectra $E_{\mathrm{gap}} > 800\,\mathrm{meV}$.

E.4 Ionization Discs around Disordered Areas

Fig. E.6**a** displays a CCI with two disordered areas of 3–5 nm extent recorded during a grid spectroscopy and already known from Fig. 7.14. Corresponding grid LDOS maps at selected energies in the occupied states are shown in Fig. E.6**b**. They reveal the presence of a circle with increased $\mathrm{d}I/\mathrm{d}V$ signal, which exhibits ≈ 3.5 nm diameter at $E - E_\mathrm{F} = -1.0$ eV and continuously shrinks when the probing energy is increased, until it merges to a point at $E - E_\mathrm{F} = -0.886$ eV with ≈ 0.5 nm extension, limited by the grid resolution.
Such rings are well-known and understood in literature. They have been observed around Si donor atoms in GaAs and studied in detail by the group of P.M. Koenraad (see e.g. Refs. [251, 305, 306]), but their observation is not limited to this semiconductor toy model system (see, e.g., Refs. [249, 250, 307]). A detailed explanation of the underlying mechanism causing their appearance is given in the article by Teichmann et al. [251]. The effect is caused by ionized donor or acceptor impurities, which become charged at a certain threshold, i.e., when the tip-induced band bending is large enough that electrons can escape in the conduction band or holes become occupied by a valence band electron. In the present case, the effect is observed in the occupied states. Hence, the defect acts as acceptor and the electrostatic potential of the tip causes a band bending to higher binding energies. At a certain threshold, the defect level, which is in the band gap in a flat band condition, is pulled below the bulk VB edge, whose electrons occupy states in the acceptor-like defect. The presence of additional charge with respect to the bulk electronic structure causes in increased current from sample to tip. Here, the increase of the ring diameter is connected to a rising absolute probing voltage, compare to the LDOS maps in Fig. 7.14**b**.
In Ref. [251] it has been found that the appearance of ionization rings in $\mathrm{d}I/\mathrm{d}V$ scans is associated with ionization discs in the corresponding CCI measurement.[30] In this case, the reduction of the lateral distance between tip and defect causes a sufficiently large band bending to ionize the defect. Indeed, an ionization disc is observed around surface point defects or disordered areas, as well, see Fig. E.7**a** (CCI) and **b** (LDOS map). The observation of these discs requires a very sharp tip, as the increase of the apparent height is very small.
It is interesting to note that the observed rings and discs in Fig. E.7 clearly deviate from a perfect circle and are not centered around the defect. One possible reason among others to explain this is that the electric potential depends on the entire tip apex. Consequently, the tip shape is reflected on the sample surface, and the contour of the detected rings and discs varies from measurement to measurement [306].

[30] Strictly speaking this disc must be present in all scans with ionization circle in $\mathrm{d}I/\mathrm{d}V$, as the additional charge tunneling from sample to tip or vice versa is compensated by a retraction of the tip in the CCI. As the tip retraction is very small it is easily overwhelmed by the fluctuations of the apparent height.

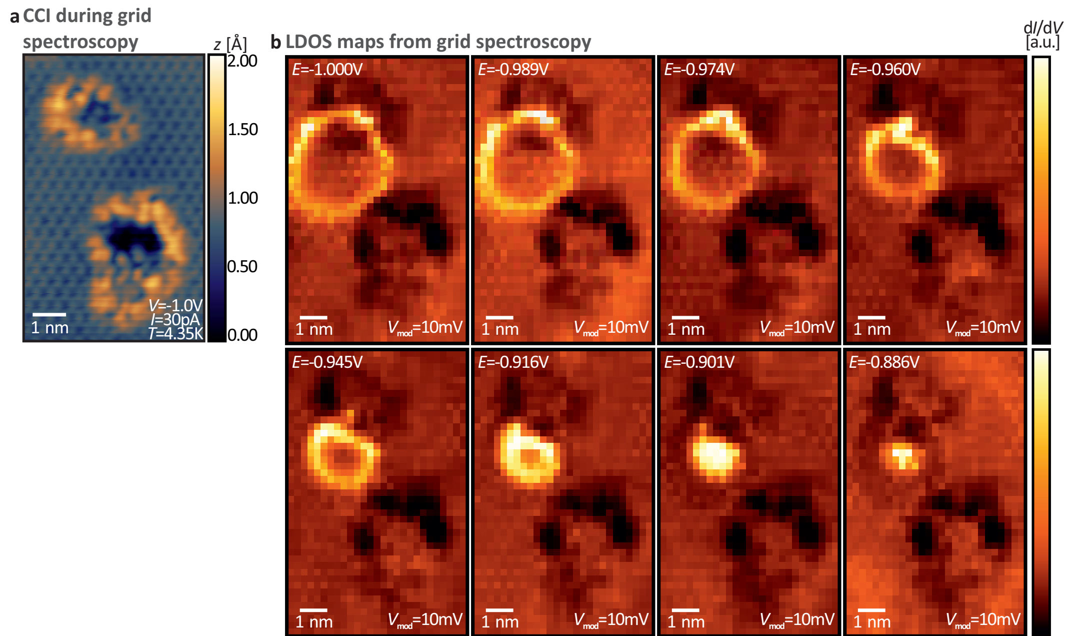

Figure E.6 Ionization rings are found around certain defects on bismuthene. **a** CCI and **b** LDOS maps at variable energy recorded during via a grid spectroscopy measurement, respectively ($V_{\mathrm{st}} = V_{\mathrm{ini}} = -1.0\,\mathrm{eV}$, $V_{\mathrm{end}} = +1.2\,\mathrm{eV}$, $I_{\mathrm{st}} = 300\,\mathrm{pA}$, $V_{\mathrm{mod}} = 10\,\mathrm{meV}$, $\Delta x = 2.41\,\text{Å}$, $\Delta y = 2.44\,\text{Å}$, 601 points per spectrum). In the LDOS maps an almost circular line of higher conductivity is seen, with increasing diameter for higher absolute bias voltage $|V_{\mathrm{T}}|$. Such ionization rings are frequently observed around defects.

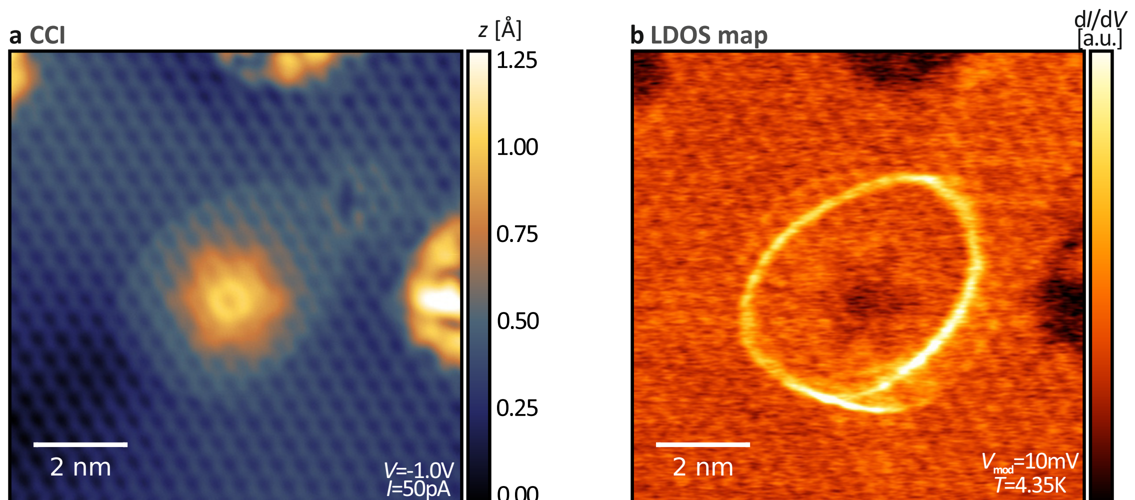

Figure E.7 **a** CCI and **b** corresponding LDOS map around a defect. In the CCI, a disc of higher apparent height is detected, which possesses the same contour as the ionization circle apparent in the $\mathrm{d}I/\mathrm{d}V$ image. Hence, within the extent of the ionization circle, i.e., at small enough diameter, the charged defect becomes ionized.

E.5 Energy Offset of Bands in ARPES ($h\nu = 47\,\mathrm{eV}$) and DFT

The evaluation of band energie offsets at $h\nu = 47\,\mathrm{eV}$, see Fig. E.8, yields the same results as discussed in the main text for $h\nu = 80\,\mathrm{eV}$ (Fig. 7.20 and Tabs. 7.1, 7.2, and 7.3).

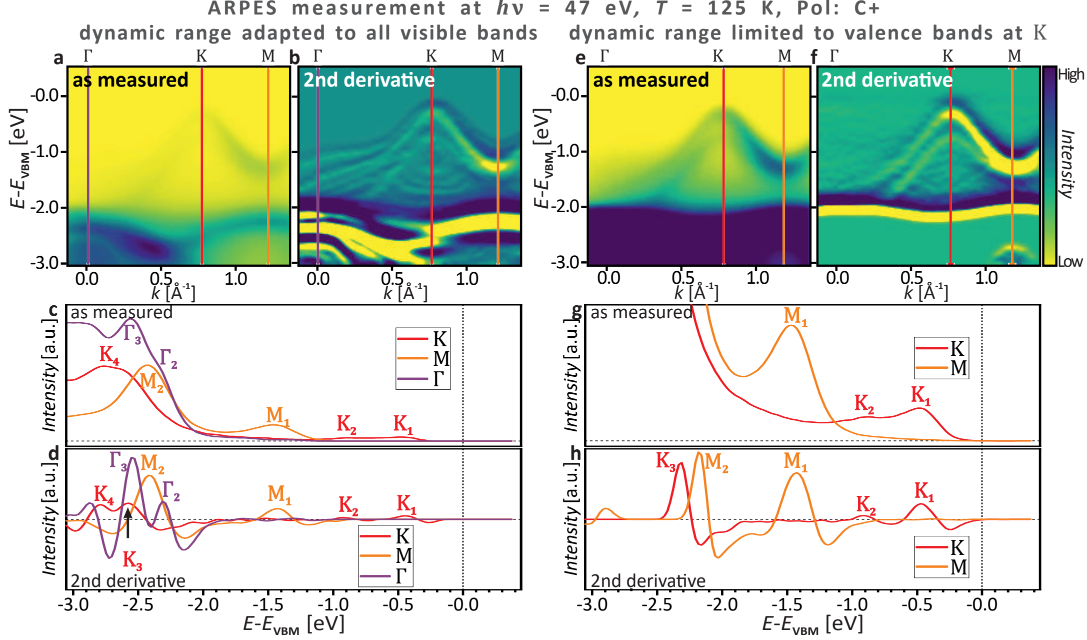

Figure E.8 **a** ARPES bandmap and **b** corresponding 2nd derivative image at $h\nu = 47\,\mathrm{eV}$. **c** and **d** Line profiles at Γ, K and M extracted from the raw data and 2nd derivative image, respectively. **e**–**h** Same as **a**–**d** but with limited dynamic range to focus on the low energy bands. All bandmaps measured at the high-resolution endstation of the SIS beamline (Swiss Light Source). Bandsmaps are smoothed with a Gaussian filter. The 2nd derivative images are smoothed with a Gaussian function before and after twofold derivation along the energy axis.

	$\mathbf{K}_2$	$\mathbf{K}_3$	$\mathbf{K}_4$	$\mathbf{M}_1$	$\mathbf{M}_2$	$\mathbf{\Gamma}_2$	$\mathbf{\Gamma}_3$
$\mathbf{K}_1$	0.464±0.070	2.129±0.035	2.333±0.035	0.983±0.039	1.964±0.034	1.856±0.036	2.088±0.034
$\mathbf{K}_2$		1.665±0.062	1.868±0.062	0.519±0.046	1.500±0.061	1.392±0.062	1.624±0.061
$\mathbf{K}_3$			0.204±0.014	−1.146±0.022	−0.165±0.011	−0.273±0.015	−0.041±0.011
$\mathbf{K}_4$				−1.349±0.022	−0.368±0.018	−0.477±0.020	−0.245±0.094
$\mathbf{M}_1$					0.981±0.020	0.873±0.023	1.105±0.020
$\mathbf{M}_2$						−0.108±0.013	0.124±0.007
$\mathbf{\Gamma}_2$							0.232±0.013

Table E.1 Binding energy offset $E(\mathrm{X}_i^{\mathrm{row}}) - E(\mathrm{X}_j^{\mathrm{col}})$ of bands at high symmetry points. The values are obtained by fitting maxima in the line profiles of the second derivative ARPES band map at $h\nu = 47\,\mathrm{eV}$ (Fig. E.8**b**/**d**). All energies in electronvolt.

	$\mathbf{K}_2$	$\mathbf{K}_3$	$\mathbf{M}_1$	$\mathbf{M}_2$	$\mathbf{M}_3$
$\mathbf{K}_1$	0.444±0.047	1.855±0.014	0.963±0.016	1.712±0.014	2.416±0.033
$\mathbf{K}_2$		1.411±0.045	0.519±0.046	1.269±0.045	1.972±0.054
$\mathbf{K}_3$			−0.891±0.009	−0.142±0.006	0.561±0.030
$\mathbf{M}_1$				0.749±0.010	1.453±0.031
$\mathbf{M}_2$					0.703±0.030

Table E.2 Binding energy offset $E(\mathrm{X}_i^{\mathrm{row}}) - E(\mathrm{X}_j^{\mathrm{col}})$ of bands at high symmetry points. The values are obtained by fitting maxima in the line profiles of the second derivative ARPES band map at $h\nu = 47\,\mathrm{eV}$ with limited dynamic range (Fig. E.8**f**/**h**). All energies in electronvolt.

F Additional Information on the Edge States of Bismuthene

F.1 Additional CCI and LDOS Maps of an Armchair Edge

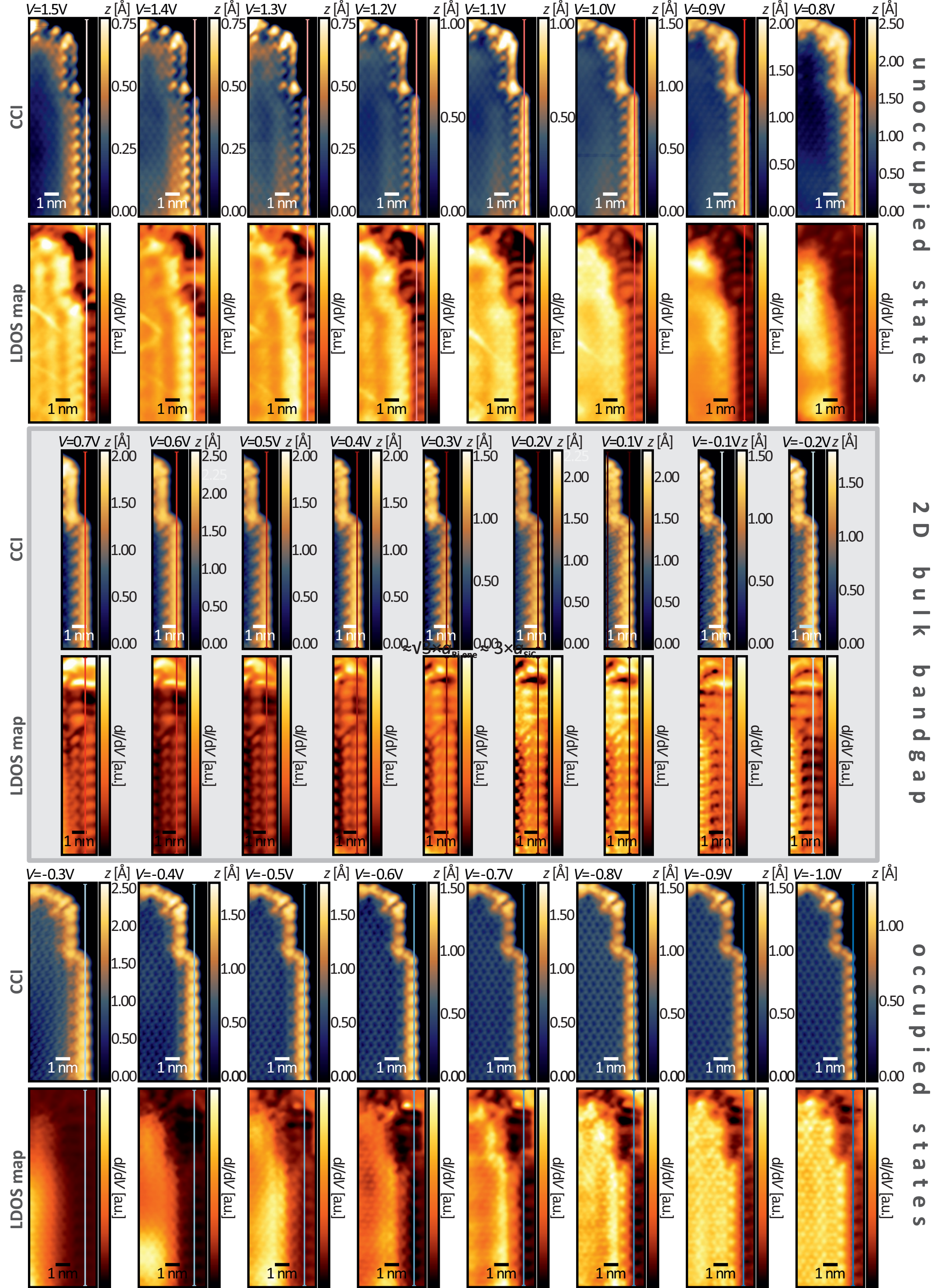

Figure F.1 Additional CCI and LDOS maps capturing an extended armchair edge with perfect ordering and a kink. Only the periodicity of an armchair edge is seen throughout all measurements and additional structures are absent. Measurement parameters: $T = 4.35\,\text{K}$, $I = 100\,\text{pA}$, $V_{\text{mod}}(V = \pm0.1\,\text{eV}) = 10\,\text{meV}$, $V_{\text{mod}}(V = \pm0.2\,\text{eV}) = 20\,\text{meV}$ and $V_{\text{mod}} = 30\,\text{meV}$ in all other scans.

F.2 Python Procedure Used for Analysis of the ZBA

The following pages show the commented Python source code used to analyze and model the ZBA STS curves with the TLL theory (Eq. 8.3).

Header. The header loads all used packages and is shown for the sake of completeness.

```
# Header
import numpy as np
import scipy.optimize as optimize
import os
#GammaFunction
from scipy.special import gamma
#convolution
from scipy import signal
from scipy.signal import savgol_filter
#curve fitting
from scipy.optimize import curve_fit
import astropy.convolution as astro
from astropy.convolution import Gaussian1DKernel
from lmfit import Model
from lmfit.model import save_model, Model, save_modelresult
```

TLL function. The *TLL* function models a TLL without thermal or instrumental broadening and is only used to normalize the lock-in spectra after scaling, as the probed signal is often spiky at $V_{\text{ini}}/V_{\text{end}}$, rendering a direct, reliable normalization with the measured signal itself impossible.
The function comprises free fit parameters, i.e., a scaling constant 'c' and offset 'o'. Normalization with use of a less complex function (power function, linear function) was attempted but produces worse results.

```
#TLL function
def TLL(V,a=0.5,c=0.3,o=0.5, T=10):
    kB=8.617e-5
    Voff=4
    conv=c*(T**a)*np.cosh((V-Voff)*0.001/(2*kB*T))*(np.absolute(gamma((1+a)/2+1j*0.001*
        (V-Voff)/(2*kB*T*np.pi))))**2+o
    return conv

TLLmodel = Model(TLL)
TLLmodel.set_param_hint('a',min=0.0, max=1.0)
TLLmodel.set_param_hint('c',min=0.0, max=1000, vary=True)
TLLmodel.set_param_hint('o',min=-0.5, max=0.5, vary=True)
TLLmodel.set_param_hint('T', vary=False )
params=TLLmodel.make_params(a=0.4, c=0.5, o=-0.2, T=95)
```

TLL function including thermal and instrumental broadening. The *nTLLwTwG* function models a TLL in the given energy range, as the TLL function. In addition, it generates a convolution to incorporate (i) thermal broadening (wT) in the form of a derivative of the Fermi distribution, and (ii) a subsequent second convolution to account for instrumental broadening (wG). Lastly, it normalizes the model curve (nTLL) and returns the resulting array. Note that α is the only free fit parameter in the given function.

```
#nTLLwTwG function
def nTLLwTwG(V,a=0.5, T=10):
    kB=8.617e-5
    Voff=-2
    length=2.5/(((max(V)-min(V))*2*np.sqrt(2*np.log(2)))/np.size(V))
    conv=astro.convolve(T**a*np.cosh((V-Voff)*0.001/(2*kB*T))
        *np.absolute(gamma((1+a)/2+1j*0.001*(V-Voff)/(2*kB*T*np.pi)))**2,
        1/(4*kB*T)*(1/np.cosh(0.001*(V-Voff)/(2*kB*T)))**2, 'extend')
    gauss=Gaussian1DKernel(length)
    convv=astro.convolve(conv, gauss, 'extend')
    nconv=convv/max(convv)
    return nconv
#It is important to set parameter hints.
#Otherwise, fitting won't work (kernel produces NANs errormessage!)
nTLLwTwGmodel = Model(nTLLwTwG)
nTLLwTwGmodel.set_param_hint('a',min=0.0, max=1.0)
nTLLwTwGmodel.set_param_hint('T', vary=False)
params=nTLLwTwGmodel.make_params(a=0.4, T=4.35)
```

Auxiliary functions. Small auxiliary functions are defined to perform array shifting, scaling, and derivation of the measured curves.

```
#shifter function:
def shifter(arr):
    i=0
    shifted=arr.copy()
    while i< np.size(arr,1):
        shifted[:,i]=arr[:,i]-4
        i+=2
    return shifted

#scale function:
def scale(unscaled,mul=1.0,off=1.0):
    scaled=unscaled.copy()
    scaled=off+mul*unscaled
    return scaled

#deriver function:
```

```
def deriver(iv, aux, T, number=1):
    i=number
    scaled=iv.copy()
    V=iv[:,0].copy()
    while i<np.size(iv,1):
        smooth=savgol_filter(iv[:,i], 25,0, deriv=0, mode='interp')
        scaled[:,i]=1000*savgol_filter(smooth,7 ,1, deriv=1, mode='wrap')
        i+=2
    return scaled
```

Normalizer function. The *normalizer* function is used to scale the lock-in signals to real $\mathrm{d}I/\mathrm{d}V$ values. Firstly, a smoothed $I(V)$ curve is derived and smoothed with use of the Savitzky-Golay filter function implemented in *Scipy* package. Next, the lock-in data are scaled to real values with help of the "scale" function. This step is necessary to make the spectra of different experimental runs or at different positions comparable. A curve fit with the *TLL* function is used to compute a model, which is fitted to the rescaled lock-in arrays. Its only use is to avoid that the subsequent normalization of the rescaled lock-in arrays is carried out with scattered values, which causes false fit results when computing α of the individual arrays with the *nTLLwTwG* function.

```
def normalizer(iv, aux, T, number=1):
    i=number
    scaled=iv.copy()
    V=iv[:,0].copy()
    while i<np.size(iv,1):
        deriv=savgol_filter(iv[:,i], 3,1, deriv=1, mode='interp')
        scalopt, scalcov=curve_fit(scale,aux[:,i],deriv)
        tll=TLLmodel.fit(scale(aux[:,i], *scalopt), a=0.4, c=0.5, o=-0.0,
                T=T, V=V, method='least_squares')
        scaled[:,i]=scale(aux[:,i], *scalopt)/max(tll.best_fit)
        i+=2
    return scaled
```

Alphawriter function. The *alphawriter* function uses the normalized STS data generated by the *normalizer function* and performs a curve fit with the *nTLLwTwG* function. After that, the best fit value of α and the respective standard error is written into a text file. The *alphawriter_redchi_ranged* is a variation of this function, which calculates the reduced χ^2 value of the fit. In this way, it is assured that only fits with reliable quality enter into the averaged value of α. The ranged output is used for the same reason. Before setting these limits, the average α value has been estimated with the unconstrained output of the *alphawriter* function.

```
def alphawriter(arr, T=77, name='filename', number=1):
    i=number
    while i < np.size(arr,1):
        V=arr[:,0]
```

```
        result= nTLLwTwGmodel.fit(arr[:,i], a=0.4, T=T, V=V,
                method='least_squares')
        u=''
        u=['\n', str((i+1)/2), '\t', str(result.params['a'].value), '\t',
                str(result.params['a'].stderr)] # array
        with open(name,'a') as outfile:
            outfile.writelines(u)
        i+=2

#Alternative version including a fit quality check and ranged output:
def alphawriter_redchi_ranged(arr, T=77, name='filename', number=1):
    i=number
    while i < np.size(arr,1):
        V=arr[:,0]
        result= nTLLwTwGmodel.fit(arr[:,i], a=0.4, T=T, V=V,
                method='least_squares')
        if (0.3<= result.params['a'].value <=0.5) and (result.redchi<0.05):
            u=''
            u=['\n', str((i+1)/2), '\t', str(result.params['a'].value),
                        '\t', str(result.params['a'].stderr)]
            with open(name,'a') as outfile:
                outfile.writelines(u)
        i+=2
```

Zeroconductance function. The *zeroconductance* function exports the zero bias conductance obtained with *nTLLwTwG model* fit into a text file. Again, the fit quality is checked by calculation of the reduced χ^2 and a ranged output is generated.

```
def zeroconductance_redchi_ranged(arr, T=77, name='filename', number=1):
    i=number
    if np.size(arr[:,0])==501:
        shiftvalue=int(10)
    elif np.size(arr[:,0])==601:
        shiftvalue=int(12)
    while i < np.size(arr,1):
        V=arr[:,0]
        result= nTLLwTwGmodel.fit(arr[:,i], a=0.4, T=T, V=V,
                method='least_squares')
        if (0.3<= result.params['a'].value <=0.5) and (result.redchi<0.05):
            u=''
            u=['\n', str((i+1)/2), '\t',
                        str(result.best_fit[int((np.size(V)-1)/2)+shiftvalue])]
            with open(name,'a') as outfile:
                outfile.writelines(u)
        i+=2
```

F.3 Parameters of the ZBA Grid Spectroscopy Measurements

T[K]	I_{st}[nA]	V_{st}[mV]	V_{ini}[mV]	V_{end}[mV]	Points	Sample	No. Anal. Spectra
4.35	1	-300	-100	100	501	4	1348
	1	-300	-100	100	501	2	46
	0.3	-100	-100	100	501	1	22
	1	-300	-100	100	501	1	8
10	1	-300	-100	100	501	2	82
15	0.3	-100	-100	100	501	1	13
	1	-300	-100	100	501	1	9
25	1	-300	-100	100	501	2	19
30	1	-300	-100	100	501	2	11
45	0.3	-100	-100	100	501	1	35
	1	-300	-100	100	501	1	33
55	1	-300	-100	100	501	2	14
77	0.3	-100	-100	100	501	1	90
	0.3	-100	-100	100	501	1	75
	1	-300	-100	100	501	1	93
95	1	-300	-100	100	601	1	169
	1	-300	-100	100	601	1	191
110	1	-300	-120	120	501	3	49

Table F.1 Parameters used in the different grid spectroscopy measurements presented in Fig. 8.13. Note that the number of spectra recorded at higher temperature is rather low as the rest time of the cryostat is fairly short when measuring at elevated temperatures using LHe caooling. For example, a measuring time of less than 30 min has been available for the experiment conducted at $T = 55$ K. Before data acquisition, the search for a suitable step edge, the piezo drift correction and the set up of the grid spectroscopy must be accomplished, such that not much time remains available for the ZBA spectroscopy measurement.

F.4 Influence of the Power-Law Exponent and Broadening Effects

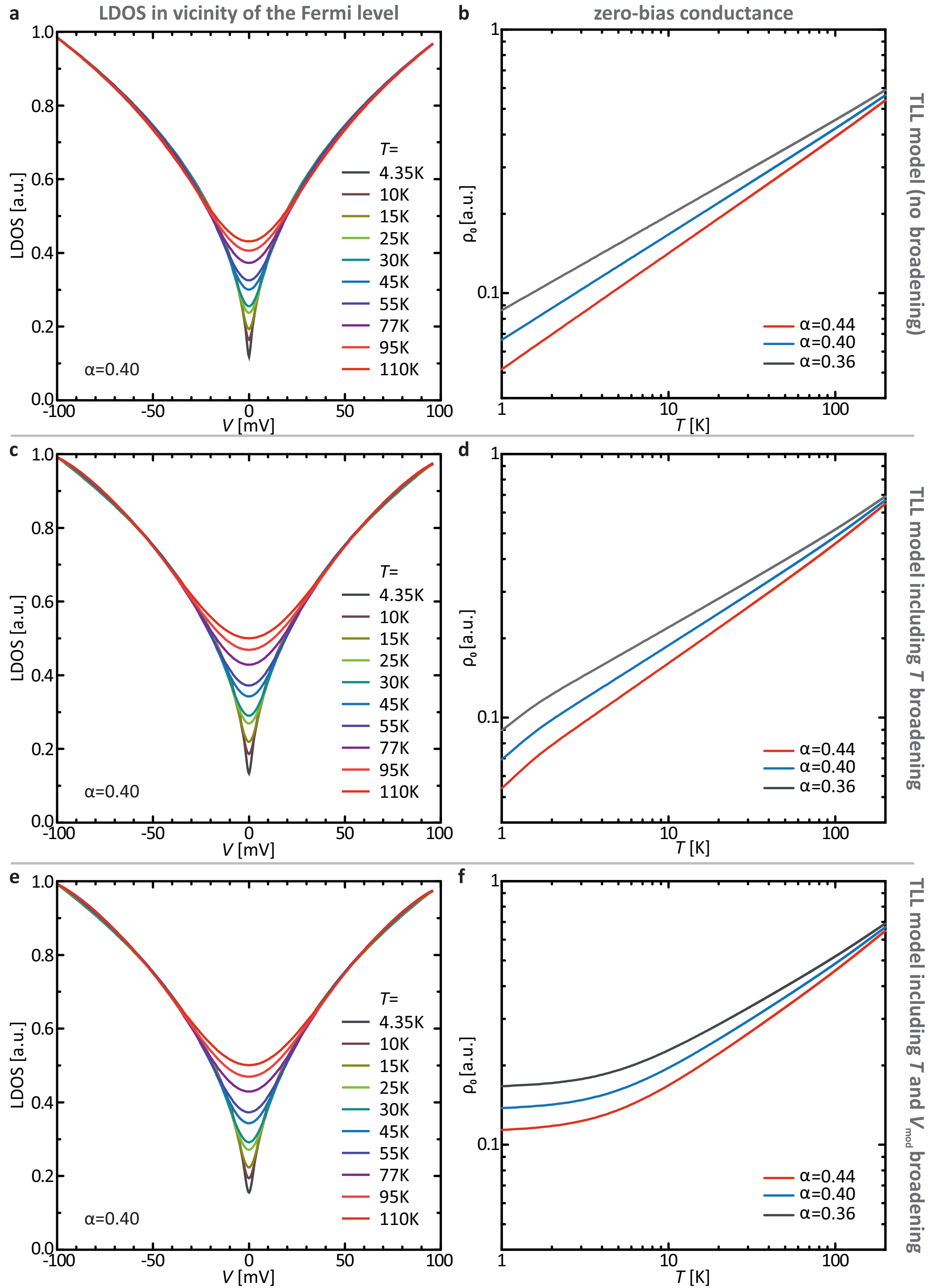

Figure F.2 Modeling of the spectral function (left column) and the zero-bias conductance (right cloumn) of a TLL with no broadening (**a**, **b**), with thermal broadening (**c**, **d**), and with thermal and instrumental broadening (**e**,**f**). Instrumental broadening has a major influence at very low temperatures, whereas the influence of thermal broadening increases mainly at larger T.

F.5 Dynamical Coulomb Blockade Theory

The DCB can be modeled quantum mechanically with the $P(E)$ theory. The $P(E)$ function describes the probability that an electron exchanges energy with the surrounding, dissipative environment, which is modeled as a frequency-dependent impedance $Z(\omega)$ [276]. The tunneling probability of a single electron is given by [277]

$$\Gamma_{\text{tip}\rightarrow\text{ sample}} = \frac{1}{e^2 R_{\text{T}}} \int\int dE\, dE'\, \rho_{\text{T}}(E)\, \rho_{\text{S}}(E' - eV)\, f(E,T) \times \\ \times [1 - f'(E' - eV, T)] P(E - E'), \tag{F.1}$$

where V is the applied bias voltage, f is the Fermi function, T is the temperature, E and E' are the energy levels of tip and sample, respectively, ρ_{T} and ρ_{S} are the DOS of tip and sample, respectively, and $P(E-E')$ describes the probability that the energy $E-E'$ is emit to the dissipative environment. Note that $E - E' < 0$ indicates that energy is absorbed from the surrounding. In elastic tunneling, the energy is conserved and $P(E-E')$ reduces to the delta function. In general, $P(E)$ is modeled by [270]:

$$P(E) = \frac{1}{2\pi\hbar} \int_{-\infty}^{+\infty} dt\, e^{[J(t) + iEt/\hbar]} \tag{F.2}$$

where [270]

$$J(t) = 2 \int_0^{+\infty} \frac{d\omega}{\omega} \frac{\text{Re}Z(\omega)}{R_K} \frac{e^{-i\omega t} - 1}{1 - e^{-\hbar\omega/k_{\text{B}}T}}, \tag{F.3}$$

with the Boltzmann constant k_{B} and the resistance quantum R_{K}. The total impedance $Z(\omega)$ of the two junction system is [270]

$$Z(\omega) = \frac{1}{i\omega C_{\text{T}} + Z_{\text{ex}}^{-1}(\omega)}, \tag{F.4}$$

where C_{T} is the capacitance of the T-junction, and the frequency-dependent impedance of the environment is [270]

$$Z_{\text{ex}}(\omega) = \frac{1}{i\omega C + 1/R}. \tag{F.5}$$

with C and R being the capacitance and resistance of the S-junction (see Fig. 8.17). The total impedance (Eq. F.4) may be rewritten with $C_{\Sigma} = C_{\text{T}} + C$ [270],

$$Z(\omega) = \frac{1}{i\omega C_{\Sigma} + 1/R} \approx \frac{1}{i\omega C + 1/R}, \tag{F.6}$$

which can be analytically solved if that $C_{\text{T}} \ll C$, which is assumed in the last step [270, 277].

The reverse tunneling probability (from sample to tip) is described by [278]:

$$\Gamma_{\text{sample}\rightarrow\text{ tip}} = \frac{1}{e^2 R_{\text{T}}} \int\int dE\, dE'\, \rho_{\text{T}}(E)\, \rho_{\text{S}}(E' - eV)\, [1 - f(E,T)] \times \\ \times f'(E' - eV, T) P(E' - E). \tag{F.7}$$

Using Eq. F.1 and Eq. F.7, total tunneling current as the difference between

$$I(V) = -e(\Gamma_{\text{tip}\to\text{ sample}} - \Gamma_{\text{sample}\to\text{ tip}}) \tag{F.8}$$

In order to simulate the probed LDOS it is necessary to know ρ_T as well as ρ_S [277, 308]. The tip DOS ρ_T is assured to be constant in the energy range of $-100\,\text{meV} \leq eV \leq +100\,\text{meV}$ by characterization with the Shockley-type surface state on Ag(111). The sample DOS is approximately constant apart from the dip at zero bias in STS, which is not inherent part of the sample's DOS as was demonstrated by measurements with varying position of E_F, compare to Figs. 8.5 and 8.6. Moreover, it can be considered constant in the nanoribbon calculations (Fig. 4.10). Consequently, it may be assumed to be fairly flat in the energy range of interest. By derivation of $I(V)$ we obtain an expression for the differential conductivity, which is probed in STS experiments [279]:

$$\frac{dI}{dV}(eV) = \frac{1}{R_\text{T}}[1 + 2\int_0^\infty dt\,\frac{\pi k_\text{B}^2 T^2}{\hbar^2}\,\text{Im}[e^{J(t)}]\cos(\frac{eVt}{\hbar})\,\text{csch}^2(\frac{\pi k_\text{B} T t}{\hbar})\,t]. \tag{F.9}$$

Bibliography

[1] E. Hittinger and P. Jaramillo: "Internet of Things: Energy boon or bane?" *Science* **364**, 326–328 (2019) (cit. on p. 1).

[2] E. Masanet, A. Shehabi, N. Lei, S. Smith, and J. Koomey: "Recalibrating global data center energy-use estimates". *Science* **367**, 984–986 (2020) (cit. on p. 1).

[3] M. M. Waldop: "More than Moore". *Nature* **530**, 144 (2016) (cit. on p. 1).

[4] A. K. Geim and K. S. Novoselov: "The rise of graphene". *Nature Materials* **6**, 183–191 (2007) (cit. on p. 1).

[5] N. R. Glavin, R. Rao, V. Varshney, E. Bianco, A. Apte, A. Roy, E. Ringe, and P. M. Ajayan: "Emerging Applications of Elemental 2D Materials". *Advanced Materials* **32**, 1904302 (2020) (cit. on pp. 1, 3, 37).

[6] P. Vishnoi, K. Pramoda, and C. N. R. Rao: "2D Elemental Nanomaterials Beyond Graphene". *ChemNanoMat* **5**, 1062–1091 (2019) (cit. on pp. 1, 37).

[7] G. Li, Y.-Y. Zhang, H. Guo, L. Huang, H. Lu, X. Lin, Y.-L. Wang, S. Du, and H.-J. Gao: "Epitaxial growth and physical properties of 2D materials beyond graphene: from monatomic materials to binary compounds". *Chemical Society Reviews* **47**, 6073–6100 (2018) (cit. on pp. 1, 37).

[8] K. Premasiri and X. P. A. Gao: "Tuning spin–orbit coupling in 2D materials for spintronics: a topical review". *Journal of Physics: Condensed Matter* **31**.19, 193001 (2019) (cit. on p. 1).

[9] M. Kim, Z. Jacob, and J. Rho: "Recent advances in 2D, 3D and higher-order topological photonics". *Light: Science and Applications* **9** (2020) (cit. on p. 2).

[10] *Creative Commons Attribution 4.0 International License*. `https://creativecommons.org/licenses/by/4.0/`. 2021 (cit. on pp. 2, 64).

[11] C. L. Kane and E. J. Mele: "Quantum Spin Hall Effect in Graphene". *Physical Review Letters* **95**, 226801 (2005) (cit. on pp. 1, 2, 32–34, 45, 47, 52, 53).

[12] C. L. Kane and E. J. Mele: "Z_2 Topological Order and the Quantum Spin Hall Effect". *Physical Review Letters* **95**, 146802 (2005) (cit. on pp. 1, 2, 32–34, 45, 146).

[13] M. Z. Hasan and C. L. Kane: "*Colloquium* : Topological insulators". *Reviews of Modern Physics* **82**, 3045 (2010) (cit. on pp. 1, 2, 27, 28, 30, 32, 35, 146).

[14] S. Rachel: "Interacting topological insulators: a review". *Reports on Progress in Physics* **81**, 116501 (2018) (cit. on pp. 1, 2, 27, 28, 34, 35, 146).

[15] B. A. Bernevig and S.-C. Zhang: "Quantum Spin Hall Effect". *Phys. Rev. Lett.* **96**, 106802 (2006) (cit. on p. 2).

[16] B. A. Bernevig, T. L. Hughes, and S. C. Zhang: "Quantum Spin Hall Effect and Topological Phase Transition in HgTe Quantum Wells". *Science* **314**, 1757 (2006) (cit. on pp. 2, 35).

[17] M. König, S. Wiedmann, C. Brüne, A. Roth, H. Buhmann, L. W. Molenkamp, Q. X. L., and Z. S. C.: "Quantum Spin Hall Insulator State in HgTe Quantum Wells". *Science* **318**, 766 (2007) (cit. on pp. 2, 35).

[18] G. Li, W. Hanke, E. M. Hankiewicz, F. Reis, J. Schäfer, R. Claessen, C. Wu, and R. Thomale: "Theoretical paradigm for the quantum spin Hall effect at high temperatures". *Physical Review B* **98**, 165146 (2018) (cit. on pp. 2, 37, 43, 45–47, 52–57).

[19] A. Molle, J. Goldberger, M. Houssa, Y. Xu, S.-C. Zhang, and D. Akinwande: "Buckled two-dimensional Xene sheets". *Nature Materials* **16**, 163–169 (2017) (cit. on pp. 2, 3, 37, 47).

[20] S. Wu, V. Fatemi, Q. D. Gibson, K. Watanabe, T. Taniguchi, R. J. Cava, and P. Jarillo-Herrero: "Observation of the quantum spin Hall effect up to 100 kelvin in a monolayer crystal". *Science* **359**, 76–79 (2018) (cit. on pp. 3, 36).

[21] L. Zhang, T. Gong, Z. Yu, H. Dai, Z. Yang, G. Chen, J. Li, R. Pan, H. Wang, Z. Guo, H. Zhang, and X. Fu: "Recent Advances in Hybridization, Doping, and Functionalization of 2D Xenes". *Advanced Functional Materials* **n/a**, 2005471 () (cit. on p. 3).

[22] G. Binnig and H. Rohrer: "Scanning tunneling microscopy—from birth to adolescence". *Reviews of Modern Physics* **59**, 615–625 (1987) (cit. on pp. 5, 10, 12).

[23] C. Davisson and L. H. Germer: "The Scattering of Electrons by a Single Crystal of Nickel". *Nature* **119**, 558–560 (1927) (cit. on p. 5).

[24] A. Einstein: "Über einen die Erzeugung und Verwandlung des Lichtes betreffenden heuristischen Gesichtspunkt". *Annalen der Physik* **322**, 132–148 (1905) (cit. on pp. 5, 19).

[25] K. Siegbahn: "Electron spectroscopy for atoms, molecules, and condensed matter". *Reviews of Modern Physics* **54**, 709–728 (1982) (cit. on pp. 5, 19).

[26] W. Kohn: "Nobel Lecture: Electronic structure of matter—wave functions and density functionals". *Reviews of Modern Physics* **71**, 1253–1266 (1999) (cit. on p. 5).

[27] T. Seyller: "Hydrogen-Saturated SiC-Surfaces: Model Systems for Studies of Passivation, Reconstruction and Interface Formation". *Materials Science Forum* **483-485**, 535–540 (2005) (cit. on pp. 5, 7, 49).

[28] N. Sieber, T. Seyller, L. Ley, D. James, J. D. Riley, R. C. G. Leckey, and M. Polcik: "Synchrotron x-ray photoelectron spectroscopy study of hydrogen-terminated $6H-$SiC0001 surfaces". *Physical Review B* **67**, 205304 (2003) (cit. on p. 5).

[29] D. Zhuang and J. Edgar: "Wet etching of GaN, AlN, and SiC: a review". *Materials Science and Engineering: R: Reports* **48**.1, 1–46 (2005) (cit. on pp. 5, 6).

[30] U. Starke: "Atomic structure of hexagonal SiC surfaces". *Physica Status Solidi B Basic Solid State Physics* **202**, 475–499 (1997) (cit. on pp. 6, 7, 165).

[31] T. Seyller: "Passivation of hexagonal SiC surfaces by hydrogen termination". *Journal of Physics: Condensed Matter* **16** (2004) (cit. on pp. 6, 7, 72, 80, 84, 97, 98, 170).

[32] H. Tsuchida, I. Kamata, and K. Izumi: "Infrared attenuated total reflection spectroscopy of 6H–SiC(0001) and (000$\bar{1}$) surfaces". *Journal of Applied Physics* **85**, 3569–3575 (1999) (cit. on pp. 6, 7, 68, 72, 170).

[33] L. I. Johansson, F. Owman, and P. Mårtensson: "High-resolution core-level study of 6H-SiC(0001)". *Physical Review B* **53**, 13793–13802 (1996) (cit. on pp. 6, 165).

[34] K. V. Emtsev, A. Bostwick, K. Horn, J. Jobst, G. L. Kellogg, L. Ley, J. L. McChesney, T. Ohta, S. A. Reshanov, J. Röhrl, E. Rotenberg, A. K. Schmid, D. Waldmann, H. B. Weber, and T. Seyller: "Towards wafer-size graphene layers by atmospheric pressure graphitization of silicon carbide". *Nature Materials* **8**, 203–207 (2009) (cit. on p. 6).

[35] N. Mishra, J. Boeckl, N. Motta, and F. Iacopi: "Graphene growth on silicon carbide: A review". *Physica Status Solidi A Applications and Material Science* **213**, 2277–2289 (2016) (cit. on p. 6).

[36] J. Chase M.W.: "NIST-JANAF Thermochemical Tables, Fourth Edition". *J. Phys. Chem. Ref. Data, Monogr. 9*, 1–1951 (1998) (cit. on p. 6).

[37] S. Glass, F. Reis, M. Bauernfeind, J. Aulbach, M. R. Scholz, F. Adler, L. Dudy, G. Li, R. Claessen, and J. Schäfer: "Atomic-Scale Mapping of Layer-by-Layer Hydrogen Etching and Passivation of SiC(0001) Substrates". *Journal of Physical Chemistry C* **120**, 10361–10367 (2016) (cit. on pp. 6, 65, 67).

[38] Q. Xue, Q. K. Xue, Y. Hasegawa, I. S. T. Tsong, and T. Sakurai: "Two-step preparation of 6H–SiC(0001) surface for epitaxial growth of GaN thin film". *Applied Physics Letters* **74**, 2468–2470 (1999) (cit. on pp. 6, 72).

[39] J. Hassan, J. Bergman, A. Henry, and E. Janzén: "In-situ surface preparation of nominally on-axis 4H-SiC substrates". *Journal of Crystal Growth* **310**, 4430–4437 (2008) (cit. on pp. 6, 64).

[40] Z. Y. Xie, C. H. Wei, L. Y. Li, Q. M. Yu, and J. H. Edgar: "Gaseous etching of 6H-SiC at relatively low temperatures". *Journal of Crystal Growth* **217**, 115–124 (2000) (cit. on pp. 6, 64, 72, 170).

[41] V. Ramachandran, M. F. Brady, A. R. Smith, R. M. Feenstra, and D. W. Greve: "Preparation of atomically flat surfaces on silicon carbide using hydrogen etching". *Journal of Electronic Materials* **27**, 308–312 (1998) (cit. on pp. 6, 7, 72, 75, 170).

[42] F. Owman, C. Hallin, P. Mårtensson, and E. Janzén: "Removal of polishing-induced damage from 6H-SiC(0001) substrates by hydrogen etching". *Journal of Crystal Growth* **167**, 391–395 (1996) (cit. on pp. 6, 62, 72, 170).

[43] J. Schardt, C. Bram, S. Müller, U. Starke, K. Heinz, and K. Müller: "LEED structure determination of hexagonal α-SiC surfaces". *Surface Science* **337**, 232–242 (1995) (cit. on p. 7).

[44] N. Sieber, B. F. Mantel, T. Seyller, J. Ristein, L. Ley, T. Heller, D. R. Batchelor, and D. Schmeißer: "Electronic and chemical passivation of hexagonal 6H-SiC surfaces by hydrogen termination". *Applied Physics Letters* **78**, 1216–1218 (2001) (cit. on pp. 7, 170).

[45] T. Seyller: "Electronic properties of SiC surfaces and interfaces: some fundamental and technological aspects". *Applied Physics A* **85**, 371–385 (2006) (cit. on pp. 7, 65, 68, 78, 80).

[46] N. Sieber, M. Hollering, J. Ristein, and L. Ley: "Photoemission Study of the Silicate Adlayer Reconstruction on Si-terminated 6H-SiC (0001)". *Materials Science Forum* **338-342**, 391–394 (2000) (cit. on p. 7).

[47] J. R. Arthur: "Molecular beam epitaxy". *Surface Science* **500**, 189–217 (2002) (cit. on pp. 8, 9).

[48] M. Henini, ed.: *Molecular Beam Epitaxy*. 1st ed. Elsevier. doi: `dx.doi.org/https://doi.org/10.1016/C2010-0-68986-3` (2013) (cit. on pp. 8, 9).

[49] F. Huber, J. Berwanger, S. Polesya, S. Mankovsky, H. Ebert, and F. J. Giessibl: "Chemical bond formation showing a transition from physisorption to chemisorption". *Science* **366**, 235–238 (2019) (cit. on p. 8).

[50] S. Valdueza-Felip: "Nitride-Based Semiconductor Nanostructures for Applications in Optical Communications at 1.5µm". Dissertation. Universidad de Alcalá (2011) (cit. on p. 8).

[51] I. Daruka and A.-L. Barabási: "Dislocation-Free Island Formation in Heteroepitaxial Growth: A Study at Equilibrium". *Physical Review Letters* **79**, 3708–3711 (1997) (cit. on pp. 8, 9).

[52] H. Güntherodt, D. Anselmetti, R. Wiesendanger, R. Behm, P. van Bentum, S. Chiang, R. Hamers, H. Hug, H. van Kempen, Y. Kuk, et al.: *Scanning Tunneling Microscopy I: General Principles and Applications to Clean and Absorbate-Covered Surfaces*. Springer Series in Surface Sciences. Springer-Verlag Berlin Heidelberg. doi: `dx.doi.org/10.1007/978-3-642-79255-7` (1994) (cit. on pp. 9, 11, 13).

[53] C. J. Chen: *Introduction to Scanning Tunneling Microscopy*. 2nd ed. Oxford University Press. doi: `dx.doi.org/10.1093/acprof:oso/9780199211500.001.0001` (2007) (cit. on pp. 9, 10, 12).

[54] J. Kügel: "3*d*-Übergangsmetallphtalocynin-Moleküle auf Metalloberflächen: Der Einfluss der *d*-Orbitalbesetzung". Dissertation. Julius-Maximilians-Universität Würzburg (2015) (cit. on p. 10).

[55] I. Ekvall, E. Wahlström, D. Claesson, H. Olin, and E. Olsson: "Preparation and characterization of electrochemically etched W tips for STM". *Measurement Science and Technology* **10**.1, 11–18 (1999) (cit. on p. 11).

[56] C. J. Chen: "Microscopic view of scanning tunneling microscopy". *Journal of Vacuum Science & Technology A* **9**, 44–50 (1991) (cit. on p. 12).

[57] J. Bardeen: "Tunnelling from a Many-Particle Point of View". *Physical Review Letters* **6**, 57–59 (1961) (cit. on p. 12).

[58] J. Tersoff and D. R. Hamann: “Theory of the scanning tunneling microscope”. *Physical Review B* **31**, 805–813 (1985) (cit. on pp. 12, 13).

[59] R. J. Hamers: “Atomic-Resolution Surface Spectroscopy with the Scanning Tunneling Microscope”. *Annual Review of Physical Chemistry* **40**, 531–559 (1989) (cit. on pp. 13, 14, 17).

[60] C. J. Chen: “Origin of atomic resolution on metal surfaces in scanning tunneling microscopy”. *Physical Review Letters* **65**, 448–451 (1990) (cit. on p. 13).

[61] M. Ternes: “Scanning tunneling spectroscopy at the single atom scale”. Dissertation. École Polytechnique Fédérale de Lausanne (2006) (cit. on pp. 15, 17, 146, 150).

[62] M. F. Crommie, C. P. Lutz, and D. M. Eigler: “Imaging standing waves in a two-dimensional electron gas”. *Nature* **363**, 524 (1993) (cit. on pp. 17, 141).

[63] S. Hüfner: *Photoelectron Spectroscopy*. 3rd ed. Springer-Verlag Berlin Heidelberg. doi: `dx.doi.org/10.1007/978-3-662-09280-4` (2003) (cit. on p. 17).

[64] C. Westphal: “The study of the local atomic structure by means of X-ray photoelectron diffraction”. *Surface Science Reports* **50**, 1–106 (2003) (cit. on p. 17).

[65] M. A. Van Hove, W. H. Weinberg, and C.-M. Chan: *Low energy electrons diffraction - Experiment, Theory and Surface Structure Determination*. Springer-Verlag Berlin Heidelberg. doi: `dx.doi.org/10.1007/978-3-642-82721-1` (1986) (cit. on p. 18).

[66] F.-J. Meyer zu Heringdorf and M. Horn-von Hoegen: “Reciprocal space mapping by spot profile analyzing low energy electron diffraction”. *Review of Scientific Instruments* **76**, 085102 (2005) (cit. on p. 18).

[67] G. Ertl and J. Küppers: *Low Energy Electrons and Surface Chemistry*. VCH Verlagsgesellschaft mbH. doi: `dx.doi.org/10.1002/bbpc.19870910223` (1985) (cit. on pp. 18, 87).

[68] H. Hertz: “Ueber einen Einfluss des ultravioletten Lichtes auf die electrische Entladung”. *Annalen der Physik* **267**, 983–1000 (1887) (cit. on p. 19).

[69] A. Damascelli: “Probing the Electronic Structure of Complex Systems by ARPES”. *Physica Scripta* **T109**, 61 (2004) (cit. on pp. 19–23, 126, 128).

[70] B. Lv, T. Qian, and H. Ding: “Angle-resolved photoemission spectroscopy and its application to topological materials”. *Nature Reviews Physics* **1**, 609–626 (2019) (cit. on pp. 20, 22, 23).

[71] G. H. Berner: “Funktionelle oxidische Heterostrukturen aus dem Blickwinkel der Spektroskopie”. Dissertation. Julius-Maximilians-Universität Würzburg (2014) (cit. on pp. 20, 21, 23).

[72] R. Claessen: *Photoelectron spectroscopy: The joys and pitfalls of the photoelectric effect*. Lecture at the ”School on UV and X-ray spectroscopies of correlated electron systems“. École de Physique Les Houches (2017) (cit. on pp. 20, 22).

[73] P. Scheiderer: “Spectroscopy of Prototypical Thin Film Mott Materials”. Dissertation. Julius-Maximilians-Universität Würzburg (2019) (cit. on pp. 23, 24, 94).

[74] M. Sing, G. Berner, K. Goß, A. Müller, A. Ruff, A. Wetscherek, S. Thiel, J. Mannhart, S. A. Pauli, C. W. Schneider, P. R. Willmott, M. Gorgoi, F. Schäfers, and R. Claessen: "Profiling the Interface Electron Gas of $LaAlO_3/SrTiO_3$ Heterostructures with Hard X-Ray Photoelectron Spectroscopy". *Physical Review Letters* **102**, 176805 (2009) (cit. on pp. 24, 94).

[75] A. D. Becke: "Perspective: Fifty years of density-functional theory in chemical physics". *Journal of Chemical Physics* **140**, 18A301 (2014) (cit. on pp. 24, 25).

[76] K. Capelle: "A bird's-eye view of density-functional theory". *Brazilian Journal of Physics* **36**, 1318–1343 (2006) (cit. on pp. 24, 25, 129).

[77] P. Hohenberg and W. Kohn: "Inhomogeneous Electron Gas". *Physical Review* **136**, B864–B871 (1964) (cit. on p. 24).

[78] W. Kohn and L. J. Sham: "Self-Consistent Equations Including Exchange and Correlation Effects". *Physical Review* **140**, A1133–A1138 (1965) (cit. on pp. 24, 25).

[79] G. Kotliar and D. Vollhardt: "Strongly Correlated Materials: Insights From Dynamical Mean-Field Theory". *Physics Today* **57**, 53–59 (2004) (cit. on p. 25).

[80] A. Pribram-Jones, D. A. Gross, and K. Burke: "DFT: A Theory Full of Holes?" *Annual Review of Physical Chemistry* **66**, 283–304 (2015) (cit. on pp. 25, 129).

[81] J. P. Perdew, K. Burke, and M. Ernzerhof: "Generalized Gradient Approximation Made Simple". *Physical Review Letters* **77**, 3865–3868 (1996) (cit. on pp. 25, 49, 65, 110).

[82] J. Heyd, G. E. Scuseria, and M. Ernzerhof: "Hybrid functionals based on a screened Coulomb potential". *Journal of Chemical Physics* **118**, 8207–8215 (2003) (cit. on pp. 25, 51).

[83] X.-L. Qi and S.-C. Zhang: "Topological insulators and superconductors". *Reviews of Modern Physics* **83**, 1057–1110 (2011) (cit. on pp. 27, 35).

[84] J. Wang and S.-C. Zhang: "Topological states of condensed matter". *Nature Materials* **16**, 1062–1067 (2017) (cit. on p. 27).

[85] W. P. Su, J. R. Schrieffer, and A. J. Heeger: "Solitons in Polyacetylene". *Physical Review Letters* **42**, 1698–1701 (1979) (cit. on p. 27).

[86] K. v. Klitzing, G. Dorda, and M. Pepper: "New Method for High-Accuracy Determination of the Fine-Structure Constant Based on Quantized Hall Resistance". *Physical Review Letters* **45**, 494–497 (1980) (cit. on p. 27).

[87] D. J. Thouless, M. Kohmoto, M. P. Nightingale, and M. den Nijs: "Quantized Hall Conductance in a Two-Dimensional Periodic Potential". *Physical Review Letters* **49**, 405–408 (1982) (cit. on p. 27).

[88] M. Fruchart and D. Carpentier: "An introduction to topological insulators". *Comptes Rendus Physique* **14**. Topological insulators / Isolants topologiques, 779–815 (2013) (cit. on pp. 27–33).

[89] B. A. Bernevig: *Topological Insulators and Topological Superconductors*. 1st ed. Princeton University Press. doi: dx.doi.org/10.1515/9781400846733 (2013) (cit. on pp. 27–30, 33).

[90] J. K. Asbóth, L. Oroszlány, and A. Pályi: "A Short Course on Topological Insulators". *Lecture Notes in Physics* (2016) (cit. on pp. 27, 29, 30).

[91] H. Zhang and S.-C. Zhang: "Topological insulators from the perspective of first-principles calculations". *Physica Status Solidi Rapid Research Letters* **7**, 72–81 (2013) (cit. on p. 27).

[92] A. Bansil, H. Lin, and T. Das: "Colloquium: Topological band theory". *Reviews of Modern Physics* **88**, 021004 (2016) (cit. on pp. 27, 43).

[93] Y. Ando and L. Fu: "Topological Crystalline Insulators and Topological Superconductors: From Concepts to Materials". *Annual Review of Condensed Matter Physics* **6**.1, 361–381 (2015) (cit. on p. 27).

[94] J. H. Dil: "Spin- and angle-resolved photoemission on topological materials". *Electronic Structure* **1**, 023001 (2019) (cit. on p. 27).

[95] C. L. Kane: "Topological band theory and the $\mathbb{Z}_2$ invariant". *Contemporary Concepts of Condensed Matter Science*. Ed. by M. Franz and L. Molenkamp. Vol. 6. Elsevier. doi: dx.doi.org/10.1016/B978-0-444-63314-9.00001-9 (2013) (cit. on pp. 28, 30, 32).

[96] David Carpentier: *Topological Properties of Matter*. Presentation at the School on UV and X-ray spectroscopies of correlated electron systems. École de Physique des Houches (2017) (cit. on p. 30).

[97] C. Wu, B. A. Bernevig, and S.-C. Zhang: "Helical Liquid and the Edge of Quantum Spin Hall Systems". *Physical Review Letters* **96**, 106401 (2006) (cit. on p. 35).

[98] A. Roth, C. Brüne, H. Buhmann, J. Molenkamp Maciejko, X.-L. Qi, and Z. S. C.: "Nonlocal Transport in the Quantum Spin Hall State". *Science* **325**, 294 (2009) (cit. on p. 35).

[99] K. Bendias, S. Shamim, O. Herrmann, A. Budewitz, P. Shekhar, P. Leubner, J. Kleinlein, E. Bocquillon, H. Buhmann, and L. W. Molenkamp: "High Mobility HgTe Microstructures for Quantum Spin Hall Studies". *Nano Letters* **18**, 4831–4836 (2018) (cit. on p. 35).

[100] P. Leubner, L. Lunczer, C. Brüne, H. Buhmann, and L. W. Molenkamp: "Strain Engineering of the Band Gap of HgTe Quantum Wells Using Superlattice Virtual Substrates". *Physical Review Letters* **117**, 086403 (2016) (cit. on p. 36).

[101] P. Leubner: "Strain-engineering of the Topological Insulator HgTe". Dissertation. Julius-Maximilians-Universität Würzburg (2016) (cit. on p. 36).

[102] J. I. Väyrynen, M. Goldstein, and L. I. Glazman: "Helical Edge Resistance Introduced by Charge Puddles". *Physical Review Letters* **110**, 216402 (2013) (cit. on p. 36).

[103] I. Knez, C. T. Rettner, S.-H. Yang, S. S. P. Parkin, L. Du, R.-R. Du, and G. Sullivan: "Observation of Edge Transport in the Disordered Regime of Topologically Insulating InAs/GaSb Quantum Wells". *Physical Review Letters* **112**, 026602 (2014) (cit. on p. 36).

[104] L. Du, I. Knez, G. Sullivan, and R.-R. Du: "Robust Helical Edge Transport in Gated InAs/GaSb Bilayers". *Physical Review Letters* **114**, 096802 (2015) (cit. on p. 36).

[105] I. Knez, R.-R. Du, and G. Sullivan: "Evidence for Helical Edge Modes in Inverted InAs/GaSb Quantum Wells". *Physical Review Letters* **107**, 136603 (2011) (cit. on p. 36).

[106] T. Li, P. Wang, H. Fu, L. Du, K. A. Schreiber, X. Mu, X. Liu, G. Sullivan, G. A. Csáthy, X. Lin, and R.-R. Du: "Observation of a Helical Luttinger Liquid in InAs/GaSb Quantum Spin Hall Edges". *Physical Review Letters* **115**, 136804 (2015) (cit. on pp. 36, 154).

[107] H. Min, J. E. Hill, N. A. Sinitsyn, B. R. Sahu, L. Kleinman, and A. H. MacDonald: "Intrinsic and Rashba spin-orbit interactions in graphene sheets". *Physical Review B* **74**, 165310 (2006) (cit. on pp. 36, 52, 53).

[108] S. Konschuh, M. Gmitra, and J. Fabian: "Tight-binding theory of the spin-orbit coupling in graphene". *Physical Review B* **82**, 245412 (2010) (cit. on p. 36).

[109] S. Zhang, S. Guo, Z. Chen, Y. Wang, H. Gao, J. Gómez-Herrero, P. Ares, F. Zamora, Z. Zhu, and H. Zeng: "Recent progress in 2D group-VA semiconductors: from theory to experiment". *Chemical Society Reviews* **47**, 982–1021 (2018) (cit. on p. 37).

[110] Y. Ren, Z. Qiao, and Q. Niu: "Topological phases in two-dimensional materials: a review". *Reports on Progress in Physics* **79**, 066501 (2016) (cit. on pp. 37, 47).

[111] C.-C. Liu, W. Feng, and Y. Yao: "Quantum Spin Hall Effect in Silicene and Two-Dimensional Germanium". *Physical Review Letters* **107**, 076802 (2011) (cit. on p. 37).

[112] Y. Xu, B. Yan, H.-J. Zhang, J. Wang, G. Xu, P. Tang, W. Duan, and S.-C. Zhang: "Large-Gap Quantum Spin Hall Insulators in Tin Films". *Physical Review Letters* **111**, 136804 (2013) (cit. on pp. 37, 47).

[113] J. Gou, L. Kong, H. Li, Q. Zhong, W. Li, P. Cheng, L. Chen, and K. Wu: "Strain-induced band engineering in monolayer stanene on Sb(111)". *Physical Review Materials* **1**, 054004 (2017) (cit. on p. 37).

[114] J. Yuhara, Y. Fujii, K. Nishino, N. Isobe, M. Nakatake, L. Xian, A. Rubio, and G. L. Lay: "Large area planar stanene epitaxially grown on Ag(1 1 1)". *2D Materials* **5**.2, 025002 (2018) (cit. on p. 37).

[115] F.-F. Zhu, W.-J. Chen, Y. Xu, C.-L. Gao, D.-D. Guan, C.-H. Liu, D. Qian, S.-C. Zhang, and J.-F. Jia: "Epitaxial growth of two-dimensional stanene". *Nature Materials* **14**, 1020–1025 (2015) (cit. on p. 37).

[116] Y. Zang, T. Jiang, Y. Gong, Z. Guan, C. Liu, M. Liao, K. Zhu, Z. Li, L. Wang, W. Li, C. Song, D. Zhang, Y. Xu, K. He, X. Ma, S.-C. Zhang, and Q.-K. Xue: "Realizing an Epitaxial Decorated Stanene with an Insulating Bandgap". *Advanced Functional Materials* **28**.35, 1802723 (2018) (cit. on p. 37).

[117] J. Deng, B. Xia, X. Ma, H. Chen, H. Shan, X. Zhai, B. Li, A. Zhao, Y. Xu, W. Duan, S.-C. Zhang, B. Wang, and J. G. Hou: "Epitaxial growth of ultraflat stanene with topological band inversion". *Nature Materials* **17**, 1081–1086 (2018) (cit. on pp. 37, 106, 111, 117).

[118] Y. Shao, Z.-L. Liu, C. Cheng, X. Wu, H. Liu, C. Liu, J.-O. Wang, S.-Y. Zhu, Y.-Q. Wang, D.-X. Shi, K. Ibrahim, J.-T. Sun, Y.-L. Wang, and H.-J. Gao: "Epitaxial Growth of Flat Antimonene Monolayer: A New Honeycomb Analogue of Graphene". *Nano Letters* **18**, 2133–2139 (2018) (cit. on pp. 37, 106).

[119] M. Fortin-Deschênes, O. Waller, T. O. Menteş, A. Locatelli, S. Mukherjee, F. Genuzio, P. L. Levesque, A. Hébert, R. Martel, and O. Moutanabbir: "Synthesis of Antimonene on Germanium". *Nano Letters* **17**, 4970–4975 (2017) (cit. on p. 37).

[120] X. Wu, Y. Shao, H. Liu, Z. Feng, Y.-L. Wang, J.-T. Sun, C. Liu, J.-O. Wang, Z.-L. Liu, S.-Y. Zhu, Y.-Q. Wang, S.-X. Du, Y.-G. Shi, K. Ibrahim, and H.-J. Gao: "Epitaxial Growth and Air-Stability of Monolayer Antimonene on PdTe2". *Advanced Materials* **29**, 1605407 (2017) (cit. on p. 38).

[121] Z.-Q. Huang, C.-H. Hsu, F.-C. Chuang, Y.-T. Liu, H. Lin, W.-S. Su, V. Ozolins, and A. Bansil: "Strain driven topological phase transitions in atomically thin films of group IV and V elements in the honeycomb structures". *New Journal of Physics* **16**, 105018 (2014) (cit. on pp. 38, 48).

[122] I. K. Drozdov, A. Alexandradinata, S. Jeon, S. Nadj-Perge, H. Ji, R. J. Cava, B. Andrei Bernevig, and A. Yazdani: "One-dimensional topological edge states of bismuth bilayers". *Nature Physics* **10**, 664–669 (2014) (cit. on pp. 38, 141).

[123] J. Voit: "One-dimensional Fermi liquids". *Reports on Progress in Physics* **58**, 977–1116 (1995) (cit. on pp. 38, 39, 41).

[124] H. Weitering: "Luttingers wake". *Nature Physics* **7**, 744–745 (2011) (cit. on p. 38).

[125] S. Eggert: "One-dimensional quantum wires: A pedestrian approach to bosonization". *arXiv*, 0708.0003. url: arxiv.org/abs/0708.0003 (2007) (cit. on pp. 38–42).

[126] T. Giamarchi: *Quantum Physics in One Dimension*. Oxford University Press. doi: 10.1093/acprof:oso/9780198525004.001.0001 (2003) (cit. on p. 41).

[127] F. Geißler: "Transport properties of helical Luttinger liquids". Dissertation. Julius-Maximilians-Universität Würzburg (2017) (cit. on pp. 42, 154).

[128] A. Ström and H. Johannesson: "Tunneling between Edge States in a Quantum Spin Hall System". *Physical Review Letters* **102**, 096806 (2009) (cit. on p. 42).

[129] M. Hohenadler and F. F. Assaad: "Correlation effects in two-dimensional topological insulators". *Journal of Physics: Condensed Matter* **25**, 143201 (2013) (cit. on pp. 42, 154).

[130] G.-F. Zhang, Y. Li, and C. Wu: "Honeycomb lattice with multiorbital structure: Topological and quantum anomalous Hall insulators with large gaps". *Physical Review B* **90**, 075114 (2014) (cit. on pp. 43, 47, 55).

[131] C.-H. Hsu, Z.-Q. Huang, F.-C. Chuang, C.-C. Kuo, Y.-T. Liu, H. Lin, and A. Bansil: "The nontrivial electronic structure of Bi/Sb honeycombs on SiC(0001)". *New Journal of Physics* **17**, 025005 (2015) (cit. on pp. 43, 47–53, 106).

[132] M. Zhou, W. Ming, Z. Liu, Z. Wang, P. Li, and F. Liu: "Epitaxial growth of large-gap quantum spin Hall insulator on semiconductor surface". *Proceedings of the National Academy of Sciences* **111**, 14378–14381 (2014) (cit. on pp. 43, 47, 48, 52, 53, 55).

[133] M. Zhou, W. Ming, Z. Liu, Z. Wang, Y. Yao, and F. Liu: "Formation of quantum spin Hall state on Si surface and energy gap scaling with strength of spin orbit coupling". *Scientific Reports* **4**, 7102 (2015) (cit. on pp. 43, 47, 48, 56).

[134] Y. M. Koroteev, G. Bihlmayer, J. E. Gayone, E. V. Chulkov, S. Blügel, P. M. Echenique, and P. Hofmann: "Strong Spin-Orbit Splitting on Bi Surfaces". *Physical Review Letters* **93**, 046403 (2004) (cit. on pp. 43–45).

[135] P. Hofmann: "The surfaces of bismuth: Structural and electronic properties". *Progress in Surface Science* **81**, 191–245 (2006) (cit. on pp. 43–45).

[136] C. R. Ast and H. Höchst: "Electronic structure of a bismuth bilayer". *Physical Review B* **67**, 113102 (2003) (cit. on pp. 43–45).

[137] P. de Marcillac, N. Coron, G. Dambier, J. Leblanc, and J.-P. Moalic: "Experimental detection of α-particles from the radioactive decay of natural bismuth". *Nature* **422**, 876 (2003) (cit. on p. 43).

[138] Z. Liu, C.-X. Liu, Y.-S. Wu, W.-H. Duan, F. Liu, and J. Wu: "Stable Nontrivial Z_2 Topology in Ultrathin Bi (111) Films: A First-Principles Study". *Physical Review Letters* **107**, 136805 (2011) (cit. on pp. 43, 45, 47).

[139] H. Mönig, J. Sun, Y. M. Koroteev, G. Bihlmayer, J. Wells, E. V. Chulkov, K. Pohl, and P. Hofmann: "Structure of the (111) surface of bismuth: LEED analysis and first-principles calculations". *Physical Review B* **72**, 085410 (2005) (cit. on pp. 43, 44).

[140] D. Wang, L. Chen, H. Liu, and X. Wang: "Electronic Structures and Topological Properties of Bi(111) Ultrathin Films". *Journal of the Physical Society of Japan* **82**, 094712 (2013) (cit. on pp. 43, 45).

[141] S. Murakami: "Quantum Spin Hall Effect and Enhanced Magnetic Response by Spin-Orbit Coupling". *Physical Review Letters* **97**, 236805 (2006) (cit. on pp. 43–45).

[142] K. Miyamoto, H. Miyahara, K. Kuroda, T. Maegawa, A. Kimura, and T. Okuda: "Peculiar Rashba spin texture induced by C_{3v} symmetry on the Bi(111) surface revisited". *Physical Review B* **97**, 085433 (2018) (cit. on pp. 44, 45).

[143] O. Prakash, A. Kumar, A. Thamizhavel, and S. Ramakrishnan: "Evidence for bulk superconductivity in pure bismuth single crystals at ambient pressure". *Science* **355**, 52–55 (2017) (cit. on p. 44).

[144] C. A. Hoffman, J. R. Meyer, F. J. Bartoli, A. Di Venere, X. J. Yi, C. L. Hou, H. C. Wang, J. B. Ketterson, and G. K. Wong: "Semimetal-to-semiconductor transition in bismuth thin films". *Physical Review B* **48**, 11431–11434 (1993) (cit. on p. 45).

[145] M. Wada, S. Murakami, F. Freimuth, and G. Bihlmayer: "Localized edge states in two-dimensional topological insulators: Ultrathin Bi films". *Physical Review B* **83**, 121310 (2011) (cit. on p. 45).

[146] K.-H. Jin and S.-H. Jhi: "Quantum anomalous Hall and quantum spin-Hall phases in flattened Bi and Sb bilayers". *Scientific Reports* **5**, 8426 (2015) (cit. on pp. 45–47, 53–55).

[147] X. Li, H. Liu, H. Jiang, F. Wang, and J. Feng: "Edge engineering of a topological Bi(111) bilayer". *Physical Review B* **90**, 165412 (2014) (cit. on pp. 45, 46).

[148] S. Reich, J. Maultzsch, C. Thomsen, and P. Ordejón: "Tight-binding description of graphene". *Physical Review B* **66**, 035412 (2002) (cit. on p. 46).

[149] R. Yu, X. L. Qi, A. Bernevig, Z. Fang, and X. Dai: "Equivalent expression of $\mathbb{Z}_2$ topological invariant for band insulators using the non-Abelian Berry connection". *Physical Review B* **84**, 075119 (2011) (cit. on p. 47).

[150] A. A. Soluyanov and D. Vanderbilt: "Computing topological invariants without inversion symmetry". *Physical Review B* **83**, 235401 (2011) (cit. on p. 47).

[151] C. Wu, D. Bergman, L. Balents, and S. Das Sarma: "Flat Bands and Wigner Crystallization in the Honeycomb Optical Lattice". *Physical Review Letters* **99**, 070401 (2007) (cit. on p. 47).

[152] C. Wu and S. Das Sarma: "$p_{x,y}$-orbital counterpart of graphene: Cold atoms in the honeycomb optical lattice". *Physical Review B* **77**, 235107 (2008) (cit. on pp. 47, 56).

[153] M. Krawiec: "Functionalization of group-14 two-dimensional materials". *Journal of Physics: Condensed Matter* **30**, 233003 (2018) (cit. on p. 47).

[154] C. Niu, G. Bihlmayer, H. Zhang, D. Wortmann, S. Blügel, and Y. Mokrousov: "Functionalized bismuth films: Giant gap quantum spin Hall and valley-polarized quantum anomalous Hall states". *Physical Review B* **91**, 041303 (2015) (cit. on p. 47).

[155] C.-C. Liu, S. Guan, Z. Song, S. A. Yang, J. Yang, and Y. Yao: "Low-energy effective Hamiltonian for giant-gap quantum spin Hall insulators in honeycomb X-hydride/halide (X = N–Bi) monolayers". *Physical Review B* **90**, 085431 (2014) (cit. on pp. 47, 53–55).

[156] Y. Ma, Y. Dai, L. Kou, T. Frauenheim, and T. Heine: "Robust Two-Dimensional Topological Insulators in Methyl-Functionalized Bismuth, Antimony, and Lead Bilayer Films". *Nano Letters* **15**, 1083–1089 (2015) (cit. on p. 47).

[157] Y. Ma, Y. Dai, C. Niu, and B. Huang: "Halogenated two-dimensional germanium: candidate materials for being of Quantum Spin Hall state". *Journal of Materials Chemistry* **22**, 12587 (2012) (cit. on p. 47).

[158] C. Weeks, J. Hu, J. Alicea, M. Franz, and R. Wu: "Engineering a Robust Quantum Spin Hall State in Graphene via Adatom Deposition". *Physical Review X* **1**, 021001 (2011) (cit. on p. 47).

[159] X. Wang, C. Xu, H. Hu, P. Wang, G. Bian, W. Tan, S. A. Brown, and T. C. Chiang: "Topological phase stability and transformation of bismuthene". *Europhysics Letters* **119** (2017) (cit. on p. 47).

[160] Z. Q. Huang, F. C. Chuang, C. H. Hsu, Y. T. Liu, H. R. Chang, H. Lin, and A. Bansil: "Nontrivial topological electronic structures in a single Bi(111) bilayer on different substrates: A first-principles study". *Physical Review B.* **88**, 1–7 (2013) (cit. on pp. 47–49).

[161] *Creative Commons Attribution 3.0 Unported License.* https://creativecommons.org/licenses/by/3.0/. 2021 (cit. on pp. 48, 52).

[162] F. Reis, G. Li, L. Dudy, M. Bauernfeind, S. Glass, W. Hanke, R. Thomale, J. Schäfer, and R. Claessen: "Bismuthene on a SiC substrate: A candidate for a high-temperature quantum spin Hall material." *Science* **357**, 287–290 (2017) (cit. on pp. 48–50, 52–55, 57–60, 108, 110).

[163] M. Stockmeier, R. Müller, S. A. Sakwe, P. J. Wellmann, and A. Magerl: "On the lattice parameters of silicon carbide". *Journal of Applied Physics* **105**, 033511 (2009) (cit. on pp. 49, 62, 77).

[164] A. Bauer, J. Kräußlich, L. Dressler, P. Kuschnerus, J. Wolf, K. Goetz, P. Käckell, J. Furthmüller, and F. Bechstedt: "High-precision determination of atomic positions in crystals: The case of 6H- and 4H-SiC". *Physical Review B* **57**, 2647–2650 (1998) (cit. on pp. 49, 62, 77).

[165] K. V. Emtsev, T. Seyller, L. Ley, L. Broekman, A. Tadich, J. D. Riley, R. G. C. Leckey, and M. Preuss: "Correlation effects at ideal SiC{0001}-(1×1) surfaces". *Physical Review B* **73**, 075412 (2006) (cit. on pp. 49, 64, 65, 105, 128).

[166] G. Kresse and J. Furthmüller: "Efficient iterative schemes for ab initio total-energy calculations using a plane-wave basis set". *Physical Review B* **54**, 11169–11186 (1996) (cit. on pp. 49, 64).

[167] G. Kresse and D. Joubert: "From ultrasoft pseudopotentials to the projector augmented-wave method". *Physical Review B* **59**, 1758–1775 (1999) (cit. on p. 49).

[168] *Private communication with Prof. G. Li, School of Physical Science and Technology, ShanghaiTech University* (cit. on pp. 50, 52, 57, 59, 60, 65, 110, 122, 135, 138, 140, 189).

[169] M. E. Levinshtein, S. L. Rumyantsev, and M. Shur: *Properties of advanced semiconductor materials : GaN, AlN, InN, BN, SiC, SiGe*. John Wiley and Sons (2001), p. 194 (cit. on p. 50).

[170] J. Heyd and G. E. Scuseria: "Efficient hybrid density functional calculations in solids: Assessment of the Heyd–Scuseria–Ernzerhof screened Coulomb hybrid functional". *Journal of Chemical Physics* **121**, 1187–1192 (2004) (cit. on pp. 50, 108).

[171] A. V. Krukau, O. A. Vydrov, A. F. Izmaylov, and G. E. Scuseria: "Influence of the exchange screening parameter on the performance of screened hybrid functionals". *Journal of Chemical Physics* **125**, 224106 (2006) (cit. on pp. 50, 110).

[172] L. Fu and C. L. Kane: "Time reversal polarization and a Z_2 adiabatic spin pump". *Physical Review B* **74**, 195312 (2006) (cit. on p. 53).

[173] T. Fukui and Y. Hatsugai: "Quantum Spin Hall Effect in Three Dimensional Materials: Lattice Computation of Z2 Topological Invariants and Its Application to Bi and Sb". *Journal of the Physical Society of Japan* **76**, 053702 (2007) (cit. on p. 53).

[174] Y. Yao, F. Ye, X.-L. Qi, S.-C. Zhang, and Z. Fang: "Spin-orbit gap of graphene: First-principles calculations". *Physical Review B* **75**, 041401 (2007) (cit. on p. 53).

[175] C.-C. Liu, H. Jiang, and Y. Yao: "Low-energy effective Hamiltonian involving spin-orbit coupling in silicene and two-dimensional germanium and tin". *Physical Review B* **84**, 195430 (2011) (cit. on p. 53).

[176] K. Wittel and R. Manne: "Atomic spin-orbit interaction parameters from spectral data for 19 elements". *Theoretica Chimica Acta* **33**, 347–349 (1974) (cit. on p. 54).

[177] *Creative Commons Attribution Non-Commercial Non-Derivatives 4.0 International License*. `https://creativecommons.org/licenses/by-nc-nd/4.0/`. 2021 (cit. on p. 54).

[178] J. C. Slater and G. F. Koster: "Simplified LCAO Method for the Periodic Potential Problem". *Physical Review* **94**, 1498–1524 (1954) (cit. on p. 56).

[179] A. A. Mostofi, J. R. Yates, G. Pizzi, Y.-S. Lee, I. Souza, D. Vanderbilt, and N. Marzari: "An updated version of wannier90: A tool for obtaining maximally-localised Wannier functions". *Computer Physics Communications* **185**, 2309–2310 (2014) (cit. on p. 58).

[180] N. Marzari, A. A. Mostofi, J. R. Yates, I. Souza, and D. Vanderbilt: "Maximally localized Wannier functions: Theory and applications". *Reviews of Modern Physics* **84**, 1419–1475 (2012) (cit. on pp. 58, 60).

[181] S. Mohr, L. E. Ratcliff, L. Genovese, D. Caliste, P. Boulanger, S. Goedecker, and T. Deutsch: "Accurate and efficient linear scaling DFT calculations with universal applicability". *Physical Chemistry Chemical Physics* **17**, 31360–31370 (2015) (cit. on p. 60).

[182] M. Östling, R. Ghandi, and C.-M. Zetterling: "SiC power devices — Present status, applications and future perspective". *2011 IEEE 23rd International Symposium on Power Semiconductor Devices and ICs*. IEEE. doi: `10.1109/ISPSD.2011.5890778` (2011), pp. 10–15 (cit. on p. 61).

[183] R. Singh and M. Pecht: "Commercial impact of silicon carbide". *IEEE Industrial Electronics Magazine* **2**, 19–31 (2008) (cit. on p. 61).

[184] K. Takahashi, A. Yoshikawa, and A. Sandhu, eds.: *Wide Bandgap Semiconductors*. Springer Nature. doi: `dx.doi.org/10.1007/978-3-540-47235-3` (2007) (cit. on pp. 61, 62, 170, 171).

[185] K. V. Emtsev, F. Speck, T. Seyller, L. Ley, and J. D. Riley: "Interaction, growth, and ordering of epitaxial graphene on SiC0001 surfaces: A comparative photoelectron spectroscopy study". *Physical Review B* **77**, 155303 (2008) (cit. on p. 61).

[186] P. Mallet, F. Varchon, C. Naud, L. Magaud, C. Berger, and J.-Y. Veuillen: "Electron states of mono- and bilayer graphene on SiC probed by scanning-tunneling microscopy". *Physical Review B* **76**, 041403 (2007) (cit. on p. 61).

[187] P. R. Tripathy, M. Mukherjee, S. K. Choudhury, and S. P. Pati: "Prospects and issues of Diamond based IMPATT Diode at MM-Wave Frequency". *Physics of Semiconductor Devices*. Ed. by V. K. Jain and A. Verma. Springer International Publishing. doi: `dx.doi.org/10.1007/978-3-319-03002-9_59` (2014), pp. 235–238 (cit. on p. 61).

[188] K. Järrendahl and R. F. Davis: "Chapter 1 Materials Properties and Characterization of SiC". *SiC Materials and Devices*. Ed. by Y. Soo Park. Vol. 52. Semiconductors and Semimetals. Elsevier. `https://doi.org/10.1016/S0080-8784(08)62843-4` (1998), pp. 1–20 (cit. on pp. 61, 171).

[189] A. Bauer, J. Kräusslich, P. Kuschnerus, K. Goetz, P. Käckell, and F. Bechstedt: "High-precision determination of atomic positions in 4H– and 6H–SiC crystals". *Materials Science and Engineering: B* **61-62**, 217–220 (1999) (cit. on p. 62).

[190] V. Borovikov and A. Zangwill: "Step bunching of vicinal 6*H*-SiC0001 surfaces". *Physical Review B* **79**, 245413 (2009) (cit. on pp. 62–64, 70, 71, 76, 172, 174).

[191] K. Hayashi, K. Morita, S. Mizuno, H. Tochihara, and S. Tanaka: "Surface Science Stable surface termination on vicinal 6H – SiC (0 0 0 1) surfaces". *Surface Science* **603**, 566–570 (2009) (cit. on pp. 62, 76).

[192] M. Camarda, A. Canino, P. Fiorenza, A. Severino, R. Anzalone, S. Privitera, A. La Magna, F. La Via, C. Vecchio, M. Mauceri, G. Litrico, A. Pecora, and D. Crippa: "Study of the Effects of Growth Rate, Miscut Direction and Postgrowth Argon Annealing on the Surface Morphology of Homoepitaxially Grown 4H Silicon Carbide Films". Materials Science Forum **740**, 229–234 (2013) (cit. on pp. 62, 63).

[193] S.-I. Nakamura, T. Kimoto, H. Matsunami, S. Tanaka, N. Teraguchi, and A. Suzuki: "Formation of periodic steps with a unit-cell height on 6H–SiC (0001) surface by HCl etching". *Applied Physics Letters* **76**, 3412–3414 (2000) (cit. on pp. 62, 64, 72).

[194] S. Nie, C. Lee, R. Feenstra, Y. Ke, R. Devaty, W. Choyke, C. Inoki, T. Kuan, and G. Gu: "Step formation on hydrogen-etched 6H-SiC{0001} surfaces". *Surface Science* **602**.17, 2936–2942 (2008) (cit. on pp. 62, 64, 72, 76, 172).

[195] H. Morkoç, S. Strite, G. B. Gao, M. E. Lin, B. Sverdlov, and M. Burns: "Large-band-gap SiC, III-V nitride, and II-VI ZnSe-based semiconductor device technologies". *Journal of Applied Physics* **76**, 1363–1398 (1994) (cit. on pp. 62, 171).

[196] K. Heinz, J. Bernhardt, J. Schardt, and U. Starke: "Functional surface reconstructions of hexagonal SiC". *Journal of Physics: Condensed Matter* **16** (2004) (cit. on pp. 63, 171, 173).

[197] T. Kimoto, A. Itoh, H. Matsunami, and T. Okano: "Step bunching mechanism in chemical vapor deposition of 6H– and 4H–SiC0001". *Journal of Applied Physics* **81**, 3494–3500 (1997) (cit. on pp. 63, 70, 76).

[198] K. Arima, H. Hara, J. Murata, T. Ishida, R. Okamoto, K. Yagi, Y. Sano, H. Mimura, and K. Yamauchi: "Atomic-scale flattening of SiC surfaces by electroless chemical etching in HF solution with Pt catalyst". *Applied Physics Letters* **90**, 202106 (2007) (cit. on pp. 63, 70).

[199] H. Deng, K. Endo, and K. Yamamura: "Competition between surface modification and abrasive polishing: A method of controlling the surface atomic structure of 4H-SiC (0001)". *Scientific Reports* **5**, 1–6 (2015) (cit. on pp. 63, 64).

[200] A. Nakajima, H. Yokoya, Y. Furukawa, and H. Yonezu: "Step control of vicinal 6H-SiC(0001) surface by H 2 etching". *Journal of Applied Physics* **97**, 4–9 (2005) (cit. on pp. 63, 64, 70, 72, 76, 170).

[201] H. Nakagawa, S. Tanaka, and I. Suemune: "Self-Ordering of Nanofacets on Vicinal SiC Surfaces". *Physical Review Letters* **91**, 226107 (2003) (cit. on pp. 64, 170).

[202] W. Wulfhekel, D. Sander, S. Nitsche, F. Dulot, A. Leycuras, and M. Hanbücken: "Regular step formation on concave-shaped surfaces on 6H–SiC(0001)". *Surface Science* **550**, 8–14 (2004) (cit. on pp. 64, 170).

[203] E. Pearson, T. Takai, T. Halicioglu, and W. A. Tiller: "Computer modeling of Si and SiC surfaces and surface processes relevant to crystal growth from the vapor". *Journal of Crystal Growth* **70**, 33–40 (1984) (cit. on p. 64).

[204] T. Kimoto, A. Itoh, and H. Matsunami: "Step bunching in chemical vapor deposition of 6H– and 4H–SiC on vicinal SiC(0001) faces". *Applied Physics Letters* **66**, 3645–3647 (2002) (cit. on p. 64).

[205] M. Ostler, F. Speck, M. Gick, and T. Seyller: "Automated preparation of high-quality epitaxial graphene on 6H-SiC(0001)". *Physica Status Solidi B Basic Solid State Physics* **247**, 2924–2926 (2010) (cit. on pp. 64, 72).

[206] N. Ohtani, M. Katsuno, J. Takahashi, H. Yashiro, and M. Kanaya: " Evolution of macrosteps on 6H–SiC(0001): Impurity-induced morphological instability of step trains ". *Physical Review B* **59**, 4592–4595 (2002) (cit. on p. 64).

[207] J. Paier, M. Marsman, K. Hummer, G. Kresse, I. C. Gerber, and J. G. Angy?án: "Screened hybrid density functionals applied to solids". *Journal of Chemical Physics* **124**, 154709 (2006) (cit. on pp. 64, 108).

[208] P. E. Blöchl: "Projector augmented-wave method". *Physical Review B* **50**, 17953 (1994) (cit. on p. 64).

[209] T. Kimoto: “Material science and device physics in SiC technology for high-voltage power devices”. *Japanese Journal of Applied Physics* **54**, 040103 (2015) (cit. on pp. 66, 178).

[210] M. Ikeda, H. Matsunami, and T. Tanaka: “Site effect on the impurity levels in $4H$, $6H$, and $15R$ SiC”. *Physical Review B* **22**, 2842–2854 (1980) (cit. on p. 66).

[211] Y. Margoninski: “The influence of inelastic electron processes on LEED beam intensities during adsorption studies”. *Surface Science* **29**, 355–362 (1972) (cit. on p. 68).

[212] P. Mårtensson, F. Owman, and L. I. Johansson: “Morphology, atomic and electronic structure of 6H-SiC(0001) surfaces”. *Physica Status Solidi B Basic Solid State Physics* **202**, 501–528 (1997) (cit. on p. 68).

[213] U. Starke, J. Schardt, and M. Franke: “Morphology, bond saturation and reconstruction of hexagonal SiC surfaces”. *Applied Physics A* **65**, 587–596 (1997) (cit. on p. 68).

[214] P. H. Weidlich, R. E. Dunin-Borkowski, and P. Ebert: “Quantitative determination of local potential values in inhomogeneously doped semiconductors by scanning tunneling microscopy”. *Physical Review B* **84**, 1–8 (2011) (cit. on pp. 70, 75, 79, 177, 178, 191).

[215] S. Landrock, Y. Jiang, K. H. Wu, E. G. Wang, K. Urban, and P. Ebert: “Origin of nanoscale potential fluctuations in two-dimensional semiconductors”. *Applied Physics Letters* **95**, 072107 (2009) (cit. on pp. 70, 75, 177).

[216] R. J. Pechman, X.-S. Wang, and J. H. Weaver: “Interactions of Br with Si(111)-7×7: Chemisorption, step retreat, and terrace etching”. *Physical Review B* **52**, 11412–11423 (1995) (cit. on p. 71).

[217] S. Doğan, D. Johnstone, F. Yun, S. Sabuktagin, J. Leach, A. A. Baski, H. Morkoç, G. Li, and B. Ganguly: “The effect of hydrogen etching on 6H-SiC studied by temperature-dependent current-voltage and atomic force microscopy”. *Applied Physics Letters* **85**, 1547–1549 (2004) (cit. on pp. 72, 74).

[218] J. Bernhardt, J. Schardt, U. Starke, and K. Heinz: “Epitaxially ideal oxide-semiconductor interfaces: Silicate adlayers on hexagonal (0001) and $(000\bar{1})$ SiC surfaces”. *Applied Physics Letters* **74**, 1084–1086 (1999) (cit. on p. 72).

[219] D. Sander, W. Wulfhekel, M. Hanbücken, S. Nitsche, J. P. Palmari, F. Dulot, F. Arnaud d’Avitaya, and A. Leycuras: “Preferential carbon etching by hydrogen inside hexagonal voids of 6H-SiC(0001)”. *Applied Physics Letters* **81**, 3570–3572 (2002) (cit. on p. 72).

[220] S. Soubatch, S. E. Saddow, S. P. Rao, W. Lee, M. Konuma, and U. Starke: “Structure and Morphology of 4H-SiC Wafer Surfaces after H2-Etching”. Materials Science Forum **483**, 761–764 (2005) (cit. on p. 72).

[221] Z. Zhang and J. T. Yates: “Band bending in semiconductors: Chemical and physical consequences at surfaces and interfaces”. *Chemical Reviews* **112**, 5520–5551 (2012) (cit. on pp. 78, 97).

[222] M. McEllistrem, G. Haase, D. Chen, and R. J. Hamers: "Electrostatic sample-tip interactions in the scanning tunneling microscope". *Physical Review Letters* **70**, 2471–2474 (1993) (cit. on pp. 78, 148).

[223] *Private communication with R. Stühler, Experimentelle Physik 4, Universität Würzburg* (cit. on pp. 81, 85, 175).

[224] M. J. X. Bauernfeind: "Bismuten auf SiC(0001): Optimierung der Substratgüte und Charakterisierung des Materialsystems". Master's Thesis. Julius-Maximilians-Universität Würzburg (2016) (cit. on p. 83).

[225] S. Glass, G. Li, F. Adler, J. Aulbach, A. Fleszar, R. Thomale, W. Hanke, R. Claessen, and J. Schäfer: "Triangular Spin-Orbit-Coupled Lattice with Strong Coulomb Correlations: Sn Atoms on a SiC(0001) Substrate". *Physical Review Letters* **114**, 247602 (2015) (cit. on p. 87).

[226] S. Tanuma, C. J. Powell, and D. R. Penn: "Calculations of electron inelastic mean free paths. IX. Data for 41 elemental solids over the 50 eV to 30 keV range". *Surface and Interface Analysis* **43**, 689–713 (2011) (cit. on p. 95).

[227] V. S. Dharmadhikari, S. Sainkar, S. Badrinarayan, and A. Goswami: "Characterisation of thin films of bismuth oxide by X-ray photoelectron spectroscopy". *Journal of Electron Spectroscopy and Related Phenomena* **25**, 181–189 (1982) (cit. on pp. 96, 99, 184).

[228] A. Pramanik, R. P. Pandeya, K. Ali, B. Joshi, I. Sarkar, P. Moras, P. M. Sheverdyaeva, A. K. Kundu, C. Carbone, A. Thamizhavel, S. Ramakrishnan, and K. Maiti: "Depth-resolved core level spectroscopy of noncentrosymmetric solid BiPd". *Physical Review B* **101**, 035426 (2020) (cit. on p. 96).

[229] B. Ulgut and S. Suzer: "XPS Studies of SiO2/Si System under External Bias". *The Journal of Physical Chemistry B* **107**, 2939–2943 (2003) (cit. on p. 97).

[230] M. Grodzicki, R. Wasielewski, S. A. Surma, and A. Ciszewski: "Formation of excess silicon on 6H-SiC(0001) during hydrogen etching". *Acta Physica Polonica A* **116**, 82–85 (2009) (cit. on pp. 97, 98).

[231] W. Mönch: *Semiconductor Surfaces and Interfaces*. Springer Series in Surface Science. Springer-Verlag Berlin Heidelberg (2001) (cit. on p. 97).

[232] D. Lide: *CRC Handbook of Chemistry and Physics, 84th Edition*. CRC Press LLC (2003) (cit. on p. 97).

[233] E. J. Telford, A. Benyamini, D. Rhodes, D. Wang, Y. Jung, A. Zangiabadi, K. Watanabe, T. Taniguchi, S. Jia, K. Barmak, A. N. Pasupathy, C. R. Dean, and J. Hone: "Via Method for Lithography Free Contact and Preservation of 2D Materials". *Nano Letters* **18**, 1416–1420 (2018) (cit. on p. 100).

[234] R. H. Miwa, T. M. Schmidt, and G. P. Srivastava: "Bi covered Si(111) surface revisited". *Journal of Physics: Condensed Matter* **15**, 2441–2447 (2003) (cit. on pp. 103, 104).

[235] R. Shioda, A. Kawazu, A. A. Baski, C. F. Quate, and J. Nogami: "Bi on Si(111): Two phases of the $\sqrt{3} \times \sqrt{3}$ surface reconstruction". *Physical Review B* **48**, 4895–4898 (1993) (cit. on p. 103).

[236] R. Z. Bakhtizin, C. Park, T. Hashizume, and T. Sakurai: "Atomic structure of Bi on the Si(111) surface". *Journal of Vacuum Science & Technology B* **12**, 2052–2054 (1994) (cit. on p. 103).

[237] J. C. Woicik, G. E. Franklin, C. Liu, R. E. Martinez, I.-S. Hwong, M. J. Bedzyk, J. R. Patel, and J. A. Golovchenko: "Structural determination of the Si(111) $\sqrt{3} \times \sqrt{3}$-Bi surface by x-ray standing waves and scanning tunneling microscopy". *Physical Review B* **50**, 12246–12249 (1994) (cit. on p. 103).

[238] P. A. Redhead: "Hydrogen in Vacuum Systems: An Overview". *AIP Conference Proceedings* **671**, 243–254 (2003) (cit. on p. 105).

[239] M. K. Gupta, A. Priyadarshi, and Z. Khan: "Hydrogen in Stainless Steel as Killing Agent for UHV: A Review". *Materials Today: Proceedings* **2**, 1074–1081 (2015) (cit. on p. 105).

[240] D. Culcer, A. C. Keser, Y. Li, and G. Tkachov: "Transport in two-dimensional topological materials: recent developments in experiment and theory". *2D Materials* **7**, 022007 (2020) (cit. on p. 108).

[241] J. Heyd and G. E. Scuseria: "Efficient hybrid density functional calculations in solids: Assessment of the Heyd–Scuseria–Ernzerhof screened Coulomb hybrid functional". *Journal of Chemical Physics* **121**, 1187–1192 (2004) (cit. on pp. 108, 110).

[242] K. Burke: "Perspective on density functional theory". *Journal of Chemical Physics* **136**, 150901 (2012) (cit. on p. 110).

[243] J. P. Perdew, W. Yang, K. Burke, Z. Yang, E. K. U. Gross, M. Scheffler, G. E. Scuseria, T. M. Henderson, I. Y. Zhang, A. Ruzsinszky, H. Peng, J. Sun, E. Trushin, and A. Görling: "Understanding band gaps of solids in generalized Kohn–Sham theory". *Proceedings of the National Academy of Sciences* **114**, 2801–2806 (2017) (cit. on pp. 110, 188).

[244] L. El-Kareh: "Rashba-type spin-split surface states: Heavy post transition metals on Ag(111)". Dissertation. Julius-Maximilians-Universität Würzburg (2014) (cit. on pp. 111, 135, 146).

[245] Z. Pedramrazi, C. Herbig, A. Pulkin, S. Tang, M. Phillips, D. Wong, H. Ryu, M. Pizzochero, Y. Chen, F. Wang, E. J. Mele, Z.-X. Shen, S.-K. Mo, O. V. Yazyev, and M. F. Crommie: "Manipulating Topological Domain Boundaries in the Single-Layer Quantum Spin Hall Insulator 1T'–WSe2". *Nano Letters* **19**, 5634–5639 (2019) (cit. on pp. 111, 116).

[246] P. Sternativo and F. Dolcini: "Tunnel junction of helical edge states: Determining and controlling spin-preserving and spin-flipping processes through transconductance". *Physical Review B* **89**, 035415 (2014) (cit. on p. 116).

[247] E. N. Lima, T. M. Schmidt, and R. W. Nunes: "Topologically Protected Metallic States Induced by a One-Dimensional Extended Defect in the Bulk of a 2D Topological Insulator". *Nano Letters* **16**, 4025–4031 (2016) (cit. on p. 116).

[248] M. M. Ugeda, A. Pulkin, S. Tang, Y. Z. Hyejin Ryu and Quansheng Wu and, D. Wong, Z. Pedramrazi, A. Martín-Recio, Y. Chen, F. Wang, Z.-X. Shen, S.-K. Mo, O. V. Yazyev, and M. F. Crommie: "Observation of topologically protected states at crystalline phase boundaries in single-layer WSe2". *Nature Communications* **9** (2018) (cit. on p. 116).

[249] D. Wong, J. Velasco, L. Ju, J. Lee, S. Kahn, H.-Z. Tsai, C. Germany, T. Taniguchi, K. Watanabe, A. Zettl, F. Wang, and M. F. Crommie: "Characterization and manipulation of individual defects in insulating hexagonal boron nitride using scanning tunnelling microscopy". *Nature Nanotechnology* **10**, 949–953 (2015) (cit. on pp. 117, 119, 192).

[250] N. A. Pradhan, N. Liu, C. Silien, and W. Ho: "Atomic Scale Conductance Induced by Single Impurity Charging". *Physical Review Letters* **94**, 076801 (2005) (cit. on pp. 119, 120, 192).

[251] K. Teichmann, M. Wenderoth, S. Loth, R. G. Ulbrich, J. K. Garleff, A. P. Wijnheijmer, and P. M. Koenraad: "Controlled Charge Switching on a Single Donor with a Scanning Tunneling Microscope". *Physical Review Letters* **101**, 076103 (2008) (cit. on pp. 119, 148, 192).

[252] W. Norimatsu and M. Kusunoki: "Selective formation of ABC-stacked graphene layers on SiC(0001)". *Physical Review B* **81**, 161410 (2010) (cit. on p. 123).

[253] L. Nyakiti, R. L. Myers-Ward, V. D. Wheeler, E. A. Imhoff, F. Bezares, H. Chun, J. D. Caldwell, A. L. Friedman, B. R. Matis, J. W. Baldwin, P. M. Campbell, J. C. Culbertson, C. R. Eddy, G. G. Jernigan, and D. K. Gaskill: "Bilayer Graphene Grown on 4H-SiC (0001) Step-Free Mesas". *Nano Letters* **12**, 1749–1756 (2012) (cit. on p. 123).

[254] A. Bostwick, T. Ohta, T. Seyller, K. Horn, and E. Rotenberg: "Quasiparticle dynamics in graphene". *Nature Physics* **3**, 36–40 (2007) (cit. on p. 126).

[255] F. Theilmann, R. Matzdorf, and A. Goldmann: "High-resolution photoemission studies at rough Cu(111) surfaces: The influence of defect scattering and disorder-dependent dephasing processes". *Surface Science* **420**.1, 33–42 (1999) (cit. on p. 126).

[256] K. R. Knox, A. Locatelli, M. B. Yilmaz, D. Cvetko, Mente ş, M. Á. Niño, P. Kim, A. Morgante, and R. M. Osgood: "Making angle-resolved photoemission measurements on corrugated monolayer crystals: Suspended exfoliated single-crystal graphene". *Phys. Rev. B* **84**, 115401 (2011) (cit. on p. 126).

[257] H. Iwasawa: "High-resolution angle-resolved photoemission spectroscopy and microscopy". *Electronic Structure* **2**.4, 043001 (2020) (cit. on pp. 126, 128, 129).

[258] F. Dominguez, B. Scharf, G. Li, J. Schäfer, R. Claessen, W. Hanke, R. Thomale, and E. M. Hankiewicz: "Testing topological protection of edge states in hexagonal quantum spin Hall candidate materials". *Physical Review B* **94**, 2–7 (2018) (cit. on p. 131).

[259] L. Van Hove: "The Occurrence of Singularities in the Elastic Frequency Distribution of a Crystal". *Physical Review* **89**, 1189–1193 (1953) (cit. on p. 133).

[260] A. Diíaz-Fernández, L. Chico, J. W. González, and F. Domínguez-Adame: "Tuning the Fermi velocity in Dirac materials with an electric field". *Scientific Reports* **7**, 8058 (2017) (cit. on pp. 135, 138).

[261] C. Pauly, K. Rasche Bertold Koepernik, M. Liebmann, M. Pratzer, M. Richter, J. Kellner, M. Eschbach, B. Kaufmann, L. Plucinski, C. M. Schneider, M. Ruck, J. van den Brink, and M. Morgenstern: "Subnanometre-wide electron channels protected by topology". *Nature Physics* **11**, 338–343 (2015) (cit. on p. 141).

[262] C. Wu, B. A. Bernevig, and S.-C. Zhang: "Helical Liquid and the Edge of Quantum Spin Hall Systems". *Physical Review Letters* **96**, 106401 (2006) (cit. on p. 141).

[263] C. Xu and J. E. Moore: "Stability of the quantum spin Hall effect: Effects of interactions, disorder, and $\mathbb{Z}_2$ topology". *Physical Review B* **73**, 045322 (2006) (cit. on pp. 141, 146).

[264] P. Sessi, M. M. Otrokov, T. Bathon, M. G. Vergniory, S. S. Tsirkin, K. A. Kokh, O. E. Tereshchenko, E. V. Chulkov, and M. Bode: "Visualizing spin-dependent bulk scattering and breakdown of the linear dispersion relation in Bi_2Te_3". *Physical Review B* **88**, 161407 (2013) (cit. on p. 141).

[265] J. Weis: "Photoelectron Spectroscopy Studies on the Wide-Gap Two-Dimensional Topological Insulator Bismuthene on 4H-SiC(0001) & Perylene as a Removable Organic Capping". Master's thesis. Julius-Maximilians-Universität Würzburg (2019) (cit. on p. 145).

[266] F. Spriestersbach: "Kalium-Dotierung des 2D Topologischen Isolators Bismuten auf SiC(0001) - eine Studie mittels Rastertunnelmikroskopie und -spektroskopie". Bachelor's thesis. Julius-Maximilians-Universität Würzburg (2018) (cit. on p. 145).

[267] F. D. M. Haldane: "Luttinger liquid theory of one-dimensional quantum fluids. I. Properties of the Luttinger model and their extension to the general 1D interacting spinless Fermi gas". *Journal of Physics C: Solid State Physics* **14**, 2585–2609 (1981) (cit. on p. 146).

[268] B. Braunecker, C. Bena, and P. Simon: "Spectral properties of Luttinger liquids: A comparative analysis of regular, helical, and spiral Luttinger liquids". *Physical Review B* **85**, 035136 (2012) (cit. on pp. 146, 153).

[269] L. Bartosch and P. Kopietz: "Zero bias anomaly in the density of states of low-dimensional metals". *European Physical Journal B: Condensed Matter and Complex Systems* **28**, 29–36 (2002) (cit. on pp. 146, 155).

[270] C. Brun, K. H. Müller, I.-P. Hong, F. Patthey, C. Flindt, and W.-D. Schneider: "Dynamical Coulomb Blockade Observed in Nanosized Electrical Contacts". *Physical Review Letters* **108**, 126802 (2012) (cit. on pp. 146, 156, 202).

[271] M. Bockrath, D. H. Cobden, J. Lu, A. G. Rinzler, R. E. Smalley, L. Balents, and P. L. McEuen: "Luttinger-liquid behaviour in carbon nanotubes". *Nature* **397**, 598–601 (1999) (cit. on pp. 150–152).

[272] V. V. Deshpande, M. Bockrath, L. I. Glazman, and A. Yacoby: "Electron liquids and solids in one dimension". *Nature* **464**, 209–216 (2010) (cit. on pp. 151, 152).

[273] C.-Y. Hou, E.-A. Kim, and C. Chamon: "Corner Junction as a Probe of Helical Edge States". *Physical Review Letters* **102**, 076602 (2009) (cit. on p. 153).

[274] J. C. Y. Teo and C. L. Kane: "Critical behavior of a point contact in a quantum spin Hall insulator". *Physical Review B* **79**, 235321 (2009) (cit. on p. 154).

[275] R. Stühler, F. Reis, T. Müller, T. Helbig, T. Schwemmer, R. Thomale, J. Schäfer, and R. Claessen: "Tomonaga–Luttinger liquid in the edge channels of a quantum spin Hall insulator". *Nature Physics* **16**, 47–51 (2020) (cit. on pp. 154–157).

[276] C. R. Ast, B. Jäck, J. Senkpiel, M. Eltschka, M. Etzkorn, J. Ankerhold, and K. Kern: "Sensing the quantum limit in scanning tunneling spectroscopy". *Nature Communications* **7** (2016) (cit. on pp. 156, 202).

[277] F. Ming, T. S. Smith, S. Johnston, P. C. Snijders, and H. H. Weitering: "Zero-bias anomaly in nanoscale hole-doped Mott insulators on a triangular silicon surface". *Physical Review B* **97**, 075403 (2018) (cit. on pp. 156, 158, 202, 203).

[278] I. Safi and H. Saleur: "One-Channel Conductor in an Ohmic Environment: Mapping to a Tomonaga-Luttinger Liquid and Full Counting Statistics". *Physical Review Letters* **93**, 126602 (2004) (cit. on pp. 156, 157, 202).

[279] P. Joyez and D. Esteve: "Single-electron tunneling at high temperature". *Physical Review B* **56**, 1848–1853 (1997) (cit. on pp. 156, 203).

[280] M. H. Devoret, D. Esteve, H. Grabert, G.-L. Ingold, H. Pothier, and C. Urbina: "Effect of the electromagnetic environment on the Coulomb blockade in ultrasmall tunnel junctions". *Physical Review Letters* **64**, 1824–1827 (1990) (cit. on p. 157).

[281] S. Glaß: "Wachstum und Struktur von hexagonalen Sn- und Bi-Lagen auf SiC(0001)". Master thesis. Julius-Maximilians-Universität Würzburg (2014) (cit. on p. 164).

[282] V. Schröder, B. Emonts, H. Janßen, and H.-P. Schulze: "Explosionsgrenzen von Wasserstoff / Sauerstoff-Gemischen bei Drücken bis 200 bar". *Chemie Ingenieur Technik* **75**, 914–918 (2003) (cit. on p. 167).

[283] W. Kern: "The Evolution of Silicon Wafer Cleaning Technology". *Journal of The Electrochemical Society* **137**, 1887–1892 (1990) (cit. on p. 170).

[284] H. Tsuchida, I. Kamata, and K. Izumi: "Infrared spectroscopy of hydrides on the 6H-SiC surface". *Applied Physics Letters* **70**, 3072–3074 (1997) (cit. on p. 170).

[285] H. Tsuchida, I. Kamata, and K. Izumi: "Si-H Bonds on the 6H-SiC(0001) Surface after H_2 Annealing". *Japanese Journal of Applied Physics* **36**, L699–L702 (1997) (cit. on p. 170).

[286] C. Hallin, F. Owman, P. Mårtensson, A. Ellison, A. Konstantinov, O. Kordina, and E. Janzén: "In situ substrate preparation for high-quality SiC chemical vapour deposition". *Journal of Crystal Growth* **181**, 241–253 (1997) (cit. on p. 170).

[287] A. A. Burk and L. B. Rowland: "The role of excess silicon and in situ etching on 4H-SiC and 6H-SiC epitaxial layer morphology". *Journal of Crystal Growth* **167**, 586–595 (1996) (cit. on p. 170).

[288] C. H. Park, B.-H. Cheong, K.-H. Lee, and K. J. Chang: "Structural and electronic properties of cubic, 2H, 4H, and 6H SiC". *Physical Review B* **49**, 4485–4493 (1994) (cit. on p. 170).

[289] V. Heine, C. Cheng, and R. J. Needs: "The Preference of Silicon Carbide for Growth in the Metastable Cubic Form". *Journal of the American Ceramic Society* **74**, 2630–2633 (1991) (cit. on p. 170).

[290] J. Aulbach: "Gold-Induced Atomic Wires on Terraced Silicon Surfaces: Formation and Interactions of Silicon Spin Chains". Dissertation. Julius-Maximilians-Universität Würzburg (2017) (cit. on p. 174).

[291] A. Kowalewski: "Bismuthene on Silicon Carbide: Substrate Preparation, Monolayer Epitaxy, and Electronic Interference Phenomena in Domain Boundaries". Master's Thesis. Julius-Maximilians-Universität Würzburg (2019) (cit. on p. 174).

[292] M. Schüler, U. De Giovannini, H. Hübener, A. Rubio, M. A. Sentef, and P. Werner: "Local Berry curvature signatures in dichroic angle-resolved photoelectron spectroscopy from two-dimensional materials". *Science Advances* **6** (2020) (cit. on p. 176).

[293] T. Y. Nikolaienko, V. S. Chuiko, and L. A. Bulavin: "The dataset of covalent bond lengths resulting from the first-principle calculations". *Computational and Theoretical Chemistry* **1163**, 112508 (2019) (cit. on p. 177).

[294] F. Gao, W. J. Weber, H. Y. Xiao, and X. T. Zu: "Formation and properties of defects and small vacancy clusters in SiC: Ab initio calculations". *Nuclear Instruments and Methods in Physics Research Section B: Beam Interactions with Materials and Atoms* **267**, 2995–2998 (2009) (cit. on p. 178).

[295] L. Torpo, M. Marlo, T. E. M. Staab, and R. M. Nieminen: "Comprehensive *ab initio* study of properties of monovacancies and antisites in 4H-SiC". *Journal of Physics: Condensed Matter* **13**, 6203–6231 (2001) (cit. on p. 178).

[296] A. Zywietz, J. Furthmüller, and F. Bechstedt: "Vacancies in sic: influence of jahn-teller distortions, spin effects, and crystal structure". *Physical Review B* **59**, 15166–15180 (1999) (cit. on p. 178).

[297] C. C. Ling, A. H. Deng, S. Fung, and C. D. Beling: "Positron lifetime spectroscopic studies of as-grown 6H-silicon carbide". *Applied Physics A* **70**, 33–38 (2000) (cit. on p. 178).

[298] L. B. Drissi and F. El Yahyaoui: "Stability, magnetic and electronic properties of SiC sheet doped with B, N, Al and P". *Bulletin of Materials Science* **40**, 1081–1086 (2017) (cit. on p. 178).

[299] T. Kimoto and J. A. Cooper: "Appendix C: Major Physical Properties of Common SiC Polytypes". *Fundamentals of Silicon Carbide Technology.* John Wiley & Sons. doi: `https://doi.org/10.1002/9781118313534.app3` (2014), pp. 521–524 (cit. on p. 178).

[300] A. Ferreira da Silva, J. Pernot, S. Contreras, B. E. Sernelius, C. Persson, and J. Camassel: "Electrical resistivity and metal-nonmetal transition in n-type doped $4H-$SiC". *Physical Review B* **74**, 245201 (2006) (cit. on p. 178).

[301] M. Bockstedte, A. Mattausch, and O. Pankratov: "Solubility of nitrogen and phosphorus in 4H-SiC: A theoretical study". *Applied Physics Letters* **85**, 58–60 (2004) (cit. on p. 178).

[302] G. Ferro and D. Chaussende: "A new model for in situ nitrogen incorporation into 4H-SiC during epitaxy". *Scientific Reports* **7**, 43069 (2017) (cit. on p. 178).

[303] B. Schuler, D. Y. Qiu, S. Refaely-Abramson, C. Kastl, C. T. Chen, S. Barja, R. J. Koch, D. F. Ogletree, S. Aloni, A. M. Schwartzberg, J. B. Neaton, S. G. Louie, and A. Weber-Bargioni: "Large Spin-Orbit Splitting of Deep In-Gap Defect States of Engineered Sulfur Vacancies in Monolayer WS_2". *Physical Review Letters* **123**, 076801 (2019) (cit. on p. 178).

[304] D. Nečas and P. Klapetek: "Gwyddion: an open-source software for SPM data analysis". *Central European Journal of Physics* **10**, 181–188 (2012) (cit. on p. 180).

[305] J. K. Garleff, A. P. Wijnheijmer, C. N. v. d.Enden, and P. M. Koenraad: "Bistable behavior of silicon atoms in the (110) surface of gallium arsenide". *Physical Review B* **84**, 075459 (2011) (cit. on p. 192).

[306] A. P. Wijnheijmer, J. K. Garleff, K. Teichmann, M. Wenderoth, S. Loth, and P. M. Koenraad: "Single Si dopants in GaAs studied by scanning tunneling microscopy and spectroscopy". *Physical Review B* **84**, 125310 (2011) (cit. on p. 192).

[307] M. C. M. M. van der Wielen, A. J. A. van Roij, and H. van Kempen: "Direct Observation of Friedel Oscillations around Incorporated Si_{Ga} Dopants in GaAs by Low-Temperature Scanning Tunneling Microscopy". *Physical Review Letters* **76**, 1075–1078 (1996) (cit. on p. 192).

[308] L. Serrier-Garcia, J. C. Cuevas, T. Cren, C. Brun, V. Cherkez, F. Debontridder, D. Fokin, F. S. Bergeret, and D. Roditchev: "Scanning Tunneling Spectroscopy Study of the Proximity Effect in a Disordered Two-Dimensional Metal". *Physical Review Letters* **110**, 157003 (2013) (cit. on p. 203).

Publikationsliste Felix Reis

- R. Stühler, **F. Reis**, T. Müller, T. Helbig, T. Schwmmer, R. Thomale, J. Schäfer, R. Claessen, *Tomonaga-Luttinger liquid in the edge channels of a quantum spin Hall insulator*, Nature Physics **16**, 47-51 (2020)

- V. A. Rogalev, **F. Reis**, F. Adler, M. Bauernfeind, J. Erhardt, A. Kowalewski, M. R. Scholz, L. Dudy, L. B. Duffy, T. Hesjedal, M. Hoesch, G. Bihlmayer, J. Schäfer, R. Claessen, *Tailoring the topological surface state in ultrathin α-Sn(111) films*, Physical Review B **100**, 245144 (2019)

- T. Rauch, V. A. Rogalev, M. Bauernfeind, J. Maklar, **F. Reis**, F. Adler, S. Moser, J. Weis, T.-L. Lee, P. K. Thakur, J. Schäfer, R. Claessen, J. Henk, I. Mertig, *Nontrivial topological valence bands of common diamond and zinc-blende semiconductors*, Physical Review Materials **3**, 064203 (2019)

- G. Li, W. Hanke, E. M. Hankiewicz, **F. Reis**, J. Schäfer, R. Claessen, C. Wu, R. Thomale, *Theoretical paradigm for the quantum spin Hall effect at high temperatures*, Physical Review B **98**, 165146 (2018)

- M. R. Scholz, V. A. Rogalev, L. Dudy, **F. Reis**, F. Adler, J. Aulbach, L. J. Collins-McIntyre, L. B. Duffy, H. F. Yang, Y. L. Chen, T. Hesjedal, Z. K. Liu, M. Hoesch, S. Muff, J. H. Dil, J. Schäfer, R. Claessen, *Topological surface state of α-Sn on InSb(001) as studied by photoemission*, Physical Review B **97**, 075101 (2018)

- **F. Reis**, G. Li, L. Dudy, M. Bauernfeind, S. Glass, W. Hanke, R. Thomale, J. Schäfer, R. Claessen, *Bismuthene on a SiC substrate: A candidate for a high temperature quantum spin Hall material*, Science **357**, 287-290 (2017)

- V. A. Rogalev, T. Rauch, M. R. Scholz, **F. Reis**, L. Dudy, A. Fleszar, M.-A. Husanu, V. N. Strocov, J. Henk, I. Mertig, J. Schäfer, R. Claessen, *Double band inversion in α-Sn: Appearance of topological surface states and the role of orbital composition*, Physical Review B **95**, 16117(R) (2017)

- S. Glass, **F. Reis**, M. Bauernfeind, J. Aulbach, M. R. Scholz, F. Adler, L. Dudy, G. Li, J. Schäfer, R. Claessen, *Atomic-Scale Mapping of Layer-by-Layer Hydrogen Etching and Passivation of SiC(0001) Substrates*, Journal of Physical Chemistry C **120**, 10361-10367 (2016)

- P. Sessi, **F. Reis**, T. Bathon, K. A. Kokh, O. E. Tereshchenko, M. Bode, *Signatures of Dirac fermion-mediated magnetic order*, Nature Communications **5**, 5349 (2014)

Danksagung

Man bekommt ja öfter den Eindruck vermittelt, Physiker seien Einzelkämpfer und würden die meiste Zeit alleine in stillen Laboren vor sich hinwerkeln. Das ist das genaue Gegenteil dessen was ich während meiner Promotionszeit erlebt habe. Daher möchte ich mich mit dem Abschluss dieser Arbeit bei zahlreichen Personen bedanken, welche in den zurückliegenden Jahren direkt oder indirekt zum Gelingen dieser Arbeit beigetragen haben.

Zuallererst möchte ich Prof. Ralph Claessen für die Möglichkeit, meine Promotion an seinem Lehrstuhl anzufertigen, danken. Durch sein persönliches Engagement ist ein prosperierender Lehrstuhl entstanden, welcher materiell hervorragend ausgestattet ist und in welchem insbesondere auch großen Wert auf das soziale Miteinander gelegt wird.

Natürlich hat er mit seinem immerwährenden Interesse, seinen kritischen Nachfragen und seinen Ideen auch ganz entscheidend zu den Forschungsergebnissen und den entstandenen Fachartikeln beigetragen. Weiterhin hat er mir die Teilnahme an zahlreichen Konferenzen, Workshops sowie an einer Sommerschule an der École de Physique des Houches ermöglicht, und ebenso die Teilnahme an Strahlzeiten bei Diamond, der Swiss Light Source und beim Berliner Electronensynchrotron. Für all diese Erfahrungen bin ich sehr dankbar.

Prof. Jörg Schäfer als meinem Doktorvater danke ich zuallerst dafür, dass er mir dieses Doktorarbeitsthema angeboten hat. Insbesondere am Anfang, als funktionierende Bismutenproben noch nicht in Sicht waren, hat er mit viel Motivation und positiver Ausstrahlung so manche triste Laborstunde bereichert und immer an das Thema, unseren Erfolg und meine Fähigkeiten geglaubt. Seine zahlreichen experimentellen Vorschläge und Problemlösungsansätze waren häufig hilfreiche Denkanstöße. Natürlich hat er ebenso ganz wichtige Beiträge zu unseren Manuskripten oder Präsentationen geliefert, insbesondere durch seine Fähigkeit, die entscheidenen Punkte einer Geschichte zu identifizieren und in den Vordergrund zu stellen - hiervon werde ich mit Sicherheit auch in Zukunft profitieren. Abgesehen davon möchte ich mich bei ihm für die vielen Ganggespräche über Physik, aber auch über lebenspraktische Dinge bedanken!

Special thanks go to *Prof. Gang Li*, who provided all the DFT calculations and derived the low-energy model of bismuthene on SiC. Thereby, he created invaluable contributions to our research project. Apart from that, I got to know him as a very modest and interested person, and I am very thankful for his great personal efforts during our cooperation. Genauso danke ich *Prof. Ronny Thomale* und *Prof. Werner Hanke* für die fundierten Erklärungen und die tolle Zusammenarbeit, die zu unseren gemeinsamen Forschungsergebnissen geführt hat.

Ein ganz großes Dankeschön gebührt den Studierenden, welche ich betreuen durfte. Ohne deren Engagement, welches bei jedem Einzelnen weit über das hinausging, was man von einem Masterstudenten erwarten kann, wäre diese Arbeit in dieser Form nicht möglich gewesen und es hätte nur halb so viel Spaß gemacht. Im Einzelnen danke ich: *Maximilian Bauernfeind*, *Raúl Stühler*, *André Kowalewski* und *Johannes Weis*. Außerdem danke ich *Stefan Glass* für den Wissenstransfer zu den ersten Probenpräparationen am Ende seiner Masterarbeit. Weiterer Dank gilt den Bachelorstudenten *Marius Will* sowie *Felix*

Spriestersbach. *Raúl Stühler* bin ich im Übrigen auch äußerst dankbar für die Bereitstellung der Espressomaschine in unserem Büro ;-)

Daneben möchte ich mich noch bei zahlreichen weiteren Kolleginnen und Kollegen an der EP4 bedanken. Ich beginne mit unseren Photoemitter-Postdocs: *Dr. Lenart Dudy*, *Dr. Victor Rogalev* und *Dr. Markus Scholz*. Allen danke ich für ihre stete Hilfsbereitschaft, die zahlreichen fachgebundenen und fachfremden Diskussionen, und nicht zuletzt für die hervorragende Atmosphäre und die "tolle" Musikauswahl im ARPES-Labor – Спасибо / Danke! Außerdem möchte ich bei meinen Doktoranden-Kollegen *Julian Aulbach* sowie *Florian Adler* für die Einarbeitung in die Labore und die zahlreichen Diskussionen zu unseren Messungen danken. Weiterhin danke ich *Prof. Michael Sing* und allen weiteren Mitgliedern des Nano- und Oxidteams, nämlich *Maximilian Bauernfeind*, *Jonas Erhardt*, *Judith Gabel*, *Ozan Kirilmaz*, *Berengar Leikert*, *Bing Liu*, *Philipp Scheiderer*, *Matthias Schmitt*, *Philipp Schütz*, *Matthias Stübinger*, *Raúl Stühler*, *Tim Wagner*, *Michael Zapf*, die alle für ein gutes Miteinander stehen und diese schöne Zeit geprägt haben.

Moreover, I would like to thank *Prof. Hugo Dil*, *Naamneh Mutaser*, *Dr. Nick Plumb*, *Prof. Milan Radovic*, *Prof. Ming Shi* and *Dr. Andrew Weber* from the SIS Beamline at the SLS in Switzerland for providing support during our beamtime.

Für das Korrekturlesen der Arbeit danke ich *Maximilian Bauernfeind*, *Dr. Louis Veyrat* und *Philipp Schütz*, und insbesondere *Dr. Victor Rogalev* sowie *Raúl Stühler*, die ein deutlich erhöhtes Pensum abgearbeitet haben.

Abschließend möchte ich *Moni Seifer* danken, die die EP4 zusammenhält und sich um die Erledigung aller nötigen Dinge kümmert. Neben der Lösung von Problemen aller Art war sie stets am Forschungsfortschritt und auch persönlichen Belangen interessiert, und die Unterhaltungen mit ihr waren immer bereichernd. Moni, danke für alles!

Eine solche Arbeit wird aber nicht nur von den Kolleginnen und Kollegen am Lehrstuhl, sondern auch durch den entsprechenden Ausgleich im Familien- und Freundeskreis ermöglicht.

Hier möchte ich zuerst *Manuel*, *Philipp* und *Simon* nennen, die mich die komplette Zeit, angefangen beim Mathe-Vorkurs bis zum Promotionsende, als Studienkollegen und schließlich gute Freunde begleitet haben. Außerdem möchte ich an dieser Stelle meinen *Freundinnen/Freunden aus Wiesen*, *Würzburg* und *Bamberg* danken (kann sie aber aus Platzgründen nicht einzeln aufzählen), weil sie mir ermöglicht haben, auch abseits der Physik viele spannende Dinge zu entdecken und zu diskutieren.

Meiner lieben *Anne* will ich für die viele Geduld und Nachsicht, welche sie in den zurückliegenden Jahren aufgebracht hat, danken – wenn ich mal wieder zu lange im Institut geblieben bin, oder ich angefressen war, weil zum Beispiel die Messsoftware abgestürzt ist (und das war beides häufiger der Fall). Sie hat generell einen wunderbaren Ausgleich geschaffen, und dafür kann ich ihr nicht genug danken :-).

Abschließend möchte ich mich bei meinen *Eltern* bedanken, die mir diesen Bildungsweg ermöglicht und mich immer unterstützt haben. Genauso möchte ich meiner *Schwester* danken, weil sie immer ein offenes Ohr für mich hatte. Danke, dass ihr für mich da seid!